ICPIG XXVI

International Conference on Phenomena in Ionized Gases

Proceedings
Volume 4
Saturday/Sunday, July 19/20

GREIFSWALD, GERMANY 2003

REPORT DOCUMENTATION PAGE

Form Approved OMB No. 0704-0188

maintaining the data needed, and completing and reviewing the collection of information. Send comments regarding this burden estimate or any other aspect of this collection of information, including suggestions for reducing the burden, to Department of Defense, Washington Headquarters Services, Directorate for Information Operations and Reports (0704-0188), 1215 Jefferson Davis Highway, Suite 1204, Arlington, VA 22202-4302. Respondents should be aware that notwithstanding any other provision of law, no person shall be subject to any penalty for failing to comply with a collection of information if it does not display a currently valid OMB control number.
PLEASE DO NOT RETURN YOUR FORM TO THE ABOVE ADDRESS.

1. REPORT DATE (DD-MM-YYYY) 14-11-2003	2. REPORT TYPE Conference Proceedings	3. DATES COVERED (From – To) 15 July 2003 - 20 July 2003

4. TITLE AND SUBTITLE	5a. CONTRACT NUMBER
XXVI International Conference on Phenomena in Ionized Gases, Vol. 4	FA8655-03-1-5023
	5b. GRANT NUMBER
	5c. PROGRAM ELEMENT NUMBER

6. AUTHOR(S)	5d. PROJECT NUMBER
J. Meichsner, ed.	5d. TASK NUMBER
	5e. WORK UNIT NUMBER

7. PERFORMING ORGANIZATION NAME(S) AND ADDRESS(ES) Ernst-Moritz-Arndt-University Greifswald Domstr. 10a Greifswald D-17489 Germany	8. PERFORMING ORGANIZATION REPORT NUMBER N/A

9. SPONSORING/MONITORING AGENCY NAME(S) AND ADDRESS(ES) EOARD PSC 802 BOX 14 FPO 09499-0014	10. SPONSOR/MONITOR'S ACRONYM(S)
	11. SPONSOR/MONITOR'S REPORT NUMBER(S) CSP 03-5023

12. DISTRIBUTION/AVAILABILITY STATEMENT

Approved for public release; distribution is unlimited.

13. SUPPLEMENTARY NOTES

Copyright 2003 ICPIG-26, Greifswald, Germany. Available from: University Greifswald, Institut fur Physik, Greifswald, Germany. The Department of Defense has permission to use for government purposes only. All other rights are reserved by the copyright holder.

14. ABSTRACT

The Final Proceedings for XXVI International Conference on Phenomena in Ionized Gases, 15 July 2003 - 20 July 2003

The scientific program covers most aspects of phenomena in ionized gases, with special emphasis on moderate-temperature plasmas. Additionally, two conference workshops (plasma light sources; reactive plasmas and surface interaction) are organized from the Local Organizing Committee.

15. SUBJECT TERMS

EOARD, Plasma Physics and Chemistry

16. SECURITY CLASSIFICATION OF:			17. LIMITATION OF ABSTRACT	18, NUMBER OF PAGES	19a. NAME OF RESPONSIBLE PERSON INGRID J. WYSONG
a. REPORT UNCLAS	b. ABSTRACT UNCLAS	c. THIS PAGE UNCLAS	UL	262+154+260 +252	19b. TELEPHONE NUMBER (Include area code) +44 (0)20 7514 4285

Standard Form 298 (Rev. 8/98)
Prescribed by ANSI Std. Z39-18

XXVI
International
Conference on
Phenomena in
Ionized
Gases

July 15 – 20, 2003
Greifswald, Germany

Editors: J. Meichsner, D. Loffhagen, and H.-E. Wagner

ICPIG 2003

Proceedings

Volume 4

Saturday, July 19, and Sunday, July 20

Organizers

Institute of Physics, Ernst Moritz Arndt University Greifswald (IfP)

Institute for Low-Temperature Plasma Physics, Greifswald (INP)

Max Planck Institute for Plasma Physics, Greifswald branch institute (IPP)

International Scientific Committee

L. C. Pitchford (chair, France)

K. Becker (USA)

R. P. Brinkmann (Germany)

R. Carman (Australia)

V. Fortov (Russia)

T. Goto (Japan)

S. Longo (Italy)

J. Mizeraczyk (Poland)

J. van der Mullen (The Netherlands)

G. Musa (Romania)

H. Pécseli (Norway)

A. Phelps (Great Britain)

Local Organizing Committee

J. Meichsner (chair, IfP)

D. Loffhagen (vice-chair, INP)

H.-E. Wagner (secretary, IfP)

J. Behnke (IfP)

J. F. Behnke (IfP)

H. Kersten (INP)

M. Kettlitz (INP)

T. Klinger (IPP)

R. König (IPP)

C. Krčka (INP)

T. Meyer (IfP)

S. Müller (INP)

V. Müller (IfP)

National Advisory Board

M. Born (Aachen)

J. Conrads (Jülich)

H. Deutsch (Greifswald)

R. Hippler (Greifswald)

H.-J. Kunze (Bochum)

A. Piel (Kiel)

G. Röpke (Rostock)

A. Rutscher (Greifswald)

U. Schumacher (Stuttgart)

R. Wilhelm (Garching)

Foreword

The International Conference on Phenomena in Ionized Gases (ICPIG) has been held every two years and covers nearly all aspects of phenomena in ionized gases. In 2003, the 26th conference is taking place in the centre of the Hanseatic city of Greifswald, located near the Baltic Sea. It is now 50 years since the first ICPIG conference was held in Oxford in 1953. The conference arrangements have been prepared by the Local Organizing Committee (LOC) in cooperation with the Institute of Physics of the Ernst Moritz Arndt University, the Institute for Low-Temperature Plasma Physics and the Max Planck Institute for Plasma Physics, Greifswald branch institute.

More than 400 scientists are expected to attend this conference from various countries, and about 400 important papers on various topics will be presented.

We would like to acknowledge the contributions of all cooperative individuals and organizations, and also to all participants form various countries.

This set of four volumes contains invited papers for oral presentation and the contributed papers which were reviewed by the Local Organizing Committee in cooperation with the national advisory board and accepted for presentation in poster sessions at the conference. For a paper to be included in these volumes, at least one of the authors had to be registered for the conference.

Invited general, topical and workshop papers as well as contributed papers are printed in four volumes (vol. 1: July 15, vol. 2: July 16, vol. 3: July 17, vol. 4: July 19 and 20). Each volume is arranged by topics corresponding to the respective poster sessions. The papers were limited in length to two pages. The responsibility for the contents and the form of each paper rests with the authors. Most of the papers are available on the website http://www.icpig.uni-greifswald.de/proceedings/.

The full text of the Invited Papers will be published in a special issue of *"Contributions to Plasma Physics"* after the conference.

The editors express their deep gratitude to Bert Krames for his technical assistance in the preparation of the conference proceedings.

July 2003   The Editors

Acknowledgement

The organizers of the 26th ICPIG wish to thank the following for their contribution to the success of this conference:
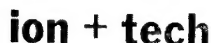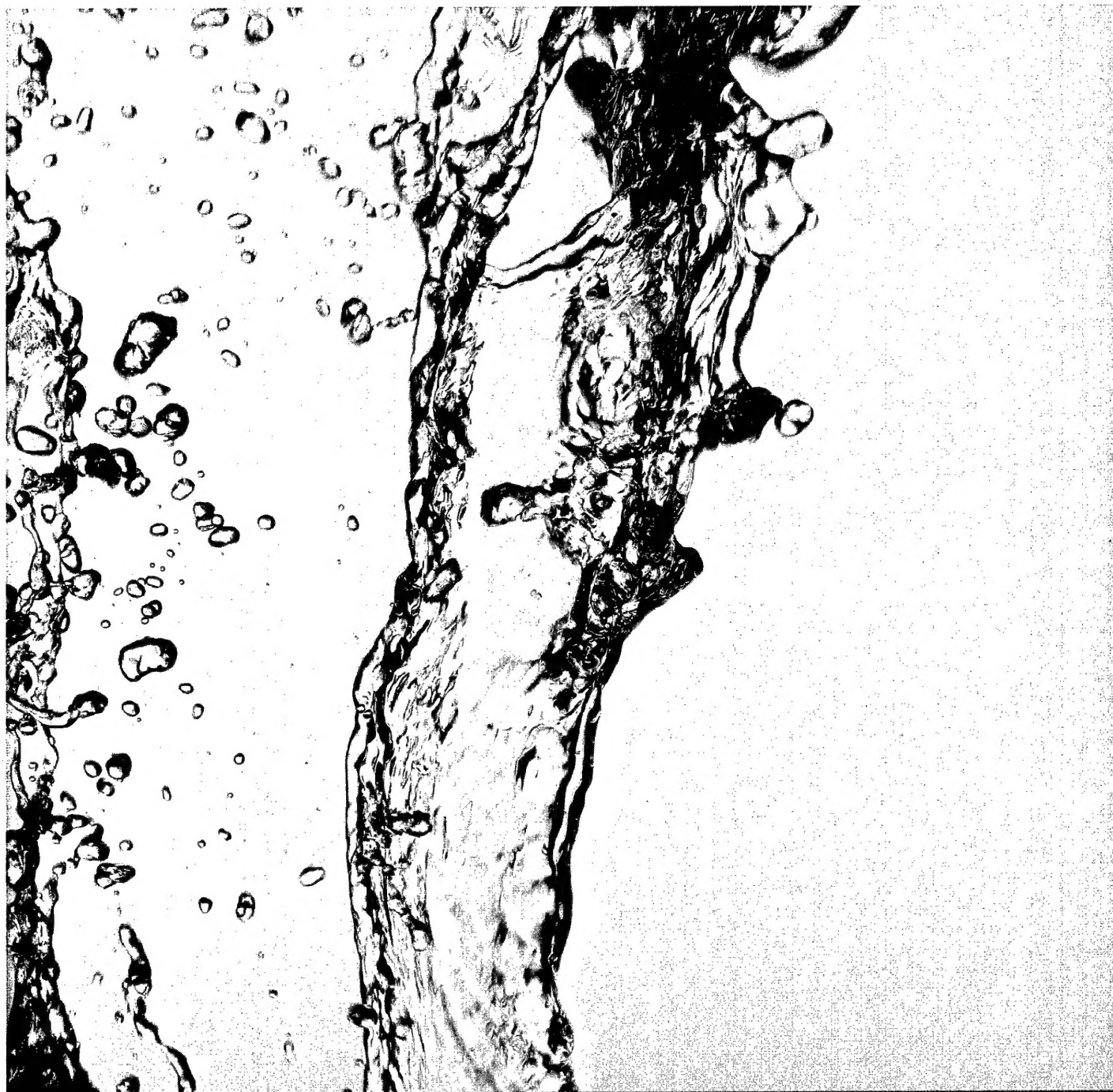
Publisher: Local Organizing Committee

Printed in Germany by: Kiebu-Druck GmbH

Ziegelhof 27

17489 Greifswald

To purchase additional copies of this publication, please contact

Prof. Dr. J. Meichsner

Ernst-Moritz-Arndt-Universität Greifswald

Institut für Physik

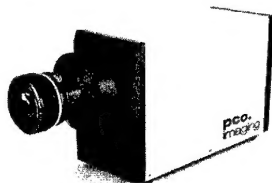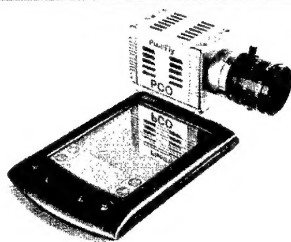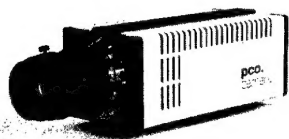Domstraße 10a

17487 Greifswald, Germany

Lieferprogramm
Januar 2003

RBM-R.Braumann GmbH
Freisinger Str. 19a
85416 Langenbach
http://www.rbm-braumann.com

EDINBURGH INSTRUMENTS
- CO / CO_2-Laser, CW, gitterabstimmbar, 1W - 200W
- CO_2-TEA Laser (z.B. MTL-3 Mini TEA-Laser, 150mJ, 50ns, 100Hz)
- optisch gepumpte FIR-Laser (40µm-1,2mm)
- Zubehör z.B. Photon Drag Detektoren, CO_2/CO Laser Spektrum Analysatoren

ELECTRO-OPTICS TECHNOLOGY
- Faraday Rotatoren und Isolatoren für 1.0 - 1.1 µm
- Breitband Isolatoren, Laser Dioden Isolatoren
- Fresnel-Rhomb Breitband Polarisationsrotator
- Silizium Photodetektoren und InGaAs Photodetektoren mit BNC Steckeranschluss
- Photodetektoren mit Vorverstärker mit BNC Steckeranschluss
- >10GHz Photodetektoren mit SMA Steckeranschluss

IST-REES
Laser Spektrumanalysatoren
- Modell E201 LSA, Auflösung 0.3nm FWHM, 350 - 1100nm
- Modell E202 LSA, Auflösung 0.4nm FWHM, 1000 - 1650nm

JDS UNIPHASE
- Argon-Ionen Laser, luftgekühlt, 5mW ... 150mW, 458 ... 514nm
- Helium-Neon Laser, 0.5mW ... 25mW, 633, 543, 594 oder 612nm
- Diodengepumpte Festkörperlaser, cw, 10mW ... 100mW, 532nm
- Diodengepumpte Festkörperlaser, gepulst, 5mW ... 500mW, 10 ... 40kHz
- Laserdioden, 200mW ... 4W, 798 ... 980nm
- Faserlasersysteme und Faserlasermodule, 9, 15 und 25W, 1,1 µm

QUANTUM TECHNOLOGY
- Elektro-Optische Modulatoren
- Modulationssysteme bis 1GHz
- Pockelszellen mit Hochspannungstreibern, Pulspicker Systeme
- SHG, THG Systeme
- Kristalle (ADA, ADP, BBO, CDA, RDA, KDP etc.)

SCITEC INSTRUMENTS
- analoge Einphasen und Zweiphasen Lock-In Verstärker
- Opto-mechanische Chopper bis 20kHz (mit Hochfrequenzzusatz)
- Pyroelektrische Detektoren (mounted/unmounted)

SPECTROLAS
- pyroelektrische Laserenergie Detektoren mit schwarzer oder keramischer Oberfläche
- VUV Laserenergie Detektor für F_2 Laser
- pyroelektrische OEM Sensoren
- Thermische Laserleistungs Detektoren
- VUV Laserleistungs Detektor für F_2 Laser
- Anzeigegerät für den Anschluss von zwei Detektoren (Energie oder Leistung) und mit RS-232 und IEEE-488 Schnittstelle
- preiswertes Komplettgerät (Detektor mit Anzeigegerät) für die Laserenergiemessung

VIII

Contents

Saturday, July 19

General Lectures

Topical Lectures

Poster Sessions

Topic 4: Coronas, sparks, surface discharges and high-pressure glows

X

XI

Topic 5: Arc discharges

XVII

Topic 15: Particle and laser beam interaction with plasmas

XXI

Sunday, July 20

Topical Lectures

General Lecture

Properties of Planar Surface Wave Excited Plasma

Masashi Kando

Department of Electrical and Electronic Engineering, Shizuoka University
Johoku 3-5-1, Hamamatsu 432-8561, Japan.

The properties of the planar surface wave plasma are discussed from the view point of electron heating in the plasma at the low pressure, referring to the experimental evidences. The role of the dielectric plate is considered. The plasma density profiles in the radial direction can be modified by controlling the microwave in the dielectric plate.

1. Introduction

The surface wave plasma in the cylindrical geometry has a long history of investigation originated from the 1970's. Extensive experimental and theoretical results obtained till now are summarized in the literatures [1]. Therefore, the present paper will be focused to the planar surface wave plasma, which was firstly reported in 1989 [2].

The planar surface wave plasmas have attracted an increasing interest in the industrial application since they can produce high-density plasmas with a large diameter at the low pressure without magnetic field. Many types of planar surface wave plasmas have been developed using several methods of the wave excitation to feed the microwave power at the top [3-4] or from the side wall [5] of the discharge chamber. The details of the planar surface plasmas have already been reported in the review paper [6]. From the view point of plasma physics, it is important to consider the mechanism of the energy transfer from microwave to electrons in such a low-pressure plasmas that the collisional electron heating is not effective: in other words, electron collision frequency is much lower than the microwave frequency. The present paper will report the experimental results related to electron heating mechanism measured at the low pressure argon in the planar surface wave plasma whose apparatus consists of a large diameter quartz plate and an annular slot antenna [4]. The role of the dielectric plate will also be discussed since some part of microwave can propagate inside the dielectric plate and interact with the plasma, which permit to modify the plasma profiles in the radial direction.

2. Experimental apparatus

The experiments were carried out in argon gas in a microwave planar plasma source. The apparatus used in the experiment has been taken into account to keep a good axial symmetry using an annular slot antenna as a surface wave launcher, for the sake of easier consideration of experimental results. The 2.45GHz microwave power of 0.2 - 2 kW is applied to produce the plasma to a cylindrical discharge chamber with 312 mm in diameter and 350 mm in height. The microwave couples to the chamber through a quartz plate with a thickness of 15 mm by an annular slot antenna backed by

a tunable cylindrical cavity [4]. The cylindrical tungsten Langmuir probes were moved along the chamber axis or rotated in the azimuthal direction to measure the plasma density and electron temperature profiles.

3. Experimental results and consideration

3.1 Hole on the axial probe current profile [7]

The axial profiles of the probe current are measured along the chamber axis as a function of the argon gas pressure, microwave power and the probe bias voltage. Figure 1 shows the typical example. The probe current rapidly increases from the quartz plate, taking a maximum at around 50 mm and then gradually decreases towards the bottom of the chamber. It is clearly shown that the hole appears on the probe current profile at a certain axial position of around 30 mm from the quartz plate and that the depth of the hole becomes small with
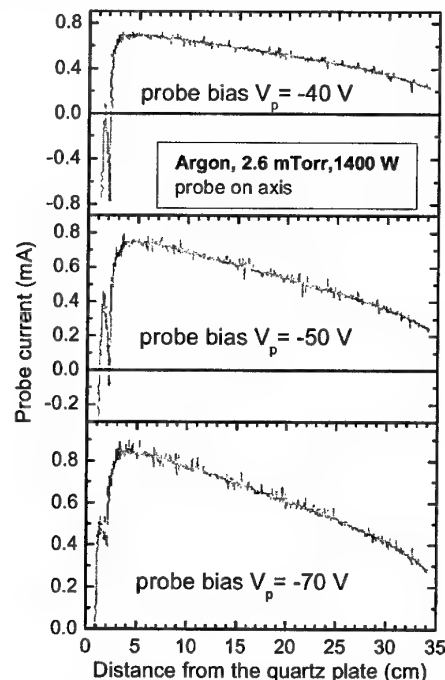
Fig. 1 Axial probe current profiles measured along the chamber axis in argon at 2.6 mTorr and absorbed microwave power of 1.4 kW for three different probe bias voltages.

decreasing the probe bias voltage from - 40 V to - 70 V, diminishing at -50 V. When the plasma potential of 20 V is taken into account, the energy of the hot electrons is estimated to be around 70 eV. It is interesting that the electron density at the hole always coincides with the cutoff plasma density $(7.4 \times 10^{16} \ m^{-3})$ for the other experimental conditions. However, the hole does not appear in the probe current profiles when they are measured under the slot antenna. This suggests that the hole creation is responsible for the microwave electric field in the axial direction.

3.2 Hot electron measurement [8]

Another experimental evidence of electron heating in the low pressure surface wave plasma is an isotropic probe characteristics measured by the specially designed probe that the plasma particles can be collected from the specified direction, as shown in Fig.2(a). Figure 2(b) shows a set of the probe characteristics measured at 100 mm from the quartz plate by the collecting surface of the

(a)

(b)
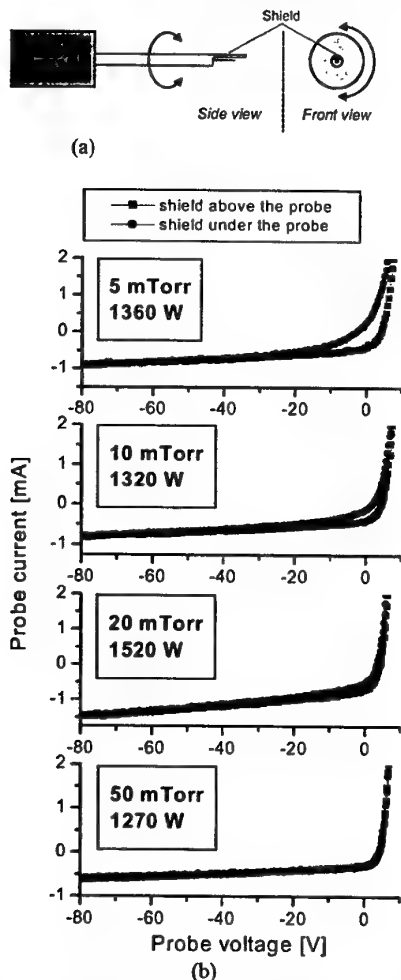
Fig.2 (a) One-side shielded Langmuir probe, (b) Probe characteristics measured at 100 mm under the quartz plate with the shield positioned above and under the probe tip.

probe facing to the quartz plate (the top of the chamber) and to the bottom of the chamber. Significant difference is observed in the region of bias voltage higher than - 40 V at the low pressure and decreases with increasing the pressure. The differences come from the high energy electron flux directed away from the quartz plate, originated at the resonance region near the quartz plate as mentioned before. Assuming the hot electron energy of 60 eV, electron mean free paths estimated at the pressure of 5, 10, 20 and 50 mTorr are 306, 153, 76 and 31 mm respectively, which can explain the directed electron flux cease at higher pressure.

3.3 Active control of plasma density profile

A tuning system for a planar surface wave plasma source [9] has been developed, based on T-junction tuning element. It can control the plasma diameter, matching and radial plasma density profile since the microwave propagation inside the quartz plate is effectively controlled by the position of three plungers of T-junction tuning element.

3. Summary

Two experimental evidences of electron heating in the low-pressure surface wave plasma have been observed by the probe measurement. The heating region is close to the quartz plate where the plasma density coincides with the cut off plasma density.

The origin of localized hot electron can be explained on the basis of the heating mechanism proposed by Aliev et al [10]. The electrons entering the plasma resonance region where the microwave electric field is enhanced can take energy from the field if their transit time through the region is short compared to the field period. Otherwise, electrons cannot gain any energy from the filed when averaged by one period of the field. The transit time estimated for hot electrons fulfill the necessary condition for transit time heating.

4.References

[1] For example, M. Moisan and J. Pelletier, "*Microwave Excited Plasmas* ", Elsevier (1992).
[2] K. Komachi, J. Vac. Sci. Technol. **A11** (1993) 164.
[3] M. Nagatsu, G. Xu M. Yamage, M Kanoh, and H. Sugai, Jpn. J.Appl.Phys. **35** (1996) L341.
[4] I. Odrobina, J. Kudela and M. Kando, Plasma Sources Sci. Technol .7 (1998) 238.
[5] F. Werner, D.Korzec and J. Engemann, Plasma Sources Sci. Technol .3 (1996) 473.
[6] H.sugai, I.Ghanashev and M.Nagatsu, Plasma Sources Sci. Technol. 7 (1998) 192.
[7] T. Terebessy, J. Kudela and M. Kando, Appl. Phys. Letters **77** (2000) 2825.
[8] J. Kudela, T. Terebessy and M. Kando, Appl. Phys. Letters **76** (2000) 1249.
[9] J. Kudela, T. Terebessy and M. Kando, Appl. Phys.Letters **80** (2002) 1132.
[10] Yu. M. Aliev, H. Schluter and A. Shivarova, "*Guided-Wave-Produced Plasmas*", Springer (2000) p206.

Plasma Phase Transition in Dense Hydrogen and Electron-Hole Plasmas

V.S. Filinov[1] , M. Bonitz[2], P. Levashov[1], V.E. Fortov[1], W. Ebeling[3] and M. Schlanges[4]

1 Institute for High Energy Density, Russian Academy of Sciences, Izhorskay 13/19, Moscow 127412, Russia
2 Fachbereich Physik, Universität Rostock, D-18051 Rostock, Germany
3 Institut für Physik, Humboldt-Universität Berlin, Invalidenstrasse 110, D-10115 Berlin, Germany
4 Fachbereich Physik, Universität Greifswald, D-17489 Greifswald, Germany

Plasma phase transitions (PPT) in dense hydrogen and electron-hole plasmas are investigated by direct path integral Monte Carlo methods (DPIMC). The phase boundary of the electron-hole liquid in Germanium is calculated and is found to agree reasonably well with the known experimental results. Analogous results are found for high-density hydrogen. For a temperature of $T = 10,000 K$ it is shown that the internal energy is lowered due to droplet formation for densities between $10^{23} cm^{-3}$ and $10^{24} cm^{-3}$.

1. Path integral Monte Carlo simulations

All thermodynamic properties of a two-component plasma are defined by the partition function Z which, for the case of N_e electrons and N_p protons, is given by $Z(N_e, N_p, V, \beta) = \frac{Q(N_e, N_p, \beta)}{N_e! N_p!}$, with $Q(N_e, N_p, \beta) = \sum_\sigma \int_V dq\, dr\, \rho(q, r, \sigma; \beta)$, where $\beta = 1/k_B T$. The exact density matrix is, for a quantum system, in general, not known but can be constructed using a path integral representation [1, 2] $\int_V dR^{(0)} \sum_\sigma \rho(R^{(0)}, \sigma; \beta) = \int_V dR^{(0)} \ldots dR^{(n)} \rho^{(1)} \cdot \rho^{(2)} \ldots \rho^{(n)} \times \sum_\sigma \sum_P (\pm 1)^{\kappa_P} \mathcal{S}(\sigma, \hat{P}\sigma') \hat{P}\rho^{(n+1)}$, where $\rho^{(i)} \equiv \rho\left(R^{(i-1)}, R^{(i)}; \Delta\beta\right) \equiv \langle R^{(i-1)}|e^{-\Delta\beta\hat{H}}|R^{(i)}\rangle$, whereas $\Delta\beta \equiv \beta/(n+1)$ and $\Delta\lambda_a^2 = 2\pi\hbar^2 \Delta\beta/m_a$, $a = p, e$. $\hat{H}$ is the Hamilton operator, $\hat{H} = \hat{K} + \hat{U}_c$, containing kinetic and potential energy contributions, $\hat{K}$ and $\hat{U}_c$, respectively, with $\hat{U}_c = \hat{U}_c^p + \hat{U}_c^e + \hat{U}_c^{ep}$ being the sum of the Coulomb potentials between protons (p), electrons (e) and electrons and protons (ep). Further, σ comprises all particle spins, and the particle coordinates are denoted by $R^{(i)} = (q^{(i)}, r^{(i)}) \equiv (R_p^{(i)}, R_e^{(i)})$, for $i = 1, \ldots n+1$, $R^{(0)} \equiv (q, r) \equiv (R_p^{(0)}, R_e^{(0)})$, and $R^{(n+1)} \equiv R^{(0)}$ and $\sigma' = \sigma$. This means, the particles are represented by fermionic loops with the coordinates (beads) $[R] \equiv [R^{(0)}; R^{(1)}; \ldots; R^{(n)}; R^{(n+1)}]$, where q and r denote the electron and proton coordinates, respectively. The spin gives rise to the spin part of the density matrix $\mathcal{S}$, whereas exchange effects are accounted for by the permutation operator $\hat{P}$, which acts on the electron coordinates and spin projections, and the sum over the permutations with parity κ_P. To compute thermodynamic functions, the logarithm of the partition function has to be differentiated with respect to thermodynamic variables, so for internal energy E we have $\beta E = -\beta \partial \ln Q / \partial \beta$

2. Numerical Results

Since the PPT in dense hydrogen is still hypothetical and has not been observed experimentally, it is reasonable to look for other systems where similar conditions exist. A suitable example is electron-hole plasma in low-temperature semiconductors, for which droplet formation is well established and observed ex-

perimentally three decades ago [3]. We, therefore, performed DPIMC simulations for electron hole plasmas.   Below the critical temperature the simulations exhibit anomalously large fluctuations and an unstable behavior of the pressure. The e-h-plasma is found to phase separate and form large droplets. The phase boundary of the electron-hole liquid (e-h-droplets) in Germanium obtained by our DPIMC method is presented in Fig. 1 together with the experimental data. We observe good agreement. Deviations may be connected with complex band structure of Germanium approximated in our simulations by a two-band parabolic mass model.

Figure 2: Pressure and energy of hydrogen for $T = 10,000K$, DFT - [5]. RPIMC - [4].

tween plasma particles is of the order of the size of a hydrogen molecule the homogeneous plasma state becomes unstable, and many-particle clusters appear. Results of one independent well tested method based on density functional theory (DFT) are presented on Fig. 2, where PPT was obtained at smaller density [5].

Figure 1: Phase boundary of the electron-hole liquid in bulk Germanium.   Experiment - [3].   Temperature is presented in units of the exciton binding energy.

Fig.2 presents results of our calculations for pressure and energy of hydrogen at $T = 10,000K$, which is well below the critical point of the PPT predicted by chemical models (around $T = 15,000K$). In our calculations between 10^{22}cm^{-3} and 10^{24}cm^{-3} calculated pressure becomes negative. We find also that in this region plasma energy is systematically lower than the RPIMC results [4]. If average distance be-

References

[1] V.S.Filinov,M.Bonitz,W.Ebeling, V.Fortov, Plasma Phys. Contr. Fusion **43** (2001) 743.

[2] V.Filinov, J.Phys.**A34** (2001) 1665.

[3] G.Thomas, T.Rice, J.Hensel, Phys.Rev.Let., **33** (1974) 219.

[4] B.Militzer, D.Ceperley, Phys. Rev. Lett. **85** (2000) 1890.

[5] H.Xu, J.Hansen, Phys. Rev.E **57** (1998) 211.

Transport Properties of Dense Laser Plasmas

M. Schlanges[1], Th. Bornath[2], P. Hilse[1], D. Kremp[2]

[1] Institut für Physik, Ernst-Moritz-Arndt-Universität Greifswald, Domstrasse 10a, 17487 Greifswald, Germany

[2] Fachbereich Physik, Universität Rostock, Universitätsplatz 3, 18051 Rostock, Germany

Generalized kinetic equations are used to investigate transport properties of dense plasmas in strong laser fields. Quantum statistical expressions are derived for, e.g., the collision frequency to account for nonlinear field phenomena as well as strong correlation effects. The influence of these effects on collisional absorption is discussed.

1. Introduction

The impressive progress in laser technology makes femtosecond laser pulses of very high intensity available in laboratory experiments. If solid targets are irradiated by such laser pulses, dense plasmas can be created relevant for astrophysics and inertial confinement fusion. To understand transport properties of intense laser–plasma interaction, a theoretical modelling of dense nonideal plasmas in strong laser fields is needed.

One of the important mechanisms of energy deposition is inverse bremsstrahlung, i.e., laser light absorption via collisional processes between the plasma particles. In strongly ionized plasmas, this absorption process is essentially governed by the electron–ion interaction usually described in terms of the electron–ion collision frequency.

A lot of work has been done up to now to consider the electron–ion collision frequeny and the dynamic conductivity, respectively, for laser plasmas under different conditions. The well-known classical theories were developed in, e.g., [1, 2, 3]. Basic equations of a rigorous quantum kinetic approach to laser plasmas were derived in Ref. [4].

We consider a fully ionized plasma under the influence of a spatially homogeneous electric field. Starting point is a generalized kinetic equation for the gauge invariant Wigner distribution function which follows from the time diagonal Kadanoff-Baym equation. The central quantity in the collision term is the self energy function. Powerful schemes are available to determine appropriate approximations for the self-energy function taking into account nonlinear field dependence as well as many–body and quantum effects relevant for high density plasmas.

2. Collisional absorption

As we are interested here in the collisional absorption by the plasma, it is obvious to start from the balance equation for the energy and for the electrical current resulting from the kinetic equation. As the collison integral is a non–Markovian one, the energy balance reads

$$\frac{dW^{\text{kin}}}{dt} + \frac{dW^{\text{pot}}}{dt} = \mathbf{j} \cdot \mathbf{E}, \qquad (1)$$

i.e., the change of the total energy of the plasma particles is equal to $\mathbf{j} \cdot \mathbf{E}$ that is in turn the energy loss of the electromagnetic field due to Poynting's theorem.

For the calculation of the collisional absorption, we start from the general balance equation for the current density of species a. It follows

$$\frac{\mathrm{d}}{\mathrm{d}t}\mathbf{j}_a(t) - n_a \frac{e_a^2}{m_a} \mathbf{E}(t)$$

$$= \sum_{b \neq a} \int \frac{d^3q}{(2\pi\hbar)^3} \frac{e_a \mathbf{q}}{m_a} V_{ab}(q) L_{ab}^<(\mathbf{q}; t, t), \qquad (2)$$

where $V_{ab}(q)$ is the Fourier transform of the Coulomb potential. The collision term is now expressed by the correlation function of the density fluctuations given by $i\hbar L_{ab}^<(t, t') = \langle \delta\rho_b(t')\delta\rho_a(t) \rangle$. For this function an appropriate approximation has to be found. In Born approximation the current can be expressed by the Lindhard dielectric function. For a harmonic field $\mathbf{E} = \mathbf{E}_0 \cos \omega t$, the field dependence is described by a Fourier series in terms of Bessel functions. This scheme allows to investigate the current density and the energy dissipation in dense weakly nonideal laser plasmas including dynamic screening, quantum effects as well as nonlinear field phenomena such as higher hamonics and multiphoton processes. The details of the investigation are presented in Ref. [6].

To include strong correlations one has to go beyond the Born approximation. An approximation which accounts for strong correlations in the ion and electron subsystems, we derived in Ref. [7]. Now, the resulting expression for the current is given in terms of dynamical structure factors and the exact density response functions. Again, the field dependence is described by a Bessel function expansion which causes the nonlinear field effects mentioned above. An important quantity is the cycle averaged dissipation of energy $\langle \mathbf{j} \cdot \mathbf{E} \rangle$. In the case of high-frequency fields, we get

$$\langle \mathbf{j} \cdot \mathbf{E} \rangle = \int \frac{d^3q}{(2\pi\hbar)^3} \frac{\epsilon_0 q^2}{\hbar^2 e_e^2} V_{ei}^2(q) \, n_i \, S_{ii}(\mathbf{q})$$

$$\times \sum_{n=-\infty}^{\infty} n\omega \, J_n^2 \left(\frac{\mathbf{q} \cdot \mathbf{v}_0}{\hbar\omega} \right) \text{Im} \frac{1}{\varepsilon_e(\mathbf{q}; -n\omega)}, \qquad (3)$$

with $\varepsilon_e^{-1}(\mathbf{q}; \omega) = 1 + (\hbar^2 e_e^2)/(\epsilon_0 q^2) \mathcal{L}_{ee}^R(\mathbf{q}; \omega)$ being the dielectric function with the density reponse function of the electron gas $\mathcal{L}_{ee}(\mathbf{q})$. As high frequency fields are considered the static ion–ion structure factor $S_{ii}(\mathbf{q})$ appears in (3) instead of the dynamical

5

one. Furthermore, J_n is the Bessel function of nth order and $v_0 = eE_0/m_e\omega$ is the so-called quiver velocity.

Often the electron–ion collision frequency ν_{ei} is discussed which is defined for the high-frequency case by (ω_p - plasma frequency)

$$\nu_{ei} = \frac{\omega^2}{\omega_p^2} \frac{\langle \mathbf{j} \cdot \mathbf{E} \rangle}{\langle \epsilon_0 \mathbf{E}^2 \rangle}. \tag{4}$$

Using the Lindhard dielectric function and neglecting ion–ion correlations (S_{ii}=1), the results follow we derived in Ref. [6]. Those results have a similar form as that of the nonlinear Dawson-Oberman model [1]. However, in our formula, the dielectric function is given by the quantum Lindhard form, whereas the dielectric theory of Decker et al. leads to the classical Vlasov dielectric function.

3. Numerical results

We compare the results obtained in the frame work of the quantum kinetic approach with the results of the classical theories. In Fig. 1 the collision frequency is shown as a function of the coupling parameter $\Gamma = (e^2/4\pi\varepsilon_0)/dk_BT$ with $d = (4\pi n/3)^{-1/3}$ for a strong field ($v_0/v_{th} > 1$). Results using the Lindhard dielectric function and $S_{ii}(\mathbf{q}) = 1$ are given by the upper curve. In the case of static screening the collision frequency is reduced.
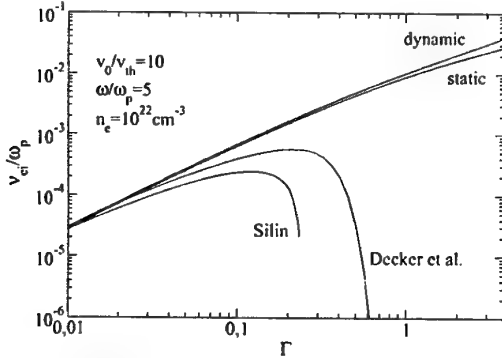
Fig. 1: Electron–ion collision frequency as a function of the coupling parameter Γ for a hydrogen plasma in a strong laser field. Comparison is given with the theory of Decker et al. and with the asymptotic formula of Silin.

For small values of Γ (weakly nonideal plasma), the classical dielectric theory of Decker et al. [1] and the classical asymptotic formula by Silin [2] give almost the same results. However, with increasing Γ, the classical curves show a sharp drop down. This behaviour results from a cutoff procedure at large wave numbers used in the classical theories. Such a cutoff is avoided in our approach automatically, and the range of applicability is extended to higher values of the coupling parameter.

As discussed above, the expression (3) generalizes the results to dense quantum plasmas including strong correlation effects.
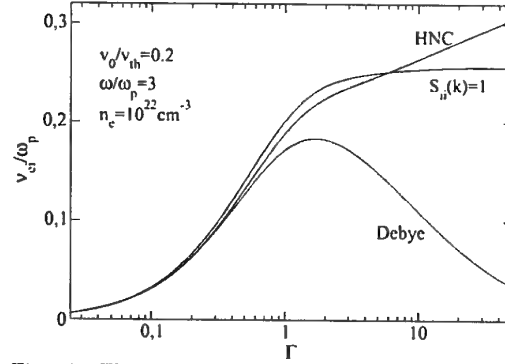
Fig. 2: Electron–ion collision frequency as a function of the coupling parameter Γ. Ion structure factors in different approximations: HNC and Debye.

Let us consider the influence of the ion-ion correlations. In Fig. 2 the collision frequency is shown using different approximations for the static ion-ion structur factor S_{ii} (in the dielectric function, we included local field corrections [7]). Here $v_0/v_{th} = 0.2$, i.e. a smaller field strength is considered. Inclusion of the structure factor in hypernetted chain (HNC) approximation decreases the collision frequency for small and moderate coupling up to $\Gamma \approx 5$ whereas an increasing behaviour follows for high values of the coupling parameter. As expected, the Debye approximation can be applied only for weak coupling. Good agreement with data obtained by simulations can be found in the range $\Gamma < 1$ [6].

References

[1] C. Oberman, A. Ron, and J. Dawson, Phys. Fluids **5**, 1514 (1962); C.D. Decker, W.B. Mori, J.M. Dawson, and T. Katsouleas, Phys. Plasmas **1** (1994) 4043.

[2] V.P. Silin, Zh. Eksp. Teor. Fiz. **47** (1964) 2254.

[3] Yu.L. Klimontovich, *Kinetic Theory of Nonideal Gases and Nonideal Plasmas* (Nauka, Moscow 1975 (russ.)).

[4] D. Kremp, Th. Bornath, M. Bonitz and M. Schlanges, Phys. Rev. **E 60** (1999) 4725.

[5] M. Schlanges, Th. Bornath, D. Kremp, M. Bonitz, P. Hilse, J. Phys. IV France **10** (2000) Pr5–323.

[6] Th. Bornath, M. Schlanges, P. Hilse, D. Kremp, Phys. Rev. E **64** (2001) 026414.

[7] Th. Bornath, M. Schlanges, P. Hilse, D. Kremp, J. Phys. A, accepted.

Super Fast Strong Radiative Z-Pinch Research in Kurchatov Institute and TRINITI

V. P. Smirnov

Director of Nuclear Fusion Institute, RRC Kurchatov Institute, Moscow, 123182, Russia

The magnetised plasma-wall transition: Theory and PIC simulation

D. Tskhakaya* and S. Kuhn

Department of Theoretical Physics, University of Innsbruck, Innsbruck, Austria
*Permanent Address: Institute of Physics, Georgian Academy of Sciences, Tbilisi, Georgia

We consider the plasma-wall boundary conditions in the presence of a strong magnetic field and discuss realistic examples when they can strongly deviate from the well-accepted classical ones.

1. Classical model of the magnetised plasma-wall transition

The plasma-wall transition (PWT) is the narrow layer between the "bulk" plasma and a conducting wall. The PWT strongly affects the particle and heat fluxes to the wall, thus influencing all plasma-wall interaction processes [1, 2]. Hence, investigation of the PWT has become a genuine branch of plasma physics. In describing the PWT it is usually assumed that $\lambda_D << \rho_i << l$, where λ_D, ρ_i and l are the Debye length, the ion Larmor radius and the charged-neutral particle collision mean free path, respectively. Under these conditions, the one-dimensional PWT can be divided into the following three parts: the Debye sheath (DS), the magnetic presheath (MP), and the collisional presheath (CP). Due to the strongly kinetic nature of the DS and the MP, fluid and gyrokinetic numerical codes are inappropriate to describe this region self-consistently. Thus, establishing realistic boundary conditions (BCs) at the MP entrance (MPE) is becoming of top importance. In addition, these BCs can be used for direct (analytical) calculations of the particle and energy fluxes to the wall [2].

The classical model of the combined DS-MP region [2,3] assumes a cut-off Maxwellian velocity distribution for the electrons, and neglects cross-field drifts. Then, the BCs at the MP entrance are

$$\Delta\phi_{MP} = \frac{T_e}{2e} \ln \frac{M_i}{2\pi m_e} \frac{T_e}{T_i + T_e}, \quad V_{MP} = \sqrt{\frac{T_i + T_e}{M_i}} \sin\alpha,$$

$$\gamma_e = \frac{\Theta_e}{T_e \Gamma_e} = 2 + \frac{e\Delta\phi_{MP}}{T_e} \approx 5, \quad \gamma_i = \frac{\Theta_i}{T_i \Gamma_i} = 2,0 \div 3.5,$$

where $\Delta\phi_{MP}$, V_{MP} and $\gamma_{e,i}$ are the potential drop between the MPE and the wall, the ion fluid velocity component normal to the wall at the MPE, and the electron and ion sheath heat transmission coefficients, respectively [3]; α is the angle between the wall and the magnetic field, e is the positive elementary charge, m_e and M_i are the electron and ion masses; $T_{e,i}$, $\Gamma_{e,i}$ and $\Theta_{e,i}$ are the temperature, the electron and ion particle and energy fluxes at the MPE. The second equation is the Bohm-Chodura condition. For simplicity we restrict ourselves to the floating case.

The aim of our work is to demonstrate that in reality the BCs at the MPE can strongly deviate from the classical ones listed above. All analytical results presented below have been checked against PIC kinetic simulations and found to be in good agreement with the latter.

2. Effects of superthermal electrons

The first question arising is the following: How correct is the assumption of Maxwellian electrons inside the PWT? Due to the low collisionality of high-energy electrons, the electron distribution at the MPE can contain a non-Maxwellian high-energy tail. In fusion plasmas this happens, e.g., during ELM (Edge-Localised Mode) activity, or during Lower Hybrid current drive and heating. In order to model a PWT of this kind one can assume that the plasma contains three electron populations [4], namely the thermal one and two high-energy electron beams propagating towards and away from the wall. The second beam corresponds to the electrons of the incoming beam, having been reflected in the DS and MP. Using the quasineutrality and the particle-conservation constrains, one can obtain the modified plasma BCs at the MPE. For low concentrations of the high-energy electron population (C_f) we get the following implicit BCs:

$$C_f = \frac{\alpha - cF(0,\sqrt{\Delta\varphi})}{F(\beta,\delta) - cF(0,\sqrt{\Delta\varphi})}, \quad \alpha = \sqrt{\pi \frac{T_i + T_e}{T_b} \frac{m_e}{M_i}}$$

$$\gamma_e = \frac{c}{\alpha}\left((2 + \Delta\varphi)F(0,\sqrt{\Delta\varphi}) + \frac{C_f}{c^3}\left(F(\beta,\delta)(2.5 + \beta^2) - c^3(2 + \Delta\varphi)F(0,\sqrt{\Delta\varphi}) + \frac{\alpha^2\Delta\varphi + \alpha\beta\sqrt{\Delta\varphi} - 0.5}{1 + 2erf(\beta) + erf(\delta)} e^{-\delta^2}\right)\right),$$

$$\beta = \sqrt{\frac{m_e}{T_b}}V_b, \delta = c\sqrt{\Delta\varphi} - \alpha, \quad c = \sqrt{\frac{T_e}{T_b}}, \quad \Delta\varphi = \frac{e\Delta\phi_{MP}}{T_e},$$

$$F(\alpha,\beta) = \frac{\exp(-\beta^2) + \sqrt{\pi}\alpha(1 - erf(\beta))}{1 + 2erf(\alpha) + erf(\beta)}.$$

where T_b and V_b are the temperature and the velocity of the high-energy electron beam, respectively. $\Delta\varphi$ and γ as functions of C_f are given in Fig. 1, from which we see that even a very low concentration of the high-energy electron population can dramatically change the BCs at the MPE.
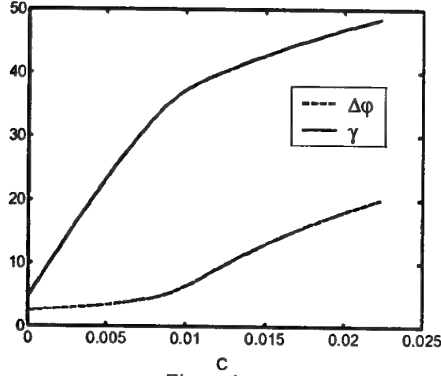
Figure 1.

3. Drift effects

Other candidates for affecting the BCs are the cross-field drifts. Here we consider the **ExB** drift as the most important one for fusion plasmas [2].

We consider a half-bounded plasma with the MPE located at $z \to -\infty$, where z is directed along the normal to the wall (Fig. 2). Let us assume that there exists an electric-field component parallel to the wall (E_y). Then, neglecting pressure terms, we can write the ion particle and momentum conservation equations for the MP [5] in the form

$$\frac{\partial}{\partial \vec{r}} n \vec{V} = 0, \quad \left(\vec{V} \frac{\partial}{\partial \vec{r}} \right) \vec{V} = \frac{e}{M_i} \left(\vec{E} + \vec{V} \times \vec{B} \right),$$

$$n \cong \exp\left(-\frac{e\phi}{T_e} \right), \qquad \frac{\partial}{\partial \vec{r}} = \left(0, 0, \frac{\partial}{\partial z} \right),$$

$$\vec{E} = \left(0, E_y(z,y), E_z(z,y) \right), \quad \vec{B} = \left(B_x, 0, B_z \right).$$

The corresponding BCs at the MPE have the following form:

$$V_x^0 = V_{\|}^0 \cos\alpha + \frac{E_y^0}{B} \sin\alpha, \ V_y^0 = 0, \ \vec{V}^0 \equiv \vec{V}\Big|_{z \to -\infty}$$

$$V_z^0 \equiv V_{MP} = V_{\|}^0 \sin\alpha - \frac{E_y^0}{B} \cos\alpha, \ E_y^0 = E_y\Big|_{z \to -\infty},$$

where $V_{\|}^0$ is the ion parallel velocity at the MPE, which is unknown yet.

It is possible to show that the system given above has a solution only if

$$V_{\|}^0 = \left(\sqrt{1 + \eta^2} - \eta \right) \sqrt{\frac{T_i + T_e}{M_i}} + \frac{E_y^0}{B} \cot\alpha,$$

$$\eta = \pm \frac{1}{2} \frac{\cot\alpha}{\sqrt{1 + T_i/T_e}} \frac{\rho_i}{L_y}, \quad L_y = \left| \frac{E_z}{\partial_y E_z} \right|_{z \to -\infty}. \tag{1}$$

Here, ρ_i is the Larmor radius and the sign of η depends on the direction of the **ExB** drift: If the drift is directed towards the wall, then η is positive, and in the opposite case it is negative.

From Eq. (1) we immediately obtaina new BC at the MPE:

$$V_{MP} = \left(\sqrt{1 + \eta^2} - \eta \right) \sqrt{\frac{T_i + T_e}{M_i}} \sin\alpha.$$

For small angles ($\alpha \ll 1$), η can easily become of the order of unity (or larger), hence the corresponding V_{MP} can significantly differ from the classical one.
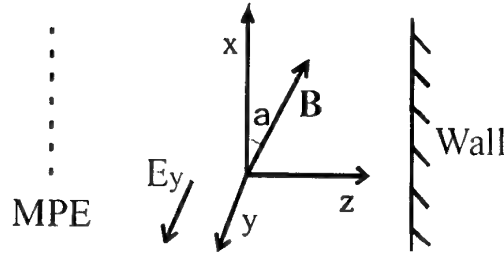
Figure 2.

Let us conclude by noting that in the extended version of this paper we will discuss two additional aspects, namely (a) the effects of a magnetic field almost parallel to the wall, and (b) the instabilities caused by secondary electrons.

References

[1] K. –U. Riemann, J. Tech. Phys. **41**, 1, Special issue, 89-121 (2000).
[2] P.C. Stangeby, The Plasma Boundary of Magnetic Fusion Devices, Institute of Physics Publishing, Bristol and Philadelphia (2000).
[3] D. Tskhakaya and S. Kuhn, J. Nucl. Mat. **313-316**, 1124-1127 (2003).
[4] D. Tskhakaya, S. Kuhn, V. Petržílka, and R. Khanal, Phys. Plasmas **9** (6), 2486-2496 (2002).
[5] D. Tskhakaya and S. Kuhn, Contrib. Plasma Phys. **42** (2–4), 302–308 (2002).

10

Plasma-Based Sterilization

Mounir Laroussi
Electrical & Computer Engineering Department
Old Dominion University
Norfolk, VA 23529

Rapid, safe, and effective sterilization is of the utmost importance when it comes to protecting the public in general and hospital patients in particular. Today, public health institutions face unprecedented challenges due to the advent of heat sensitive reusable medical tools and due to the appearance of heat resistant microorganisms such as prion, the protein which causes Creutzfeldt-Jacob disease, more commonly known as "mad cow disease". Conventional sterilization methods such as autoclaving and Ethylene Oxide (EtO) are inadequate in these cases. Non-equilibrium "cold" plasmas have recently been shown to be a very promising alternative, potentially capable of overcoming the above-mentioned challenges. In addition to not damaging the articles to be sterilized, cold plasmas proved to be very effective due to the synergistic effects of free radicals and UV photons, which interact with the cells of microorganisms on the atomic and molecular levels.

1. Introduction

Sterilization was concisely defined by S. S. Block [1] as " any process or procedure designed to entirely eliminate microorganisms from a material or medium". It can be achieved by chemical and/or physical means, such as heat, chemical solutions and gases, and radiation [1]. Most conventional sterilization techniques are associated with some level of damage to the material or medium supporting the microorganisms. This does not present a problem in cases where material preservation is not an issue. However, in cases where it is imperative not to damage the materials to be sterilized, conventional methods are either not suitable at all or offer very impractical and/or tedious and time consuming solutions. This situation led to a drive to develop new techniques as effective as established ones, but with added superior characteristics such as short processing times, non-toxicity, and medium preservation. Amongst these new methods, non-equilibrium atmospheric pressure plasmas have been shown to present a great promise [2] -[4].

2. Conventional Sterilization Methods

From early times human have realized that sunlight is a good sterilization agent. It offers some degree of protection from infection with pathogenic microorganisms. However, through the years, more controllable sterilization methods have been developed. Here we briefly discuss a few of these methods.

Sterilization by Heat: Both moist heat and dry heat can be used. Moist heat is generally applied by a device known as an "autoclave", which produces pressurized steam (15 psi) at 121 °C. Exposures of 20 minutes usually result in complete sterilization. Dry heat can be applied by infrared radiation or incineration. Heat sterilization is applicable only if damage by heat and/or moisture is not a problem.

Sterilization by Gases: The most widely used gas in this method is Ethylene Oxide (EtO). It is used in medical applications to sterilize heat sensitive items. Ozone (O_3) is another gas used to disinfect water and to preserve food from spoilage. Ozone is known to interfere with cellular respiration.

Sterilization by EM Radiation: Microwaves, ultraviolet radiation, gamma-rays, and X-rays can be used to inactivate microorganisms. Each type of EM radiation affects cells in a different way. Ultraviolet radiation (UV), in the 220-280 nm range, for example, directly affects the DNA of cells. Ionizing EM radiation affects the cells of microorganisms by causing physical and biochemical changes in the DNA. EM radiation is used for the preservation of food, treatment of sewage, and for the sterilization of medical products.

Sterilization by Particle Radiation: Electrons, a-particles, and protons can be used in this method. However, electrons have been the particle of choice. In particular, electron beam irradiation is presently used for various decontamination purposes.

3. Low Temperature Plasmas

Relatively large volume low temperature plasmas are traditionally generated at reduced pressures. However, for practical sterilization/decontamination purposes, to have a vacuum system-based device would be inconvenient and expensive. Therefore, methods to generate large volume plasmas at or near atmospheric pressure were adopted. In this paper, the emphasis is on atmospheric pressure "cold" plasma devices. For an extensive coverage on the sterilization application of low-pressure plasmas, the reader is referred to reference [5].

Today, cold plasmas at atmospheric pressure can be generated by various methods. Amongst these, the Dielectric Barrier Discharge (DBD) [6], the Resistive Barrier Discharge (RBD) [7], and the Atmospheric Pressure Plasma Jet (APPJ) [8] have been especially researched in the past few years. The RBD can be driven by DC or AC power sources, the DBD requires frequencies in the kHz range, and the APPJ uses a 13.56 MHz RF power source. These devices can generate relatively large volumes of non-equilibrium, low temperature plasmas at or near atmospheric pressure.

Air or other gas mixtures can be used. The plasmas produced by these devices have typically electron densities in the 10^9 cm^{-3} – 10^{11} cm^{-3} range, plasma power densities in the 10 – 300 mW/cm^3, and gas temperatures generally below 100 °C. They are sources of UV, visible, and IR radiation, and free radicals such as O and OH which play important roles in the destruction of microorganisms.

4. Sterilization/Decontamination by Low Temperature Plasmas

Historically, it was Siemens [9] who in 1857 used an atmospheric pressure plasma (corona discharge) to generate ozone to disinfect water. Later, Menashi [10] used a corona discharge to sterilize the surface of materials. In the mid-nineties Laroussi [2], [3] used a DBD – based diffuse discharge at atmospheric pressure to decontaminate biological media. Other experiments soon followed using various discharge configurations to destroy both gram-negative and gram-positive bacteria, as well as other microorganisms such as viruses.

Kinetics of Inactivation: The concept of inactivation or destruction of a population of microorganisms is not an absolute one. This is because it is impossible to determine if and when all microorganisms in a treated sample are destroyed [1]. Therefore, experimental investigation of the kinetics of cell inactivation is paramount in providing a reliable temporal measure of microbial destruction.

One kinetics measurement parameter, which has been used extensively by researchers studying sterilization by plasma, is what is referred to as the "D" value (Decimal value). The D-value is the time required to reduce an original concentration of microorganisms by 90%. Since survivor curves are plotted on semi-logarithmic scales, the D-value is determined as the time for a one $\log_{10}$ reduction.

To date, the experimental work on the germicidal effects of atmospheric pressure plasmas has shown that survivor curves (CFUs versus time) take different shapes depending on the type of microorganism, the type of the medium supporting the microorganisms, and the method of exposure. Single-slope, dual-slope, and multi-slope survivor curves have all been reported. The D-value of each phase of the dual-slope and multi-slope curves are generally different (seconds to minutes range), indicating different interaction processes in these phases between the plasma and the biological media.

5. Cells Inactivation Factors

Effects of the UV: UV affects the cells of bacteria by inducing the formation of thymine dimers in the DNA. This inhibits the bacteria's ability to replicate properly. By comparing the killing kinetics of UV radiation from a low-pressure mercury vapor lamp and that of atmospheric pressure cold plasma, Laroussi [3] concluded that UV does not play the prominent inactivation role in atmospheric pressure plasmas. This

claim was later supported by the work of Herrmann et al. [4] and others.

Effects of the Reactive Species: It has always been recognized that the reactive species, generated in a high pressure non-equilibrium discharge through electron impact excitation and dissociation, play an important role in its germicidal characteristics. Several investigators showed that discharges containing oxygen have a strong germicidal effect: The D-value decreases if a certain amount of oxygen is added. This is due to the presence, in such discharges, of oxygen-based active species such as atomic oxygen and ozone. Other radicals such as OH have also been found to play an important role in the inactivation process.

Effects of Charged Particles: Mendis et al. [11] suggested that charged particles may play a very significant role in the rupture of the outer membrane of bacterial cells. They showed that the electrostatic force caused by charge accumulation on the outer surface of the cells' membrane could overcome the tensile strength of the membrane and cause its rupture. They claim that this scenario is more likely to occur for gram-negative bacteria, the membrane of which possesses an irregular surface.

6. Conclusions

Low temperature, atmospheric pressure plasmas have been shown to possess very effective germicidal characteristics. Their relatively simple and inexpensive designs, as well as their non-toxic nature, give them the potential to replace conventional sterilization methods in the near future. This is a most welcome technology in the healthcare arena where re-usable, heat sensitive medical tools are becoming more and more prevalent.

7. References

[1] S. S. Block, *Encyclopedia of Microbiology* 4 (87) Academic Press, 1992.

[2] M. Laroussi, *Bull. Amer. Phys. Soc. Div. Plasma Phys.* 40 (1995) 1685.

[3] M. Laroussi, *IEEE Trans. Plasma Sci.* 24 (1996) 1188.

[4] H. W. Herrmann, I. Henins, J. Park, and G. S. Selwyn, *Phys. Plasmas* 6 (1999) 2284.

[5] M. Moisan, J. Barbeau, S. Moreau, J. Pelletier, M. Tabrizian, and L'H. Yahia, *Int. J. Pharmaceutics* 226 (2001) 1.

[6] S. Kanazawa, M. Kogoma, T. Moriwaki, and S. Okazaki, *J. Appl. Phys. D: Appl. Phys.* 21 (1988) 838.

[7] M. Laroussi, I. Alexeff, J. P. Richardson, and F. F. Dyer, *IEEE Trans. Plasma Sci.* 30 (2002) 158.

[8] A. Scutze, J. Y. Jeong, S. E. Babyan, J. park, G. S. Selwyn, and R. F. Hicks, *IEEE Trans. Plasma Sci.* 26 (1998) 1685.

[9] W. Siemens, *Poggendorfs Ann. Phys. Chem.* 12 (1857) 66.

[10] W. P. Menashi, U. S. Patent No. 3,383,163, 1968.

[11] D. A. Mendis, M. Rosenberg, and F. Azam, *IEEE Trans. Plasma Sci.* 28 (2000) 1304.

Plasma processing of materials at the atomic scale

N St J Braithwaite & T Matsuura
The Open University, Oxford Research Unit, OX1 5HR, UK

Plasma etching is finding new applications beyond the microelectronics industry. There are new challenges in the devising and controlling of plasma-surface interactions.

1. Introduction

A new generation of electromechanical devices is emerging that indirectly interface the processing power of microelectronics with the macroscopic world of human life. These are micro-electromechanical systems (MEMS) and their close relatives, micro-opto-electromechanical systems (MOEMS) and nano-electromechanical systems (NEMS); for brevity the single acronym MST will be used to imply the whole family of micro and nano systems technologies.

Conventional process technologies that have evolved for the manufacture of microelectronics to a very large scale of integration (VLSI) are amenable to adaptation for the fabrication of MST devices [1]. As a result, silicon is widely used as the base material for MST and plasma enhanced chemical vapour deposition and plasma etching are mandatory tools for shaping it. However, specifications of the manufacturing processes required for MST can be different by orders-of-magnitude from those in VLSI processes because of the contrasting quantity of material involved: microelectronics is still predominantly based on a planar geometry whereas MST devices are more often than not fully three dimensional. Nevertheless, the principal characteristics of processes based on low pressure, electrical discharge plasmas are still advantageous. For instance, plasmas exploit electrical energy to stimulate enhanced chemical reactivity to provide an etching medium. Furthermore, space charge sheaths at plasma boundaries introduce directionality in the rates of surface reactions through the bombardment by high energy ions. In addition, plasma processes are 'dry' – a fact that allows most of the fabrication sequence to be done without the repeated washing and drying necessary if wet chemical routes are used.

Tailoring processes for the plasma etching of silicon is of particular importance for a wide variety of MST demands. Key developments include robust and reliable control of atomic-order surface adsorption, surface diffusion and surface reactions in plasma etch processes. These surface mechanisms control the vertical and lateral etch rates as well as the etch-selectivity, all of which must be optimized in order to fabricate functional structures. Most of the previous work on etching mechanisms concentrates on reactions that are enhanced by ion-bombardment, and there has been much less on surface diffusion or adsorption processes. Existing models deal only with a sub-set of the key parameters in what is a multi-dimensional problem. Moreover, they generally deal with essentially planar silicon structures, whereas there is now a need to describe the significantly more complex 3D processes required for MST devices.

2. Plasma etching

In the plasma etching process, surface material is removed as volatile molecules formed in chemical combinations between the surface atoms and species originally activated in the plasma. The relatively hot electrons (1-10 eV) that predominate in low pressure gas discharges are particularly effective activators.

2.1 Vertical (anisotropic) etching
Of particular interest in etching features for MST devices is a process that cuts deep into the bulk silicon. The so-called 'switched etch process' achieves this in a succession of deposition and etch steps through which anisotropic etching is promoted. The sides of features are typically protected by a thin layer of fluorocarbon polymer deposited from radicals generated in a fluorocarbon plasma (Fig 1.). After only a few seconds of deposition, the plasma composition is switched to provide an etching medium based on SF_6. Fluorine atoms, liberated by the inelastic collision processes in the plasma, etch those areas that are cleared of polymer by a strongly directed flux of energetic ions crossing the space-charge sheath at the interface between plasma and surface. The sidewall passivation is repaired by further cycles of deposition every few minutes. Though a very successful basis for fabricating MST devices this approach has a number of inherent limitations: sidewall passivation involves relatively thick complex hydrocarbon polymer films that are often difficult to remove; the sidewall profile has a characteristic scalloped edge linked to the multi-step procedure; chamber walls accumulate polymeric coatings that are a potential source of particulate contamination.

Fig 1 Plasma – source of active species and ions
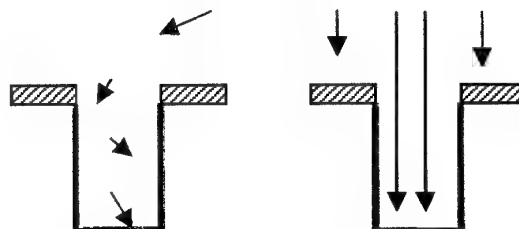
2.2 Lateral (isotropic) etching

Etchant species can diffuse considerable distances across a silicon surface before becoming chemisorbed. This can fuel etching on sites not directly exposed to the plasma. Observations of etch profiles, particularly the persistence of sharp ridge shapes and of nature of undercut immediately beneath the mask, indicate that surface diffusion can be significant in the fluorine based etching of silicon [3]. Figure 2 shows heavily undercut features in silicon produced by an *isotropic* etching environment that nevertheless fails to 'polish' the sharp edges defined by the original mask.
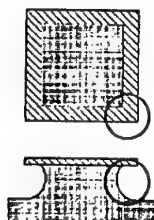
Fig. 2 Silicon etched under aluminium mask (10x10 μm) may show necking – sketches based on SEMs [3]

The rate of lateral etching of polycrystalline silicon exhibits strong aspect ratio effects on the submicron-scale, indicating different surface diffusion rates for different etchant species [4].

3. Controlling plasma etching

There are two approaches to controlling plasma-surface interactions in an etching environment. One uses chemistry; the other is based on control engineering.

The potential of atomic order control of adsorption and reaction has been demonstrated by studying the etching of silicon and related materials, atomic layer by atomic layer [5]. The etching proceeds in a succession of steps during which monolayers are chemi-sorbed and subsequently removed by ion bombardment. The growth of a monolayer is a self-limiting process that can be revealed through studies of etch rate. This then suggests a 'sharper' alternative to the switched etch process described above, with monolayer chemi-sorbtion replacing polymer passivation. Table 1 is a summary of adsorbent species and plasma gases used by Matsuura [5] for the etching of silicon using this approach. Sidewall passivation by these self limiting processes exploits atomic scale phenomena and is accordingly simpler, faster and capable of achieving finer scale features.

MST devices require considerable quantities of silicon to be removed by plasma etching. The rate of etching is determined by the concentrations of the species involved (e.g. atomic fluorine and various bombarding ions). Thus there is a demand for denser plasma sources. At the same time the electron temperature in the plasma affects the relative amounts of the active species that are created. Accordingly, a versatile source would have independent control over plasma density, the distribution of electron energies and the energy of ion bombardment. A way of coping with a multidimensional space for process parameters is to employ 'intelligent' optimization and control. Diagnostic data obtained *in-situ*, can be fed back to an Artificial Intelligence (AI) platform that controls the processing plasma. Recently this approach has been used to map the operational parameter space in terms of ion bombardment flux and energy [2]. The AI control has been mostly rule-based (including the application of fuzzy logic to achieve multi-variable control). More recently tuning and optimization has been done using the methods of genetic algorithms, simulated annealing, and differential evolution. These are all based on the idea of searching a parameter space to find an optimum or near-optimum, avoiding the local optima while not having to search exhaustively the whole parameter space.

4. References

[1] I W Rangelow and Loeschner, Reactive ion etching for MST fabrication *J Vac Sci* Tech **B13** (1995), 2394

[2] P. Verdonck, A. Goodyear, R. D. Mansano, P. R. J. Barroy and N. St. J. Braithwaite, *J. Vac. Sci. Tech.*, **B20**(3) (2002) p.791.

[3] T. Matsuura, J. Murota, T. Ohmi and S. Ono, 1992 *Int. Conf. on Solid State Devices and Materials*, Tsukuba, (August 26-28, 1992),.418-419; T. Matsuura, J. Murota, T. Ohmi and S. Ono, Proc. *Symposium on Highly Selective Dry Etching and Damage Control* (The Electrochemical Society, Pennington, NJ, **PV93-21** (1993), pp.141-148.

[4] T. Matsuura, J. Murota, Y. Sawada and T. Ohmi, *Appl. Phys. Lett.*, **63**(20) (1993), 2803; T. Matsuura, T. Sugiyama and J. Murota,, *Surf. Sci.*, **402-404**(1998), .202; T. Matsuura, Y. Honda and J. Murota, *Appl. Phys. Lett.*, **74**(23) (1999),.3573

[5] J Al-Kuzee, T Matsuura, L Nolle, A A Hopgood, P D Picton, N St J Braithwaite, *First Technological Plasma Workshop Dec 2002, Warwick*, 'Intelligent Control of Low Pressure Plasma Processing'.

Adsorbant	Plasma	Remarks
Cl radical	Ar/Cl$_2$	1/2ML etching for (100), depends on orientation
Cl$_2$ molecule	Ar/Cl$_2$	1/4ML etching for (100), depends on orientation
N radical	N$_2$	~2ML nitridation
N ions	N$_2$	~4ML nitridation

Table 1. Typical self-limiting conditions for plasma monolayer (ML) silicon etch processes established by Matsuura et al.

Practical plasma immersion ion implantation for stress regulation, treatment of insulators and complex shapes

M.M.M. Bilek, R.N. Tarrant, T. W. H. Oates, D. T. Kwok, D. R. McKenzie

School of Physics, University of Sydney, NSW, Australia 2006

Abstract: Plasma immersion ion implantation has been attracting the interest of research groups around the world over the last two decades. The technique has been developed to the stage where it is a well-established technique for a number of materials processing applications, such as plasma nitriding. Recent research has focussed on developing the method for a range of new applications, including stress regulation, surface treatment of insulators and complex shaped workpieces. The state of development of these new and technologically important applications will be discussed in this paper.

1. Introduction

Plasma immersion ion implantation (PIII) was first investigated in the late 1980s as an alternative to extracted ion beams for achieving ion implantation of a workpiece [1,2]. The advantages were identified to be the high flux of impinging ions and the conformal nature of the implantation, which reduced the need to rotate the workpiece during treatment. PIII utilises the application of short, high-voltage pulses to a substrate immersed in a plasma from which ions are drawn across a high voltage sheath and implanted into the substrate surface. As a competitor to beam line methods, PIII also has some disadvantages. These include difficulties accessing very high ion energies due to electric breakdown occurring across the plasma sheath and the larger energy spread of implanted ions, including a considerable proportion of low energy ions. The low ion energies are due to the finite rise and fall times of the high voltage pulse. Recent simulation work on the sheath dynamics has shown that the major low energy ion contribution is due to the pulse rise-time despite the fact that it is usually shorter than the fall-time[3].

PIII can also be applied during film deposition to modify the properties of the film during growth [4,5,6], most importantly the intrinsic stress and preferred orientation or texture. In the first section of this paper we present some of the recent findings of our group pertaining to the reduction of stress in growing films. Although it is straightforward to apply a voltage directly to a conductive workpiece, the treatment of insulators with PIII is complicated by the dielectric response of the workpiece and the build up of charge on its surface during the implantation process. Our recent studies of these phenomena and ways to avoid or reduce their effects are presented in the second section of this paper with a focus on the sheath dynamics. The extent to which a PIII surface treatment is conformal depends on the behaviour of the plasma sheath around it. Difficulties can arise when treating complex shaped workpieces, particularly those with curvatures of small radii such as sharp points or edges. The last section of this paper discusses the sheath behaviour leading to these difficulties.

2. Stress regulation

PIII, when applied during a physical vapour deposition (PVD) process, has been shown to significantly reduce the level of intrinsic stress in the growing film[6]. Our recent experimental results show that this effect is observed in carbon, titanium nitride and aluminium nitride systems (i.e. in all of the materials we have studied to date) deposited using a cathodic arc plasma. Because this group of materials contain a variety of microstructures, including crystalline cubic and hexagonal, as well as amorphous microstructures, we believe that the observed reduction in stress is a universal phenomenon which could be applied to all films deposited using PVD processes. Stress relief is observed for pulse biases exceeding approximately 500 eV in the materials we have studied.

Figure 1 shows the relationship between the pulse voltage – frequency product and the intrinsic stress in thin films of carbon. The pulse length was kept at 20 μs throughout this series of depositions, while the pulse bias was varied between 1.7 and 20 kV. Pulse frequencies of 200, 800 and 1200 Hz were used.
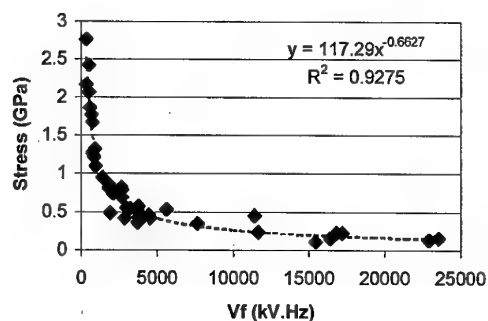
Figure 1: Film stress in cathodic arc deposited carbon treated with PIII during deposition, plotted against the pulse bias voltage-frequency product.

The majority of the points from all data sets (200, 800 and 1200 Hz) lie on a curve given by the fitting function

$y=117.29x^{-0.6627}$, where y is the value of residual stress in GPa and x is the Vf product. The curve shows that when Vf is low, increases in Vf yield large increments of stress relaxation. As Vf increases, increments of stress relief achievable from further increases in Vf are progressively smaller. This can be attributed to the fact that once a significant portion of the film's volume has been treated with *thermal spikes* (small heated volumes surrounding the impact sites of the high energy ions), the effectiveness of subsequent spikes is reduced. As the density of treated surface regions increases, incoming impacts have a non-negligible probability of overlapping with a volume already relaxed by a previous thermal spike. This issue of thermal spike overlap has been discussed in detail and an upper bound for its value has been estimated numerically in a previous paper [6].

3. Insulators and complex shapes

PIII treatment of insulating materials such as polymers has attracted much interest in recent years. Polymer surfaces can be hardened and made more wear resistant by ion implantation. They may also be coated with metallic thin films. The use of PIII during the film deposition dramatically improves adhesion of these films to the polymer substrate.

The insulating nature of the substrates, however, introduces additional difficulties to the PIII process. The dielectric properties of the substrate determine the voltage that initially appears on the surface in contact with the plasma for a given applied bias voltage. As ions are implanted into the surface it charges positively further reducing the voltage on the surface. This reduction in voltage on the surface throughout the duration of the bias pulse leads to a gradual collapse of the sheath and progressively lowers the energy of the ions implanted.
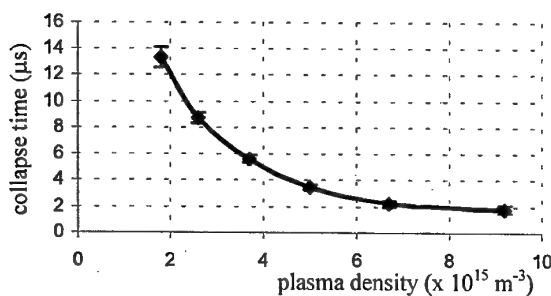
Figure 2: Time for sheath to collapse down to 5 mm as a function of the cathodic arc plasma density at an applied bias of 5 kV as measured by a Langmuir probe.

We have used small Langmuir probes to measure the sheath collapse under a variety of cathodic arc plasma and PIII pulsing conditions. The probe tip was biased to +90 V so that it drew a steady electron current when immersed in the plasma and ceased to draw current when positioned in the electron depleted sheath region.

To investigate the effect of plasma density on the collapse of a sheath around an insulator we placed the probe inside the sheath (5 mm from the substrate surface) and measured the time it took for the sheath to collapse back past the probe for a range of plasma density values. The measured data is plotted, in Figure 2, shows that as the plasma density is increased the time for the sheath to collapse decreases. This indicates that the PIII treatment of insulators is best conducted in plasmas of low density while keeping the applied bias pulse length as low as possible. Because of the finite rise time of the pulse, the use of shorter pulses coupled with the influence of surface charging will enhance the energy spread and low energy ion proportion in the treatment of insulators as compared with conducting substrates.

Practical workpieces such as tools and medical components present further difficulties due to their intricate shapes, particularly associated with points and corners. The equilibrium sheath width in these locations is smaller, making these points more susceptible to electric breakdown. Ion focusing effects also occur making treatments at corners inhomogeneous. These effects need to be better understood and accounted for in further development of practical PIII processing methods.

4. Conclusion

Since its introduction two decades ago, PIII has been shown to be a versatile technique for the surface modification of materials. Aside from its use to for ion implantation, in combination with PVD methods such as cathodic arc deposition, it yields good quality thin film coatings with greatly reduced levels of intrinsic stress and excellent adhesion. There are difficulties associated with the behaviour and dynamics of sheath that occur when employing PIII with insulating substrates and with substrates of complex shape. An improved understanding of the evolution of the sheath will enable the selection of optimum process parameters on a case by case basis.

5. References

[1]   J.R. Conrad, J.L. Radtke, R.A. Dodd, F.J. Worzala, *Journal of Applied Physics*, vol. 62, p. 4591, 1987.

[2]   J. Tendys, I.J. Donnelly, M.J. Kenny, J.T.A. Pollock, *Applied Physics Letters*, vol. 53, p. 2143, 1988.

[3]   D.T.K. Kwok, M.M.M. Bilek, D.R. McKenzie and P.K.Chu, *Applied Physics Letters*, (in press) 2003.

[4]   I. G. Brown, X. Godechot, K.M. Yu, *Applied Physics Letters*, vol. 58, p. 1392, 1991.

[5]   A. Anders, *Surface & Coatings Technology*, vol. 93, p. 157, 1997.

[6]   M.M.M. Bilek, D.R. McKenzie, R.N. Tarrant, S.H.N. Lim and D.G. McCulloch, *Surface & Coatings Technology*, vol. 156, p. 136, 2002.

Topic 4

Coronas, sparks, surface discharges and high-pressure glows

Analytical and numerical studies of non-stationary corona in long air gaps

N.L.Aleksandrov, E.M.Bazelyan[*], R.B.Carpenter[**], Jr., M.M.Drabkin[**], and Yu.P.Raizer[***]

Moscow Institute of Physics & Technology, 141700 Dolgoprydny, Moscow region, RUSSIA
[*]Krzhizhanovsky Power Engineering Institute , 117927 Moscow, RUSSIA
[**]Lightning Eliminators & Consultants, Inc., USA
[***]Institute for Problems in Mechanics, RUSSIA

The properties of a non-stationary corona in which the front of space charge has not bridged the gap are studied analytically and numerically for different one-dimensional geometries. It is shown that an analytical theory is applicable for describing the development of the non-stationary corona at any shape of applied voltage. The characteristics of a non-stationary corona differ greatly from those of a stationary corona. For the same applied voltage the current of non-stationary corona can be much higher than the current under steady conditions. The effect of aerosol ions on the properties of a corona near a grounded object is numerically studied under thunderstorm conditions.

1. Introduction

A non-stationary transient regime of a corona discharge (when the front of space charge has not bridged the gap) is initiated in any laboratory non-uniform gap after the voltage application. This regime is of particular importance under natural conditions when corona is ignited near the top of a high grounded object or near other extremities (tips of trees, bushes, grass, etc.) in the thundercloud electric field. It has been shown [1] that the corona space charge hinders the initiation of an upward leader from the object top and consequently is favourable to the protection of the object against lightning.

The purpose of this work is to analytically and numerically study the main characteristics of a non-stationary corona for different one-dimensional electrode configurations (concentric spheres, coaxial cylinders and emitting plane).

2. System of equations

A corona discharge is described by the balance equations for the density of charge carriers and Poisson's equation. The boundary condition is that the electric field near the coronating electrode is equal to the corona onset field. In addition, we use the condition that the voltage drop along the discharge gap is equal to the applied voltage $U(t)$.

3. Results obtained

In a non-stationary case, there exist an exact analytical solution for one-dimensional electrode geometries and on assumption that the discharge current is time-independent [2]. (This is valid only for a certain

voltage shape.) A generalization of this analytical approach to any voltage shape has been given in [1]. By using this approach to describe a non-stationary corona between concentric spheres with inner radius r_0 and outer radius R_0, we obtain the expression for the discharge current

$$i = 2\pi\varepsilon_0 \sqrt{\frac{\mu U_m^{3}}{6\tau\left(\frac{t}{\tau}-1+e^{-t/\tau}\right)}\left(1-e^{-t/\tau}\right)^2} \quad (1)$$

for the applied voltage shape

$$U = U_m\left(1-e^{t/\tau}\right). \quad (2)$$

Here, μ is the ion mobility. Equation (1) is valid for $r_0 \ll R \ll R_0$, where R is the radius of the space charge front.
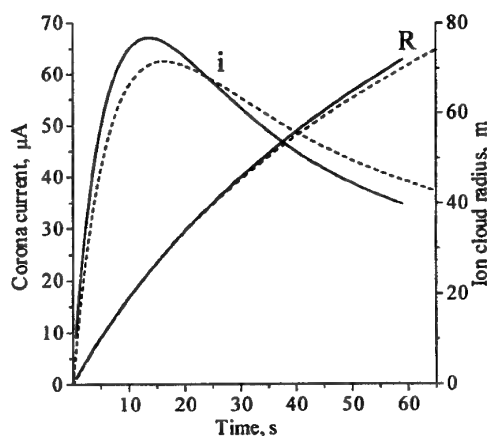
Fig. 1. The ion cloud radius R and corona current i calculated (solid curves) numerically and (dashed curves) analytically, respectively. $r_0 = 1$ cm, $R_0 = 10^3$ m, $U_m = 1$ MV and $\tau = 10$ s.

The analytical approach used was verified by comparison with the results of a computer simulation. Figure 1 shows that the approximations used in the analytical theory introduce an accepted error.

Our analytical and numerical study shows that for the same applied voltage the current of a non-stationary corona can be much higher than the current of a stationary corona. Figure 3 shows a transition from a non-stationary corona between concentric spheres to a stationary regime. The current was numerically calculated for various rise times of the voltage, t_f. The shorter is t_f, the higher is the peak current.
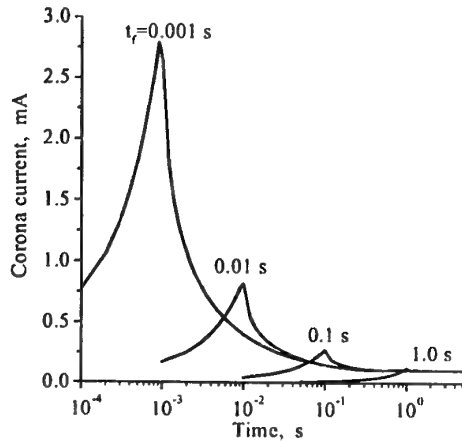
Fig. 2. The transient corona current in the gap between concentric spheres for $r_0 = 1$ cm and $R_0 = 5$ m. The voltage rises linearly up to 300 kV at $0 < t < t_f$ and is constant at $t > t_f$.

Expressions similar to (1) were obtained also for the case of coaxial cylinders and for the case of an emitting plane. (The latter one simulates a corona ignited in a thundercloud electric field near tips of trees, bushes or buildings distributed over a large area of the earth surface.)

The analysis of the results shows that the dependence of the current of a non-stationary corona upon the mobility μ of charge carriers is weaker than that of the current of stationary corona. For a well developed non-stationary corona and at a given instant, we have $i \sim \mu^{1/2}$ for spherical electrodes, a weaker dependence ($i \sim \ln(\mu^{1/2})$) for coaxial cylindrical electrodes and no μ - dependence for plane electrodes.

For each electrode geometry there exists a critical shape of applied voltage (or that of the external field in the plane case) at which the corona current is time-independent. This occurs at $U \sim t^{1/3}$ in the spherical case and at $E_0 \sim t$ in the plane case; the cylindrical case is intermediate between the spherical and plane cases. If U increases in time faster, the corona current also increases; if U increases slower, the current decreases in time.

The density of corona current from coronating earth's surface is controlled by the evolution in time of a thundercloud electric field above the space charge layer rather than by electric field at ground level.

4. Effect of aerosol ions

The characteristics of a corona discharge initiated in a thundercloud electric field near grounded objects can be effected by the formation of aerosol ions [3]. In order to estimate the effect, we numerically simulated the properties of a non-stationary corona developed from an isolated spherical anode of radius $r_0 = 10$ cm by taking into account aerosol ions. Our kinetic model for ions was similar to that used in [3]. Figure 3 shows the calculated radial distributions of the densities of light and aerosol ions at $t = 60$ s when the ion cloud radius reached 120 m. Aerosol ions are important only at large distances from the electrode at which the total ion density drops down to the initial density of neutral aerosol particles, $N_{a0} \sim 10^5$ cm^{-3}.
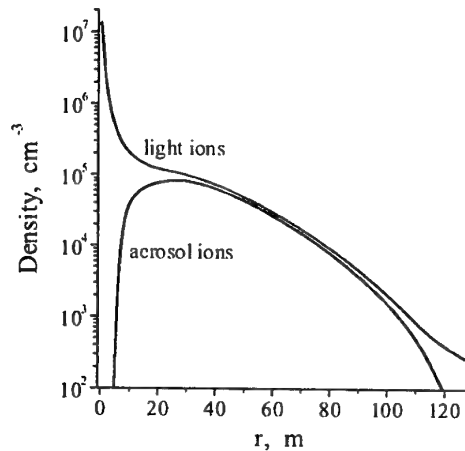
Fig. 3 The radial distributions of the densities of light and aerosol ions around a solitary sphere of radius 10 cm at $t = 60$ s. The voltage rises linearly up to 4 MV for 30 s and is constant at $t > 30$ s.

5. References

[1] N. Aleksandrov, E.M. Bazelyan, R.B. Carpenter et al, *J.Phys. D: Appl.Phys.*, **34** (2001) 3256.
[2] E.M.Bazelyan, Elektrichestvo, **6** (1990) 60.
[3] S. Chauzy and C. Rennela, *J. Geophys. Res.*, **90** (1985) 6051.

Non-stationary corona around multi-electrode system in external electric field

N.L.Aleksandrov, E.M.Bazelyan[*], R.B.Carpenter[**], Jr., M.M.Drabkin[**], and Yu.P.Raizer[***]

Moscow Institute of Physics & Technology, 141700 Dolgoprydny, Moscow region, RUSSIA
[*]Krzhizhanovsky Power Engineering Institute , 117927 Moscow, RUSSIA
[**]Lightning Eliminators & Consultants, Inc., USA
[***]Institute for Problems in Mechanics, Russia

A non-stationary corona in which the front of space charge has not bridged the gap is studied by considering a multi-electrode equipotential system in an unsteady electric field. Onset electric field and the evolution in time of discharge characteristics (discharge current, injected space charge, etc.) are numerically calculated versus the distance between electrodes. Conditions are obtained that corona near a real multi-electrode system can be simulated by charge emission from a plane in an electric field exceeding some threshold.

1. Introduction

A corona discharge developed from a system of closely-spaced equipotential electrodes occurs under natural conditions (point discharges at the tips of trees, bushes, leaves, grasses and other sharp objects under thunderstorm conditions) and in engineering practice.
A plane which emits ions in an unsteady external electric field exceeding some threshold, $E_{0\ cor}$, can be considered as a limiting case of a real plane system with numerous identical coronating points. Such an emitting plane has the following unique properties. (i) The current density through the plane, j, is controlled only by the rise rate of an external electric field E_0 ($j = \varepsilon_0 \partial E_0 / \partial t$, where ε_0 is the gas permittivity) and is independent of the ion mobility. (ii) Space charge injected into the gap from a unit plane area cannot be higher than $\sigma_{max} = \varepsilon_0 E_{0\ max}$, where $E_{0\ max}$ is the maximum external electric field. (iii) Due to charge injection, the electric field on the plane is maintained at a constant level equal to the onset threshold $E_{0\ cor}$.
The purpose of this work is to determine conditions that a corona ignited near a real multi-electrode system in an unsteady external electric field behaves similarly to an emitting plane.

2. Computer model

A large number (>5000) of identical electrodes are assumed to be uniformly distributed over a conductive plane. Each electrode, being a grounded hemisphere of radius r_0, is placed at height h above the plane. The distance between adjacent electrodes is D. The effect of the charge of grounding conductor is neglected in calculating the electric field and corona characteristics; that is, the conductor is assumed to be infinitely thin. A corona is ignited in a uniform electric field $E_0(t)$.
The discharge is described by the balance equations for the ion densities and Poisson's equation. The boundary condition is that the electric field near the coronating surfaces is equal to corona onset field. Light molecular ions and aerosol ions are considered; their mobilities and rate of ion conversion are taken from [1]. The initial density of neutral aerosol particles is assumed to be 10^5 cm^{-3}.
Our calculations include two steps: the determination of onset external electric field and calculation of corona characteristics.

3. Conditions for corona ignition

The external electric field $E_{0\ cor}$ in which a corona is ignited near the electrode tops depends on the ratios h/r_0 and D/h. Our calculations show that the onset field $E_{0\ cor}$ for the multi-electrode system is close to that for the solitary electrode at $D/h > 2$. The value of $E_{0\ cor}$ increases as the distance between electrodes decreases. This is explained by a screening effect of the charges located on adjacent electrodes. As a result, the onset field triples at $D/h = 0.25$.

4. Results

An external uniform electric field E_0 above the plane is assumed to rise linearly with a rate of 0.9 kVm^{-1}s^{-1} from an onset field of $E_{0cor} = 2.1$ kVm^{-1} for $0 < t < 20$ s and is constant for $t > 20$ s. Figure 1 shows the evolution in time of the corona current from a given electrode in the system for $h = 10$ m, $r_0 = 5$ cm and various D. Each curve is normalized to its own maximum corona current $I_{max} = i\ (t = 20$ s$)$.
In the case of a solitary hemispherically tipped electrode, the current of non-stationary corona must (i) increase linearly with time when E_0 rises linearly with time and (ii) decrease as $i \sim t^{-1/2}$ when E_0 is time-independent [2]. In figure 1, curve 1 shows that, at large ratios D/h, each electrode in the system behaves as a solitary electrode. In a multi-electrode system with small values of D/h, the corona current must (i) be constant when E_0 rises linearly with time and (ii)

decline steeply down to zero when E_0 is constant. Figure 1 shows that our calculations for small D/h correlate well with such an evolution in time of the current. Here, the calculated current rises only in the beginning until the ion clouds developed from individual electrodes unite into one common space charge layer. At intermediate D/h, the curves also behave in an intermediate way.
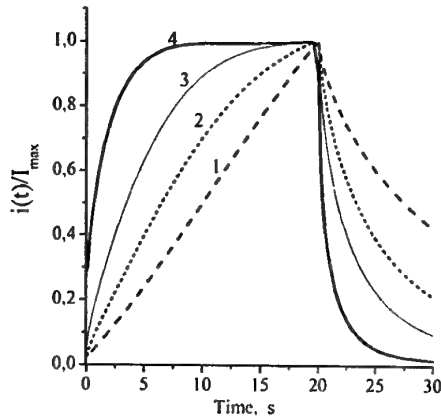
Fig. 1. The evolution in time of the corona current from a given electrode in the system with D/h = (1) 5, (2) 3, (3) 2, and (4) 1. The values of I_{max} correspond to 0.88; 3.53, 7.55; and 14.5 μA, respectively.

It is known that the injection of space charge into the gap leads to the electric field stabilization near a coronating surface. The same effect is likely near the plane covered with a large number of electrodes once the individual ion clouds have united into one plane space charge layer.

Figure 2 shows the evolution in time of the electric field on the plane under a given hemispherical electrode for various D/h. The front of space charge developed from any electrode tip covered distances of 35-40 m for 20 s. The electric field on the plane has not stabilized for D/h = 5, whereas this field stopped to rise and was close to $E_0{}_{cor}$ already at $t > 3$ s after the corona ignition for D/h = 1. Hence it follows that, under thundercloud conditions, the measurement of the electric field on the ground surface covered with numerous coronating points provides an information about the onset threshold for such a multi-point system rather than about the electric field strength of a thundercloud.

Unlike the case of a steady corona, the current of non-stationary corona is not proportional to the ion mobility μ. The more non-uniform is the undisturbed electric field in front of the expending space charge cloud the stronger is the effect of μ. For instance, an increase in μ by a factor of four must (i) lead to doubling the current in the case of a solitary spherical electrode [2] and (ii)
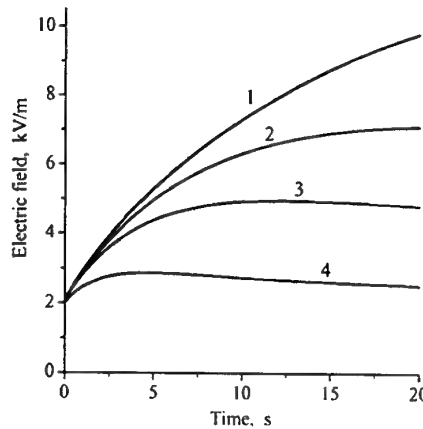
Fig. 2. The evolution in time of the electric field on the plane under a given hemispherical electrode for D/h = (1) 5, (2) 3, (3) 2, and (4) 1. The curves correspond to the same conditions as those in Fig. 1.

affect the current of a multi-electrode system only in the beginning of the process until the individual ion clouds unite into one space charge layer; thereafter, the current is independent of μ (j $=\varepsilon_0\partial E_0/\partial t$). Consequently, the effect of μ can vary in time, in agreement with results given in figure 3 which shows the ratio of the calculated corona currents at μ = 6.0 and 1.5 $cm^2V^{-1}s^{-1}$. The calculations were made for a solitary electrode and the electrode system with D = 10 m.
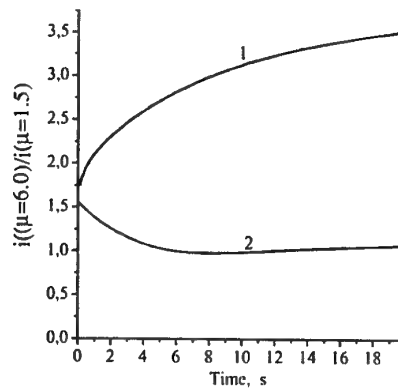
Fig. 3. Ratio of the calculated corona currents at μ = 6.0 and 1.5 $cm^2V^{-1}s^{-1}$. The calculations were made for (1) a solitary electrode and (2) the electrode system with D = 5 m.

5. References

[1] S. Chauzy and C. Rennela, *J. Geophys. Res.*, **90** (1985) 6051.

[2] N. Aleksandrov, E.M. Bazelyan, R.B. Carpenter et al, *J.Phys. D: Appl.Phys.*, **34** (2001) 3256.

22

Investigation of a pulsed positive corona in multipoint-to-plane configuration

M. Magureanu, N. B. Mandache

National Institute for Lasers, Plasma and Radiation Physics
Str. Atomistilor, nr. 111, P.O.Box MG-36, Bucharest-Magurele, ROMANIA

A pulsed corona discharge of positive polarity, in multipoint-to-plane configuration was studied. The distance between pins was optimised for obtaining maximum discharge current at a given voltage. At constant voltage the frequency and amplitude of the current pulses are controlled by a self-triggered spark-gap switch.

1. Introduction

Corona discharges are non-thermal, chemically active plasmas, which receive considerable attention both in connection to their numerous applications [1], and also from a theoretical point of view [2,3].

The present investigation of a pulsed positive corona in multipoint-to-plane configuration is concentrated especially on the influence of the geometry and electrical circuit on the discharge characteristics.

2. Experimental arrangement

The experimental arrangement is shown in Fig. 1. In a cylindrical discharge chamber, the high voltage electrode, consisting in an array of tungsten pins, with 100 μm tip diameter, is placed at approximately 40 mm above a grounded circular grid.
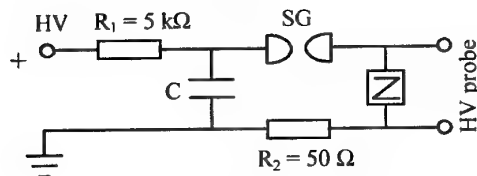
Fig. 1. Experimental set-up

The voltage generator supplies up to 30 kV, charging the capacitor $C = 1$ nF, which is discharged by means of a self-triggered spark-gap switch (SG). The discharge voltage was measured by a high voltage probe (Tektronix P6015, $R_p = 100$ MΩ) and the discharge current was determined from the voltage fall on a 50 Ω resistor in series with the grid electrode. The voltage and current waveforms are monitored by an oscilloscope (Tektronix TDS 320). The radiation emitted by the plasma is collected by an optical fiber and monitored with a photomultiplier.

The experiments were performed at atmospheric pressure; a fan was used to produce a continuous flow of air through the discharge chamber.

3. Results and discussion

3.1. Single point to plate configuration

Typical voltage and current waveforms are shown in Fig. 2, for a single pin as high voltage electrode, at 24 and 28 kV applied voltage.
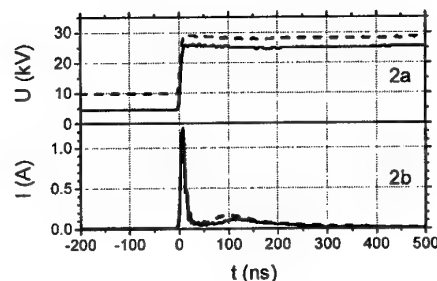
Fig. 2. Typical voltage (2a) and current (2b) waveforms

The rise time of the voltage (10 to 90%) is 7-8 ns, and the voltage rise rate is approximately 2 kV/ns.

The first current peak is a displacement current, which charges the capacitance of the electrode system. This total geometrical capacitance, determined by fitting the calculated dV / dt to the first current peak, is ~1 pF.

The real discharge current is the second, smaller peak, which is confirmed by the temporal correspondence with the radiation emitted from the plasma.

Increasing the applied voltage leads to an increase in current and to a decrease of the time interval between the displacement current and the discharge current. This time interval is connected to the inception probability, which is higher for higher applied electric fields [4]. An increase of the voltage leads also to higher repetition frequency of the pulses, from 450 Hz at 24 kV to 900 Hz at 28 kV. The frequency is controlled in addition by the spark-gap switch operation.

3.2. Influence of the number and position of pins

Adding a second pin leads to an increase of the discharge current. However, if the pins are placed very close to each other, the current remains similar to the value for a single pin. This behavior is most likely due to interactions of the electric fields near adjacent pins. Simulations of pulsed corona in wire-plate configuration [5,6] predict also interference effects on the electric field distributions near neighboring wires, consisting in the reduction of the electron density and electric field in the streamer head, as the spacing between wires decreases.

In the present experiments, the distance between the two pins was varied from 3 to 24 mm. At constant applied voltage (28 kV), the current increases linearly from 190 to 280 mA when increasing the spacing

between pins from 3 to 10 mm, and remains around 250 mA for distances longer than 10 mm.

Fig. 3 shows the discharge current as a function of the number of pins, at 28 kV applied voltage and a distance between adjacent pins of 10 mm.
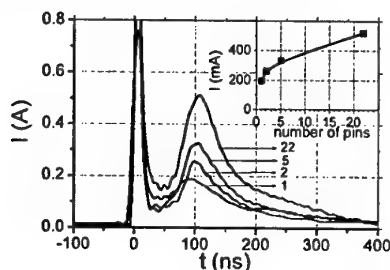
Fig. 3. Discharge current vs. the number of pins

The current is higher as the number of pins increases, reaching more than 500 mA for an array of 22 pins. The maximum number of pins used was limited by the dimensions of the discharge chamber and the optimum spacing between pins. Therefore, in the following experiments this array of 22 parallel pins, placed at 10 mm from each other was used as high voltage electrode.

3.3. Influence of the gap length of the switch

Fig. 4 shows the discharge current waveforms at constant applied voltage (28 kV) for three values of the gap length of the spark-gap switch: $d_{SG} = 3,5$ and 7 mm, and also the average current as a function of voltage.
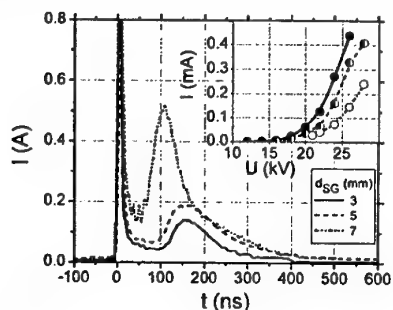
Fig.4. Discharge current waveforms for U = 28 kV and current-voltage characteristics for $d_{SG} = 3, 5, 7$ mm

For small gap lengths of the switch, the discharge current is relatively low (140 mA) and increases to more than 500 mA when increasing the gap length to 7 mm. However, the average current is higher for smaller gap lengths at constant applied voltage. This is due to the higher repetition frequency of the pulses for small gap length (1400 kHz, for $d_{SG} = 3$ mm and U = 24 kV) as compared to longer gap lengths (450 Hz, at $d_{SG} = 7$ mm) at the same voltage.

Fig. 5 shows the voltage waveforms on a long time scale for $d_{SG} = 3$ and 7 mm at 24 kV. For the small gap between the electrodes of the switch, a relatively low potential difference between them (~15 kV) is sufficient for breakdown, while the necessary voltage drop for the

longer gap length is higher (22-23 kV). Since the time constant of the voltage decrease after the breakdown is the same, the repetition frequency of the pulses is higher for small gap lengths as compared to the frequency corresponding to longer gaps.
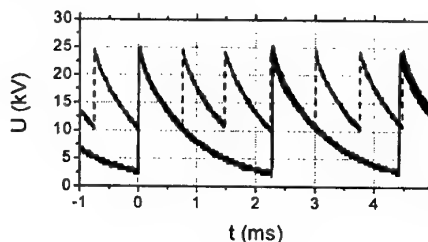
Fig. 5. Voltage waveforms for $d_{SG} = 3$, 7 mm and 24 kV

For small gap lengths, the corona high voltage electrode stays continuously at 10-11 kV, over which the pulses are superimposed. In these conditions, the lower values of the discharge current could be due to the lower amplitude of the voltage pulses.

4. Conclusions

The electrical characteristics of a pulsed multipoint-to-plane positive corona discharge were studied.

In the multipoint configuration the discharge current is higher as compared to the single point corona. Another advantage, especially for plasma-chemical applications, is the significantly higher active volume of the multipoint discharge: almost the entire cross section of the discharge chamber is filled with plasma.

Both the position and the number of pins used as high voltage electrode influence the characteristics of the discharge. The discharge current is higher as the number of pins is increased. Small distances between adjacent pins cause interactions between simultaneously propagating streamers due to changes in the electric field distribution near the pins, therefore the optimum spacing, where this interference effect ceases, was found to be 10 mm.

The functioning of the spark-gap switch determines the repetition frequency and the amplitude of the current pulses, at constant applied voltage, therefore the gap length of the switch is an important parameter in this configuration.

References

[1] J.-S. Chang, P. A. Lawless and T. Yamamoto, IEEE Trans. Plasma Sci. **19** (1991) 1152

[2] J. Chen and J. H. Davidson, Plasma Chem. Plasma Process. **22** (2002) 1

[3] A. A. Kulikovsky, IEEE Trans. Plasma Sci. **25** (1997) 439

[4] E. M. van Veldhuizen and W. R. Rutgers, J.Phys. D: Appl. Phys. **35** (2002) 2169

[5] Y.-H. Kim and S. H. Hong, IEEE Trans. Plasma Sci. **30** (2002) 168.

[6] G. V. Naidis, J. Phys. D: Appl. Phys **29** (1996) 779

Spontaneous Branching of Anode-Directed Discharge Streamers: Conformal Analysis and Numerical Results

U. Ebert[1,2], B. Meulenbroek[1], C. Montijn[1], A. Rocco[1], and W. Hundsdorfer[1]

[1]CWI, P.O.Box 94079, 1090 GB Amsterdam, The Netherlands

[2]Dept. Physics, TU Eindhoven, 5600 MB Eindhoven, The Netherlands

We recently have identified a simple mechanism of spontaneous streamer branching [1, 2]. Here we discuss when this instability occurs, we present new numerical results, and we present a reduced model in which the instability can be studied analytically.

1. Observations and minimal model

Discharge streamers appear in the initial stages of natural sparking as well as in many plasma reactors. Streamers also play a role in the recently observed upwards sparking from clouds towards the ionosphere [3]. Frequently streamers do branch.

It is generally accepted that the properties of streamers are determined by space charge effects. Space charges enhance the field at the rapidly propagating head of the ionized streamer channel and create an active ionization zone that now can be visualized by fast CCD cameras [4].

We investigate the **minimal model** for anode-directed streamers in a non-attaching and non-ionized gas. It is a "fluid model" with impact ionization in local field approximation, with drift and diffusion of charged particles between abundant neutral particles, and with space charge effects through the Coulomb equation of electrostatics. In dimensionless units [1, 2], the model for electron density σ, ion density ρ and electric potential Φ has the form:

$$\partial_t \, \sigma - \nabla \cdot (\sigma \, \mathbf{E} + D \, \nabla \sigma) = \sigma \, |\mathbf{E}| \, \alpha(|\mathbf{E}|) \, ,$$
$$\partial_t \, \rho = \sigma \, |\mathbf{E}| \, \alpha(|\mathbf{E}|) \, ,$$
$$\rho - \sigma = \nabla \cdot \mathbf{E} \quad , \quad \mathbf{E} = -\nabla \Phi \, ,$$

where $\alpha(|\mathbf{E}|)$ in our numerical work is approximated by the Townsend expression $e^{-1/|\mathbf{E}|}$.

2. Two transitions, the Firsov limit

The avalanche-to-streamer-transition is a classical concept, it occurs when the space charge $\rho - \sigma$ is not negligible anymore. In the streamer phase, the interior of the ionized channel is screened from the externally applied field, the field at the active head is enhanced. This field enhancement makes the streamer propagate more rapidly than the avalanche.

In our recent numerical evaluation of the minimal model [1, 2], we applied an external field twice as high as previous authors [5]. Ionization gradients were much steeper and the field enhancement much stronger, and the streamer splitted spontaneously. We interpret this as a second "transition": the streamer head accumulates enough charge to approach the limit of "ideal conductivity" according to

the old concept of Lozansky and Firsov [6]. However, the simple parabolic front shape solution [6] found for the "ideally conducting" streamer at the time is just one possible solution of the problem. Actually, we show that the head dynamics of a streamer in this limit can be surprisingly rich, and that branching is a generic instability:

3. Head dynamics of Firsov-streamers

3.1 Numerical results, adaptive grid

Spontaneous streamer branching was found in the numerical studies of M. Arrayás, A. Rocco, W. Hundsdorfer and U. Ebert [1, 2]. This work is presently being extended by C. Montijn, W. Hundsdorfer and U. Ebert. Specifically, an adaptive grid for the ionized regions has now been implemented which allows for finer grid spacing and more rapid calculations. The numerical discretization has been reinvestigated, and a larger parameter range is presently being tested. We will present our state of the art.

3.2 Analytical approach, conformal mapping

The simplest sketch of the dynamics of our Firsov streamers consists of the following building blocks: the interior of the streamer is equipotential, its boundary moves everywhere with a local velocity $\mathbf{v} = \mathbf{v}(\mathbf{E})$ where $\mathbf{E}$ is the local field, and the exterior is non-ionized and charge-free, so $\nabla^2 \Phi = 0$. The field $\mathbf{E} = -\nabla \Phi$ far from the streamer is specified; we presently consider the case where this far field is constant.

The problem of a moving boundary of arbitrary shape in 2 dimensions can be reduced to a one-dimensional problem by conformal mapping methods. Such methods have been developed previously for the study of interfacial instabilities in two-fluid-flow, the so-called Saffman-Taylor problem. With the last simplification of $\mathbf{v}(\mathbf{E}) \propto \mathbf{E}$, the complex dynamics of the ionization boundary in some cases can be solved even fully analytically. We present the solutions recently found by B. Meulenbroek, A. Rocco and U. Ebert. They reproduce the transients and the branching instability as observed in the numerical solutions.

4. References

[1] M. Arrayás, U. Ebert, W. Hundsdorfer, Phys. Rev. Lett. **88**, 174502 (2002); accompanied by Nature: http:www.nature.com/nsu/020408/020408-4.html, and by Phys. Rev. Focus: http://focus.aps.org/story/v9/st19.

[2] A. Rocco, U. Ebert, W. Hundsdorfer, Phys. Rev. E **66**, 035102(R) (2002).

[3] V.P. Pasko, M.A. Stanley, J.D. Mathews, U.S. Inan, T.G. Wood, Nature **416**, title page and p. 152-154 (2002).

[4] E.M. van Veldhuizen, P.C.M. Kemps, W.R. Rutgers, IEEE Trans. Plasma Sci. **30**, 162 (2002); E.M. van Veldhuizen, W.R. Rutgers, J. Phys. D: Appl. Phys. **35**, 2169 (2002).

[5] P.A. Vitello, B.M. Penetrante, and J.N. Bardsley, Phys. Rev. E **49**, 5574 (1994).

[6] E.D. Lozansky and O.B. Firsov, J. Phys. D: Appl. Phys. **6**, 976 (1973).

Comparison of Experimental Measurements and Theoretical Description for Cathode-Directed Streamer

S Pancheshnyi, M Nudnova, D Opaits, A Starikovskii

Moscow Institute of Physics and Technology, Dolgoprudnyi, Russia, e-mail:pon@neq.mipt.ru

At this work complex study of positive streamer development in N_2/O_2 mixtures at pressure range 0.1–2.0 atm has been performed. Experimental measurements of streamer discharge dynamics have been compared with direct numerical simulation within the scope of 2D hydrodynamics approach. Self-consistent analytical model that allows with the use of known potential of the high-voltage electrode to obtain associated values of the streamer parameters was developed and verified.

1. Experimental Setup

Discharge section comprises cube chamber 20x20x20 cm. There is a possibility to pump up to 10^{-2} torr and to heat the chamber. Special optical windows are made of quartz to register optical emission in a wavelength range of 190-600 nm. A rotating-interrupter generator was used as a pulsed voltage supply. The high-voltage pulses were fed through a coaxial electric cable to the high-voltage connector of the discharge system. Repetitive frequency of the high-voltage pulses was 1.2 kHz, voltage amplitude in the cable was 15 kV, high voltage pulse on the half-height was 50 ns. A calibrated back-current shunt placed in the break of the shield of the feeding coaxial cable was used to control electrical parameters of the pulses. The emission spectroscopy technique was used to analyze a cathode-directed streamer discharge. The densities of excited molecules were determined and the reduced electric field in the streamer head was estimated [1].

2. Direct Numerical Simulation in 2D Geometry

Streamer discharge modeling was performed for pure N_2 and it mixtures with O_2 at different pressures at positive voltage up to 100 kV and interelectrode distance up to 20 cm. The modeling was performed in the hydrodynamic approximation for 2D geometry [2]. Numerical model considered balance equations for charged particles:

$$\frac{\partial n_e}{\partial t} + \text{div}\,(\vec{v}_e \cdot n_e) = S_{ion} + S_{photo} - S_{rec}$$
$$-S_{att} + S_{det}$$
$$\frac{\partial n_p}{\partial t} = S_{ion} + S_{photo} - S_{rec}$$
$$\frac{\partial n_n}{\partial t} = S_{att} - S_{det}$$

Here n_e, n_p and n_n – densities of electrons, positively and negatively charged ions, $\vec{v}_e$ – drift velocity in a local electric field $\vec{E}$, S_{ion}, S_{photo}, S_{rec}, S_{att} and S_{det} – rates of ionization, photoionization, electron-ion recombination and electron attachment/detachment

respectively. Electric field distribution $\vec{E}$ in the gap was calculated by Poison's equation:

$$\vec{E} = -\nabla\varphi$$
$$\Delta\varphi = -\frac{e}{\varepsilon_0}(n_p - n_e - n_n)$$

3. Analytical Description

In [2] on the base of theoretical investigation and numerical modeling of streamer discharge in 2D geometry an analytical model of the cathode directed streamer head was proposed. The model allows us, with the use of known streamer head potential, to obtain values of the head radius and peak electric field in the head. According to the model, electron flux into the streamer channel is to be compensated by a flow of intensively multiplying electrons from the pre-ionization region in front of the streamer head.

4. Acknowledgments

[1] S.V. Pancheshnyi, S.V. Sobakin, S.M. Starikovskaya, A.Yu. Starikovskii *Discharge Dynamics and the Production of Active Particles in a Cathode-Directed Streamer* // Plasma Physics Reports **26** (2000) 1054.

[2] S.V. Pancheshnyi, S.M. Starikovskaia, A.Yu.Starikovskii *Role of Photoionization Prosesses in Propagation of Cathode-Directed Streamer* // Journal Physics D: Applied Physics **34** (2001) 105.

Mechanism of Negative Corona Pulses in CO_2 - SF_6 Mixtures

A.Zahoranová, M. Simor, D. Kovácik and M. Cernák

Faculty of Mathematics, Physics, and Informatics,Comenius University, Mlyn. dolina F2, 842 48 Bratislava, Slovakia

Abstract
Current waveforms of first negative corona pulses have been measured in CO_2-SF_6 mixtures over a pressure range extending from 6.65 kPa to 50 kPa and various overvoltages. Effects of changing cathode secondary electron emission were studied using a copper cathode coated by CuI and graphite. The results indicate a positive-streamer discharge mechanism and important role of field emission processes at pressure above 30 kPa.

1. Introduction

Mixtures of SF_6 with other less expensive gases such as air, N_2 and CO_2 are extensively investigated as a cheaper and environmentally attractive option to pure SF_6. Also, comparing to pure SF_6, there are indications of the superior dielectric characteristics of these mixtures in non-uniform field conditions and in the case of projection-initiated breakdown. Since in these conditions the breakdown criteria often can be interpreted as the negative corona-onset voltage [1,2,3], it is apparent that a better understanding of the negative corona mechanism in SF_6 and the SF_6 containing mixtures can help to optimize their insulation performance.

In a recent series of papers [4,5] it has been concluded that in air-SF_6 and N_2-SF_6 mixtures containing less than approximately 10 % of SF_6 the negative corona pulse is associated with the formation of a cathode-directed streamer-like ionizing wave in the immediate vicinity of the cathode [6]. However, in the mixtures containing more than 10 % of SF_6 the ionizing wave was quenched and, consequently, the discharge was governed by the Townsend ionization mechanism fed by cathode γ_p - emission processes. This work is now being extended to study the negative corona pulse mechanism in CO_2-SF_6 mixtures.

2. Experimental results and discussion

The point-to-plane electrode system consisted of a hyperbolically capped Cu-cathode with a value of tip curvature radius of 0.1mm situated 12 mm from a planar stainless steel anode. The experimental set-up and procedure were similar to those given in Refs. [4,5]. To clarify the role of γ_p – emission processes, copper iodide and graphite, which have exceptionally high and exceptionally low photoelectric yields, respectively, were used as alternative cathode surface materials to cooper [4,5,7,8].

Figure 1 shows the first corona current pulses measured in CO_2-SF_6 at a pressure of 6.65 kPa for the SF_6 percentage varied from 0% to 30%. From Fig.1 it is apparent that increasing the SF_6 content a more significant reduction in the step height on the pulse leading edge than in the pulse maximum was observed, which is in contrast to the observed discharge behaviour in SF_6 with N_2 and air mixtures [4,5].
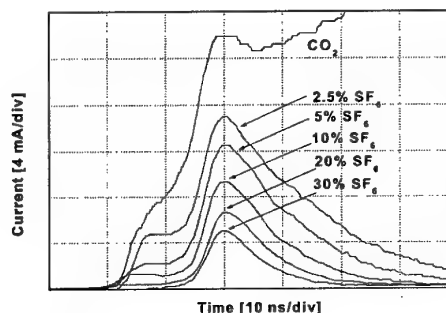
Fig. 1: Current pulse waveforms taken for various SF_6 admixtures at a gap voltage value of 3 kV and a pressure of 6.65 kPa.
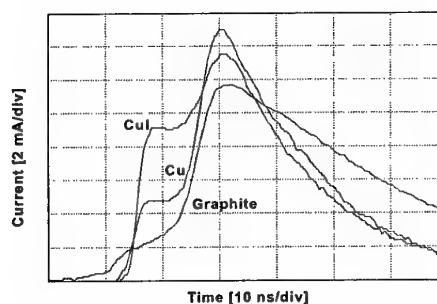
Fig. 2: First negative corona pulses measured using the Cu-cathode, the CuI-cathode and the graphite-coated cathode for CO_2 at a pressure of 6.7 kPa with 2.5% SF_6 at gap voltage value of 3 kV.

Figure 2 compares the first corona pulses measured at a pressure of 6.7 kPa using the copper cathode, CuI-coated cathode, and graphite-coated cathode for 2.5% of SF_6. The observed sensitivity of the step height and relative insensitivity of the pulse maximum to the changing the cathode γ_p – emission, which are identical with the discharge behaviour observed in SF_6-air and SF_6-N_2 mixtures [4,5], are also in a good agreement with the above mentioned streamer-based hypothesis for the discharge mechanism [6].

The first corona current pulses measured in CO_2-SF_6 at a pressure of 50 kPa for SF_6 content varied from 0% to 30% are shown in Figs. 3(a)-(b).
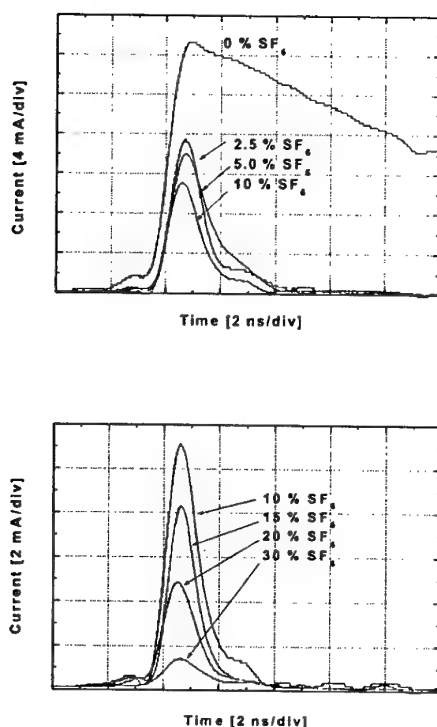
Fig. 3: Current pulse waveforms taken at a gap voltage value of 5 kV and a pressure of 50 kPa for SF_6 admixtures (a) 0%-10%; (b) 10%-30%.

At a pressure of 50 kPa the step on the pulse leading edge in pure CO_2 is less discernible than at 6.67 kPa apparently due to an increased collisional quenching of photon-emitting excited states and absorption of photons in the gas. The decrease may also be due to increased electron attachment near the cathode surface [9].
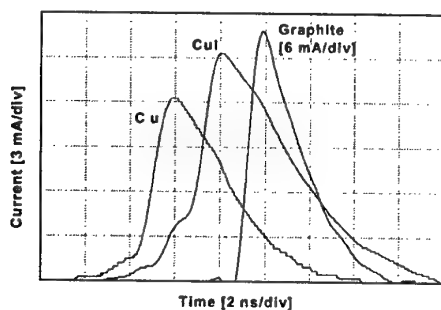
Fig. 4: First negative corona pulses measured using the Cu-cathode, CuI-coated cathode, and graphite-coated cathode at a pressure of 50 kPa in CO_2 + 2.5% SF_6, and at gap voltage value of 5.5 kV.

Figure 4 exemplifies the effects of changing of the cathode γ_p - emission using 2.5% of SF_6 and gap voltage of 5.5 kV, where the step on the pulse leading edge was

clearly seen. In a close correspondence with the results shown in Fig. 2 and with the streamer-based hypothesis the graphite coating led to a dramatic reduction of the step on leading edge, while the CuI coating led to a well pronounced increase of the step. However, in a contrast to the results measured at a reduced pressure of 6.65 kPa, at 50 kPa the graphite coating resulted in a marked increase of the pulse magnitude. The observed effect of the graphite cathode coating observed at higher gas pressures is the same as that studied in more detail in work [5] for the discharge in N_2-SF_6 mixtures. On this base, and in line with the recent studies of other authors [10-12], we hypothesize that this effect can be an indication that with increasing gas pressure and consequently increasing gap voltage the field emission becomes to play an important role in the discharge mechanism.

3. Conclusions

The above results interpreted in terms of the streamer-based hypothesis suggest that the effect of adding SF_6 to CO_2 was primarily to quench the Townsend multiavalanche ionization processes, while the effect on the positive streamer ionization processes was much less pronounced. This is in contrast to our results obtained in similar experimental conditions in air-SF_6 and N_2-SF_6 mixtures [4,5], where the observed effect was opposite. One may therefore speculate that the stronger streamer quenching in N_2-SF_6 mixtures, and the resulting more efficient corona stabilization effects can be responsible for higher dc breakdown voltages measured at pressures less that 0.2 MPa in N_2-SF_6 mixtures, comparing to those measured in CO_2-SF_6 mixtures [13].

References
[1] A. H. Cookson, *Proc. IEE*, Vol. A **128** (1981) 303
[2] P. Espel, A. Gilbert, P. Domens, G. Riquel and J. Paillol, *Proc. XIII Int. Conf. on Gas Discharges and their Applications (University of Strathclyde, Glasgow, 3-8 September 2000)* ed S J MacGregor (2000)381
[3] W. Pfeiffer, D. Stolz, and J. Wolf, *Proc. 9th Int. Conf. Gas Discharges and their Applications (Venezia 1988)* 315
[4] J. Kúdelcík, A. Zahoranová, K. Choma, M. Cernák *Contr. Plasma Phys.* **42** (2002) 546
[5] A. Zahoranová, J. Kúdelcík, J. Paillol and M. Cernák, *J. Phys. D : Appl Phys* **35** (2002) 762
[6] M. Cernák, T. Hosokawa, and I. Odrobina, *J. Phys. D* **26** (1993) 607
[7] M. Cernák and T. Hosokawa, *Austral.. J. Phys* **45** (1992)193
[8] M. Cernák, T. Hosokawa, S. Kobyashi and T. Kaneda *J. Appl. Phys.* **83** (1998) 5678
[9] R. V. Hodges, R. N. Varney and J. F. Riley *Phys. Rev. A* **31** (1985) 2610
[10] T. Reess and J. Paillol *J. Phys D* **30** (1997) 3115
[11] P. Espel, J. Paillol, T. Rees, A. Gilbert and P. Domens, *J. Phys. D* (2002) **35** 318
[12] J. Paillol, P. Espel, T. Reess, A. Gilbert and P. Domens J. *Appl. Phys.* **91** (2002) 5614
[13] Y. A. Safar, N. H. Malik and A. H. Qureshi *IEEE Trans. on El. Ins.* EI-17 (1982) 441

Synchronized Generation of Positive Surface Streamer Discharge in Atmosphere

Yasuhide Kashiwagi,   Masakuni Chiba,   Haruo Itoh,
Kisarazu National College of Technology   The University of Tokyo Chiba Institute of Technology

Under certain conditions, streamers are generated simultaneously from two electrodes on the same plane. The synchronization is found to be produced by light emitted from the first streamer. Not only the light of the UV region, but also VUV, is effective.

1. Introduction

Lichtenberg figure method has been used for studies on surface discharge since its development in 1777. With this method, Pedersen [1] described synchronized generation of surface discharges using five electrodes on an insulator surface. After that, studies on surface discharge continued, but it would seem that the synchronization mechanism remains unclear. Recently, Chiba et al. [2] demonstrated that the cause of synchronization between two streamers which started from two different electrodes in parallel connection is attributable to the initial electron emitted from the insulator surface by illumination from the first streamer.

We have also examined the relationship of synchronization mechanisms of streamers and energy of photons radiated from the first streamer. It is considered that the phenomenon includes some important processes as the supply of initial electron: not only surface discharge, but also barrier discharge [3]. In particular, barrier discharge is a frontier of recent discharge plasma technology for development of a practical apparatus.

2. Experimental Procedure

Figure 1 shows a front view of the experimental setup. Standard lightning impulse voltage (1.2/50 μs) which has several tens of kilovolts peak value was applied to the parallel connected electrodes. The two electrodes were placed on an insulator plate made of acrylic resin. It is a square plate of side 300 mm and thickness 10 mm and has an aluminum back electrode. The back electrode is also a square plate of side 350 mm and thickness 10 mm ; it is grounded through a resistor put on the shielded box. Both terminals of the resistor were connected to a digital waveform recording system. Current and applied voltage were recorded by the system simultaneously. Dust figures were obtained on the insulator plate using photocopier toner. Observations were repeated several tens to a hundred times according to demand. It was judged that the streamers were synchronized if only one or two streamers occurred within a 100 ns

interval in the current waveform. In that case, the obtained symmetrical dust figures had the same diameter as circles on the insulator plate. Probabilities of synchronization were determined for all experiments. A shading plate or an optical filter indicated by H in the figure was used to intercept discharge light or to limit the short side of wavelength of the light passing through a territory between the parallel electrodes, respectively. Several pieces of shading plate with different length or several optical filters were prepared for the purpose.

Figure 1   Experimental setup
A: Spherical Gaps,   B: Acrylic Resin Insulator,
C: Back Electrode,   D: Current Measuring System,
E: Insulator,   F: Metallic Bar, G: Voltage Divider,
H: Shading plate or Optical Filter

3. Results and Discussions

Without the shading plate, two streamers originated from both electrodes were synchronized with almost 100 % probability. The result is plotted by the open circle in Fig. 2. We call that synchronization of surface discharge. In contrast, if the shading plate was mounted on the middle point of the two electrodes, the probability of synchronization decreased remarkably to almost zero, as shown by the open triangles in the same figure. As length of the shading plate increased, probabilities decreased, as shown by the open squares in the same figure. Results suggest that the initial electrons emitted from an insulator near another electrode by illumination of the first streamer decrease with increase of the shortest
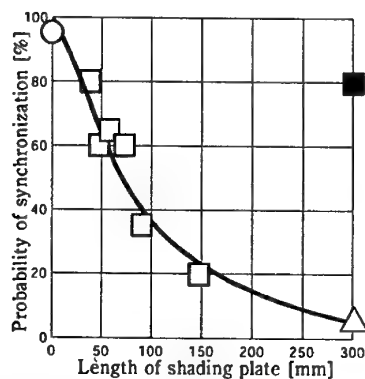
Figure 2
Probability of synchronization as a function of length of shading plate.
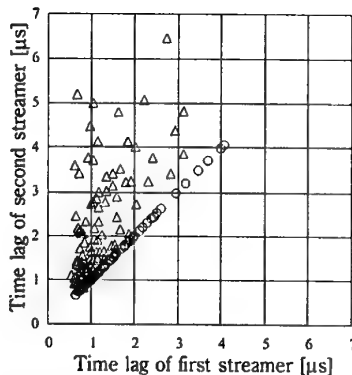
Figure 3
Time lags of first and second streamer.
Open triangle : With shading plate
Open circle : Without shading plate
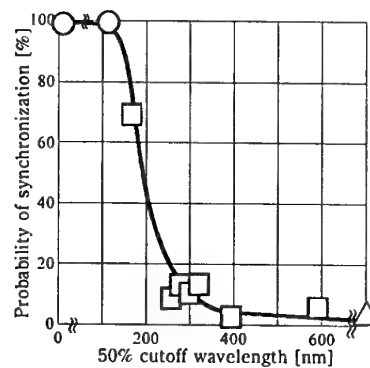
Figure 4
Probability of the synchronization as a function of cutoff wavelength of the filters

light pass along the surface of the insulator plate. Nevertheless, with the shading plate, the probability returned to above 80 %, as plotted by a closed square in the figure, when both electrodes were illuminated by ultraviolet light. UV is emitted from low-pressure mercury lamp that was fixed over the electrode system.

In the case where probability is approximately 100 %, the time lags of the first and second streamer are almost equal, as shown by the open circles in Fig 3. These time lags, which are observed in each current waveform of the one shot experiment, lie on a straight line in the graph. The horizontal axis of T_1 is a time lag of the first streamer; the vertical axis of T_2 is also a time lag of the second (another electrode) streamer from the origin of the applied impulse voltage to the electrodes, respectively. Cases of the open circles on the straight line as shown in the Fig. 3 correspond to plots indicated by the open circle in the Fig. 2. In contrast, the open triangle plots in the Fig. 3, i.e. T_2s become longer than T_1s give low synchronization probabilities, as shown by the open triangle in the Fig. 2.

It is supposed that UV light from the first streamers can introduce synchronization of surface streamers through the initial electron supply by the first streamers. Optical filters were used to investigate wavelength dependency of synchronization probability. Open circles of zero and 112 nm on the horizontal axis in Fig. 4 achieved 100 % probability of synchronization through one hundred times measurements without the shading plate and using an MgF2 filter, respectively. In cases where filter of 350 nm cutoff or longer were used, probabilities sharply decreased and reached almost zero. The plot indicated by an open triangle in Fig. 4 is the result with shading plate of 300 mm and shows the non-synchronization of streamers.

For cases where distances between electrodes were changed, a similar tendency to that in Fig. 2 was recognized by experiments.

It is considered that the short side of the wavelength against the light required for the generation of synchronization is about 250 nm. This value corresponds almost to 5 eV and is the minimum energy for photoemission from the insulator surface [4], [5]. Our results also satisfied the necessity of photo-ionization near the insulator surface and the photoelectron emission from the insulator surface for interpretation of progression of dust figures experimentally and through computer simulation [6].

4. Conclusions

In order to investigate the relationship between synchronization probability and the wavelength of light radiated from the first streamer, more detailed experiments than the experiments described in previous papers were performed. Results confirmed that UV and VUV from the first streamer induced synchronization between the two streamers. That is not only UV but also VUV, radiated from the first streamer triggers the second one.

References

[1] P. O. Pedersen, On the Lichtenberg Figures Part I. A Preliminary Investigation (1919) Andr, Fred, Høst & Søn, København
[2] e.g. M. Chiba, et al., The papers of technical meeting on Electrical Discharges, IEEJ, ED-92-114 (1992) (in Japanese)
[3] U. Kogelschatz, IEEE Trans. Plasma Sci. 30 (2002) 1400-1408
[4] Y. Gosho, M. Saeki, Jpn. J. Appl. Phys. 28 (1989) 1939
[5] M. Yumoto, T. Sakai, Trans. IEE Jpn. 109A (1989) 1-8 (in Japanese)
[6] M. Tanaka, Y. Murooka, K. Hidaka J. Appl. Phys. 61 (1987) 4471

Vacuum breakdown of sub-micrometer gap with pointed electrode

Y.Hirata*, K.Ozaki**, K.Fukatani*, T.Takenaka*, U.Ikeda*, and T.Ohji*

* Dept. of Adaptive Machine Systems, Graduate School of Eng., Osaka University

2-1, Yamada-oka, Suita, Osaka 565-0871, Japan

** National Institute of Advanced Industrial Science and Technology, Chubu

2266-98, Anagahora, Shimo-shidanmi, Moriyama-ku, Nagoya 463-8560, Japan

Vacuum breakdown of very small gap in the range of 30nm to 2f m, between a pointed cathode of thin tungsten wire and a plane anode of stainless steel, was experimentally investigated. The experimental setup, which consists of both electrodes and precise positioning mechanisms actuated by piezoelectric devices, was installed in scanning electron microscope (SEM). Breakdown voltage decreases with decrease of gap spacing and/or radius of curvature at the tip of cathode. Theoretical consideration shows that the evaporation from the anode surface heated by field emission current is dominant factor of triggering vacuum breakdown.

1. Introduction

Recently, various materials processing techniques have been actively developed in order to produce micro-machines and/or micro-robots used for medical instruments, sensors, inspection/repair of piping in nuclear power plants or chemical process plants, and so on. The silicon based micro-parts have been almost produced by means of a photolithography which is frequently used in fabrication of semiconductor ICs. On the other hand, the metal based parts have been shaped by LIGA process and/or focused ion beam (FIB) process. These precise processes are based on the material removing technique; photo-chemical reaction, laser ablation and ion beam sputtering.

However, a micro-joining technique, which includes welding and solid state bonding, will be surely required to produce or assemble more complex structure of the micro-parts. In order to carry out micro-welding successfully, heat power must be precisely controlled and concentrated on the microscopic area. Accordingly, in addition to laser and/or electron beam, of which the beam size can be focused or varied, micro-discharge is possible to be adopted as the heat source. Because the energy generated in the electric discharge partly flows into both of the cathode spot and the anode spot, which are very small regions formed on the surface of each electrode. The energy released from these local areas is spent on heating, melting and evaporation of the electrode material. The goal of the present research and development is to achieve micro-sized welding by use of discharge energy, which is 1/1000 scale-down compared with conventional welding as now practiced widely.

In this paper, in order to establish the discharge condition with a pointed electrode as the first step of micro-welding, vacuum breakdown of very short gap, between a pointed tungsten cathode and a plane stainless steel anode, was experimentally investigated. And the shape and the size of melting spots on the anode surface were also examined.

2. Experimental apparatus and procedure

The experimental setup mainly consists of the pointed tungsten cathode of 0.1 mm in diameter, the stainless steel plate anode, the electric circuit and the actuators for adjusting the gap length. The cathode tungsten is mounted on the piezoelectric device, which is used as a fine adjusting actuator that controls the gap length with the accuracy in the order of nanometer. The piezoelectric device is set on a positioning stage driven by pulse-motor, which is a coarse adjusting device. This experimental setup is installed in a SEM in order to carry out the *in-situ* observation of both electrodes before and after micro-discharge.

The shape of the electrode tip affects on the breakdown of the gap or the current distribution of the discharge. The use of the tip having a small radius of curvature increases the local electric field of the gap near the tip. And it may limit the area of electric current flow into the specimen surface. Accordingly, the tip of the tungsten wire is sharpened by electrochemically etching in the 10% NaOH solution. For the plane anode, the surface of stainless steel is buff-polished.

The following procedure was employed in the experiment. With the aids of SEM observation, the tungsten electrode was gradually brought nearer and then softly contacted with the anode surface by driving the actuators. This position was adopted as the origin of the distance for discharge gap spacing. And the gap length was adjusted and determined from voltage applied to the piezoelectric device.

3. Experimental results and discussions

Fig. 1 shows SEM images of both electrodes before and after electrical breakdown. As seen in Fig.1 (b), the melted area is formed at the specimen surface just under the tungsten electrode. This melted spot size seems to depend on the no-load voltage, the gap length and the shape of electrode tip.
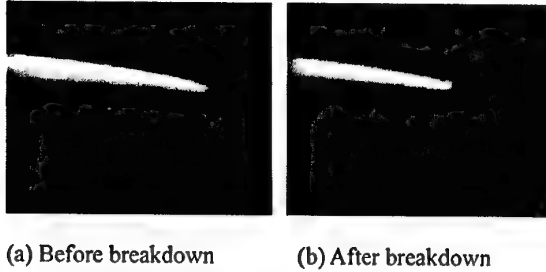
(a) Before breakdown   (b) After breakdown
Fig. 1 In-situ observation of both electrodes before and after the electrical breakdown.

Fig. 2 shows the relationship between the gap length and the breakdown voltage. When the curvature radius of the tungsten electrode tip is kept constant, the breakdown voltage decreases with decrease of the gap length, and goes down to about 20 volt at the gap length of 30nm. At the same gap length, the breakdown voltage increases with increase of the curvature radius. From the experimental results, the nominal field strength across the gap for the occurrence of breakdown gives the value in the range between $2 \cdot 10^8 \cdot 1 \cdot 10^9$V/m. Therefore, it is deduced that the field emission current from the cathode plays important roles for the initiation of breakdown.
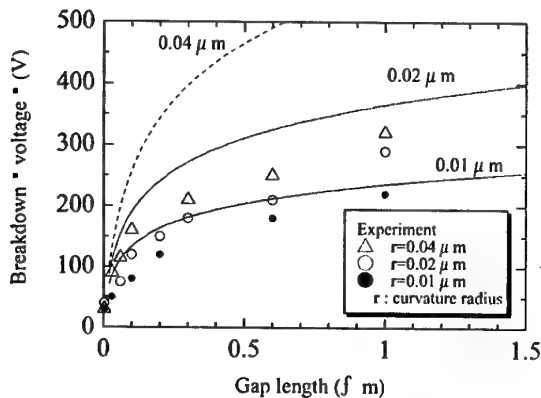
Fig. 2 Change of the breakdown voltage by the gap length between pointed cathode and plane anode in SEM vacuum environment.

Then, the field strength at each point of the electrode surface was calculated on the assumption that the electrode shape is axial symmetric. Next, the field emission current distribution was calculated using Fowler-Nordheim equation. The emitted electron is accelerated by the voltage applied between the cathode and the anode. So, the power density distribution at the anode surface can be calculated as shown in Fig. 3.
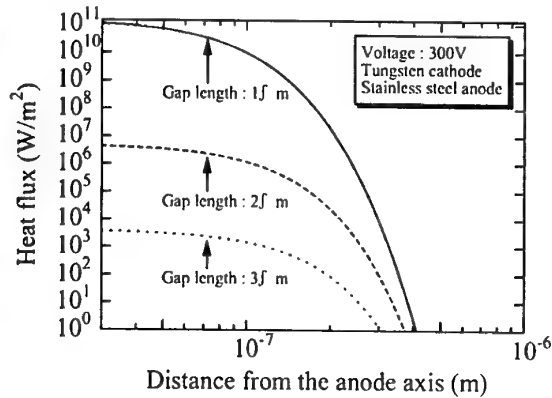
Fig. 3 Heat flux distribution at the anode surface by field emission current as a function of gap length.

As seen, the heat flux or the power density of emission current is concentrated within the radius of $0.1\int$ m and it greatly increases with decrease of the gap length. Accordingly, the very small area of anode surface is rapidly heated up. The temperature distribution at the anode surface can be obtained through the calculation of heat conduction. The solid line and dotted lines in Fig. 1 indicate the calculated results of the relationship between the gap length and the voltage applied, that the temperature of the anode surface reaches boiling point of stainless steel. The calculated voltage is higher than the experimental breakdown voltage, but it seems to be the measure of breakdown. Because the evaporation in vacuum occurs sufficiently at the temperature lower than boiling point. Therefore, the accelerated electrons from the cathode collide with the metal vapor and the avalanche-like accumulation of electrons and ions rapidly occurs in the gap, that is, the breakdown occurs.

4. Conclusions

(1) Vacuum breakdown of sub-micrometer gap between the pointed cathode and the plane anode is governed by the gap length and the curvature radius of cathode tip.
(2) The evaporation from the anode surface heated by the field emission current triggers the electrical breakdown.

Investigation of nonstationary modes of atmospheric pressure needle-to-plane gas discharge and streamer propagation

V. Golota, L. Zavada, B. Kadolin, V. Karas', I. Paschenko, S. Pugach and A. Yakovlev

Department of Nonequilibrium Lowtemperature Plasmachemistry,

National Science Center "Kharkov Institute of Physics and Technology",

Akademicheskaya St. 1, Kharkov 61108, Ukraine

The experimental investigation of current and radiation dynamics in nonstationary atmospheric pressure needle-to-plane gas discharge in dried air, ambient air and oxygen are presented.

1. Introduction

High-pressure needle-to-plain gas discharge is investigated with the purpose of its application in plasma-chemical reactors of ozone synthesis. It is known, that at atmospheric pressure in oxygen-contained gases a various modes of discharge can be realized in the needle-to-plane electrode geometry.

Investigations of nonstationary modes of atmospheric pressure needle-to-plane gas discharge with positive potential at the needle and streamer propagation were carried out. Both oscillograms of discharge current light emission from different cross-section of the gap and for various oxygen-contained gas mixtures (dried air, ambient air, oxygen) were studied.

2. Experiment

The experimental setup is showed in fig. 1. The needle-to-plane electrode system was located in the discharge chamber (volume 1 dm^3) with controlled gas feeding. The gas pressure was an atmospheric. The positive DC voltage was applied to the needle electrode. The discharge voltage was varied from 3 to 15kV.

There was a quartz window in the chamber for registration of the discharge radiation. The light-tight shield with 1 mm slit, which disposed transverse to the discharge channel, covered quartz window of the chamber. The moving of slit along discharge gap allowed obtaining the dynamics of light emission.

The radiation from the slit was focused by a quartzy condenser on an entrance slit of monochromator and then was registered by FEM. All dynodes were shunted by high frequency capacitors for correct measuring of short light pulses.

The discharge current and FEM's signals were displayed by double-channel oscilloscope Tektronix TDS-210. The current pulse from FEM was measured on the noninductive 50 Ω resistor. The discharge current was measured by the high frequency current probe using 75 ns delay line (for compensation of time delay between FEM's current signal and a light pulse).
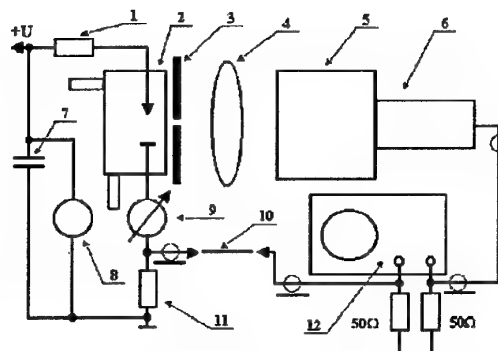
Fig. 1. Experimental setup. 1 – ballast resistor 100 κΩ, 2 – discharge chamber, 3 – shield with 1 mm slit, 4 – quartz condenser, 5 – monochromator MDR-12U, 6 - FEM-39A, 7 - capacitive filter of voltage, 8 - kilovoltmeter, 9 - microammeter, 10 – 75 ns delay line, 11 – current probe, 12 - oscilloscope Tektronix TDS-210.

3. Experimental results

The analysis of the oscillograms of a discharge current and optical signals has allowed identifying two modes of the nonstationary streamer discharge. The first mode corresponds to the case when streamers do not reach the cathode. (see osc. 1 and 2 from fig. 2). Second mode corresponds to bridging of the gap by the streamer channel (see osc. 4 and 5 from fig. 2). Section BC of the V-I characteristic in fig. 4 corresponds to first mode of streamer discharge and section CD – to the second.

The following features between the first and second modes of discharge are existed: 1) the formation and propagation of a secondary ionization wave after bridging of interelectrode gap by a streamer; 2) influence of a field emission on current dynamics and rate of streamer propagation near the cathode. Besides at mode crossover the discontinuous change of repetition frequency of current pulses was observed.
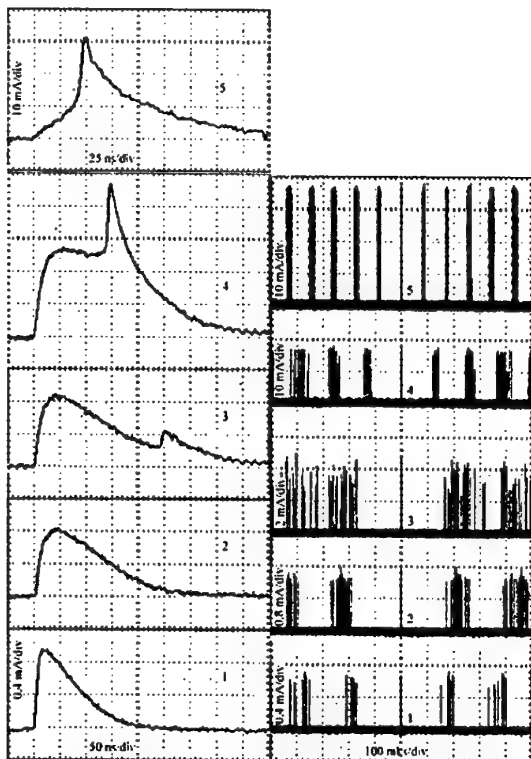
Fig. 2. Oscillograms of discharge current pulses in ambient air (interelectrode gap is 11 mm).
1 - U=4.8 kV, I_{cp}=1.5 μA; 2 - U=6 kV, I_{cp}=3.5 μA;
3 - U=6.2 kV, I_{cp}=3.8 μA; 4 - U=6.4 kV, I_{cp}=4.2 μA;
5 - U=11 kV, I_{cp}=50 μA.

The dependence of streamer propagation rate vs. location of its head in the gap was obtained from analysis of light emission dynamics. Near electrodes the streamer propagation rate increased, and in middle of the gap it decelerated.

It was noted that current pulse parameters and dynamics of streamer propagation for various oxygen-contained gas mixtures were very different. For example, the repetition frequency of streamers in oxygen was ~100 kHz, while in ambient air it was ~10 kHz).
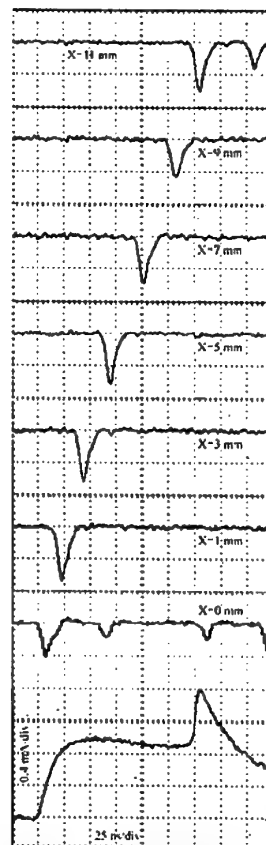
Fig. 3. Oscillograms of discharge current pulse in ambient air and FEM's current pulses from different areas of the interelectrode gap (11 mm). U=6.4 kV, I_{cp}=4.2 μA.
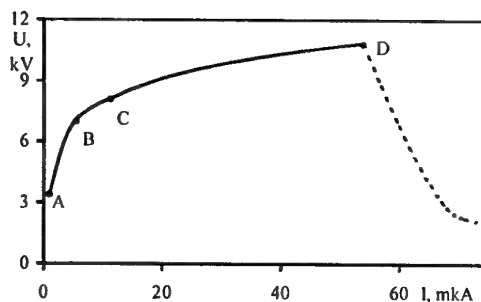
Fig. 4. The typical voltage-current characteristic of atmospheric pressure needle-to-plane gas discharge. AB – stationary mode (positive corona), BD – nonstationary streamer discharge, BC – - streamers do not reach the cathode, CD – streamer bridge the gap.

36

Ozone synthesis in atmospheric pressure needle-to-plane gas discharge

V. Golota, B. Kadolin, V. Karas', I. Paschenko, S. Pugach and A. Yakovlev

Department of Nonequilibrium Lowtemperature Plasmachemistry,
National Science Center "Kharkov Institute of Physics and Technology",
Akademicheskaya St. 1, Kharkov 61108, Ukraine

The research of negative, positive coronas and also a nonstationary streamer discharge was carried out. The synthesis of O_3 and emission spectrum of NO and atomic oxygen O on wave length 777.1 nm was investigated experimentally. The concept of ozone synthesis in atmospheric pressure gas discharge was offered.

1. Introduction

Most industrial ozone generators are the classical DBD setups. However, recently, attention is also attracted to ozone generators on high-pressure needle-to-plane gas discharge.

As is well known the basic reaction of ozone synthesis is $O_2 + O + M \rightarrow O_3 + M$. The concentrations of O_2 and M set by feeding gas composition. The main task is increasing of O generation efficiency, i.e. increasing of O_2 dissociation rate.

Electron energy distribution defines the dominant dissociative processes. Thus, it is possible to attempt to adjust discharge parameters with the purpose of effective generation of atomic oxygen, and therefore synthesis of ozone, if the chain of O_2 dissociation processes is known.

Nonstationary streamer discharge (SD), positive (PC) and negative (NC) coronas in the needle-to-plane electrode geometry was experimentally investigated. The analyses of peculiarities and similarity of physical processes of these discharges will allow determining the mechanism of dissociation O_2.

2. Experiment

The needle-to-plane electrode system was located in the hermetically chamber with controlled air feeding. The air pressure was an atmospheric. There was a possibility to apply to needle-electrode both positive and negative DC voltages. There was a quartz window in the chamber for registration of a radiation spectrum of discharge. There was no possibility to control O concentration. Therefore we observed the discharge byproducts such as O_3 and NO, and also radiation of atomic oxygen O on wave length 777.1 nm.

3. Results

For all three types of discharges the voltage-current characteristics with simultaneous monitoring of O_3 concentration were measured. The obtained dependences for the positive potential on the needle are represented in fig. 1.
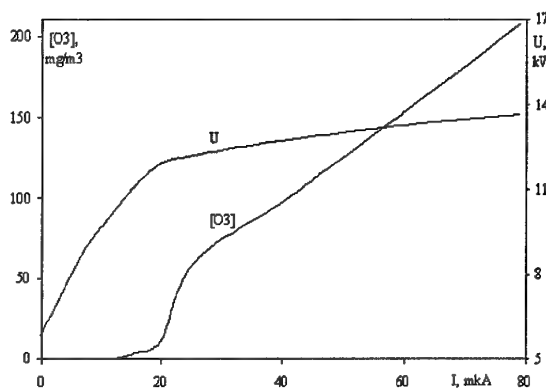
Fig. 1. V-I characteristic and O_3 concentration for the positive potential on the needle.

It is possible to observe the abrupt change on the current-voltage characteristic. This point separates the positive corona and nonstationary streamer discharge [1].

The radiation spectrums in a wave band 200÷300 nm were obtained with the purpose to register the γ-NO system (fig. 2) for all three types of discharges.

Some of the experimental and analytical results of physical processes of nonstationary streamer discharge, positive and negative coronas are presented in the table 1. Column 1 of this table is a power consumption w for ozone synthesis in SD, PC and NC normalized on power consumption of SD w_{sd}. Also, the ratios of γ-NO (0-1) intensity to intensity of $IV^+ N_2$ (0-1) $(I_{\gamma NO(0-1)}/I_{IV^+ N_2(0-1)})$ and O-radiation (777.1 nm) intensity to $II^+ N_2$ (0-3) intensity $I_{O(777.1)}/I_{II^+ N_2(0-3)}$ are presented in Columns 2 and 3 respectively. The Column 4 of the table explains the role of negative ions for SD, PC and NC [2].

streamer discharge

negative corona

positive corona
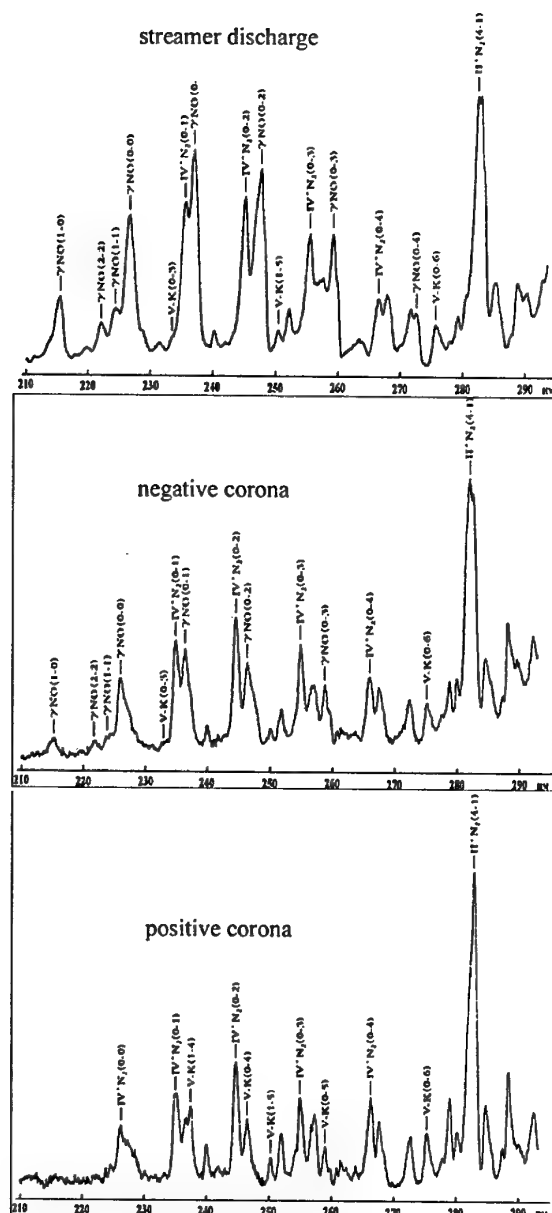
Fig. 2. Discharge radiation spectrum.

Table 1. Experimental results.

	1	2	3	4
	$\dfrac{w}{w_{sd}}$	$\dfrac{I_{\gamma NO(0-1)}}{I_{IV^+N_2(0-1)}}$	$\dfrac{I_{O(777.1)}}{I_{II^+N_2(0-3)}}$	Negative ions
SD	1	1.32	0.2	This mode is controlled by negative ions
NC	~2	0.91	0.1	Negative ions determine pulse regime
PC	>10	≈0	0.03	Negative ions practically are absent

4. Concept

Strong correlation between presence of negative ions in discharge, i.e. processes of attachment, and O_2 dissociation byproducts are observed (table 1). Thus, it is possible to conclude that the main channel of atomic oxygen generation is the process of dissociative attachment of electrons to O_2 molecules (table 2).

Table 2. The main dissociative processes.

№	Process	Threshold, eV	Ref.
1	$O_2 + e \rightarrow O^- + O$	4.2	[3]
2	$O_2 + e \rightarrow O + O + e$	5.58	[4]
3	$O_2 + e \rightarrow O + O\left(^1D\right) + e$	8.4	[5]

It is possible to draw a conclusion, that the processes of ionization and O_2 dissociation are separated in time and/or in space, and the atomic oxygen density can not be more then electron density in the current channel.

So, the effective dissociative processes must be realized in two stages. In the fist one the required level of ionization in the streamer channel can be reached by reduced electric field 1000 Td and more. In the second one the reduced electric field must quickly decrease to the value ~100 Td where processes from the table 2 effectively occur. The special shape of power pulse can optimize these conditions as against the DC power supply.

The present concept has allowed us to elaborate the ozone generator on nonstationary streamer discharge with following parameters: O_3 concentration - 2÷4 %, power consumption - 8÷13 Wh/gO_3, feeding gas – 20 % N_2 + 80 % O_2.

5. References

[1] A.A. Bruev, V.I. Golota, L.M. Zavada, B.B. Kadolin, V.I. Karas', I.A. Paschenko, S.G. Pugach, Problems of Atomic Science and Technology, 1 (2000) 50-53.

[2] Loeb L.B., Fundamental Processes of Electrical Discharge in Gases, N.Y., 1939

[3] D. Rapp, P. Englander-Golden, J. Chem. Phys., 43 (1965), 1464.

[4] K. Klopovsky, T. Rakhimova, Moscow State University, private comm. 1994.

[5] B. Eliasson, U. Kogelschatz, Asea Brown Boweri Forschungszntrum CH-5405, Baden, KLR 86-11C, June. 1986.

2D structure of nitrogen molecular bands radiation of microdischarges in DBD in N_2-O_2 mixtures: Experimental results

R. Brandenburg[1], K. V. Kozlov[2], H.-E. Wagner[1], P. Michel[1], Yu.V. Yurgelenas[3]

[1] University of Greifswald, Institute of Physics, Domstrasse 10 a, 17489 Greifswald, Germany
[2] Moscow State University, Department of Chemistry, 119899 Moscow, Russia
[3] General Physics Institute RAS, Moscow, Russia

Results of spatio-temporally resolved optical emission spectroscopy of single filaments in a dielectric barrier discharge in nitrogen containing 3% of oxygen are presented. Results of numerical modelling are discussed, too.

1. Introduction

Dielectric barrier discharges (DBD) are known to consist of many filaments or microdischarges (MDs). Due to their small dimensions (typically mm) and short duration (in the nanosecond-range) there is a lack of experimental data seizing their two-dimensional propagation. This contribution reports about our first attempts of the investigation of MD development in axial and radial direction.

2. Experimental technique

The discharge cell consists of two semi-spherical electrodes, both covered by glass and mounted with a gap distance of 1.4 mm (see figure 1).
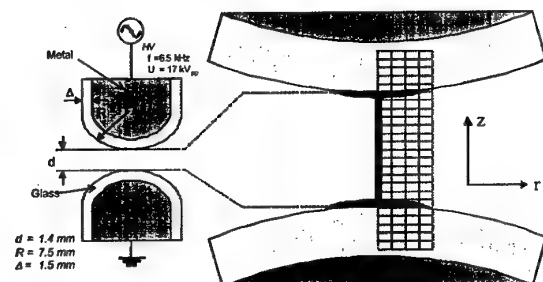
Figure 1: Electrodes and schematic drawing of the spatial scanning

The DBD was generated in a flowing gas-mixture of nitrogen with 3% admixture of oxygen. At these conditions the microdischarges have a good reproducibility in electrical characteristics and position [3]. Using a lens, the discharge area was imaged to an optical slit, adjustable and movable in vertical as well as in horizontal direction. For vertical motion of the slit a stepper motor, for horizontal movement a micro-controller was used. By changing the horizontal slit position the single filaments can be scanned along the discharge axis z (resolution $\Delta z = 0.1$ mm) for a chosen radial discharge area (resolution $\Delta r = 0.2$ mm). The technique of Cross-correlation spectroscopy (CCS) allows a time resolution of about 0.1 ns. A detailed description of the experimental set-up and the CCS-method is given in [2].

3. Experimental results and discussion

The emission spectrum of a filamentary BD in the mixture (N_2 + 3% O_2) mainly consists of the 2nd positive system of nitrogen (SPS) and the 1st negative system of N_2. In figure 2 for the 0-0 transition of the SPS at $\lambda = 337.1$ nm spatio-temporally resolved intensity distributions are shown for two different radial positions. The intensity is coded in grey-scale in logarithmic steps.
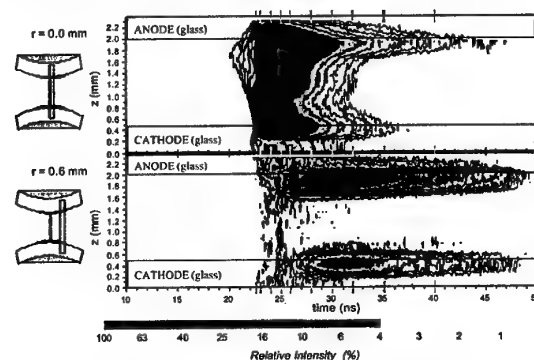
Figure 2: Spatio-temporally resolved intensity distributions for different radial positions - top: centre; bottom: outside

In the picture for the centre (top) a cathode-directed ionising wave and an anode glow is seen. These phenomena have been discussed in detail elsewhere [2]. For the fastest outside position investigated in the experiments (r = 0.6 mm, bottom) radiation is only see on the dielectric surfaces. From the comparison of the two pictures one can already suggest, that at the surfaces the discharge spreads radially.

To resolve the radial structure of MD in the volume the radial resolution of $\Delta r = 0.2$ mm is to low. It is known, that the radius of a MD does not exceed 0.4 mm [4, 5]. The 2D structure of MD propagation is summarized in figure 3 at different times. The stage of the cathode directed ionizing wave is discussed in attention to numerical modelling presented in [6]. Short after its arrival at the cathode (approx. t = 24 ns in time-scale used here, but t = 32.0 ns in [6]) the radiation radius along the gap in direction from the anode to the cathode decreases. Numerical modelling in [7] has demonstrated that the decrease of the radiation radius is not characteristic for a streamer. One possible reason of this

difference given in [6] is the effect of a preliminary electron background to MD propagation. Another possible explanation is a small horizontal jitter of the MD position during the measurements.

The discharge processes on the dielectric surfaces shows a outward directed propagation at both electrodes. Due to an electron accumulation at the microdischarge tip on the anodic dielectric a radial component of the electric field E is formed. Therefore after the formation of the cathode-directed luminosity wave and the anode glow the MD spreads at the dielectrics (see in fig. 3 for $t \geq 28$ns), forming a funnel-shaped MD-foot [2]. The electron accumulation leads to a decrease of the local electric field in the discharge centre,

Figure 3: Spatial structure of the microdischarge evolution
(radial co-ordinate r always at position 0; 0.2; 0.4 and 0.6mm for every time step t; at t = 22.5ns the cathode directed wave has nearly arrived at the cathode)

but not yet in the surrounding area. So in the MD-centre the signal decreases and the maximum of the signal propagates outwards (beginning from t = 28ns). In the following the negative surface charge growths radially and the signal continues to move to the outside with decreasing intensity and a velocity of about 0.1 mm/ns. Similar, on the cathodic dielectric a positive surface charge -responsible for the observed Lichtenberg-figures [2]- is spreading with decreasing value and the discharge creeps over the dielectric surface. An influence of the semi-spherical electrode geometry can be seen by the slight move of the outside spreading maximum in vertical direction (see fig 3). The surface discharge phenomena are not included in the numerical model presented in [6].

4. Conclusions

The evolution of a microdischarge in nitrogen-oxygen mixture was measured by Cross-correlation spectroscopy in axial and radial direction. The results visualise the discharge propagation. In the volume even before the cathode directed ionising wave arrives the electrode a decreasing of the radiation channel towards the cathode is observed. The microdischarge dynamics on the dielectric surfaces is characterised by an outward creeping radiation maximum. These observation confirms with previous experimental and numerical modelling results [2] and can be explained by the dynamics of surface charging processes.

5. Acknowledgements

6. References

[1] R. Brandenburg, K.V. Kozlov, A. Morozov, H.-E. Wagner, P. Michel: "Dielectric barrier discharges in nitrogen/oxygen mixtures", *These Proccedings*

[2] K.V. Kozlov, H.-E. Wagner et.al., *J. Phys. D: Appl. Phys.*, **34** (2001) 3164

[3] V.I. Gibalov, G.J. Pietsch., *J. Phys. D: Appl. Phys.*, **33** (2000) 2618

[4] B. Eliasson, U. Kogelschatz, *IEEE Trans. on Plasma Sci..* (1991), vol. 19, no. 2, 9. 309

[5] V.G. Samojlovic, V.I. Gibalov, K.V. Kozlov: "Physical chemistry of the barrier discharge", 2nd Edition, Düsseldorf: DVS-Verlag, 1997

[6] Yu.V. Yurgelenas, R. Brandenburg, K.V. Kozlov, H.-E. Wagner: "2D structure of nitrogen molecular bands radiation of barrier discharge in N_2-O_2 mixtures: numerical modelling", *These Proceedings*

[7] Yu.V. Yurgelenas, H.-E. Wagner: "Modelling of the spatio – temporal structure of nitrogen molecular bands radiation by streamer discharge channel in air", *These Proceedings*

Two-dimensional structure of nitrogen molecular bands radiation of microdischarges in DBD in N_2-O_2 mixtures: Numerical model

Yu.V. Yurgelenas[1], R. Brandenburg[2], K.V. Kozlov[3], H.-E. Wagner[2]

[1] General Physics Institute RAS, Vavilova str. 28, Moscow, 119991, Russia, yvyurg@mail.ru
[2] University of Greifswald, Institute of Physics, Domstrasse 10a, Greifswald, 17489, Germany
[3] Moscow State University, Department of Chemistry, Moscow, 119899, Russia

Two-dimensional structure of the microdischarge channel radiation in the second positive (0,0) molecular band of nitrogen in dielectric barrier discharge in nitrogen-oxygen mixtures between parallel plane electrodes is investigated by means of numerical modelling. The numerical results are applied for the explanation of experimental results.

1. Introduction

Recent years highly spatio-temporally resolved experimental investigations using cross-correlation spectroscopy technique [1] were performed for the spectroscopic diagnostics of microdischarge local parameters in dielectric barrier discharges (DBD) in air. Usually the radial structure of the discharge channel was not taken into account however simulations [2] showed non-uniform radial profiles of streamer channel radiation. In recent investigation [3] the two-dimensional (both radial and axial) structure of microdischarge channel radiation was obtained experimentally. To explain the experimental results [1,3] numerical modelling of the single microdischarge evolution at the initial stage is made.

2. Mathematical model of DBD dynamics and radiation

Dielectric barrier discharge in a parallel-plane geometry with discharge gap d as shown in fig. 1 is considered. Atmospheric pressure gas in the gap consists of (100-p)% N_2 and p% O_2. The constant applied anode voltage U_0 and the cylindrical symmetry of the microdischarge channel are supposed. Dielectric permittivity of glass is $\varepsilon = 5$.
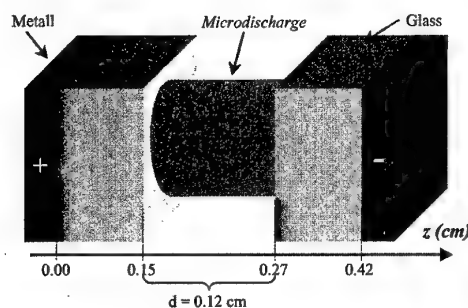
Figure 1: Geometry of DBD discharge.

Microdischarge plasma dynamics is described by the set of continuity equations for charged and excited species densities and Poisson equation for electrical potential [4]. Sources of particles by plasma kinetics both photoionization are taken into account. All the reactions rates are supposed to be dependent on the local reduced electric field strength.

The only two secondary processes: ion emission from the near-cathode dielectric surface (emission coefficient γ_i=0.01) and photoionization of a gas are included.

No charged or excited particles inside the gap at the initial state any are assumed. Single filament in DBD is initiated by single electron going directly from the near-cathode dielectric surface.

In the most previous simulations "single initial electron" was substituted by many (100-1000 and more) electrons and initial electric field was high enough following avalanche-to-streamer transition. This seems to be non-realistic for short gaps and can lead to incorrect conclusions as to DBD development stages.

Spontaneous radiation intensity for the (0-0) transition of the second positive system ($\lambda = 337.1$ nm) is calculated analogously to [5].

In the simulations of the experimentally measured quantities ideal spatial resolution is supposed. As the local radiation intensity the number of photons directed from the line crossing the point with coordinate (r,z) per surface area unit per time (photons/cm^2/s) is used.

3. Results of the numerical simulation and discussion

1) p=20 (artificial air), d = 0.12 cm (conditions [1]).
For U_0 = 9.18 kV the two-dimensional distribution for 337.1 nm is presented for t =54.5 ns (filament arrival time at the cathode) in fig. 2, the axial dependence of discharge parameters is shown in fig. 3 and spatio-temporal radiation distribution is presented in fig. 4.

By the modelling results (fig. 3) after avalanche stage the relatively long time Townsend phase (till t=50 ns) characterized by charged particles accumulation takes place. Then it transforms to cathode-directed ionizing wave usually observed as filament.

As it is seen (fig. 2), initial decreasing of the radiation radius along the gap takes place, analogously to the corresponding experimental pictures in [3]. This is not characteristic for the streamer discharge radiation [5].

Under the term "streamer" let us denote a self-consistent ionization wave which: 1) has sufficiently high own electric field strength for propagation, 2) produces enough electrons before the tip (by photoionization) so

its movement is independent of possible electrons background. So we can distinguish between ionization waves controlled by preliminary background and "self-consistent" streamers. From the results [3] one can conclude that along almost all the gap the filament is not a real streamer and its dynamics is controlled by electrons background formed at the Townsend phase.

It can be seen in fig. 3, the ionization wave (from 50 ns, radius is decreasing, fig. 2) is following by real streamer (from 54 ns, radius is increasing), possessing almost constant concentration at the tip.

The simulated relatively long time near-anode radiation at the initial stage (fig. 4) is in accordance to the experimental results [1].

2) For $p=3$, $d = 0.14$ cm (conditions in [3]), and $U_0 = 10.4$ kV the picture is presented in fig. 5 (for $t = 32$ ns). A decrease of the radiating channel along all the gap is seen. This confirms our conclusions because in this case the electrons attachment rate is lower and the effect of electrons background is expected to become more important than for $p=20$.

Both the experimental and numerical results testify to principal role of 2D dynamics of microdischarges so any reliable modelling must be at least two-dimensional.

4. References

[1] K.V. Kozlov, H.-E. Wagner, R Brandenburg, P. Michel, *J. Phys. D.* **34** (2001) p. 3164.

[2] Yu.V. Yurgelenas, 7th *Int. Symp. on High Pressure Low Temp. Plasma Chemistry (HAKONE VII)*, Greifswald/GER (2000) vol.1, p.169.

[3] R. Brandenburg, K.V. Kozlov, H.-E. Wagner, P. Michel, Yu.V. Yurgelenas: Two-dimensional structure of nitrogen molecular bands radiation of microdischarges in DBD in nitrogen-oxygen mixtures: Experimental results, *These Proceedings.*

[4] A.F. Diyakov, Yu.K. Bobrov, A.V. Sorokin, Yu.V. Yurgelenas: *Principal Physics of Electrical Breakdown of gases* (1999) MPEI Publishers, Moscow (in Russian).

[5] Yu.V. Yurgelenas, H.-E. Wagner: Modelling of the spatial – temporal structure of nitrogen molecular bands radiation by streamer discharge channel in air, *These Proceedings.*

Figure 3: Axial distributions of electrons concentration at the axis for different times, time in ns.
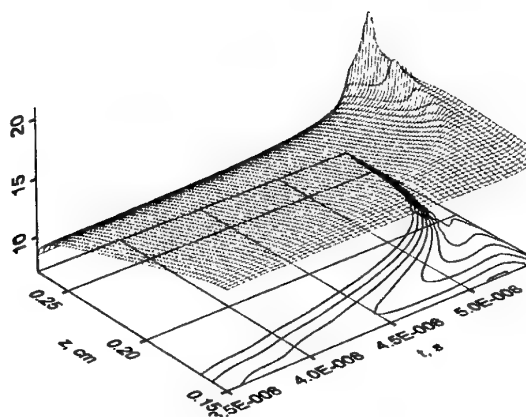
Figure 4: Spatio-temporal dependence for radiation before microdischarge bridging the gap at $\lambda = 337.1$ nm, in photons / cm / s (decimal logarithms), low level 15, step 0.25 .

Figure 2: Radiation distribution at $\lambda = 337.1$ nm for p= 20 and t=54.5 ns, in photons / cm^2 / s (decimal logarithms), low level 16.5, step 1/2.
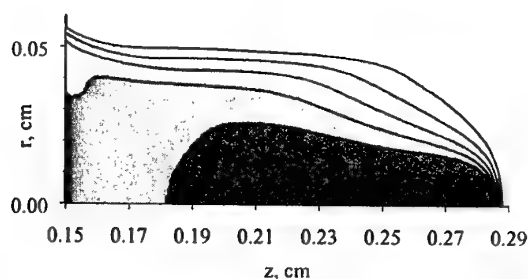
Figure 5: Radiation distribution at $\lambda = 337.1$ nm for p= 3 and t= 32 ns, in photons / cm^2 / s (decimal logarithms), low level 16.5, step 1/2.

Behaviour of dielectric barrier discharges in nitrogen / oxygen mixtures

R. Brandenburg[1], K.V. Kozlov[2], A.M. Morozov[2], H.-E. Wagner[1], P. Michel[1]

[1] University of Greifswald, Institute of Physics, Domstrasse 10 a, 17489 Greifswald, Germany
[2] Moscow State University, Department of Chemistry, 119899 Moscow, Russia

Dielectric barrier discharges have been investigated in binary mixtures of nitrogen and oxygen by means of spatio-temporally resolved optical emission spectroscopy. The content of oxygen was varied within the range 0.5-97%. Qualitatively, no profound influence of the gas composition on the discharge behaviour has been found. Observed quantitative changes in the luminosity distributions depending on the oxygen content in a mixture, may be explained by the role of collisional quenching of nitrogen excited states by the O_2 molecules.

1. Introduction
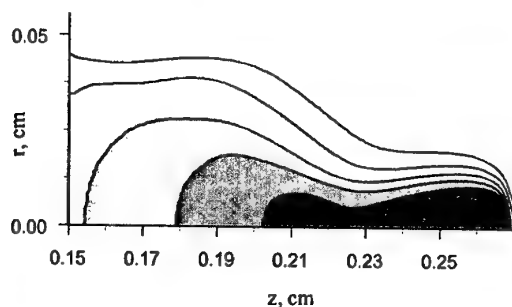
Barrier discharges (BDs) in oxygen-containing gas mixtures consist of many tiny filaments (microdischarges - MDs) of nanosecond duration. Due to their small dimensions (typically, a few mm) and short lifetimes, there is a lack of experimental data related to their spatial structure and evolution, that are needed to provide an adequate quantitative theoretical description for the MD development. To fill this lag in understanding the mechanism of BDs (MDs), systematic investigation for the case of binary gas mixtures (N_2+O_2) of variable composition have been undertaken.

2. Experimental set-up

The BD was generated in a flowing gas mixture of nitrogen and oxygen in a discharge cell consisting of two semi-spherical electrodes, both covered by glass (gap width d = 1.4 mm). The content of oxygen was varied in the range of 0.5-97 %. An applied sinusoidal voltage (frequency f = 6.5 kHz) with amplitudes U(peak-to-peak) = 16-19 kV was used to sustain the discharge with 1-3 MDs per half cycle. The BD was investigated by current oscillography, optical emission spectroscopy, and cross-correlation spectroscopy (CCS) for spatio-temporally resolved measurements of the MD evolution. A detailed description of the experimental set-up and the CCS method is given in [1]. Therefore the most important measurement characteristics are summarised: the spatial resolution along discharge axis is 0.1 mm, while 0.3 mm in radial direction, the wavelength accuracy is 0.3 nm, the resolution over the fine time scale is 0.1 ns, and additionally the measurements are resolved over the phase of driving sinusoidal voltage with T/16 (T = 1/6.5 kHz = 153 µs).

3. Results and discussion

In pure nitrogen, a diffuse ("glow", Townsend-like) BD is generated [2]. But an admixture of even some hundred ppm of oxygen leads to the transition to the filamentary mode, characterised by the occurrence of MDs. In the case of more than 1% O_2, a profound filamentary discharge is observed [3]. Furthermore, the filamentary mode itself is affected by the oxygen content. For low oxygen content, the MDs occur almost always at the

same value of the phase of the applied voltage. The same effect of MD reproducibility dependence on the gas composition is clearly seen in the current oscillograms. Visually it is found out that for low oxygen content, the MDs appear to burn at a steady state position between the electrode tips, while for the higher oxygen concentration, more diffuse shining discharge is observed.

An increase in oxygen content is found to result in characteristic changes in the emission spectrum. In all cases, the 2nd positive system of N_2 (SPS) dominates the spectrum. For low oxygen concentrations (0.5 and 1%), a weak signal of the NO_γ-system is clearly seen, while for higher values (more than 10%), the 0-0 transition of the 1st negative system of nitrogen (FNS) is observed. In fig. 1 only a part of the spectrum, presenting three different vibritional transitions (v'→v''= 0→3, 1→4, 2→5) of the SPS is shown. The structure of the SPS depends on the oxygen content. In the vibrational distribution for pure nitrogen and 0.5 % O_2 the 0-3 transition is the most intensive band, which is in contrast to the corresponding Franck-Condon factors (FCF). These observed overpopulation of the v'=0-level suggest that indirect mechanisms (e.g. via N_2-metastable states) are dominating the excitation process. The structure of the SPS-spectrum for higher oxygen admixture is in better agreement with the FCFs, thus referring to direct electronic excitation.

The plots of spatio-temporally resolved intensity distributions of selected spectral bands (SPS and FNS) for several gas mixtures are presented in fig. 2. Qualitatively, no significant difference in the microdischarge behaviour can be found here. The discharge evolution is characterised by a cathode directed luminosity wave followed by a glow at the anode. The velocity of the cathode directed luminosity wave (ionisation wave) seems to be independent of the gas composition (see fig. 3). However the higher oxygen content, the faster the decay of the SPS-signal (figure 4). Assuming the relaxation of the $N_2(C)$ density to be caused by spontaneous radiation and collisional quenching, reasonable agreement between measured and calculated data can be obtained:

$$\frac{1}{\tau_{eff}} = \frac{1}{\tau_0} + K_{N_2} n_{N_2} + K_{O_2} n_{O_2} \approx K_{N_2} n_{N_2} + K_{O_2} n_{O_2}$$
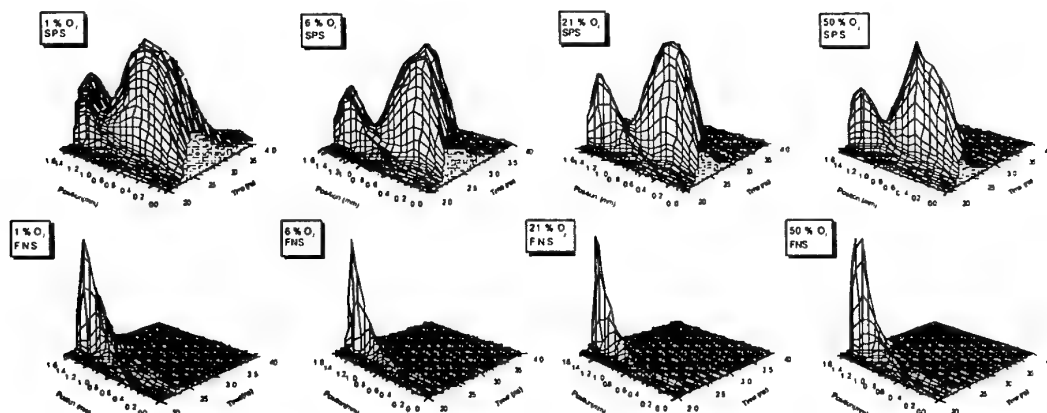
Figure 2: Spatio-temporally resolved intensity distributions for SPS and FNS,
0-0 transitions at $\lambda = 337$ nm and $\lambda = 391$ nm respectively (cathode at position 1.5 mm, anode at 0.1 mm)

where τ_0 is the radiative lifetime, K_X are the rate coefficients for de-excitation of $N_2(C)$ by $X = N_2$, O_2 taken from [4] and n_X are the densities of the species in the ground state. At atmospheric pressure the collisional quenching dominates. The best agreement between measured and calculated effective lifetimes is obtained in the case of stable microdischarge behaviour (3 vol. % O_2 admixture to N_2).
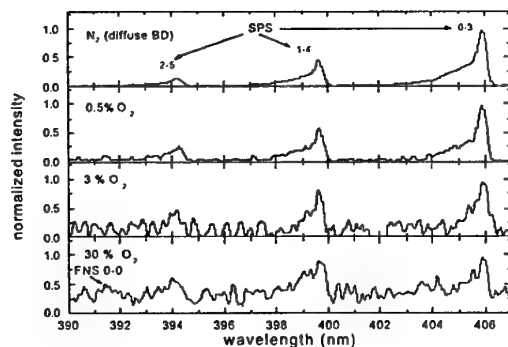
Figure 1: Comparison of emission spectra fragments for different gas mixtures
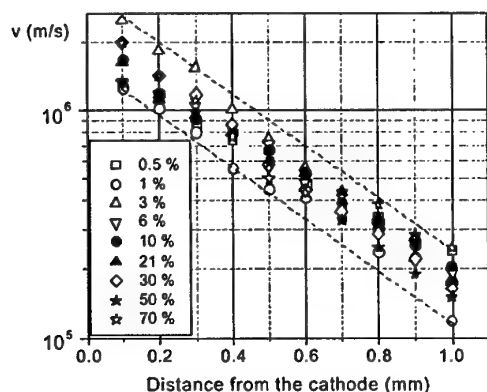
Figure 3: Velocity of the cathode directed wave as a function of axial co-ordinate and gas composition
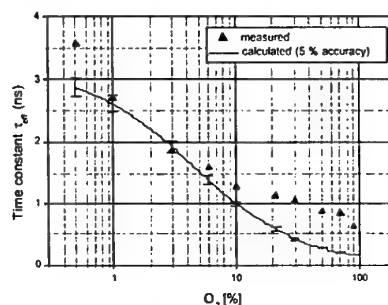
Figure 4: Effective lifetimes τ_{eff} for the SPS-signal

4. Summary

Qualitatively, no profound influence of the gas composition on the discharge behaviour has been found. Observed quantitative changes in the luminosity distributions depending on the oxygen content may be explained by the role of collisional quenching of nitrogen excited states by the molecules O_2.

5. Acknowledgements

6. References

[1] K.V. Kozlov, H.-E. Wagner, R. Brandenburg, P. Michel., *J. Phys. D: Appl. Phys.*, **34** (2001) 3164

[2] N. Gherardi, G. Gouda, E. Gat, A. Ricard, F. Massines, *Plasma Sources Sci. Technol.*, **9** (2000) 340

[3] R. Brandenburg, K.V Kozlov, N. Gherardi, P. Michel, C. Khampan, H.-E. Wagner, F. Massines, *Proc. of 8th Int. Sym. on High Press. Low Temp. Plasma Chemistry*, Pühajärve/EST, 2002, vol. 1, 28

[4] K.B. Mitchell., *J. Chem. Phys.*, **53** (1970) 1795

Diffuse dielectric barrier discharges in nitrogen-containing gas mixtures

R. Brandenburg[1], H.-E. Wagner[1], P. Michel[1], D. Trunec[2], P. Stahel[2]

[1] University of Greifswald, Institute of Physics, Domstrasse 10 a, 17489 Greifswald, Germany

[2] Department of Physical Electronics, Masaryk University, Kotlarska 2, 61137 Brno, Czech Republic

Diffuse dielectric barrier discharges are investigated in mixtures of nitrogen with several noble gasses (He, Ne, Ar). The results show that the discharge remains in the diffuse mode at relatively high content of the noble gases, which is contrary to the admixture of oxygen to nitrogen.

1. Introduction

Under special conditions dielectric barrier discharges (or barrier discharges, BD) can be operated in a diffuse mode, often called homogeneous mode or atmospheric pressure glow discharge (APGD). The diffuse BD in helium, nitrogen and neon has been intensively investigated by plasma diagnostics and numerical modelling [1 - 5]. The decisive criterion for the generation of a diffuse BD is the presence of charge carriers at a low electric field, i.e. a memory effect responsible for the production of primary electrons below breakdown voltage, otherwise microdischarges are formed. Several processes for this has been discussed as Penning ionisation due to metastable collisions [3] or electron desorption from the dielectric surface [4]. It was found out that the diffuse BD in nitrogen is a Townsend-like discharge, while the helium respectively neon diffuse BD is characterised by the formation of a cathode fall. For the case of diffuse BD in N_2 systematic measurements have shown that already oxygen admixtures of some hundreds of ppm lead to the generation of the usual filamentary mode. On the other hand diffuse BD could be generated in mixtures of nitrogen and argon with up to 70 % of argon content [6]. In this contribution we report the experimental study of diffuse BD in mixtures of nitrogen with the noble gases argon, helium or neon. The discharge voltage and current are measured and spatio-temporally resolved optical emission spectroscopy is performed. The aim of this work is the investigation of the transition between the two different types of diffuse BD and the selection of the conditions leading to the generation of either the Townsend-like or the glow-like form. By understanding the transition it might be possible to learn more about the elementary processes leading to a diffuse BD instead of a filamentary one.

2. Experimental technique

The BD is generated in flowing gas-mixtures between two semi-spherical electrodes covered by glass (1.5 mm thick), mounted with a gap distance of 1.4 mm. These special electrodes are usually used for the investigation of single microdischarges in the filamentary form [7]. The applied sinusoidal voltage (frequency f = 6.5 kHz) and the total discharge current are recorded with an oscilloscope (Tektronix TDS 380), the optical emission spectrum is investigated with a monochromator (Jobin Yvon Triax 320) and spatio-temporally resolved

emission spectroscopy can be performed with the modificated set-up for cross-correlation spectroscopy [7].

3. Experimental results and discussion

The discharge behaviour representative for all gas mixtures under investigation is shown in fig. 1 for the helium-nitrogen mixtures. The burning voltage (i.e. the minimum voltage needed to sustain the diffuse discharge after first ignition) and the transition voltage (i.e. the voltage needed to cause the formation of microdischarges) are shown as a function of the gas composition. To distinguish between the discharge modes current oscillograms as shown in fig. 2 are used.
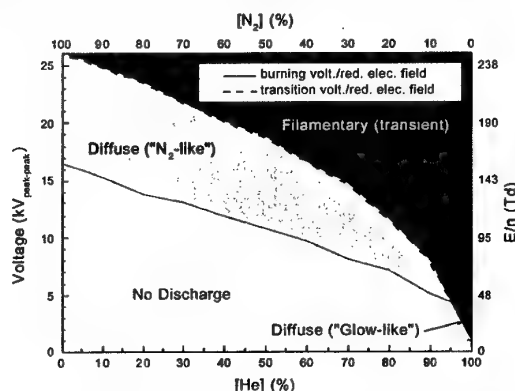
Figure 1: Burning and transition voltages in He-N_2-BDs (applied sinusoidal voltage with frequency f = 6.5 kHz)

Remarkably high content of the noble gases (up to 80 %) can be admixed to nitrogen without changing the diffuse nature of the discharge (see fig. 2b), if the applied voltage is chosen properly. Both threshold voltages decrease with the noble gas content and the interval for diffuse BD formation narrows. For almost pure helium/ neon the "Glow-like" type of barrier discharge is generated like in [1], while in pure argon a filamentary discharge is observed (see fig. 2a). The transition to the filamentary mode begins with the occurrence of regular oscillations in the discharge current (fig. 2c).

The luminosity distributions of diffuse BD in the mixtures of noble gas and nitrogen have their maximum nearby the anode (see fig. 3). This additionally proves that a Townsend-like discharge as in the case of pure nitrogen is formed. The oscillations described above are also present
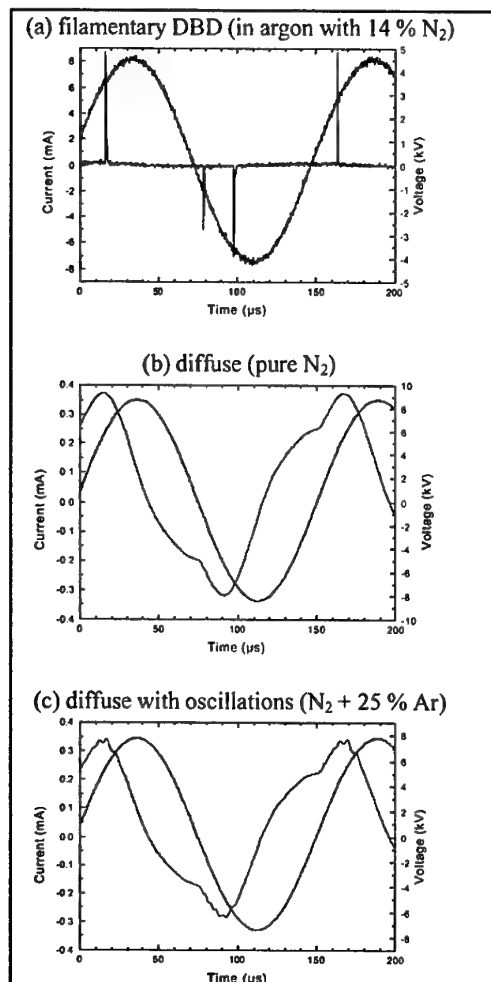
Figure 2: Voltage and current oscillograms
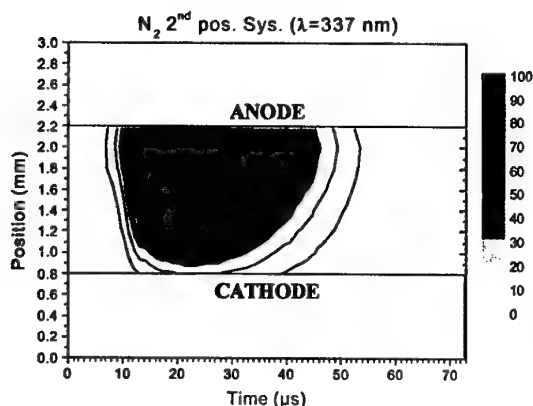
Figure 3: Results of spatio-temporally res. OES. 2nd positive system of N$_2$ (0-0 transition at 337 nm), conditions as in fig. 2c (Ar + 25 % N$_2$)

in the discharge luminosity of the second positive system of nitrogen (fig. 3) as well as of excited atomic argon. Both signals follows the discharge current in time. Furthermore the γ-spectrum of NO is observed in the

spectra. But this signal is delayed about 25 μs against current and other intensities. The NO-signal is mainly caused by excitation via metastable N$_2$(A) molecules. In contrast N$_2$(C) and Ar* excitation are initiated by electrons. One can conclude, that the oscillations describe an instability of the diffuse BD finally leading to the microdischarge formation.

The physical behaviour of the presented results is rather complex and not understood in detail up until now in atmospheric pressure discharges. The interpretation includes a multitude of processes. Some important are summarized in the following: The values of the first Townsend ionisation coefficient α are greater for noble gases than for N$_2$, resulting in the decrease of the threshold voltages in noble gas / nitrogen mixtures (comp. figure 1). Furthermore, in such discharges metastables of nitrogen and noble gases are formed. Via different Penning ionisation processes these metastables form effectively molecular nitrogen ions (N$_2^{+}$, N$_4^{+}$), affecting to the diffuse discharge mode.

4. Conclusion

Electric and spectroscopic diagnostics confirms that the admixture of noble gases argon, neon and helium to a diffuse, Townsend-like BD in nitrogen does not change the nature of the discharge significantly. A detailed interpretation of the results remains to future investigations.

5. Acknowledgements

6. References

[1] F. Massines, A. Rabehi, P. Decomps, R.B. Gadri, P. Segur, C. Mayoux, *J. Appl. Phys.*, **83** (1998) 2950

[2] N. Gherardi, G. Gouda, E. Gat, A. Ricard, F. Massines, *Plasma Sources Sci. Technol.*, **9** (2000) 340

[3] P. Segur, F. Massines, *Proc. 13th Int. Conf. on Gas Discharges and Their Appl.*, 2000, Glasgow/UK, p. 15

[4] Yu.B. Golubovskii, V.A. Maiorov, J.F. Behnke, J. Behnke, *J. Phys. D: Appl. Phys.*, **35** (2002) 751

[5] D. Trunec, R. Brandenburg, P. Michel, D. Pasedag, H.-E. Wagner, Z. Navratil, *Proc. of 8th Int. Symp. of High Pressure Low Temperature Plasma Chemistry (HAKONE VIII)*, 2001, Pühajärve/EST, vol. 1, p. 63

[6] R. Kozakov, V. Lebedev, A. Sonnenfeld, J.F. Behnke, *Proc. of 7th Int. Symp. of High Pressure Low Temperature Plasma Chemistry (HAKONE VII)*, 2001, Greifswald/GER, vol. 1, p. 184

[7] K.V. Kozlov, H.-E. Wagner, R. Brandenburg, P. Michel, *J. Phys. D: Appl. Phys.*, **34** (2001) 3164

Spatio-temporal development of the diffuse barrier discharge in nitrogen

R. Brandenburg[1], V. A. Maiorov[2], Yu. B. Golubovskii[2], H.-E. Wagner[1],
K. V Kozlov[3], J. F. Behnke[1], J. Behnke[1], P. Michel[1]

[1] University of Greifswald, Institute of Physics, Domstrasse 10 a, 17489 Greifswald, Germany
[2] St. Petersburg State University, Physical Faculty, Ulianovskaja 1, Petrodvorets, 198904 St. Petersburg, Russia
[3] Moscow State University, Department of Chemistry, 119899 Moscow, Russia

Results of spatio-temporally resolved optical emission spectroscopy of the diffuse dielectric barrier discharge in nitrogen are presented and compared with results of numerical modelling. The model is taking into account the surface processes and involves the special electrode geometry used in the experiment.

1. Introduction

Within the last few years diffuse barrier discharges (BD) often referred to as homogeneous BD or as atmospheric pressure glow discharges (APGD) became an object of intensive experimental and theoretical investigations [1]. The diffuse BD in nitrogen has been investigated by means of voltage-current ocsillography, short exposure time photography, optical emission spectroscopy (OES) [2, 6] as well as numerical modelling [3, 4].

The criterion to generate a diffuse BD is the presence of carrier charges at a low electric field, i.e. a memory effect responsible for the production of primary electrons below a voltage leading to filament formation. Several processes has been discussed as Penning ionisation due to metastable collisions [3] or electron desorption from the dielectric surface [4]. In these contribution results of spatio-temporally resolved emission spectroscopy are presented and compared with results of numerical modelling including the surface processes.

2. Experimental technique

Diffuse BD generated in pure flowing nitrogen and a discharge gap of 1.0 mm was investigated with a modified experimental set-up already used for diagnostics of filamentary barrier discharges [5, 6]. Especially the same semi-spherical electrodes (thickness of the glass was 1.5 mm) were used (see figure 1a). Due to the combined action of a single photon counting device and an electrically triggered pattern generator time resolution of 2.3 µs has been archived. The spatial resolution along the discharge axis was 0.2 mm by using stepper motor controlled imaging optics.

3. Model

The model of the diffuse BD was based on the system of fluid equations coupled with the Poisson equation. The details of the model and the solution method can be found in [4].

Special attention was paid to the influence of the electrode geometry. To simulate qualitatively small deviations from plane geometry, electrodes were divided into radial pieces (see figure 1b), and the axial electric field was assumed to be dependent on the radius.

The densities of excited states $A^3S_u^+$ and $C^3?_u$ of nitrogen were calculated on the basis of the corresponding balance equations. Since the lifetime of the metastable state is determined by the frequency of quenching by impurity (NO) atoms, this lifetime was chosen arbitrarily ($3 \cdot 10^4$ s^{-1}) in order to fit the experimental results.
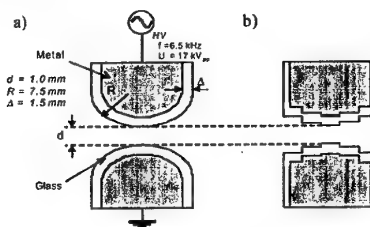
Figure 1: Electrode arrangement used
in the experiment (a) and in the model (b)

4. Results and discussion

The emission spectrum of the diffuse BD in nitrogen consists of the second positive system of nitrogen (SPS), NO_γ-bands and band of ON_2-excimer at 557 nm [2]. For 0-0 transition of the SPS and 0-3 transition of NO_γ the spatio-temporally resolved intensity distributions are shown in figure 2. In the pictures the time scale slightly exceeds the period of the driving voltage ($1/T = 1/6.5$ kHz $= 153$ µs) and the upper electrode is the cathode within the first half period. The intensity is coded in grey-scale in logarithmic steps. The calculated density of the $N_2(C)$-molecules is shown in figure 3a. Since the effective life times of the excited states are orders of magnitude smaller than the characteristic time scales for density evolution, the pictures 2a and 3a can be compared directly. Furthermore it is known that the excitation of the NO(A) state is dominated by N_2-metastable collisions [2, 6]. Therefore the calculated densities of the $N_2(A)$-densities is shown in figure 3b and can be directly compared with the NO_γ-signal.

All intensity distributions as well as density profiles shows the maximum near the momentarily anode. The SPS respectively the $N_2(C)$-density growths exponentially towards the anode and between the two half widths no signal is seen. Since the $N_2(C)$ excitation is initiated by electrons [2] this demonstrates that the
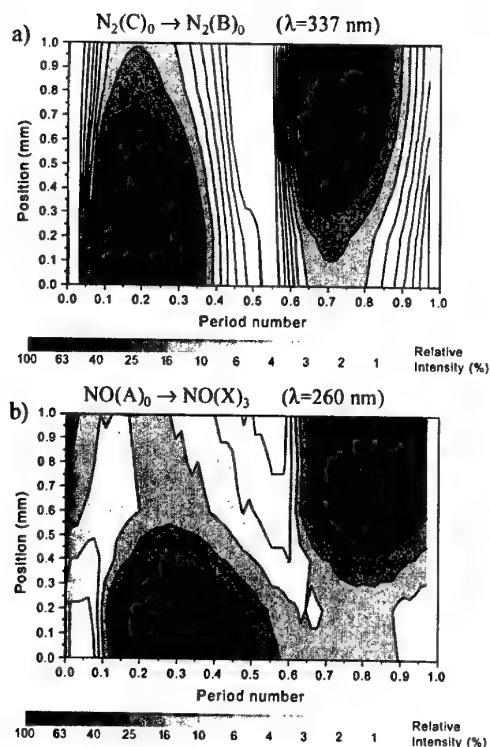
Figure 2: Results of spatio-temporally resolved OES
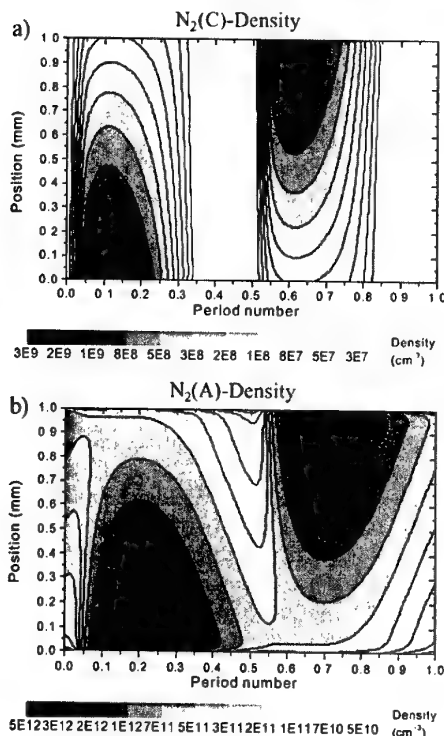
Figure 3: Results of numerical modelling

diffuse BD in nitrogen is a Townsend-like discharge, i.e. no large space charges distorting the electric field are produced and finally an exponential growth of the electron current towards the anode is observed. The NO_{γ} signal resp. NO(A)-density distribution is delayed against the SPS resp. $N_2(C)$ and both profiles shows a similar slower decay. A better correspondence of the measured SPS intensities with numerical modelling results of $N_2(C)$ density than in previous simulations is obtained [6]. There the surface processes and the special electrode contour had not been considered. This result points out the importance of the electron desorption process from the cathode (i.e. the previous anode). A similar good qualitative agreement was observed for measured and calculated discharge current. In planned experiments a plane parallel discharge cell will be used to investigate the influence of surface contour in more detail.

5. Conclusion

A general qualitative agreement between experiment and model is observed, referring to the importance of surface processes, in particular electron desorption from the cathode. Future experimental investigations will be dedicated to a planar electrode geometry in order to have a better comparability with the numerical modelling results.

7. References

[1] S. Kanasawa, M. Kogoma, T. Moriwaki, S. Okazaki, *J. Phys. D: Appl. Phys.*, **21** (1988) 838

[2] N. Gherardi, G. Gouda, E. Gat, A. Ricard, F. Massines, *Plasma Sources Sci. Technol.*, **9** (2000) 340

[3] P. Segur, F. Massines, *Proc. 13th Int. Conf. on Gas Discharges and their Appl.*, 2000, Glasgow/UK, 15

[4] Yu.B. Golubovskii, V.A. Maiorov, J.F. Behnke, J. Behnke, *J. Phys. D: Appl. Phys.*, **35** (2002) 751

[5] K.V. Kozlov, H.-E. Wagner, R. Brandenburg P. Michel, *J. Phys. D: Appl. Phys.*, **34** (2001) 3164

[6] R. Brandenburg, K.V Kozlov, N. Gherardi, P. Michel, C. Khampan, H.-E. Wagner, F. Massines, *Proc. of 8th Int. Sym. on High Pressure Low Temperature Plasma Chemistry (HAKONE VIII)*, 2002, Pühajärve/Estonia, vol. 1, 28

Widening of the electron avalanche in a barrier discharge due to the photoemission

Yu. B. Golubovskii[1], V. A. Maiorov[1], J. Behnke[2], J. F. Behnke[2]

[1] St. Petersburg State University, Physical Faculty, Ulianovskaja 1, Petrodvorets, 198904 St. Petersburg, Russia
[2] University of Greifswald, Institute of Physics, Domstrasse 10 a, 17489 Greifswald, Germany

The evolution of the narrow electron avalanche in a barrier discharge is studied via two-dimensional fluid model. If the photoemission is taken into account as a primary source of electrons at the cathode, the electron avalanche initiates a quasi-homogeneous glow discharge. This discharge is about 10 ns in duration; it covers all the electrode area.

1. Introduction

One of the methods to produce homogeneous glow plasma at atmospheric pressure is to use the barrier discharge. In most common gases, such as N_2 or air, as the barriers are made of glass or Al_2O_3, only Townsend discharge is homogeneous [1]. The reason is that this discharge mode is stable relative to radial fluctuations in distinction with the glow mode [2].

However, there is a way to produce homogeneous glow discharge in N_2 at low (50 Hz) frequency by using electret "Mylar" barriers [1]. A possible mechanism of its initiation is the subject of the present work.

2. Source of initial electrons in a DBD

The experimental profile of current in Townsend discharge [1] can be obtained in a model if desorption is assumed to be the primary source of electrons at the cathode [3]. At 50 Hz, low value of dU/dt does not allow to obtain the glow mode in presence of the desorption. The charge transfer causes the screening of the slowly growing external voltage, and the overvoltage necessary for the development of a glow mode cannot be obtained. This overvoltage can occur if no electrons are emitted from the cathode. Absence of charge loss is the feature of electrets, so this mechanism is probable in the case of Mylar barriers. After the overvoltage is obtained, any incident electron may initiate the breakdown. The remarkable widening of a resulting avalanche can be caused only by the photoemission.

3. Model

The model is based on 2D fluid equations for electrons and ions as well as Poisson equation. Following [3], only direct ionization is taken into account. The photoemission is introduced in accordance with [4].
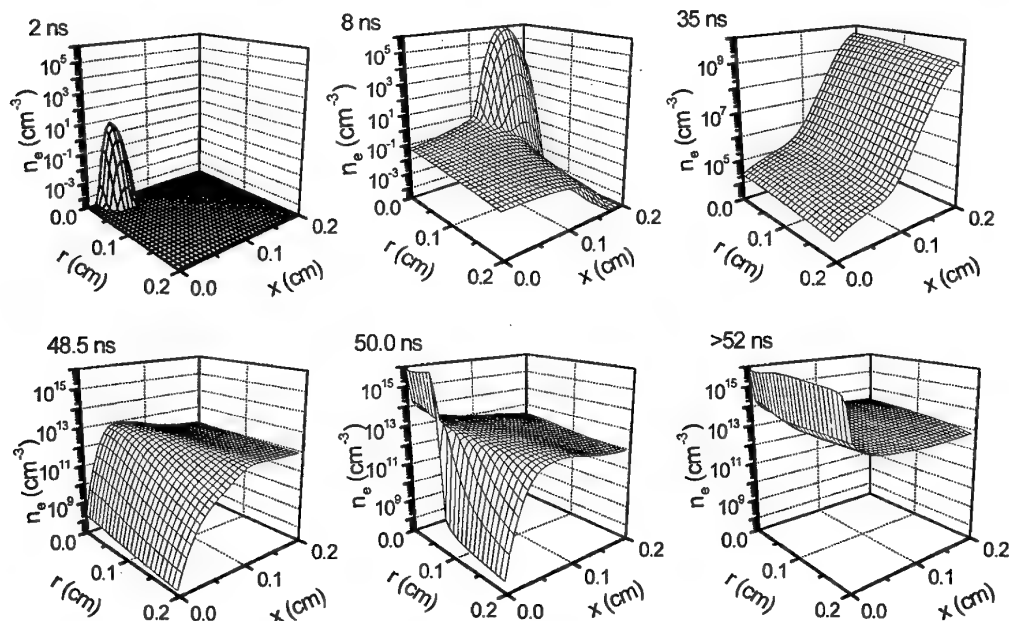
Fig. 1. Electron density distribution in different phases of the breakdown.
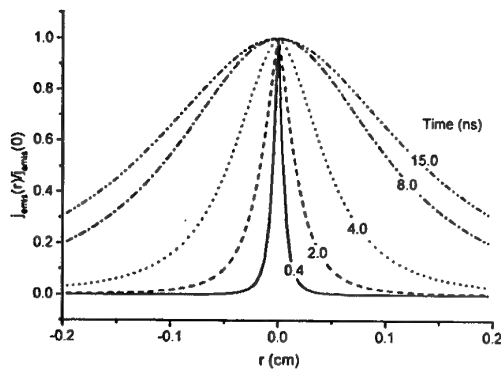
Fig. 2. Profile of emission current in different phases.

Fig. 3. External current pulse in 2D and 1D models.

The system is solved numerically for the discharge geometry similar to [1], i.e., gap width 0.2 cm, barrier width 0.35 cm, $\varepsilon=3.3$. The discharge radius is chosen to be 0.5 cm. The working gas is nitrogen. The external voltage is equal to 13 kV.

The initial electron density is chosen to have Gaussian profile both in radial and axial directions ($\Delta x=\Delta r=0.005$ cm). The maximum is at $x=r=0$; its value is 1 cm^{-3}.

4. Results and discussion

In figure 1 one can see different stages of breakdown. First stage is the drift of the initial avalanche towards the anode (t<10 ns) and its growth due to the ionization. Since the overvoltage is not very high, the charged particle density in the avalanche does not achieve the value necessary for the formation of a streamer (n~10^{12} cm^{-3}). Therefore, after the initial avalanche reaches the anode (t≈15 ns), it is adsorbed.

The UV photons produced by fast electrons in the avalanche hit the cathode and cause the photoemission. The essential widening of the electron density due to this process can be seen in figure 1 for t = 8 ns. This widening is illustrated by figure 2, where the emission current is shown in different discharge phases.

The external voltage is chosen so as

$$\exp(\alpha L) > \frac{1}{\gamma_{eff}}, \qquad (1)$$

where α is the Townsend ionization coefficient and γ_{eff} is the effective secondary emission coefficient (in the case of photoemission $\gamma_{eff} = \gamma_{ph} / 2$). Therefore, the electron density grows in time due to this overvoltage even after the disappearance of the initial avalanche. The Townsend phase of the discharge can be observed in figure 1 at t=35 ns.

After the electron density at the anode attains the critical value, a streamer front is formed. This front runs rapidly in the cathode direction (Figure 1, t=48.5 ns).

Since the electron density was maximal at r=0, the streamer front near the axis of symmetry reaches the cathode earlier (cf. the instability of the streamer front [2]). At t=50.0 ns the streamer front reaches the cathode
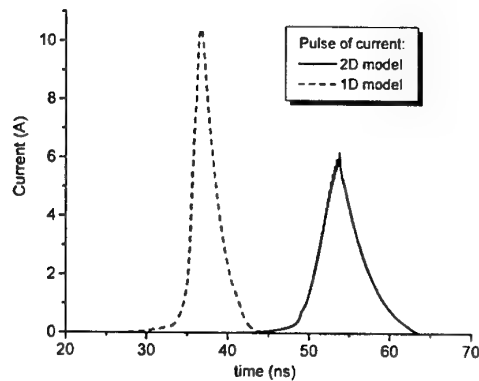
for r < 0.1 cm and do not for larger radii.

At t > 55 ns one can see the final stage of the breakdown. The electron density attains its maximal value in all radial points, and the current becomes to decrease (see also figure 3).

The effect of delay of the streamer front for remote radial points causes the widening of the current peak in comparison with that without delay (1D model). The difference in current pulses is seen in figure 3. Larger electrode area may lead to even stronger widening of the current peak up to some tens of nanoseconds.

5. Conclusion

It is shown that, in presence of the photoemission and in absence of any other emission processes, even one incident electron may cause a quasi-homogeneous glow discharge covering all the electrode area. At low frequencies, this effect may be the origin of the homogeneous glow barrier discharge.

The delay of the streamer front far from the position of the initial avalanche may cause the increase of the duration of the current pulse.

6. Acknowledgements

7. References

[1] J. Tepper and M. Lindmayer, *Proc. of HAKONE VII* (Greifswald, 10-13 Sept. 2000), Vol. 1, p. 38

[2] V.A. Maiorov, Yu.B. Golubovskii, J. Behnke, J.F. Behnke, *Proc. of this conference*

[3] Yu.B. Golubovskii, V.A. Maiorov, J. Behnke, J.F. Behnke, *J. Phys. D: Appl. Phys.* **35** (2002) 751

[4] G. E. Georghiou, R. Morrow, A. C. Metaxas, *J. Phys. D: Appl. Phys.* **34** (2001) 200

On the radial instability of a homogeneous barrier discharge in nitrogen

V. A. Maiorov[1], Yu. B. Golubovskii[1], J. Behnke[2], J. F. Behnke[2]

[1] St. Petersburg State University, Physical Faculty, Ulianovskaja 1, Petrodvorets, 198904 St. Petersburg, Russia
[2] University of Greifswald, Institute of Physics, Domstrasse 10a, 17489 Greifswald, Germany

The temporal development of small radial disturbances of the cathode current in a barrier discharge in nitrogen is studied by means of a 2D fluid model. It was found that Townsend discharge mode is stable, whereas in glow mode disturbances of all radii grow with time. Therefore, the domain of discharge homogeneity coincides with that of existence of Townsend discharge. The homogeneity domains are obtained for both linearly increasing and sinusoidal voltages. The filamentation is induced by increase of the voltage growth rate as well as gap width.

1. Introduction

The barrier discharge is a widely used source of non-equilibrium plasma at high pressure. This discharge can be homogeneous even as the reduced gap width *pd* is high (hundreds of Torr cm).

Up to now, different types of the homogeneous barrier discharge are studied experimentally [1-3]. In nitrogen, as the classic equipment (e.g. plane parallel electrodes with glass barriers) is used, only Townsend discharge can be obtained [2,3].

The one-dimensional (1D) simulation of this discharge [4] can succeed in the description of the experimental data, but it is not able to explain the nature of the homogeneity. The 2D modelling [5] reveals different behaviour of radial disturbances in Townsend and glow modes. The growth of fluctuations is a probable way to the filamentation.

This work is devoted to the extensive analysis of the instability of a homogeneous barrier discharge in N_2 relative to radial fluctuations. The homogeneity domains are obtained on the basis of the notions developed.

2. Model

At high pressures and small currents, it is possible to reduce greatly the number of particles responsible for the discharge characteristics and simplify remarkably the kinetics of ionization in N_2 [4]. The effective quenching of excited states, particularly of the metastable state $a'^1\Sigma_u^-$, makes the chemoionization and the stepwise ionization negligibly small. The vibrational temperature in nitrogen is close to room temperature because of the diffusion of vibrationally excited molecules to the barriers. The prevailing type of ions in a homogeneous barrier discharge in nitrogen is N_4^+. This ion is produced in fast conversion processes.

Thus, only the direct ionization is responsible for the discharge maintenance; to describe the discharge, one must calculate only the density of electrons and N_4^+ ions. The calculation is based on the two-dimensional fluid equations coupled with the Poisson equation for the potential. At the barriers, the desorption of electrons ($v_{des}=10^4$ s^{-1}) is taken as a source of an initial cathode current.

3. Stability of different discharge modes

To analyse the barrier discharge for the stability, it is necessary to know which qualitatively different modes can exist in the framework of the one-dimensional model. The following discharge parameters are used: gap width L=0.1 cm, dielectric barrier width l=0.01cm (ε=1), surface density of particles at the barriers σ=10^{10} cm^{-2}. The phase of active discharge is modelled via the assumption of the linearly increasing voltage. Different discharge modes are obtained by changing the voltage growth rate dU/dt.

The electrical characteristics of the discharge in different modes are shown in Fig. 1. At small dU/dt, Townsend mode can be observed (Fig. 1a). The cathode current in this mode is amplified in a weakly disturbed electric field. As the voltage growth rate increases (Fig. 1b), damping oscillations of the current occur due to the influence of spatial charge. However, the discharge is also Townsend. More rapid voltage growth (Fig. 1c) changes the discharge behaviour greatly. As U_{gap} attains a certain value, a strong current peak (units of A/cm^2) is observed. In this mode, the field is strongly disturbed by spatial charge.
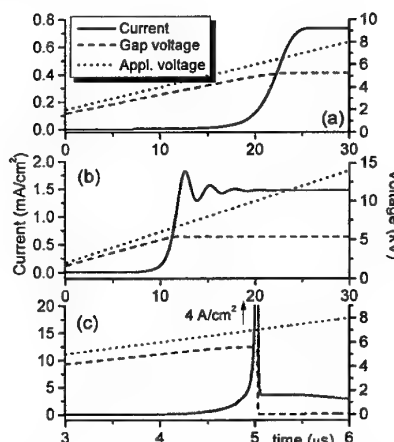
Fig. 1. Different modes of barrier discharge. (a) dU/dt = 2x10^8 V/s, Townsend mode; (b) dU/dt = 4x10^8 V/s, multipeak Townsend mode; (c) dU/dt = 10^9 V/s, space-charge dominated (glow) mode
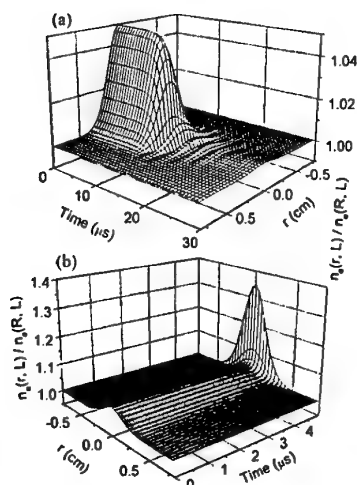
Fig. 2. Evolution of the normalized electron density at the anode in (a) Townsend and (b) glow modes

These modes are analysed for the stability using a small (5%) radial perturbation of the cathode current. The object of study is the electron density at the anode, normalized to that in a non-disturbed discharge.

In both Townsend modes (e.g. Fig. 2a, oscillative mode), the disturbance of the cathode current is strongly damped. Stronger cathode current causes the earlier shielding of the field by surface charge and reduction of the Townsend coefficient in a disturbed domain.

In glow mode, larger spatial charge in a disturbed domain causes earlier formation of an ionization wave (streamer). Therefore, one can see the growth of a disturbance.

The fluctuations of all radii behave similarly. In Townsend discharge they are damped, which testifies its stability. On the contrary, the glow mode is unstable; therefore, in the real discharge it must turn into the filamentary mode immediately.

4. Domains of homogeneity

The immediate consequence from the results of the previous section is that the domain of discharge homogeneity coincides with the domain of existence of Townsend discharge and can be studied via 1D model.

For linearly increasing voltage, the diagram of discharge modes is shown in Fig. 3. It is seen that as the gap width L or the voltage growth rate dU/dt increases, the discharge tends to be filamentary. The decrease of the barrier width reduces the homogeneity domain.

The study of the stability of a discharge at sinusoidal voltage (Fig. 4) allows to take into account the gas heating. This process decreases the domain of homogeneity (Fig. 4, curve B) and improves the agreement with the experiment [2]. At room temperature, the estimation of the boundary of homogeneity by the corresponding dU/dt (solid curve) is successful.
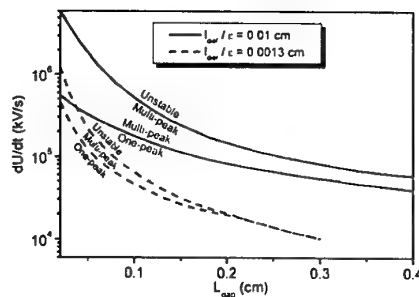
Fig. 3. Diagram of the modes for a barrier discharge at linearly growing external voltage
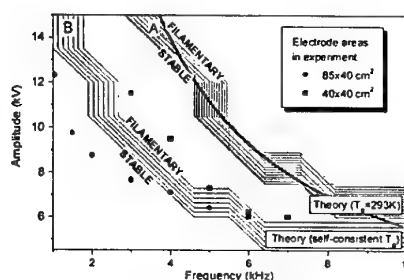
Fig. 4. Diagram of the modes for a barrier discharge at sinusoidal voltage. Dots, experiment [2]; multistroke curves, calculation; solid curve, estimation by dU/dt

5. Conclusion

The two-dimensional study shows that the space-charge dominated mode of a barrier discharge in N_2 is unstable and must be filamentary. Only Townsend mode is homogeneous. The calculations of the homogeneity domains are performed; the theory agree well with the experiment as the gas heating is taken into account.

6. Acknowledgements

7. References

[1] F. Massines et al, J. Appl. Phys. 83 (1998) 2950

[2] E. Croquesel, N. Gherardi, S. Martin and F. Massines, Proc. of HAKONE VII (Greifswald, 10-13 Sept. 2000), Vol. 1, p. 88

[3] J. Tepper and M. Lindmayer, Proc. of HAKONE VII (Greifswald, 10-13 Sept. 2000), Vol. 1, p. 38

[4] Yu. B. Golubovskii, V. A. Maiorov, J. Behnke, J. F. Behnke, J. Phys. D: Appl. Phys. 35 (2002) 751

[5] Yu. B. Golubovskii, V. A. Maiorov, J. Behnke, J. F. Behnke, Proc. of 16th ESCAMPIG (Grenoble, 14-18 July 2002), Vol 1, p. 235

Optical diagnostics of atmospheric pressure glow discharge in nitrogen with admixture of organosilicon

Z. Navrátil, P. Sťahel, D. Trunec, V. Buršíková, A. Brablec

Department of Physical Electronics, Masaryk University, Kotlářská 2, 611 37 Brno, Czech Republic

The atmospheric pressure glow discharge in nitrogen with small admixture of different organosilicons compounds such as hexamethyldisilazane and hexamethyldisiloxane was studied by means of emission spectroscopy. The deposited films were studied by means of indentation techniques.

1. Introduction

In the industrial applications there is a great effort to develop techniques to control the surface properties of materials. There is a wide range of plasma enhanced chemical vapour deposition (PECVD) methods enabling to prepare coatings with well-defined wetting and sticking behaviour and good mechnical properties.

The disadvantage of the low pressure PECVD techniques is that they demand expensive vacuum pumping systems. Moreover, there are difficulties to arrange the deposition system for large area depositions. Recently plasma deposition at atmospheric pressure becomes a promising technology due to its economical and ecological advantages. During last years there is a great interest in atmospheric pressure glow discharges (APGD) especially in the industrial applications. The glow discharge in different pure gases can be easily generated [1, 2, 3, 4], but in nitrogen which is from the technological point of view the most suitable gas the small admixture of oxygen to nitrogen can lead to the generation of filamentary dielectric barrier discharge instead of APGD [4]. The objective of the present work is to study the APGD in nitrogen with small admixture of different organosilicon compounds such as hexamethyldisilazane – $C_6H_{19}Si_2N$ and hexamethyldisiloxane – $C_6H_{18}Si_2O$. These mixtures can be used for plasma deposition of thin films with desired surface and bulk properties.

2. Experimental

The deposition of thin films was carried out by atmospheric pressure glow discharges with the operation frequency of 5 kHz. The APGD was carried out between two electrodes covered with insulating glass plates. The type of discharge as concerns the filamentary or glow mode was determined from the current-voltage measurements. The films were deposited from different mixtures of organosilicons (hexamethyldisilazane – HMDSZ, hexamethyldisiloxane – HMDSO) with nitrogen on glass substrate put on the bottom electrode. The nitrogen was bubbled through liquid HMDSZ or HMDSO monomers to evaporate the monomer from the liquid to gaseous state. The nitrogen with organosilicon vapors was mixed with pure nitrogen. The flow rate of the pure nitrogen was 8l/min, the electrode gap was 1 mm and the supplied power was 30 W in all cases.

The emission spectra from the discharges were recorded with TRIAX550 spectrometer and some parameters such
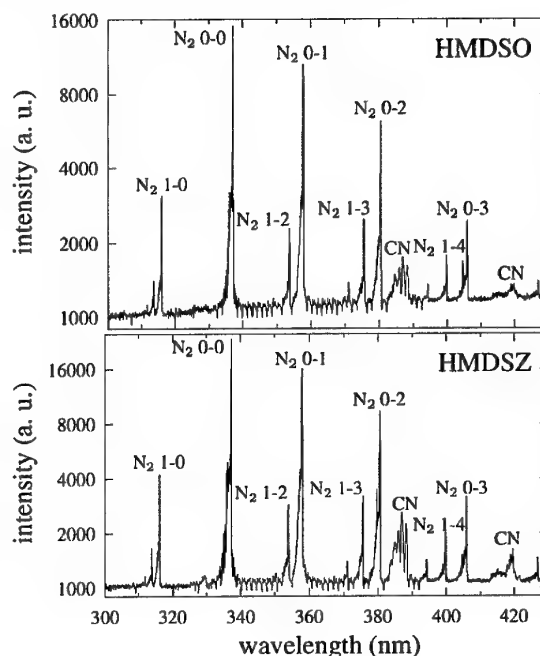
Figure 1: Emission spectra of APGD in nitrogen with admixture of HMDSO or HMDSZ.

as vibration temperature of nitrogen were determined. The mechanical properties were studied by means of the depth sensing indentation technique using a Fischerscope H100 tester.

3. Results and discussion

Fig. 1 shows the typical emission spectra of the APG discharge in nitrogen with a small admixture of monomer (hexamethyldisiloxane or hexamethyldisilazane). The spectra were recordered in the range of 300 – 800 nm. However, above 430 nm only second spectral order of grid was observed.

Spectra consist of the molecular bands of second positive system of nitrogen ($C^3\Pi_u \to B^3\Pi_g$) and in case of the APGD in nitrogen with monomer two CN bands of CN violet system ($^2\Pi \to {}^2\Sigma$) were observed. The first one at 388 nm was more intensive than the second one at 422 nm. Vibrational bands of nitrogen with a corresponding change of vibrational quantum number $\Delta v = -2, -3$ were used to calculate the vibrational temperature. De-

hexamethyldisiloxane		hexamethyldisilazane	
flow rate $(lmin^{-1})$	T (K)	flow rate $(lmin^{-1})$	T (K)
0.0	1883 ± 67	0.0	1769 ± 95
0.3	2011 ± 100	0.2	1802 ± 68
0.6	1967 ± 110	0.5	1940 ± 69
1.2	1962 ± 85	1.2	1887 ± 65

Table 1: Vibrational temperature of nitrogen determined for different flow rates of organosilicones.
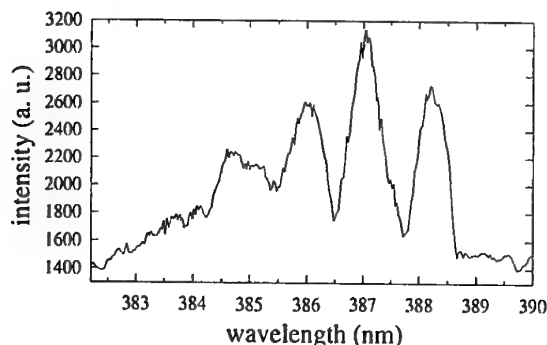
Figure 2: Structure of CN band with position at 388.3 nm.

termined values of vibrational temperature for different concentrations of organosilicones are listed in Table 1.

The structure of the CN band with the position at 388 nm is plotted on the Fig. 2. This CN band was used for calculation of the integral intensity of the band. Fig. 3 shows the integrated intensity of the CN band vs. flow rate of organosilicon mixed to the pure nitrogen. The exponential increase of the integrated intensity was observed for both types of monomer, but in case of HMDSZ the integrated intensity was much higher.

The measurement of the discharge voltage and current is presented in Fig. 4. Whereas applied voltage is si-
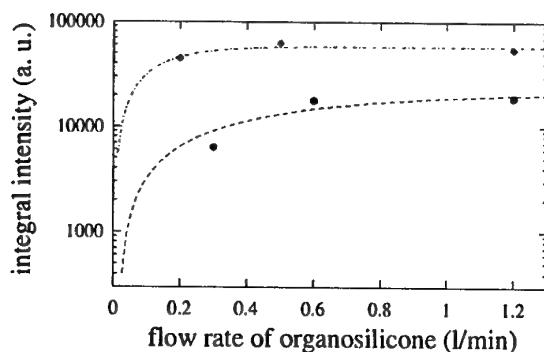
Figure 3: Dependence of integrated intensity of CN band on flow rate of hexamethyldisiloxane (full circle) and hexamethyldisilazane (full square).
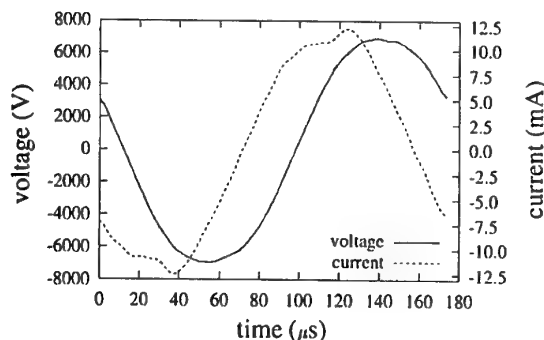
Figure 4: Time variation of current and applied voltage of APG discharge.

nusoidal, the current consists of two parts. The sinusoidal current course corresponds to capacitive current, the small peak represents the current of the APG discharge.

Deposited films were homogeneous and microhardness was in the range from 0.2 to 0.3 GPa. The elastic modulus ranged from 10 to 25 GPa. The films showed high ductility and good adhesion to the substrate.

4. Conclusion

It was found that APGD can be generated not only in pure nitrogen but also in nitrogen with a small admixture of organosilicons. In case of higher concentration of HMDSO or HMDSZ the APG mode changes to filamentary mode. The APGD was studied by means of emission spectroscopy and the vibrational temperature of nitrogen was determined. The vibrational temperature varied from 1800 to 2000 K and only lightly depended on concentration of monomer added to the nitrogen. The properties of thin films were studied by means of the indentation technique, the hardness of films was about $0.2-0.3$ GPa.

5. Acknowledgements

6. References

[1] S. Kanazawa, M. Kogoma, T. Moriwaki, S. Okazaki, *J. Phys. D: Appl Phys.* **21** (1988) 838.

[2] N. Gherardi, G. Gouda, E. Gat, A. Ricard, F. Massines, *Plasma Sources Sci. Technol.* **9** (2000) 340.

[3] D. Trunec, A. Brablec, J. Buchta, *J. Phys. D: Appl. Phys.* **34** (2001) 1697.

[4] R. Brandenburg, K. V. Kozlov, F. Massines, P. Michel, H.-E. Wagner, *Proceedings of HAKONE VII, Greifswald 10-13 Sept. 2000* **1** (2000) 93.

Study of a helium atmospheric pressure dielectric barrier discharge at 100 kHz

R. Foest[1], V. A. Maiorov[2,3], Yu. B. Golubovskii[2], J. F. Behnke[3], M. Schmidt[1]

[1] Institute of Low-Temperature Plasma Physics, F.-L.-Jahnstrasse 19, 17489 Greifswald, Germany
[2] St. Petersburg State University, Physical Faculty, Ulianovskaja 1, Petrodvorets, 198904 St. Petersburg, Russia
[3] University of Greifswald, Institute of Physics, Domstrasse 10 a, 17489 Greifswald, Germany

A homogeneous atmospheric pressure glow discharge is obtained in helium at 100 kHz. The electrical characteristics of the discharge are measured and compared with the results of the model. The calculations agree well with the experiment when a small admixture of nitrogen is assumed and the destruction of the helium excimers is strong enough. A multi-peak structure of the current is observed at higher amplitudes of the external voltage.

1. Introduction

Non-thermal plasmas are widely used for plasma processing. Atmospheric pressure plasmas require practically no vacuum devices. The atmospheric pressure dielectric barrier discharge (DBD) has been used for a long time, starting with the ozone generation by Siemens 1857. The DBD is mostly a filamentary one, however, a homogeneous DBD was found in He and later in other gases too [1]. Studies of the homogeneous He discharge cover the frequency region of 50 Hz to 50 kHz with two dielectric barriers in the gap. In our work we extend the frequency region to 100 kHz. Moreover, only one electrode is covered by a glass dielectric. The other electrode is plain aluminium.

2. Experimental technique

The experiments were carried out in a cylindrical glass vessel (d=200 mm, l=400 mm, Fig. 1), which is, along with the measuring method of the electrical parameters, described elsewhere [2]. Residual gas pressures are about 20 Pa. The upper electrode (80x15mm, covered with glass) is powered with a sinusoidal voltage while the lower Al electrode is connected to ground by R_m or C_m resp.
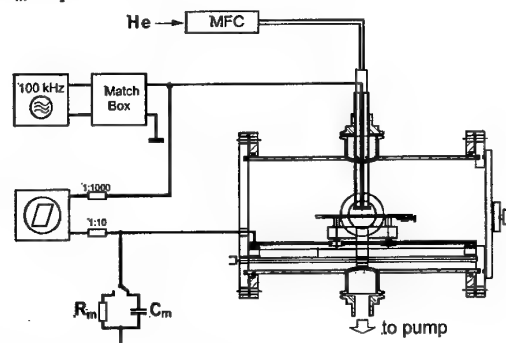
Fig. 1. Experimental set-up

The electrode distance was kept at 1.5 mm for the experiments described here.

3. Model

The simulation of the homogeneous barrier discharge is based on the continuity equations for electrons, ions, and metastable atoms and molecules, and the Poisson equation. The mobility, diffusion, excitation and ionization coefficients are calculated on the basis of the Boltzmann equation. The interaction between plasma and electrodes is described by boundary conditions. We assume the emission coefficients γ to be equal to 0.05 for glass and 0.1 for metal. Electron desorption plays no role in the glow discharge.

In helium, relatively large densities of metastable states can occur due to their ineffective destruction [3]. Hence, different ionization channels must be considered to describe the helium discharge properly (Fig. 2).
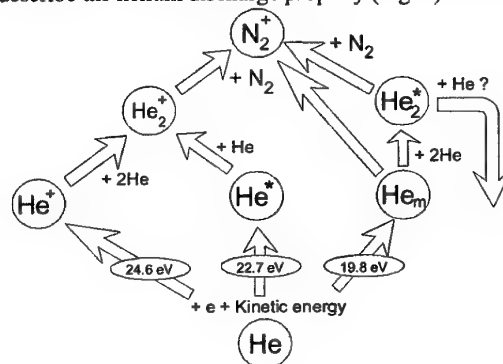
Fig. 2. Channels of ionization in helium

Besides the direct ionization, there is the Hornbeck-Molnar process, i.e., the ionization by collision of highly excited states with helium atoms, and the most effective Penning ionization. At high pressure, the conversion of ions causes the formation of impurity (N_2) ions within the time of 0.1 μs.

4. Results and discussion

We applied amplitudes of the sustaining voltage between 0.66 and 1.63 kV and obtained the homogeneous glow discharge throughout the whole range.

The experimental and calculated electrical characteristics of the discharge at 1.2 kV are shown in Fig. 3. Theory and experiment are in good agreement.
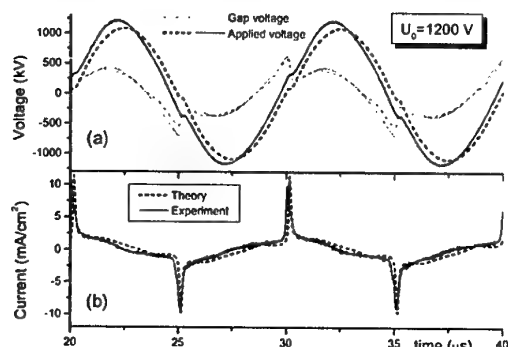
Fig. 3. Comparison of the experimental and theoretical curves of gap and applied voltages (a) and current (b)

The breakdown occurs as the gap voltage attains the value of 0.6 kV. In this phase, the applied voltage is slightly disturbed due to the nonideality of the power supply (in the theory, we use the external resistance R=50 kΩ). Positive and negative current peaks have different amplitudes; the larger peak occurs when the metal electrode serves as cathode.

We should note the following aspect of the ionization kinetics. When the ionization scheme shown in Fig. 2 is used, the excitation of metastable helium is followed by ionization with almost 100% efficiency. The breakdown voltage in this case is about 0.3 kV. Therefore an effective destruction mechanism for metastable states has been assumed to achieve better agreement with the experiment. A possible mechanism is the transition of a vibrationally excited excimer molecule to the radiating state via collision with a helium atom. The destruction frequency in our model is taken to be 10^6 s^{-1}.
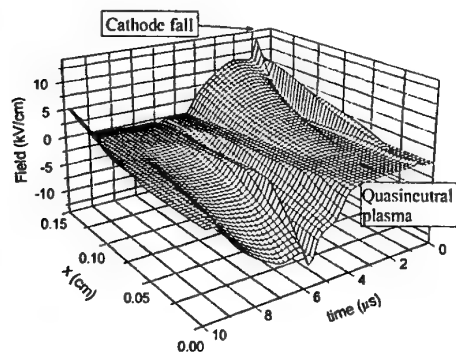
Fig. 4. Distribution of electric field in space and time

Besides the electrical characteristics, the model provides the spatial distributions of internal plasma characteristics. In Fig 4 the distribution of the electric field is shown.

During the breakdown, a cathode fall region with strong electric field is developed. After this phase, a positively charged cathode sheath and quasi neutral plasma region with zero field can be seen. The strong field in the cathode region can accelerate the ions efficiently, which can be useful for surface modification applications.
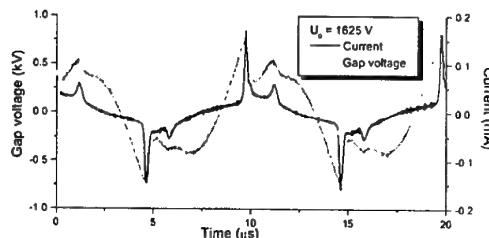
Fig. 5. Current and gap voltage for two-peak mode

At higher amplitudes, a second current peak is observed (Fig. 5). Such a multi-peak structure was observed by other authors too [4], where it was proven that the second peak corresponds to the breakdown at the periphery of the discharge gap.

5. Conclusion

We consider the study of the homogeneous DBD in He as a valuable contribution to the understanding of the discharge mechanism. The promising results of the simulation encourage us to study other gas mixtures too and to apply the model to gases with a technical relevance to surface treatment.

6. Acknowledgements

7. References

[1] U. Kogelschatz, B. Eliasson, W. Egli, *J. Phys. IV France* 7 (1997) C4
[2] R. Foest, F. Adler, F. Sigeneger, M. Schmidt, *Surf. Coating Technol.* **163-164C** (2003) 305
[3] Yu. B. Golubovskii, V. A. Maiorov, J. Behnke, J. F. Behnke, *Proc. of HAKONE VIII* (Pühajärve, Estonia, 21-25 July 2002; http://www.ut.ee/hakone8) Vol 1 p 48
[4] Mangolini L. et al., *Appl. Phys. Lett.* **80** (2002) 1723

Determination of gas temperature in cathode fall of the self-sustained normal atmospheric pressure dc glow discharge

V.I. Arkhipenko, A.A.Kirillov, L.V. Simonchik, S.M. Zgirouski

Institute of Molecular and Atomic Physics NASB, F.Skaryna Ave. 70, 220072 Minsk, Belarus

The result of gas temperature measurements in cathode region of atmospheric pressure glow discharge in helium are presented. Temperature was determined using molecular bands of the first negative system of nitrogen (0,1) and OH ($A^2\Sigma^+$-$X^2\Pi_i$) (0,0) band. The obtained results are compared with calculated one using one-dimensional model of the cathode fall taking into account the volumetric heat generation.

1.Introduction

Gas temperature is one of main characteristic of a discharge gases, as it determines gas density and, as consequence, other discharge parameters. In [1] were determined main parameters of cathode fall, namely, the electric field profile, cathode fall thickness, current density, heat flux to the cathode. Gas temperature in mentioned work was measured only in negative glow. The aim of present investigation is a reception of the temperature distribution in cathode fall of the self-sustained normal atmospheric pressure glow discharge in helium.

2. Experimental

The self-sustained normal atmospheric pressure dc glow discharge was created in the pressurized chamber between two electrodes: the weakly rounded tungsten anode (diameter 6 mm), and flat circular steel cathode (diameter 30 mm) [1]. Interelectrode gap was about 4 mm. Experiment was fulfilled at discharge current of 1
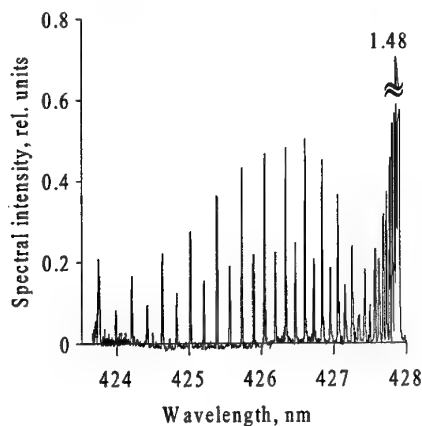
Fig. 1. Spectrum of the N_2^+ (0,1) band

Ampere. The impurities concentration in helium flow (H_2, N_2, O_2, Ar, CO_2, CO, Ne, H_2O) wasn't exceeding 0.02 %. The intensive water cooling of cathode was ensured due to its special design.

The enhanced image of glow discharge using two objectives was focused onto entrance slit of the scanning 0.5-meter double diffraction monochromator of high resolution MDD500x2. At diffraction gratings with 1800 line per millimeter the inverse linear dispersion is
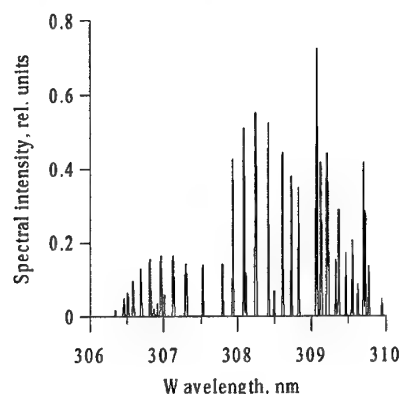
Fig. 2. Spectrum of the OH (0,0) band

0.52 nm/mm. Band spectra of the (0,1) N_2^+ and (0,0) OH used for gas temperature determination are shown in fig. 1 and 2. At that the separate spectral lines have Gaussian profiles with halfwidth about 0.0065 nm.

3. Evaluation of gas temperature

The method of the relative rotational line intensity of molecular gases was used at determination of gas temperature [2]. Band of (0,1) of $N_2^+(B^2\Sigma_u^+ - X^2\Sigma_g^+)$ was chosen because it is free from superposition with other spectral lines. The rotational line of R-branch with N'>6 are used only. The necessary wavelengths for identification of rotational lines were calculated according [3].

Intensity of a doubling of rotational lines of R–branch at presence of boltzmann equilibrium is defined as

$$I_{N'} = \text{const} v_N^4 S_{N'} g_{N'} (2N'+1)\exp\left\{-\frac{hcF(N')}{kT}\right\},$$

where $v_{N'N''}$ – frequency of optical transition; $g_{N'}$ – statistical weight caused by nuclear spin ($g_{N'}$ = 1 for even number N' and $g_{N'}$ = 2 for odd number N'); F(N') – magnitude of rotational term of the excited electron state; S_N=N'/(2N'+1) – Hönl–London factor of R–branch convolute on doubling line structure [4]. To

h convolute on doubling line structure [4]. To determine the temperature using experimental spectra a graph of dependence $\ln(I_{N'}/G_{N'})$ against the rotational term energies, where $I_{N'}$ – measured intensity of doubling, and $G_{N'} = v^4_{N'} S_{N'} g_{N'} (2 N'+1)$. The line doubling $\Delta_{N'}$ is increased while number N' is increased and becomes equal 0.0053 nm at N'=21. Therefore, at determination of the experimental values $I_{N'}$ the profile change of doubling structure against the rotational line number was taken into account. In case of linear dependence of $\ln(I_{N'}/G_{N'})$ on F(N') it can talk about boltzmann distribution of population of molecule levels N'. At that the angle of regression slope will determine the rotational temperature.

Intensities of rotational lines of hydroxyl molecule at presents of boltzmann equilibrium is as follow

$$ I_{BN'} = \text{const} v_{BN'} A_{BN'} (2J' +1)\exp\left\{-\frac{hcF(N')}{kT}\right\} , $$

where B – branch number, $v_{BN'}$ – frequency of optical transition, $A_{BN'}$ – Einstein's coefficient of spontaneous emission, J – full angular moment, F(N') – magnitude of rotational term of excited electron state. Values of the level energies and Einstein coefficients was taken from [5, 6]. As consequence, gas temperature is determined on line slope pictured the dependence $\ln[I_{BN'}/v_{BN'}A_{BN'}(2J+1)]$ on F(N').

4. Results and discussion

The atmospheric pressure glow discharge is characterized the small dimensions of cathode regions and high heat release. As it is shown in [1], the cathode fall thickness is about 70 μm and maximal electric field
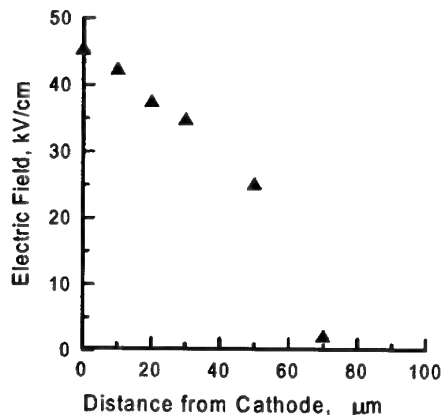
Fig. 3. Axial distribution of the electric field strength

strength ~45 kV/cm. Axial distribution of electric field in cathode fall is shown in fig. 3. Large quantity of heat generation in this narrow region takes place. Heat rejec-

tion from cathode fall is carried through the water-cooled cathode.

In fig. 4. the gas temperature determined in cathode fall using both the N_2^+ and OH bands is presented. As it seen, the values of temperatures in end of cathode fall (>70 μm) are in reasonable agreement. However these temperatures differ close cathode surface. Difference is
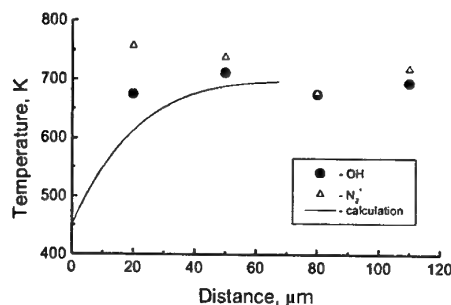
Fig. 4. Temperature distribution in cathode fall.

about 100 K and is more then experimental error. High temperature value obtained using the N_2^+ band, in our opinion, is explained by a acceleration of N_2^+-ions in strong electric field close cathode surface.

Calculated temperature distribution obtained using the model of cathode fall developed by Baranov-Smirnov [7] is pictured in fig. 4 (solid curve). Good correspondence of calculated temperature to measured one using the OH band is observed at distances more then 20 μm. Sharp decrease of gas temperature close cathode we can't resolve because the spatial resolution of our optical system is about 25 μm.

5. References

[1] V.I. Arkhipenko, S.M .Zgirouski, A.A. Kirillov, L.V. Simonchik, *Plasma Phys. Reports* 28 (2002) 930.

[2] V.N. Ochkin, S.Yu. Savinov, N.N.Sobolev, *Trudy PhIAN* 157 (1985) 6.

[3] K.A. Dick, W. Benesch, H.M. Crosswhite, S.G. Tilford, R.A. Gottscho and B.W. Field , *J. Molec. Spectr.* 69 (1978) 95.

[4] G. Herzberg, *Molecular spectra and molecular structure. 1. Spectra of diatomic molecules,* N.Y.: D. van Nostrand (1951).

[5] J.A. Coxon, *Can. J. of Phys.* 58 (1980) 933.

[6] I.L. Chidsey, D.R. Crosley, *J. Quant. Spectrosc. Radiat. Transfe* 23 (1980) 187.

[7] G.A. Baranov, S.A. Smirnov, *Techn. Fiz.* 44 (1999) 1305.

Comparison of parallel and serial resonance circuits for generation of surface barrier discharges

M.Teschke, D. Korzec, J.Engemann, R. Kennel

Forschungszentrum für Mikrostrukturtechnik-*fmt*, University of Wuppertal,
Rainer Gruenter Straße 21, 42119 Wuppertal, Germany

Two different principles of power supplies for generation of planar dielectric barrier discharges at atmospheric pressure were investigated. The comparison of parallel and serial resonance circuits has been made and the power loss mechanism in both cases has been studied. A power supply based on serial resonant circuit of plasma source has been developed.

1. Introduction

Atmospheric pressure planar dielectric barrier discharges (PDBD) are used on a large scale in industry for applications like ozone production for gas and water purification [1], film deposition and surface treatment of polymers or other materials [2]. With increasing effective area of the discharge electrode grows the need for effective and low-loss power.

Different discharge excitation principles are possible. For laboratory applications high voltage amplifiers are often used, whose output stage is operated within the active range. The disadvantage of this approach is high electrical power loss. Therefore it is unsuitable for the industrial applications. Besides, appropriate amplifiers for high voltage (several kV) and high power are very expensive. For that reason resonant power supplies are frequently used, which utilize the strongly capacitive characteristics of the plasma sources. Nevertheless also in this case the electrical losses are not negligible and this is the subject discussed in the present work.

2. Electrical characteristics of PDBD

The typical investigated system of the surface barrier discharge (SBD) [3] consists of two electrodes separated by 0.4 mm thick, high purity Al_2O_3 ceramic plate. The discharge electrode consist of 27 interconnected 1 mm wide and 45 mm long strips. On the opposite side the induction electrode is formed as a 70 mm × 50 mm rectangle. A sinusoidal signal with a frequency in the range of 5-20 kHz and voltage amplitude 2-6 kV is applied between the electrodes.

Without plasma the electrical behavior of the source is almost purely capacitive. Only a small real component of the power, caused by the dielectric losses, is to be considered. During the discharge rises this real component considerably by the power consumption of the plasma. The energy from the power supply is transferred into the plasma during partial discharges (PD). The resulting current pulses are in the range of nano- to microseconds and are superposed on the capacitive current. The voltage breaks down during the pulse duration more or less strongly (see figure 1).

or less strongly (see figure 1).
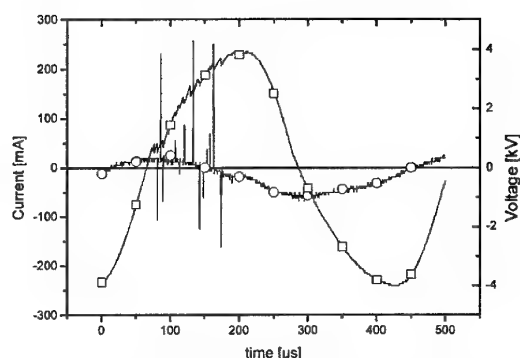
Figure 1. Typical current-voltage characteristics (o = current, □ = voltage) of a SBD-source in 80% N_2 , 20% O_2 operated with an parallel resonant power supply (Lifetech)

3. The resonant power supply

In principle two types of resonant power supply are possible: parallel and serial [4].
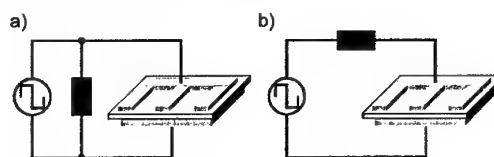
Figure 2. a) Parallel and b) serial resonant circuit.

A coil or a transformer with large main inductance or strain inductance is connected to the plasma source. The circuit formed by the inductance and the capacity of the plasma is connected to the power supply working at the resonant frequency. At higher power this excitation can be done with low electrical losses only with rectangular or pulse voltage signal.

The common way to operate a plasma source is to apply a voltage from the transformer which is connected parallel to it. In this way the plasma source and the main coil of the transformer work as a parallel resonant circuit.

When the rising time of the applied voltage is very short as in the case of rectangular or pulsed voltage the capacity of the plasma source behaves like a short cut. The strongly rising current produces high power losses in the wire resistances and in the output stage of the power supply.

The advantage of a serial resonant circuit is that the coil limits the current rise in normal operation mode but also when an accidental short cut occurs in the plasma source.

Power supply delivers energy in the resonant circuit in each half period. As long as plasma is still off, more and more energy is stored in the circuit. To ignite the plasma some energy has to be consumed, the voltage breaks down and the capacity of the plasma source changes very fast involving a change in the resonant frequency. This means that the resonant circuit is not any more stable.

In order to overcome this disadvantage two methods are proposed:
1. The energy in the circuit has to become much higher using for example capacities parallel to the plasma source. This makes the voltage drop weaker.
2. The frequency of the power supply has to be adjusted permanently to the resonant frequency of the circuit. This has been realized by the use of "current zero point detection" method.

The method 1 has the disadvantage that the parallel capacities stabilize the voltage too restrictive. More and more energy will be transferred in the plasma and this can cause the damage of the plasma source. To avoid this, a second coil L_{cpl} has been introduced in the circuit in order to adjust the coupling between plasma source and power supply. This limits the current between the parallel capacity and the plasma source.
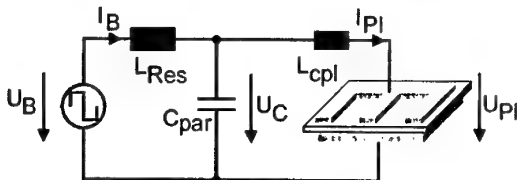
Figure 3. The resonant circuit consists of L_{Res} and C_{Par}. Coupling is realised by L_{cpl}.

4. The current synchronizing method

If an ideal serial resonant circuit is powered with a rectangular shaped voltage signal, the current reaches the zero point exactly at the moment of switching the voltage. This fact can be used to synchronize the frequency of power supply with the resonant frequency.

A technical problem is the detection of the current zero point [5] from the noisy signals produced by the plasma. This problem was solved by use of the „dynamic hysteresis". The sensitivity of detection varies in

time. The sensitivity reaches a maximum just before the current crosses its zero level and gets the minimum immediately after this.

5. Results

With this new power supply concept it is possible to operate the atmospheric pressure plasma sources in a low loss way and with the possibility to vary the power coupled into the plasma.

Figure 4 shows the current and voltage characteristics of the plasma source with (figure 4b) and without (figure 4a) the coupling inductance L_{cpl}.

The difference is obvious. The current peaks are limited strongly. If no coupling coil is used, the lifetime of the plasma source is reduced from hundreds of hours to maximal one hour. In this last case the plasma source gets much hotter.
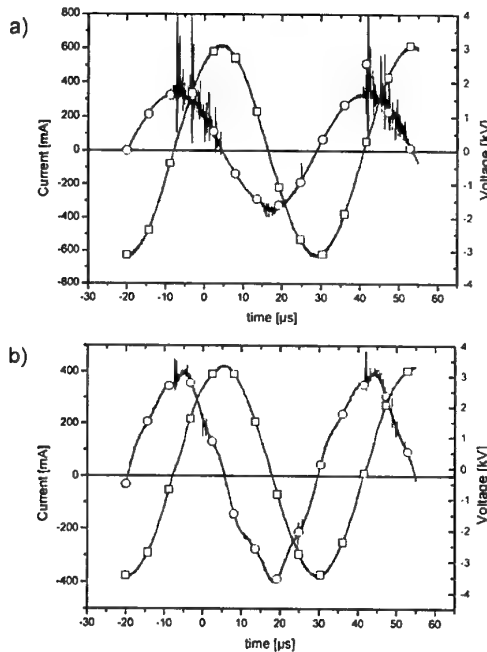
Figure 4. Current and voltage characteristics of a plasma source powered by the serial resonance voltage supply without (a) and with (b) $L_{cpl} \approx 1mH$ (o = current, □ = voltage).

References:

[1] S. Masuda et al, IEEE Tr. Industry Appl. **24** (1988) 223
[2] Stefecka et al, Proc. XXV ICPIG, Nagoya, Japan, 17-22 July 2001, Vol. 4, pp. 45-46
[3] E. Finantu-Dinu et al, PSE 2002, Garmisch-Partenkirchen, Sept. 9-13, 2002
[4] J.Kunze et al, IEEE Ind. Appl, 1992, Vol 1, pp. 750-753
[5] R. Kennel, atp, 28.Jg, **12**/1986, pp. 580-582

Investigation of the surface barrier discharge topology by use of intensified CCD camera

E.G. Finantu-Dinu, D. Korzec, J. Engemann

Forschungszentrum für Mikrostrukturtechnik-*fmt*, University of Wuppertal,
Rainer Gruenter Straße 21, 42119 Wuppertal, Germany

The topology of surface barrier discharges (SBD) at atmospheric pressure in ambient air is investigated with an intensified CCD camera. The distributions of partial discharges (PD) over the alumina surface for different exposition times and different topological features of the electrode are presented and related to the temporal PD sequences. The excitation frequency is 3.7 kHz. The voltage amplitudes are in the range of 2-5 kV.

1. Introduction

The very promising type of dielectric barrier discharge (DBD) for plasma processing is surface barrier discharge (SBD) [1]. It is generated on the dielectric surfaces by alternating electrical voltage in arrangements with a structured discharge electrode on a dielectric surface and a plane induction electrode on the reverse side of the dielectric. The main applications of the SBD are ozone generation [1], exhaust gas decomposition [2] and more recently surface treatment and film deposition at atmospheric pressure [3]. Important information about the mechanism and structure of the surface discharge can be obtained from time resolved voltage and current of the discharge electrode [4] and form investigation of high speed and sensitive CCD photographs [5]. Strong influence on the PD development has the layout of the discharge electrode. It was shown by electrical measurement [4] and by electrical simulation [6]. In this work the influence of the electrode layout on the PD is investigated by use of ICCD.

2. Experiment

The discharge system described in detail in [4] consists of two electrodes separated by 0.4 mm thick, high purity Al_2O_3 ceramic plate. The discharge electrode comprises 447 holes with diameter of 1.45 mm, organized in 19 rows. Such hole is the dark circle in Fig. 1a. On the opposite side the induction electrode is formed as a 70 mm $\times$ 50 mm rectangle. A sinusoidal signal with a frequency of 3.7 kHz and voltage amplitude 2-5 kV is applied between the electrodes.

The ICCD camera PRINCETON Instruments 576-G/1 gated by pulse generator PRINCETON Instruments PG 200 is used for taking short time, down to 10 ns duration, pictures of the SBD. The sufficient sensitivity is achieved by electro-thermal cooling of the ICCD chip down to -35 C°. The macro-objective allows the magnification sufficient for observation of single PDs.
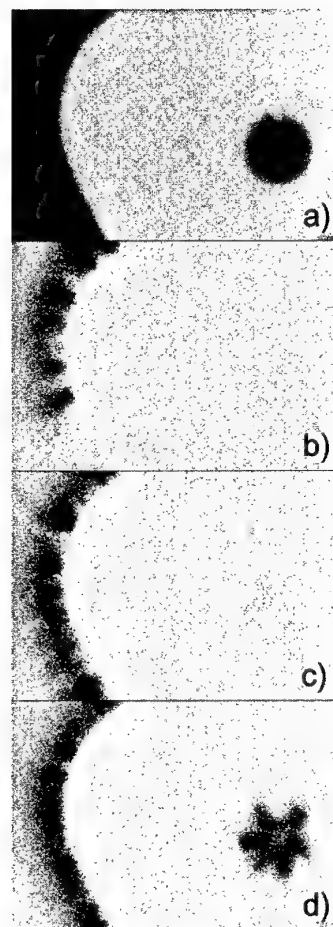
Fig. 1: Influence of the electrode edge shape on the sequence of PD ignitions. a) The electrode without discharge. The dark areas represent the Al_2O_3 surface. b), c) and d) are the inverted pictures (discharge is black) of PDs with voltage amplitudes of 3.5, 4.0 and 4.5 kV respectively. Exposition time is 10 ms.

3. Results and discussion

The shape of the electrode edge has strong influence on the ignition voltage and PD density. In Fig. 1a the fragment of the SBD electrode is shown, having three types of edge shape: convex (left top corner), linear (left low corner) and concave (hole in the electrode at the right side). With increasing voltage the PDs at the convex part of the electrode edge ignite first (Fig. 1b), followed by the linear part (Fig. 1c) and finally by concave shaped holes (Fig. 1d). It can be explained by increasing maximum electric field with increasing grade of electrode edge convexity and is in agreement with electrical measurements [4] and field simulations [7].
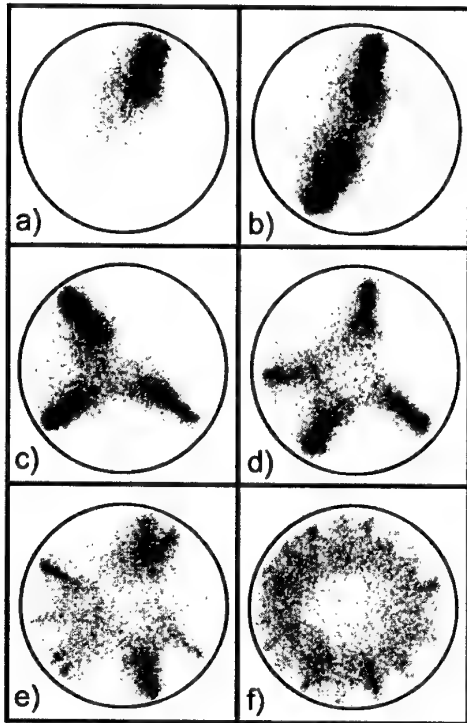
Fig.2: The inverted pictures of the discharge in the hole in the electrode (as shown in Fig. 1a). The electrode edge is shown as a circle. The exposition time is 10 ms. The voltage amplitude for a), b), c) and d) is 3.9 kV, for e) is 4.4 kV and for f) is 4.9 kV.

The observation of the SBD in the hole of the discharge electrode confirms the predictions of electrical simulation of the PD development by use of PSPICE circuit simulator. For observation time much longer than the voltage excitation period of about 0.3 ms and low voltage, it can be seen that the PDs ignite preferentially at the same position in subsequent cycles, resulting in "discrete" discharge pattern (see Fig. 2a-d). The positions of frequent PD occurrence are geometrically as far as possible, because of the repelling forces of the

charge stored at the ceramic surface. This effect is less pronounced at higher voltages (see Fig. 2e and 2f) at which PDs are distributed more evenly around the electrode hole edge.

For exposition times shorter than voltage excitation period but much longer than the typical PD duration, more than one PD within exposure time can be observed. The distance between these PDs is sufficient to avoid
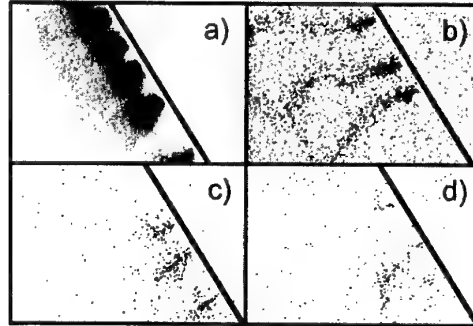
Fig.3 The inverted pictures of the discharge at the linear part of the electrode edge (as shown in Fig. 1a). The electrode edge is shown as a line. The exposition times are a) 10 ms, b) 10 μs, c) 1 μs and d) 0.1 μs. The voltage amplitude is in all cases 4.9 kV.

the suppression of the subsequent PD by the electrical charge stored during an earlier PD (see Fig. 3b and 3c).

What is somewhat surprising is, that for exposure times as short as 100 ns, still more than one PD structure can be recognized (see Fig. 3d). It means, that PDs can ignite almost simultaneously at two positions. These positions can be apart from each other. For example concurrent existence of PD at the linear part of the electrode and in the hole is observed. It means that in the time scale of a single PD, the ignited PD is not disabling the ignition of subsequent PD.

Acknowledgements:

References:

[1] S. Masuda et al, *IEEE Tr. Industry Appl.* **24** (1988) 223.
[2] S. Masuda et al, *IEEE Tr. Industry Appl.* **29** (1993) 781.
[3] Štefečka et al, *Proc. XXV ICPIG*, Nagoya, Japan, 17-22 July 2001, Vol. 4, pp. 45-46.
[4] E. Finantu-Dinu et al, *PSE 2002*, Garmisch-Partenkirchen, September 9-13, 2002.
[5] A. B. Savaliev and G. J. Pietsch, Hakone VIII.
[6] M. Teschke et al, *PSE 2002*, Garmisch-Partenkirchen, September 9-13, 2002
[7] D. Korzec et al, *Asian European Plasma Surface Engineering AEPSE 2001*, Nagoya, Japan

Interpretation of the current signal collected from surface barrier discharge electrodes

D. Korzec, E.G. Finantu-Dinu, J. Engemann

Forschungszentrum für Mikrostrukturtechnik-*fmt*, University of Wuppertal,
Rainer Gruenter Straße 21, 42119 Wuppertal, Germany

The current signal measured at the grounded electrode of the surface barrier discharge (SBD) excited in the frequency range 1-10 kHz is typically distorted by electric circuitry oscillations in MHz range. Numerical techniques for extraction of the partial discharge (PD) current signals with durations in ns range are proposed.

1. Introduction

The surface barrier discharge (SBD) [1] and insulated surface barrier discharge (ISD) [2] are very promising types of dielectric barrier discharges (DBD). Their main applications are ozone generation [1], exhaust gas decomposition [3] and more recently surface treatment and film deposition at atmospheric pressure [4]. The electrical measurements [5] show strong influence of excitation voltage and frequency, electrode layout and coating material on the PD development. The measured current represents the response of the electric circuitry connected to the electrode on the discharge current. In this work the method for determination of the discharge current from the measured current is proposed. It is based on the fast FOURIER transform (FFT).

2. Experiment

The discharge system described in detail in [5] consists of two electrodes separated by 0.4 mm thick, high purity Al_2O_3 ceramic plate. The surface of the discharge electrode is coated by diamond like carbon (DLC) or polymeric film. On the opposite side the induction electrode is formed as a 70 mm × 50 mm rectangle. A sinusoidal voltage with a frequency of 3.7 kHz and amplitude in range 2-5 kV is applied between the electrodes. For current measurements the digital oscilloscope Tektronix TDS 7254 with a high frequency AC current probe CT6 is used.

3. Results and discussion

The typical current waveform for DLC coated ISD electrode is shown in Fig. 1a. The "spikes" easier recognizable in magnification shown in Fig. 1b, are related to partial discharges (PD) but show the PD currents overlapped with oscillations in MHz range [5]. These oscillations are interpreted as response of the RLC circuitry connected to the discharge electrode on
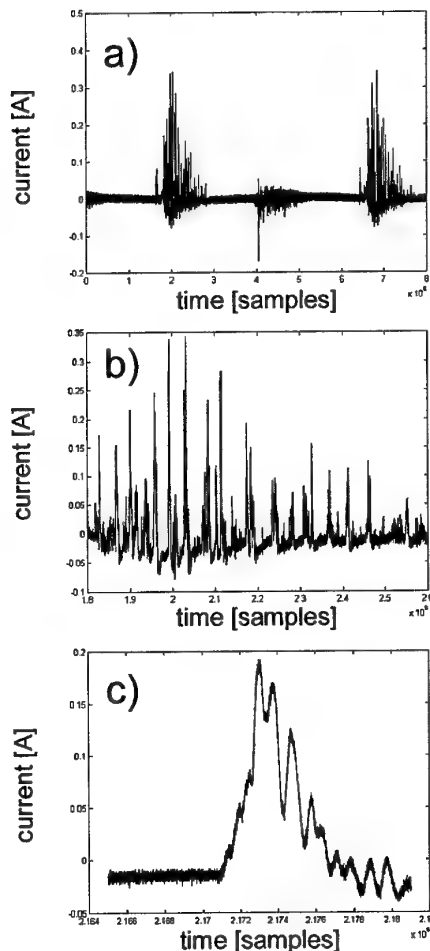
Fig. 1: Typical current signal of ISD in 10% oxygen + 90% nitrogen gas mixture at 700 mbar. a) Entire excitation cycle, b) signal segment and c) PD response of the circuitry. Sample = 0.1 ns. Coating: 1 μm DLC.

the PD current. Assuming a DIRAC pulse excitation put on the serially connected resistance R, capacitance C and inductance L, the response of the circuit is given as:

$$g(t) = \frac{1}{\sqrt{LC}} \exp\left(-\frac{R}{2L}t\right) \sin\left(\frac{t}{\sqrt{LC}}\right)$$

One of parameters having strong influence on the oscillation frequency is the length of wires connecting the electrode system to the coaxial cable. In Fig. 2 the examples of the PD signal for two different connection

current of single PD can be considered as a convolution of the real PD current and the circuit response on DIRAC impuls. In such case the real PD current can be obtained following the algorithm presented graphically in Fig. 4.

In first step the FFT of the measured signal x(t) and of the dumped RLC-oscillation g(t) are calculated. Than the signal transform X(f) is divided by the oscillation transform G(f). From the result the inversion FOURIER transform (IFFT) is determined, which gives the real PD current Y(t). Also overlapping signal of subsequent PDs can be de-convoluted by use of this scheme (see Fig. 3).

Fig.2: The response of the circuitry for two oscillation frequency a) 16.8 MHz to b) 20 MHz, due to different lengths of wire connections to the electrode.

wire lengths are shown. For technically useful electrode geometries it is not possible to eliminate the electric connections inductance completely. The measured
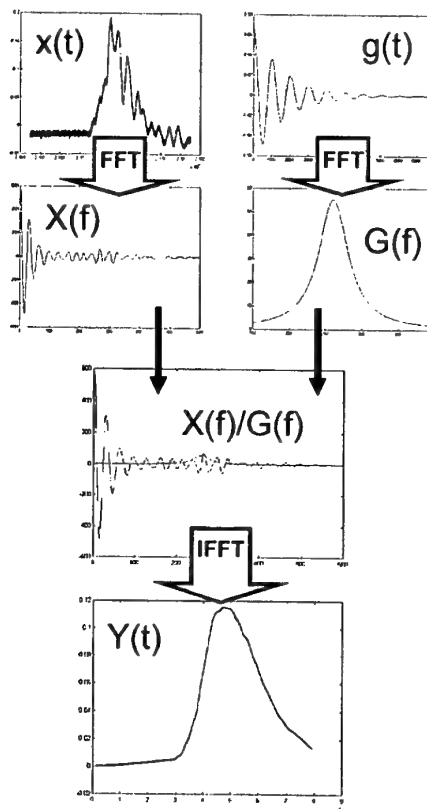
Fig.4: Principle of numerical removal of the electric circuit oscillation from the measured current signal.

Fig.3: Deconvoluted current signal for overlapping PDs.

References:

[1] S. Masuda et al, *IEEE Tr. Industry Appl.* **24** (1988) 223.
[2] D. Korzec et al, *Asian European Plasma Surface Engineering AEPSE 2001*, Nagoya, Japan.
[3] S. Masuda et al, *IEEE Tr. Industry Appl.* **29** (1993) 781.
[4] Štefečka et al, *Proc. XXV ICPIG*, Nagoya, Japan, 17-22 July 2001, Vol. 4, pp. 45-46.
[5] E. Finantu-Dinu et al, *PSE 2002*, Garmisch-Partenkirchen, September 9-13, 2002.

The incorporation of heating effects in atmospheric pressure gas discharges

A P Papadakis[1], G E Georghiou[2] and A C Metaxas[3]

[1]Electricity Utilization Group (EUG), Department of Engineering, University of Cambridge, Cambridge, CB2 1PZ, UK
[2]Electronics and Computer Science Department, University of Southampton, Highfield, Southampton, SO17 1BJ, UK
[3]St John's College, University of Cambridge, Cambridge, CB2 1TP, UK

E-mail:ap263@eng.cam.ac.uk, geg@ecs.soton.ac.uk, acm@eng.cam.ac.uk,

Abstract

The latest extension of the FE-FCT algorithm used for the solution of gas discharge problems is presented in this paper. The solution of Navier Stoke's equations is coupled to the continuity and Poisson's equations to account for the heating effects of the neutral gas species in near atmospheric pressure gas discharges. Adaptive meshing techniques that adjust the mesh in time are also incorporated, so that the highly transient phenomena involved can be captured. Results are presented for the development of avalanches and streamers in a 1 mm uniform field gap in air at atmospheric pressure, in order to validate the new algorithm. The assumption adopted by many authors to date, namely, that there is no significant heating involved early in the development of such a discharge is investigated.

1. Introduction

The detailed analysis of the spark discharge is important in the design of lasers, exhaust filters and for the protection of microwave systems. Experiments have shown that the spark discharge development after the avalanche and the primary streamer is highly dictated by the heating effects of the neutral gas.

2. Theory

In order to incorporate heating effects in near atmospheric pressure gas discharges, as manifested by the heating of the neutral gas species, the Navier Stoke's equations (conservation of mass, momentum and energy for the neutral gas) need to be coupled to the continuity equations for charged particles (electrons, positive and negative ions) and Poisson's equation for the electric field. The equations are solved in two-dimensional cylindrical axisymmetric coordinates. A Finite Element Flux Corrected Transport method (FE-FCT) has been developed and used for the transport equations [1]. The primary purpose of this work is to validate the new part of the algorithm, i.e. that of the Navier Stoke's in the presence of the continuity equations and Poisson's equations, following the validation of the Navier Stoke's algorithm in [2]. Furthermore, this is the natural progression of previous work by the authors, as they have already simulated the same configuration assuming no heating effects. In this way, the assumption for no heating effects and the validation of the coupling of the Navier Stokes with the Poisson and the continuity equations is achieved. As expected, it has been proven that there is no considerable heating during the avalanche and primary streamer stage and that heating does not significantly affect their development.

3. Adaptive Meshing

The complexity of the new model (coupling of the above three sets of equations) and the computational demand makes the solution of such problems using conventional software very difficult, therefore the authors have developed their own algorithm in C++. An adaptive mesh generator has also been developed such that computational needs are considerably reduced, making it possible to analyse heating effects not only in short gaps, but also in long gaps. The error indicator used for the refinement of the adaptive meshing is the one used by Lohner [3]. The error estimator in multidimensional form is as follows:

$$E^i = \sqrt{\frac{\sum_{k,l}(\int_{\Omega} N_k^i N_l^j d\Omega . U_j)^2}{\sum_{k,l}(\int_{\Omega}|N_k^i|[|N_l^j U_j| + \varepsilon(|N_l^j||U_j|)]d\Omega)^2}}$$

where E^i is the error indicator value at node i, N_K^l is the shape function of node i in element k, N_L^J is the shape function of node j in element l and U_j is the value of the variable chosen to be used as error indicator at node j and ε is a factor varying from 0 to 1. The value of ε is chosen depending on the algorithm used to solve the partial differential equation, since the term following ε is added as noise filter, so that any loss of monotonicity such as wiggles or ripples are not refined. The authors have used three different variables for error indication, which are the electron density, the positive ion density and the modulus of the electric field.

The advantages of the above error indicator are that it is fast to calculate, it is dimensionless, it varies from 0 to 1 such that prefixed tolerances and many variables as error indicators can be used and that it is reliable for steady state and highly transient applications, as in the case of the development of the spark discharge.

4. Results

In the configuration used to test the heating effects, a voltage of 5600 V is applied between two parallel plates of distance 1 mm apart in ambient air. As an initial condition, a single electron is released at a distance of 1×10^{-4} m from the cathode.

Figure 1 shows the electron density two-dimensional plot as the streamer propagates towards the cathode. Densities of the order of 10^{20} particles/m^3 are in agreement with primary streamer propagation theory.
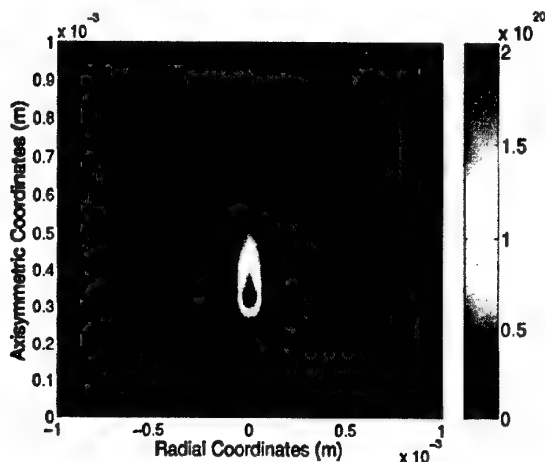
Figure 1: Two-dimensional axisymmetric plot of the electron density of the primary streamer at time t = 4.61 ns.

Figure 2 is a temperature distribution plot during the propagation of the primary streamer towards the cathode. It can be seen that a temperature rise of a few degrees occurs. To test the ability of the heating effects in changing the propagation of the avalanche and the primary streamer, early in its development, it was assumed that all the energy from the electrons, positive and negative ions is transferred to the neutral particles as Joule heating, when charged particles collide with the neutral particles. Taking this into consideration, it is evident that heating does not affect the propagation of the avalanche and primary streamer.

5. Conclusions

As expected, no significant heating arose during the avalanche and streamer propagation that could affect the discharge, and hence the long-held assumption of no heating is justified.

It is now possible to analyse the heating effects of neutral gas species in atmospheric or near atmospheric pressure gas discharges. Heating effects can also be simulated in long gaps, due to the adaptive mesh generator developed. With the densities of the charged particles and the electric field increasing at later stages of the discharge, the heating effects will no longer be negligible, but will dictate the development and behaviour of the spark.
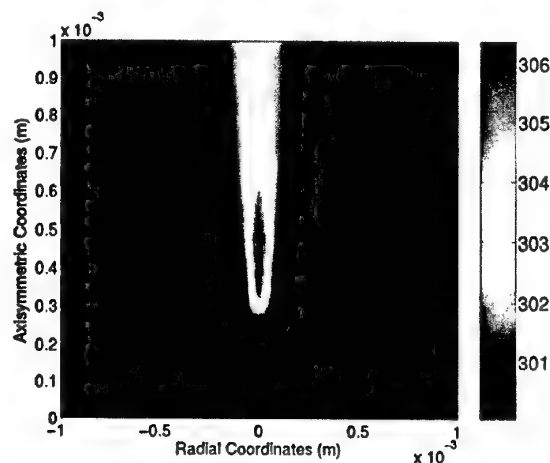
Figure 2: Two-dimensional plot of the temperature during the propagation of the streamer at time t = 4.61 ns.

6. References

[1] G.E. Georghiou, R. Morrow and A.C. Metaxas, Journal of Physics D: Applied Physics, *Two-dimensional simulation of streamers using the FE-FCT algorithm* **33** (2000) L27-32.

[2] A.P. Papadakis, G.E. Georghiou and A.C. Metaxas, XIV International Conference on Gas Discharges and their Applications, *Towards the simulation of spark discharges* **2** (2002) 272-275.

[3] R. Lohner, Computer Methods in Applied Mechanics and Engineering, *An adaptive finite element scheme for transient problems in CFD* **61** (1987), 323-338, North Holland.

DC Diaphragm Discharge in Water Solutions

Zdenka Stara, Frantisek Krcma

This contribution is focused on the investigation of the non-pulsed DC diaphragm discharge in water solutions. The optical emission spectroscopy was used for investigating the light spectrum of the diaphragm discharge in the solution. The light intensity was dependent on the initial discharge conditions.

1. Introduction

The electrical discharges in liquids have been a subject of research during a few last years [1, 2]. Especially point to plane and coaxial geometry were used. The high voltage used for creating the discharge was usually pulsed. Therefore, this work is focused on the diaphragm discharge with an applied non-pulsed DC high voltage which combination is not so common. The diaphragm discharge is also called „electrodeless" discharge because the electrodes does not disturb the discharge process.

2. Experimental setup

A batch discharge reactor was used in our experiments (Fig. 1) [3]. It consists of two parts with one stainless steel electrode in each part (negative, positive). The dielectric diaphragm with a small pinhole (PTFE, 0.25 mm) separated the both parts. The electrodes were installed in the distance of 2 cm from the diaphragm.
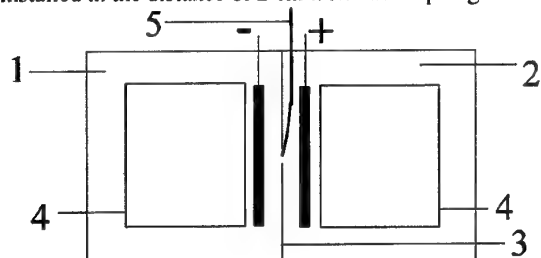
Fig. 1: The scheme of the batch reactor; 1 – negative part, 2 – positive part, 3 – diaphragm with pin hole, 4 – cooling boxes with ice-pack, 5 – optical fibre.

A non-pulsed DC high voltage from 1.4 to 2.8 kV was applied on the electrodes. To protect liquid before heating by the discharge, two cooling boxes with icy water were placed in the both parts of our reactor. NaCl

and Na_2HPO_4 salts were used to obtain the defined conductivity of initial demineralized water.

The optical emission spectroscopy was used for investigating the light spectrum of the diaphragm discharge in the solution. Especially hydroxyl radicals and some elements contained in salt (Na) were determined by this method.

3. Results and discussion

During the experiments the emission spectra of the discharge were observed. The investigation was focused on the emission intensity of the hydroxyl radicals generated by the diaphragm discharge. The observations were done in both salts (NaCl and Na_2HPO_4) and the discharge conditions were varied; the applied high voltage was used in the range 1.4 – 2.8 kV, the initial conductivity was 400 or 550 $\mu S \cdot cm^{-1}$ (the maximum hydrogen peroxide generation is reached at these two conductivities [3]). It was found that the light intensity of hydroxyl radicals decreases in both salts during the discharge. In Fig. 2 is shown an example of the OH integral intensity (306.5 – 318 nm) as a function of time.
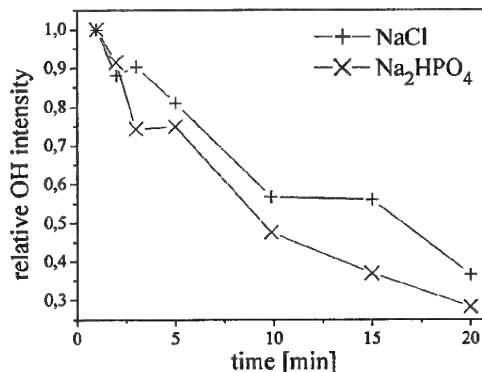
Fig. 2: The OH integral intensity as a function of time.

The evolution of this dependence might be caused by the decrease of OH radicals in the synthetic reaction which leads to the production of the hydrogen peroxide. This phenomenon was a subject of previous studies [3]. The influence of the applied high voltage on the emission intensity is demonstrated in Fig. 3. The increasing OH integral intensity with increasing voltage is evident from this picture and it corresponds with the increase of the hydrogen peroxide production as it was observed recently [3] and it is demonstrated in Fig. 4.
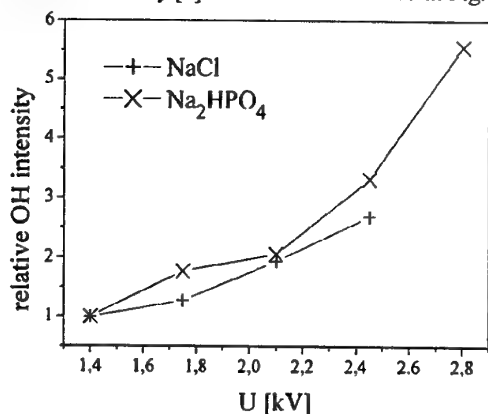
Fig. 3: The OH integral intensity as a function of the applied voltage.
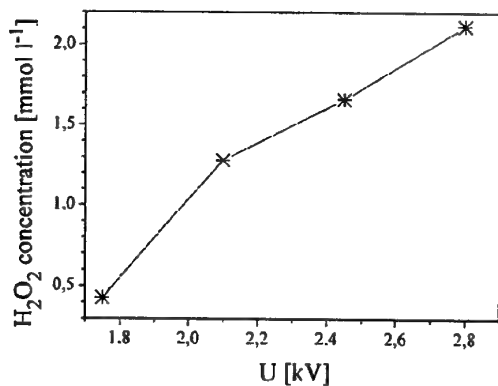
Fig. 4: Hydrogen peroxide generation as a function of applied voltage (3mM NaCl, initial conductivity 300 μS/cm)

The OH emission intensity also depends on the initial conductivity of the solution and used salt. The production of the hydroxyl radicals is higher in case of Na_2HPO_4 salt (see Fig. 3) and increases with the increase of the initial solution conductivity.

An interesting phenomenon was observed - the initial conductivity increased in time. The magnitude of the

conductivity change was higher in the positive part of the reactor. In both parts the final conductivity had stabilized on the constant value after 60 minutes of the experiment. The increase was caused by metallic traces involved from electrodes by the electrolysis.
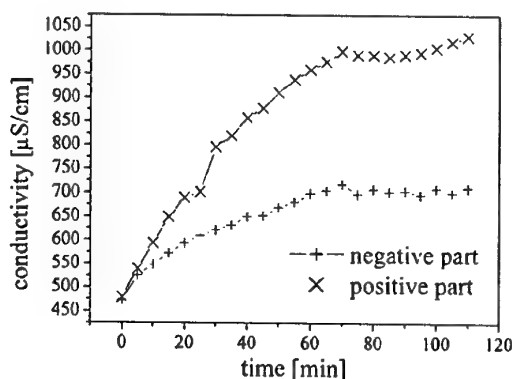
Fig. 5: Conductivity changes (5 mM NaCl, 2.8 kV)

4. Conclusion

The results of the optical emission spectroscopy applied on the non-pulsed DC diaphragm discharge are presented in this contribution. The OH integral intensity was counted and shown as a function of time and applied voltage. The light intensity decreases during the discharge and increases with increasing high voltage. The initial conductivity of the liquid also affects the light spectrum. The dependence of the emission intensity of hydroxyl radicals on the applied salt was studied.

5. Acknowledgement

6. References

[1] A. A. Joshi, B. R. Locke, P. Arce, W. C. Finney, *Hazard. Mater.* **41** (1995) 3.

[2] P. Sunka, V. Babicky, M. Clupek, P. Lukes, M. Simek, J. Schmidt, M. Cernak, *Plasma Source Sci. Tech* **8** (1999) 258.

[3] F. Krcma, Z. Stara, *Chemical Papers* **96** (2002) 82.

Improvement in the Performance by Changing Electrode Shape in Barrier Discharge type ESP

Hideyuki Ando[1], Yosuke Kuroda[1], Yoshihiro Kawada[1], Takeo Takahashi[1], Yoshiyasu Ehara[1], Tairo Ito[1], Akinori Zukeran[2], Yoshihiro Kono[2], Kouji Yasumoto[2]

1) Musashi Institute of Technology,1-28-1,Tamazutsumi,Setagaya-ku,Tokyo 158-8557,Japan
2) Fuji Electric Co.Ltd.,1-11-2,Osaki, Shinagawa-ku, Tokyo 141-0032,Japan

In general corona discharge is used in ESP (Electrostatic Precipitator). The corona discharge type ESP can remove DEP (Diesel Exhaust particles) at high collection efficiency but at low removal efficiency for NOx and re-entrainment phenomena due to low resistivity and particle agglomeration on the electrode. Barrier discharge is effective for removal NOx. Therefore, we are used Barrier discharge in ESP. In this paper, we investigated the plate type, punched hole type, and grid type electrode. As results, energy efficiency of particle collection becomes high with punched hole and grid type electrode than with plate type electrode. And then, punched hole type achieved high collection efficiency as comparison with plane type electrode at the same power consumption.

1. Introduction

The electrostatic precipitator (ESP) has been used extensively to decontaminate polluted gases and to clean air because of high collection efficiency. One of the major tasks of ESP applications is to increase visibility and to clean the air in the highway tunnels. The conventional ESP eliminates suspended particles traceable to diesel exhausted particle. ESP with DC corona discharge precharger little removes NOx[1]. Therefore, we propose barrier discharge type ESP to remove particles and NOx simultaneously. Barrier discharge is effective for removal NOx. Barrier discharge type ESP has been investigated to remove suspended particles [2]. The aim of this study is to improve energy efficiency for particle collection and NOx removal with several electrode shapes. This present version electrode shapes are changed from plane to punched hole, to grid pattern type. Several electrode shapes become the change of barrier discharge condition.

2. Experimental Methods

The schematic experimental system is shown in Fig.1. Particle generated by the diesel engine. The diesel exhaust gases is diluted with air in the mixing chamber, and then boosted through the duct and enter to ESP. The gases cleaned by ESP pass through the induced fan and then exhausted. The mean gas velocity in the duct is 1.5m/s constant in all test condition. The number density of suspended particle is measured by the particle counter (PC, RION KC-01C, measured particle size d > 0.3μm). The sampling locations are upstream and downstream of the ESP. This present version ESP is barrier discharge type. The barrier discharge type ESP electrode configuration is shown in Fig.2. These barrier discharge electrodes are the aluminum plate (0.5mm thick) sandwiched by two glass plates (0.5mm thick), electrode length is 45mm(aluminum), and 65mm(glass plate). In here, 3 varieties of aluminum plate electrode shapes are used as illustrated in Fig.3. The punched hole type electrode has many holes, The diameter of a hole is
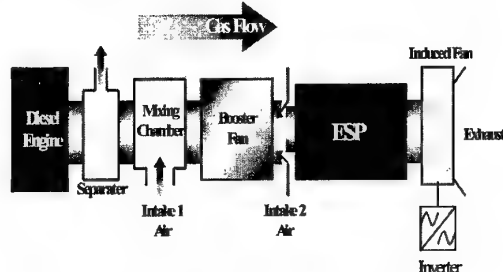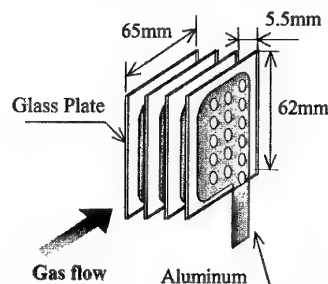
Fig.2 Electrode configuration of barrier discharge type electrostatic precipitator.

a)Plane b)Punched hole c)Grid Pattern
(φ3.1mm)
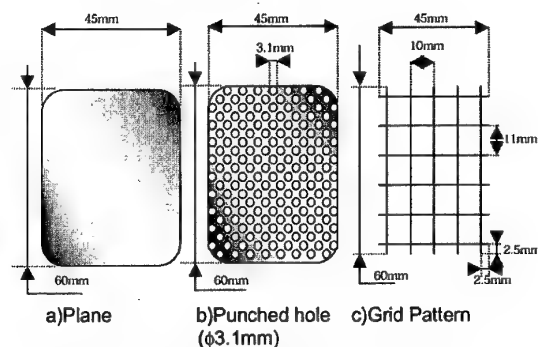
Fig.3 Test shapes of aluminum plate electrode

Fig.1 Schematic diagram of experimental system

3.1mm. The grid pattern type electrode consists of tungsten wire with 0.26mm diameter, these wires are laid out such as grid pattern. These aluminum plate electrodes are applied high voltage (AC50Hz). The discharge power is measured by the Lissajous figure (V-Q plots) on oscilloscope.

3. Results and Discussion

Discharge current for several electrode shapes as a function of applied voltage is shown in Fig.4. At the same applied voltage, discharge current at punched hole type becomes high, discharge current at grid pattern type becomes low as compared with plane type electrode. As for gird pattern type electrode, discharge current becomes low due to decrement of the electrode area. Electric field intensity distribution as the punched hole type electrode is shown in Fig.5. This figure is analyzed with ANSYS 6.0 (Ansys Inc. Electric field analysis with a finite-element methods). The electric field intensity at edge of punched holes type electrode is 1.2 times stronger than at plane type electrode. Especially, electric field intensity around the punched
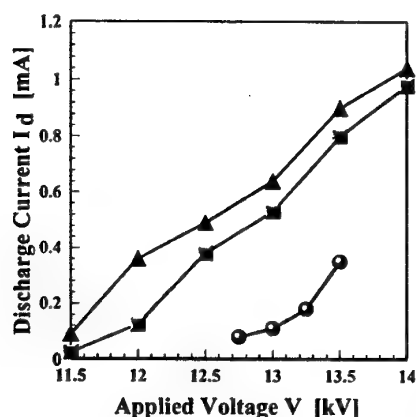
Fig.4 Discharge current as a function of applied voltage. Plots indicate electrode shapes ;
■:Plane type , ▲:Punched hole type,
●:Grid pattern type electrode.
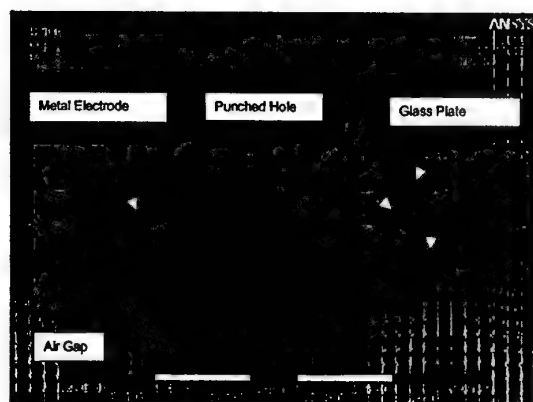
Fig.5 Electric field intensity distribution as the punched hole type electrode

hole becomes high. Hence, because of this field intensity increment, discharge current at punched hole type electrode becomes high as shown in Fig.4.

Discharge power as a function of collection efficiency is shown in Fig.6. Collection efficiencies at punched hole type and grid pattern type electrodes become high in comparison with plane electrode. Additionally, collection efficiency increases up to 95 percent with increasing discharge power at punched hole type. It has been shown that energy efficiency for particle collection is improved when deference in electric field intensity exists in barrier discharge.

4. Concluding Remarks

Energy efficiency for particle collection is tested by changing barrier discharge electrode shape. Consequently, it has been shown that energy efficiency for particle collection is improved when the difference in electric field intensity exists in barrier discharge area. Additionally, using punched hole type electrode achieved high collection efficiency as comparison with plane type electrode at the same power consumption.

We would like to thank Mr. T.Nakahara and Dr. H.Kishida at Musashi Institute of Technology for their valuable comments and discussion.

5. References

[1]K.Ohtuka et al "Oxidation Characteristics of Nitrogen Monooxide in Corona Discharge Field"(In Japanese), Proc. Inst. Electrostatics Jpn., Vol.9, No.5, pp.346-325 (1985)
[2] Y.Kawada et al "Particle agglomeration on the electrodes in electrostatic precipitator with barrier discharge system"Xth Asian Conference on Electrical Discharge, Kyoto Japan (2000)
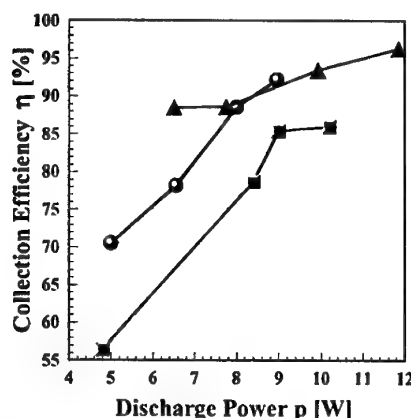
Fig.6 Collection efficiency for several electrode types as a function of discharge power.
■:Plane type , ▲:Punched hole type,
●:Grid pattern type electrode.

Topic 5

Arc discharges

THE ION FUNCTIONS OF ONE-DIMENSIONAL ACTIVE PLASMA LAYER OF HIGH-CURRENT GAS DISCHARGES

Vladimir P. Shumilin

All-Russian Electrotechnical Institute. Krasnokazarmennaya, 12, Moscow, 111250, Russia.

Active plasma layer (APL) is a quasineutral plasma area bordering with cathode space charge layer. All generated in APL ions get to cathode. In [1] it has been shown, that in intensive discharges there is a multiple gas compression in APL. In the present work the important characteristic of discharges, P_0, equal to number of ions coming on cathode in recalculation on one neutral flying from cathode is considered. The dependence of this value on parameters of discharge is named an ion function. The low-voltage case, when energy of cathode electrons does not exceed several neutral ionization energies, and the high-voltage case, when density of primary electrons current in APL is supposed to be a constant, but their average energy changes only, are discussed.

1. One-dimensional APL

Let there be emitted an electron current with density $j_{e0} = j_e(0)$ and a neutral flow with density $q_0 = q(0)$ and average directional velocity $v_0 = 0.5\sqrt{8T_0 / \pi M}$, along an axis x, which is normal to a flat homogeneous surface of cathode, where T_0 - temperature of cathode in energy unities, M - neutral mass. Ions with current density $j_i(x) \geq 0$ and neutral flow with density $q_{back}(x) \geq 0$ move to cathode. Neutral backflow is caused partly by resonant charge exchanged ions ($q_{ch}(x)$), partly by presence of gas on anode boundary of APL ($q_{ex}(x)$).

Obviously, in stationary APL the conservation of heavy particles flow takes place

$$Q(x) - Q_{back}(x) - P(x) = D = const, \qquad (1)$$

where neutral flows are normalized to quantity q_0; $P(x) = j_i(x) / eq_0$; e - the elementary charge. If $D = 0$, we deal with an non-consumed operating mode of cathode. When $D < 0$ cathode immerses gas, if $D > 0$ material of cathode is constantly spent.

Let's write down a simplified system of the continuity equations for neutrals and ions, and the equation for energy flow of primary electrons in APL

$$dN / ds = -\alpha(V)KN - \beta PN, \qquad (2)$$

$$\omega^{-1} dN_{ex} / ds = -\alpha(V)KN_{ex} - \beta PN_{ex}, \qquad (3)$$

$$dP / ds = -\alpha(V)K(N + N_{back}), \qquad (4)$$

$$d(KV) / ds = W(V) dP / ds, \qquad (5)$$

where $\omega = v_0 / v_g = \sqrt{T_0 / T_g}$; $v_g = 0.5\sqrt{8T_g / \pi M}$ - average velocity of directed to the cathode neutral flow in the region of anode boundary of APL; neutral densities are normalized to quantity n_0 ($q_0 = n_0 v_0$); $s = n_0 \sigma_m x$; σ_m - the peak value of electron-neutral ionization cross-section; $\lambda = v^2 / 4\delta^2$; $\varepsilon(s)$ - average primary, accelerated in cathode space charge layer,

electron energy; φ_i - neutral ionization potential; $\alpha(V) = \sigma_i(V) / \sigma_m$; $\beta = \sigma_n / \sigma_m$; $\sigma_i(V)$ and σ_n - ionization and resonant charge exchange cross-sections, respectively; $K = j_e(s) / eq_0$; $W(V) = w(V) / e\varphi_i$; $w(V)$ - average energy a primary electron spends for one act of ionization. Thus we consider, that all ion current acting on cathode is generated due to ionization by primary electrons in APL, and neutral "burning" occurs due to ionization by primary electrons and resonant charge exchange processes. Slow electrons ionization and recombination processes in APL are neglected.

From (2) and (3) we shall receive $N_{ex} = \omega(\Pi - D)(\Pi / N)^\omega$, where $\Pi = Q(s_a)$ - normal transparency of APL ($\Pi \geq 0$; $\Pi \geq D$); s_a - APL thickness, so taking (1) into account we shall have

$$N + N_{back} = kN + (\omega + 1 - k)(\Pi - D)(\Pi / N)^\omega - \\ - (k-1)(P + D) \qquad (6)$$

where $k = 1 + v_0 / u$; u - average velocity of charge exchanged neutrals ($u > v_0 \geq v_g$).

In the ionization mode (when $i_0 \ll i_{0m}$, where $i_0 = j_{i0} / j_{e0}$, and i_{0m} - the peak value of i_0, achievable at the complete cathode electrons relaxation in APL) the flow of charge exchanged neutrals in APL is small, therefore, by setting in (1) $Q_{ch} = 0$, we find $P(N) = N - (\Pi - D)(\Pi / N)^\omega - D$, and since $P(1) = P_0$, then

$$P_0 = 1 - \Pi^{\omega+1} - D(1 - \Pi^\omega). \qquad (7)$$

2. Low-voltage APL

In this case, when $V_0 \leq 3 \div 4$, it is possible to account, that $V(s) = V_0 = const$ and $W(V) = W(V_0) = W_0 = const$, so using (5) we find

$$K = i_{0m}^{-1}[P + P_0(i_{0m} / i_0 - 1)], \qquad (8)$$

73
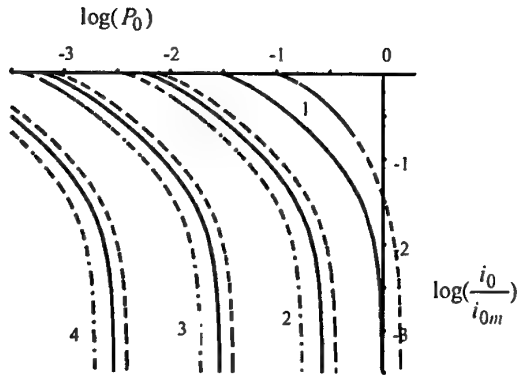
Fig.1. The ion functions of low-voltage APL, received by the numerical solution (11) at $i_{0m}\chi = 50$, $k = 3/2$ and $\omega = 2$. Solid lines are plotted at $D = 0$, dotted - at $D = -0.5$, and dash-dotted - at $D = 0.5$. Groups of curves 1, 2, 3 and 4 correspond to transparences $\Pi = 10^{-6}$, $\Pi = 0.9$, $\Pi = 0.99$ and $\Pi = 0.999$, respectively.

$$i_{0m} = V_0 / W_0. \qquad (9)$$

It is known, that at the large energies of electrons ($V \gg 1$) $W(V) \cong 2$ for every gas. At the small energies we shall account, that $W \to \infty$ at $V \to 1$. Therefore the dependence $W(V)$ can be approximated by the expression $W(V) = 2V/(V-1)$. For dependence $\alpha(V)$ we put $\alpha(V) = (V-1)/V$. Then using (9) we find

$$i_{0m} = (V_0 - 1)/2. \qquad (10)$$

From (2) and (4) taking (8) into account we receive

$$N[(1+i_{0m}\chi)P + A]dP/dN = (P+A)(N+N_{back}), \qquad (11)$$

where $\chi = \beta/\alpha(V_0)$, and $(N+N_{back})$ is defined by (6); $i_{0m}\chi = \beta V_0 / 2 \gg 1$, $A = P_0(i_{0m}/i_0 - 1)$.

3. High-voltage APL

Let's consider, that in this case initial energy of electrons is much greater than the energy loss for one act of ionization $V_0 \gg W(V_0)$, that is approximately $V_0 \geq 10$. We shall restrict voltages from above to the requirement of applicability of approximation $\alpha(V) = (V-1)/V$ to within the coefficient $\cong 2$. Then $V_0 \leq 50$.

Obviously, in the high-voltage case it is practically always possible to account, that primary electrons do not transfer in slow group, and spend on ionization only the energy, that is $K(s) \cong K_0 = const$. In this case from (5) we shall receive $i_0 = (V_0 - V_a)/2 - \ln(V_0/V_a)/2$, where $V_a = \varepsilon(s_a)/e\varphi_i$; $\varepsilon(s_a)$ - average energy of an electron beam leaving APL. Setting $V_a = 1$, we shall have
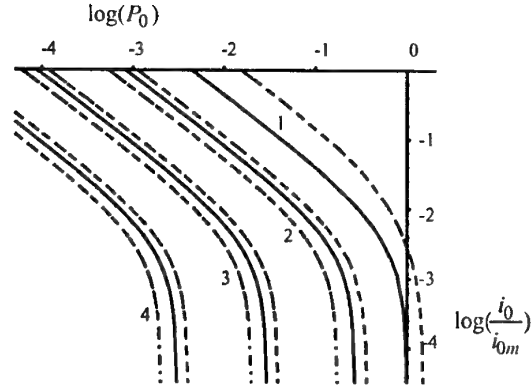
Fig.2. The ion functions of high- voltage APL, received by the numerical solution (13) at $V_0 = 30$, $\beta = 50$, $k = 3/2$ and $\omega = 2$. Solid lines are plotted at $D = 0$, dotted - at $D = -0.5$, and dash-dotted - at $D = 0.5$. Groups of curves 1, 2, 3 and 4 correspond to transparences $\Pi = 10^{-6}$, $\Pi = 0.9$, $\Pi = 0.99$ and $\Pi = 0.999$, respectively.

$$i_{0m} = (V_0 - 1)/2 - \ln(V_0)/2 \approx V_0/2. \qquad (12)$$

The basic equation determining the high-voltage APL ion function, we shall receive from (2), (4), (5) and (12)

$$N[\alpha(V)P_0 + i_0\beta P(V)]dV/dN = 2i_0(N + N_{back}), \qquad (13)$$

where

$$P(V) = P_0[V - V_a - \ln(V/V_a)]/2i_0, \qquad (14)$$

and $(N + N_{back})$ is defined by (6).

4. Conclusion

In high-current discharges there is strong "burning" of gas in APL ($\Pi \ll 1$). Thus in ionization mode ($i_0 \ll i_{0m}$) gas is kept near to cathode due to ionization ($P_0 \approx 1$). In charge exchange mode ($i_0 = i_{0m}$) gas is kept due to resonant charge exchange processes ($P_0 \ll 1$), and in the high-voltage case charge exchange efficiency grows due to increase in APL thickness.

5. Acknowledgements

6. References

[1] Zharinov A.V. *Proc. of XXV ICPIG*. Ed. by Toshio Goto. Japan: Nagoya University, 3 (2001) 335.

Thermo field emission in high current arc discharge

V.V.Choulkov

All-Russian Electrical Engineering Institute
111250, Krasnokazarmennaya 12, Moscow, Russia

The effect of ion electrical current on the electron thermo field emission from metal surface of cathode in high current arc has been investigated. An electron emission process are considered as follow. One electron emitted due to field of ions in cathode layer is captured by ion to form an exited neutral atom which is then ionized by the electrical field. It is shown that in high current arc random fluctuation of electrical field induced by ions contributes significantly to this kind of emission. The electron emission coefficient is calculated for a variety of arc parameters and surface conditions. The mechanism of electron emission in arc discharge are discussed.

1.Introduction

One of a basic problem high current arc discharge is a problem of electron emission from metal cathode surface. Extremely high density of current at cathode surface, which exceed 10^7 A/cm^2 and more at rather low voltage of discharge burning, testifies that a mechanism of generation of electrons at the cathode of high current arcs differs from known mechanisms such as field emission or electron-ion emission [1] and is more effective, than in glow discharges. Estimations show, that a current of thermo emission with Schottky correction, arising due to a field of spatial charge of the cathode layer, is not enough for achievement of that current density. The electric field that is necessary for effective emission should be at least on the order more. In [2] a current of electron emission in view of random fluctuation of electric field has been calculated. In [3-7] influence of a field of ions was considered in more detail within the framework of mechanism emission which results from tunnel transition electron from a surface of the cathode in field of the ion falling on the cathode, with the subsequent ionization the formed exited atom by an electric field. However in the calculations of ionization of exited atoms average value of electric field has been used. It does not allow to take into account influence of parameters of a layer of spatial charge and underestimates the calculated emission coefficient. A task of the given work is research of influence of parameters a cathode layer of an electric arc on mechanism electron emission and fluctuations of electric field induced by ions.

2. The simulation model

Let's consider the cathode layer of an electrical arc with density of ions n_i. The electric field E near surface equals to the sum of a fields of ions E_i

$$E_i = \frac{Ze}{r_i^3} r_i$$

where r_i- distance from a point under observation to an ion, Ze is an ion charge. As the position of ions are random values the field of spatial charge also will have an accidental value. The electric field is characterized by function of distribution of field which is density of probability W (E) presence of field E in a point r and which is determined by the following expression

$$W(E) = \int ... \int \delta \left(E - \sum_{i=1}^{n} E_i \right) d^3 r_1 d^3 r_2 ... d^3 r_n \tag{1}$$

Integration in (1) has been carried out on all volume of cathode layer V, and $n = Vn_i$, r_i is a random variables with homogeneous density of distribution on volume of spatial charge.

Boundary conditions to (1) were set by introduction of mirror charges relative to surface of the cathode.

The rate of electron emission was determined by emission coefficient γ which was amount of electrons, formed as a result of falling one ion on a surface of the cathode.

$$\gamma = \int_0^\infty W(E) \int_\infty^d \int_0^\infty N_{ex} v_i (E, \varepsilon) d\varepsilon dx dE \tag{2}$$

where N_{ex} is exited atoms density with exited energy ε, v_i is frequency of ionization of exited atom, d is a distance on which the atom deexitation occurs on the cathode surface.

N_{ex} was determined using continuous equation

$$\frac{d(uN_{ex})}{dx} = \frac{J_{tf}}{e} \sigma - v_i N_{ex} \tag{3}$$

where u is an exited atom velocity which has been chosen to be equal ion velocity because ion-atom exchange process, J_{tf} is a electron thermo field emission current which determined from Richardson-Dushman formula (where electric field strength is equal to the sum of a field of a spatial charge and a field of the

falling ion); σ is a Coulomb electron-ion collisions cross section. Frequency of ionization of exited atoms was determined from [8].

3. Computational results and discussion

The integral (1) was computed by Monte-Carlo method. The computed probability distribution of amplitude of electric field near cathode surface is presented on fig. 1 in dimensionless value for five values of layer thickness l_d. Field is presented in unit $E_0 = 2.603 e n_i^{2/3}$, layer length is presented in $d_0 = (4\pi n_i/3)^{-1/3}$. All distribution are computed for point located at distance $d_0/2$ from cathode surface.
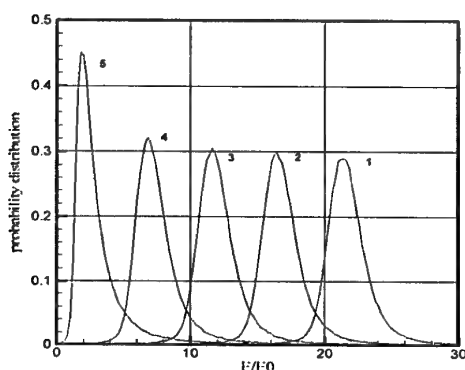
Fig.1 The electric field distribution near cathode surface
1 – l_d = 5, 2 – l_d = 4, 3 – l_d = 3, 4 – l_d = 2, 5 – l_d = 1

One can see that for layer length about (3-5)d_0 and more the probability distribution can be presented as Holtsmark distribution displaced an amount macroscopic field of charge. For small layer the shape of probability distribution changes. The amplitude of probability distribution extend up to value 0.45 and high field part of the distribution rises.
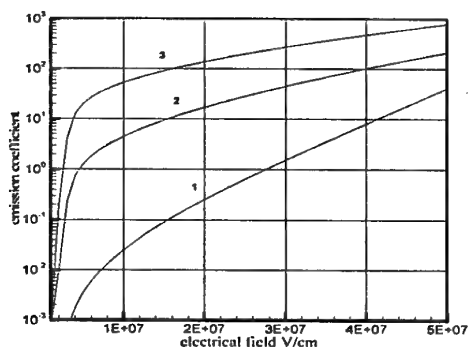
Fig. 2 The emission coefficient dependence on electric field l_d = 5; curve 1-T=3000°K, 2 - T=5000°K, 3 -T=7000°K
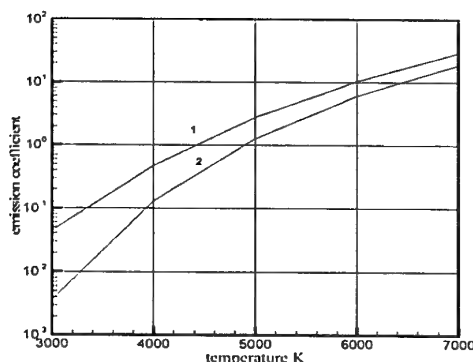
Fig. 3 The emission coefficient dependence on surface temperature E=5·10^6 v/cm with (curve 1) and without(2) field fluctuation; $l_d = 2$.

Fig. 2 and 3 present emission coefficient γ computed from (2) as a function surface temperature and macroscopic electrical field . On figure 3 curve 1 presents calculation γ with field fluctuation, curve 2 presents data computed without considering field fluctuation. One can see the significant difference between both curves.

From Mackeown theory of cathode layer at constant layer voltage drop we see that the thickness of the layer l_d depends on ion current density J_{ion} how $J_{ion}^{-1/6}$. So for big J_{ion} one faces condition where $l_d \leq 1$. ($l_d \approx 1$ at $J_{ion} \approx 10^7 A/cm^2$). It means that random fluctuation of electrical field plays most important role in electron emission at cathode of such electrical arcs.

Acknowledgments

References

[1] G.Kesaev *Cathodic processes of an electric arc* Moscow Science 1968
[2] G.Ecker, K.G.Müller *J.Appl. Phys.* **30** (1959) 1466
[3] R.R. Newton *Phys. Rev.* **73** (1948) 1122
[4] A.A.Porotnikov,B.B.Rodnevich *Zh.Tech.Fiz.* **46** (1976) 2094 (in Russian)
[5] V.S.Gvozdetsky, J.L.Vasenin *Surface* #3 1985 15 (in Russian)
[6] Ph.Testé and J-P Chabrerie *J.Phys.D:Appl.Phys.* **29** (1996) 697
[7] C Spataru, D Teillet-Billy, J P Gauyacq, P Testé, J-P Chabrerie *J.Phys.D:Appl.Phys.* **30** (1997) 1135
[8] L.D. Landau, E.M.Lifshitz *Quantum mechanics*, Moscow Science 1974

EXPERIMENTAL STUDY OF SOLAR ARRAY-PLASMA INTERACTION

B.V. Vayner[*], D.C. Ferguson, and J.T. Galofaro.

NASA/ Glenn Research Center, Cleveland, Ohio 44135

The results are presented of an experimental study of arc phenomena and snapover for five types of solar array samples immersed in xenon plasma. I-V curves are measured, and arc and snapover inception voltages, essential parameters, and arc rates are determined. It is shown that the array with wrapthrough interconnects has the highest arc threshold and the lowest current collection. Coverglass design with overhang results in decrease of current collection and increase of arc threshold. Doubling coverglass thickness does not improve measured array parameters. Both arc inception voltage and current collection increase significantly with increasing a sample temperature to 80 C. Arc sites have been determine by employing a video-camera. The results obtained seem to be important for the progress toward employment of high- voltage solar array in Low Earth Orbit.

1. Introduction.

The main obstacle to the implementation of a high-voltage solar array in space is arcing on the conductor-dielectric junctions exposed to the surrounding plasma. One obvious solution to this problem would be the installation of fully encapsulated solar arrays which were not having exposed conductors at all. However, there are many technological difficulties that must be overcome before the employment of fully encapsulated arrays will turn into reality. An alternative solution to raise arc threshold by modifications of conventionally designed solar array looks more appealing, at least in the nearest future. A comprehensive study of arc inception mechanism[1] suggests that such modifications can be done in the following directions: i) to insulate conductor-dielectric junction from a plasma environment (wrapthrough interconnects); ii) to change a coverglass geometry (overhang); iii) to increase a coverglass thickness; iiii) to outgas areas of conductor-dielectric junctions. The operation of high-voltage array in LEO produces also the parasitic current power drain on the electrical system. Moreover, the current collected from space plasma by solar arrays determines the spacecraft floating potential that is very important for the design of spacecraft and its scientific apparatus. In order to verify the validity of suggested modifications and to measure current collection five different solar array samples have been tested in large vacuum chamber. Each sample (36 silicon based cells) consists of three strings containing 12 cells connected in series. Thus, arc rate and current collection can be measured on every string independently, or on a whole sample when strings are connected in parallel. The heater installed in the chamber provides the possibility to test samples under temperature as high as 80 C that simulates the LEO operational temperature. The experimental setup is described below.

2.Experimental setup

Low Earth Orbit (LEO) plasma environment was simulated in two different vacuum vessels: 1) small bell jar (45 cm diameter and 75 cm height); 2) large vacuum tank (1.8 m diameter and 3 m height). The vacuum equipment provided pressure as low as 0.5 µTorr. One Penning source was installed in a small tank to generate argon (or xenon) plasma with electron density $n_e=(0.1\text{-}10)\cdot10^5$ cm^{-3} , temperature T_e=1-1.2 eV, and neutral gas pressure p=(0.7-7)$\cdot10^{-5}$ Torr which could be kept steady during the experiment. To supply large tank with plasma the hollow cathode was installed, and it provided plasma with lower electron temperature T_e=0.5-0.8 eV and the same density. Later this hollow cathode was exchanged on Kaufman source that generated plasma with close parameters. To measure plasma parameters, Langmuir probes with diameter 2 cm were employed (one in bell jar and two in large tank). To determine an ion distribution function and to improve measurements of electron temperature one retarding potential analyzer (RPA) was mounted on the bottom of large tank. It was found that the ion (xenon) thermal flux in the experiment is about three times lower than ram ion flux in LEO, and the electron temperature is 5-10 times higher than in ionosphere. However, the number densities are simulated with a quite high accuracy, and one can believe that the results of high-voltage experiments in vacuum chambers are fairly adequate to the outcomes of processes in LEO plasma. To control plasma chemical composition (particularly, water vapor and oil partial pressures) a quadruple mass spectrometer was installed in large vacuum tank.

---

[*]Ohio Aerospace Institute, Cleveland, USA

The sample (or set of samples) is vertically mounted in the middle of the chamber, and it is biased to a voltage power supply through a capacitor and a 10 kΩ resistor network back to ground. An additional power supply (Solar Array Simulator-SAS) is used to generate electrical field perpendicular to the dielectric side surface for investigating arc inception on semiconductor-dielectric junction and inception of sustained discharges between adjacent strings. Diagnostic equipment includes two current probes to measure discharge current and SAS current, and one voltage probe that allows us to register voltage pulse on the sample during the discharge. To measure optical spectra of arc plasma an intensified CCD camera with optical spectrometer is installed. The most probable arcing sites are determined by employing a video camera and VCR. Most experiments were performed at room temperature (15C), but some tests had been done at the temperature +80 C simulating the exposure of solar array to full sun in LEO.

3. Experimental results.

Each string (12 cells in series) of five types of solar arrays was tested separately, and measurements revealed significant differences in arc rates even for strings belonging to one sample. There are two reasons explaining such observations: manufacturing process peculiarities and geometrical design of a sample. Manufacturing peculiarities demonstrate themselves when one compares arc parameters for two outer strings and finds considerable differences. And arc sites are located mostly on interconnects for middle string while great part of arcs on outer strings has been observed on cell edges. To preserve the homogeneity of collected data one common experimental procedure is used for all measurements of arc inception voltages and arc rates: 1) string is initially biased to voltage well below an expected arcing threshold; 2) 15-30 minute time interval is allowed to register (or to not register) an arc; 3) voltage is increased on 10-20 V; 4) arc rate is defined as an average over a respective time span. Some results of measurements are shown in Fig.1.

Short electrostatic discharges studied above are certainly undesirable events that must be prevented for reliable operation of the spacecraft. However, this kind of transients are not damaging solar array irreversibly. Sustained discharges initiated between adjacent cells with a few tens volt potential difference are much more dangerous because they can destroy cells and underlying substrate that results in considerable loss of power. Three samples have been tested against an inception of sustained arc between two strings. Test starts with lower limits on SAS voltage and current. After the registration of 5-10 arcs these parameters are gradually changed and more arcs are generated until initial sign of sustained discharge is seen on the oscilloscope. This sign represents the SAS current pulse that continues much longer than original arc. The corresponding SAS current and voltage are considered as threshold parameters because even a small increase of them (10 V and 0.25 A) results in spectacular event shown in Fig. 2. In this case the sustained discharge has been quenched after 20 s by

turning SAS off. Significant area of the sample around arc site was damaged. Threshold parameters depend on solar array design. (For details see Ref. [2]).
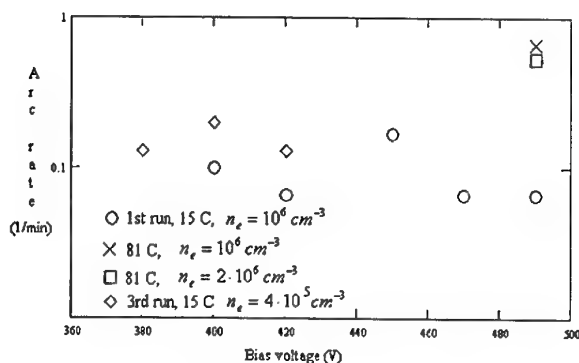
Fig.1. Arc rates are shown under different conditions for the middle string with coverglass thickness 150 μm.
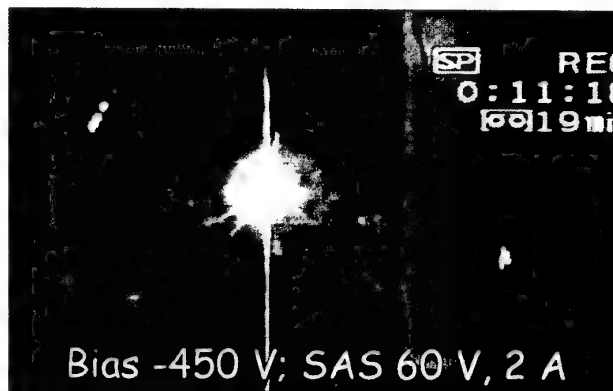
Fig.2. One frame of a 20 s long video record of a sustained arc.

Comprehensive tests of five different types of solar array samples in simulated LEO plasma environment have demonstrated that the highest arc threshold (440 V) can be achieved for an array with wrapthrough interconnects if edges of strings are not exposed to the plasma. This design is also effective in decreasing of an array current collection. The design with exposed interconnects but with coverglass overhang also provides significant improvement comparatively to the conventional design. Particularly, arcing on the sample cannot be initiated at potentials below 300 V even under room temperature, and arc threshold increases to 420 V under temperature 72 C. The increase of coverglass thickness itself appears to be useless in this respect.

References

1. Vayner, B.V., Galofaro, J.T., and Ferguson, D.C. Proc.XXth ISDEIV, 2002, Tours, France, pp.80-83

2. Vayner, B.V., Galofaro, J.T., and Ferguson, D.C. Journal of Spacecraft and Rockets, 2003, in press.

78

Behaviour of the cathode active surface temperature in the steady-state diffuse mode of HID lamps

M. Cristea[1], G. Zissis[2]

[1] University "Politehnica" of Bucharest, Department of Physics, Splaiul Independentei 313, 77206 Bucharest, Romania; e-mail: mcristea@physics1.physics.pub.ro
[2] University Paul Sabatier of Toulouse, Center of Plasma Physics and Application of Toulouse, Route de Narbonne 118, Toulouse, France

1. Introduction

Generally, the topics of functioning model of high intensity discharge (HID) lamp electrode presents a big scientific interest. A lot of lamp properties and lamp efficient functioning are in strong relationship with the cathode operation. The non-linear equation of heat transfer influence the electronic emission mechanism (Schottky amplified thermionic emission, thermofield emission or field emission).

Many authors developed theoretical model in order to calculate the electrode temperature distribution [1, 2], the arc attachment modes or the transition between different mode [3].

In this paper we analyse, in the case of diffuse cathode mode functioning, the influence of some external parameters on the cathode active surface temperature.

2. Theoretical model

In the HID lamp the high value of discharge current is given by the high electron emission. This is possible by a low work emission function and by high emissive surface temperature. The second condition request a refractory material (generally tungsten), and the first condition request the material like barium or thorium deposed as a thin film on the active surface of the electrode. But, during the functioning lamp, this film is very sensitive at the sputtering and vaporisation processes trough the temperature distribution. The temperature distribution in the bulk electrode can be obtained by solving the heat transfer equation with mixed boundary conditions. These conditions modell the plasma-electrode interaction (Neuman conditions - using the heat flux continuity equation) or are imposed like Dirichlet condition (the temperature at the electrode end, or at the active emissive zone). Due to the vessel envelope blackening in the electrode vicinity, the measurement by pyrometric technique is very difficult to be carried out. For this reason we consider that any method to calculate the active surface temperature is very helpful.

In this paper we propose a method to estimate the active surface temperature and the behaviour at various external parameters changing.

The model is based on the following assumptions:
- The lamp electric discharge is considered to be in the steady-state regime;
- we suppose a lower cathode electric field ($E < 10^7 V/m$), a low pressure, a high current intensity and a weak cooling of the electrode; in this situation a lower current density is obtained and the diffuse mode is favoured [3, 4]; the attachement of the arc is very stable;
- for the electrode functioning in diffuse mode, the emissive surface cover all the front electrode surface; sometimes, a lateral part of tungsten electrode rod participate at the electric discharge (especially in the case of high pressure sodium lamps), but this case is included in our model by the increasement of active surface radius;
- all plasma - electrode interactions are in stationary regime,so, the change of surface temperature due to these interaction are unexistent;
- we suppose also that the stationary temperature distribution assure a stationary discharge current;
- we suppose that the electron current density is due to the field-enhanced thermionic emission caused by lowering of the potential barrier in the presence of an electric field (Schottky effect) (j_e^{th}) and by secondary emission by γ-Townsed process (j_e^{sec}).

The electron current density components are given by the relations:

$$j_e^{th} = AT^2 \exp\left(\frac{e\varphi(E_k)}{k_B T}\right) \quad (1)$$

$$\varphi(E_k) = \varphi_0 - \Delta\varphi(E_k); \Delta\varphi(E_k) = \left(\frac{eE_k}{4\pi\varepsilon_0}\right)^{1/2} \quad (2)$$

$$j_e^{sec} = \gamma j_i \quad (3)$$

Here, $A = 4\pi e m_e k_B^2 / h^3$ represents the Richardson-Duschmann constant, φ_0 is the electrode material work function, $\Delta\varphi$ is the Schottky correction of work function. e and m_e represent the electron charge

respectively mass, k_B is the Boltzmann constant, h is the Planck constant, ε_0 is the free space permitivity and E_k is the electric field intensity in the cathode fall.

The relation of ion current density returning to the electrode (j_i), to the electron current density leaving the electrode (j_e), was determined by Waymouth [5]:

$$j_i = \beta j_e = \beta\left(j_e^{th} + j_e^{sec}\right) \qquad (4)$$

The cathode field is related to the ion current density, j_i and potential drop, V_k, by the equation:

$$E_k^2 \approx \frac{4 j_i}{\varepsilon_0}\left(\frac{m_i V_k}{2e}\right)^{1/2} \qquad (5)$$

with m_i the ion mass.

The magnitude of the cathode fall is somewhat larger than the mercury ionisation potential, being usually 12 – 16 V.

At the discharge current density j, we find the following equation:

$$j = \frac{1+\beta}{1-\gamma\beta} A T^2 \exp\left(-\frac{e\varphi(E_k)}{k_B T}\right) \qquad (6)$$

which give the electrode active surface temperature.

3. Results of the model

The model is used to calculate the active surface temperature of a d.c lamp cathode. We fix the discharge current and the value of β-Waymouth coefficient. The active surface temperature is calculated via electric field strenght. The electric field at the cathode surface is calculated from ion current density and cathode fall using Mackeon equation. The algoritm steps are as follows:

- the start with the value of total current density j, impozed by the external current discharge and electrode geometrie;

- the calcul of the ion density current $j_i = \beta j /(1+\beta)$ for a fixed β-Waymouth coefficient;

- afther that, the electric fiel intensity in the cathode vicinity E_k is calculate from equation (5);

- with E_k, the electrode material work function correction $\Delta\varphi$ is calculated;

- the active temperature surface is obtained with equation (6) by iterative mechanisme in order to have the total calculated current equal with imposed discharge current; the active surface temperature is ajusted until convergence.

An analysis of active temperature dependence on the front electrod radii, curent intensity discharge and β-Waymouth coefficient is caried out. The

influence of γ-Townsend coeficient on the active surface temperature is shown to be weak. Also, the active surface temperature dependence on the electrode material work function is analysed.

As exemple, the active surface temperature dependeces on the discharge current and on the β-Waymouth coefficient are presented in Fig. 1, respectively, Fig. 2.
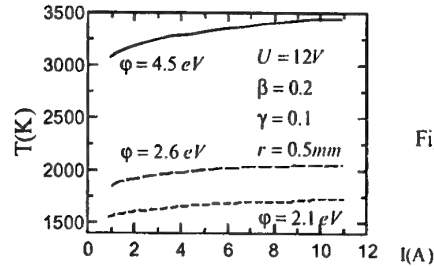
Fig.1.
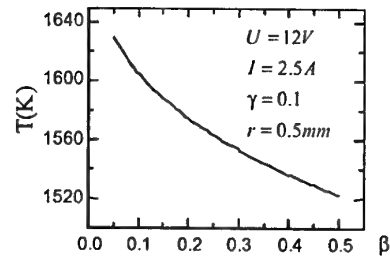
Fig. 2.

This type of analysis can be extended in the case of more realistic cathode emmision. In this case, as it was shown by Coulombe and Meunier [6], is more efficient to use a tratement of Murphy and Good for electron emission instead of Richardson-Duschmann emission mechanisme corrected by Schottky effect.

But, the simplified model presented in this work, is easy to be used to give the Dirichlet condition on the top of cathode for the heat transfer equation in the cathode.

4. Acknowledgement

References

[1]. M. S. Benilov, M. D. Cunha, *J. Phys. D: Appl. Phys.* **35** (2002) 1736 – 1750.

[2]. P. Tielemans, F. Oostvoegels, *Philips J. Res.* **38** (1983) 4-5, 214-223.

[3]. R. Botticher, W. Botticher, *J. Phys. D: Appl. Phys.* **33** (2000) 367 – 374.

[4]. S. Lichtenberg, D. Nandelstadt, L. Dabringhausen, M. Redwitz, J. Luhmann, J. Mentel, *J. Phys. D: Appl. Phys.* **35** (2002) 1648 – 1656.

[5]. J. F. Waymouth, Electric Discharge Lamps, Cambridge, (1971), MA: MIT Press.

[6]. S. Coulombe, J-L. Meunier, *J. Phys. D: Appl. Phys.* **30** (1997) 776 – 780.

High Intensity Arc by Means of the Head-on Collision of Two Supersonic Jets

Kouichi Ikeda*   Tatsuya Osafune**   Tadashi Amakawa*   Fumio Higashino**

*Central Research Institute of Electric Power Industry, 2-6-1 Nagasaka, Yokosuka-shi, Kanagawa-Ken 240-0196, Japan
**Tokyo University of Agriculture & Technology, 2-24-6 Nakacho, Koganei-shi, Tokyo, 184-8588, Japan

The head-on collision of two supersonic jets in the arc was tested to intensify the arc brightness. Consequently, the temperature in the stagnation region of the arc and the arc brightness increased.

1. Introduction

Powerful arc lamps have the potential for surface treatments such as remelting, alloying, vitrification, etc. The purpose of this study is to produce higher temperature flows in the arc column. In this experiment, the head-on collision of two supersonic jets is utilized to elevate the temperature in the stagnation region of the arc column. This method may be expected to produce the following phenomena: first, when shock waves generate in the arc column and the gas develops irreversible adiabatic compression, temperature and pressure of the gas rise, and second, when the jets blow and constrict the arc, temperature and potential gradient of the arc column rise.

2. Experimental Conditions

Fig.1 shows the experimental apparatus. The combination of plasma torch and flat electrode was defined as "single torch" and the combination of plasma torch and plasma torch was defined as "twin torch". Either single torch or twin torch was placed vertically facing each other in the test chamber. Argon test gas of around 1.0 MPa was supplied to the nozzle in order to produce a supersonic flow. In order to study the behavior of the gas, ultra high speed camera whose minimum exposure time is 10 ns was used. The radiation was observed using a power meter and a spectrometer with ICCD.

Fig.2 shows shape of nozzles and visualization of gas by shadowgraph technique. Two kinds of micronozzles with 1.7 mm throat diameter, a normal and a Laval nozzle, were designed. The nozzles were tested to find the optimal conditions for the flow system. Mach number of the Laval nozzle was about 1.7, which was estimated by the ratio of total pressure to static pressure and Mach angle. The pressure in the stagnation region was estimated indirectly by means of stagnation pressure without electric discharge.

The temperature in the stagnation region was estimated by comparing the intensities of argon continuum. When the radiance was estimated measuring arc radiation intensity, the arc was regarded as perfect diffusing radiator of column or sphere.

The D.C. arc current was adjusted to around 60 A.

3. Results

Fig.3 shows the supply pressure dependence of temperature in the stagnation in case of twin torch. As the supply pressure increased from 0.4 MPa to 0.9 MPa, the temperature did not change greatly. The temperature in case of the Laval nozzle was about 15,000 K and around 3,000 K higher than that in case of the normal nozzle. The difference was caused by the conversion of the kinetic energy of the flow into the thermal energy. According to the compressible fluid theory, the gas temperature through the shock wave might rise to 20,000 K when Mach number of the supersonic flow was 1.7. The difference between the theoretical value and the data shown in Fig.3 was considered that the specific heat ratio became small because of argon ionization.

Fig.4 shows the radiance of the arc. The radiance in case of twin torch exceeded that in case of single torch. This was caused by the pressure rise in the stagnation region formed by opposed jets. In addition, the radiance in case of the Laval nozzle exceeded that in case of the normal nozzle. That was caused by irreversible adiabatic compression. It was effective to intensify the arc brightness in case of the Laval nozzles mounted on twin torch. The maximal radiance existed at the supply pressure when the gas through the Laval nozzle might expand correctly.

4. Conclusion

This paper deals with a new proposal to brighten arc. It is expected that the pressure and temperature in the stagnation region of the plasma torch were elevated by means of the head-on collision of two supersonic jets. The experiments to verify the validity of the principle were performed using plasma torches on which micronozzles were mounted. When the Laval nozzle

was used to create supersonic flow instead of the normal nozzle, the temperature in the stagnation region was around 3,000 K higher and the radiance could be doubled. Maximal radiance was obtained for the optimally expanded supersonic flow. Therefore, it is considered that our proposal was effective for the intensification of arc brightness.
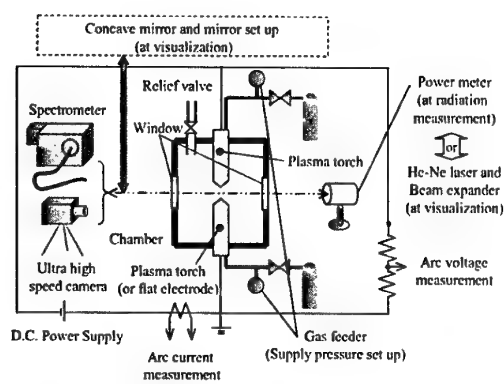
5. Acknowledgements

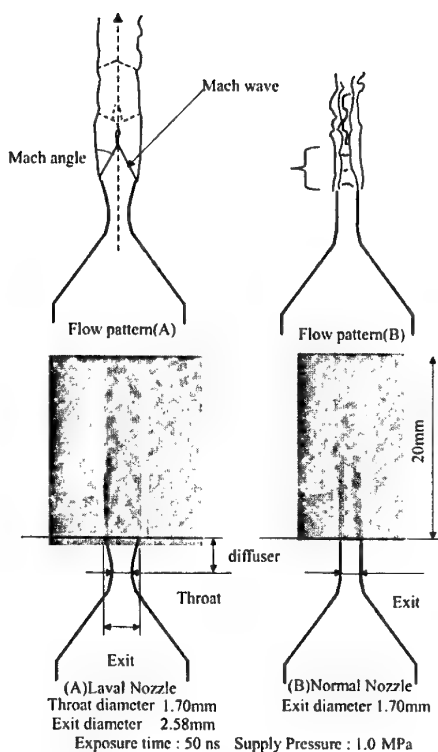Fig.1 Schematic diagram of experimental apparatus.

Fig.2 Shape of nozzles and visualization of gas by shadowgraph technique.
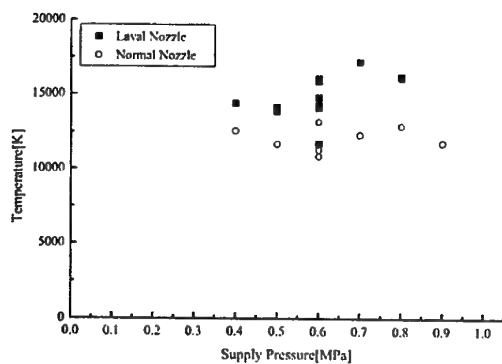

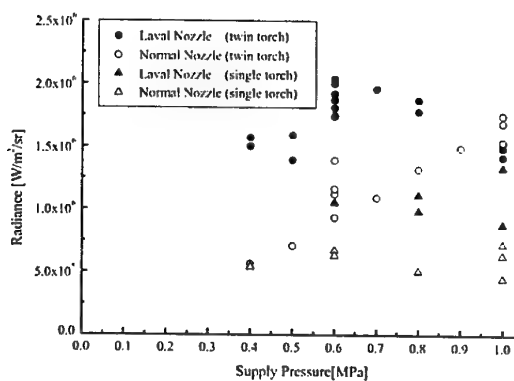Fig.3 Supply pressure dependence of temperature.

Fig.4 Supply pressure dependence of radiance.
(arc current : 50-70A)

Modelling of axial magnetic field effect on electric arc in ablation capillaries

A. Wolny, J. Piotrowski

Gdańsk University of Technology

Modelling of the axial magnetic field effect on the arc voltage of an arc burning in a gas-evolving chamber using Niemeyer's model of ablation arcs is discussed. The results support the assumption that the arc voltage rise is due to the increasing gas generation.

1. Introduction

In previous publications [1,2] the authors showed a significant effect of the axial magnetic field on the arc voltage of an arc burning in gas-evolving capillary chambers. Under similar conditions the magnetic field perpendicular to the arc column caused no voltage changes. It was noticed that the axial field influenced the arc voltage almost proportionally. The highest voltage increase was recorded for organic materials. At the field density reaching several tesla, the arc voltage rise by 300%, and more was observed, Fig. 1.
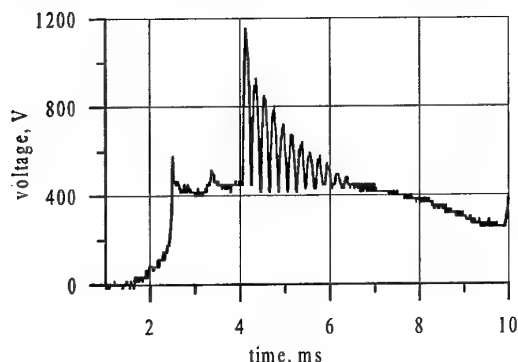

Fig. 1. Effect of high frequency axial magnetic field on ablation arc voltage: PE capillary, 1–mm $\varnothing$ [2]

When the arc was stabilised by a ceramic capillary or quartz-sand the magnetic field effect was negligible.

2. Discussed phenomenon

The arcing voltage is proportional to the arc deposited power. Hence, followed the above-given observations the presence of magnetic field influences the energy balance of an arc burning in a gas-evolving capillary, or in other words – arc cooling conditions. Moreover, it was noticed that such influence can only be exerted by the axial magnetic field component contracting the arc column. Thus, it can be assumed that the observed process consists of the following steps:

reduction of the arc column diameter → increase of the arc resistance → increase of power deposition → the arc temperature rise → intensification of radiation → abundant evaporation of walls → improvement of the convection cooling effect → further reduction of the arc column diameter leading to the adjustment of energy balance.

The assumption of such procedure permits to rely on ablation arc models in the modelling of the magnetic field effect on the arcing voltage. To practical models belongs that one developed by Niemeyer [3], and improved later by Ruchti Niemeyer [4]. These authors provided in addition practical examples of calculations complemented with experiments.

3. Application of Niemeyer's model

Niemeyer's model is cylindrical, one-dimensional and isothermal. It consists of two-layer cylindrical arc column, with current conducting central core and the outer layer filled with hot wall vapours. In this model the only flowing mass source is the vaporising chamber wall. The boundary temperatures can be defined easily. The outer temperature is dependent on the pyrolysis of wall material and the inner one, defined for the surface separating the layers, is connected with the assumed plasma conductivity. For approximate calculations both of them can be considered nearly constant.

The deposited energy in the current conducting core is inversely proportional to the plasma conductivity and cross-sectional area of the core. It is partly transferred to the chamber wall causing its vaporisation, and partly taken off by the cool stream of vapours generated by the wall streaming axially.

The axial magnetic field contracts the arc column core and reduces its cross section raising this way the energy deposited, and consequently, the arc plasma enthalpy, temperature, radiation, and vapour flow streaming from the walls increasing the pressure.

The hydromagnetodynamic equations describe above-discussed processes, if plasma parameters and radiation conditions are known. Niemeyer applied black-body model.

Since the magnetic field does not increase the energy of charged particles, its only effect is the arc core diameter reduction. Hence, the analysis of the magnetic field influence can be roughly performed based on the latter process.

## 4. Simulation of magnetic field effect

In the simulation material parameters were calculated based on the Kovitya's model [5], and functions of temperature and pressure were designed. Although a lot of materials were tested, PTFE was selected as the wall

material to facilitate comparison of the obtained results with those of Niemeyer [3].

In the first step the simulation was performed under Niemeyer's conditions, next arbitrary reduction of the arc core diameter was applied, and finally the needed magnetic field density was found.

The stagnation point temperature, pressure, electric field were calculated.

The results of simulation for 3–mm $\varnothing$, and no magnetic field conditions are provided in Fig. 2. Experimental check point has been marked.
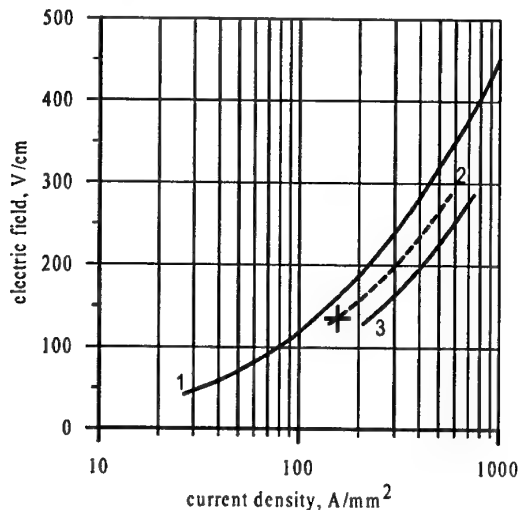
Fig. 2. Electric field along the arc column under no magnetic field conditions: 1 – Niemeyer's calculation, 2 – j for full arc cross section, 3 – j for actual arc core, $\ddot{\mathrm{i}}$ – the ratio of the measured current to the full arc cross section

5. Experimental

In experiments PTFE capillary were used with the length of 20 mm and diameters taken from the range of 1÷3 mm. Currents were supplied from capacitors.
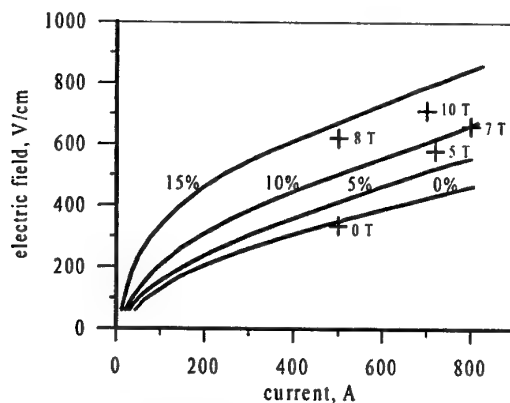
Fig. 3 Effect of arc core contraction on the arc electric field in a PTFE capillary of 1–mm $\varnothing$.

In Fig. 3 and Fig. 4 the simulation curves are marked with the percentage of arc core contraction. Next to the points of experimental measurements rounded applied magnetic field density is shown.
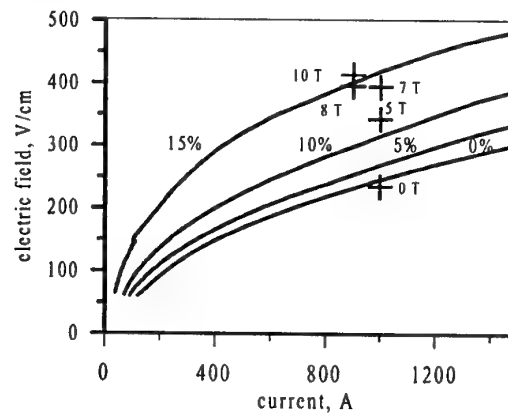
Fig. 4. Effect of arc core contraction on the arc electric field in a PTFE capillary of 2–mm $\varnothing$.

6. Discussion

Calculations were performed at the stagnation point, while measurements average values varing along the enclosure. Thus, making comparisions that fact should be taken under consideration.Quite maderate reduction in the arc diameter raises significantly the arc voltage, but the magnetic field rather needs radical changes.

7. Conclusions

Simplified simulation of the effect of axial magnetic field on the arc burning in gas-evolving capillary by exclusive consideration of reduction of the arc core diameter provides results convincing that this is the basic phenomenon responsible for the significant rise of arcing voltage.

A strong impulse of axial magnetic field can be used for the enforcement of current transfer from the arc to a parallel device.

8. References

[1] A. Wolny, J. Piotrowski, *Int. Conference on Gas Discharges,* Glasgow UK (2000) 182.

[2] J. Piotrowski, *Int. Conf. on Switching Arc Phenomena,* Lodz Poland (2001) 127.

[3] L. Niemeyer, *IEEE Trans. PAS-97* 3 (1978) 950.

[4] C.B. Ruchti, L. Niemeyer, *IEEE Trans. PS-14* 4 (1986) 423.

[5] P. Kovitya, *IEEE Trans. PS-12* 1 (1984) 38.

Time resolved recording of arc spot formation on cold cathodes

S. Frohnert, J. Mentel

Ruhr-University of Bochum, Fundamentals of Electrical Engineering, D-44780 Bochum

An experimental set-up is presented, which allows to investigate the interaction of a dense plasma with a cold cathode. The ignition of arc attachments is recorded by electrical measurements, high-speed photography and time resolved spectroscopy. The electrodes are prepared in different ways for reproducing fine microscopic surface structures. Pictures and measurements are shown for a polished Al-electrode.

1. Introduction

The electrodes of cold HID-lamps are heavily stressed during lamp ignition by a high voltage pulse. For a reduction of this load by an improved electrode design, a better understanding of the ignition is desired. The ignition may be decomposed into two different processes. One process is the formation of charge carriers and of a bulk plasma in the lamp volume. A broad knowledge is available concerning these processes. The other process is the establishment of an electron emission at the cathode, which is sufficiently high to transfer an arc current. The understanding of this process resulting in the formation of an arc spot is rather incomplete. If the arc is extinguished immediately after ignition the electrode surface shows the formation of craters by melting and vaporization of the electrode material [1]. One explanation for the emission of electrons is that microscopic structures on the electrode surface are heated by the high energy of the incoming ions. To investigate the influence of the surface structure on the ignition of arc spots independently of the processes in the discharge volume, a special experimental set-up was developed [1]. An arc ignited between two electrodes in a pure argon atmosphere (0.106 MPa) is blown magnetically against a third so-called commutation electrode CE. The ignition is recorded by electrical measurements, high-speed photography and time resolved spectroscopy. The electrodes are prepared in different ways for reproducing fine microscopic surface structures. First measurements are made with polished electrodes of copper, aluminium, graphite, palladium and tungsten. After that, electrodes of tungsten and palladium were prepared with pulverized tungsten/palladium. For comparison electrodes of palladium were annealed at temperatures of 1273K after polishing to produce a cleaner surface.

2. Experimental set-up

The experimental set-up shown in Fig.1 consists of a pair of horn electrodes, an anode (A) and a cathode (C) between which an arc is ignited by a high voltage breakdown. After the ignition the arc is blown magnetically against a diaphragm (D) which is positioned horizontally above the horn electrodes. The third electrode CE ($\varnothing = 2$mm) is arranged perpendicularly to the arc axis in the center of the diaphragm aperture. The whole discharge arrangement is enclosed in a vacuum tight chamber equipped with windows for optical observation. The electrical set-up can be divided into four circuits, the ignition circuit (S1, R_3, R_4 and C_1, charged onto the voltage $U_1 = 1.8$kV), the arc circuit (current source I_0, R_1, D_1 and R_4), the circuit of commutation (CE, D_3) and a circuit for acceleration of commutation (S2, C_2 and R_2). By closing the switch S1, the arc between the horn electrodes is brought into operation with a constant current of $I_0 = 25$A. By the resistance R_4 the cathode potential is raised up to 250V, so that CE is negatively biased against the arc plasma. By applying a magnetic field (B) in addition to the thermal lift, the plasma is blown against the diaphragm and the CE. After a time of a few hundred μs the current of the arc is taken over by the new cathode. This is marked by a steep current increase through the CE. The experiment is stopped by triggering the thyristor T_1. To record the initiation and the development of arc spots by high-speed photography, it is necessary to produce a trigger signal before a current through the CE can be measured. As shown in Fig.1 an optical trigger signal is generated by using a laser diode (LD), whose wavelength is adjusted to a strong atomic line of the filling gas (in case of argon a line at 811.531 nm). If the arc plasma passes the diaphragm the radiation of the laser diode is partly absorbed. This is detected by a sensitive photodiode PD. The signal of the PD is used to generate time delayed trigger signals for all cameras and to trigger the switch S2 which connects the negative pin of C_2 (charged onto a voltage U_2) with CE. By applying the voltage U_2 the commutation process is more accelerated and timed.

3. Measurements

The arc current (I_B) and the current through the CE (I_c) are recorded by current probes Cp1 and Cp2 (shown in Fig.1). Pictures are taken with a high-speed CCD-camera (PROXITRONIC) which allows exposure times down to 5 ns and also with a streak camera (Hamamatsu) which makes it possible to record the development of arc spots on the CE. Generally the Proxitronic is triggered by the current in-
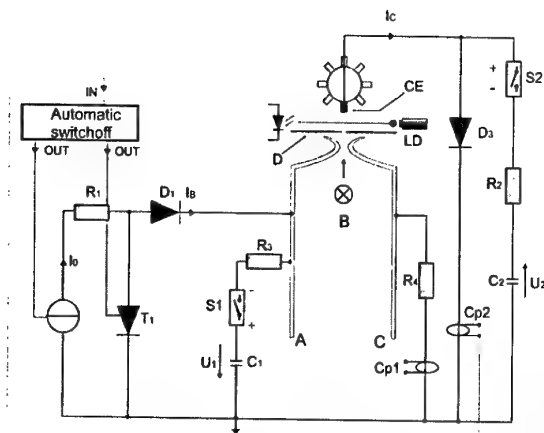
Figure 1: Experimental set-up

Figure 2: Proxitronic image: ignition on polished Al; $U_2 = 600$V, plasma channel between the bulk plasma and a luminous layer in front of the CE; $T_{delay} = 300$ns.

crease of I_c and the streak camera by the signal of the laserdiode. In some cases (for Cu, Al, Pd and C) the trigger time for the Proxitronic is delayed in addition by a digital delay generator to examine the arc attachment at different times during the increase of I_c. These series of pictures can only give a overview about the development of arc attachment, because only one picture can be taken per ignition. Spectroscopic measurements are taken with different spectral resolutions with a intensified CCD-camera (Dicam Pro, PCO), operated in double shutter mode. This mode allows to get two separate pictures with a minimum of time delay of 1 μs between them showing as in Fig.3 changes of the spectrum with time. Measurements are made at different voltages U_2 from 0V up to 950V. Furthermore SEM images are taken of the electrodes before and after a number of ignitions. In some cases (for Al and Pd) only one ignition is executed, where the current through the CE is switched off after 700ns. The given examples in Fig.2 and 3 are characteristic for the two different operating modes: $U_2 = 0$V and $U_2 > 300$V.
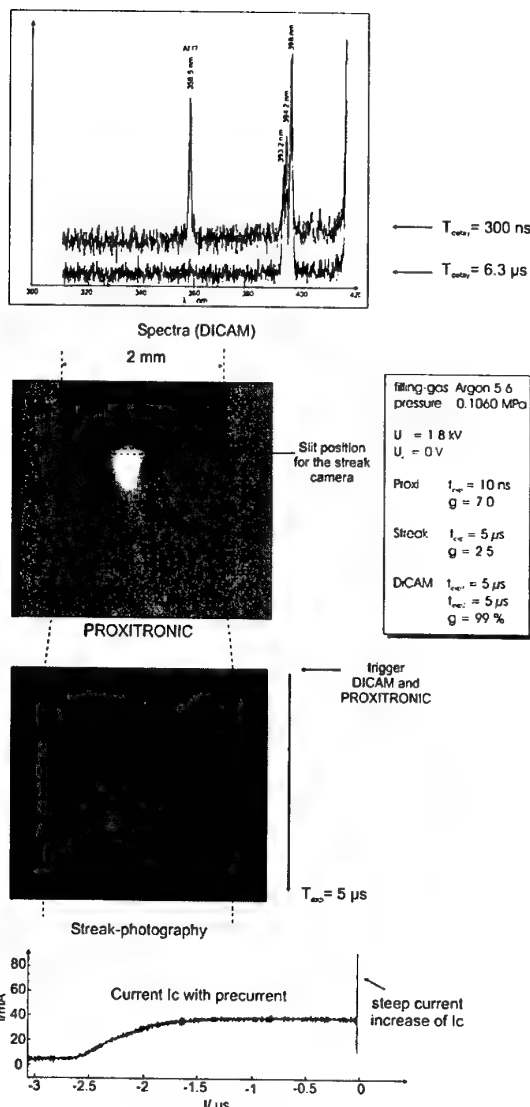

Figure 3: Ignition on polished Al; $U_2 = 0$V. recorded with high-speed cameras DICAM and PROXITRONIC, streak camera and current probe.

4. Acknowledgements

5. References

[1] J. Schein. M. Schumann, D.Nandelstädt. J.Mentel "Investigations of the ignition of arc spots on cold cathodes in a noble gas atmosphere", IEEE Trans. Plasma Sci., vol 25, pp. 897-904, 1997.

Ag-DLC tribological film deposition by double thermionic vacuum arc

I. Mustata, G. Musa, M. Blideran, V. Zaroschi, A. M. Lungu, C.P. Lungu and K. Iwasaki*

National Institute of Lasers, Plasma and Radiation Physics, Magurele-Bucharest, PO Box MG-37, Romania
*Japan Ultra-high Temperature Materials Research Institute, 573-3, Okiube, Ube, Yamaguchi 755-0001, Japan

A new type of plasma discharge, thermionic vacuum arc (TVA) was used to prepare Ag-DLC composite films to be used as anti-friction layer in automotive applications. The deposition method and film properties are presented.

1. Introduction

A new class of advanced materials with controlled tribological properties and environmental friendliness is currently developed in order to be applied in the automotive industry as anti-friction layer for plain bearing by using electron cyclotron resonance - direct current (ECR-DC) sputtering [1-2]. Thin film deposition process by thermionic vacuum arc (TVA), a new discharge type in pure metal vapor plasma, might become one of the most suitable technologies to improve significantly the tribological properties of the surfaces covered with different materials. TVA can be ignited only in high vacuum (HV) or ultra high vacuum (UHV) conditions between a heated cathode surrounded by an electron focussing Whenelt cylinder and an anode (crucible) containing the material to be deposited [3-4]. Due to the continuous electron bombardment of the anode (positively charged with controllable high voltage supply) by the accelerated thermo-electrons coming from the grounded cathode the anode material first melts and afterwards starts to evaporate ensuring a steady state concentration of the evaporated atoms in the cathode-anode space. At further increase in the applied high voltage, a bright discharge is established inside the vacuum vessel in the vapors of the pure anode material. The energy of ions of the TVA plasma can be directly controlled and established at needed value even during arc running by changing the cathode heating current and anode potential. As mentioned in a recently published paper, ion bombardment ensures better quality of the deposited thin film [5].

2. Experimental setup and method

The experimental set-up is shown in Fig. 1. The cathode of each of two guns consisted of heated tungsten filament surrounded by molybdenum Whenelt cylinder, which had an aperture of 10 mm in diameter. The filament for the silver discharge was made of a tungsten wire of 0.6 mm in diameter while the filament for the carbon discharge was made of thoriated tungsten wire of 3 mm in diameter. The filaments were arranged in the apertures of the Whenelt cylinders in the plane of their front surface. A hydrogen free graphite rod 20 mm in length and 10 mm in diameter was used as the carbon anode in the carbon discharge case and silver grains of 5 mm in diameter filed the anode crucible in the silver discharge case. The inter-electrode gap was adjusted in

the range of 4-8 mm. The ion energy was evaluated by using a retarding field analyzer of multiple mesh type.

The film composition was measured by using an X-ray fluorescence (XRF) analyzer in the quantitative mode and the crystallographic state of carbon included in the prepared films by a Laser-Raman spectrometer by using 514.4 nm wavelength radiation of an Ar ion laser, 5 mW power and 1 μm spot diameter.
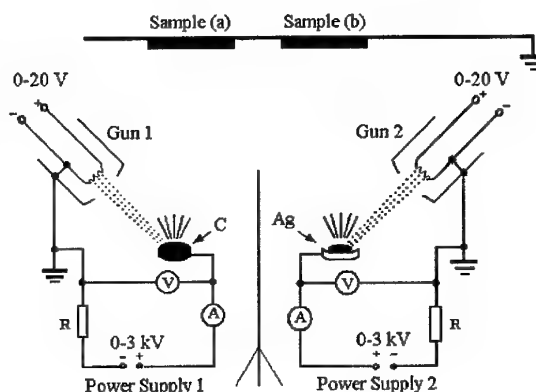

Fig.1 Experimental set-up.

The film morphology was analyzed by using an atomic force microscope (AFM) in contact mode. The coefficient of friction of the deposited film was measured by using a ball-on-disk tribometer at room temperature and 50% relative humidity of air. A bearing steel ball of 6 mm in diameter was used as a counter material. Load of 5 N and sliding radius of 4 mm were chosen. The sliding speed was kept at 0.1 m/s in all the measurements.

3. Results and discussion

Following parameters were fund to control the TVA: Arc current; I_{arc}, Cathode thermoelectronic current, (controlled by the heated cathode temperature); T_c, Inter-electrode distance; d, The angle between an imaginary perpendicular line on the anode and the axis of the heated cathode. Because both the cathode of TVA and the vacuum vessel are at earth potential the plasma has a positive potential against the vacuum vessel wall, that is roughly equal to the cathode potential fall. In these circumstances, the sample (and the growing layer too) is subjected to an intense

bombardment by both evaporated atoms and energetic ions during the film deposition.

The ionic energies in the vicinity of the substrate holder were found to be in the range of 50-300 eV. The high ionic energies led to the formation of composite films with a smooth morphology as was shown by the AFM analysis. The surfaces of the deposited films reproduced properly the initial roughness of the bronze used as substrates, and the "planarization" of the coated surface was not observed, allowing the coating to keep the embeddability of foreign particles in the running-in process of the engine bearings.

X-ray fluorescence of the prepared films showed a concentration of 44.82mass%C in the sample (a) fixed close to the C anode and 19.27mass%C in the (b) sample fixed close to the Ag containing crucible.
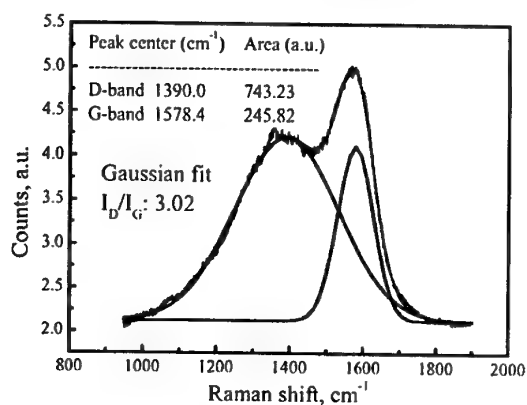

Fig.2 Typical Raman spectrum and Gaussian fit of the 2 peaks assigned asD-band and G-band.

Carbon was incorporated into the composite films as DLC phase, as defined recently by Ferrari and Robertson [6] with a large ratio of characteristic D-band/G-band. Figure 2 shows a typical spectrum of the prepared film and a Gaussian fit made in order to separate the D and G peaks. The D and G peaks are characteristic of the sp^2 sites of all disordered carbons at 1350 and 1570 cm-1, respectively. Development of the D band indicates disordering of graphite but ordering of an amorphous carbon structure; its intensity is proportional to the number and size of sp^2 clusters, while its width is more related to a narrower distribution of clusters with different order and dimensions. The G-band of graphite involves the in-plane bond-stretching motion of pairs of carbon sp^2 atom; this mode does not require the presence of sixfold rings and so it occurs at all sp^2 sites. [6] The influence of carbon incorporation into the film as DLC led to a drastic decrease in the coefficient of friction tested in dry condition. Figure 3 shows the frictional behavior of the Ag-DLC films compared to that of the bronze substrate.

The reduction of the coefficient of friction can be observed for both the coatings compared to that of bronze substrate. A drastically decreases in the coefficient of friction of the Ag-DLC coating with

increasing carbon content was observed during the ball-on-disk test in dry conditions. This suggests the predominant influence of the DLC acting as a solid lubricant inclusion in the silver matrix.
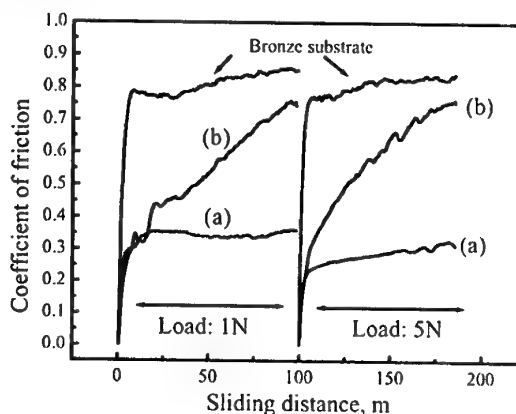

Fig.3 Coefficient of friction versus sliding distance.

Due to the ion bombardment the thin films are compact and very smooth with no columnar structure. Due to the incident energetic ions, the adherence of the thin film to the substrate increases remarkably. In this case the adherence was directly related to the value of the energy of ions, increasing with the energy of ions. Taking into consideration the peculiarities of the carbon film deposition, TVA is considered to be one of the most adequate technologies for this field of applications. Indeed, due to the ensured high purity of the deposition process (in vacuum vessel only carbon and silver being introduced besides refractory metals used as electrodes) completely hydrogen free carbon film can be obtained. At the same time, TVA technology ensure high efficiency in producing high energy ions spent to heat carbon which needs temperatures higher than 4000K.

Because of vacuum conditions and high sublimation temperature of the carbon, and relative low melting temperature of the silver the main energy losses are practically only by radiation. Taking these advantages into account TVA is expected to be very promising for preparation of Ag-DLC tribological coatings.

4. References

[1] K. Iwasaki, C. P. Lungu, S. Takayanagi, K. Ohkawa, Int. J. of Applied Mechanics and Engineering 7 (2002) 351.

[2] C. P. Lungu, K. Iwasaki, Vacuum 66 (2002) 385.

[3] G. Musa, H. Ehrich, J. Schuhmann, IEEE Transactions of Plasma Science, 25 (1997) 386.

[4] H. Ehrich, J. Schuhmann, G. Musa, A. Popescu, I, Mustata, Thin Solid Films 333 (1998) 95.

[5] C. Biloiu, H. Erich, G. Musa, J. Vac. Sci. Technol. A19 (2001) 757.

[6] A. C. Ferrari, J. Robertson, Phys. Rev. B 61 (2000) 14095.

Plasma of free burning electric arc between composition electrodes in air

A.N.Veklich[1], I.L.Babich[1], V.Ye.Osidach[1], L.A.Kryachko[2], R.V.Minakova[2]

[1]Taras Shevchenko Kyiv National University, 64, Volodymyrs`ka Str., Kyiv 01033, Ukraine
e-mail: van@univ.kiev.ua

[2]Institute of Materials Technology Problems NAS of Ukraine, lab.29, 3, Krizhanivs`ky Str., Kyiv 03142, Ukraine
e-mail: 29min@ipms.kiev.ua

This paper deals with spectroscopy investigations of plasma of free burning electric arcs in air between electrodes from composition materials on the base of cooper (Cu, Cu-W, Cu-Mo, Cu-Mo-LaB₆) and silver (Ag, Ag - CdO, Ag – Ni).

1. Introduction

A problem of developing of reliable interrupting devices, where ignition of electric arc often is realised, can not be resolved without careful analysis of processes which take place in the arc and its electrodes. Furthermore, an electric arc, being generated at contact disconnection, results in considerable material erosion of contacts. This causes the decrease of device efficiency and limits reliability of its activity.

In this paper the processes occurred in a free burning electric arc in air between electrodes from composite materials on the base of cooper *(Cu, Cu-W, Cu-Mo, Cu-Mo-LaB₆)* and silver *(Ag, Ag - CdO, Ag – Ni)* were studied. Such arc is model of arcs arising between contacts of current disconnectors of electric circuits.

2. Experimental Set-up

The arc was ignited between the end surfaces of the non-cooled electrodes. The discharge gap l_{ak} was of 2, 4, 6 or 8 mm. The diameter of the rod electrodes was of 6 mm. To avoid the metal droplets appearing a pulsing mode was used: the current pulse up to 30 A was put on the "duty" weak-current (3.5 A) discharge. The pulse duration ranged up to 30 ms. The quasi-steady mode was investigated.

Because of the discharge spatial and temporal instability the method of the single tomographic recording of the spectral line emission was used. A 3000-pixel CCD linear image sensor (B/W) Sony ILX526A accomplished fast scanning of spatial distributions of radiation intensity. It allows the recording of the radial distributions of nonstationary arc radiation intensity in arbitrary spatial sections simultaneously.

Just as previously spectrometer [1-2], the using of the monochromator with the significant astigmatism allowed excluding additional focusing optics from the optical path of given spectrometer. The CCD linear image sensor is directly aligned with sagittal focal plane of monochromator behind its exit slit. This slit is located in the meridional focal plane. Such technical decision enables to increase aperture ratio of the device and to register spatial distribution of radiation intensities along an entrance spectral slit of monochromator in a given spectral range. The observed spatial distributions of spectral line intensities can be approximated by Gaussian function and transformed into local distribution by Abel inversion. Our developed software provides such procedure on the base of Bockasten technique [3].

The synchronisation of operation of the CCD linear image sensor with the external electrical circuit is stipulated. The ISA interface slot of IBM PC in a control and data exchange is used.

In a combination with a Fabry-Perot interferometer (FPI) the spectrometer provides simultaneous registration of spatial and spectral distribution of radiation intensities. Thus, the spectrometer allows measuring contours of spectral lines in different spatial points of plasma volume.

3. Results and Discussions

3.1 Electric arc between electrodes from composition materials on the base of cooper *(Cu, Cu-W, Cu-Mo, Cu-Mo-LaB₆)*

The radial profiles of temperature are determined in the average cross section of the discharge gap l_{ak} = 2, 4, 6 and 8 mm in air at arc currents 3.5 and 30 A. The temperature profiles are obtained from relative intensities of copper spectral lines 510.5 and 521.8 nm. Because of the discharge spatial and temporal instability the statistical treatment of obtained data was carried out. The spectral sensitivity of the experimental set-up was taken into account.

As recently was found the some secondary structure on a surface of electrodes can be realised during the discharge operation [4]. Therefore we studied our plasma in a two different modes. In the first mode the measurements of radial distributions of spectral line intensities were carried out as a statistical average value during the series of current pulses (30A) putted on the "duty" weak-current discharge (3.5 A). In this case the secondary structure on a surface of electrodes was realised. To avoid the influence of such secondary structure during the discharge operation in an another mode we measured the radial distribution of spectral line intensities as a statistical average value of single current pulses of an electric arc between smoothed surface of electrodes.

The radial temperature profiles of the arc between Cu-Mo-LaB$_6$ electrodes in two different modes are measured. In the first mode of the arc operation we investigated plasma of the discharge between smoothed surface of electrodes. The next mode corresponds to the case of electrode surfaces covered by a secondary structure, which is realised under the arc activity.

From the comparison of obtained results the key role of the condition of the surface electrode follows. Really the presence of the secondary structure must decrease the erosion of the electrode material. As a result the amount of lightly ionised metal vapours in a discharge gap must be decreased. Therefore at the same arc currents the temperature in plasma column must be higher in case of secondary structure on a surface of electrodes.

It was interesting to compare the influence of composition of the electrodes on the plasma parameters. Additionally investigations of radial profiles of temperature in the arc discharge between pure copper electrodes were carried out. We carried out the similar investigations of plasma of electric arc between Cu-Mo and Cu-W electrodes in the first mode of the arc operation as well.

We can compare obtained radial temperature profiles of the arcs between Cu-Mo-LaB$_6$ electrode surfaces with a secondary structure and between copper electrodes. From these results follows that in arcs with discharge gaps 4, 6 and 8 mm at the arc current 30 A the axial temperatures are higher in case of Cu-Mo-LaB$_6$ electrodes. This phenomenon can be cased by both the additions of the Mo-LaB$_6$ to copper in such composition and a secondary structure of electrode surfaces. In case of discharge gap 2 mm such behaviour of axial temperatures are not observed. It is natural because the plasma of such arc probably is not in a local thermodynamic equilibrium. Such effect was observed in plasma of a short free-burning electric arc between copper electrodes [5].

The increasing of both the temperature and the efficiency of the plasma torch as a tool in the electrical erosion cutting is probably one of the factors, which determine the productivity of the dimensional treatment in the presence of the boron-containing compounds.

We compared radial temperature profiles of the arc between Cu, Cu-Mo, Cu-Mo-LaB$_6$ and Cu-W electrodes also. The arcs between composition electrode surfaces with a secondary structure were investigated in this case. The essential influence of the additions to the electrode materials on the arc plasma temperature is found [6].

3.2 Electric arc between electrodes from composition materials on the base of silver (Ag, Ag-CdO, Ag-Ni)

As the width of the spectral line AgI 466,8 nm is determined by the quadratic Stark effect, i.e. the width of the spectral line is proportional to the electron density

N_e in the discharge, the variation of its value means the variation of this plasma parameters.

It was found that the width of the spectral line in a case of the pure silver electrodes is comparable with the FPI instrumental contour (free spectral range of the FPI $\Delta\lambda$ = 0.36 nm). The width of this line increases in an arc between Ag-Ni electrodes. It caused by increasing of the electron density in the discharge plasma.

The obtained results are in a good agreement with earlier published [7]. The matter is that in a spark plasma the electron density increases at the using of the composition electrodes made from the pure metals. This effect is especially visible with increasing of their particles dispersity. For instance, in a case of pure copper $N_e/(10^{18}$ cm$^{-3}) =1.48$. In a case of pure tungsten this parameter equals 0.57 and in a case of a composition Cu-W it equals 1.92 with an average size of particles $r_{av}= 0.3$ μm.

We also measured the radial profiles of temperature in plasma of the arc between Ag-CdO. These profiles are obtained from relative intensities of spectral lines CdI 479.9, 508.5 and 643.8 nm. It is necessary to pay attention to unusual low temperature value (about 4000 K) in such discharge plasma. It can be caused by the significant amount of cadmium vapours in a gap. The matter is that the melting temperature of Cd is lowest among metals (~300°C), which are usually used in the production of the composition materials.

4. Conclusions

Based of spatial profiles of the temperature and electron density the model of the investigated plasma can be developed. It is visible from the analysis of the obtained results that the processes occurred in the discharge gap are determined by erosion of the electrode material and condition of its surface.

5. References

[1] A.N.Veklich, V.A.Zhovtyansky, *J. Appl. Spectroscopy* **50** (1989) 359.
[2] I.L.Babich, A.N.Veklich, V.A.Zhovtyansky, *J. Appl. Spectroscopy* **51** (1990) 1028.
[3] K.Bockasten, *J.Opt.Soc.Am.* **51**(1961) 943.
[4] I.L.Babich, A.N.Veklich, V.Ye.Osidach, G.A.Zykov, A.P. Kresanova, R.V. Minakova, *15th International Symposium on Plasma Chemistry. Orleans, France* **III** (2001) 1003.
[5] A.N.Veklich, *PhD Thesis, Taras Shevchenko Kyiv University* (1997) (in Russian).
[6] I.L.Babich, V.Ye.Osidach, V.I.Sobovoy, A.N.Veklich, *Czechoslovak Journ. of Physics* **52**, **Supplement D** (2002) D731.
[7] L.I.Kostenetskaya, I.I.Kravcevich, A.P.Kresanova, R.V. Minakova, A.V.Smirnov, *Electrical contacts. Institute of Materials Technology Problems NAS of Ukraine* (1983) 17(in Russian).

On the Nature of the Voltage Fluctuations in the Plasmatron with Self-Established Arc Length

O.A. Sinkevich, E.Kh.Isakaev, S.V. Kalinin, S.L. Ochkan

Science and Engineering Center for Energy Efficient Processes and Equipment, Associated Institute for High Temperatures, Russian Academy of Sciences, Izhorskaya 13/19, Moscow, 127412, Russia, emin-isakaev@mtu-net.ru

In a plasmatron, when the cathode is placed centrally, the channel wall serves as an anode, and length of an arc is self-established, voltage fluctuations have a specific ramp-like shape. This shape of the voltage fluctuation has the regular component generated by downstream elongation of the electric arc and its consequent rerouting and a noise generated by different processes going on inside the plasmatron [1-5]. The downstream elongation of the electric arc explains the first slow stage of the voltage fluctuation. The second stage – a steep fall of the voltage – is explained by the electric breakdown between the hot arc core within the axis and the anode spot on the plasmatron channel. The "breakdown" observed during the self-establishment of the arc length in the flow occurs mainly under the influence of dynamic interaction of electric currents of the different parts of the arc.

The displacement of the anode end of the arc when the cathode end is fixed to its central place at the conical cathode must generate without fall fluctuations of the current path near the position of the unstable equilibrium under the influence of the Ampere force. The velocity of the plasma flow is maximal at the axis, so the part of the current channel is entrained downstream while the "fastening" point at the anode, where the arc ends, lags behind because the plasma has zero velocity at the wall. The entertainment and the elongation of the arc in the downstream direction raise the length of the current path by $\delta l(t)$ and the arc voltage by $\delta U(t) = E_l \delta l(t) = E_l V(r = 0) t$, $E_l \approx$ Const. The displacement of the far end of the current path from the axis wakes up an interaction of different parts of the current channel – the radial Ampere force appears that was absent before. The interaction of anti-parallel currents from different parts of the current path leads to the rerouting of the anode end of the arc. This shunting process makes the arc voltage lower. It is very fast compared with the stage of linear increase of the voltage.

The dependency of the main fluctuation frequency on external parameters assuming that the electric arc shunting process in a plasmatron with gas flow and self-established arc length is determined by electrodynamic interaction of the currents from different parts of the current path may be found. We define the characteristic fluctuation frequency as:

$$f = \frac{d(kG)}{dt}/G, \qquad (1)$$

where $k(t) = 2\pi \iint \rho V r dr / G$.

The characteristic fluctuation frequency could be found from the dynamic equation of an arc and for arbitrary values of the magneto hydrodynamic interaction parameter (MHDIP) $N = jBd/P$ may br represented in the next form:

$$f = \xi_1 I^2 \mu_0 / Gd \quad + \xi_2 G / \rho_0 d^3 =$$
$$= I^2 \mu_0 / Gd \, (\xi_1 + \xi_2 / N). \qquad (2)$$

Here ξ_1, ξ_2 are a non-dimensional coefficients. The coefficients ξ_1 and ξ_2 depending on the geometric factors differ from 1. They can be calculated using the numerical solution of the non-stationary 3D magnetogasdynamic problem for the arc shunting or determined from the experiment. Numerical solution of this non-stationary 3D problem is also a hard problem so we have obtained ξ_1, ξ_2 from our experiments.

Experimental dependencies of the fluctuation frequency on the flow rate for different currents and on the current for different flow rates were experimentally investigated in argon and nitrogen [4]. The investigation of the mechanism governing the rerouting (shunting) of the current path in a plasmatron channel with self-established electric arc length is performed for the axisymmetric configuration where the cathode is placed centrally and the channel wall serves as an anode. The formula was found from the analysis of the dynamics of the current channel determining the dependency of the characteristic frequency of the voltage oscillations on the external parameters of the problem: the electric arc current, the flow rate of the working gas and the characteristic diameter of the duct. This formula generalizes the results of the investigations of the voltage oscillations in the plasmatron channel with self-established electric arc length performed by different authors in a wide range of external parameters [1-4].

It follows from (2) that, according to the MHDIP, the different kinds of the dependency of voltage oscillation frequency on the flow rate may be observed. Under the greater values of the MHDIP ($N = jBd/P \gg 1$) the characteristic frequency of voltage oscillation falls with

the increase of the flow rate. If the MHDIP is much less than 1 the characteristic frequency of voltage oscillation grows with the increase of the flow rate and practically doesn't depend on the current.

Fig. 1 Non-dimensional frequency f^* on the current for

different gas flow rates
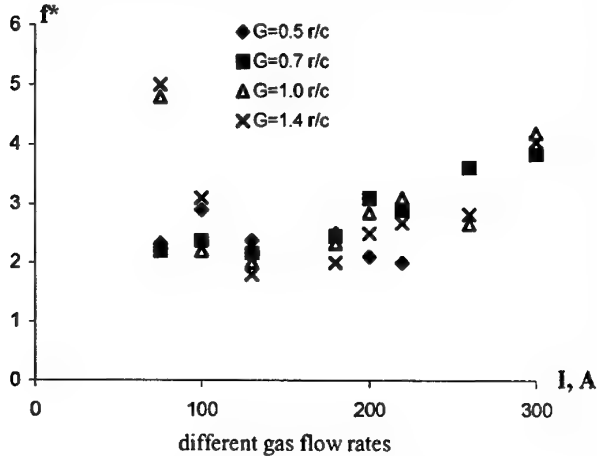
The dependency of the non-dimensional frequency $f^* \equiv f(I^2\mu_0/Gd)^{-1} = (\xi_1 + \xi_2 / N)$ on the current for different flow rates of a plasma-forming nitrogen is presented in the fig. 1. For analyzing the fluctuations in plasmatron, one should take into account that for high currents the influence of the current-convection instability [6,7] might be more significant making the arc-conducting channel pulsate.

References

[1] M.T. Dooly, W.K. McGregor, L.E. Brewer: Characteristics of the Arc in a Gerdien – type plasma generator, AIAA Journal, 32 (1962) 99.

[2] J.K. Harvey, P.G. Simpkins, B.D. Adcock: AIAA Journal, 33 (1963) 213.

[3] M. Leylavergne, Z. Duan, J.F. Coudert, P. Faushais, J.Heberlein: Progress in Plasma Processing of Materials, Eds. P. Fauchais and J. Amouroux, Begell House Inc. N.Y., Wallingford U.K., 1999 443.

[4] E.Kh. Isakaev, V.K. Korolev, S.A. Tereshkin, A.S. Tyuftyaev, O.A. Sinkevich: Ibid. 13.

[5] M.F. Zhukov, A.S. Koroteev, B.A. Uryukov: Applied dynamics of thermal plasma, Novosibirsk, Nauka, 1975 (in Russian).

[6] V.I.Artemov, Ju.S.Levitan, O.A.Sinkevich: Instabilities and turbulence in a low temperature plasma, Moscow, Moscow Power Engineering Institute, 1994 (in Russian).

[7] A.V. Nedospasov, V.D. Khait: Oscillations and instabilities in a low temperature plasma, Moscow, Nauka, 1979 (in Russian).

Experimental determination of temperature, electronic density and air pumping in an oxygen plasma cutting arc

L.M. Girard[*], Ph. Teulet[*], M. Razafinimanana[*], A. Gleizes[*], F. Camy-Peyret[#] and G. Caillibotte[#]

[*]Centre de Physique des Plasmas et de leurs Applications de Toulouse (CPAT) UMR 5002, Université Paul Sabatier, 118 Rte de Narbonne, 31062 Toulouse cedex 4, France

[#]Air Liquide, Centre Technique des Applications de Soudage (CTAS), 13 Rue d'Epluches, Saint-Ouen l'Aumône, BP 24, 95311 Cergy Pontoise cedex, France

Abstract: This paper deals with the experimental characterization of an oxygen plasma cutting torch. Optical spectroscopic methods were performed to determine temperature, electronic density and nitrogen rate values. This study concerned the region situated under the shock wave located in the immediate vicinity of the nozzle exit.

1. Introduction

Several investigations about oxygen plasma cutting torch were realized previously in our laboratory [1-2]. They deal with an arc model, but few experiments were made to validate this numerical treatment. The jet is supersonic and turbulent, with the presence of a shock wave in the immediate vicinity of the nozzle exit. Pressure relaxes to the atmospheric pressure on a short distance, in the order of few millimeters. The study presented in this paper concerns the region under this shock wave, where the LTE assumption is valid. Results about temperature, electronic density, and air pumping in the plasma jet will be reported.

2. Device presentation

2.1. Torch configuration

The plasma cutting torch is an OCP 150 system marketed by "Air-Liquide" company. The simplified torch design is shown in figure 1. The injected gas is first argon for arc striking, then oxygen when the arc is transferred to the metal workpiece. In our configuration, the plate to be cut is a rotating disk (the anode) situated further down at 15 mm, allowing spectroscopic measurements. In the real cutting configuration, this distance would be 3 mm from the nozzle exit.
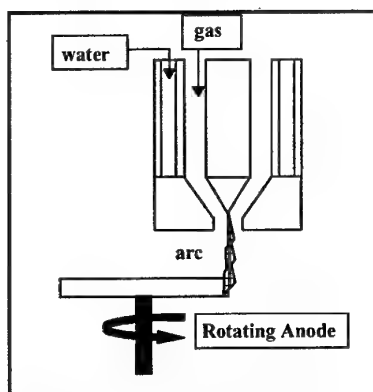
Figure 1 : Torch Configuration

2.2. Experimental setup

In the acquisition device, an optical system, which magnification equals 2.0, allows horizontal (x) and vertical (z) scans. The lines are selected by a Jobin-Yvon monochromator. A Hamamatsu CCD camera transforms the integrated intensities in electric signals received by a computer.

2.3. Experimental conditions

Spectroscopic measurements were performed under the shock wave, for different axial positions z= 3, 6, 9, 10 and 12 mm along the jet. The arc current is fixed at 60 A and the voltage is 200 V, for an oxygen flow rate of 6.5 l.min^{-1}.

3. Diagnostic methods

3.2. Electronic density

The electronic density was deduced from the Stark broadening of the OI oxygen line at 645,6 nm and the H Balmer α line at 656,3 nm, according to Griem theory [3-4]. Apparatus function is neglected (~0.04 nm). It is noteworthy that the pumping of nitrogen doesn't change significantly the electronic density, since the nitrogen ionization energy value is very near the oxygen one.

Method related to the continuum emission was performed to determinate the electronic density. The contributions of the radiative recombination and Bremsstrahlung (e-ions and e-atoms) were calculated [5].

3.1. Temperature determination

The Folwer-Milne method [6] was applied for the temperature determination. This technique requires an axial temperature of the plasma greater than the temperature corresponding to the maximum emission (for the OI 777.3 nm and the OI 884.6 nm, the maximum emission temperature is 15500 K at atmospheric pressure). Nevertheless, this method depends strongly both on the pressure and the plasma

composition. Temperature profiles can also be obtained by combining the plasma composition, under LTE assumption, with the electronic density values deduced from Stark Broadening measurements.

3.3. Nitrogen pumping in the plasma jet

In our experimental conditions, the molecular species N_2 and N_2^+ are negligible in comparison to NI atoms. Moreover, NII ions must be taken into account. The atomic NI nitrogen density is calculated from the Boltzmann's law and the emissivity of the NI 744,3 nm line. Since the air proportion entering the plasma doesn't influence the ratio NI/NII [5], the atomic ion NII density can be easily deduced. The nitrogen rate is finally obtained from the Dalton's law [5].

4. Results

4.1. Temperature profiles

Two points can be mentioned from the figure 2. The first concerns the temperature decrease as long one go far from the nozzle exit. The second is about the crossing point of the curves due to the plasma expanding for high z values.
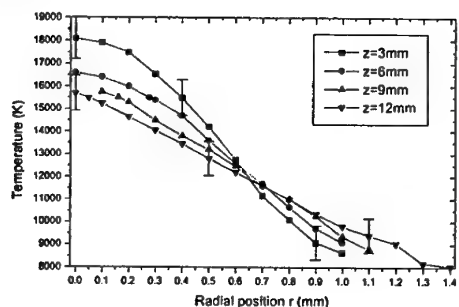
Figure 2 : Temperature profiles

4.2. Electronic density

The continuum method gives electronic density values higher than the values for an oxygen plasma at atmospheric pressure (figure 3). This discrepancy may be explained by the too low continuum intensity.
On the other hand, one can note a good agreement between the electronic density given by Stark Broadening of Hα and OI 645.5 nm lines and the LTE values. This result indicates the LTE assumption is valid for z=10 mm, excepted on the plasma edges.

4.3 Nitrogen rate in the plasma

Whatever the considered axial z position, the nitrogen rate on the axis stays lower than 10% (figure 4) in spite of turbulence. The nitrogen rate grows approximately to the air values for external part of the plasma.
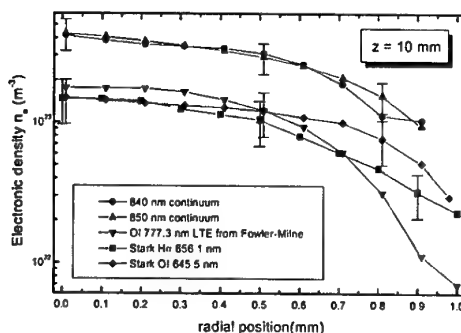
Figure 3 : electronic density profiles
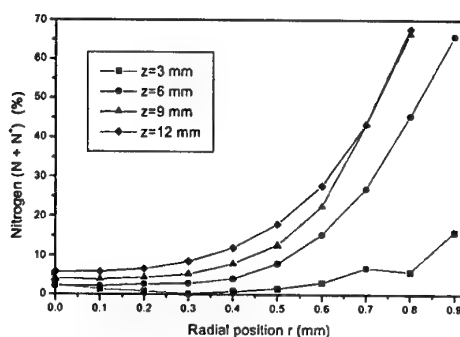
Figure 4 : Nitrogen rate

5. Conclusion and perspective

Other spectroscopic measurements have been done in the shock wave and at the nozzle exit. These results will be presented soon. Furthermore, in real cutting configuration, we intend to study the energy transfer from the arc to the plate, and the influence of different parameters such as speed on the shape of the cut kerf. Measurements based on the use of thermocouples, a CCD camera and a pyrometer are planned.

6. References

[1] P. Freton, University Paul Sabatier (Toulouse 3), Thesis, (2002).
[2] P. Freton, J.J. Gonzalez, A. Gleizes, F. Camy-Peyret and G. Caillibotte, *J. Phys. D: Applied Phys.* 35 (2002) 115.
[3] Griem H.R., Plasma Spectroscopy, Mc Graw-Hill, New York, (1964).
[4] Griem H.R., Spectral lines broadening by plasma, Academic Press, New York, London, (1974).
[5] Y. Cressault, University Paul Sabatier (Toulouse 3) Thesis, (2001).
[6] Vacquié S, *L'arc électrique*, Editions Eyrolles et CNRS éditions, (2000).

Metallic atoms concentrations measurements in an industrial low voltage circuit breaker using broad band absorption spectroscopy

S. Guillot, D. Hong, J. M. Bauchire, E. Le Menn, G. Pavelescu [a], F. Gentils [1], C. Fiévet [1] and C. Fleurier

GREMI, UMR 6606 CNRS - Université d'Orléans, B.P. 6744, 45067 Orléans Cedex 2, France
[1] Schneider Electric, Centre de Recherche, 38050 Grenoble Cedex 9, France
[a] On leave from National Institute for Optoelectronics, Bucharest-Magurele, Romania

In order to investigate the electrical arc in low voltage circuit breakers, metallic atoms concentrations measurements were performed using broad band absorption spectroscopy. From absorption spectrum in 510-523 nm range, copper atom concentration, electron temperature and silver atom concentrations were determined with LTE assumption. Absorption spectrum in spectral range around 430 nm enables to determine the iron atom density.

1. Introduction

In low voltage circuit breaker (LVCB) for high current, the arc established at contacts opening is usually moved by self-generated force towards the quenching area. For the development of such devices, it is necessary to have detailed knowledge about the behaviour of the moving arc. Because of the very complex processes involved, many experimental investigations and computer simulations of the arc in LVCB have been done by several teams [1]. In a previous paper [2], we have reported time resolved optical emission spectroscopy and imaging measurements in a LVCB adapted from an industrial device. These measurements revealed that metallic atoms (Copper, Silver and Iron) were presents in the air plasma arc. In order to determine the concentrations of these atoms, we have performed broad band absorption spectroscopy measurement using a bright radiation source developed in this purpose [3]. This investigation is useful for the modelling and the design of the LVCB. In this paper, we present some of measurement results. More results and information will be given during the conference.

2. Experimental set-up

The LVCB is shown in figure 1. An electrical arc is created during the discharge of a capacitor bank, when the separation of two contacts mounted on fixed and movable copper electrodes occurs. Then the arc expands and reaches the quenching area consisting of two symmetrical chambers. Materials of the contacts on copper fixed and movable electrodes are respectively silver-carbon and silver-carbon-tungsten. The quenching chambers consist of parallel arc splitter plates of different lengths. These steel plates are disposed on plastic holders. More details are given in reference [2].

The optical set-up is illustrated in figure 2. The radiation source light, driven by an optical fibre called F_Z, is polarised before going through the absorption medium (arc). The optical fibre F_{abs} collects polarised transmission light and one half of light emitted by the arc, while the fibre F_{emi} collects the other half of light. A spectrometer coupled with an intensified 2D CCD

camera is used to convert simultaneously these two optical signals into two spectra. The subtraction of these two spectra gives the transmission spectrum of the absorption medium. More details concerning acquisition system are given in references [2,3].
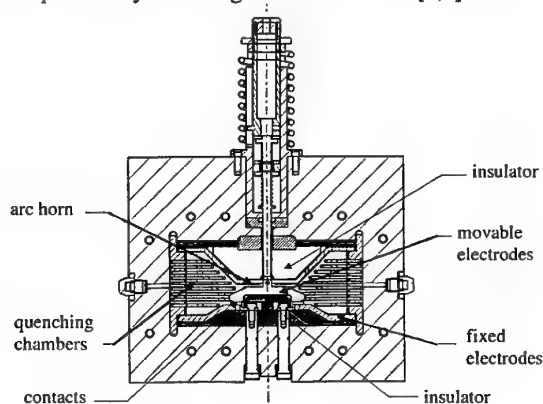

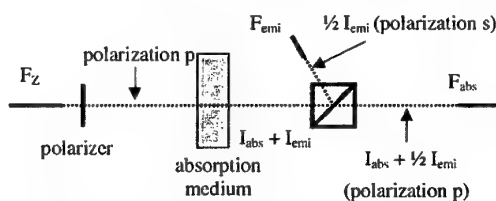Fig. 1. Industrial low voltage circuit breaker.

Fig. 2. Optical absorption measurement set-up.

3. Results and discussions

In figure 3, the spectrum (a) is the spectrum in range of 510-523 nm from the radiation source which emits as a black body of about *80 000 K* during more than 1 μs [3]. This spectrum is required without arc in LVCB. The optical opening time of ICCD camera is set to 1 μs during this experiment. The spectra (b) and (c) corresponding to light collected respectively by F_{abs} and F_{emi}, are required simultaneously when an arc is present in the LVCB. Measurement was done at 3 ms after the beginning of the current (i.e. 2 ms after the opening of the contacts) whose peak value was about 5 kA.
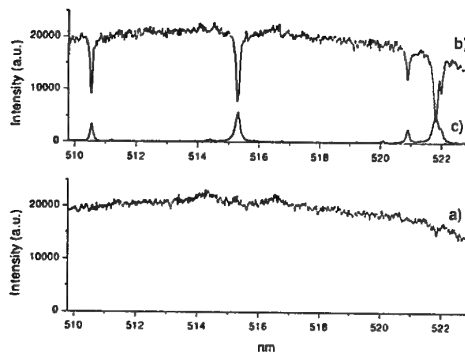
Fig. 3. a) spectrum I_a without absorption of arc,
b) and c) spectra I_b and I_c from F_{abs} and F_{emi}.

From these three spectra, the transmission spectrum is derived with calculating of $(I_b-I_c)/I_a$ and is given in the figure 4. The five main absorption lines are respectively CuI 510.55, 515.32, 521.82, 522.01 nm and AgI 520.91 nm.
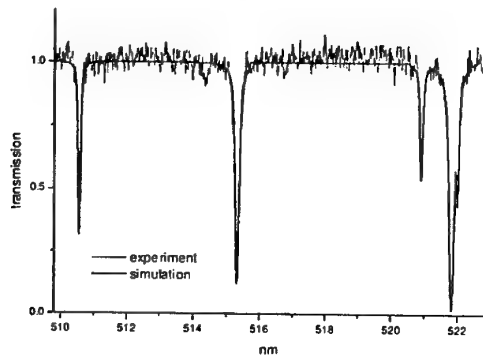

Fig. 4. Transmission spectrum and its best fit.

This transmission spectrum is fitted by a synthesised spectrum given by the relation :

$$t = e^{-\alpha_T(\lambda) L} * F_a$$

where L is the length of the absorbing medium which is supposed homogeneous, F_a is the apparatus function of detection system and * is convolution operator. The theoretical value of the absorption coefficient α_T is given by the following relation :

$$\alpha_T(\lambda) = \frac{\lambda^4 A_{ul}}{8\pi c} \frac{g_u}{g_l} N_l S(\lambda)$$

Here λ is the wavelength, A_{ul} is the transition probability between the upper level u and the lower level l, g_l and g_u are respectively the statistical weights of these two levels, c is the speed of light in vacuum and finally, N_l is the population of the atom in lower level. (Here the stimulated emission term is neglected). $S(\lambda)$ represents the normalised true line profile which has a nearly Lorentzian shape in our case.

$$S(\lambda) = \frac{1}{\pi} \frac{w}{(\lambda - \lambda_0)^2 + w^2}$$ where λ_0 is the wavelength

at line centre and w is the HWHM of the true line profile. So, the best fit of line transmission spectrum enables to determine the population of atoms in the lower energy level of the corresponding transition.

The best fit shown in figure 4 yields copper atom density in the four lower levels listed in the table 1. In this experiment, the uncertainty is estimated to be *30%*.

Table 1 Spectroscopy data and population in lower level

CuI line (nm)	E_l (eV)	g_l	A_{ul} (s^{-1})	N_l (m^{-3})
510.55	1.39	6	1.949×10^6	3.9×10^{20}
515.32	3.79	2	1.034×10^8	5.4×10^{18}
521.82	3.82	4	1.221×10^8	1.1×10^{19}
522.01	3.82	4	2.180×10^7	1.2×10^{19}

With LTE assumption, the population of an excited level is linked to the one of fundamental level by the Boltzmann law. In this case, if one plots $\ln(N_l/g_l)$ as a function of E_l, the slop should be $-1/T_e$ with T_e in eV when E_l is in eV. The Boltzmann's diagram yields an electron temperature of 0.77 eV. Since the energy gap between the two lower levels of the two CuI lines (510.55 and 515.32 nm) is as large as 2.4 eV, the uncertainty is quite good, and is estimated to be *20%*. The total concentration of copper atom is 1.4×10^{21} m^{-3}.
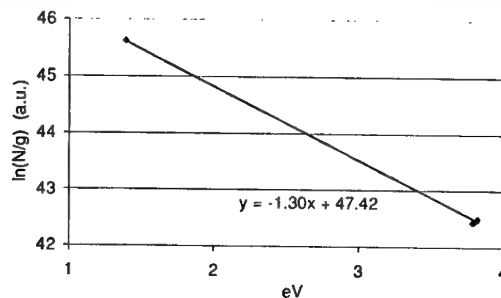
Fig.5 Bolztmann diagram from four CuI lines

The best fit of transmission spectrum yields a concentration of 2.0×10^{18} m^{-3} for the lower level of AgI 520.91 nm. A total silver atoms concentration can be yielded with LTE assumption, it is 2.5×10^{20} m^{-3}.

Measurements were also performed for the iron lines in spectral range around 430 nm. Results will be presented during the conference.

4. References

[1] M. Lindmayer, proceedings of the XIV Int. Conf. on Gas Discharges and their Applications, **2** (2002) 318-324.

[2] S. Guillot, J. M. Bauchire, E. Le Menn, C. Fleurier, C. Fiévet and F. Gentils, proceedings of 15th ISPC, **III** (2001) 1097-1100.

[3] D. Hong, G. Sandolache, K. Lan, J. M. Bauchire, E. Le Menn and C. Fleurier, Plasma Sources Sci. Technol. **12** (2003) 1-7.

A broad band radiation source for optical absorption spectroscopy measurements in single shot transient media

D. Hong, S. Guillot, G. Sandolache [a], J. M. Bauchire, E. Le Menn and C. Fleurier

GREMI, UMR 6606 CNRS - Université d'Orléans, B.P. 6744, 45067 Orléans Cedex 2, France
[a] On leave from NILPRP - Laboratory 22 P.O. Box MG 36, R-76900 Bucharest-Magurele, Romania

In order to investigate the post-arc period and the hot gas regions surrounding the electrical arc in circuit breakers, a broad band radiation source has been developed to perform absorption spectroscopy measurements. The radiation spectrum has been characterised both temporally and spectrally in order to determine the best operating conditions to produce an intense and continuous radiation spectrum. Absorption tests have been performed on the hot gas region of a low voltage rail gap circuit breaker.

1.Introduction

Optical absorption spectroscopy (OAS) is a technique commonly used to diagnose media where light emission is either missing or very weak. The use of this technique for rapidly transient media produced on a single shot basis or at very low and irregular repetitive rate, needs high spectral intensity sources presenting a very broad band spectral emission at the same time.

In order to perform such absorption measurements, a high intensity and very broad band transient source was developed. It consisted in an electrical discharge using the well-known Z-Pinch effect. At plasma ignition, fast discharge current flows in a very thin layer, called current sheet, at the surface of the inner wall of a cylindrical tube. This current sheet is driven by a self-generated Lorentz force towards the tube axis. When the current sheet collapses on the axis, the plasma becomes very dense due to a snowplow effect during compression, which drives all the particles towards the axis. In addition the plasma temperature strongly increases as a result of the conversion of the current sheet kinetic energy into thermal energy at the moment of collapse. This moment is referred to as the pinch time. With appropriate initial conditions, the continuous plasma radiation becomes extremely intense at the pinch time while the spectral lines are totally smeared out in the continuum background. Under our specific conditions, an electron density N_e above $10^{20}\,cm^{-3}$ is obtained. Consequently, on the one hand the bremsstrahlung and the radiative recombination, both depending on N_e^2, produce a very intense continuous emission and, on the other hand the spectral lines are strongly broadened by the Stark effect. In addition light observation along the tube axis allows to obtain a large optical thickness for both the continuous radiation and the spectral lines so that the global emitted spectrum is very close to the black body radiation at a temperature of about $80\,000\,K$ [1].

Investigations of arc re-strike phenomena were performed on a low voltage rail-gap circuit breaker by C. Fiévet et al [2]. It appears that the hot gas left behind the moving arc plays a major part in the re-strike process. The OAS measurement that enable to determine the composition and temperature of this gas and the concentration of each species, can provide valuable information for understanding of the arc re-strike phenomena. Tests of absorption measurements have been performed on a similar circuit breaker.

2. Z-pinch investigation

The experimental set-up of the Z-pinch is given in [1]. A streak camera is used to observe the plasma self-compression dynamic in Quartz tube. Optical fibre is used to collect plasma light through hole drilled in the centre of electrode. Both photo-diode signal and Streak camera photo show a giant light peak at the pinch time.
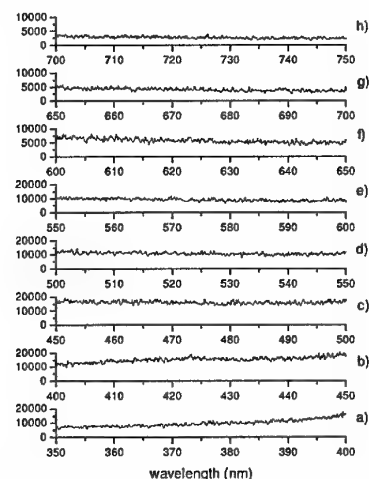

Fig. 1. Spectrum in the *350-750 nm* range at pinch time.

Time resolved end-on spectral measurements in a spectral range from 328 to 340 nm were performed at different instants during the discharge [1]. The spectra are recorded by a spectrometer ACTON 750 coupled with an intensified 2D CCD. Between *2* and *4 μs*, the spectral intensity is very weak and negligible. At *6 μs*, the plasma arrives on the axis and the emission in this wavelength range is dominated by Ar III lines (*328.61, 331.16, 333.61, 334.47, 335.84 nm*, etc.). At pinch time included in the observation period from *8* to *10 μs*, the

continuum emission becomes very intense while the spectral lines totally disappear due to the high electron density of the plasma. The plasma radiation is very close to a black body emission at this moment. At times between *14* and *16 μs*, Ar II lines (*335.09, 337.7, 338.85 nm*, etc.) appear but Ar III lines are still present.

At the pinch time, the whole spectrum in the range *350* to *750 nm* is shown in Fig. 1. The emission is flat, so it is very suitable for atomic or molecular absorption measurements.

3 Absorption measurement

Absorption measurement was performed with the experimental set-up designed for investigation of the breaking operation in low voltage circuit breakers [1-2]. One ms after the beginning of the current, a mobile contact is opened, and an arc is created in circuit breaker. Due to the Lorentz force, the arc moves away between the two rails towards the quenching area. As there is a strong erosion of the copper electrodes and, possibly, of the limiting walls, the hot gas behind the arc is composed of air, copper, and other species usually carbon and hydrogen since the walls are generally made of plastic material. Because this hot gas plays an important role in the arc-re-strike phenomenon, its investigation is useful for the modelling and the design of the circuit breaker.
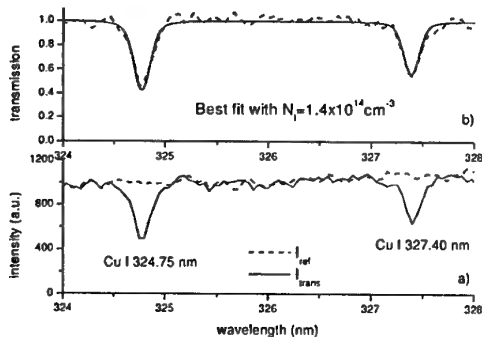
Fig. 2. a) Absorption spectrum of copper atom resonance *Cu I* lines *324.75* and *327.40 nm*; b) transmission spectra and its best fit.

In Fig. 2-a), an absorption spectrum of the two copper resonance Cu I lines Cu I *324.75* and *327.40 nm* is given. I_{ref} is the non-absorbed incident intensity and I_{trans} is the transmitted intensity. This measurement was performed at a position of *6 cm* from the arc ignition area and about *1 ms* after the arc has passed through. The relative intensity $R_M = I_{trans}/I_{ref}$ is plotted in Fig. 2-b). The theoretical value of the absorption coefficient α_T is given by the following relation, where $S(\lambda)$ represents the normalised true line profile :

$$\alpha_T(\lambda) = \frac{\lambda^4 A_{ul}}{8\pi c} \frac{g_u}{g_l} N_l S(\lambda)$$

Where the physical quantities are represented by the symbol commonly used and the stimulated emission term is neglected.

The best fit shown in Fig. 2-b) yields copper atom density of about 1.4×10^{14} cm^{-3} and a half width of *0.016 nm* (the same width was attributed to these two lines because they belong to the same multiplet). In our case the uncertainty can be estimated to be *30%*.

A Swan bands (0,0) and (1,1) absorption spectrum of the C_2 obtained in this experiment is shown in Fig. 3. Theoretical simulation of the rotational and vibrational structure of these molecular bands yields a C_2 concentration of about 1.3×10^{15} cm^{-3} and a rotation temperature of about *3 000 K*. The uncertainties are estimated to be also about *30%*.
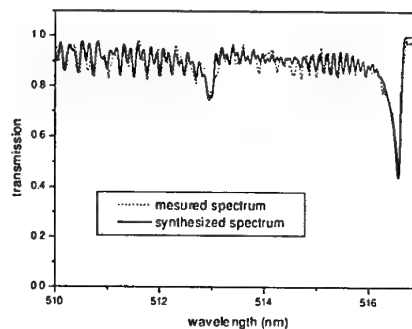
Fig. 3. C_2 absorption spectrum of Swan bands (0,0) and (1,1) (experiment and simulation).

4. Conclusion

A Z-pinch light source has been developed to perform optical absorption spectroscopy. Optimal working conditions have been set to obtain an intense and continuous radiation spectrum at the pinch time. Feasibility tests of optical absorption spectroscopy using this source have been performed on the hot gas and vapour produced in a low voltage rail gap circuit breaker. These rather simple measurements already provide quite interesting information about the hot gas left behind the arc.

5. References

[1] D. Hong, G. Sandolache, K. Lan, J. M. Bauchire, E. Le Menn and C. Fleurier, Plasma Sources Sci. Techno. 12 (2003) 1-7.

[2] C. Fiévet, M. Barrault, P. Petit, P. Chevrier, C. Fleurier and V. André, J. Phys. D : Appl. Phys. **30** (1997) 2991-2999.

98

Emission spectroscopy investigations on the low voltage circuit breaker

[1]V. Braic, [1]G. Pavelescu, [1]F. Gherendi, [1]M. Braic, [2]D. Pavelescu ,
[3]C. Fleurier, [3]D. Hong, [3]J.P. Bauchire, [1]M. Balaceanu

[1]National Institute for Optoelectronics, P.O.Box MG 05, 76900 Bucharest, Romania
[2]"POLITEHNICA" University of Bucharest, Spl.Independentei 313, 77206, Bucharest, Romania
[3]GREMI UMR 6606 CNRS Université d'Orléans - BP 6744 - 45067 Orléans Cedex 2 – France

The vacuum arc plasma produced during the electrode separation in the low voltage circuit breaker has been investigated by time resolved emission spectroscopy. The paper presents preliminary results concerning the influence of an axial magnetic field on the diffuse arc plasma. Some results of investigations on arc interruption failures in the constricted mode are also presented.

1. INTRODUCTION

The information concerning arc plasma parameters that lead to the successful or unsuccessful current interruption process is important for the technical improvement of the vacuum circuit breakers. Relating to the electrode activity and optical shape of the arc column, three main modes in the vacuum electric arc are developing: diffuse, columnar and constricted. In the case of nominal regime of the electrical network for the currents up to 4 kA (diffuse mode of the arc), the interruption is always successful after the first half-period current arcing time. For the overload and short circuit regimes (columnar and constricted modes of the arc) and currents higher than 10 kA, the current interruption could be successful, partially unsuccessful (the interruption occurs only after the second half period arching time) or totally unsuccessful (the interruption is not possible).

In this paper we present the results of the diagnostic by time-resolved emission spectroscopy of the vacuum arc plasma generated during electrode separation of a real vacuum circuit breaker. The investigations were focused on the diffuse and constricted modes, in the cases of nominal and short circuit regimes.

2. EXPERIMENTAL SET UP

The experimental set-up, reproducing exactly the conditions in a low voltage electrical network, was presented in a previous paper [1]. A stainless steel vacuum chamber with classical Cu-Cr50 electrodes (30 mm diameter, 3.5 mm gap) was used. In this structure, a variable axial magnetic field (AMF) up to 100 mT/kA was produced using Helmholtz type coils.

The test current simulates the rating current (1÷4 kA) and the short circuit current (10÷50 kA). Also, an imposed asymmetrical degree and adjustable half-period of the testing current can be provided by the electrical supply unit. The arcing moment can be set within ~500 µs error using an ultra fast electro-mechanical device, based on Thompson electrodynamic effect. The half-period of the current was set at 16 ms. The vacuum chamber pressure was always $10^{-7} \div 10^{-8}$ mbar.

Time-resolved emission spectroscopy was performed using an Acton SP750 spectrograph coupled to a gated micro-channel plate (MCP) intensified CCD detector (512×512 pixels). A bundle of 19 optical fibers, placed in a single column, matched the spectrograph entrance. The opposite end of the bundle with circularly disposed fibers collected the arc light, for different positions of the arc column sampled using a multiple slit collimator (parallel splitter plates of 680 mm length, 2 mm apart). A number of 16 MCP gates per single shot were recorded, with the gate width of 500 µs.

The measurements were performed in a wide spectral range (350-750 nm), and finally were focused on two spectral ranges, centered on 385 and 515 nm, where experimental lines were observed and also atomic data for Cr and Cu lines could be found.

3. RESULTS AND DISSCUSION

The influence of the AMF of about 820mT on the arc emission was analyzed. The typical time-resolved spectra for 3.4 kA arc current, with and without AMF, are presented in Fig. 1. The spectra are showing a change in plasma chemical composition during the arc evolution, less prominent in the presence of the axial magnetic field.
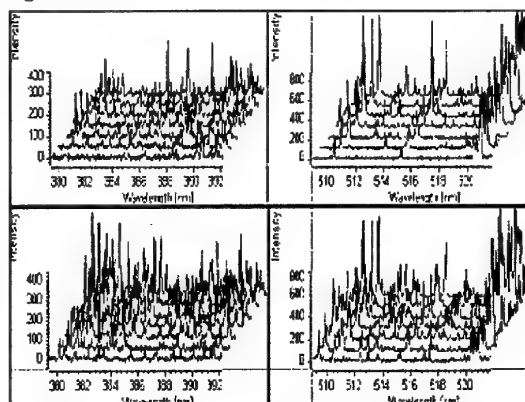

Fig.1 Time-resolved spectra - time as the third dimensions (AMF in the lower pictures)

99

This behavior is the result of the multiple particle jets production at the cathode, combined with the fast movement and short lifetime of the cathode spots during the arc. The jets dispersion is lower when an AMF is applied, which collimates the jets of charged particles around the electrode axis. Application of the magnetic field causes an enhanced excitation and ionization of the Cu and Cr atoms, by the trapped electrons, compared with the absence of the magnetic field. The presence of the AMF leads to a lower resistivity in the arc column, meaning lower energy dissipation in the plasma and lower contacts erosion.

Spectroscopic diagnosis was used to determine the excitation temperature of the atomic and ionic species using Boltzman graph method. Preliminary results on the diffuse mode regime showed a lower temperature than expected, of about 7000 K [2]. Data processing for different moments of the arc evolution revealed that Boltzman plot of the line intensities was not always a straight line. This led to the conclusion that the plasma in the diffusion mode is not in local thermodynamic equilibrium (LTE) [3],[4] and another method to characterize the diffuse mode plasma is necessary.

The experimental device has the ability to reproduce the behavior of a vacuum circuit breaker in real operation condition. This peculiarity allows to generate successful interruption, as well as partially unsuccessful interruptions as it is illustrated in Fig 2 in the case of constricted mode.
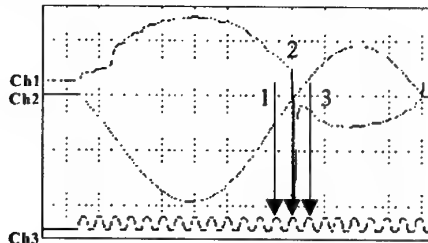
Fig. 2 *Partially* unsuccessful interruption *19.8 kA (Ch1: 20V/div; Ch2: 5 kA/div; Ch3: 10 V/div; 2ms/div)*

Using single shot time resolved spectroscopy on partially unsuccessful interruption, in the case of 19 kA peak current, the evolution of the arc emission during the arcing was analyzed. The spectroscopic successive measurement shots around current zero (CZ) can be observed in Fig. 3 at different moments of the arc evolution, indicated by arrows on the CCD gate oscillogram (Fig. 2). As shown in Fig.3, Cu II ions (508.83, 509.38, 512.77 nm) are present in larger amounts after the arc reignition than Cr II, though the 50%Cu - 50%Cr electrodes composition. The observed higher CuII, in comparison with CrII, may be determined by their different ionisation threshold. With the assumption of LTE in the constricted mode, from spectroscopic data (neutral Cu lines 510.55, 515.32, 520.08, 521.28, 521.82 nm), plasma temperatures of $5800 - 7000^0$ K were estimated around CZ. These temperatures are not far from the plasma temperature in the high current arcing period. On this basis, it is

possible to conclude that the plasma, in a similar state as in the arcing time, was present between the electrodes in the moment of the CZ, providing the appropriate media for reignition. Near CZ the presence of a minimum charge density leading to the arc reignition is expected.
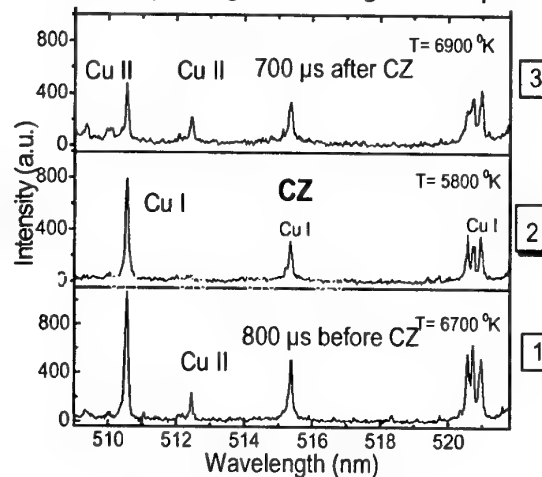
Fig. 3 Emission spectra around CZ

The measurements will be continued with absorption spectroscopy of the arc plasma in order to determine the plasma concentration around CZ and to establish the maximal value of the ion concentration for successful interruption.

4.CONCLUSIONS

Single shot time resolved emission spectroscopy of plasma in the low voltage vacuum circuit breaker for different working regimes revealed:

- Since the presence of the AMF stabilizes the arc plasma in the diffuse mode, a stronger effect is to be expected due to the higher values of the magnetic field (created by the current itself) in the constricted mode.
- Plasma temperature around CZ in partially unsuccessful interruption, approximately the same as in the arcing time, shows that the plasma is not sufficiently recombined, providing the appropriate media for reignition.

REFERENCES
[1] D. Pavelescu, S. Nitu, G. Dumitrescu, V. Trusca, IEEE Trans. Plasma Science, **27**, 4 (1999) 938
[2] F. Gherendi: *"Study of the transition from a diffuse mode to anode mode of the vacuum circuit breaker arc"*, PhD thesis, GREMI, University of Orleans (2002)
[3] A. Anders, S. Anders, J. Phys.D: Appl. Phys. **24**, (1991) 1986
[4] P. Malkin, J. Phys.D:Appl.Phys.**22** (1989) 1005

A STUDY OF THE CHARACTERISTICS OF THE PLASMA AIR ARC USED FOR CUTTING METALS

Tudor Stanciu

Technical University of Moldova, Power Engineering Faculty
168, bd. Stefan cel Mare, Chisinău, 2004, Moldova
tel.(3732) 237617, FAX (3732) 234187,
e-mail : stanciu@mail.md

The plasma air arc used for cutting metals must ensure an important heat transfer efficiency to metal during the cutting. More important parameter that ensure a great efficiency of cutting metals is the integral pressure of the outgoing plasma arc. In this paper are given the results of the experimental study of the influence of parameters of plasma torch with the antivortex generator on the integral pressure.

1. Introduction

In the plasma arc torch with the copper electrode with the cavity for cutting metals the vortex transport of the gas is used to ensure the decreasing of the electric erosion of the copper electrode and the space stabilisation of the electric arc, particularly in the nozzle channel [1]. This is necessary to prevent the appearance of a double arc that is very dangerous for the nozzle.

But the integral pressure of the plasma flux, in which the tangential component of the velocity predominates over the axial velocity, quickly decreases from the exit of the nozzle [1]. At the same time the diameter of this flux significantly increases. As a result the velocity and the deep of cutting diminish but the width of cut increases.

To increase the integral pressure of the outgoing plasma flux, to decrease his diameter, as well as to increase a capacity of cut it is necessary to increase the axial component of the velocity.

To eliminate these disadvantages a new plasma arc torch with the antivortex generator was elaborated, the principle of the work and its application for cutting metals is given below.

2. Experimental set-up and method of study of the gas dynamic characteristics

The principle scheme of the plasma arc torch is shown in the figure 1. The particularity of this torch in comparison with the other torch [1] is the utilization of a metallic antivortex generator (4) installed between the vortex generator (3) and the nozzle (2). On the both sides of the antivortex generator the chambers (5) and (6) are created in which the gas arrives via the tangential channels (7). The channels on the both sides are in opposite directions. This is necessary to create two opposite vortices.

The vortex created in the chamber (6), having the opposite direction, will compensate partially or totally the gas vortex issues from the chamber (5) to the nozzle.

Consequently the tangential component of the velocity of the plasma flux decreases but the axial

component increases on the issue of the nozzle. The vortex generator ensures the insulation between the cooper electrode with the cavity (1) and the nozzle (2).

The diagnostic includes the capacitor transducer (8) with a Pitot tube for measurement of the integral pressure, the camera with filters (9) to take pictures and the microphotometer (10) to study the radiation capacity and the radial distribution of the temperature of the outgoing plasma arc (11).
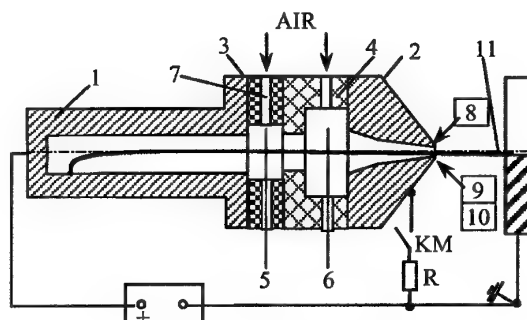
Figure 1. Experimental set-up.

3. Experimental results

The integral pressure of the outgoing plasma arc was measured at 3 to 35 mm from the outside of the nozzle for the values of the arcing current between 200 and 300 A and the values of the flow rate from 0.75 to 1.5 $g \cdot s^{-1}$. The diameters of the nozzle channel and the cavity of copper electrode were respectively 4 and 12 mm. The length of the nozzle channel and the cavity of the electrode were respectively 6 and 30 mm.

The distribution of integral pressure of the outgoing plasma arc for different values of the arcing current is shown in fig.2.

The integral pressure increases when increasing the arcing current. At the distance 3 mm from the nozzle the integral pressure increases from $3 \cdot 10^4$ to $6 \cdot 10^4$ $N \cdot m^{-2}$ when increasing the arcing current from 200 to 300 A (fig.3, curves 1 and 3).
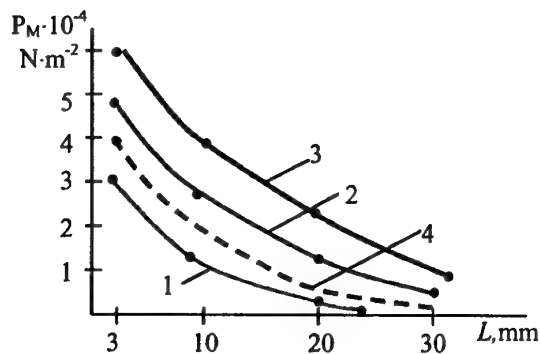
Fig.2. Distribution of integral pressure of the plasma arc torch with the antivortex generator for arcing current, A: 1 -200; 2 -250; 3 -300; 4 -250 (without antivortex generator).

For the same parameters the integral pressure, for the arcing current 250 A, is approximately 40% greater than for the plasma arc torch without antivortex generator (curves 2 and 4 respectively).

The integral pressure increases about 1.4 ...1.6 times when increasing the flow rate G of the air from 0.75 to 1.5 $g \cdot s^{-1}$ (fig.3, curves 1,2).

4. Conclusions

The utilisation of the antivortex generator ensures the increasing of the integral pressure of the outgoing plasma arc approximately from 1.4 to 1.6 times. The diameter of the plasma flux at the distance 3 mm from the nozzle, for the same values of the current and the flow rate, is 1.15 time less than without antivortex generator. As a result a deep of cutting increases up to about 40% but a width of cut decreases to 15%.
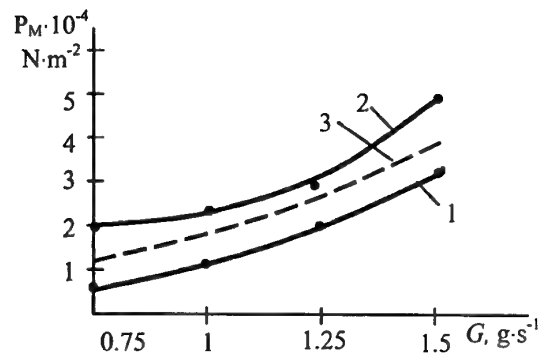
Fig.3. Correlation between the integral pressure and the flow rate for the plasma arc torch with the antivortex generator for arcing current, A: 1-200; 2-300; 3 -300 (without antivortex generator).

5.Acknowledgements

6.References

1. V. Pogora, I. Protsouc, T. Stanchou. Etude et optimisation de l'Installation de Coupage des Métaux par la Torche à plasma d'air. UIE Congress on electricity Applications, 1, Birmingham, UK (1996).

Laser exposure of high-pressure arc electrodes

M. Sieg, B. Nehmzow, M. Kettlitz, H. Schneidenbach, and H. Hess

Institute for Low-Temperature Plasma Physics
Friedrich-Ludwig-Jahn-Strasse 19, D-17489 Greifswald, Germany

The influence of a laser exposure of an arc electrode working alternatively as anode or as cathode on the discharge voltage and on the electrode temperatures is studied.

1. Introduction

Over the next years, electrodes will be the essential means for feeding electrical energy into an arc discharge lamp. The voltages which arise in the immediate neighborhood of the electrodes (electrode sheath voltage – ESV) represent a non-negligible part of the total arc voltage. They will, however, not contribute to the light output but are rather necessary to maintain the unhindered flow of charge carriers from the electrodes into the plasma column and vice versa.

A quantitative understanding of the corresponding electrode processes should lead to minimizing the ESV in order to improve the luminous efficacy of the discharge lamp. Although there are many attempts to model the cathode processes until recently [1-4], a final decision for a certain model for a given parameter range could not be made up to now [5]. Looking for effects which could be used to discriminate different cathode theories, we chose laser exposure of the electrodes. This additional heating impressively influences the arc voltage and the electrode temperatures, and the effects depend on the exposed electrode (cathode or anode). The results should be used for comparison with different electrode (cathode) models and may contribute to the development of an appropriate anode model.

2. Experiment

2.1. Experimental set-up

A vertically operated high-pressure discharge was studied the electrodes of which were exposed by a diode laser ($\lambda = 808$ nm; $P_{max} = 37.3$ W). The laser was side-on directed on the upper part of the electrode just below the tip. Its beam diameter at the electrode surface was 0.5 mm. The discharge was driven by a current source. The temperatures along the electrodes were determined by a pyrometer IS10 (IMPAC; 0.7 - 1.1 µm) the observation direction of which was at an angle of 90° compared with the laser beam. To diminish the influence of the laser radiation, a notch filter (10^{-4} at the laser wavelength) was used for the pyrometer.

2.2. Discharge configuration and operation mode

The experiments were done in conventional 150-W silica-lamp vessels which are modified by using longer electrodes. Thanks to this measure, the electrode tips are situated in the cylindrical part of the vessel making them accessible for undisturbed optical observations. The electrodes consist of pure tungsten and have a diameter of 0.5 mm. The lamps were filled with 22 mg mercury operating in the unsaturated mode which leads to a working pressure of about 6 bar. This pressure was determined by comparison with similar mercury discharges [6] which were thoroughly investigated earlier. The lamp was vertically operated and driven by a rectangular-wave current (1.9 A, 0.05 Hz). The lower electrode was exposed in a pulsed mode.

2.3. Determination of the absorbed laser power

The percentage η of the laser output power P_L, which is absorbed by the electrode surface, is an essential input for later discussions. In the case of laser heating only (no discharge!), this quantity can be determined by measuring the temperature distribution $T(z)$ along the electrode axis from top (axial coordinate $z = z_1$) to an axial position z_0 ($< z_1$) well apart from the laser-heating region. The absorbed laser power follows immediately from the simplified global energy balance:

$$\frac{4}{\pi d^2} \eta P_L = \left(\lambda \frac{dT}{dz} \right)_{z_0} + \sigma \left(\varepsilon_t T^4 \right)_{z_1} + \frac{4\sigma}{d} \int_{z_0}^{z_1} \varepsilon_t T^4 dz \quad (1)$$

where σ is the Stefan-Boltzmann constant. The thermal conductivity coefficient λ and the total emissivity of the electrode surface ε_t were taken from [7]. It results a laser power input efficiency $\eta = 0.12$. This value has been verified by solving the one-dimensional heat conduction equation with constant power input in the electrode tip region. The measured and computed axial temperature distributions agree very well.

3. Results

3.1. Change of arc voltage under exposure

The low frequency of 0.05 Hz corresponds to a quasi-stationary discharge operation. In this operation mode, the laser was always directed at the same electrode (the lower one) which alternatively serves as cathode and anode. The laser power was switched on only for three seconds during each half-cycle starting three seconds after the phase change (see Fig. 1). This operation mode ensures that stationary conditions were reached in the discharge after the change of polarity and further that the temperature increase due to the laser exposure can reach its maximum value.
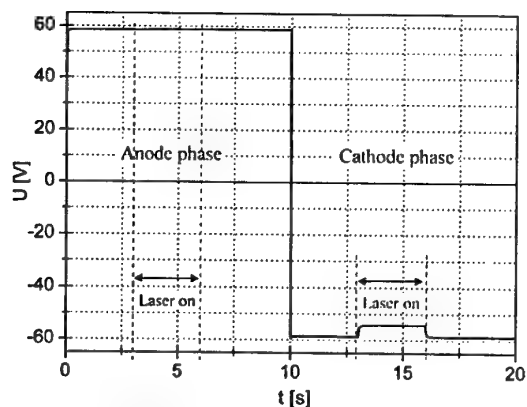
Fig. 1: Arc voltage with laser exposure of the lower electrode during the anode and the cathode phase

At first glance, only during the cathode phase there is a noticeable influence of the laser radiation. The arc voltage is decreased – the maximum laser power of 37.3 W gives rise to a voltage decrease of 4.4 V (Fig. 2). At a higher resolution of the arc voltage in the anode phase, however, there can also be seen a weak influence of the laser (arc voltage changes of about 0.1 V).
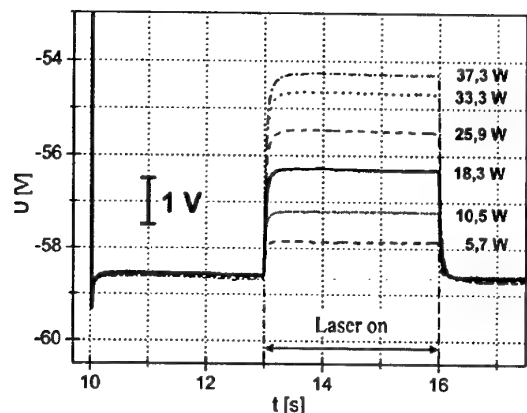

Fig. 2: Arc voltage during pulsed exposure of the cathode

3.2. Change of temperature under exposure

In Fig. 3, the pyrometrically measured temperature of the electrode tip can be seen as a function of time during the operation mode shown in Fig. 1 (rectangular-wave current, laser pulse during the anode and the cathode phase). The most striking feature is the enormous heating of the anode compared with the cathode. Because of the limited calibrated measuring range we can only compare the heating up to a laser power of 18.3 W. In this case, the anode temperature without laser is about 40 K lower than the cathode temperature (2955 K compared with 2995 K). During the laser pulse the anode temperature becomes higher by about 300 K (3255 K) and the cathode temperature only by about 50 K (3045 K); that means a difference in the influence of laser heating of 250 K.
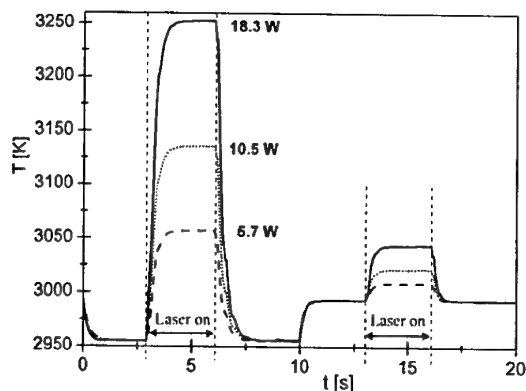
Fig. 3: Temperature at the electrode tip in the anode and cathode phase with laser exposure (cf. Fig. 1)

4. Discussion

The laser radiation hits a target (the tungsten electrode) which is in the cathode phase 40 K hotter than in the anode phase (laser power 18.3 W). This should not make a difference in the percentage of the absorbed laser power, therefore we will assume that in both phases the same amount of laser power is available for the heating of the corresponding electrode. The exposure of the anode causes a temperature increase of the electrode tip of about 300 K, and the change of the arc voltage is negligible. The exposure of the cathode, however, causes a temperature increase of only 50 K, and the arc voltage is simultaneously reduced by about 2.4 V.

This difference leads to the conclusion that in the cathode phase the absorbed laser power is mainly used not for an additional heating of the electrode but for substituting a part of the power which is usually delivered by the cathode fall.

5. References

[1] H. Schmitz and K.-U. Riemann, J. Phys. D: Appl. Phys. **35** (2002) 1727.
[2] M. S. Benilov and M. D. Cunha, J. Phys. D: Appl. Phys. **35** (2002) 1736.
[3] P. Flesch and M. Neiger, J. Phys. D: Appl. Phys. **35** (2002) 1681.
[4] R. Bötticher and W. Bötticher, J. Phys. D: Appl. Phys. **33** (2000) 367.
[5] W. Nandelstädt et al., J. Phys. D: Appl. Phys. **35** (2002) 1639.
[6] A. Kloss et al., J. Appl. Phys. **88** (2000) 1271.
[7] D. R. Lide, Ed., *Handbook of Chemistry and Physics*, CRC Press, Boca Raton, 1993 –1994, **12**-137 and **10**-299

Acknowledgment

On the electrode sheath voltage in high-pressure argon, xenon and mercury discharges

M. Sieg, B. Nehmzow, M. Kettlitz, H. Hess, L. Dabringhausen*, S. Lichtenberg*, M. Redwitz*, O. Langenscheidt* and J. Mentel*

Institute for Low-Temperature Plasma Physics, Friedrich-Ludwig-Jahn-Str. 19, D-17489 Greifswald, Germany
*Ruhr University of Bochum, Fundamentals of Electrical Engineering, Universitätsstraße 150, D-44780 Bochum, Germany

The electrode sheath voltage and the electrical field strength are measured in high-pressure argon, xenon and mercury discharges. There are significant differences in the shape of the ESV of mercury discharges compared with the rare gases.

1. Motivation

High-pressure discharge (HID) lamps have a widespread application in lighting because of their high luminous efficacy. A main problem in the operation of such lamps is a shortening of the lamp life due to a blackening of the lamp wall. The deposited material comes from the erosion of the electrodes and can also lead to the destruction of the electrode. The processes in the plasma sheaths near the electrodes are responsible for heating and the undesirable erosion of the electrodes.

The electrode design and the operating conditions are decisive for the properties of HID lamps. For instance, the power loss in the sheath near the electrodes is not negligible. This is true especially for low-power lamps. The corresponding electrode sheath voltage (ESV) is strongly influenced by the electrode material, the electrode design and the plasma composition. To reveal this influence partially, the ESV is measured in high-pressure argon, xenon and mercury discharges.

2. Experiment

The experiments in Ar and Xe are performed in the model lamp developed in Bochum [1]. Fig. 1 shows the schematic view of the experimental set-up. The discharge tube is made of fused silica ($\varnothing_i = 9$ mm). Electrode holders are inserted into the ends of the discharge tube and contain the tungsten electrodes ($\varnothing = 0.5 - 1$ mm, $l = 13$ mm).

The electrode holders can be moved in the tube by stepping motors and therefore the electrode distance can be varied during operation. The arc length was varied between 1 and 30 mm. The tube was carefully evacuated before the measurements and then filled with argon or xenon at pressures between 1 and 3 bar.

For determining the electric field strength and the ESV in discharges, the used method consists of a voltage measurement at discharges with different lengths but with otherwise identical properties of the plasma column. The electric field strength was then derived from the slope in a plot showing voltage versus gap length. From the same graph, the ESV was obtained by extrapolation to zero for the electrode gap. The underlying assumption is that the arc voltage U_{arc} is composed of the column voltage (field strength E times gap length l) and the ESV (U_{A+C}):

$$U_{arc} = E \times l + U_{A+C}. \qquad (1)$$
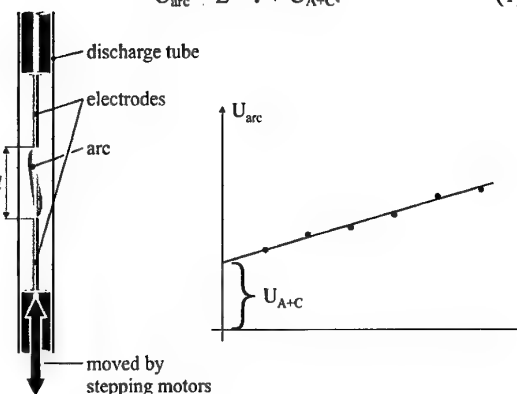
Fig. 1: Schematic view of the experimental set-up for the determination of the electrical field strength and ESV.

For the experiments in Hg we used lamps with different electrode-gap lengths but with otherwise identical geometric and filling conditions for obtaining a very similar arc plasma [2, 3]. The lamps are operated vertically, have an inner diameter of 16 mm and electrode gaps between 28 and 60 mm. The thoriated tungsten electrodes have a diameter of 0.7 mm and are surrounded by a tungsten coil.

The similarity was checked by determining plasma temperature and pressure from spectroscopic measurements of the Hg lines 546 nm and 577/579 nm and the wall temperature with a pyrometer (Varioscan, Jenoptik).

All discharges were operated with a 50 Hz sinusoidal current delivered by a current amplifier (FM1295, Feucht).

Simultaneously to the spectroscopic measurements pictures of the electrode region are taken with a camera (Flashcam, PCO) to control the position of the arc spot at the electrode surface.

The temperatures along the electrodes were determined by a pyrometer (IS10, impac) in the spectral range from 0.7 to 1.1 μm. The input power from the plasma to the electrodes can be determined from the recorded T-slope.

3. Results

The measured electrode sheath voltage and the electrical field strength for a Xe discharge are shown in figure 2. For a better illustration the sinusoidal current is plotted too. ESV and field strength are time-dependent. After current zero a jump of ESV and field strength is followed by an increase of the values leading to a maximum of the field strength of about 8 V/cm at 1.5 ms followed by a slight decrease until the change of polarity. The ESV has its maximum of 16 V at 2 ms and the following decrease is similar to that of the electric field strength.
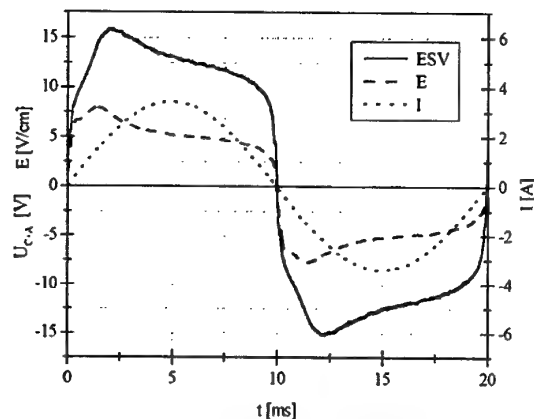
Fig. 2: Current, ESV and field strength of a Xe discharge (2 bar, tungsten electrode diameter 0.5 mm).

Although the operating conditions are only similar but not identical for all discharges, a typical behaviour for each element can be deduced. In figure 3 the ESV is compared for a discharge in Hg (I_{eff} = 3 A, p = 6 bar, $\varnothing_{El}$ = 0.7 mm), Ar (I_{eff} = 3 A, p = 3 bar, $\varnothing_{El}$ = 0.7 mm) and Xe (I_{eff} = 2.4 A, p = 2 bar, $\varnothing_{El}$ = 0.5 mm). The time dependence of the ESV in mercury is strongly pronounced. After a voltage maximum of 55 V during the rising current which corresponds to re-ignition, the current attains its maximum at a medium voltage and decreases then with initially slightly rising voltage which finally goes to zero. There are, however, two significant differences in the ESV compared with the rare gases:

1. a very pronounced "ignition" peak earlier and much higher than in the rare gases and
2. a remarkable voltage minimum near zero in the first quarter of a half cycle.

This voltage minimum does not appear in a calculated cathode fall for Hg [4]. If we attribute this difference to the anode, it would correspond to a negative anode fall

of more than 10 V which occurs around 2 ms after current zero [5].

Neither Xe nor Ar show such a strong time dependence. The ESV curves of the rare gases are more flat and only Ar shows a small dip in the ESV in the beginning of current flow. A similar behaviour can be seen for Hg discharges at 5 kHz [3].

The pronounced "ignition" peak is due to the fact that in the Hg discharge a spot mode occurs at the electrode whereas the rare gases show a diffuse mode in this parameter range. For lower discharge currents in rare gases also a spot mode occurs and the ESV has in that case also a higher ignition peak as in the Hg discharge but no minimum.
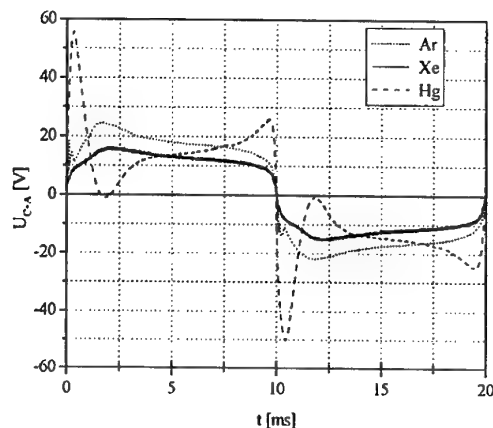
Fig. 3: Comparison of the ESV for a Hg, Xe and Ar discharge.

4. References

[1] L. Dabringhausen, D. Nandelstädt, J. Luhmann, J. Mentel, *J. Phys. D: Appl. Phys.* **35** (2002) 1621.
[2] G. Hartel, H. Schöpp, H. Hess, L. Hitzschke, *J Appl. Phys.* **85** (1999) 7076.
[3] A. Kloss, H. Schneidenbach, H. Schöpp, H. Hess, L. Hitzschke, B. Schalk, *J. Appl. Phys.* **88** (2000) 1271.
[4] R. Bötticher, W. Bötticher, *J. Phys. D: Appl. Phys.* **34** (2001) 1110.
[5] H. Pursch, H. Schoepp, M. Kettlitz, H. Hess, *J. Phys. D: Appl. Phys.* **35** (2002) 1757.

5. Acknowledgement

Plateau variation of arc current near the interruption limit in a gas circuit breaker

M. Borghei* and J. Mahdavi**
*Physics Department,Islamic Azad University,Karaj,Iran
**Electrical Engineering Department ,Sharif University of Technology, Tehran ,Iran

The electric arc is one of the basic switching elements in power engineering and the study of its behavior will help to a better understanding of related phenomena. In this paper we discuss one of this special behavior, its reason and necessary models to describe this variation that have been observed occasionally in our measurements.

1. Introduction

Current interruption requires that the interelectrode gap of a breaker changes from a conductive plasma into an insulating gas. This transition, which occurs around current zero, is governed by the dynamic behavior of the electric arc interacting with the network and the quenching gas (mixture of sulfurhexafluoride and nitrogen 75%/25%).

If we limit ourselves to thermal processes, the dynamic behavior of the plasma column can be taken into account by writing an energy balance equation such as below [1]:

$$dQ/dt = P_{in} - P_{out}$$

Where Q is the accumulated energy, P_{in} is the electrical input power (joule losses), and P_{out} is the removed power (by conduction, convection, radiation,...).

2.Test conditions:

The post arc current is recorded in our experiment with a particular device, the principle of which has been reported before [2], in a circuit of 4kV/11kA and a gas mixture of sulfurhexafluoride and nitrogen (75%/25%) as interrupting gas with p=2 bar N_2 and p=1 bar SF_6.

3. Recorded results:

Measurements of arc current and voltage are shown in (Fig.1). As we mentioned above the arc behavior is the result of the balance between cooling and heating effects and the study of the arc plasma will helps us in understanding the main parameters which successful breaking depends on. In the case of sufficient cooling, the electrical conductivity in the interelectrode gap will tend towards reduction and the arc current will have a tendency towards zero. However, after the current becomes zero, the transient recovery voltage drives a post arc current through the quenching arc plasma resulting in a heating effect. The balance between these effects may cause a decay of the plasma and current interruption such as shown in Fig.1.a or reheating of the gas to a well-conductive arc column which is termed "thermal re-ignition" as in Fig.2.b [3].
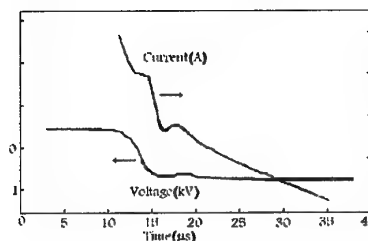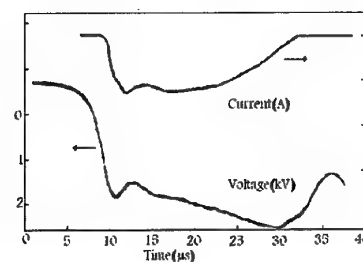
Figure 1: Interruption in the gas mixture [4].
a-With post arc current and plateau variation.
b-Re-ignition.

Thermal re-ignition occurs when there is an energetic surplus, that is when the power brought to the arc is greater than that removed. This idea, suggested by A.M. Cassie, shows that the interruption phenomenon is not an instantaneous process and that interaction with the network significantly influences the switching process. This paper concentrates on an arc interruption process that deals with thermal arc-circuit interaction as found in other gas puffer circuit-breakers and a brief discussion on a necessary model to recognize such a variation of the plasma arc current.

4.Electrical arc modelling:

There are two most commonly used types of models from simple to very complicated: black box and physical models. The first ones describe the interaction of a switching arc and the related electrical circuit during an interrupting process via a mathematical form (differential equation), and the electrical behavior is more important rather than the internal physical processes. However, the second ones include the physical processes in detail. It has to be noted that each of these models must be used in its correct range, and outside this range unacceptable errors will appear. Also it should be noted that in order to predict the plateau variation in the post-arc current we must use physical models taking into account physical processes such as conduction, convection, radiation, and so on [5]. Black box models can be applied only in cases where the switching process is governed by the arc conductance and can not be used in other cases such as for the dielectric region of the interruption process [6].

5.Conclusion:

In this paper our first aim was to recall phenomena on which successful breaking depends, and second to study the interruption in a typical gas puffer circuit-breaker. In our measurements plateau variation of post arc current was observed: this behavior is not predicted by black box models and we had to use physical models instead. Less plateau duration is equal to less probability of re-ignition and more probability of successful interruption.

6.References:

[1] WG 13-01, Electra no **149** (1993) 41-71.
[2] J. Mahdavi et al., IEE Proceedings **132** (1985) 285.
[3] E. Shade et al., IEEE Trans.on PES **10** (1982) 141.
[4] M. Borghei et al., J. Plasma Fusion Res. Series **5**, (2002), in press.
[5] A. Gleizes et al., IEEE Trans.on PS **1** (1991) 16.
[6] WG 13-01, Electra no **118** (1988) 65-79.

The "hunting effect" in the cathode region of a vacuum arc

G. A. Mesyats and S. A. Barengolts*

Institute of Electrophysics, Ural Division, RAS 106 Amundsen St., Ekaterinburg 620016
*Natural-Science Research Center, Institute of General Physics, RAS
Bd. L2, 38 Vavilov St., Moscow 117942 sb@nsc.gpi.ru

The interaction of liquid-metal droplets with plasma jets in the cathode region of a vacuum arc is considered based on the ecton model of a cathode spot. It is shown that the heating of a droplet which is in the zone of operation of a cathode spot can result in the transition of the droplet into the plasma state.

1. Introduction

When investigating the parameters of the cathode plasma with the use of fast laser diagnostics, *Batrakov* and co-workers [1] detected dense plasma blobs at distances of several micrometers from the cathode surface. The plasma density in these blobs was $\sim 10^{20}$ cm^{-3}, which is close to that immediately in cathode spots. We believe that the appearance of plasma blobs at a cathode is related to the interaction between the plasma jets and droplets ejected by the cathode spot of a vacuum arc.

It is well known that the cathode spot of a vacuum arc ejects plasma jets whose velocity is $\sim 10^{6}$ cm/s and liquid-metal droplets flying with a velocity of $\sim 10^{4}$ cm/s [2, 3]. These plasma jets are formed due to a high energy density in cathode microvolumes heated by the Joule mechanism by a high-density current. The high energy density leads to explosion-like disintegration of the cathode, accompanied by explosive electron emission. The liquid metal is splashed off the cathode spot region in the form of droplets and jets under the action of the reactive force occurring upon the ejection of high-velocity plasma jets. The droplet sizes depend on the arc current. For copper, gold, and palladium, at currents close to the arc threshold current i_{thr}, the droplet size distribution has a maximum at about 0.1–0.2 μm and the number of droplets leaving the cathode per unit charge is $\sim 10^{7}$ C^{-1} [4]. An increase in current increases the droplet size; thus, for $i \gg i_{thr}$ droplets of size up to ten micrometers are observed. Almost 90% of the droplet mass leave the cathode at an angle < 20° to the cathode plane with a velocity of $\sim 10^{3}$–10^{4} cm/s [2, 3].

A cathode spot has an internal structure which shows up in the existence of individual cells, the lifetime of each cell being $\sim 10^{-8}$ s [2]. In this connection, the operation of a cathode spot is accompanied by cyclic ejection of plasma jets and liquid-metal droplet. Besides, the cathode spot itself is in continuous chaotic motion. The great difference in ejection velocities between the plasma and the droplets may give rise to a situation where a cathode plasma jet hits a droplet. This resembles a shot of a hunter at a flying bird; therefore, we have called this phenomenon the "hunting effect".

2. Interaction between plasma jets and droplets in the cathode region of a vacuum arc

Let us consider a noncharged droplet in a flow of quasi-neutral plasma ejected by a cathode spot. For the energy flux density P_i transferred to the droplet per unit time by plasma jet ions we can write

$$P_i = \frac{j_i\left(\overline{E}_i + \overline{U}_i - Z\varphi\right)}{eZ},\qquad(1)$$

where j_i is the ion current density; Z and $\overline{E}_i$ are the ion average charge and energy, respectively; φ is the work function of an electron; $\overline{U}_i = \sum_i f_i U_i$ is the average ionization potential, and f_i is the fraction of the ions of charge multiplicity i.

Upon interaction with a droplet, electrons transfer to the droplet their kinetic energy and the energy equal to their work function:

$$P_e = \frac{j_i\left(2kT_e + \varphi\right)}{e},\qquad(2)$$

where T_e is the electron temperature.

An investigation of the ion flow from the plasma of a vacuum arc has shown that the ion current toward the anode is proportional to the arc current I with a factor $\alpha \approx 0.1$ [5]. Correspondingly, for the ion current density we can write

$$j_i = \frac{\alpha I}{S},\qquad(3)$$

where S is the cross-sectional area of the plasma jet at the site of its interaction with a droplet.

In view of relations (1)–(3), the expression for the specific energy w received by a droplet of radius R_d from a plasma jet has the form

$$w = \frac{3\alpha I t\left(\overline{E}_i + \overline{U}_i + 2ZkT_e\right)}{4SZR_d\rho e},\qquad(4)$$

where ρ is the density of the cathode material. Note that, according to (4), the specific energy is inversely proportional to the droplet radius.

Let us use the ecton model of a vacuum-arc cathode spot [2] to analyze the plasma jet parameters involved in equation (4). According to the ecton model, a cathode spot consists of individual cells, each emitting a portion of electrons – an ecton. The current of a spot cell is about twice the threshold current of the arc operation. As the arc current is increased, the spot cells are grouped in the close vicinity of one to another since, in this case, conditions are realized which are more energetically profitable for the repetition of ecton processes. As this takes place, the plasma parameters are established due to the operation of an individual cell of the spot upon explosion-like disintegration of a portion of the cathode under the action of a high-density current. A simulation of the ecton processes has shown that the ionization processes occur within a narrow (of the order of a micrometer) region near the cathode and further the charge state of the arc plasma remains practically unchanged [6]. The ions, under the action of the electron pressure gradient, acquire directional velocities of the order of 10^6 cm/s within distances as small as several micrometers. Taking this into account, to estimate the ion flow parameters $\overline{E_i}$ and $\overline{U_i}$ involved in equation (1), we can use their values measured away from the cathode. Let us consider a cathode made of copper, the material most extensively studied from the viewpoint of cathode phenomena and arc plasma properties. The kinetic energy of ions and the average ionization potential for Cu are, respectively, 56 eV and 20.4 eV [7, 8]. The electron temperature near the cathode is ~ 3–4 eV [6]. Correspondingly, for a copper cathode, the energy transferred to a droplet by ions and electrons (bracketed term in (4)) is ≈ 90 eV.

The droplet fraction of the cathode erosion plays an important role in the self-sustaining of an arc discharge [2]. As a droplet breaks off a cathode, a thin bridge is formed. The ion current from the cathode plasma, which closes on the droplet, flows through the bridge. Since the ratio of the droplet surface area to the bridge cross-sectional area may be great, the current density in the bridge may reach high values sufficient for the bridge to explode and an ecton to appear. The characteristic time of the ecton process is ~ 20–30 ns [2]. With a velocity of 10^4 cm/s, a droplet will move off the cathode surface for a distance not over 2–3 µm. If a droplet of diameter 0.1–0.2 µm, having broken off the cathode, is in the region of propagation of a plasma jet formed during the operation of an ecton, then, according to (4), for an ecton current of 3.2 A, $w > 10^4$ J/g is achieved within 20–30 ns even if the plasma expansion is spherically symmetric, i.e., $S = 2\pi r^2$, where r is the distance from the cathode. This specific energy corresponds to a droplet temperature higher than 2 eV and, as revealed in a study of the electrical explosion of conductors and the initiation of explosive electron

emission [2], it is suffice for a material to go from the condensed to the plasma state.

We have shown above that a dense plasma can be generated during the operation of an individual cathode spot cell. An increase in current increases the number of ectons and makes the droplet larger. When a spot moves to a new site and the droplet formed during the operation of the previous spot appears in the zone of its action, coarse plasma blobs may appear at a certain distance from the cathode surface. This process is quite probable since the velocity of motion of the spot over the cathode surface (~ 10^4 cm/s) is comparable to the velocity of flight of the droplet.

Let us consider the interaction of a droplet with a collectivized plasma jet produced by an ensemble of simultaneously operating ectons. To estimate the ion current density, we use the data of *Daalder* [9] according to which, for a current of 100 A, the cathode spot diameter is 10 µm. In this case, for a droplet of radius $R_d = 0.5$ µm being 5 µm away from the cathode surface and a plasma jet with an expansion angle of 60° [10], at $t = 30$ ns the specific energy is over 10^4 J/g.

3. Conclusion

Thus, the above analysis based on the ecton model has demonstrated that dense plasma blobs can be formed near a cathode due to the interaction between the plasma jets and droplets ejected by the vacuum arc cathode spot.

4. Acknowledgement

5. References

[1] A.V. Batrakov, B. Jüttner, S.A. Popov, *et al.*, *Pisma Zh. Exp. Teor. Fiz.* **75** (2002) 84.

[2] G.A. Mesyats, *Ectons in a Vacuum Discharge: The Breakdown, the Spark, and the Arc.* Nauka, Moscow (2000).

[3] *Handbook of Vacuum Arc Science and Technology.* Ed. by R.L. Boxman, P.J. Martin, and D.M. Sanders. Noyes Publications, Park Ridge, (1995).

[4] T. Utsumi and J.H. English, *J. Appl. Phys.* **46** (1975) 126.

[5] C.W. Kimblin, *J. Appl. Phys.* **44** (1973) 3074.

[6] S.A. Barengolts, G.A. Mesyats, and D.L. Shmelev, *Zh. Eksp. Teor. Fiz.* **120** (2001) 1227.

[7] G.Yu. Yushkov, E.M. Oks, A. Anders, and I.G. Brown, *J. Appl. Phys.* **88** (2000) 5618.

[8] I.G. Brown, *Rev. Sci. Instrum.* **65** (1995) 3061.

[9] J.E. Daalder, *IEEE Trans. Pow. App. Syst.* **93**, (1974) 1747.

[10] M.P. Reece, *Proc. IEE* **110** (1963) 793.

Topic 19

Highly ionized, low-pressure plasmas (plasma thrusters, ion sources and surface treatment)

Very-Near-Field Plume Model of a Hall Thruster

F. Taccogna[1], S. Longo[1,2], M. Capitelli[1,2]

[1] Department of Chemistry, University of Bari, Italy
[2] IMIP-CNR sect. Bari, Italy

Plasmadynamic phenomena of a stationary plasma thruster (SPT-100) plume in the very-near-field region have been studied by using a two-dimensional axysimmetric numerical code based on a combination of Particle in Cell (PIC) simulation for ion component (Xe^+ and Xe^{++}) and fluid description for electrons. The model can reproduce qualitatively several experimental observations.

1. Introduction

Stationary plasma thrusters (also called closed electron drift thruster of the Morozov type) [1] are ion thrusters with high specific impulse and low thrust that make them suitable for satellite station keeping or orbit transfer.

A major concern in the use of these devices is the possible damage their plumes may cause to the host spacecraft and to communication interference of satellites. Indeed an electric thruster, such SPT-100, in operation produces, besides high energy ions (Xenon for his inert and low ionization potential property) responsible of the thrust and electrons emitted to neutralize the positive space charge, also neutral propellant atoms and low energy ions created by charge exchange (CEX) collisions between ions and un-ionized propellant (in which electrons are transferred) or by electron impact ionization of neutral atoms. They are more influenced by the self-consistent electric fields that cause slow ions to propagate radially and to flow upstream, while gaining energy.

Thus, the structure of the plasma plume exhaust from the thruster is of great interest and several models [2-5] have been developed simulating the plasmadynamic of the exhaust plume in the far-field region. The modelling of the plasma plume of electric thrusters in the very-near-field plume region (z<0.2 m from the thruster exit plane) is important because there are many new aspects to take in account as plasma sheath effect, magnetic field effect, non isothermal electrons, electron-neutral collisions and so on.

2. Numerical model

Due to particular geometry of the problem each quantity is given in terms of axisymmetric coordinates (r,z) and we assume no variation in the azimuthal direction.

In the PIC technique, ions are considered as macro-particle and their charge are deposited onto a computational grid using the cylindrical weighting functions. Ions are loaded into the simulation at each time step to simulate the exit flow. The ion exit conditions (radial position and velocity components) are given in ref. [5] on the basis of fitted experimental data.

In order to know the electron charge density, one differentiates the momentum conservation equation and substituting the laplacian of the electric potential with the source term of Poisson equation the following differential non linear equation for the electron charge density results:

$$\frac{k_B T_e}{e}\nabla^2 ln\rho_e + \frac{k_B}{e}\nabla ln\rho_e \cdot \nabla T_e - \frac{\rho_e}{\varepsilon_0} - B_r\frac{\partial v_{e I}}{\partial z} + \frac{k_B}{e}\nabla^2 T_e + \frac{\rho_i}{\varepsilon_0} = 0 \tag{1}$$

with boundary conditions given by (see Fig. 1):

$$\begin{cases} S_1 \to \rho_e = -\rho_i \\ S_2 \to \rho_e = \rho_\infty \\ L_1 \to \frac{\partial \rho_e}{\partial r} = 0 \\ L_2, L_3, L_4 \to \rho_e = \rho_\infty \end{cases}$$

In eq. (1), $v_{e,t}=v_{i,t}$ since the particle flow across the magnetic field is ambipolar (current-less) and we consider only the radial component of the magnetic field (dipol approximation).
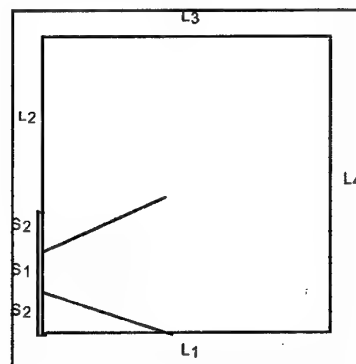
Fig. 1 - Scheme of the simulation domain.

The solution is obtained by the iterative Newton-Raphson method discretizing the laplacian with a 5-points formula in cylindrical coordinates and using a successive-over-relaxation (SOR) scheme.

Once the electron charge density is computed, the electrostatic potential is determined by solving Poisson's equation.

Knowing the electron density we can solve the electron energy conservation equation for the temperature where we neglect the unsteady and convection terms and we consider the following ionization energy sink term:

$$Q_e = \dot{n}_e E_i \tag{2}$$

with $\dot{n}_e = k_{T_e} n_e n_{Xe}$ the volumetric ionization rate and E_i the Xenon ionization energy. We calculate the electron impact ionization rate coefficient $k(T_e)$ on the basis of e/Xe cross-section data [6] fitted to the following polynomial expression:

$$k(T_e) = 4.5243 \times 10^{-15} - 4.4952 \times 10^{-15} T_e + 1.1776 \times 10^{-15} T_e^2 -$$
$$2.5515 \times 10^{-17} T_e^3 - 2.3932 \times 10^{-18} T_e^4 + 9.7869 \times 10^{-20} T_e^5$$
$$(3)$$

Substituting the ideal gas equation we have

$$\kappa_e \nabla^2 T_e + \nabla \kappa_e \cdot \nabla T_e = -Q_e \qquad (4)$$

where the electron thermal conductivity is included by the following fitting formula (including the electron collision effect) [7]:

$$\kappa_e = A T_e^n \quad \text{with} \quad \begin{cases} A = 6.9 \times 10^{-12} & n = 5/2, & T_e \leq 2eV \\ A = 2.08 \times 10^{-3} & n = 1/2, & T_e > 2eV \end{cases}$$
$$(5)$$

Eq. (4) is solved with the following boundary conditions:

$$\begin{cases} S_1, S_2 \rightarrow T_e = const \\ L_1 \rightarrow \dfrac{\partial T_e}{\partial r} = 0 \\ L_2, L_3, L_4 \rightarrow T_e = T_\infty \end{cases}$$

and we come back to the electron momentum conservation equation until we reach convergency.

The ions are moved under the influence of the self-consistent electric field integrating numerically the equations of motion using the leap-frog algorithm .

Collisional processes are modeled between move steps using a TPMC method [8] to simulate Xe-Xe$^+$ and Xe-Xe^{++} (momentum and charge transfer) collisions, and a volumetric production method to simulate neutral ionization by electron impact.

3. Results

The behavior of the plasma potential is reported in Fig. 2. We can see the potential wall structure developing spontaneously that capture ions to neutralize electrons trapped by magnetic field. In fact we note a peak near the centerline at the small axial position that is attributed to electrons confined by magnetic field cusp formed by the thruster magnetic coils.
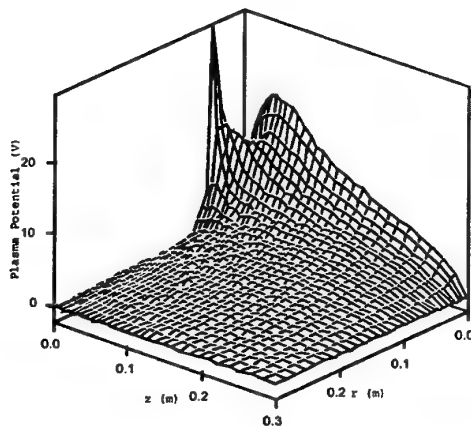
Fig. 2 - Plasma potential surface.

Figure 3 shows the radial profiles of electron temperature measured [9] at different axial locations The peak structure in front of the discharge channel (28mm<r<50mm) decreases in magnitude and broadens as the electrons move away axially from the thruster in agreement to the fact that electrons continue to cool down. We note a discrepancy between the model and experimental values in the very low radial and axial positions due to neutralizer position effect. The high experimental values of temperature at radial distances greater than 70 mm for z=10 mm can be due to a reduction of thermal electrical conductivity caused by electron-ion collisions.
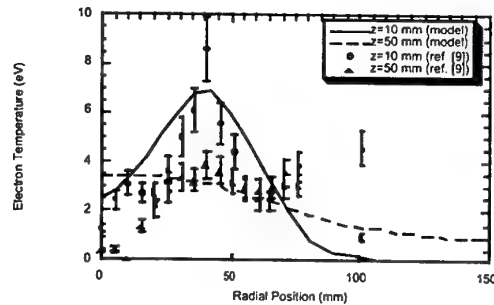
Fig. 3 - Measured [9] and computed electron temperature as a function of radial position for different axial position.

Acknowledgements

References

[1]   V. V. Zhurin et al, *Plasma Source Sci. Technol.* **8** (1999) R1-R20.

[2]   D. Y. Oh et al, *J. Propulsion and Power* **15** (1999) 345-357.

[3]   I. D. Boyd, D. B. VanGilder, M. Keidar, *J. Spacecr. Rockets* **37** (2000) 129-136.

[4]   F. Taccogna, S. Longo, M. Capitelli, *AIAA paper* **2000-2345** (2000).

[5]   F. Taccogna, S. Longo, M. Capitelli, J. *Spacecr. Rockets* **39 (3)** (2002) 409-419.

[6]   G. Colonna, L. D. Pietanza, M. Capitelli, *AIAA Paper* **2000-2349** (2000).

[7]   R. Samanta Roy, *Ph. D. thesis, MIT* (1995).

[8]   K. Nanbu, Y. Kitatani, *J. Phys. D: Appl. Phys.* **28** (1995) 324-330.

[9]   S. Kim, J. E. Foster, A. D. Gallimore, *AIAA paper* **96-2972** (1996).

114

Double Sheath Associated with Negative Ion Extraction from a Plasma Containing Negative Ions

H. Amemiya and G. Fuchs*

The Institute of Physical and Chemical Research, Hirosawa, Wako, Saitama-Pref. Japan 351-0198
*Institut für Plasmaphysik, Association EURATOM-FZJ, Jülich 52425, Germany

The double sheaths formed by plasmas that contain thermal electrons, as well as positive and negative ions has been investigated. The negative ion beam that can be extracted under these conditions is given as a function of the electric potential, the density ratio and the Langmuir limit. The result is useful when it comes to extract ion beams from negative ion sources.

1. Introduction

Double sheaths set up by electron emission [1] and a counter–stream [2] can be tailored to give optimum extraction of beams with regard to the Langmuir limit. Double sheaths containing negative ions are scarce [3]. In a previous work the effect of negative ions within a plasma upon electron beam extraction has been investigated [4]. This paper deals with double sheaths whereby the plasmas on both sides do contain negative ions. This is of practical interest if one wants to optimize negative ion beams from an NBI source.

2. Model

Consider a double layer formed by two plasmas, both containing negative ions. From the lower potential side (potential $V=0$), thermal electrons and negative ions flow with current density J_e and J_n. Particle densities $n_{e1}(V)$, $n_{n1}(V)$ are given by

$$n_{e1} = \frac{J_e}{e\sqrt{2e(V+V_e)/m}}, \; n_{n1}\frac{J_n}{e\sqrt{2e(V+V_n)/M_n}}, \; (1)$$

where V_e and V_n are the potentials equivalent to the initial energy, m, M_p, M_n, are electron, positive and negative ion masses. Positive ions get reflected and their density $n_{p1}(V)$ within the sheath is

$$n_{p1}(V) = N_{p1}\exp(-eV/\kappa T_p), \qquad (2)$$

where N_{p1} is the boundary value. From the high plasma potential side ($V=V_a$) positive ions flow with current density J_p, such that the density becomes

$$n_{p2}(V) = J_p/e\sqrt{2e(V_a-V+V_o)/M_p}, \quad (3)$$

whereby the initial velocity is given by v_o according $eV_o = M_p v_o^2/2$. Electrons and negative ions are reflected. Their densities are

$$n_{e2} = N_{e2}\exp[-e(V_a-V)/\kappa T_e],$$

$$n_{n2} = N_{n2}\exp[-e(V_a-V)/\kappa T_n], \qquad (4)$$

where T_e, T_n, T_p, are the temperatures and N_{e2}, N_{p2}, N_{n2} are the densities at the boundary.

3. Formulation

The right hand side of Poisson's equation is

$$N(V)/\varepsilon_o = -n_{e1} - n_{n1} + n_{p1} - n_{e2} - n_{n2} + n_{p2}, \; (5)$$

where ε_o is the dielectric constant in vacuum.

Introducing the following normalization,
$\xi=x/\lambda_D$, $\lambda_D=(\varepsilon_o \kappa T_e/N_{p1}e^2)^{1/2}$, $\eta=eV/\kappa T_e$, $\eta_e=eV_e/\kappa T_e$, $\eta_n=eV_n/\kappa T_e$, $v_{e1}=N_{e1}/N_{p1}$, $v_{n1}=N_{n1}/N_{p1}$, $v_{e2}=N_{e2}/N_{p2}$, $v_{n2}=N_{n2}/N_{p2}$, $q=N_{p2}/N_{p1}$, $\gamma_n=T_e/T_n$, $\gamma_p=T_e/T_p$, $j_e=J_e/J_o$, $j_n=J_n\sigma_n/J_o$, $j_p=J_p\sigma_p/J_o$, where $\sigma_n=(M_n/m)^{1/2}$, $\sigma_p=(M_p/m)^{1/2}$, $J_o=N_{p1}e(2\kappa T_e/m)^{1/2}$, Poisson's equation now reads

$$d^2\eta/d\xi^2=-e\rho/\varepsilon_o, \; \rho=N/N_{p1} \qquad (6)$$

$$\rho = -\frac{j_e}{\sqrt{\eta+\eta_e}} - \frac{j_n}{\sqrt{\eta+\eta_n}} + \exp(-\gamma_p\eta) + \frac{j_p}{\sqrt{\eta_a-\eta+\eta_o}}$$

$$-qv_{e2}\exp[-(\eta_a-\eta)]-qv_{n2}\exp[-\gamma_n(\eta_a-\eta)], \; (7)$$

and the conditions at the plasma boundaries are
1) Quasi neutrality : $\rho=0$ at $\eta=0$, η_a.
2) Zero derivative of space charge density
   $d\rho/d\xi=0$ at $\eta=0$, η_a.
3) Zero electric field: $d\eta/d\xi=0$ at $\eta=0$, η_a.

Multiplying $d\eta/d\xi$ on both sides of (6) and integrating, we obtain the stress $(d\eta/d\xi)^2/2$, which automatically satisfies the condition $d\eta/d\xi=0$ at $\eta=\eta_a$. At $\eta=0$, then we obtain

$$0 = 2j_e(\eta_e^{1/2} - \sqrt{\eta_a+\eta_e}) + 2j_n(\eta_n^{1/2} - \sqrt{\eta_a+\eta_n})$$

$$+[1-\exp(-\gamma_p\eta_a)]/\gamma_p + 2j_p(\sqrt{\eta_a+\eta_o} - \sqrt{\eta_o})$$

$$+qv_{e2}\{\exp(-\eta_a)-1\} + qv_{n2}\{\exp(-\gamma_n\eta_a)-1\}/\gamma_n. \; (8)$$

The double layer does form, if eqn.(8) together with the boundary conditions is satisfied.

4. Double sheath with high potential

Putting $\exp(-\eta_a)\ll 1$, $\exp(-\gamma_p\eta_a)\ll 1$, $\exp(-\gamma_e\eta_a)\ll 1$ and $\exp(-\gamma_n\eta_a)\ll 1$ and $\eta_e=\eta_n$, we get

$$\frac{j_e+j_n}{\eta_e^{1/2}} = 1 + \frac{j_p}{\sqrt{\eta_a+\eta_o}}, \qquad (9)$$

115

$$\frac{j_e + j_n}{\sqrt{\eta_a + \eta_e}} = \frac{j_p}{\sqrt{\eta_o}} - q(v_{e2} + v_{n2}), \qquad (10)$$

$$\frac{j_e + j_n}{2\eta_e^{3/2}} - \gamma_p + \frac{j_p}{2(\eta_a + \eta_o)^{3/2}} = 0, \qquad (11)$$

$$\frac{j_e + j_n}{2(\eta_a + \eta_e)^{3/2}} + \frac{j_p}{2\eta_o^{3/2}} = q(v_{e2} + \gamma_n v_{n2}), \quad (12)$$

$$\eta_e = \eta_n = \frac{1 + j_p /(\eta_a + \eta_o)^{1/2}}{2\gamma_p - j_p /(\eta_a + \eta_o)^{3/2}}, \qquad (13)$$

$$\eta_o = \frac{q(v_{e2} + v_{n2}) + (j_e + j_n)/\eta_a^{1/2}}{2q(v_{e2} + \gamma_n v_{n2}) - (j_e + j_n)/\eta_a^{3/2}}. \quad (14)$$

η_n and η_o given by (13) and (14) correspond to the Bohm criterion determining the ion fluxes. η_e (or η_n) increases from $1/(2\gamma_p)$ as η_a is decreased or j_p is increased. η_o increases from $1/(2\gamma_n)$ for the negative ion-rich plasma as η_a is decreased or j_e and j_n are increased. η_o tends to $1/2$ of the simple sheath if $j_e = j_n = 0$ and $\eta_a \gg 1$.

From (8), we obtain the Langmuir limit as

$$(j_e + j_n)(\sqrt{\eta_a + \eta_n} - \sqrt{\eta_n}) - j_p(\sqrt{\eta_a + \eta_o} - \sqrt{\eta_o})$$
$$= 1/\gamma_p - q(v_{e2} + v_{n2}/\gamma_n). \qquad (15)$$

If η_a is extremely large, the limit is modified as

$$j_e + j_n \cong j_p. \qquad (16)$$

Without j_n, we recover $J_e = (M_p/m)^{1/2} J_p$. Without j_p, we obtain $J_n = (M_p/M_n)^{1/2} J_p$, i.e. the negative ion beam is governed by the positive ion beam, and determined by the square root of the mass ratio.

5. Calculations and Results

We have five equations to determine the unknowns η_o, η_e, $j_e + j_n = j_{en}$, j_p and q from the known values η_a, v_{e2}, v_{n2}, γ_n and γ_p. We define $j_{en} = j_e + j_n$. This nonlinear system has been solved by
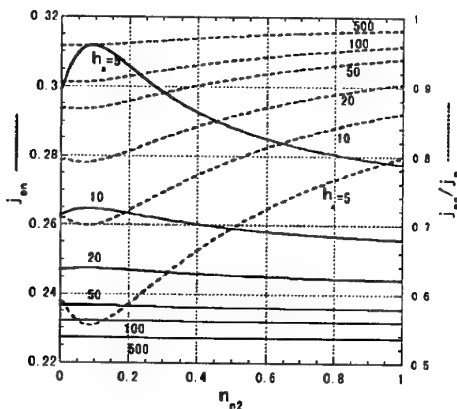
Fig. 1. j_{en} and j_{en}/j_p vs v_{n2} for $\eta_a = 10$ and $v_{e2} = 0.3$.

iteration starting with $\eta_o = 1/2$, $\eta_n = 1/(2\gamma)$ to get j_{en}, j_p and q. Afterwards new values for η_o and η_n, e.t.c were determined.

In Fig.1 for $\eta_a = 10$, $\gamma_n = \gamma_p = 10$, the beam density j_{en} has a maximum at a v_{n2} while η_a is small but becomes almost constant for higher η_a. This behavior holds in a wide range.

Fig. 2. η, η' and ρ vs ξ for $\eta_a = 10$, $\gamma_n = \gamma_p = 10$.
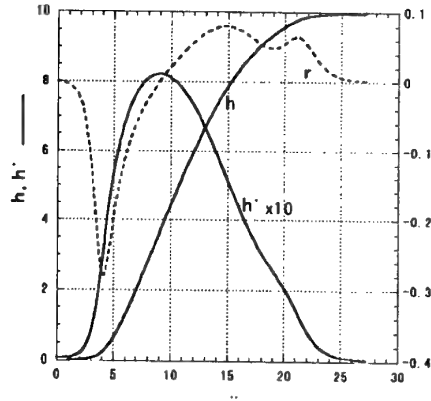
In Fig. 2 showing the profile of the double sheath, ρ is not symmetric as in the beam-free case, showing a narrow dip near the low potential side and a small bump on the higher side, though it was confirmed that the integral of ρ over the entire region is 0. For $v_{n2} = 0.1$, η shows a wavy structure near η_a, suggesting a triple layer. As v_{n2} is increased above 0.1, η, η' and ρ resemble those of $v_{n2} = 0$. Therefore, except the cases with a triple layer, the sheath thickness δ (normalized by λ_D) can be defined by the distance between $0.01\eta_a$ and $0.99\eta_a$. δ deviates from $\eta^{4/3}/j_{en}^{1/2}$, as η_a is decreased.

6. Conclusion

The double sheath theory has been extended to the case when a beam of negatively charged ions is extracted from a plasma containing such particles. Results are presented for the current densities of positively and negatively charged species, profiles of space charge, electric field and potential within the sheath. The potentials at the sheath edge will help to better understand the extraction of negative ions from negative ion sources.

References

[1] Prewett P.D. & J.E.Allen: *Proc.R.Soc.Lond*, A. **348** (1976) 435.
[2] Levine J.S. & F.W. Crawford: *J.Plasma Phys.* **23** (1980) 223
[3] Verheest F: *J. Plasma Phys.* **42** (1989) 395.
[4] Amemiya H., B.M.Annaratone and J.E.Allen: *J. Plasma Phys.* **60** (1998) 81.

Radiofrequency glow discharges used for optical emission spectroscopy : an experimental and analytical approach

L.Therese, Ph. Guillot, and Ph. Belenguer

Centre de Physique des Plasmas et Applications de Toulouse,
Université Paul Sabatier, 118 route de Narbonne, 31062 Toulouse Cedex, France

1. Introduction

Glow discharge optical emission spectroscopy (GD-OES) is an analytical technique widely used for elemental and depth profiling analysis of materials [1]. The technique is based on the analysis of the optical emission of atoms sputtered from the cathode and excited in the plasma. Radio frequency excitation of the glow discharge (RF-GD-OES) is developed for quantitative analysis of non-conductive samples.
Capacitively coupled radio frequency discharges have been extensively studied both experimentally and theoretically over the past decade in the context of plasma processing for the microelectronics industry and thus these discharges are fairly well understood [2-3].
The operating conditions used in RF-GDOES are, however, different than those standardly used in plasma processing, leading to a discharge behavior quite unusual and it is our aim to understand this behavior.

2. Experimental set-up

The experimental set-up is based on the industrial Jobin Yvon Horiba RF-5000 instrument on which the optical components have been removed, as material analysis is not considered here. The source used is a 4 mm diameter cylindrical copper electrode facing a plane electrode. The plane electrode is the sample itself and the gap space between the two electrodes is maintained by a toroidal joint. The 13.56 MHz radiofrequency voltage is applied on the back of the sample with a cylindrical applicator through a blocking capacitor. A matching box insures the coupling between the generator and the source. A Pirani gauge is used to monitor the pressure inside the reactor.
One problem of major concern in measuring the discharge current in radiofrequency discharges is removing the capacitive current due to the reactor capacitance. Applying a radiofrequency voltage of the form $V = V_{rf} \cos(\omega t)$, to the back of the sample, give rise to a capacitive current ($C_s \, dV/dt$), where C_s is the system capacitance. This current is much higher than the total discharge current. The method for suppressing this capacitive current in the GD-OES instrument is based on the technique perfected on the GEC (Gaseous Electronics Conference) reference cell. More detailed information can be found in reference [4]. Similar measurements for lower frequency discharges have been performed by Hoffmann' group using a different technique [5].

A diagram of the plasma reactor and electrical measurement system is shown figure 1. The two current probes used are Solar 9323-1 of Rogowski type. The windings of the probes are essentially the secondary windings of a toroidal transformer. The RF cable, carrying the current to be measured, acts as the primary winding of the transformer. The voltage probe is a Tektronix P5100, 100x. A high performance oscilloscope, Tektronix TDS 7104 is used. The vacuum variable capacitor is a Jennings C/GCS -100-15 picofarads.
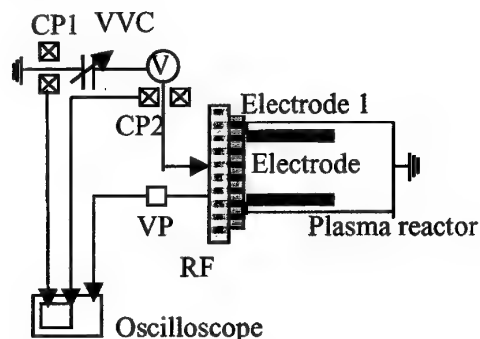
Figure 1: Schematic diagram of the electrical measurement technique. CP1 and CP2, Current Probes, VVC, Vacuum Variable Capacitor, VP,Voltage Probe.

3. Results

In this section, we will study the results obtained for a radiofrequency discharge in argon at 950 Pascal, 13.56 MHz and for a titanium sample at 10 watts. In the first part of this chapter we will show the experimental measurements of the current and voltage, in the second part we will analyze the results with the help of an analytical approach.

Figure 2 shows the current and voltage measured on the two lines (reactor and variable capacitor) for a radiofrequency cycle. We can see on this figure that the measured currents are capacitive currents; the phase shift between the currents and the voltage is close to 90 degrees. We notice that the two currents are very similar, therefore the total discharge current will be only a small part of the total current. The amplitude of the total current is about 1.2 A. The current on the two electrodes has to be identical over a radiofrequency cycle. The surface of the two electrodes being different,

the voltage exhibits a large bias, the voltage is shifted to negative values. The voltage and the current are measured on the back of the sample, the small electrode. The measured voltage is of the form $V(t) = Vrf\ cos(\omega t) + Vbias$, under our conditions we find $Vrf = -350$ V, $Vbias = -260$ V. That means that the sample is a cathode for most of the cycle. It is during the cathodic part of the cycle when the voltage is negative on the sample that the electrode is sputtered.

On figure 3, we present the total discharge current obtained by subtracting the 2 previous measured currents. The maximum amplitude is about 0.25 A, at half cycle.

The discharge current is the sum of three terms corresponding to the electron, ion and displacement current. It is possible to extract the displacement current from the measured total current if we assume that the electric field contracts and expands in a similar way.
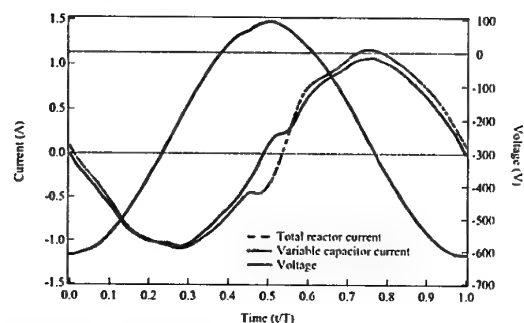
Figure 2 : Voltage and current time variations over a radiofrequency cycle. Titanium, 950 Pa, 13.56 MHz, 10 Watts.
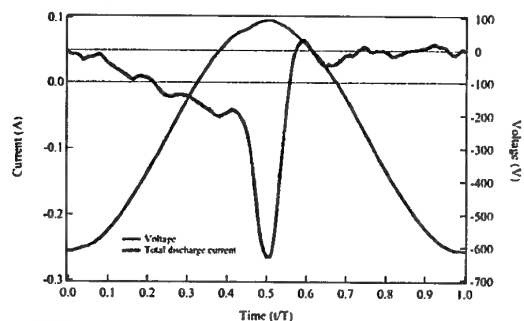
Figure 3 : Voltage and total discharge current time variations over a radiofrequency cycle.

4. Analytical Considerations

To calculate analytically the displacement current, we need to make an assumption on the temporal variation of the electric field on the electrode. We assume a linear decrease of the electric field in the sheath and a parallel slope decrease and increase of the sheath. The last assumption is to consider that all the applied potential is completely distributed in the sheath; there is no positive column.

The applied potential $V(t) = Vrf\ cos(\omega t) + Vbias$. At time $t=0$, $V = Vrf + Vbias$

If all the potential is distributed in the sheath we have $E0 = -2\ (Vrf + Vbias)/d0$, $E0$ being the electric field on the electrode and $d0$ the sheath length at time $t=0$. $E0$ and $d0$ are the maximal values of $E(t)$ and $d(t)$ as the applied potential is maximal at $t=0$. As we have a constant slope at any time we have $E(t)/E0 = d(t)/d0$. We can easily get the following relation:

$$E(t) = E_0 \left(\frac{V(t)}{Vrf + Vb} \right)^{0.5}$$

We can calculate the displacement current:

$$Id = S\mathcal{E}_0 \frac{dE}{dt} \quad \text{where S is the sample surface}$$

The best agreement between the calculation and the experimentally deduced displacement current is obtained for $E0 = 65$ kV cm^{-1}. Knowing E_0, and the displacement current it is possible to have access to important information on the discharge characteristics, we will present here these results.

5. Conclusion

We measured the total current and the voltage time variations for a radiofrequency discharge using a titanium sample at 13.56 MHz, 950 Pa and 10 watts in argon. From these measurements, we were able to electrically characterize the discharge and to get information on the plasma. We found that the plasma is only extended a few millimeters from the sample surface, 2.6 mm, and has a rather high density.

6. References

[1] *Glow Discharge Optical Emission Spectroscopy*, eds.. Payling R., Jones D. and Bengston A., John Wiley Sons, New York, 1997.
[2] *Nonequilibrium Processes in Partially Ionized Gases*, eds. Capitelli M. and Bardsley J. N., Plenum Press, New York, 1990; **220**: 155.
[3] *Modeling Collisional Low-Temperature Plasmas*, Special Issue, IEEE Trans. Plasma Sci, 1991; 2. Press, London, 1998.
[4] Hargis P. J. *et. al.*, Rev. Sci. Instrum., 1994; 65: 140.
[5] Bogaerts A., Wilken L., Hoffmann V., Gijbels. and, Wetzig K., Spectrochimica acta: part B, 2001; 56: 551.

Surface destruction and change of solids properties under the plasma influence.

A.L. Bondareva, G.I. Zmievskaya

Keldysh Institute of Applied Mathematics Russian Academy of Sciences

Interactions between ions beams and solids or plasma and solids result in changing of solids properties as well as ions beams or plasma characteristics. The influence of blistering on solids properties are examined in the paper. The stochastic model of blistering is presented. The evolution of distribution functions of bubbles versus bubbles sizes and coordinates in lattice is received. The depth dependences of porosity and tensions, which are created by bubbles, are calculated using the distribution functions.

1. Introduction.

The study of phenomena of interaction between plasma or ions beams and solids surface is very important for technologies. It concerns with cosmophysics, nanotechnology and controlled thermonuclear reactor. The phenomena result in change of surface relief and properties of materials. Experiments in space and thermonuclear experiments are very difficult and expensive. In this connection, computer simulation of such processes is very important.

This paper is devoted to computer simulation of fluctuation stage of high-temperature blistering. Blistering is phenomenon of development of gas bubbles in solids surface layer. Such gas bubbles are named blisters. Blistering results from irradiation of solids surface by ions of bad soluble gases. The fluctuation stage is very short, but it determines further development of blistering. The duration of the stage is 10^{-4} sec approximately. Bubbles sizes are approximately $10A$ during this stage.

The behaviour of gas-vacancy pores in Ni crystal lattice under the influence of He ions with energy from 1 keV to 35 keV and radiation dose from 10^{16} to 10^{19} ions/cm^2 is examined in this paper. Such terms can arise in solar wind and thermonuclear reactor. The temperature of material T is $0.4 \cdot T_{melt} \leq T \leq 0.6 \cdot T_{melt}$, T_{melt} is melting temperature of Ni.

2. Stochastic model of blistering and equations.

The stochastic model of fluctuation stage of high-temperature blistering had been put forward by authors [1,2]. Brownian motion model of particles with variable mass was accepted as a basis. Blistering investigation deals with computer simulation of superposition of the stochastic processes of bubbles sizes change and bubbles migration in crystalline lattice. It is possible because processes of increase of bubbles sizes and bubbles migration in lattice have appreciably different time scales. Solution of kinetic equations for Brownian motion model is non-linear problem. Therefore authors use stochastic analog method to solve these kinetic equations. Main idea of this method is change of kinetic equations by their stochastic analogs and

solution of stochastic differential equations. Scheme of splitting on physical processes and coordinates was used for solution of examined problem. The system of four stochastic differential equations was received after the splitting. Increase of size, migration on lattice, fusion of bubbles, exit of blisters on surface and bubbles destruction on it are examined in this paper. The stochastic equation for size change is following

$$\frac{dg}{dt} = -\frac{1}{kT}D(g,t)\frac{\partial \Delta\Phi(g,\vec{r},t)}{\partial g} - \frac{1}{2}\frac{\partial D(g,t)}{\partial g} + \sqrt{2D(g,t)}W_g(t)$$

$t_0 \leq t \leq T_k, \quad g(t_0) = g_0 \in [g_{0min}; g_{0max}], \quad g(t) > 2$

g is bubble size, $\Delta\Phi(g,\vec{r},t)$ is Gibbs potential, $D(g,t)$ is diffusion coefficient in sizes space, $W_g(t)$ is Wiener process, T_k is duration of fluctuation stage. $\frac{\partial \Delta\Phi(g,\vec{r},t)}{\partial g}|_{g=g_{cr}} = 0$, g_{cr} is "critical" size of blister.

$\Delta\Phi(g_{0min},\vec{r},t) = \Delta\Phi(g_{0max},\vec{r},t) = \Delta\Phi(g_{cr},\vec{r},t) - kT$, $g_{0min} < g_{cr} < g_{0max}$.

$\Delta\Phi(g,\vec{r},t)$ and $D(g,t)$ nonlinearly depend from bubble size. Heterogenous condensation on bubbles surfaces, difference between chemical potential of phases, surface tension on bubbles surface, elastic reaction of solids lattice, nonequivalence of bubbles position in lattice, break of connections of crystal lattice are considered using $\Delta\Phi(g,\vec{r},t)$ and $D(g,t)$.

The stochastic equation for depth is following

$$z(t) = z(t_0) + \int_{t_0}^{t} H_z(\tau,x(\tau),y(\tau),z(\tau))d\tau + \int_{t_0}^{t} \sigma(\tau,z(\tau))dW_z(\tau)$$

$$H_z(\tau,x(\tau),y(\tau),z(\tau)) = -\frac{1}{\gamma M_g}\frac{\partial U}{\partial z} - \frac{1}{2}\frac{\partial D_z}{\partial z}$$

$$\sigma_z(z,t) = \sqrt{2D_z(z,t)} \quad U = U_{bb} + U_{bs}$$

W_z is Wiener process, z is depth of bubble from surface under irradiation, M_g is blister mass, x, y, z are bubble coordinate in crystal lattice, D_z is diffusion coefficient, U_{bb} is interaction potential between blisters by phonons and oscillation of electron density, U_{bs} is potential of

interaction between bubbles and surface.

$$U_{bb} = \sum_{j \neq i}^{N} [\frac{0.6 \cdot b_r + a_r \cos(c_r(\vec{r}_i - \vec{r}_j))}{|\vec{r}_i - \vec{r}_j|^3} -$$

$$b_r \frac{(x_i - x_j)^4 + (y_i - y_j)^4 + (z_i - z_j)^4}{|\vec{r}_i - \vec{r}_j|^7}]$$

a_r, b_r c_r are model coefficients, $\vec{r}_i$ and $\vec{r}_j$ are radius-vector of two interactive bubbles. Two bubbles can fusion if fusion condition is carried out. The fusion condition is $|\vec{r}_i - \vec{r}_j| \leq \frac{r_{He}}{a}(g_i^{1/3} + g_j^{1/3}) + \Delta_f$. Δ_f is model parameter. $0 \leq \Delta_f \leq a$, a is lattice parameter, r_{He} is radius of He atom.

Authors modified Artem'ev method to solve the stochastic equations and used new method to solve system of four concerned with each other stochastic equations with nonlinear coefficients.

The developed model allows to receiv the following characteristics: distribution function of bubbles from bubbles size and position on crystal lattice, mathematical expectations and dispersions of bubble size and distance from surface, evaluations of porosity of solids layers and tensions in layers.

3. Conclusions.

1. According to classical theory bubbles destroy if their sizes are less than g_{cr} and bubbles increase if their sizes are more than g_{cr}. However, numerical experiments demonstrate that blisters can increase if their sizes are more than g_{0min} and less than g_{cr}. Bubbles can destroy if their sizes belong to interval from g_{cr} to g_{0max}. The part of increased blisters with sizes $\in [g_{0min}; g_{cr}]$ is larger than the part of destroyed blister with sizes $\in [g_{cr}; g_{0max}]$.

2. The bubbles migration into the surface under irradiation if bubble radius is less than 5 A, otherwise bubbles stop;

3. Layer-like structure of near-surface layer is discovered. Layers with accumulation of bubbles alternate with layers where number of blisters is small;

4. The greatest porosity is observed on depths of $\sim 0.85 \cdot R_p$ and $\sim 0.35 \cdot R_p$, R_p is middle depth of projection run; The porosity of solid layers from depth at time of finish of fluctuation stage is shown on Figure 1. The depths of two biggest maximums of porosity correspond to depths of development of two kinds of blisters. The depth $\sim 0.85 \cdot R_p$ conforms to depth of "large" bubbles. And the depth $\sim 0.35 \cdot R_p$ agrees with "small" bubbles.

5. Rate of increasing of bubble size reduces if blister size is bigger than 12 A. This phenomenon connects with great number of connections breaks in crystal lattice;
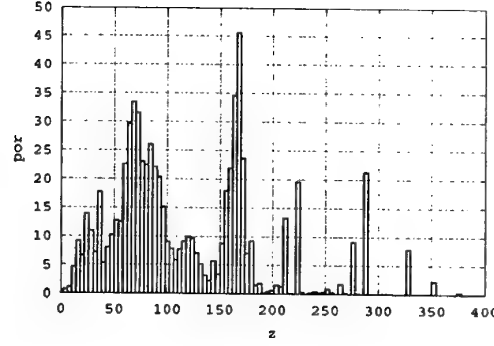
Figure 1: The porosity of solid layers from depth at time of finish of fluctuation stage is represented on this picture. The depth from surface (z) is measured in lattice parameters. 0 is surface. 400 corresponds to $2 \cdot R_p$. The porosity is considered as ratio of layer porosity from porosity of all sample at initial time.
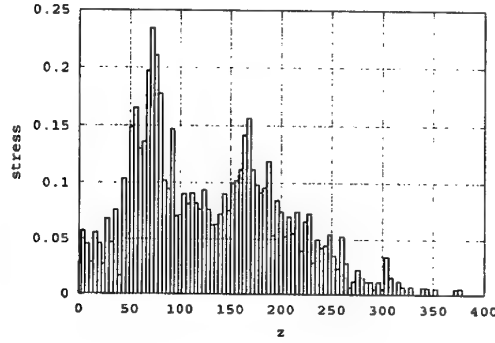
Figure 2: This figure shows the tensions in solid layers at finish time. The tension is measured in $2 \cdot 10^9 Pa$. The depth from surface (z) is measured in lattice parameters. 0 is surface. 400 corresponds to $2 \cdot R_p$.

6. Tensions in solid layers at finish time are shown on Figure 2. Largest tensions are observed on depths $\sim 0.85 \cdot R_p$ and $\sim 0.35 \cdot R_p$. Stress is pronounced near surface.

7. Distribution functions of bubbles from sizes and coordinates in lattice are nonequilibrium.

4. References

[1] A.L. Bondareva, G.I. Zmievskaya, *in book Mathematical Models of Non-Linear Excitations, Transfer, Dynamics and Control in Condensed Systems and Other Media*, Plenum Publishing Corporation, editor L. Uvarova, New-York (1998) 241.

[2] A.L. Bondareva, G.I. Zmievskaya, *XXV ICPIG Proceedings* 3 (2001) 187.

N$^+$ ion implantation effects on microhardness properties of stainless steel 52100

M. Ghoranneviss[1], A. Shokouhy[1], Amir. H. Sari[1], H. Hora[2,3], M.Talebi Taher[1], A.E.Abhari[1]

[1] Plasma Physics Research Center, Science and Research Branch, I. A. U. Iran
[2] Faculty of Electr.Engineering, University of Applide Science, Deggendorf, Germany
[3] Dept. Theoretical Physics, University of New South Wales, Sydney 2052, Australia

1. Introduction

Ion implantation has been used to modify the mechanical properties of a wide range of metals and alloys using plasma techniques for ion sources and plasma surface treatment [1-2]. It is well known for producing a modification in the structure of the superficial layers of metals by formation of new crystalline phases, meta stable or amorphous, and thus to improve the surface properties [3]. By ion implantation we are able to change the chemical composition, phase and structure of near – surface layers, i.e. the very parameters of a material which predetermine, to a great extent,its mechanical, optical, electrophysical, corrosive properties.

It has been establish that nitrogen implantation into metals can alter their surface properties such as friction, wear, corrosion, etc [4].

Nitrogen is the most common ion used for metallurgical application when the ions penetrate the surface of the workpiece, some of them peg microcracks, some fill lattice spaces in crystalline structures, and some react chemically to form compounds, giving new lattice properties [5].

When treated surfaces wear, the atoms trapped interstitially in the metal structures become dislodged and may diffuse deeper into the surface. As this process continues, the atoms continue to close up micro cracks. This discourage crack propagation in the work piece and lead to better abrasion resistance. It can also prevent the ingress of oxygen and other potentially corrosive compounds.

In this paper, the results of our experiments, are given concerning the influence of High-dose in surface hardening.

corresponding author : a_shokouhy@yahoo.com

2. Experimental and Results

First, samples, as stainless steel disks containing 1.52 wt% Cr. as the major alloying elements, with a thickness of 4 mm, were mechanically polished and cleaned by acetone and methanol, using ultrasonic device.

Disks were implanted with dosed ranging from 1×10^{16} to 3×10^{19} N$^+$/cm^2 at an energy of 90 keV. In every cases, the substrates temperature was kept at $224^\circ C$.

Beam current and accelerator voltage during the experiment were 5 mA and 105 kV, respectively. Vacuum before implantation process was $4.8\times10^{-4}\, pa$ and during implantation it was better than $1.6\times10^{-3}\, pa$. Comparison of unimplanted sample microhardness, with implanted one, shows increasing about 41.6% at dose of 1×10^{19} N$^+$/cm^2. Figure 1, presents the Vickers hardness(HV), profile, versus Nitrogen irradiation dose at the energy of 90 keV.
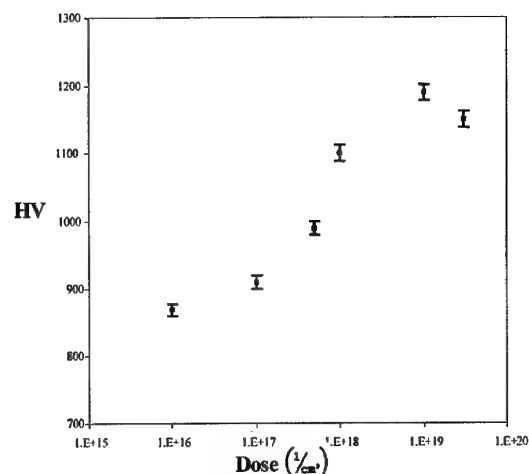
Fig. 1. Micro hardness measurement profile versus dose variations

As this profile shows, the microhardness increase with accumulation of dose up to 1×10^{19} N^+/cm^2, and then decrease at dose of 3×10^{19} N^+/cm^2. It may be because of saturation of the implanted layer by nitrogen.
A great role in the surface hardening is obviously played by different crystalline phases of iron nitrides produced as a result of nitrogen ion implantation into stainless steel targets [6-7]. Hardness measurements and wear reduction of 52100 steel by implantation of oxygen, aluminum and carbon dioxide have been reported [8].
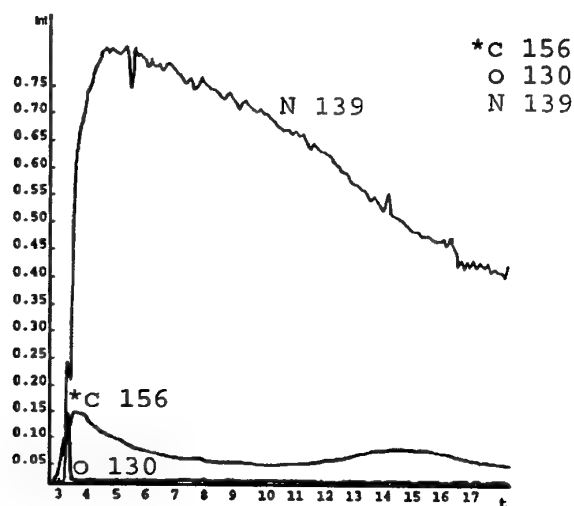
Fig. 2. Elemental Analysis for stainless steel sample implanted by 1×10^{19} N^+/cm^2.

Figure 2, shows nitrogen distribution in the surface of a sample at dose of 1×10^{19} N^+/cm^2. using GDS instrument which confirm theoretical distribution of nitrogen implantation into stainless steel.
Also the elemental analysis of Oxygen, and Carbon on the surface have been carried out using GDS instrument (fig2.)

3. Conclusion

Hardness increasing could be because of dislocation fixing by nitrogen deposition (as figure 2 shows) in steel crystalline. Also high chromium existence in 52100 steel, can cause formation of chromium nitride phases, and this may be another reason of hardness increasing.

4. References

[1]   H.Parchami, M.Ghoranneviss, A.Shokouhy, J.Plasma Fusion Res.Vol.5(2002)000.

[2]   A.H. Sari, Hantehzadeh, M.R, Ghoranneviss, M., 25th ICPIG, Nagoya, Japan, July 2001, paper 17a52.

[3]   H. Herman, Nucl. Instr . and Meth, B 182/183 (1981) 887.

[4]   S. Lucas, G. Terwagne and F. Bodart Nucl. Instr. and Meth. B50 (1990) 401.

[5]   E. Wooley, Materials World, Vol., 5 no.10, (1997) 515.

[6]   J. Salik, J. appl. Phys. 57, 1328(1985).

[7]   F. G. Yost, S. I. Picraux, D.M. Follstaedt, L.E. Pope and J.A. KNAPP, This solid film, 107, 287(1983).

[8]   K.Langguth, A.Kluge, H.Ryssel, Nucl. Instr . and Meth, B 59/60(1991) (1991) 718.

Characteristics of pulse magnetron discharge with power supply from a capacitor energy storage

A.I. Kuzmichev[1], Yu.I. Melnyk[1], V.Yu. Kulikovsky[2], P. Bohac[3], L. Jastrabik[3]

[1] National Technical University "Kiev Polytechnical Institute", Pr. Pobedy 37 KPI-2230, Kiev 03056 Ukraine
[2] Institute for Problems of Material Science, Academy of Sciences of Ukraine, Krzhyzhanovsky 3, Kiev 04142 Ukraine
[3] Institute of Physics, Academy of Sciences of the Czech Republic, Na Slovance 2, CZ-18221 Praha-8 Czech Republic

The peculiarities of pulse sputtering magnetron discharge in conditions of low-voltage power supply from capacitor energy storage are considered. Discharge current-voltage characteristics is shown to depend on pulse duration. The pulse packet regime ensures stable arc-free maintenance of the discharge at long time operation.

1. Introduction

Magnetron sputtering systems (MSS) are widely used in thin film technology, however, the practice constantly brings forth new problems and development of new more efficient MSS does not interrupted. The abilities of MSS in many respects are defined by their operation mode and power supply features. As an example of this, one can mention the intensively developed pulse sputtering [1]. The new approach allows to reduce working temperature at high power level, to increase an instantaneous plasma density and to stimulate chemical reactions on coated surfaces, to prevent glow-to-arc transitions on magnetron targets in reactive gases. Different circuits can be used for pulse discharge generation. A large charged capacitor periodically connected to a magnetron may be employed for this goal, too. The capacitor serves as an energy storage and a current transformer for a power supply source that is the discharge current magnitude can be much higher than the maximum permissible current of the power source. However the capacitor appears as a constant voltage which equals to the burning voltage of magnetron discharge and commonly is less than the firing voltage. The paper deals with the peculiarities of pulse magnetron operation with such energy source.

2. Experimental set-up

The experiments were performed using sputter deposition machine Z550M with planar "balanced magnetic field" magnetrons. A schematic drawing of the pulse magnetron circuit is shown in Fig. 1, where E – primary power source (controlled thyristor rectifier SSV-3.5) operating in constant mean power mode, C – capacitor energy storage, VT – switch IGBT transistor, VD – isolation diode, R_1 – ballast resistor for the auxiliary discharge (starting-up glow) with low current of 10-30 mA, PA – peak ampermeter. A capacitor/transistor circuit is known to have near-zero output impedance and this allows to have very high discharge current which is defined in such case only by

magnetron current-voltage characteristics (CVC) [2]. A small resistor R_0 was employed for limiting the maximum current in the magnetron circuit.
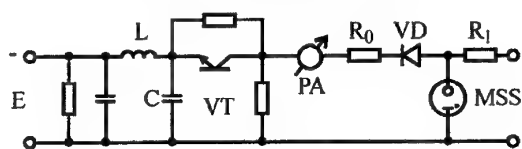
Fig.1. Schematic drawing of the MSS circuit

3. Results and discussion

Fig.2 shows diagrams of discharge voltage and current where τ – pulse duration, τ_f – formative time for pulse discharge or fall time for magnetron voltage.
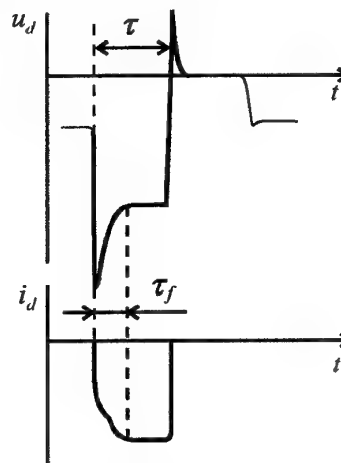
Fig.2. Discharge voltage (u_d) and current (i_d) diagrams

Fig.2 clearly demonstrates the delay in building-up of pulse discharge current after pause. The value of τ_f is about 50 µs at Ar pressures of 0.2-3 Pa and peak currents of up to 30 A that is much bigger than $\tau_f \sim 5$ µs in case of the modulator on the base of electronic tubes

[3]. In our case, the value of E (400-600 V) is close to the maintaining or burning voltage of the magnetron discharge; in [3], E was about 2 kV and this voltage was applied to the magnetron during the formative time. Fig. 3 shows CVC of the pulse magnetron discharge at the end of current pulses for different τ. One can see the smaller τ the higher the discharge resistance is and only after 100 μs CVC becomes independent on τ. Thus, at small τ the pulse discharge operates in high-voltage mode and the square-wave current becomes triangular.

a

b
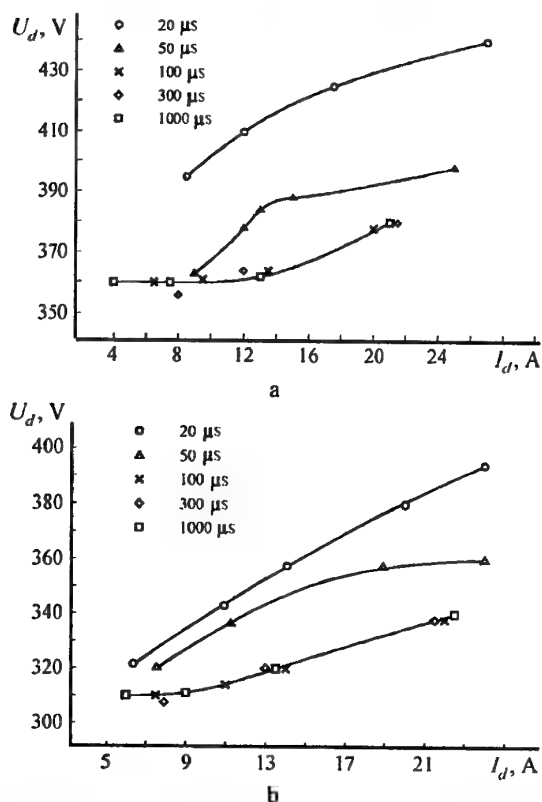
Fig.3. Current voltage characteristics of the magnetron discharge at Ar pressures of 0.19 Pa (a) and 2 Pa (b). Target material is Ti.

The thin line in Fig.2 is a voltage diagram of the auxiliary discharge which creates primary ionization, this glow discharge stabilizes arising and maintenance of the powerful pulse discharge [3]. When auxiliary discharge was put out the delay in firing pulse discharge may be very large up to some milliseconds. The near-zero voltage period after current pulse is a result of excess afterglow plasma conductivity and this period may serve as a measure of plasma decay time.

Adding reactive gases (N_2, CH_4, etc) to the discharge chamber is known to cause sparking and arcing on the magnetron target [1,2] but when we used short pulses ($\tau < 50$ μs at I_d of up to 30 A) these phenomena vanished as we decreased the time for charging dielectric films on the target. Electron current from decaying afterglow plasma and, maybe, the positive

voltage overshootings (Fig.2) promote discharging the films and prevent from accumulation of the critical positive charge. However we have the problem how to work with long pulses. Obviously, the best approach is splitting long pulses into short pulses with small current pauses between them that is use pulse packets instead of continuos long pulses. Such a pulse regime was proposed and successfully employed earlier [3,4]. Fig.4 shows oscillograms for discharge in the pulse packet mode and one can see the stable arc-free work of the magnetron with graphite target is possible even at τ in second'th range.
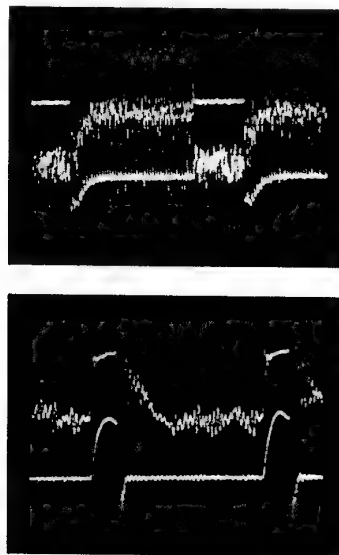
Fig.4. Oscillograms of current (upper traces) and voltages (lower traces) in the pulse packet regime. The upper oscillogram (2 s/div) shows whole packets, the lower oscillogram (20 μs/div) shows three pulses, separated by pauses of 20 μs, from the packet. Material of the target is graphite. Polarity of signals is negative.

4. References

[1] S. Schiller, K. Goedicke, J. Reschke, V. Kirchhoff, S. Schneider, F. Milde, *Surf. Coat. Technol.* **61** (1993) 331.

[2] R.A. Scholl, *Surf. Coat. Technol.* **98** (1998) 823.

[3] S.V. Denbovetsky, R. Hippler, A.I. Kuzmichev, V.Yu. Kulikovsky, S.U. Nisimov, S.B. Sidorenko, *Electronics and communication (Kiev)* **8(2)** (2000) 195 [in Russ.].

[4] A.I. Kuzmichev, *Electronics and communication (Kiev)* **4** (1998) 384 [in Russ.].

On the working regime of a pulsed duopigatron ion source

V. Braic, G. Pavelescu, M. Braic, M. Balaceanu

National Institute for Optoelectronics, POBox MG05, 76900 Bucharest, Romania

A pulsed duopigatron ion source operated in hydrogen atmosphere is investigated. Plasma parameters were determined using a plane Langmuir probe. Experimental observations of self oscillations occurring in one of the two working regimes were put into evidence. The development of the self- oscillations depending on the gas pressure and magnetic field intensity was analysed.

Introduction

Most common devices used to observe a rich variety of phenomena in collisionless plasma discharges are plasma sources with magnetic field and hot emissive filaments as cathodes. Nowadays there is an increasing interest in studying pulsed ion sources as the duopigatron one, because of their behavior presenting self excited oscillations or chaotic patterns depending on some external parameters.

The aim of this work is to analyze the influence of the gas pressure and of the magnetic field intensities on the characteristics of the self-oscillations developed in the pulsed duopigatron source.

Results and discussion

The classical configuration (hot cathode-intermediate electrode-reflecting electrode anode) of a pulsed duopigatron ion source was used to investigate the transition from a chaotic pulsed plasma towards the development of self-excited oscillations with a frequency of $25 \div 30$ kHz. The cathode of the duopigatron ion source is supplied continuously and a negative electrical pulse (10 Hz, 250 μs duration) is applied to the cathode anode gap [1]. The intermediate and the reflecting electrodes are biased automatically via serial resistors.

The ion source was operated mainly in 99.99% hydrogen atmosphere, but other gases (N_2, O_2, Ar) were used during the investigations. The pressure working regime was in the range $5.10^{-5} \div 6.10^{-3}$ mbar.

The dense, pulsed plasma expands into the working chamber where it was investigated. The discharge current is max. 30 A at a frequency of $1 \div 10$ Hz, with a $20 \div 300$ μs pulse duration. A plane Langmuir probe was used to determine carrier concentration, electron temperature and plasma potential in a cylindrical volume around the axis of the working chamber. To investigate the time evolution of the expanding plasma, the probe characteristics were determined using a digitising oscilloscope and a data acquisition system.

Two working regimes of the ion source were evidenced. In the normal one (for pressures higher than 10^{-4} mbar) the discharge current displays a normal rectangular shape with the same pattern as the applied pulsed voltage. Fig.1 illustrates the shape of the voltage and the discharge current as obtained on the oscilloscope display at a pressure of 1.9×10^{-3} mbar.
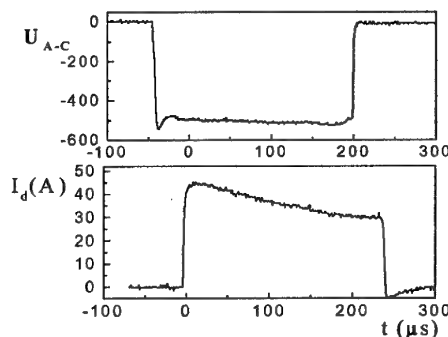
Fig.1 The shape of the voltage U_{A-C} and the discharge current pulse I_d at a pressure of 1.9×10^{-3} mbar

At relatively high pressures ($p > 10^{-3}$ mbar) the plasma characteristics display a continuous variation during the discharge pulse, as presented in Fig. 2 for electron density/ temperature and in Fig. 3 for plasma potential.
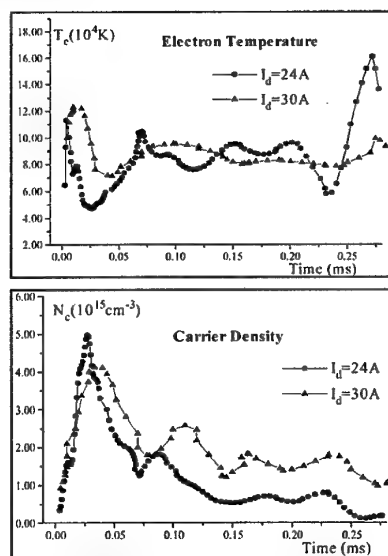
Fig. 2 Electron density (a) and electron temperature(b) variation during the discharge pulse

The analysis reveals that during pulse duration all these parameters reach a maximum with a delay of about

1÷2μs from the applied pulse. The plasma potential and the electron temperature show a saddle pattern in the middle of the impulse and a sharp increase at the pulse end. The increase of electron temperature and plasma potential after the driving pulse cut-off may be ascribed to the destruction of the double layer structure located nearby the anode, which suddenly transfers its energy to the plasma.
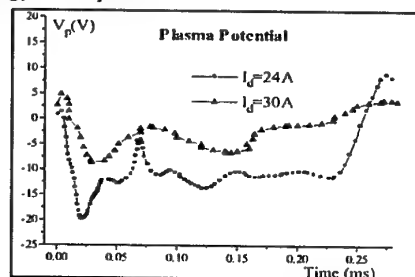
Fig. 3. Plasma potential V_p variation during the discharge pulse

In the lower pressure regime ($p<10^{-4}$ mbar) self excited oscillations of the discharge current during the applied pulsed voltage are exhibited, independently of the gas nature, pulse frequency and duration. The occurence and the shapes of these oscillations present a great dependence on the gas pressure (Fig.4). The amplitude of the oscillations of the discharge current is limited by the filament temperature ("temperature limited current regime"[4]), being slightly dependent on the discharge voltage and not strongly dependent, as reported in [3].
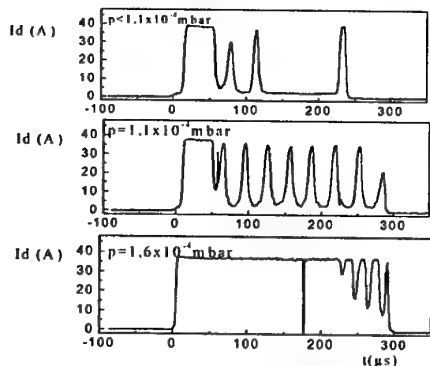
Fig. 4. Shape of the discharge current at different H_2 working pressure

As it was already reported [2], [3], plasmas produced in devices with thermoemission and applied external magnetic field may present under certain conditions an oscillating behaviour, mainly due to a lack of carriers in front of the electrodes where a double layer is formed. In our configuration, self-oscillations are developing in a narrow pressure range: $1.6x10^{-4}$ mbar ÷ $1.1x10^{-4}$mbar. At a certain pressure ($1.2 x10^{-4}$ mbar) the oscillations exhibit a structured sinusoidal form, far from the chaotic appearance exhibited at higher pressures. In Fig.5 the correlation between the oscillating feature of the discharge current I_d and the anode voltage can be seen: the anode voltage measured

with respect to the ground presents minima corresponding to the maxima in the discharge current.
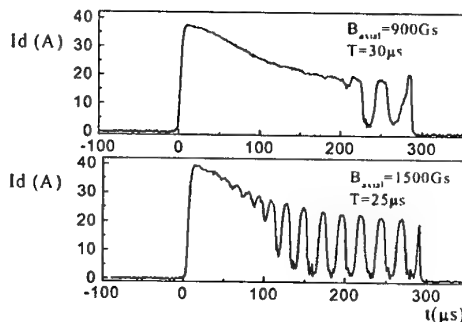
Fig. 5 Correlation between anodic voltage (U_a) and discharge current (I_d), $p=1.2 x10^{-4}$ mbar

The increase of the magnetic field, accompanied by a reduced charged particle loss to the walls at low electron densities determine the development of the oscillations through the entire pulse duration. Different oscillations corresponding to 900 Gs and 1500 Gs are presented in Fig. 6. The self-oscillations develop as distinctive patterns from the beginning towards the end of the pulse, as the magnetic field intensity increases.
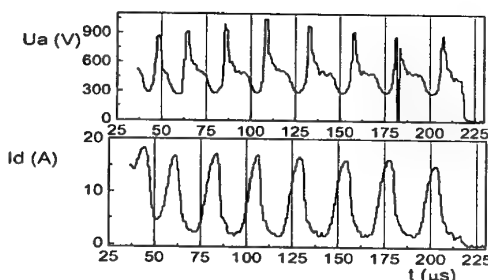
Fig. 6. Shape of the discharge current for different magnetic fields values

The time dependence of the discharge current I_d suggests that the density of the primary electrons and consequently the ionisation process is also variable in time. In our opinion the oscillations in the discharge current with frequencies at about 25÷30 kHz suggest an ionic space charge build-up followed by disruption.

Conclusions

The investigation of a pulsed duopigatron ion source evidenced the development of self excited oscillations with 25÷30 kHz at low pressures and high magnetic fields, determined by an ionic space charge build-up followed by disruption.

References

[1]. V.Braic, Rev.Optoelectronics, **4/3** (1997), 31
[2]. D.L.Morse, Phys.Fluids, **8/3** (1965) 516
[3]. C.Arnas Capeau, G.Bachet, F.Doveil, Le Vide: Sci. Tech. Appl..**275** (1995) 321
[4]. R.A.Bosch, R.L.Marlino, Contrib.Plasma Phys. **26** (1986) 1

126

A Plasma Source with LaB$_6$ Hollow Cathode for a Diagnostic Beam Injector

V.I.Davydenko, P.P.Deichuli, A.A.Ivanov, A.Kreter[*], B.Schweer[*], G.I.Kuznetsov,
V.V.Mishagin, N.V.Stupishin, G.I.Shul'zhenko

Budker Institute of Nuclear Physics, 630090, Novosibirsk, Russia

[*]Trilateral Euregio Cluster, Institut fur Plasmaphysik, Forschungszentrum Juelich GmbH,

Association EURATOM-KFA, P.O.B. 1913, D-5170, Juelich, Germany

1. INTRODUCTION

The hydrogen neutral beams are widely used to diagnose the plasma in magnetic fusion devices. The beams are extracted from the plasma generated by a plasma source, accelerated to desired energy and subsequently neutralized in a gas target. The critically important characteristics of the plasma source are the composition and the source lifetime. A presence of the molecular ions in the plasma results in appearing of atoms in the beam with energies E, E/2, and E/3, where E is the determined by accelerating voltage (E=eU). For example, the plasma sources of the diagnostic injectors developed for TEXTOR and TCV tokamaks [1,2], which are based on RF-discharge, has a long enough lifetime (many thousands shots) for a pulse duration 2-10 sec. At the same time, the proton fraction in the RF-plasma is about only 60% by current [2,3].

The plasma produced in an arc-discharge plasma source generally has a higher proton fraction (80-90%) [4]. For the plasma source developed in Novosibirsk and its modifications [1,4], the plasma density near the anode hole is quite high, of the order of 10^{21}m^{-3} and electron temperature is ~5 eV. For these parameters, the gas puffed into the anode region is to be almost completely ionized and the molecular ions are dissociated. The plasma generated near the anode orifice expands towards the plasma grid and its density falls dawn to ~ 10^{18}m^{-3}. Due to this density reduction, the additional gas ionization in the expansion volumes becomes negligible and additional molecular ions do not appear. This type of arc-discharge plasma source with a cold cathode is used in the neutral beam injectors with a pulse duration limited to ~0.5s or less [4]. The main disadvantage here is a limited lifetime of the plasma source parts due to their intensive erosion.

In this paper, a modification of the arc discharge plasma source is described, in a hollow cathode with internal LaB$_6$ electron emitter is used instead of the cold metal cathode. This plasma source is developed for a hydrogen beam diagnostic injector. It is expected that this plasma source has longer lifetime operating in a few second pulses and generates a plasma with lower molecular fraction compared to RF-based plasma source [2].

2. PLASMA SOURCE

2.1 General design

General layout of the plasma source is shown in Fig.1. It consists of an anode (3), gas-discharge channel (2), cathode assembly, magnetic coil (4), an array of permanent magnets (5) to transport the plasma flow to plasma grid and the cooling system. The gas-discharge is sustained between copper anode and a hollow cathode with internal LaB$_6$ electron emitter. The discharge channel is formed by a stuck of isolated metallic washers with internal diameter varying from 5 to 7 mm. The plasma production is increased by application of a longitudinal magnetic field about 0.1 T in anode region, which is formed by the coil (4). The gas (hydrogen) is supplied through the gap between the anode and the nearest washer, and into the cathode chamber. The washers, cathode and anode have intensive water cooling.

The beam is extracted and accelerated by a four-electrode ion-optical system (6) with 163 holes each of 4mm in diameter. The diameter of plasma emitter at plasma grid is about 70mm to provide 2 A ion beam current.

2.2 Multipole peripheral magnetic field
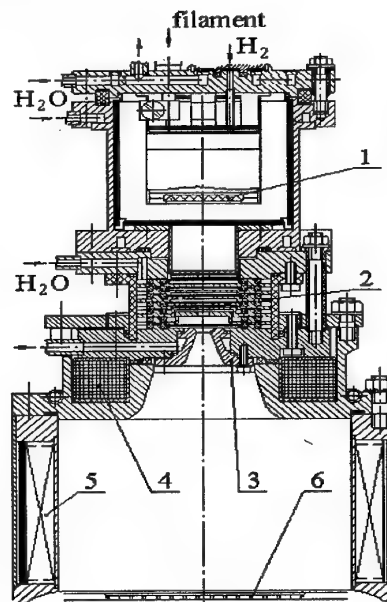
Fig.1. The plasma source with hollow LaB$_6$ cathode.
1- LaB$_6$ tablet, 2- discharge channel, 3- anode, 4 – magnetic coil, 5 – permanent magnets, 6 – electrode of acceleration system.

To obtain the required current density of a plasma emitter of 0.1-0.2 A/cm^2 the high density plasma jet expands from the anode of the plasma source into a cylindrical volume with peripheral magnetic field. The field is formed by an array of 16 permanent magnets, which provides magnetic picket fence configuration near the wall. The $Nd_{15}Fe_{77}B_8$ permanent magnets have 80 mm length and 9x12 mm cross-section. Magnetic field strength at inner wall of the expander is 0.2T and falls down along the radius to less than 0.01 T at 2 cm distance from the wall. This peripheral magnetic field increases the plasma density at the plasma grid by approximately 2 times reflecting a plasma from the wall and at the same time improves the uniformity of plasma flow at the ion emitter plane.

2.3 Hollow Cathode with internal LaB$_6$ emitter

Lanthanum hexaboride has a high emission electron current up to 20-40 A/cm^2 at rather moderate temperatures. We have introduced a LaB$_6$ electron emitter into the hollow cathode to increase efficiency of plasma production. The LaB$_6$ disk has 30 mm in diameter and 3 mm thickness. The LaB$_6$ tablet is supported by graphite rings and is heated by radiation of a wound tungsten wire. The discharge is initiated by applying a 20-50 V voltage between the tablet and the body of hollow cathode.

3. EXPERIMENTAL RESULTS

The discharge current was varied from 80 to 350 A. Fig. 2 shows the discharge voltage-current characteristic. The dependence was measured with 750 Gs longitudinal magnetic field near anode opening. The discharge current ~270 A was enough to extract 2 A ion beam.

The typical value of the heating power of the tablet was 650 W. The temperature of LaB$_6$ tablet was measured by an optical pyrometer. The temperature required for stable operation was found to be about 1700^0 C. At the same time, it was observed that due to the tablet extra heating during the discharge really 1450^0 C initial temperature was enough. The transition time from initial temperature to a steady-state was measured to be up to 0.2 s.

The radial profile of the plasma flow density measured at the plane of the first (plasma) grid is shown in Fig.3. The required non uniformity of ±10% was obtained inside a circle with diameter of 68mm, which enables to extract the beam with this diameter.

As it was already mentioned, the lifetime is a critical parameter for the arc-discharge plasma source. By now, about 1000 shots were made with pulse duration 1 s without noticeable damages to the source components. Several 2 s shots also were also made without critical damages to the source.
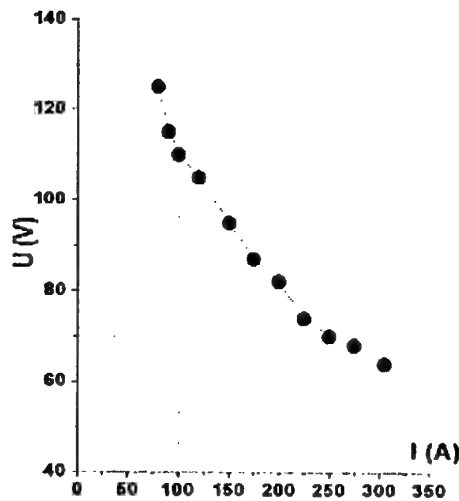
Fig. 2. Discharge voltage-current characteristic .
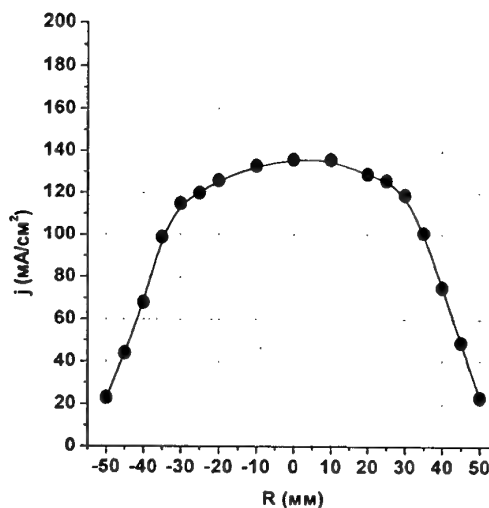
Fig.3. Radial profile of the plasma flow density.

REFERENCES

[1] A.A.Ivanov, V.I.Davydenko, et al, 19th IAEA Fusion Energy Conference, Lyon, France, 14-19 October 2002, Book of Abstracts, IAEA-CN-94, p.101.

[2] A.A.Ivanov, V.I.Davydenko, P.P.Deichuli, et al, Rev. Sci. Instruments, v.71, No.10, pp.3728-3735 (2000)

[3] A.A.Ivanov et al, Preprint 2002-41, Budker Institute of Nuclear Physics, Novosibirsk, Russia

[4] G.F.Abdrashitov, V.I.Davydenko, et al, Rev. Sci. Instr., 2001, v.72, N1, p. 594-597

128

Electrical diagnostics of a macroscopic rf plasma display panel cell

B. Caillier, Ph. Guillot, J. Galy, L.C. Pitchford, J.P. Boeuf.
Centre de Physique des Plasmas et Applications de Toulouse,
Université Paul Sabatier, 118 route de Narbonne, 31062 Toulouse Cedex, France

1. Introduction

Although Plasma Display Panels (PDPs) are now produced industrially, their luminous efficiency is still low, on the order of 2 lumens per watt (lm/W) or less, and needs to be increased up to 5 lm/W. Research efforts are directed toward the increase of efficiency by optimization of the electrode and cell design or by seeking more efficient discharge regimes. Recently some attempts at operating PDP cells in a RF regime have been made[1]. The RF regime is much more efficient than the usual dielectric barrier discharge ac regime because the better electron confinement allows lower operating voltages. Less energy is therefore dissipated in ion heating in the sheaths, and the lower electric field allows a more efficient energy deposition into xenon excitation (the efficiency of the PDP cell is directly related to the UV emission of the xenon resonant and excimer states[2,3,4]). It was shown experimentally[1] and with numerical simulations[2,3,4] that the efficiency of RF PDP cells can be up to 4 times larger than that of standard ac PDP cells for RF frequencies on the order or larger than 40 MHz. The application of RF power at 40 MHz to a 42 in. Plasma Display Panel is however a big challenge because of the large capacitive currents and because the wavelength of the electric field at this frequency is not large with respect to the panel dimensions (and the electrodes are no longer equipotential). More work is necessary to study the practical feasibility of RF PDPs.

In this paper we present electrical characteristics of the plasma in a "macro-cell" which is related to a real PDP cell by scaling laws (constant pd, pt, and E/p, where p is the gas pressure, d is the gap spacing, t is time or reciprocal of the frequency, and E is the electric field). The macro-cell is 100 times larger than a real PDP cell, but the pressure is 100 times lower. To the extent that gas chemistry does not affect the electrical properties, the scaling laws are valid and can be used apply our measurements to PDP conditions. We present electrical measurements of the power dissipated in the cell and compare them with results from simulations in PDP conditions.

2. Experimental set-up

The macro-cell is represented in Fig. 1. The cell walls are made out of glass (0.5 cm width). The cell is pumped, baked at 300 °C for several hours, filled with a Xe(4%)-Ne gas mixture at 5 torr, and sealed. The electrodes are placed outside the glass vessel (capacitive coupling) on the external faces. The gas gap is 3 cm; the electrode spacing is 4 cm.
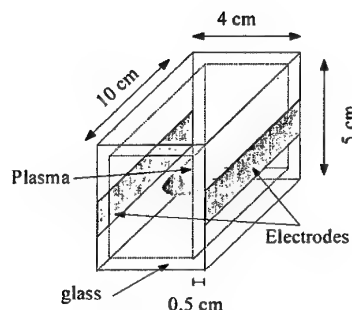
Fig. 1: "Macro-cell" used in the experiments. In the results presented in this paper, each electrode entirely covers one cell face (dimensions 10 cm x 5 cm).

The voltage frequency is varied between 1 MHz and 3 MHz (which would correspond to 100 MHz to 300 MHz for a real PDP cell).

The power dissipated in the cell is measured with two methods. The first one is the Lissajou method which is illustrated in Fig. 2. The voltages across the discharge electrodes from the oscilloscope are plotted as a function of the voltage across a capacitor in series. The power is obtained by measuring the area of the Lissajou curve (Fig. 2):

$$P = \frac{1}{T} \int I_D V_D dt = \frac{C}{T} \int V_D dV_C$$
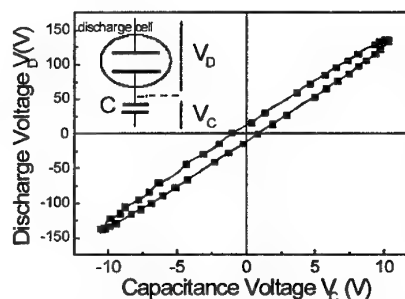
Fig. 2: Example of power measurements with the Lissajou method (conditions: Xe(5%)-Ne, 4 torr, 150 V, 3 MHz)

The second method is a simple bridge method where the capacitor C_V (Fig. 3) is adjusted so that the

voltage V_1 and V_2 are equal for given applied voltage when there is no plasma in the cell. When the plasma is ON, the power is deduced from the measurement of (V_2-V_1).
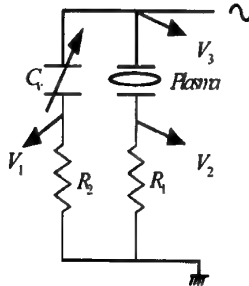
Fig.3: Scheme illustrating the electrical measurement with a bridge method.

3. Results

Figure 4 shows the power measured as a function of applied RF voltage amplitude for different frequencies.
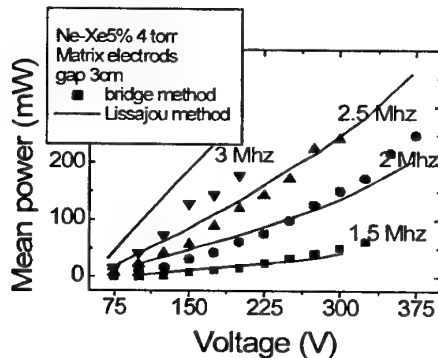
Fig. 4 : Measured mean power versus applied voltage for different frequencies with two different methods (see text)

The two methods gives similar results except for the higher frequency case where the discharge is more capacitive and the accuracy of the measurement needs improvement.

The measured power was compared with results from a 1D fluid simulation of the discharge[4]. As seen in Fig. 5, the simulation results strongly depend on the secondary electron emission coefficients on the dielectric surface. A reasonable fit is obtained when the secondary emission of neon ions is taken to be 0.05 (0.005 for xenon ions). Note that the glass wall is not coated with MgO in these experiments.
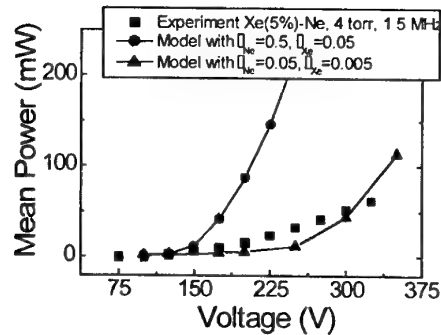
FFig.5 : Measured and simulated mean power as a function of RF voltage amplitude for two values of the second Townsend coefficient.

The shape of the power vs voltage curve suggests that the discharge operates in the α regime (i.e. power dissipation due to the sheath oscillation is dominant).

The calculated plasma density is on the order of a few 10^8 cm^{-3} for a frequency of 1.5 MHz at 100 V RF voltage amplitude. This is in rough agreement with the estimation based on the analysis of the current waveform assuming that the discharge can be represented by an equivalent circuit composed of a resistor (bulk plasma) in series with the sheath capacitance (deduced from the optical measurement of the sheath thickness).

Infrared xenon and neon visible emission from the cell have also been measured as a function of applied voltage and frequency. From these results, we infer that the efficiency for power deposition in xenon excitation decreases with increasing voltage for a given frequency. The results, when compared with ac PDP measurements, show that the power is much more efficiently dissipated into xenon excitation in a RF PDP cell. These results will be further described in the poster.

References

[1] J. Kang, J. SID 8, 223 (2000); J. Kang, W. G. Jeon, O. D. Kim, J. W. Song, J. P. Boeuf, and M. H. Park, IDW'99 Proceedings, p. 691 (1999); J. Kang, O. D. Kim, W. G. Jeon, J. W. Song, J. Park, J. R. Lim and J. P. Boeuf, IDW'00 Proceedings, p. 643 (2000).

[2] S. Cany, J. Kang, C. Punset, and J. P. Boeuf, IDW'99 Proceedings, p. 751 (1999).

[3] M. Kurihara and T. Makabe, J. Appl. Phys. 89, 7756 (2001).

[4] L.C. Pitchford, J. Kang, C. Punset, and J.P. Boeuf, J. Appl. Phys. 92, 6990 (2002)

[5] B. Caillier, et al, "Plasma Display Cell Operating in a RF Regime" ,ESCAMPIG 2002, I-355.

130

Ion Heating in a Supersonic Plasma Flow for an Advanced Plasma Thruster

A.Ando, S.Fujimura, T.Yagai, Y.Hosokawa, K.Hattori and M.Inutake,

Department of Electrical Engineering, Tohoku University,
Aoba05, Sendai 980-8579, Japan, akira@ecei.tohoku.ac.jp

Ion heating experiments are performed in a fast flowing plasma with an ion Mach number of nearly unity. RF waves with an ion cyclotron range of frequency is excited by a pair of loop antennas located at a divergent magnetic nozzle. Increase of plasma thermal energy $W_\perp$ measured by a diamagnetic coil is observed when the waves are excited with various azimuthal mode numbers in several magnetic nozzle configurations. It is most effective to heat ions of plasma flow to excite the waves with an azimuthal mode number of $m= \cdot 1$. The heating efficiency is larger in the magnetic beach configuration than that in the uniform one.

1. Introduction

Recently a plasma flow is found to play an important role in space and fusion plasmas. Intensive researches to develop a fast flowing plasma with high particle and heat fluxes are required in basic plasma-physics as well as various industrial and space applications.

A magnetic-nozzle acceleration and ion heating in a fast flowing plasma attracts much attention in the advanced electric propulsion system. In the Variable Specific Impulse Magnetoplasma Rocket (VASIMR) project, the combined system of the ion cyclotron heating and the magnetic nozzle is proposed to control a ratio of specific impulse to thrust at constant power [1].

Plasma acceleration in a divergent magnetic nozzle has been successfully demonstrated in the HITOP device, where a transonic plasma flow (M_i is nearly unity) is converted into a supersonic one (M_i increases up to 3) through a divergent magnetic nozzle where no $j \cdot B$ acceleration is exerted [2-4].

Though an ion heating in a magnetically-confined plasma has been precisely investigated both theoretically and experimentally in many researches, few attempt of a direct ion heating for fast flowing plasmas by radio-frequency waves has been done. The condition of ion cyclotron resonance is expected to change drastically by the effect of a Doppler shift in a fast flowing plasma.

In this experiment we have performed an ion heating experiment in a supersonic plasma flow produced in the HITOP device. Either axisymmetric ($m=0$) or non-axisymmetric ($m= \cdot 1$ and $\cdot 2$) mode waves near the ion cyclotron frequency is launched by a pair of loop-type antennas set in a diverging magnetic field. It is found that the plasma thermal energy measured by a diamagnetic loop coil increases when the waves are launched as a beach-heating configuration. The heating effects are compared in various wave excitation mode numbers and in several magnetic nozzle configurations.

2. Experimental Setup

Experiments are carried out in the HITOP device. It consists of a large cylindrical vacuum chamber (diameter $D = 0.8m$, length $L = 3.3m$) with eleven main and six auxiliary magnetic coils, which generate a uniform magnetic field up to 0.1T. Various types of magnetic field configurations can be formed by adjusting the external coil current.

A magneto-plasma-dynamic arcjet (MPDA) is installed at one end-port of the HITOP. It has been developed as a representative device for a space thruster [5] and is also utilized as a supersonic plasma flow source [3]. The MPDA has a coaxial structure and the plasma is accelerated axially by a self-induced electro-magnetic force, $F_z=J_r \cdot B_\theta$ where J_r is a radial discharge current and B_θ is self-induced azimuthal magnetic field.

Discharge current I_d up to 10kA is supplied by a pulse-forming network (PFN) system with the quasi-steady duration of 1ms. A high density (more than $10^{20}m^{-3}$) and high Mach number (M_i up to 3) plasma flow can be generated.

Plasma flow characteristics are measured by several diagnostics installed on the HITOP device. Profiles of ion Mach number and plasma density along and across the field lines are measured by a movable Mach probe and an array of 13-channel Mach probes set at 1.7m downstream of the MPDA outlet in the HITOP [6].
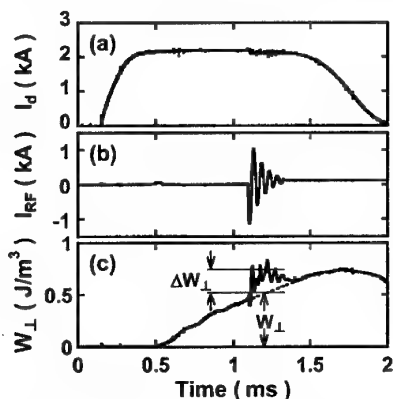
Fig.1 Temporal evolutions of (a) discharge current, (b) antenna current, (c) diamagnetic signal. The m= $\cdot$ 1 mode waves are excited in the magnetic-beach configuration .

3. Experimental Results

A pair of loop antennas with 60mm in diameter is used for the wave excitation [7]. Employing a Faraday shield reduces electrostatic coupling between the antenna and the plasma. The antennas are set at Z=1.0m downstream of the MPDA. The antenna current is supplied by a pulsed oscillation power-supply, which consists of a condenser and a gap-switch. The azimuthal mode number m of the exciting wave can be changed by adjusting the combination of the antenna-current direction.

In the present experiments, an argon gas is used due to a relatively low excitation frequency of about 20kHz. Figure 1 shows typical waveforms of the discharge current I_d, the antenna current I_{RF} and an observed diamagnetic signal $W_\perp$ under the condition of m= $\cdot$ 1 for the wave excitation mode. The plasma thermal energy $W_\perp$ is measured by a diamagnetic loop coil located at Z=2.2m. Though the antenna current damps rapidly due to the lack of power supply capability, the diamagnetic coil signal increases during the excitation.

The electron and ion temperature are almost equal at about 2eV and the density is $2 \cdot 10^{19} \mathrm{m^{-3}}$. Plasma flow velocity can be estimated to be about 6km/sec by Mach probe measurements and a time delay of ion saturation current signals. It takes about 0.2ms for the Ar plasma to flow from the antenna position to the diamagnetic coil position. The $W_\perp$ signal, however, increases without such a delay time as shown in Fig. 1(c), which indicates that the waves propagate and absorbed in the downstream region. The wave phase velocity is about 10^5 m/s, which is measured by a phase shift of two magnetic probe signals located at axially-different positions.

We varied an azimuthal mode number of the excited waves by changing the coil arrangement. Figure 2 shows time evolutions of the diamagnetic signals with

Fig.3 Three types of magnetic configurations. The wave is excited in $\omega/\omega_{ci}<1$ region and propagates downward approaching to the region of (a) $\omega/\omega_{ci}<1$,(b) $\omega/\omega_{ci}=1$, (c) $\omega/\omega_{ci}>1$. The wave amplitudes are measured in these configurations. The doted line corresponds to the case without plasma

three types of the azimuthal mode number, m=0, $\cdot$ 1, $\cdot$ 2. The increment ratio of the thermal energy ratio $\Delta W_\perp/W_\perp$ is the largest in the case of m= $\cdot$ 1.

Wave amplitude and phase shift are measured by magnetic probes at several axial positions in a uniform magnetic field. The obtained dispersion relation agrees well with that of shear Alfven waves. Damping of the excited wave amplitudes are measured and shown in Fig.3. The wave damping and the increment of $W_\perp$ are larger in the diverging magnetic configuration (type c) in these three types of magnetic configurations. The dependence on the magnetic strength does not show clear indication of the cyclotron resonance region. It should be caused by the Doppler effect of fast flowing ions.

References

[1] F.R.ChangDiaz, et.al. Proc. of 36th Joint Propulsion Conf., (Huntsville), **AIAA-2000-3756**, (2000). pp. 1-8.
[2] A.Ando, et.al., J. Plasma Fusion Res. SERIES, **4** (2001) 373.
[3] M.Inutake, et.al., J. Plasma Fusion Res., **78** (2002) 1352.
[4] M.Inutake, et.al., Proc. of 26th Int. Conf. on Phenomena in Ionized Gases, (2003,Greifswald).
[5] R.G.Jahn., Physics of Electric Propulsion, McGRAW-HILL, NewYork, 1968, pp. 196-256.
[6] A.Ando, et.al., Proc. of 25th Int. Conf. on Phenomena in Ionized Gases, (Nagoya, 2001) Vol. 2, pp.195.
[7] Yagai T., et.al., Proc. 11th Int. Congress on Plasma Physics, (Sydney, 2002), ICPP-2002, paper No.482.

Fig.2 Temporal evolutions of diamagnetic signals in the three types of azimuthal mode number, (a) m=0, (b)m= $\cdot$ 1, (c)m= $\cdot$ 2.

Topic 13

Waves and instabilities, including shock waves

Oscillations of the positive column plasma caused by propagation of ionization wave and the two-dimensional structure of striations

Yu.B. Golubovski[†], R.V. Kozakov[‡], C. Wilke[‡] and V.O. Nekutchaev[§]

[†] Saint-Petersburg State University, ul. Uljanovskaja, 1, 198504, Russian Federation

[‡] Insitute of Physics, University Greifswald, Domstr., 10a, 17489, Germany

[§] Ukhta Industrial State University, ul. Senjukova 13, Ukhta, 167300, Russian Federation

Time resolved measurements of the electron energy distribution function (EEDF) and plasma potential in longitudinal and radial directions under the presence of S- and P- striations in neon were performed. The potential was measured with high spatial resolution by means of simultaneous displacement of electrodes relative to stationary probe in different radial positions. A method of decomposition of the spatio-temporal structure of the potential is proposed. The potential is shown to be composed of the plasma oscillations and the ionization wave potential. Experiments revealed two-dimensional structure of the striation potential field. Qualitative considerations of the origins of this structure are discussed.

1. Introduction

Plasma of the positive column of glow discharge is stratified under wide range of discharge conditions. Propagation of the ionization waves (striations) is accompanied by ocsillations of the plasma potential. These oscillations should be taken into account when measuring spatial potential profile [1]. Correct measurement of potential allows one to analyse electrons kinetics in striations. In this paper the space and time resolved measurements of the potential within striation are presented. Two-dimensional structure of the potential in the stratified positive column is investigated. Decomposition method of the spatio-temporal potential distribution in terms of potential oscillations and wave propagation is proposed.

2. Experimental setup and measurement technique

Measurements were carried out in discharge tube with inner diameter of 40 mm and distance between electrodes of 55 cm. Electrodes were moveable in axial direction allowing direct space resolved measurements in positive column. The probe was moveable in radial direction. Spatial resolution in axial direction was limited by the length of the probe which was equal to 1.5 mm. Measurements were carried out in neon discharge at pressures $p = 1.5$ Torr for S-striation and $p = 1.0$ Torr for P-striation. Discharge current in both cases was equal to 10 mA. Potential drops over striation lengths were equal to 19 V for S-striation at length L_S equal to 10.15 cm and 9.5 V over $L_P = 5.1$ cm for P-striation. Values of mean electric field were equal $E_0 = 1.9 V/cm$ in both cases.

3. Decomposition of the measured potential onto wave and oscillations

Let us suppose that measured space-time potential structure has a form of

$$\Phi_{\text{exp}}(x,t) = -E_0\, x + \Phi_{\text{wav}}(x - vt) + \Phi_{\text{osc}}(t).$$

Eliminating the potential created by the constant electric field $E_0\, x$ and introducing substitution ($\xi = x - vt, t$) one becomes a matrix in the form

$$\tilde{\Phi}_{\text{exp}}(\xi,t) = \Phi_{\text{wav}}(\xi) + \Phi_{\text{osc}}(t) \qquad (1)$$

where $\tilde{\Phi}_{\text{exp}}(\xi,t) = \Phi_{\text{exp}}(x,t) + E_0\, x$. It is seen from (1) that when the ξ value is constant, the term on the left hand side of (1) gives $\Phi_{\text{osc}}(t)$ and when the t is constant it gives $\Phi_{\text{wav}}(\xi) = \Phi_{\text{wav}}(x - vt)$.

This allows one to expand the measured space-time potential structure onto the potential of ionization wave, that depends on $x - vt$ and potential oscillations depending only on time. Results of such decomposition are shown in figure 1.

4. Two-dimensional structure of ionization waves

Two-dimensional structure of the potential in the striations is shown in figure 2. It is clearly seen, that the potential which was measured with the help of the moveable electrodes and probe has a form of superposition of the steady-state positive column potential $\varphi^{(0)}(x,r) = -E_0\, x + \varphi_0(r)$ and the two-dimensional potential of ionization wave $\tilde{\varphi}(x,r)$. Radial potential profile is periodically changed in the direction of wave propagation.

Two-dimensional potential perturbations could be analysed on the basis of ion motion equation, which can be written in the following form

$$\frac{\partial n(\varphi)}{\partial t} + b_i \text{div}(n(\varphi)\text{grad}(\varphi)) = I(\varphi) \qquad (2)$$

where the electron density $n(\varphi)$ and ionization rate $I(\varphi)$ are the functions of the radial potential. Both of them can be considered as the sum of the values for the axially homogeneous positive column and small

135
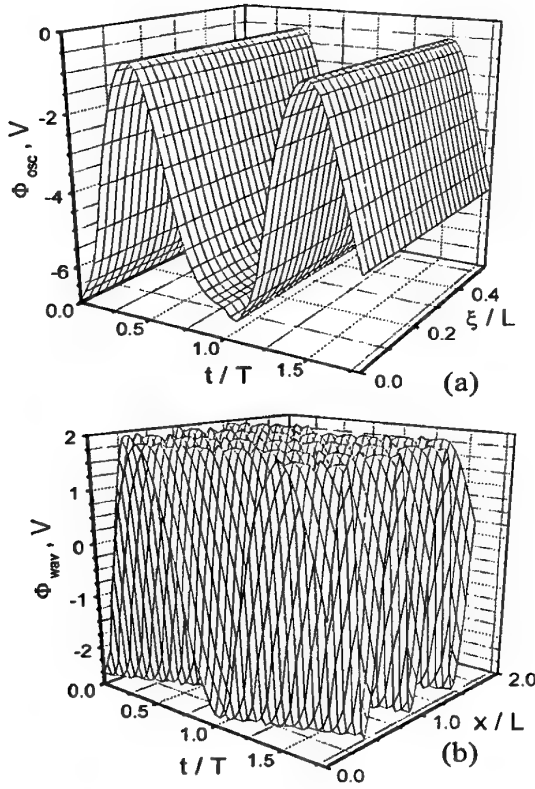
Figure 1: Decomposition of the measured spatio-temporal potential onto potential on oscillations and wave. a - oscillations of the plasma potential as a whole, b - potential of the ionization wave.

Figure 2: Measured two-dimensional structures of the potential in S-(a) and P-(b) striations.

wave-like additions. Let us suppose that potential perturbations have the form of the wave which propagates in longitudinal direction x with an amplitude depending on r.

$$\tilde{\varphi}(x,r) = \Phi(r) \exp(ikx) \exp(\delta t)$$

Scale $k = 2\pi/L$ of the axial inhomogeneity is defined by electron kinetics and remains constant. Longitudinal gradients could be neglected as far as the wavelength is much longer than the tube radius $L \gg R$. Linearized equation for the wave amplitude $\Phi(r)$ has the following form

$$\frac{1}{r}\frac{\partial}{\partial r} r \frac{\partial \Phi}{\partial r}$$
$$+ \left(\frac{1}{b_i n} \frac{\partial n}{\partial \varphi} \delta - \frac{1}{b_i n} \frac{\partial I}{\partial \varphi} + \frac{1}{nr} \frac{\partial}{\partial r} r \frac{\partial n}{\partial r} \right) \Phi = 0$$
$$(3)$$

Equation (3) with the boundary condition

$$\left. \frac{\partial \Phi}{\partial r} \right|_{r=R} = 0$$

is an eigenvalue problem where the eigenvalues determine a sign of disturbance decrement δ and eigen-

functions define a form of this disturbance. Similar eigenvalue problem for the electron density perturbation was considered in paper [2]. It can be shown [2] that the largest decrement δ corresponds to the first alternating-sign eigenfunction resulting in the radial potential perturbation in the following form

$$\Phi(r) = J_0 \left(t_1 \frac{r}{R} \right)$$

Where t_1 is the first root of Bessel function of first order $J_1(t_1) = 0$.

5. Acknowledgements

6. References

[1] Yu.B. Golubovskii, V.O. Nekuchaev and N.S. Ponomarev, *Tech. Phys.* **43** (1998) 3.

[2] Yu.B. Golubovskii, V.I.Kolobov and L.D. Tsendin, *Zh. Tekh. Phys.* **56** (1986) 1.

136

Hall-MHD surface waves in flowing solar-wind plasma slab

R. Miteva and I. Zhelyazkov

Faculty of Physics, Sofia University, BG-1164 Sofia, Bulgaria

We study the influence of a steady flow velocity on the dispersion characteristics of Hall-magnetohydrodynamic forward and backward sausage and kink surface waves travelling along a solar-wind plasma slab. Both surface modes, being Alfvén waves in an immovable layer, become super Alfvénic ones in flowing slab with increased dispersion at small wave numbers for forward waves and at large wave numbers for backward waves, respectively.

1. Motivation

Recent observations made by two *HELIOS* spacecrafts have confirmed the existence of fine structures in high-speed solar-wind flows. Satellite measurements of plasma characteristics such as the magnetic field, the velocity and density of the plasma are important to understand the different plasma wave modes which may occur. However, wave analysis requires further information and special tools in order to be able to identify which set of modes is contributing to observed wave features [1]. While the magnetohydrodynamic (MHD) waves (acoustic, Alfvén and magnetosonic modes) possess frequencies much below the ion cyclotron frequency ω_{ci}, the frequency range of Hall-MHD waves is expanded up to ω_{ci}. Recall that Hall-MHD theory is relevant to plasma dynamics occurring on length scales shorter than an ion inertial length ($l_{\text{Hall}} < c/\omega_{pi}$, where c is the speed of light and ω_{pi}—the ion plasma frequency) [2]. Assuming the solar-wind plasma is structured due to different plasma/mass densities inside and outside the slab [3], the Hall length scale for a solar-wind flux tube at 1 AU with ambient magnetic field $B_0 = 3.6 \times 10^{-9}$ T (and accordingly ion cyclotron frequency $\omega_{ci}/2\pi = 0.055$ Hz), electron number density $n_e = 2 \times 10^6$ m^{-3}, electron temperature $T_e = 2 \times 10^5$ K is $l_{\text{Hall}} = 160$ km. The Alfvén speed is $v_A = 56$ km s^{-1}, sound speed being $v_s = 52$ km s^{-1} and hence the plasma β equals approximately unity. The slab steady flow speed is $v_0 \approx 400$ km s^{-1}.

2. Basic equations and relations

Consider a flowing plasma slab of uniform density ρ_o and thickness $2x_0$, bounded by immovable plasmas of densities ρ_e, the interfaces being the surfaces $x = \pm x_0$. The uniform magnetic field $\mathbf{B}_0$ and the steady flow velocity $\mathbf{v}_0$ point in the z direction. The wave vector $\mathbf{k}$ lies also along the z axis and its direction is the same as that of $\mathbf{B}_0$ and $\mathbf{v}_0$ for forward waves and opposite for backward waves, respectively. The basic equations for Hall-MHD waves are the linearized equations governing the evolution of perturbed plasma density $\delta\rho$, pressure δp, fluid velocity $\delta\mathbf{v}$ and wave magnetic field $\delta\mathbf{B}$ [4],

$$\frac{\partial}{\partial t}\delta\rho + (\mathbf{v}_0 \cdot \nabla)\,\delta\rho + \rho_0\nabla \cdot \delta\mathbf{v} = 0,$$

$$\rho_0\frac{\partial}{\partial t}\delta\mathbf{v} + \rho_0\,(\mathbf{v}_0 \cdot \nabla)\,\delta\mathbf{v} + \nabla(\delta p + \frac{1}{\mu_0}\mathbf{B}_0 \cdot \delta\mathbf{B})$$
$$- \frac{1}{\mu_0}\,(\mathbf{B}_0 \cdot \nabla)\,\delta\mathbf{B} = 0,$$

$$\nabla \cdot \delta\mathbf{B} = 0,$$

$$\frac{\partial}{\partial t}\delta\mathbf{B} - (\mathbf{B}_0 \cdot \nabla)\,\delta\mathbf{v} + \mathbf{B}_0\nabla \cdot \delta\mathbf{v} + (\mathbf{v}_0 \cdot \nabla)\,\delta\mathbf{B}$$
$$+ l_{\text{Hall}}\frac{v_A}{B_0}\mathbf{B}_0 \cdot \nabla\nabla \times \delta\mathbf{B} = 0,$$

$$\frac{\partial}{\partial t}\delta p + (\mathbf{v}_0 \cdot \nabla)\,\delta p + \gamma p_0\nabla \cdot \delta\mathbf{v} = 0,$$

where $v_A = B_0/(\mu_0\rho_0)^{1/2}$ and $\gamma = 5/3$. The pressure perturbation δp is related to the mass density perturbation $\delta\rho$ via $\delta p = v_s^2\delta\rho$, where $v_s = (\gamma p_0/\rho_0)^{1/2}$ is the sound speed. Following the way of solving the above set of equations developed in Ref. [4], after Fourier transforming all perturbed quantities $\propto g(x)\exp(-i\omega t + ikz)$, we derive two coupled second order differential equations for δv_x and δv_y. All other perturbed quantities are expressed in terms of δv_x and δv_y. By applying the boundary conditions for continuity of $\delta v_x/(\omega - \mathbf{k} \cdot \mathbf{v}_0)$, the full perturbed pressure δp_{total} (kinetic + magnetic), the y-component of perturbed wave electric field δE_y, and the x-component of perturbed electric displacement $\delta D_x = \varepsilon_0\,(K_{xx}\delta E_x + K_{xy}\delta E_y)$ (where K_{xx} and K_{xy} are the low-frequency components of the plasma dielectric tensor [5]) at the interfaces, we arrive at the dispersion relations of Hall-MHD sausage and kink surface waves presented symbolically in the form

$$\mathcal{D}\,(\omega, k, v_0, B_0, l_{\text{Hall}}, x_0, \beta, \rho_o, \rho_e) = 0.$$

Solving numerically the waves' dispersion relations we get the wave phase velocity ω/k (being Doppler-shifted inside the slab), normalized with respect to the Alfvén speed v_{Ao}, as a function of the dimensionless wave number kx_0 with four entry parameters, notably the ratio $\rho_o/\rho_e = 4$, the plasma $\beta = 1$, the ratio $l_{\text{Hall}}/x_0 = 0.4$, and the Alfvén Mach number v_0/v_{Ao} lying in the range 7–8 (because the steady flow velocity v_0 is not a constant, but swinging around the aforementioned value of 400 km s^{-1}).

3. Results and discussion

It is well known that sausage and kink surface waves are normal modes of a spatially bounded MHD flux tube. For a flowing plasma slab one can distinguish two kind of waves: forward and backward ones assuming that the positive direction is defined by the steady flow velocity $\mathbf{v}_0$. Figures 1 and 2 show the dispersion curves of forward sausage and kink waves.
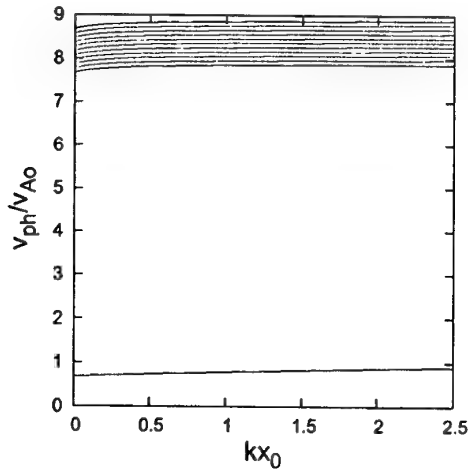
Figure 1: Forward Hall-MHD sausage waves
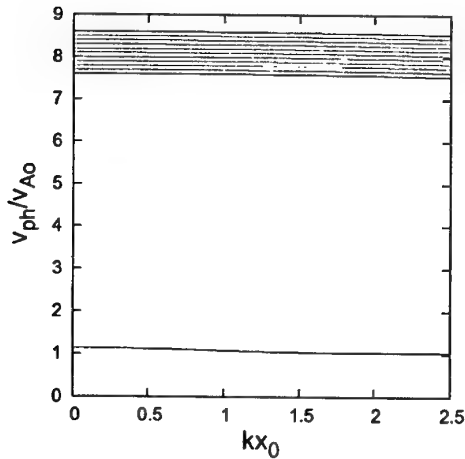
Figure 2: Forward Hall-MHD kink waves

Next two figures 3 and 4 present the dispersion characteristics of backward waves. It is seen, first, that all waves, being Alfvén waves without flow, become super Alfvénic ones with flow. Second, the dispersion of forward waves is slightly modified with small kx_0's by the flow speed while that of the backward waves is visibly changed for large dimensionless wave numbers. Moreover, the phase velocity of each surface wave can be presented in the form [6]

$$\frac{\omega}{k} = \frac{\rho_o}{\rho_o + \rho_e} v_0 \pm \text{Hall-MHD } v_{ph},$$
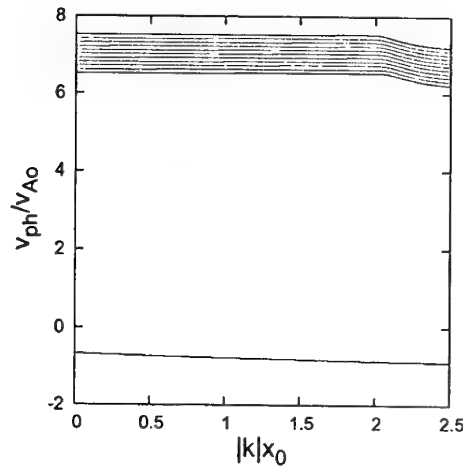
Figure 3: Backward Hall-MHD sausage waves
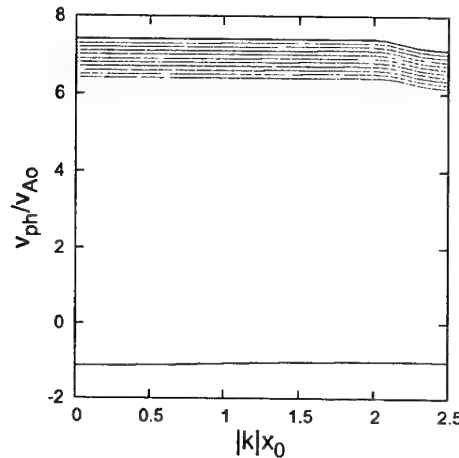
Figure 4: Backward Hall-MHD kink waves

where Hall-MHD v_{ph} is the phase velocity which the wave possesses in an immovable plasma slab.

4. References

[1] C. Vocks, U. Motschmann, K.-H. Glassmeter. *Ann. Geophysicae* **17** (1999) 712.

[2] J.D. Huba, *Phys. Plasmas* **2** (1995) 2504.

[3] C.-Y. Tu, E. Marsch, *Space Sci. Rev.* **73** (1995) 1.

[4] I. Zhelyazkov, A. Debosscher, M. Goossens, *Phys. Plasmas* **3** (1996) 4346.

[5] D.G. Swanson, *Plasma Waves* (Academic Press, San Diego, 1989), p. 53.

[6] S. Chandrasekhar, *Hydrodynamic and Hydromagnetic Stability* (Oxford University Press, Oxford, 1960).

A new explanation of the instability of high intensity discharge operated in high frequency

Yang Zheng Ming Chai Guo Sheng   Zhang Ming

R&D center for special light sources of Guang Dong Province
Bright Star Light & Electricity Ind.Co.,Ltd.

Abstract

Analysed the irrationality of so called "acoustic resonance" theory,that was suggested forty years ago to explain the instability of high frequency arc generated in high intensity discharge lamp. Presented a new idea that the ion oscillation in plasma is the culprit of instability of high frequency arc.

1.Introduction

The arc instability of high intensity discharge (HID) generated in high pressure lamp with high frequency operation was studied for forty years[1, 2, 3, 4, 5, 6, 7]. Researchers found that the high pressure xenon lamp and all other high pressure discharge device were unstable while it is operated in high frequency from decade KHz to few hundred KHz, they also found that a kind of acoustic wave always accompanied with instable high frequency arc and the frequency of acoustic wave is always double of discharge. The brightness and all other parameters such as current and potential drop of unstable arc were also fluctuated with a frequency around few to decade Hz, mean while the arc was curved and shivered.

All researchers and papers published explain the above phenomena in a same way . All of them firmly believe the theory of so called" acoustic resonance" effect. The main points of this theory is as following:

Inside the high frequency operated discharge tube gas is heated intermittent by arc with a frequency double of discharge. Gas is heated by input current while it is positive or negative peak ,but it is condensed while discharge polarity change because of zero input power, then the partical wave or said pressure wave is created. This is the reason of acoustical wave generating. If the acoustical wave is resonate with the wall of arc tube, then a standing wave forms and the discharge become unstable. The resonate frequency lower the amplitude of standing wave bigger and the discharge instability more serious. For the lowest resonate frequency that means the half of acoustic wave length is just equal to the diameter of arc tube, perhaps the arc will be extinguished or even broken the arc tube because of acoustic wave resonance .

In the past forty years especially last fifteen years.,the arc instability was a main barrier for developing the high frequency electronic ballast for metal halide lamps. Experts did their best to overcome the problem of so called "acoustic resonance" ,but not successful.

2. The theory of acoustic resonance is not correct

Our research find that the theory of acoustic resonance is not correct to explain the phenomemon of instability of high frequency arc.

2.1 Gas temperature can not be changed with the frequency double of arc

Inside a operating high frequency arc tube the gas temperature is from 1000K near tube wall to 6000K at the core of arc and the gas pressure is around 20 bar. As a medium with very high pressure and very high temperature the heating capacity of plasma gas is very large. It is not easy to change the temperature within a short time catch up with discharge frequency. In fact , the temperature of gas inside a operating arc tube is almost keep constant without obvious fluctuation even while discharge polarity change .

2.2 Acoustic wave is only found from the instable arc but not stable one

The acoustic wave is only found from instable arc,but never discovered from a stable arc. If according to the theory of acoustic resonance,This kind of pressure wave should be always generated from any kind of high frequency arc either stable or not because of the alternating input power. This is an evidence to prove that the acoustic wave is not caused by gas temperature fluctuation but from other sources, the temperature fluctuation of high frequency arc can be neglected even if exist .

According to the theory of acoustic resonance, the temperature fluctuation and also the amplituede of pressure wave of high frequency arc should be bigger for lower frequency discharge, but researchers did not found

this kind of wave from an arc which the frequency is below 2KHz and all arc below this frequency is always very stable. This is another evidence proving that the temperature fluctuation can be neglected .

2.3 Parameters fluctuation of instable arc is only few Hz

According to the theory of acoustic resonance, the frequency of acoustic wave is double of discharge. Usually the arc instability is only found in the frequency range from few KHz to few hundred KHz. But the fluctuation of arc brightness and other discharge parameters of an instable arc is discovered only few times per second and changes all the time. It is not found any relations between acoustic wave and brightness fluctuation from any instable arc .

3. A new explanation of instability of high frequency arc

The main points of the new explanation for high frequency arc instability we suggest are as follow:

3.1 Acoustic wave is not exist in a stable arc

No one find acoustical wave form a stable arc even it is operated in high frequency and no one find obvious temperature fluctuation from it,even it is heated by high frequency input power.
Even acoustic wave radiate from an unstable arc, but it still is not found temperature fluctuation with the frequency double of discharge.

3.2 Instability of high frequency arc is caused by plasma oscillation

Plasma oscillation is the source of acoustical wave and causes arc instable. For a DC discharge or a discharge the frequency below 2KHz the plasma oscillation is a random process, it attenuated very fast because of collisions with atoms [8] .But for high frequency discharge the ion oscillations will respond with field and amplified by it, if the frequency of ion oscillation is resonant with field ,then a stable ion oscillation appear. The frequency of ion oscillation is just equal to the field frequency inside discharge. The huge number of ions oscillated together and accompanied by huge number of atoms because of momentum transfer by collions between them must create a pressure wave .This is the acoustic wave found for forty years, and it is only a product of ion oscillation could be found from instable arc but not the culprit of arc instability.
Ion oscillation is the culprit which causes arc instable. In a arc ions and electron will separated because of ion

oscillation, then the different part of the arc will charged to different polarity , the force between the different parts of the arc and the wall of tube lost balance , the path of arc will be curved and shivered because of the positive part and negative parts of arc shift in the space. This is the reason which causes discharge parameters and brightness fluctuation.

3.3 Ion oscillation creats acoustical wave

Obversly,the acoustical wave is created by ion oscillation but not temperature fluctuation. This is the reason why it is only found from an unstable plasma ,but not stable arc.

4 . Conclusion

Arc instability of high frequency discharge can not be explained by the so called "Acoustic Resonance" theory. But it is very easy described by the idea of ion oscillation, and also some experiments about arc instability are matched with the theory of ion oscillation very well. The only way to overcome the difficulty of arc instability is to control the process of ion oscillation,but not the resonant conditions between acoustic wave and arc tube shape.

Reference:

[1] Gallo C F, Courtnet J E. *Acoustical resonances in modulated xenon and krypton compact arc lamps.*Applied Optics, (1967) 6 (5): 939

[2] Schafer R, Stormberg H P. *Investigations on the fundamental longitudinal acoustic resonance of high pressure discharge lamp.* J Appl Phys, (1978) 49 (5):2680

[3] Gallo C F, Lama W L. *Acoustical resonances in modulated compact arc lamps.* Applied Optics, (1977) 16 (4): 819

[4] Witting H L.*Acoustic resonances in cylindrical high pressure arc discharge.* J Appl Phys,(1978) 49 (5): 2680

[5] Daveport J M, Petti R J. *Acoustic resonance phenomena in low wattage metal halide lamps.* Journal of IES, April (1985):633

[6] Wada S, Okada A, Morii S. *Study of HID lamps with reduced acoustic resonances.* Journal of IES,Winter (1987):162

[7] Hans-Juergen Faehnrich, Erhard Rasch.*Electronic ballast for metal halide lamps.* Journal of IES, Summer (1988):131

[8] Gordon Francis.*Ionization Phenomena in Gases.* (1960):249

Moving striations in a low-pressure argon plane discharge. Self-consistent kinetic model

A.V. Fedoseev, G.I. Sukhinin

Institute of Thermophysics, Novosibirsk, 630090, Russia

In the paper, a self-consistent iterative kinetic model of stratified low-pressure argon glow discharge in plane geometry is presented. It is shown that striations moving from the anode to the cathode side of the positive column can be obtained from the consideration of non-local Boltzmann equation for electron distribution function and non-stationary continuity equation for ions coupled with Poisson equation for electric field.

1. Introduction

It is known that the positive column of a low-pressure glow discharge in inert gases often exists in a stratified form. Usually striations manifest themselves as moving waves. There were a lot of attempts to describe this phenomenon (see, for example, [1]). However, in most papers stratification was considered under the assumption of quasineutrality of the positive column, and the electric field was introduced from some additional consideration without taking into account the Poisson equation.

The stratification of a discharge is a collective phenomenon of mutual influence of electron and ion plasma components. In the paper, electron kinetics is considered on the basis of non-local Boltzmann equation coupled with the non-stationary ion balance equation and Poisson equation.

2. Model

A plane low-pressure discharge (p<1 Torr) is considered in self-consistent way. The influence of edge effects is neglected and the electric field is assumed to be axial.

The non-local Boltzmann equation in two-term approximation for the isotropic part of electron energy distribution function (EEDF) written in total energy–space coordinate representation was used:

$$\frac{\partial}{\partial z}\left[\frac{U}{3H(U)}\frac{\partial}{\partial z}f_0(\varepsilon,z)\right] = \frac{\partial}{\partial \varepsilon}\left[2\frac{m}{M}U^2 N_g Q^d(U)f_0(\varepsilon,z)\right] + \sum_k UN_g Q_k^{in}(U)f_0(\varepsilon,z) - \sum_k (U+U_k^{in})N_g Q_k^{in}(U+U_k)f_0(\varepsilon+U_k^{in},z),$$ (1)

where N_g is gas density, U is kinetic energy of electron, $\varepsilon = U - e_0\varphi(z)$ is total electron energy, $\varphi(z)$ is potential distribution in the positive column (PC) of the plane discharge between the edge of the PC (z = 0 cm) and the anode (z=20 cm).

For ions, the non-stationary continuity equation in the drift approximation was considered:

$$\frac{\partial n_i}{\partial t} + \frac{\partial}{\partial z}(n_i \mu_i E) = n_e v_I,$$ (2)

$v_I(z)$ is the direct ionization frequency, which in this paper is omitted, μ_i is ion mobility coefficient.

The coupling of the electron and ion components is provided by the Poisson equation for self-consistent electric field

$$\frac{\partial E_z}{\partial z} = 4\pi e_0(n_i - n_e),$$ (3)

For the solution of the system (1-3), the iterative numerical procedure was used. To obtain the first approximation of distribution function $f_0^0(z,U)$, the parabolic equation (1) was solved as an initial boundary value problem from higher to lower total energies in some proposed electric field $E^0(z)$. The numerical code is based on the solution of tridiagonal linear system of discrete form of Eq. 1, which is analogous to the Crank-Nikolson scheme [2]. Usually the constant field was chosen as the initial one. From the $f_0^0(z,U)$, the electron density distribution $n_e^0(z)$ was obtained. With the help of Eqs.(2-3), a new approximation of electric field $E(z)$ was found, and the procedure was repeated until successive iterations of the electric field were converged. Usually ten iterations were enough for the procedure convergence. The final axial electric field distribution $E(z)$ did not depend on the initial approximation $E_0(z)$.

3. Results

As a result of numerical calculations, spatial evolution of the isotropic part of EEDF was obtained (see, Fig.1).
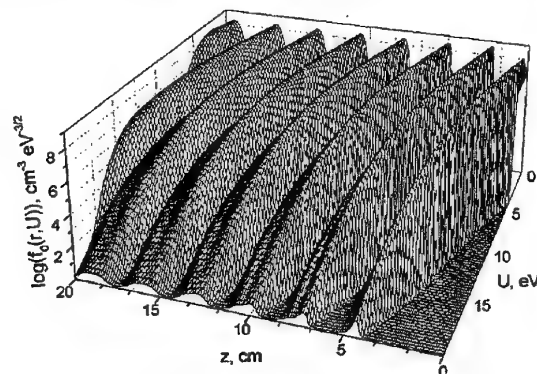
Fig.1. Three-dimensional representation of the isotropic EEDF starting from the cathode side edge (z=0) of PC toward the anode (averaged electric field E=4 V/cm, p=0.5 Torr).

141

It was found that the iterative process is converging only for the case of moving striations. In plane discharge, the solution for ion density and electric field were looked for in the form $n_i = n_i(v_i t - z)$, $E = E(v_i t - z)$, with the striation velocity $v_i = \alpha \mu_i E_0$, $0 < \alpha < 1$.

The velocities of moving striation have the value of averaged ion drift velocity, $v_i = \alpha \mu_i E_0$, with parameter $0 < \alpha < 1$. For $\alpha \leq 0.25$ the used iterative procedure does not converge. With the increase of $\alpha > 0.25$, the peaks of electric field in striations are decreased.

In Fig. 2, an example of self-consistent field distribution is presented. It is seen that electric field distribution has non-sinusoidal peak-like structure. The electron density distribution is almost in anti-phase with respect to electric field.
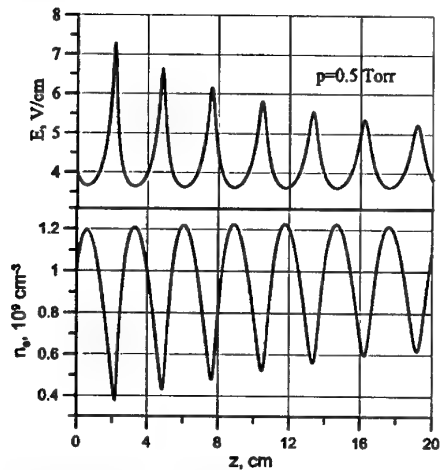
Fig.2. Electric field and electron density distributions in plane striated argon glow discharge ($\alpha=0.5$).

It is found that for argon pressures p>1.5 Torr striations are damped due to energy losses in elastic collisions. For lower pressures, elastic losses result in small decay of striations to the anode side of PC.
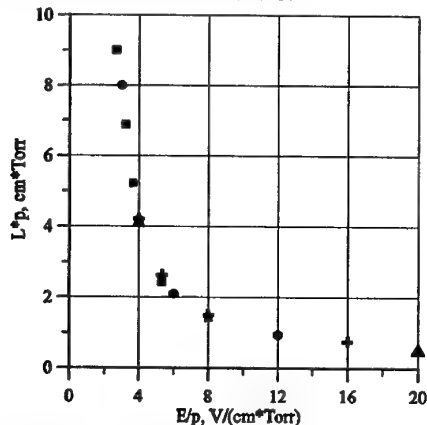
Fig.3. Striation length dependence on reduced electric field in plane glow discharge.

In Fig.3, the dependence of striation length on reduced electric field is shown. Results calculated for different argon pressures and electric fields fall into the unified curve. For given E/p, the striation length is inversely proportional to gas pressure, $L \sim 1/p$. The length L slightly exceeds the minimal length necessary for an electron to attain the first excitation threshold $L > U_1/e_0 E_0$.

In Fig. 4, the distribution of volume charge is shown for averaged field $E=4$ V/cm and p = 0.5 Torr. It is seen that double layers are formed in stratified PC. Relative deviation from the quasineutrality has the order of 10^{-2}-10^{-3}.
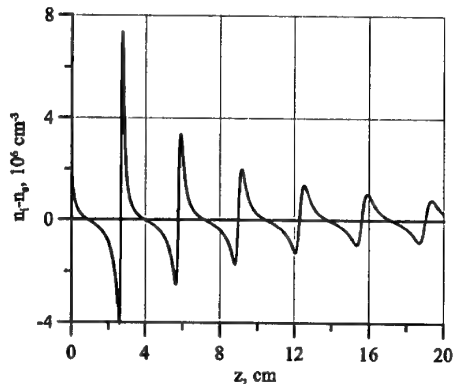
Fig.4. Volume charge distribution in stratified PC.

4. Conclusions

It this paper, a self-consistent model of moving striation in argon is presented. Non-local Boltzmann equation, non-stationary ion balance equation, and Poisson equation were considered simultaneously with the help of iterative procedure.

It was found that for low-pressure gas conditions the stratified regimes cannot be realized for the case of standing striations. However, consideration of moving striations permits us to receive a converged solution of the problem. Only the moving striations with the velocities directed from the anode to the cathode adjust the phase shifts between electric field and electron density distribution. The resonant amplification of peaks of distributions takes place.

The presented kinetic model is applied for low-pressure inert gases. At intermediate pressures, the stepwise ionization from metastable states should be taking into account. In this case, system of Eqs.(1-3) has to be supplemented with corresponding balance equation for matastable particles

5. References

[1] Yu. B. Golubovskii et al. *Plasma Sources Sci. Technol.* **11** (2002) 309.
[2] F.Sigeneger, R. Winkler, Contrib. Plasma Phys. **36** (1996) 551.

Self-consistent kinetic approach to stratified regimes of a low-pressure spherical discharge

G.I. Sukhinin, A.V. Fedoseev

Institute of Thermophysics, Novosibirsk, 630090, Russia

A spherical glow discharge with a central point-like anode has been studied in self-consistent kinetic approach. The model includes non-local Boltzmann equation coupled with non-stationary ion balance equation, and Poisson equation for radial electric field. For low-pressure argon, the model permits to obtain moving striations in a spherical glow discharge.

1. Introduction

Spherical striations were observed in low-pressure glow discharge around point-like anode [1]. It was found that for different discharge conditions the radii of striations in a positive column of discharge obey relationship $r_{k+1}/r_k \approx$ const (geometric series) or $r_{k+1} - r_k \approx$ const (arithmetical progression). The reason for such different behavior of spherical striations is not clear yet. In [2], spherical striations were modeled in a given peak-like electric field. However, the solution of [2] was not self-consistent.

In the paper, this problem is studded on the basis of non-local Boltzmann equation for electron distribution function coupled with non-stationary balance equation for ions, and Poisson equation for self-consistent electric field.

2. Model

The model includes:

1. The non-local Boltzmann equation in two-term approximation for isotropic part of electron energy distribution function (EEDF) written in "total energy–space coordinate (radius from point-like anode)" representation:

$$\frac{1}{r^2}\frac{\partial}{\partial r}\left[\frac{r^2 U}{3H(U)}\frac{\partial}{\partial r}f_0(\varepsilon,r)\right] =$$
$$\frac{\partial}{\partial\varepsilon}\left[2\frac{m}{M}U^2 N_g Q^d(U)f_0(\varepsilon,r)\right] + \quad (1)$$
$$\sum_i UN_g Q_k^{in}(U)f_0(\varepsilon,r) -$$
$$\sum_i (U+U_k^{in})N_g Q_k^{in}(U+U_k)f_0(\varepsilon+U_k^{in},r)$$

where N_g is gas density, U is kinetic energy of electron, $\varepsilon=U-e_0\varphi(r)$ is total electron energy, $\varphi(r)$ is radial dependence of spherical discharge potential in the positive column (PC), $E(r)=-\partial\varphi/\partial r$ is electric field in the positive column of a spherical discharge. Eq. (1) is parabolic equations with source terms representing elastic, inelastic and ionizing electron-atom collisions.

2. The non-stationary continuity equation in drift approximation for ions

$$\frac{\partial n_i}{\partial t} + \frac{1}{r^2}\frac{\partial}{\partial r}(r^2 n_i \mu_i E) = n_e v_I, \quad (2)$$

$v_I(r)$ is the direct ionization frequency, μ_i is ion mobility coefficient.

3. Poisson equation for self-consistent electric field:

$$\frac{1}{r^2}\frac{\partial(r^2 E(r))}{\partial r} = 4\pi e_0 (n_i - n_e). \quad (3)$$

The solution of the system (1-3) was looked for in the region from the edge (r=R) of the positive column to the central anode with appropriate boundary conditions.

The iterative numerical procedure for the solution of the striation problem is used. At the first step, in order to obtain the first approximation of distribution function $f_0^0(r,U)$, the parabolic equation (1) is solved in some proposed electric field $E^0(r)$. From the $f_0^0(r,U)$, the electron density distribution $n_e^0(r)$ and the ionization frequency $v_I^0(r)$ are obtained. With the help of Eqs.(2-3), new approximation of electric field $E(r)$ is found and the procedure is repeated until successive iterations of electric field are converged. Usually ten iterations are enough for the procedure convergence, and the final electric field distribution $E(r)$ does not depend on the initial approximation of $E_0(r)$. However, the voltage drop is kept constant.

3. Results

It was found that the iterative process is converging only in the case of moving striations. In spherical discharge, the solution for ion density and electric field are looked for in the form

$$n_i(t,r) = n_i^0\left(\frac{R}{r}\right)^\beta \bar{n}_i\left(v_i^0 t - \frac{R}{(3-\beta)}\left(\frac{r}{R}\right)^{3-\beta}\right) \quad (4)$$

$$E(t,r) = E^0\left(\frac{R}{r}\right)^{2-\beta} \bar{E}\left(v_i^0 t - \frac{R}{(3-\beta)}\left(\frac{r}{R}\right)^{3-\beta}\right) \quad (5)$$

where n_i^0 and E^0 are characteristic values of ion density and electric field at r=R, $\bar{n}_i(t,r)$ and $\bar{E}(t,r)$ are dimensionless functions presenting waves moving with the phase velocity $v_{st} = v_i^0(r/R)^{2-\beta}$, the constant $v_i^0 = \alpha\mu_i E^0$ has the order of ion drift velocity. It should be noted that for $\alpha<0.25$ (standing striations corresponds to $\alpha=0$) the iterative process is not converged. Below all results are presented for $\alpha=0.5$. In the general case, parameter β can be in the range $\beta=1$-2. For $\beta=2$, average field and striation velocity v_{st} are constant. Ion and electron densities vary inversely proportional to the square of the distance r from the anode. Such dependencies were obtained in drift-diffusion

approximation of a spherical glow discharge [3]. For $\beta=1$, the average electric field and densities n_i, n_e vary inversely proportional to r. In this case, the striation velocity decreases with the increase of the distance from the anode.

In Fig. 1, an example of self-consistent field distribution and electron density is presented for argon pressure p=0.5 Torr. It is seen that average electric field is modulated by several non-equidistant striation peaks.
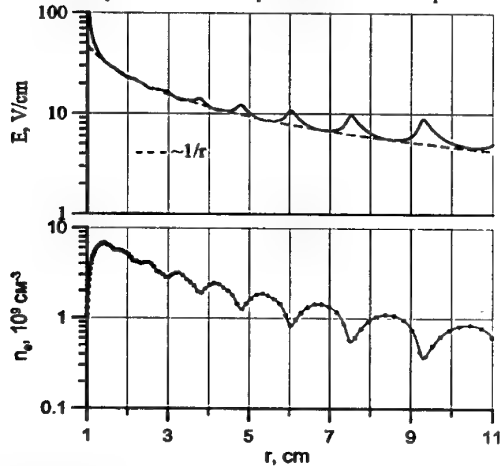
Fig.1. Electric field and electron density radial distributions in spherical striated glow discharge for $\beta=1$, p=0.5 Torr.

The radii of striation obey the geometric series law $r_n \approx r_1 \beta^n$ (see, Fig. 2). Such dependence was observed in experiments [1] (however, not for argon but for the mixture of N_2 with small addition of acetone).
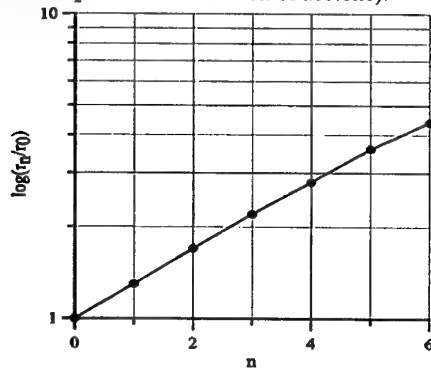
Fig.2. Dependence of striation radii r_n on the number of striation, n, for the case $\beta=1$.

According to the energy balance equation

$$\frac{1}{r^2}\frac{d}{dr}(r^2 j_{er}(r)) = P^f(r) - P^{el}(r) - \sum_k P^{in}_k(r) \qquad (6)$$

the difference between energy gain from the electric field $P^f(r)$ and the energy loss in elastic $P^{el}(r)$ and all inelastic collisions $P^{in}_k(r)$ is compensated for by the spatial divergence of the energy current density, see Fig.3. It is seen that there is a phase shift between the maximum of energy gain in the field and maximum of

energy losses in the inelastic collisions, which, in fact, stimulates the propagation of waves (moving striations).
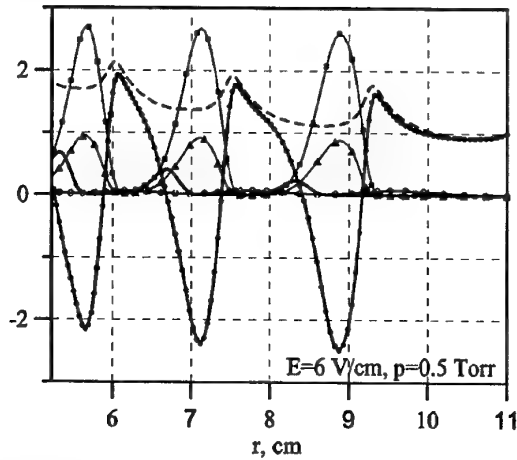
Fig.3. Normalized energy balance terms. ●●●● divergence term, - - - - gain from electric field, ⊖⊖⊖ loss by elastic collisions, ■■■ loss by excitation $E_1=11.27$ eV, ▲▲▲ loss by excitation $E_2=11.7$ eV, solid line - loss by ionization $E_i=15.7$ eV.

4. Conclusions

A spherical glow discharge has been studied in self-consistent kinetic consideration of moving striations.

It is shown that two types of plasma parameters distributions are possible in a stratified spherical discharge: 1) constant averaged field in the spherical discharge gap and electron density $n_e(r)\sim r^{-2}$ with peaks due to striations, and 2) averaged field and electron density are inversely proportional to the distance from the anode. Both regimes were observed in experiments. It is still not clear why real system in PC of spherical glow discharge chooses one of these alternatives.

The presented kinetic model is applied for low-pressure inert gases. For the pressures p>1.5 Torr striation are damped due to energy losses in elastic collisions. In these cases, it is necessary to take into account the excitation of molecule metastable levels and radiative processes.

Special attention should be paid to ionization and recombination processes, which equalize creation and loss of charged particle on the striation length.

5. References

[1] O.A.Nerushev, S.A.Novopashin, V.V.Radchenko, G.I.Sukhinin, *JETF Letters* **66** (1997) 711.
[2] F. Sigeneger, G.I. Sukhinin, R. Winkler, *Plasma Chemistry and Plasma Processing* **20** (2000) 87.
[3] G.I. Sukhinin, A.V. Fedoseev, *ICPIG-2003*.

144

Auto-oscillations of a spherical glow discharge in drift-diffusion approximation

G.I.Sukhinin, A.V. Fedoseev

Institute of Thermophysics, Prospect Lavrentyev, 1, Novosibirsk, 630090, Russia

A spherical glow in low-pressure nitrogen for transition from abnormal to Townsend regimes of a spherical discharge has been studied. The model includes non-stationary drift-diffusion equations for electrons and ions coupled with Poisson equation for radial electric field. The auto-oscillations of plasma parameters are obtained.

1. Introduction

A spherical discharge was observed for the first time in 1997 [1]. It was realized in the gap between a central point-like anode and surrounding it cathode.

This paper presents the drift-diffusion numerical study of a spherical glow discharge in nitrogen in a wide range of gas pressures and electric circuit parameters. Oscillating regimes were obtained for transition regimes from abnormal to Townsend discharge forms.

2.Model

A volume spherical discharge was studied in the drift-diffusion approximation. Non-stationary balance equations for electrons and ions were used:

$$\frac{\partial n_e}{\partial t} + \frac{1}{r^2}\frac{\partial(r^2 n_e u_e)}{\partial r} = \left|n_e u_e\right| N\alpha_{ion}(E/N) - \beta_{rec}n_e n_i , \qquad (1)$$

$$\frac{\partial n_i}{\partial t} + \frac{1}{r^2}\frac{\partial(r^2 n_i u_i)}{\partial r} = \left|n_e u_e\right| N\alpha_{ion}(E/N) - \beta_{rec}n_e n_i , \qquad (2)$$

where $E(r)$ is the radial course of the electric field, N is gas density, β_{rec} is two-body dissociative recombination coefficient in $e+N_2^+ \rightarrow 2N$ collision, α_{ion} is ionization coefficient,. Electron and ion fluxes are presented by drift and diffusion terms:

$$n_e u_e = -\mu_e E n_e - D_e \frac{\partial n_e}{\partial r}; \quad n_i u_i = \mu_i E n_i - D_i \frac{\partial n_i}{\partial r}, \quad (3)$$

The ionization and diffusion coefficients, electron and ion drift velocities, $W_{e,i}=\mu_{e,i}E$, were taken in the local field approximation. The electric field was obtained from the Poisson equation:

$$-\frac{1}{r^2}\frac{\partial}{\partial r}(r^2 \frac{\partial \varphi}{\partial r}) = 4\pi e(n_i - n_e), \quad E(r) = -\frac{\partial \varphi}{\partial r}, \quad (4)$$

Equations (1-4) were solved as the initial problem with boundary conditions for electron and ion fluxes at the cathode and anode. At the initial time step, small electron and ion densities ($\sim 10^4 cm^{-3}$) were set equal to each other, and the Coulomb's distribution was set for the initial radial distribution of the electric field.

In the model, it was assumed that a spherical discharge covers the entire cathode surface (abnormal regime of a glow discharge, subnormal and Townsend discharges). For the numerical solution of Eqs.(1-4), an implicit finite difference scheme was used. As boundary conditions for the Poisson equation, there was used discharge potential U_{dis}, which was recalculated with the help of the Ohm law: $U_{dc}=U_{dis}-RJ_c$, where U_{ps} is the

potential of power supply, R is the active resistance of external electric circuit and J_c is the conduction current at the cathode.

3. Results

Calculations were carried out for different gas pressures ($0.1 \le p \le 3.5$ Torr) and parameters of electric circuit (U_{ps}=1-3.5 kV, R=10-25 kΩ). Radius of the central anode was fixed (a=1cm), the radius of the spherical cathode was R_c=12.5 cm. These parameters correspond to conditions of [1] in which spherical stratification of glow discharge was observed.

As a result of numerical calculations the radial distributions of electron, ion, and bulk charge densities, electric field and potential of discharge were obtained.
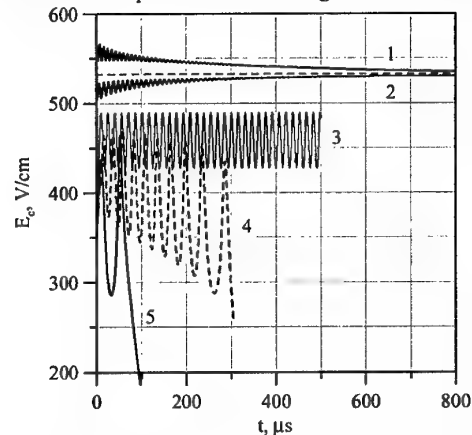
Fig.1. Relaxation (1-2) of electric field at the cathode (R_c=25cm) for different $\Delta U_{ps} = U_{ps}^*(p) - U_{ps}$ and auto-oscillation (3) Decaying regimes (curves 4-5) p=3.5 Torr, and different power supply voltages U_{ps}.

It was found that steady state conditions in abnormal regimes of the spherical glow discharges were formed if sufficient voltage of power supply U_{ps} was applied. In this case, after sudden change U_{ps}, decaying transitional oscillation of all plasma parameters to new stable conditions arose. In Fig.1, the example of such relaxation from two different initial values of power supply is shown. The curves 1 and 2 present transition from U_{ps}=1500V and U_{ps}=1350V to U_{ps}=1400V, correspondently. It is seen that the system (for transitions from different initial states) works out the

steady state condition, which corresponds to the new voltage of power supply.

For small supply voltage U_{ps} (smaller than some critical value U_{ps}^*) at a given gas density, a spherical discharge turns into auto-oscillating (self-maintaining) regimes or into decaying modes. For critical value U_{ps}^*, almost sinusoidal oscillation of electric field and conduction current are realized.

It should be stressed that the critical voltage U_{ps}^* is realized only for gas pressures higher than some critical value p* depending on the radius of spherical discharge R_c. For spherical discharge gap R_c=12.5 cm and active resistance of external electric circuit R=20 kΩ, the critical values are p*≈1.9 Torr and U_{ps}^* ≈ 800 V. The oscillation frequency for this case is f ≈ 30 kHz. For higher gas pressure p=3.5 Torr, U_{ps}^* ≈1250V, f = 60 kHz. This regime is shown in Fig.1 (curve 3).

Frequencies of oscillations correspond to the time of ions move from the center of cathode fall to the cathode surface where they cause secondary emission of electrons.

In Fig.2, radial distributions of electric field for oscillating regime of a spherical discharge at different moments are presented (U_{ps}=1.25kV, p=3.5 Torr). It is seen that the amplitude of electric field changes considerably in every point of discharge gap.
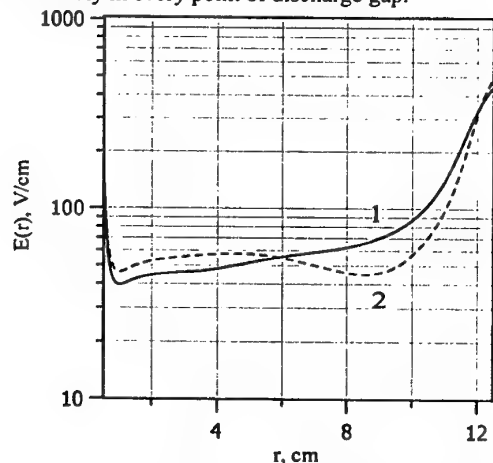
Fig.2. Radial distributions of electric field at two different moments 1 and 2 with interval Δt=12,5 μs, corresponding to anti-phase of oscillation.

It was found that for some regimes with $U_{ps} < U_{ps}^*(p)$ the second oscillating mode appeared. The frequency of this mode is two times smaller than the first one. The amplitude of this additional mode increased with the increase of $\Delta U_{ps} = U_{ps}^*(p) - U_{ps}$. The example of such a bifurcation is presented in Fig.3 for p=4 Torr, U_{ps}^* =1300 V, ΔU_{ps} = 25 V.

The nature of such complex oscillations is connected with the "breathing" of the width of cathode layer.

For larger ΔU_{ps}, the oscillating processes become aperiodic, and a discharge turns into the decaying mode (see, Fig.1, curves 4-5).
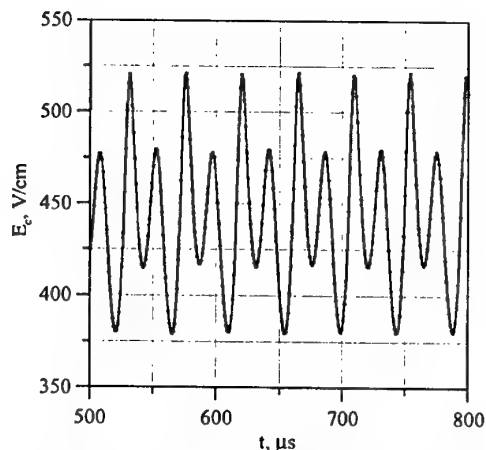
Fig.3. Bifurcation of the period of electric field oscillations $E_c(t)$ at the cathode. The curve is superposition of two modes with frequencies f_1 ≈ 45.5 kHz, f_2 ≈ 22.7 kHz, and amplitudes E_1 ≈52 V/cm, E_2 ≈27 V/cm.

4. Conclusions

A DC spherical glow discharge has been studied by means of self-consistent drift-diffusion approximation in a wide range of gas pressure and electric circuit parameters.

In transition regime between abnormal and Townsend regimes of discharge burning, auto-oscillating and decaying modes were obtained. All discharge parameters (conduction current, ion and electron densities, and electric field) oscillated in the whole range of the spherical discharge gap with the frequencies f~10-100 kHz.

The nature of such oscillations is connected with the periodical ionization of molecules in the cathode sheath by electron impact, drift of ions to the cathode surface and secondary emission of electrons from the cathode.

In certain cases, the bifurcation of the main mode of oscillation was obtained. The second oscillating mode with two time smaller frequency appeared due to the doubling of the cathode layer width during one half of the oscillation period.

Similar oscillations have been observed in the experiments (see, for example [2]) in the transition region from Townsend discharge to a glow discharge.

5. References

[1] O.A.Nerushev, S.A.Novopashin, V.V.Radchenko, G.I.Sukhinin, *JETF Letters* **66** (1997) 711.

[2] V.N.Melekhin et al., *Sov. Phys. Tech.* **32** (1987) 274.

Acknowledgements

Resonance effects of the electron distribution function formation in spatially periodic fields

Yu.B. Golubovskii[†], R.V. Kozakov[‡], C. Wilke[‡], J. Behnke[‡] and V. Nekutchaev[§]

[†] Saint-Petersburg State University, ul. Uljanovskaja, 1, 198504, Russian Federation

[‡] Insitute of Physics, University Greifswald, Domstr., 10a, 17489, Germany

[§] Ukhta Industrial State University, ul. Senjukova 13, Ukhta, 167300, Russian Federation

Calculations of the election energy distribution function (EEDF) in the striation-like sine modulated electric field are performed. Dependence on a spatial period length was investigated. Calculations were made for discharge conditions pR=2 Torr cm and i/R= 5 mA/cm and electric field E/p= 1.9 V/cmTorr. The presence of the resonances on the EEDF and macroscopic parameters are demonstrated. These resonances correspond to S- and P- striations that could be observed in experiments. The interpretation of the results, based on the analytical approximation of the numerical solution is proposed.

1. Introduction

Resonant EEDF formation in the spatially periodic electric fields occurs in the case when electron energy balance is governed by inelastic processes and the energy losses in elastic collisions over the period length are negligible. This kind of energy balance occurs in gas discharges at small currents and low pressures in inert gases.

Resonant EEDF formation was investigated in several papers. Analytical solution of the Boltzman equation was obtained in paper [1]. It was shown that the relaxation process of an arbitrary initial EEDF in the homogeneous electric field has a form of damped oscillations with energy period $U_{res} = U_{ex} + \Delta U$ and spatial period $L_{res} = U_{res}/E_0$, where U_{ex} is the excitation energy, ΔU is the small energy losses in elastic collisions and E_0 is the period-averaged electric field.

In spatially periodic electric field the EEDF is formed which depends resonantly on the value of spatial period [2]. EEDF has a specific maximum whose formation was explained as bunching effect due to the small energy losses in elastic collisions [1] and due to the presence of several excited states [3].

Present work is devoted to the analysis of the EEDF formation in the spatially periodic electric fields, study of the resonance behaviour of the EEDF and their interpretation.

2. EEDF in the spatially periodic electric fields

2.1 Kinetic equation

Boltzman equation for the isotropic part of the distribution function f_0 in variables of total energy $\varepsilon = U + e\varphi(x)$ and space coordinate x, where U is the kinetic energy and $e\varphi(x)$ is the potential energy of the electron, can be written as

$$\frac{\partial}{\partial x} D_\varepsilon(v) \frac{\partial f_0(\varepsilon, x)}{\partial x} + \frac{\partial}{\partial \varepsilon} V_\varepsilon(v) f_0(\varepsilon, x)$$
$$= v\nu^*(v) f_0(\varepsilon, x) - v'\nu^*(v') f_0(\varepsilon + U_{ex}, x) \quad (1)$$

where $D_\varepsilon = v^3/3\nu(v)$, $V_\varepsilon = 2m^2\nu(v)v^3/M$, $\nu^*(v)$ is the total frequency of inelastic processes and $\nu(v)$ is the frequency of elastic collisions. Velocities v and v' are related by the energy conservation law $mv'^2/2 = mv^2/2 + U_{ex}$. For numerical analysis of the equation (1) it has to be completed by the appropriate boundary conditions

$$f_0(\varepsilon, x)|_{U \to \infty} = 0 \qquad \left.\frac{\partial f_0(\varepsilon, x)}{\partial x}\right|_{U=0} = 0 \quad (2)$$

2.2 Calculation procedure

Equation (1) with the boundary conditions (2) was solved numerically by Cranc-Nicolson algorithm [4]. Calculations were performed for the electric fields with modulation degree $\alpha = 0.9$ and value of mean electric field $E_0 = 1.9\,V/cm$ which corresponds to the discharge conditions under the pressure $p = 2.0\,Torr$ and current $I = 10\,mA$. First it was solved for the case of the homogeneous electric field E_0 in order to obtain the value of the resonance spatial period L_{res} which was found to be equal $9.8\,cm$. Then equation (1) was solved for the different values of the spatial period L in the range $4 - 12\,cm$ which includes values of the first $L = L_{res}$ and second $L = L_{res}/2$ resonances. The values of the frequencies of the inelastic processes were increased by two orders of magnitude in order to obtain sharper resonance behaviour of the EEDF.

2.3 Results of the calculations

As the numerical analysis was performed for the increased values of the inelastic frequencies, the solution strives to that in the "black wall" approximation with the zero boundary condition at the excitation threshold $f_0(\varepsilon, x)|_{U=U_{ex}} = 0$. Results of the calculations near the first resonance are shown in figure 1. It is seen that at $L = L_{res}$ the EEDF has a strong modulation which decreases at other values of L. Analytical solution of (1) under "black wall" approximation could be obtained [1] in the form of series expansion relative to the small parameter
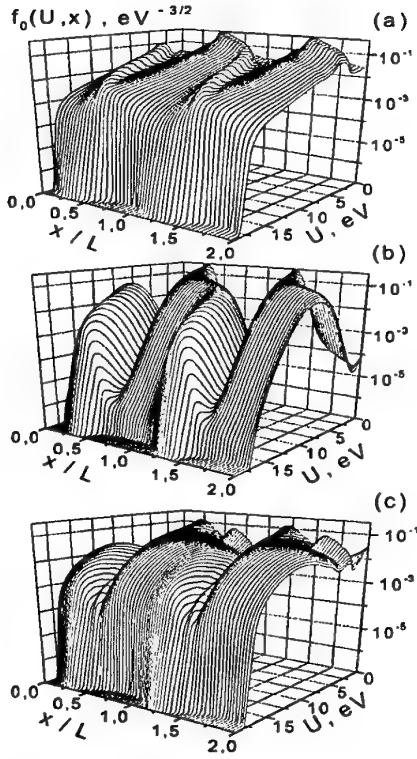
Figure 1: EEDFs calculated in the spatially periodic electric fields with modulation degree $\alpha = 0.9$ for the values of spatial period: (a) $L = 0.9L_{res}$, (b) $L = L_{res}$ and (c) $L = 1.1L_{res}$.

$\delta = 6m^2\nu^2(v_1)U_{ex}/(M(eE_0)^2)$ as follows

$$f_0(\varepsilon, x) = \sum_{i=0} f_0^{(i)}(\varepsilon, x)\delta^i \tag{3}$$

The main term of the expansion (3) can be written as

$$f_0^{(0)} = \Phi(\varepsilon) \int_x^{x_{ex}(\varepsilon)} \frac{dx}{D_\varepsilon} \equiv \Phi(\varepsilon)F(\varepsilon, x) \tag{4}$$

where $\Phi(\varepsilon)$ is the amplitude of the distribution function and $F(\varepsilon, x)$ is the function which is formed in given electric fields when the losses in elastic collisions are neglected.

Accurate numerical solution of equation (1) could be approximated by expression (4). In this case the amplitude $\Phi(\varepsilon)$ can be obtained from the expression

$$\Phi(\varepsilon) = \frac{f_0(\varepsilon, x)}{F(\varepsilon, x)}$$

where $f_0(\varepsilon, x)$ is the strict numerical solution in electric fields with different spatial periods L and $F(\varepsilon, x)$ is given by expression (4).
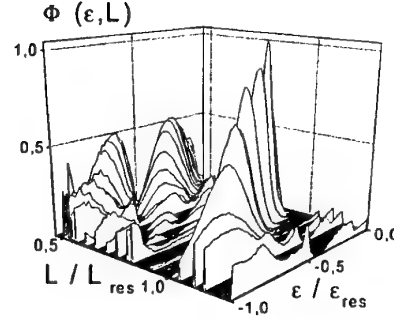
Figure 2: Amplitude of the distribution function $\Phi(\varepsilon)$ calculated for different values of spatial period L.

It is seen from figure 2 that $\Phi(\varepsilon)$ depends resonantly on the value of the spatial period L of electric field.

3. Linear theory of the EEDF formation in weakly modulated periodic electric fields

In the electric fields with small modulation degree an analytical approach to solution of the kinetic equation is possible [1]. It can be shown that the EEDF depends resonantly on the value of the spatial period L. The dependence of the periodic part of the amplitude $\tilde{\Phi}^{(0)}(k)$ on the value of the spatial period L can be written as

$$\tilde{\Phi}^{(0)}(k) = \Phi_{hom}^{(0)} \frac{-ik\beta}{\exp\left(ik(1+\delta A)\right) - 1 + \delta^2\mathcal{B}k^2}$$

where $\Phi_{hom}^{(0)}$ is the amplitude of the EEDF in homogeneous field, $k = 2\pi L_{res}/L$ is the dimensionless wavenumber and β, A, $\mathcal{B}$ are the parameters dependent on the modulation degree of the electric field.

4. Acknowledgements

5. References

[1] L.D. Tsendin, *Sov. Fiz. Pl.* **2** (1982).

[2] F. Sigeneger and R. Winkler, *Plasma Chem. Plasma Process.* **4** (2001) 429.

[3] F. Sigeneger, Yu.B. Golubovski, I.A. Porokhova, and R. Winkler, *Plasma Chem. Plasma Process.* **18** (1998) 153.

[4] R. Winkler, G. Petrov, F. Sigeneger and D. Uhrlandt, *Plasma Sources Sci. Technol.* **6** (1997) 118.

148

The parametric instability of the cyclotron radiation in the absence of resonant particles

M.A. Erukhimova, M.D. Tokman

IAP RAS, Nizhny Novgorod, Russia

The effect of the simultaneous amplification of two waves due to their parametric cyclotron interaction with modulated ensemble of nonresonant particles is investigated. The mechanism of energy exchange between field and particles in this effect is analyzed.

1. Introduction

This work continues theoretical investigations of unusual regimes of generation of coherent radiation by ensembles of classical charged particles started a few years ago. In these new regimes the simultaneous amplification of two HF waves is provided by their parametric cyclotron interaction with modulated electron ensemble which is stable against generation of these waves separately. The main interest was attracted by so-called maser without inversion (MWI) [1]-[4],-classical analog of quantum effect of inversionless amplification [5].

This paper is devoted to the investigation of another interesting regime of such parametric instability. It is the amplification of bichromatic cyclotron radiation in the absence of resonant particles [2]. The second regime in contrast to the first one where the amplification mechanism corresponds to the parametric interaction with modulated *active* susceptibility can be named as the amplification in *reactive* medium.

2. The model

The effect of amplification of coherent radiation by ensemble of nonresonant particles was revealed in paper [2]. In that particular scheme two Brilluin components of the waveguide mode with the same transverse structure (with respect to the constant magnetic field $\mathbf{B} = \mathbf{z_0}B_0$) and different (but close) frequencies $\mathbf{E} = \mathbf{y_0}\sum_{j=1}^{2} ReE_j exp\left(ik_\perp x + ik_{||j}z - i\omega_j t - i\frac{\pi}{2}\right)$, that are resonant to the electrons with momentum components $p_{||}^R$, $p_\perp^R$ at the first harmonic of the cyclotron frequency $\omega_j = eB_0/mc\gamma_R + k_{||j}v_{||}^R$, interact with ensemble of electrons with momentum components close (but not equal) to the resonant values. The electron ensemble is described by the unperturbed distribution function, modulated on the longitudinal coordinate at the initial moment providing the parametric coupling of HF waves

$$f = f_0\left(p_{||}, p_\perp^2/2\right) +$$
$$f_M\left(p_{||}, p_\perp^2/2\right)cos\left(\varphi_M + \left(k_{||1} - k_{||2}\right)z\right).$$

The analysis in [2] based on linearised kinetic equation in truncated variables has shown that due to the specific dependence of synchronism detunings on

momentum which takes into account both relativistic cyclotron detuning and Doppler shift:

$$\Delta_j = \omega_j - eB_0/mc\gamma - k_{||j}v_{||},$$

it is possible to set such modulation of distribution function, that Δ_1 and Δ_2 oscillate in opposite phase. The dependence $f_M\left(p_{||}, p_\perp^2/2\right)$ must be the antisymmetric function of $\left(p_{||} - p_{||}^R\right)$. As consequence the oscillations of corresponding susceptibilities (medium responses on the first and second field) will be "antiphase". Then if all particles are out of the resonance with waves (there is no partial synchronism), i.e.

$$\Delta_j\left(p_{||}, p_\perp\right)t \gg 1 \tag{1}$$

but there is parametric synchronism

$$\left(k_{||1} - k_{||2}\right)\left(v_{||} - v_{||}^R\right)t \ll 1 \tag{2}$$

the parametric coupling of two waves will assume their simultaneous amplification. The linear increment of such amplification is found in [2].

3. The mechanism of energy exchange

The results of previous analysis [2] do not make clear the mechanism of energy exchange between bichromatic field and "nonresonant". Note that this effect is accompanied by amplification of two waves simultaneously but not by scattering from the field of one frequency to another, as in standard induced scattering. In order to clarify the mechanism of energy exchange in investigated process we solve nonlinear equations of particle motion going to the accompanying frame of references where the frequencies of two waves are equal. Note that in this system the standard induced scattering is accompanied by no energy exchange with the medium.

Consider two circulary polarized waves propagating along the constant magnetic wave. The electric and magnetic field can be written as:

$$\mathbf{E} = Ree_+E(z)e^{-i\omega t}, \mathbf{B} = Ree_+B(z)e^{-i\omega t} + B_0\mathbf{z_0}$$
$$E(z) = E_0\left(e^{ikz} + e^{-i\varphi - ikz}\right), \mathbf{e_+} = \mathbf{x_0} + i\mathbf{y_0}.$$

Consider the relativistic equations of particle motion in this field

$$\dot{\mathbf{p}} = Re\left(-eE(z)\mathbf{e_+}e^{-i\omega t} - \frac{e}{c}\left[\mathbf{v}, B(z)\mathbf{e_+}e^{-i\omega t} + B\mathbf{z_0}\right]\right)$$
$$\dot{\mathbf{r}} = \mathbf{v} = \frac{\mathbf{p}}{m\gamma}.$$

Suppose that momentum components of relativistic particles are close to the resonant values so that resonant parameter is large:

$$R = |v_\perp|^2 \, \omega/c^2 \Delta_0 \gg 1,$$

and Doppler shift is much smaller that cyclotron detuning:

$$kv_\| \ll \Delta_0,$$

where $\Delta_0 = \omega - eB_0/mc\gamma$.

Since the electron is not resonant to the field (condition (1)), the electron makes large number of oscillations in the wave, so its motion can be presented as superposition of slow part and term oscillating in the wave field: $\mathbf{p} = \left(P_\| + \tilde{p}_\|\right)\mathbf{z_0} + Re\left(P_\perp + \tilde{p}_\perp\right)\mathbf{e}_+ exp\left(-i\left(eB_0/mc\gamma_0\right)t\right)$.

We develop the theory of perturbations with respect to the wave amplitude, which is set to be rather small so that $\omega\left|\tilde{v}_\|\right|/\Delta_0 c \ll 1$. We finally obtain the expression for the evolution of electron energy averaged over large number of oscillations in wave field in the square approximation:

$$\frac{d}{dt}\langle w\rangle = \frac{1}{2m\gamma_R}\left(\frac{d}{dt}|P_\perp|^2 + \frac{d}{dt}\left\langle|\tilde{p}_\perp|^2\right\rangle + \frac{d}{dt}P_\|^2 + \frac{d}{dt}\left\langle\tilde{p}_\|^2\right\rangle\right).$$

It can be found that the change of transverse energy is $4\omega/\Delta_0 \gg 1$ times larger than change of longitudinal energy. In tern averaged transverse energy consists of energy of gyrorotations $w_\perp^{gr}$ and averaged oscillatory energy $w_\perp^{osc}$. Their time derivatives

$$\frac{d}{dt}w_\perp^{gr} \propto \left(-R^2 + 2R\left|\frac{V_{\perp 0}}{c}\right|^2 - 2R\right)\left(V_{\|0}\frac{\partial|E|^2(Z(t))}{\partial Z}\right)$$
$$\frac{d}{dt}\langle w_\perp^{osc}\rangle \propto \left(R^2 - 2R\left|\frac{V_{\perp 0}}{c}\right|^2 - 2R\right)\left(V_{\|0}\frac{\partial|E|^2(Z(t))}{\partial Z}\right)$$

approximately compensate each other. The remainder of this compensation defines the change of full electron energy:

$$\frac{d}{dt}\langle w\rangle = -\frac{\omega}{\Delta_0^3}\frac{e^2}{m\gamma_0}\frac{|V_{\perp 0}|^2}{c^2}\left(V_{\|0}\frac{\partial}{\partial Z}|E|^2\left(Z(t)\right)\right) \quad (3)$$

The sign of energy change is constant if $kV_\| t < \pi$ (condition (2)). This sign depends on the sign of synchronism detuning Δ_0. If $\Delta_0 > 0$ the energy of particle decreases if it moves in direction of stronger field. In this case the decrease of energy of gyro-rotations prevails over increase of averaged oscillatory energy. If $\Delta_0 < 0$ the situation is opposite.

Now the role of modulation of electron ensemble on the longitudinal momentum becomes obvious. If at every position Z electrons moves with the same longitudinal velocity number of electrons receiving and losing energy are equal. But setting the initial modulation on z of longitudinal velocity of electrons in ensemble in correspondence with spatial dependence of field amplitude, so that $\varphi_0 = \varphi_M + \frac{\pi}{2} + \pi Sign\left(\Delta_0\right)$, the decrease of the energy of electron ensemble due to its interaction with nonresonant wave field is obtained.

Note that the expression (3) is correct for relativistic particle, moving in the field of standing wave and constant magnetic field. In the absence of magnetic field the motion of nonrelativistic particle is accompanied by the conservation of its full energy. So in this system this mechanism of parametric amplification can not be realized. But if magnetic field is not zero the full energy of nonrelativistic electron changes in correspondence with conservation law for the sum of kinetic energy and the energy of interaction between magnetic moment of oscillating in wave field electron and magnetic field. So the effect of amplification without resonant particles is realized also in this more simple situation. But the analysis of this effect for different ensembles of electrons has shown that the presented here system with relativistic particles close to resonance seems to be the most perspective for possible applications, since it is important to compare the energy contributed by electrons to the amplified HF radiation with energy input necessary for preparation of initial modulation.

4. Conclusion

In the conclusion let us underline the principal difference between the investigated regime of parametric amplification "without resonance" and the standard induced scattering. It is important that in the considered here effect the time of interaction must be restricted by condition (2), i.e. all particles must stay in the parametric synchronism with the waves during interaction. The condition (2) in particular leads to breaking of the low of conservation of photon number in the interaction process, i.e. to the breaking of the Manley-Rowe relation, which forbids such amplification process at the infinite time of interaction.

5. References

[1] Gaponov-Grekhov A.V., Tokman M.D., *JETP* **85** (1997) 640.

[2] Erukhimova M.A., Tokman M.D., *JETP* **91** (2000) 255.

[3] Erukhimova M.A., Tokman M.D., *Radiophysics and Quant. Electr.* **44** (2001) 176.

[4] Erukhimova M.A., Tokman M.D., *Plasma Phys.Reps.* **27** (2001) 868.

[5] Kocharovskaya O., *Phys.Rep.* **219** (1992) 175.

Effect of ion-parallel viscosity on the propagation of Alfvén surface waves

Nagendra Kumar and Himanshu Sikka

Department of Mathematics, K.G.K.(P.G.) College, Moradabad-244001 (U.P.) India

The paper analyzes the damping of the Alfvén surface waves via ion parallel viscosity at a single magnetic interface. The dispersion relation is obtained and characteristics curves are drawn for the real and imaginary phase speeds. The modes thus obtained are two damped Alfvén modes propagating in a way such that when one mode dies new mode appears after a certain propagation gap. The results are applicable for the situation in solar wind at AU for values obtained from the spacecraft data.

1. Introduction

Alfvén waves have been widely discussed in space plasma and their ubiquitous presence in the solar wind was demonstrated by [1]. They lose energy as they propagate outward from the Sun. If we consider solar wind as the part of the corona we can undoubtfully say that Alfvén waves lead to coronal heating. The wave damping in solar wind is not well understood. In what follows we study the viscous damping of Alfvén surface waves propagating at the magnetic interface in the solar wind. The Braginskii viscosity ([2], [3], [4] and [5]) is a tensor with terms η_0, η_1, η_2, describing viscous dissipation and terms proportional to η_3 and η_4 as nondissipative and describe wave dispersion related to the finite ion gyroradius. Since $\omega_{ci}\tau_i$ can typically be of the order of 10^6 in the solar wind, where ω_{ci} is the ion cyclotron frequency and τ_i is the ion collision time, the term η_0 'parallel viscosity' becomes far more important than all other terms.

2. Basic equations

We consider an incompressible and viscous magneto-fluid of uniform density under the assumption, when $\omega_c\tau \gg 1$. Since the viscous dissipation is dominated by the term proportional to ion-parallel viscosity, conventionally denoted by η_0^i, the viscous term gets reduced to ([6] and [7])

$$-\eta_0^i \nabla \cdot [(I - 3\hat{\mathbf{B}}\hat{\mathbf{B}})\hat{\mathbf{B}}\hat{\mathbf{B}} : \nabla \mathbf{v}], \qquad (1)$$

where $\hat{\mathbf{B}}$ is a unit vector in the direction of magnetic field. In terms of cartesian coordinates equation (1) simplifies to

$$+\eta_0^i \left(-\frac{\partial^2}{\partial x \partial z}, -\frac{\partial^2}{\partial y \partial z}, 2\frac{\partial^2}{\partial z^2}\right) v_z = \eta_0^i \mathbf{D} v_z. \qquad (2)$$

Taking the mass density to be uniform and constant, the associated kinematic viscosity coefficient is $\nu_{ion} = \eta_0^i/\rho$.

The relevant linearized incompressible MHD set of equations when the viscous dissipation is dominative by the term proportional to ion parallel viscosity, are

$$\frac{\partial \mathbf{v}}{\partial t} = -\nabla p^T + \frac{1}{4\pi\rho}(\mathbf{B}_0 \cdot \nabla)\mathbf{b} + \nu_{ion}\mathbf{D}v_z, \qquad (3)$$

$$\frac{\partial \mathbf{b}}{\partial t} = \mathbf{B}_0 \cdot \nabla \mathbf{v}, \qquad (4)$$

$$\nabla \cdot \mathbf{v} = 0, \nabla \cdot \mathbf{b} = 0, \qquad (5)$$

where $\mathbf{B}_0 = B_0\hat{z}$; $\mathbf{v}$ and $\mathbf{b}$ are the perturbed velocity and magnetic field, and p^T is the total pressure (plasma and magnetic).

Equations (3)-(5) can be Fourier-analysed, assuming all perturbed quantities $\alpha\, g(x)\exp(-i\omega t + ik_z)$ i.e. $\partial/\partial t = -i\omega, \partial/\partial x \neq 0, \partial/\partial y = 0$, and $\partial/\partial z = ik_z$, to obtain the second order differential equation for the $x-$ component of velocity, v_x,

$$\frac{d^2}{dx^2}v_x - m^2 v_x = 0, \qquad (6)$$

where

$$m^2 = \frac{\omega^2 - k_z^2 v_A^2}{\omega^2 - k_z^2 v_A^2 + 3i\omega\nu_{ion}k_z^2}.$$

We consider plasma media occupying half spaces $x < 0$ and $x > 0$. The solution to equation (6) in the respective regions $x < 0$ and $x > 0$ is given by

$$v_{xo} = A_o e^{m_o x}, \quad x < 0, \qquad (7)$$

$$v_{xe} = A_e e^{-m_e x}, \quad x > 0, \qquad (8)$$

where A_o and A_e are arbitrary constants and subscripts 'o' and 'e' stand for the regions $x < 0$ and $x > 0$ respectively. We have imposed the conditions $m_o > 0$ and $m_e > 0$, and $v_x \to 0$ as $x \to \pm\infty$ to represent surface waves. Across the interface $x = 0$, we impose the boundary conditions that the normal component of velocity v_x and total pressure p^T (gas plus magnetic) must be continuous.

3. Dispersion relation and Discussion

Using the boundary conditions, we derive the dispersion relation in normalized form for the surface waves

$$(x^2 - 1 + 2ixV_0)^2 r^2 m_0^2 = m_e^2(x^2 - a_{Ae}^2 + 2ixV_e)^2, \qquad (9)$$

where

$$x = \frac{\omega}{k_z v_{Ao}}, \quad V_0 = \frac{\nu_{ion,o}k_z}{v_{Ao}}, \quad V_e = \frac{\nu_{ion,e}k_z}{v_{Ae}},$$

$$a_{Ae} = v_{Ae}/v_{Ao}, \quad r = \frac{\rho_o^2}{\rho_e^2},$$

151

$$m_o^2 = k_z^2 \frac{(x^2 - 1)}{x^2 - 1 + 3ixV_o},$$

and

$$m_c^2 = k_z^2 \frac{(x^2 - a_{Ae}^2)}{x^2 - a_{Ae}^2 + 3ixV_c}.$$

Here $\nu_{ion,o}$ and $\nu_{ion,e}$ are the kinematic viscosity co-efficients, and v_{Ae} and v_{Ao} are the Alfvén velocities on either side of the interface. In the absence of ion-parallel viscosity, the dispersion relation reduces to

$$\frac{\omega^2}{k^2} = \frac{\rho_o v_{Ao}^2 + \rho_c v_{Ae}^2}{\rho_o + \rho_c} \qquad (10)$$

which is the well known dispersion relation for Alfvén surface waves in an incompressible fluid. In order to know the nature of waves in our case we need to study the equation (9). On setting $V_e = \alpha V_{o,,}$ where $\alpha = \frac{\nu_{ion,e}}{\nu_{ion,o}}$, we solve numerically the dispersion relation (9) for phase speeds as a function of V_0 in the context of a situation in solar wind at 1 AU. The ratio of current plasma densities on either side of the interface, ρ_0/ρ_c is taken 0.2. The values of real and imaginary phase speeds are obtained from the values of x in units of v_{A0}. Figs. 1 and 2 show the variations of real and imaginary phase speeds with the parameter V_0 for $r = 0.04$, $a_{Ae} = 0.44$ and $\alpha = 0.5$. It is evident from the figures that the Alfvén surface waves propagating along the interface are damped waves. It is also found that there are only two damped modes of Alfvén surface waves which do not propagate simultaneously; the later mode propagates with slower speed than previous one. It is seen from figure 1 that the speed of Alfvén surface wave decreases as ion-parallel viscosity increases. This wave becomes evanescent at a critical value of $V_0=0.55$. After the disappearance of this mode a new second mode arises from 0.6 whose phase speed decreases with the increase in the value of the parameter V_0. It is also notable that there is a small region from $V_0 = 0.55$ to 0.6 where there is no propagation of either of the wave. This region is called a non propagation region. Figure 2 depicts the damping rate of the wave with the parameter V_0. Damping of the mode increases as V_0 increases but decreases after the value of 0.9. Thus the modes of surface waves become damped owing to ion-parallel viscosity in an incompressible fluid.

Acknowledgements

References

[1] J.W. Belcher and L. Davis, *J. of Geophys. Res.*, **76** (1971) 3534.

[2] S.I. Braginskii, *Transport Processes in Plasmas, Rev. Plasma Phys.* **1** (1965) 205
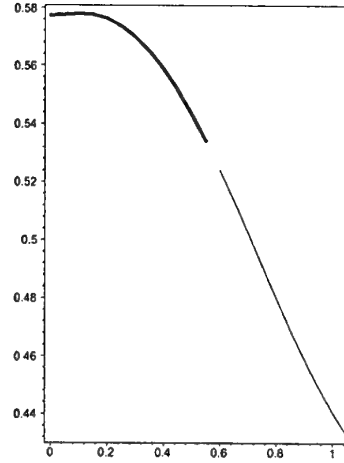
Figure 1: Variation of real phase speeds ω_R/k with parameter V_0. Dark line represents first mode while light line represents second mode of Alfvén surface waves.
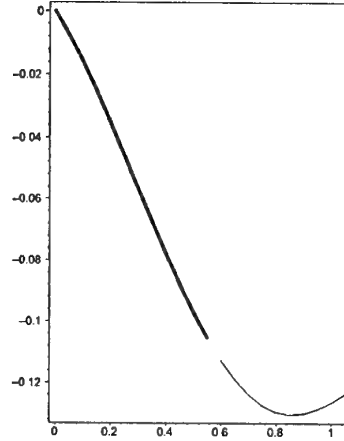
Figure 2: Variation of imaginary phase speeds ω_I/k with parameter V_0. Dark line represents first mode while light line represents second mode of Alfvén surface waves.

[3] R. Balescu, *Transport Processes in Plasmas*, North Holland, Amsterdam, **1** (1988) 247.

[4] D.L. Book, *NRL Plasma Formulary (Revised)*, U.S. Naval Research Laboratory, Washington, D.C. (1990).

[5] M.S. Ruderman, R. Oliver, R. Erdélyi, J.L. Ballester and M. Goossens, *Astron. Astrophys.*, **354** (2000) 261.

[6] D. Montgomery, *J. Geophys. Res.*, **97** (1992) 4309.

[7] S. Oughton, *J. Plasma Phys.*, **56** (1996) 641.

Temperature measurements in a shock wave created by a cutting plasma torch.

P. Freton, J.J. Gonzalez, A. Gleizes.

CPAT, UMR CNRS 5002, Université Paul Sabatier, 118, route de Narbonne, 31062 Toulouse cedex (France).
e-mail : freton@cpat.ups-tlse.fr

Abstract : This paper deals with the spectroscopic study of an oxygen plasma cutting torch. A particular attention is taken on the measurements in the shock wave created by this kind of configuration and an original method is presented for measuring temperature in this shock.

Introduction

Since ten year, cutting plasma processes try to rival with laser cutting systems. For this, a new plasma torch generation called "high energy density torch" [1] was developed by industrials in the middle of the nineties. This new generation of torch has very particular characteristics : a low current intensity (between 30 and 100A), a flat cathode, oxygen as plasma gas, very small nozzle diameter (around 1mm) and the plasma created is generally supersonic with the presence of a shock wave at the nozzle exit. Up to day engineering expertise based on observations of the cutting quality has allowed this process to progress. But now, more theoretical studies are needed for a better understanding of the arc behaviour. If some papers exist about "the traditional" plasma cutting systems [2][3], there are very few works about this new generation of torches[4]. This is probably due to the difficulties of making spectroscopic measurements in these cutting plasma especially in the wave shock zone.

In this communication, we purpose an original method for a spectroscopic study of this zone. Measurements are made on a torch commercialised by Air Liquide. We present first the studied configuration and the experimental set-up. After, the spectrum emitted by the plasma in the visible wavelengths is shown. The particular method is then proposed to determine the temperature and the electronic densities in the shock wave. Finally, measurement of the plasma temperature is proposed.

1 Experimental configuration

The system studied is an OCP150 torch. The diameter of the nozzle is equal to 1mm, the current intensity used for this paper is 60A. Oxygen is taken as plasma gas and injected through a swirl in top of a flat cathode situated in a pressure chamber. The arc discharges in air at atmospheric pressure. In a real cutting configuration, the metal piece to be cut is taken as anode and the distance between the nozzle exit and the workpiece is equal to few millimetres. With this short distance, spectroscopic measurements are difficult. Consequently, for practical considerations, the arc is transferred on the side of a rotating anode and stretched on 15mm. This configuration is presented on figure 1. It

enables us to make spectroscopic measurements. An optical system collects the light emitted by the plasma on the entry of a THR1000 Jobin Yvon monochromator. The light intensity is converted in an electrical signal by a 1024x128 Hamamatsu photodiode matrix. The optical system gives a magnitude of 2 and enables to analyse any points of the plasma in the radial and axial directions. With 128 pixels, we can obtain all the light emitted by a section of plasma of 1.5mm height. Measurements were performed with an inlet pressure of 4.2atm.
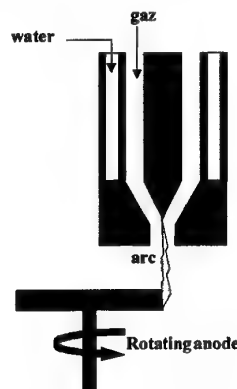
Figure 1 : Experimental configuration.

2 Spectral analysis of the light emitted by the arc

Before studying spectral emission of the plasma, an image of the arc created in the experimental configuration was obtained and enables us to situate the shock wave in an axial location between 0.5 and 2mm from the nozzle exit. This shock is due to the adaptation of the pressure in the chamber to the atmospheric pressure. Consequently, the light emitted on the axe of the plasma at 1mm from the nozzle was collected and the spectrum obtained is presented in figure 2. At low wavelengths, we can observe the presence of ionic lines of oxygen (between 4000 and 5000Å) whereas at upper wavelengths (6000-8500Å) only atomic lines are present. For spectroscopic analysis only the ionic line at 4647Å and atomic line at 6455Å are used. The line 6455Å is Stark widened

and can so be used for electronic densities determination[5].
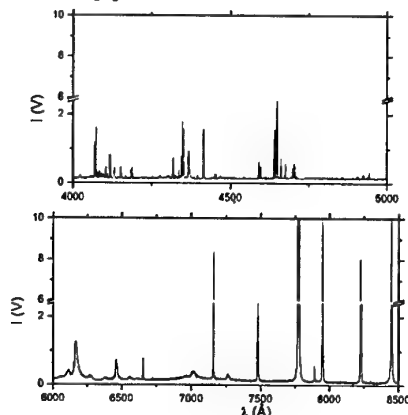
Figure 2 : Spectre of the light emitted by the arc in the shock zone.

3 Assumptions – method for the measure of the temperature

For spectroscopic measurements, we assume the plasma to be in LTE and to be optically thin for the wavelengths studied [6]. The local emissivity of the lines are determined from the Abel inversion. As the pressure of the plasma varies radially and axially and is unknown, the classical method of emission spectroscopy cannot be used. Instead, we purpose an iterative method for determining local temperature and local electronic densities :

-1- We assume a temperature T_0 and another $T_1=T_0+10K$.
-2- From the measurement of the ionic line intensity, and from the Boltzmann law, we determine the oxygen ion populations N^1_{O+} and N^0_{O+} at the respective temperature T_1 and T_0.
-3- From the experimental Stark broadening of the line 6455Å the electronic densities N^1_e and N^0_e at T_1 and T_0 are obtained.
-4- While $\left(N^1_{O+} - N^1_e\right)\cdot\left(N^0_{O+} - N^0_e\right)$ is positive, we increment by 10K T_0 and T_1 and go back on point 1 else the temperature sought is between T_0 and T_1.
This method does not depend on local composition and pressure and enables to determine the local temperature of the plasma. The electronic densities is also obtained.

4 Results

The field of temperature obtained between 0.5 and 2.1mm from the nozzle exit is presented in figure 3. We can quote the presence of local maximum of temperature on the axe. This maximum around 19400K is situated at the exit of the shock wave. It is due to the conservation of the

energy in the fluid. Effectively, at this location, there is a stagnation point, velocities of the plasma decrease and so temperature increases in order to conserve the total energy of fluid. Radially, the temperature decrease very quickly from 19000K on the axe to 15000K at 0.5mm. This denotes the very fine diameter of the plasma flow for a such cutting configuration.
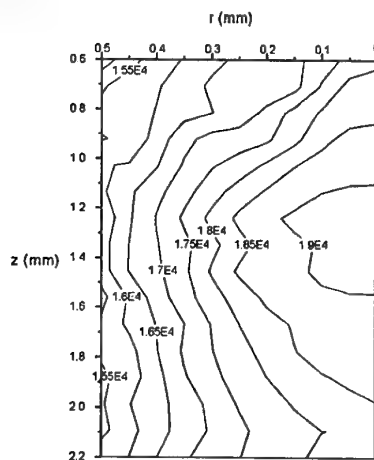
Figure 3 : Temperature (K) of the plasma in the shock wave zone.

Conclusion

A specific spectroscopic method for measuring temperature in the shock wave created by a cutting plasma torch is presented. This method, based on LTE consideration and electronic and ionic population measurements enables to estimate the local temperature of the plasma. A local maximum of the temperature equal to 19400K is fount on the axis.

References

[1] Swan, Washington University courses, USA www.tadda.wsu.edu/201/plasma2/history.htm.
[2] Nemchinsky V.A, J. Phys. D., (31), 21, (1998), pp3102-3107.
[3] Ramakrishnan S., Shrinet V., Polivka F.B., Kearney T.N. and P Koltum, J. phys. D., (33), 18, (2000), pp288-2299.
[4] Pardo C., Gonzalez Aguilar J., Rodriguez Yunta A. and Calderon M.A.G, J. phys. D., (32), 17, (1999), pp2181-2189.
[5] Wiese W.L. and Murphy P.W., Physical review, (131), 5, (1963), pp2108-2115.
[6] Boulos I., Pfender E., Fauchais P., « Thermal plasma, Fundamentals and applications », v1, Plenium Press-New york, (1994).

Electronic circuits during oscillations of an anode double layer

Valentin POHOAŢĂ, Gheorghe POPA, Roman SCHRITTWIESER* and Codrina IONIŢĂ *

Plasma Physics Department, "A. I. Cuza" University, Bd. Carol I No. 11, RO-6600 Iaşi, Romania
*Institute for Ion Physics, University of Innsbruck, Technikerstr.25, A-6020 Innsbruck, Austria

A so-called fireball is formed in front of a positively biased planar electrode (anode) inserted into a diffusive plasma produced by a multipolar confinement system. We have investigated the entire electronic circuit, through which the current is flowing during the nonlinear oscillations of the fireball. An annular ring electrode placed in front of the anode allows the identification of the ionic or electronic nature of the currents flowing through some parts of the circuits.

1. Introduction

A fireball (FB) is a localized zone of higher plasma density and luminosity, confined by an anode double layer (DL), which is produced by additional excitation and ionization processes due to electrons accelerated towards a positively biased electrode, immersed in a homogeneous low density plasma [1]. Recently, new results on the control of fireball oscillations have been reported [2], whereas the process of formation and the dynamic of these plasma formations was related to self-organisation processes [3]. Here we present experimental results about the electronic circuits involved in the oscillations of the fireball.

2. Experimental set-up
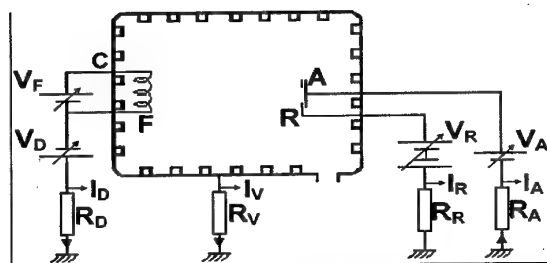
Fig. 1 *Schematic of the Iasi single multipolar confinement plasma machine. The Rd, Rv,Rr and R a are of the order of 10 ohm.*

The experiments were carried out in the multipolar plasma machine of the University of Iaşi (Fig.1). The cylindrical vessel has a diameter of 30 cm and 40 cm length. A diffusive argon plasma is produced by a hot cathode discharge inside a magnetic multiple polar confinement system, between the tungsten filament (F) as cathode (C) and the cylindrical wall as main anode. Operating parameters were: gas pressure $p = 10^{-3}$ mbar, discharge voltage $V_D = -50 \div -80$ V, discharge current within the range of $I_D = 10 \div 40$ mA.

Typical plasma parameters measured by both, Langmuir and emissive probes, were: plasma potential with respect to the grounded anode $V_p \cong +1.5$ V, plasma density in the range of $n = (1 \div 5) \times 10^8$ cm^{-3} and electron temperature $T_e = 1.5 \div 2$ eV. A plane Ta-electrode (A) with a diameter of 1 cm was inserted into the plasma and biased positively ($50 < V_A < 250$ V) to create the fireball.
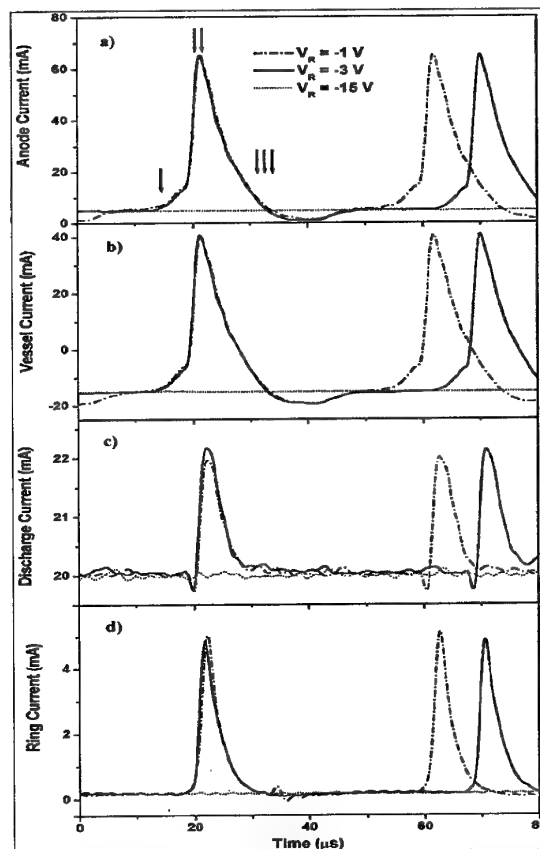
Fig. 2 *Typically time series of the oscillations of (a) the anode current I_A ; (b) the vessel current I_V (for the sake of clarity with inverted sign) (c) the plasma discharge current I_D and (d) the ring current I_R (ionic current) $V_A = 145$ V, $n = 1.5 \times 10^8$ cm^{-3}. For $V_R = -15$ V (dotted line) no fireball is formed and the plasma is stationary.*

An additional ring-shaped electrode R of 2.5 cm external diameter and 1 cm inner diameter was mounted concentrically 0.2 mm in front of the electrode A in order to control the oscillations [2] and to identify the nature of currents involved in the mechanism of the formation and dynamics of the fireball. Moreover, the experimental arrangement permits the electrical separation of the discharge vessel or main anode from ground so that also the vessel current I_V can be measured together

with the discharge current I_D, the anode current I_A and the ring current I_R, respectively.

3. Experimental results

Typical steady state (dotted lines) and oscillatory behaviours (full lines) of the currents I_A, I_V, I_D and I_R are presented in Fig. 2. They show a relaxation type oscillation, similar to that reported by Bin Song et al. [1], with the peak current (labelled II) being about one order of magnitude larger than the minimum (labelled I) of I_A. The oscillations are characterised by a fast increase (I to II), when the fireball is forming, and a slower decay (II to III) when it disappears.

In the steady state regime or during the minimum of the anode current (labelled as III in Fig. 2), when the conditions for the fireball formation are not given, the discharge works as a simple d.c. hot cathode discharge with two anodes: the electrode A and the discharge vessel (= main anode).
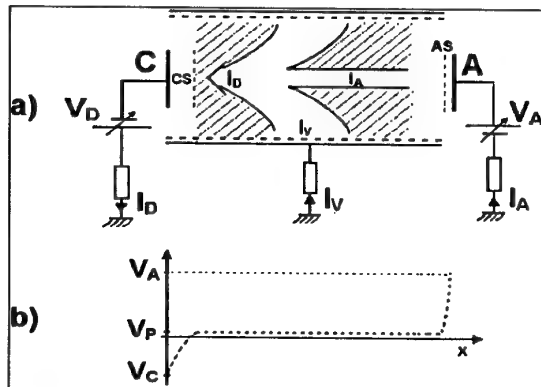
Fig. 3. *Schematic diagrams of the main currents (a) and of the axial potential profile (b) between the cathode C and anode A for a one-dimensional model for both, the steady state regime and the dynamic regime, without fireball (slow phase).*

The plasma is rather homogeneous in the chamber with a potential of about +1.5 V with respect to the main anode but separated from the hot cathode by the ion-rich space charge (CS) of the cathode fall and by a thin electron-rich space charge (AS) from the anode. The discharge current I_D, measured in the circuit of the cathode, is given by:

$$I_D = I_A + I_V, \tag{1}$$

where I_A is the current through the anode A and I_V is the current flowing through the main anode. A possible circuit, including the main anode and anode A is equivalent to a plane probe (anode A) biased positively with respect to the reference electrode (discharge vessel) and its current might be neglected with respect to the main discharge current.

During the fireball formation there is an important change in the electronic circuit. In Fig. 4 a schematic diagram is presented of the currents (a) flowing in the system during the maximum of the anode current I_A

during its oscillations, and of the corresponding potential profile (b).
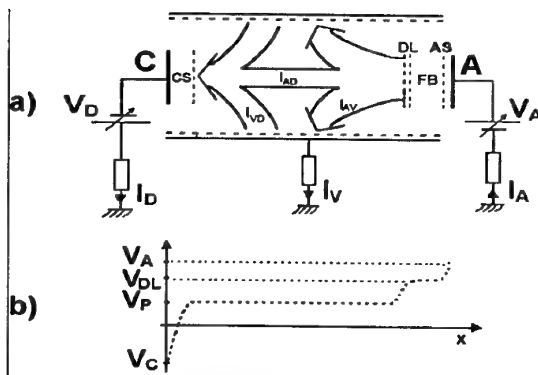
Fig. 4. *Schematic diagrams of the main currents (a) and of the axial potential profile between the cathode C and the anode A in one-dimensional model during the maximum of the anode current in the oscillatory regime. V_A, V_{DL}, V_P are the potentials of the anode A, of the plasma in the fireball region and of the main plasma region, respectively.*

In this case the fireball reaches its maximum spatial extension of about 7 cm in front of the anode [2], and the axial profile of the plasma potential corresponds qualitatively to Fig. 4b. In this case the electrons accelerated towards the anode A produce ionisations and excitations of the argon atoms so that the fireball region consists of a rather high density and luminosity plasma region, separated from the anode by a thin electron-rich sheath (AS) and from the main plasma by a double layer (DL). The potential drop across the latter ($V_{DP} - V_A$) is of the order of the ionisation potential of argon. Also important is the fact that during this stage the plasma potential in the main chamber increases significantly by some tens of volts so that the role of the discharge vessel is strongly changed. It might be considered as a cold cathode in a circuit which contains the anode A and the discharge vessel. In this case the main result is that equation (1) for the main discharge current remains valid but this time I_V is an ionic current as also the ring current I_R (Fig. 2d).

4. References

[1] Bin Song, N. D'Angelo and R.L. Merlino, *J. Phys. D: Appl. Phys.* **34**, 1789 (1991).

[2] V. Pohoață, G. Popa, R. Schrittwieser, C. Ioniță and P.C. Balan, *Proc. Joint Conf. ESCAMPIG 16 and ICRP 5* (Grenoble, France, 2002), Contr. Papers, vol. 2, p. 187.

[3] C. Avram, P.C. Balan, M. Sanduloviciu, R. Schrittwieser, *Proc. XXIVth Int. Conf. Phenomena in Ionized Gases* (Warsaw, Poland, 1999), Vol. I, p. 11.

Langmuir probe study of the floating potential fluctuations in the dc cylindrical magnetron discharge

P. Kudrna[1,2], M. Holík[1,2], O. Bilyk[1], A. Marek[1], J.F. Behnke[2], E. Martines[3], M. Tichý[1,2]

[1] Charles University in Prague, Faculty of Mathematics and Physics, Department of Electronics and Vacuum Physics, V Holešovičkách 2, 180 00 Prague, Czech Republic

[2] Ernst-Moritz-Arndt-University Greifswald, Institute of Physics, Domstrasse 10a, 17487 Greifswald, Germany

[3] Consorzio RFX, Associazione Euratom-ENEA sulla Fusione, corso Stati Uniti 4, 35127 Padova, Italy

The plasma potential fluctuations in the cylindrical magnetron discharge were measured using the Langmuir probes. The power density spectra were calculated in the range of magnetic fields 10 to 40 mT, pressures 1.5 to 7 Pa and discharge currents 100 and 200 mA.

1. Introduction

The cylindrical magnetrons are nowadays widely used as technological systems e.g. for creating thin films of superconductive or special magnetic properties. In the cylindrical magnetron the symmetry and homogeneity of the magnetic field simplifies both the theoretical and experimental investigations. In our previous experimental studies we already reported the presence of fluctuations of the plasma potential [1]. Fluctuations manifest as the unwanted noise added to the Langmuir probe voltage and in the increased noise of the measured current. The amplitude of the fluctuations significantly increases when the magnetic field increases above the value of approximately 20 mT. In this contribution the more detailed experimental study of the plasma potential fluctuations in our cylindrical magnetron system is presented.

2. Experimental system

Our construction is in more detail described in [2]. Briefly, the cylindrical magnetron is in the so-called post configuration and consists of cylindrical cathode mounted co-axially inside of the anode. The discharge volume is axially limited by means of two disc-shaped limiters, which are connected to the cathode potential. In our device the diameters of the cathode and anode are 18 mm and 60 mm respectively. The length of the discharge volume is 300 mm. The homogeneous magnetic field is created by six coils and is parallel with the common axis of the system. To prevent overheating both the coils and the cathode, they are water-cooled.

The system is constructed as high vacuum. The pumping unit consists of the combination of the turbomolecular and rotary pumps. The ultimate pressure is in the order of 10^{-3} Pa. During the experiments with the magnetron discharge the argon working gas slowly flows through the system at typical flow rate below 1 sccm (standard cubic centimetre per minute). The flow is adjusted by means of the MKS flow controller with the pressure signal at the reference input - thus keeping the constant pressure in the discharge chamber.

The system is equipped with 5 ports for inserting the Langmuir probes. Ports are distributed at the distances of 60 mm from each other along the discharge vessel.

The probes could be inserted radially into the system. For the purpose of measuring the frequency vs. wave number spectra we used a twin Langmuir probe with two tips separated by the distance 1.7 mm. The tungsten cylindrical probes had diameter 47 μm and length 2.5 mm. The probe tips were parallel and laid in the plane that was perpendicular to the magnetic field lines.

3. Estimation of the power spectra

The Langmuir probes were used without the bias voltage. That is, their floating potential signal was sampled using the digital oscilloscope (Tektronix TDS 520A) and samples h_n were transferred to the computer via the GPIB interface

$$h_n^{(i)} = h^{(i)}(n \cdot \Delta t), \qquad (1)$$

where $h^{(i)}(t)$ is the probe voltage with respect to the anode, Δt is the sampling interval and integer n ranges from 0 to the number of samples N-1. Superscript (i) denotes number of realisation (measurement). Then the discrete Fourier transform of the sampled data was calculated by means of the FFT (j represents imaginary unit):

$$H_m^{(i)} = \sum_{n=0}^{N-1} h_n^{(i)} \exp \frac{-2\pi j mn}{N}. \qquad (2)$$

The estimate of the Fourier transform of the voltage $h^{(i)}(t)$ at the discrete frequencies $m\Delta f$ is given by

$$H^{(i)}(m \cdot \Delta f) = \Delta t \cdot H_m^{(i)}, \qquad (3)$$

where $\Delta f = 1/(N\Delta t)$. The estimate of the power spectral density is then

$$S(f) = \left\langle \frac{1}{N\Delta t} \left| H^{(i)}(f) \right|^2 \right\rangle. \qquad (4)$$

Here the angle brackets represent the statistical ensemble average over large number of realisations (range of (i) was typically 100).

4. Frequency vs. wave number spectra

We attempted to analyze the wave behavior of the potential fluctuations of the magnetron discharge. For that purpose the spectra derived from the fluctuations measured simultaneously from two Langmuir probes were evaluated according to the method developed in

[3]. At first the wave number was expressed for each frequency from the phase shift between the signals at the two probes (denoted by subscripts 1 and 2) and the known distance Δx between the probes:

$$k^{(i)}(f) = \frac{\arg H_2^{(i)}(f) - \arg H_1^{(i)}(f)}{\Delta x} \quad (5)$$

Using the wave number and the average power density at the two probes $[S_1^{(i)}(f) + S_2^{(i)}(f)]/2$ the histogram $S(f,k)$ can be built by the ensemble averaging the same way as in [3]. The range of (i) was also typically 100.

It is interesting to note that this method can be looked at as the frequency domain version of the classic method of so-called z-t diagrams. This analog method was used for visualization of ionization waves in glow discharges in time domain, see e.g. [4,5].

5. Results

Figure 1 shows the dependence of the measured power density spectrum on the magnetic field at the pressure 3 Pa and the discharge current 200 mA. In the range up to several kHz the increase of the fluctuations amplitude with the increasing magnetic field is seen. The peaks on the curve taken at the magnetic field 20 mT are probably connected with the noise of the discharge power supply rather than with special fluctuation modes.
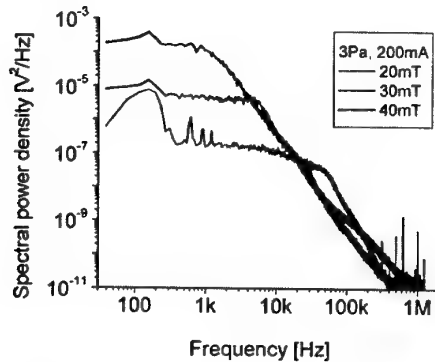
Figure 1. Example of power signal density spectrum with the magnetic field strength as parameter.
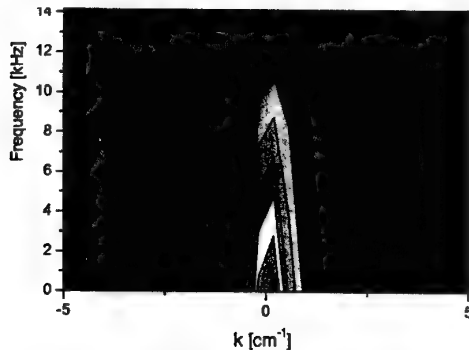
Figure 2. $S(k,f)$ histogram at 30 mT, 1.5 Pa and 200 mA. The distance between the two Langmuir probes was 1.7 mm.

The spectra derived from the fluctuations measured simultaneously from two Langmuir probes were also evaluated. Figure 2 shows the typical frequency vs. wave number histogram. It is seen from the figure that until approximately 15 kHz the phase shift between the fluctuations measured at the two probes is negligible, i.e. that the fluctuations at the positions of the two probes are well correlated.

6. Discussion

In the work [3] several fluctuation modes were observed in a planar dc magnetron device. The modes were present only when the discharge power and the neutral gas pressure were above a certain threshold. Their frequency spacing decreased when the neutral gas pressure was raised. Consequently, increasing of the pressure lead to a more turbulent state.

We investigated the fluctuations in the described cylindrical magnetron system in the range of magnetic fields 10 to 40 mT, for pressures from 1.5 to 7 Pa and at discharge currents 100 and 200 mA. Within this range of parameters we always found only one fluctuation mode, similar to that in figure 2. In other words the fluctuation in our system are the "synchronous oscillations" rather that travelling waves detected in the planar magnetron configuration. In the future we plan to refine the measurements by using the A/D card with better bit resolution.

7. Acknowledgments

8. References

[1] P. Kudrna, E. Passoth, Contrib. Plasma Phys. 37 (1997) 417.
[2] J.F. Behnke, J. Rusz, P. Kudrna, M. Tichý, Czech. J. Phys. 50/S3 (2000) 419.
[3] E. Martines, R. Cavazzana, G. Serianni, M. Spolaore, L. Tramontin, M. Zuin, V. Antoni, Phys. of Plasmas 8 6 (2001) 3042.
[4] T. Kopiczynski, Z. Zakrzewski, O. Štirand, Proc. 11th ICPIG Prague (Czech Republic), page 481, J. Phys. D (Appl. Phys.) 7 (1974) 1402.
[5] Z. Zakrzewski, T. Kopiczynski, R. Rusakiewicz, O. Štirand, Czech. J. Phys. B24 (1974) 885.

158

Drift Waves in a Helicon Plasma

Olaf Grulke [†], Christiane Schröder, and Thomas Klinger

Max-Planck-Institute for Plasma Physics, EURATOM Association, Greifswald, Germany

[†] also: Ernst-Moritz-Arndt University, Greifswald, Germany

Drift waves are studied in a high density helicon plasma in linear magnetic geometry. Drift waves are destabilized in the pressure gradient region by the ambient magnetic field acting as the control parameter. Saturated drift modes as well as turbulent states are observed by spatiotemporal probe diagnostics. Their propagation and radial mode structure is related to the time averaged plasma density and plasma potential profiles.

1. Introduction

Drift waves play an important role in many dynamical processes in magnetized plasmas. The early studies were already motivated by the enhanced transport of plasma across the magnetic field [1]. In this context drift waves have gained attention during the last two decades because experimental findings as well as numerical simulations strongly suggest a strong contribution of drift waves to the development of turbulence in the edge plasma of fusion devices [2, 3]. This paper presents observations of drift waves in a high density plasma in homogeneous magnetic field geometry. Particular attention is paid to a controllable destabilization of single coherent modes.

2. Experimental Setup

The experiments were conducted in the linear VINETA device [4] schematically shown in Fig. 1. It consists of for identical modules, each with a separate set of magnetic field coils and power supply. In the present experiments the device is homogeneously magnetized with a spatial magnetic ripple of less than 1%. The plasma is produced by a conventional helicon plasma source, located at one end of the discharge chamber. At an rf input power of typically 2.5kW a peak plasma density of $\approx 1 \cdot 10^{19} \mathrm{m}^{-3}$ is achieved at a relatively low electron temperature of 3eV. Time averaged plasma profiles are obtained by spatially resolved electrostatic probe measurements and evaluation of the probe characteristics. A typical radial profile of the plasma density and the plasma potential is shown in Fig. 2. The plasma density is of almost perfect Gaussian shape. The plasma potential is positive and shows a flat top in the core, whereas in the gradient regions the potential decreases parabolically. These profiles
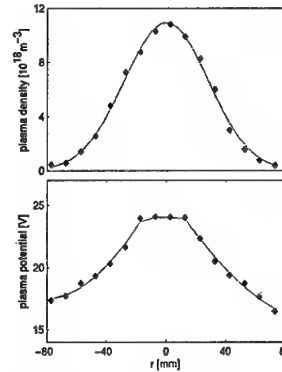
Figure 2: Measured radial profiles of the plasma density and the plasma potential as obtained by probe measurements (markers). A Gaussian is fitted to the density profile, two parabolic function are fitted to the plasma potential gradients.

lead to two important consequences. First, the $E \times B$ rotation of the plasma is strongly sheared in the density gradient region. Second, the $E \times B$ rotation is anti-parallel to the electron diamagnetic drift direction. Fluctuations of the plasma density are measured by constantly biased probes. The ion saturation current is taken as proportional to density fluctuations, i.e. electron temperature fluctuation are neglected. These probes are operated as single probes or as an azimuthal 64 probe array recording simultaneously fluctuations on an azimuthal plasma circumference [5].

3. Results

Destabilization of drift waves is achieved using the ambient magnetic field as control parameter. This directly changes the effective ion gyroradius ϱ_s, whereas the time-averaged plasma profiles turned out to remain essentially uninfluenced. Consequently, the ratio between effective ion gyroradius and density gradient scale length ϱ_s/L_n is changed via the magnetic field, which directly controls driving of the drift waves. In Fig. 3 recordings of density fluctuations together with the respective frequency-mode number spectra are shown for three different magnetic fields. For $B = 75\mathrm{mT}$, Fig. 3 (b), a single coher-
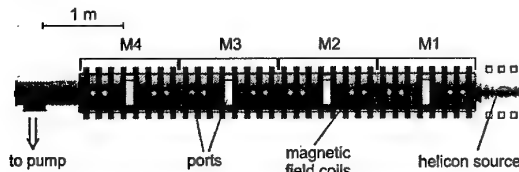
Figure 1: Schematic drawing of the VINETA device.
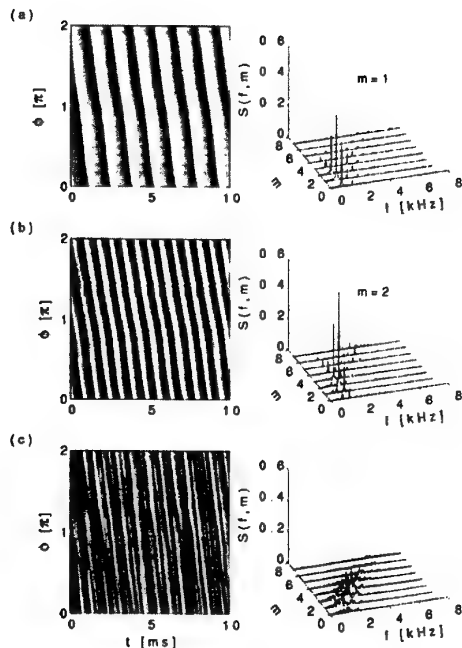
Figure 3: Spatiotemporal diagram of drift wave density fluctuations as obtained with an azimuthal probe array for different magnetic field strengths $B = 60\mathrm{mT}$ in (a), $B = 75\mathrm{mT}$ in (b), and $B = 90\mathrm{mT}$ in (c). Additionally, the respective frequency-mode number spectra are shown.

ent $m = 2$ drift mode is observed with two maxima and two minima around a plasma circumference. The frequency-mode number spectrum is strongly peaked at this mode and a frequency of 1kHz. This frequency corresponds to a phase velocity of the drift wave given by the electron diamagnetic drift Doppler shifted by the plasma $E \times B$ rotation, which reduces the propagation speed. The mode structure in a plane perpendicular to the ambient magnetic field is measured via cross-correlation measurements. Density fluctuations in an azimuthal plane are correlated to density fluctuations at a fixed spatial position in the maximum density gradient region. Fig. 4 shows the respective values of the cross-correlation function at a fixed time instant. The $m = 2$ mode structure is clearly observed. The correlation decreases towards the plasma core, where the density gradient vanishes. Coherent fluctuations are found to the far outer boundary of the density profile. The mode structure is distorted in radial direction, which can be addressed to the sheared rotation of the plasma column.

Changing the magnetic field dramatically influences the drift dynamics. For lower magnetic field, Fig. 3 (a), the dominant frequency is lowered and a $m = 1$ drift mode dominates. Increase of the magnetic field, Fig. 3 (c), destabilizes different modes, which
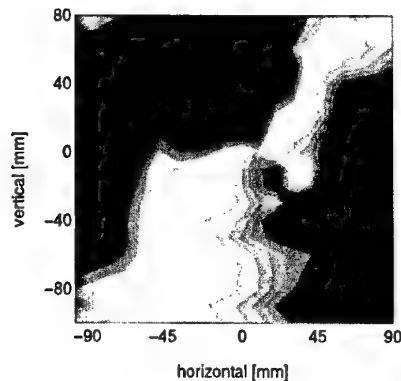
Figure 4: Cross-correlation measurement in a azimuthal plane perpendicular to the ambient magnetic field. Shown are the values of the cross-correlation function at a fixed time delay between a fixed and a scanning probe.

interact nonlinearly and lead to a weakly developed turbulent state. The spectrum here is broadened and no coherent modes are observed in the spatiotemporal diagram.

4. Conclusions

An experimental study of drift waves in a high-density helicon discharge is presented. It is shown that via the magnetic field good control over the dynamical states of drift waves is achieved, most likely by changing the drift scale length ϱ_s. By this control parameter coherent modes can be destabilized as well as mode interaction regimes and weakly developed turbulence. For low magnetic field, i.e. large ϱ_s, modes with low mode numbers are predominantly destabilized. For higher magnetic fields the dominant mode number increases and single drift modes with mode numbers ranging from $m = 1 \dots 6$ can be observed. For high magnetic fields nonlinear mode coupling results in weakly developed turbulent state.

[1] N. D'Angelo and R. W. Motley, Phys. Fluids **6**, 422 (1963).

[2] J. W. Connor, G. F. Counsell, S. K. Erents, S. J. Fielding, B. LaBombard, and K. Norel, Nucl. Fusion **39**(2), 169 (1999).

[3] B. Scott, Plasma Phys. Controlled Fusion **39**(3), 471 (1997).

[4] C. M. Franck, O. Grulke, and T. Klinger, Phys. Plasmas **9**(8), 3254 (2002).

[5] A. Latten, T. Klinger, A. Piel, and T. Pierre, Rev. Sci. Instrum. **66**(5), 3254 (1994).

160

Investigation of Alfvén waves in a helicon plasma

Albrecht Stark[1], Olaf Grulke[1,2], Thomas Klinger[1,2]

1) Max-Planck-Institute for Plasma Physics, EURATOM Association, D-17491 Greifswald, Germany

2) Ernst-Moritz-Arndt University, D-17489 Greifswald, Germany

Helicon wave sustained discharges provide high density plasmas needed to investigate Alfvén waves under laboratory conditions. In the present paper kinetic Alfvén waves were successfully launched in a helium plasma. A good agreement is found between the measured and the theoretically predicted dispersion behaviour. The damping can be associated both to collisional and Landau damping.

1. Introduction

Alfvén waves are known to play a major role in the dynamics of magnetized plasmas. Motivated by their importance in plasma heating, transport of energy, and information about perturbations in the magnetic field topologies, Alfvén waves have been subject of intense research in laboratory, space and astrophysical plasmas [1]. Two different principal modes of Alfvén waves can be observed, both propagating below the ion cyclotron frequency. Firstly, magneto-acoustic waves propagate perpendicular to the ambient magnetic field B_0. Secondly, shear Alfvén waves propagate along the magnetic field lines. The kinetic and inertial regime of Alfvén wave propagation can be distinguished, depending on the plasma-beta value, where beta is given by the ratio between kinetic and magnetic pressure. For $\beta > m_e/m_i$, which is for $T_e \gg T_i$ equivalent to $v_A < v_{th,e}$, Alfvén waves are kinetic. Here $v_A = B/(\mu_0 m_i n_i)^{1/2}$ is the Alfvén velocity and $v_{th,e} = (kT_e/m_e)^{1/2}$ is the electron thermal velocity. For $\beta < m_e/m_i$ Alfvén waves are inertial.

For laboratory experiments on Alfvén waves, a challenge is always their extremely long wavelengths. This requires first of all a large plasma device. Because of $v_A \propto n_i^{-1/2}$, a high plasma density leads to reasonably short wavelengths being smaller than the device dimension. At such high densities $\beta \simeq 0.5 \ldots 8.5\, m_e/m_i$ and one is mostly in the kinetic regime. The kinetic treatment of ion dynamics in magnetized plasmas yields an expression for the dispersion of shear Alfvén waves as [2]

$$\frac{\omega^2}{k_\parallel^2} = v_A^2 \left(1 + k_\perp \rho_s^2\right) . \qquad (1)$$

Here $\rho_s = c_s/\omega_{ci}$ is the so-called ion sound gyro-radius and the wave number is $k = k_\perp + k_\parallel$. Collisionless damping is important in the kinetic regime and the damping rate for Alfvén waves reads

$$\gamma = \frac{1}{2}\left(\frac{\pi}{2}\right)^{1/2}\left(\frac{m_e}{m_i}\right)^{1/2}\frac{k_\perp^2 v_A^2}{\omega_{ci}^2}\,|k_\parallel|\,v_s , \qquad (2)$$

with the ion cyclotron frequency $\omega_{ci} = eB/m_i$ and the ion sound speed $v_s = (kT_e/m_i)^{1/2}$.

2. Experimental Setup

Experiments were conducted in the VINETA device [3]. Figure 1 shows a schematic diagram of the experimental device. The vacuum chamber consists of four identical modules, 0.4 m in diameter and 1.2 m in length. The four chambers are immersed in a set of 36 magnetic field coils ($B_0 \le 100$ mT). The plasma source is placed at the one end of the device. A right hand half-turn helical antenna is driven with rf $5 - 30$ MHz and electric power of up to 2.5 kW in cw-mode and 6 kW in pulsed mode. Three different discharge modes, capacitive, inductive, and helicon mode can be established. Plasma-densities are found to be in the range of $10^{16} - 10^{19}$ m^{-3}. The electron temperature is in the range $1 - 5$ eV.

Alfvén waves are launched using a single-loop antenna, which surface normal is oriented perpendicular to the background magnetic field. The relative induced magnetic field perturbation $\delta B/B_0$ is in the range of a few percent. Alfvén-waves are detected with $\dot{B}$-probes by measuring the induced voltage proportional to the magnetic field fluctuations [4]. A computer controlled high-resolution two-dimensional (radial-axial) probe positioning system is used for measurements of propagating wave fronts. Helium is used as filling gas. The neutral gas pressure is in the range of $0.1 - 2$ Pa. At maximum magnetic field $B_0 = 100$ mT the ion gyro-frequency is $f_{ci} = 382$ kHz around which the $\dot{B}$-probe is already sufficiently sensitive (note that the induction voltage of the probe scales as $U_{ind} \propto \omega$).
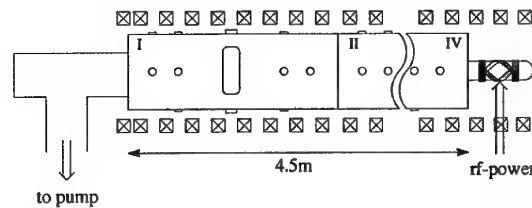
Figure 1: Schematic diagram of the VINETA device. The device consists of four identical modules. Only one complete module is shown in the schematic (module I). On the l.h.s. it is indicated the vacuum pump. On the r.h.s. the helicon source is located.
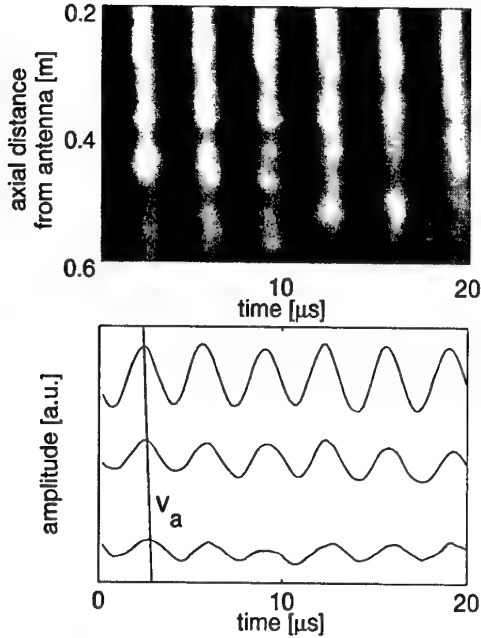
Figure 2: Top: Spatio-temporal measurements of propagating magnetic field fluctuations measured with $\dot{B}$-probes. Bottom: Selected timeseries at axial distances 0.2 m, 0.4 m and 0.6 m relative to the exciter antenna.

In a helium plasma we achieved sufficiently high densities to ensure $\beta \sim m_e/m_i$.

3. Results and Discussion

Experimental data from $\dot{B}$-probe measurements at exciter frequency 300 kHz are shown in Figure 2 (top diagram). The VINETA device is operated in the helicon mode at high rf power and $B_0 = 0.1$ T. The amplitude of magnetic fluctuations in axial direction is plotted gray-scale-coded position vs. time. The diagram shows a regular pattern of propagating signals. The bottom diagram in Figure 2 shows three timeseries taken at 0.2 m, 0.4 m and 0.6 m axial distance to the exciter-loop. A sinusoidal propagating wave-type signal is clearly observed. Two different informations can be derived from the diagram: The phase velocity $v_{ph} = 1.2 \cdot 10^6$ m/s of and the damping length $\delta = 0.5$ m.

The excitation frequency is varied in the range $160 - 330$ kHz and a dispersion diagram is obtained as shown in Figure 3. The errorbars are given by uncertainties in the $\dot{B}$-probe phase detection. The calculated dispersion relation of a kinetic shear Alfvén wave, equation (1), is plotted as solid line in the same diagram. The parameters used are $n_i = 3 \cdot 10^{17}$ m^{-3}, $B_0 = 0.1$ T and $k_\perp \approx 0$ is assumed. There is very good agreement between theory and observation.
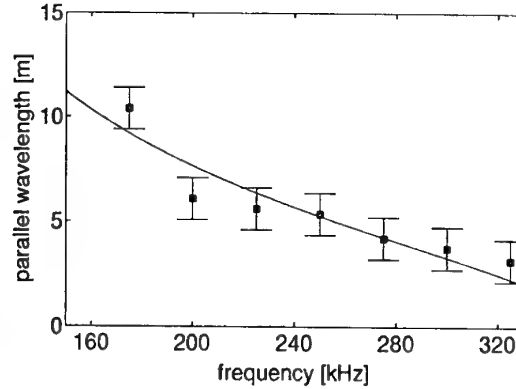
Figure 3: Dispersion diagram of the observed Alfvén waves. The dispersion relation (1) of kinetic shear Alfvén waves is indicated by a solid line.

4. Summary and Conclusion

Kinetic Alfvén waves have been successfully launched in a high-density helium helicon plasma. The dispersion relation of kinetic Alfvén waves could be fully confirmed. The present observations support results recently obtained in a different machine [5]. We note that our measurements are based on the evaluation of the full (averaged) magnetic wave field and not only on a two-point measurement. The relatively strong damping can be assigned to two different mechanisms: Collisional damping is clearly of significance ($\nu_e \approx 800$ kHz). At $\beta \sim 1$ ion Landau damping is known to be strong, too [2]. Work is in progress to make a quantitative analysis of propagation and damping of kinetic Alfvén waves in a helicon plasma.

Acknowledgement

References

[1] R. Cross, *An Introduction to Alfvén waves*, Adam Hilger, Bristol 1988.

[2] N.F. Cramer, *The Physics of Alfvén waves*, Wiley-VCH, Berlin 2001.

[3] C.M. Franck, O. Grulke, T. Klinger, *Phys. Plasmas*, **9** (8) (2002) 3254-3258.

[4] C.M. Franck, O. Grulke, T. Klinger, *Rev. Sci. Instr.*, **73** (11) (2002) 3768-3771.

[5] J. Hanna, C. Watts, *Physics of Plasmas* **8**(9) (2001) 4251-4254.

Whistler wave dispersion measurements near the ion gyro frequency

Albrecht Stark[1], Christian Franck[1], Olaf Grulke[1,2], Thomas Klinger[1,2]

1) Max-Planck-Institute for Plasma Physics, EURATOM Association, D-17491 Greifswald, Germany

2) Ernst-Moritz-Arndt University, D-17489 Greifswald, Germany

Investigation of ion whistler waves under laboratory conditions is difficult because of the long wavelength. In the VINETA device electromagnetic waves around the ion gyro frequency have been successfully launched. For frequencies above the ion gyro frequency the waves are identified as R-waves. Below the ion gyro frequency the measurements cannot be explained by R-wave or L-wave dispersion alone. In a heuristic way the observed dispersion is described by the difference wavelength of R-wave and L-wave.

1. Introduction

Whistler waves have been subject of research for almost one century [1]. Excited by lightning whistler waves, low frequency electromagnetic plasma waves, are known to propagate in the ionosphere along magnetic field lines. Because of their dispersion, high frequencies propagate faster then low frequencies and therefore, whistling tone bursts of descending frequency can be observed. Ion whistler waves, with a different dispersion behaviour, were observed by satellites [2]. But until today, there was no observation of L-waves in laboratory plasmas.

Waves in magnetised plasmas can be distinguished in wave propagation parallel and perpendicular to the ambient magnetic field. Whistler waves are of the type $k \parallel B_0$. Starting with a cold plasma dispersion relation, an expression for waves with $k \parallel B_0$ such as

$$\frac{k_\parallel^2 c^2}{\omega^2} = 1 - \frac{\omega_{pe}^2 + \omega_{pi}^2}{(\omega \pm \omega_{ci})(\omega \mp \omega_{ce})} \qquad (1)$$

is found [3]. Here $\omega_{ps}^2 = (n_e q_s^2 / m_s \epsilon_0)$ is the plasma frequency and $\omega_{cs} = |q_s| B_0 / m_s$ the gyro frequency of the species s. The dispersion relation contains two different modes, where the first (upper choice of signs) is the R-wave and the second (lower choice) is the L-wave. The ion gyro frequency represents a resonance for L-waves, and the propagation is limited to frequencies below this resonance. Waves propagating in this regime are called ion whistler waves.

In multicomponent plasmas a separate resonance occurs for each ion species. The frequency regime of propagation depends on the ion species as well as on the relative ion concentrations. At a certain frequency between two neighbouring ion gyro frequencies the dispersion of R-wave and L-wave intersect. A mode coupling of R-mode to L-mode can occur at this crossover frequency [4]. Measurements of the dispersion behaviour provides a diagnostic tool for ion concentrations as as well for plasma composition. This diagnostic tool has already been used to determine ionospheric plasma composition, but the observations partially deviate from standard models [5]. Laboratory measurements could be helpful to clarify this.
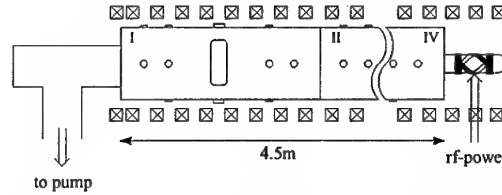
Figure 1: Schematic diagram of the VINETA device. The device consists of four identical modules (I-IV). Only one complete module is shown in the schematic (module I). On the l.h.s. the vacuum pump is indicated and the helicon source is located on the r.h.s.

2. Experimental Setup

Experiments were carried out in the linear VINETA device [6], plotted in Figure 1. The vacuum chamber is made up of four identical modules of 0.4 m in diameter and 1.1 m in length and is immersed in a set of 36 magnetic field coils ($B_0 \leq 100$ mT). The plasma source (a right hand half-turn helical antenna) is placed at one end of the device. The antenna is driven with rf of $5 - 30$ MHz and power of up to 2.5 kW in cw-mode and 6 kW in pulsed mode. Depending on gas pressure, magnetic field strength and power, three different discharge modes can be established (capacitive, inductive, and helicon mode). Plasma densities are in the range of $10^{16} - 10^{19}$ m^{-3} and electron temperature in the range $1 - 5$ eV.

Whistler waves are launched by a loop antenna with 30 mm in diameter [7]. The antenna is placed centrally in the device and its surface normal is oriented parallel to the ambient magnetic field. In order to induce a magnetic field perturbation $\delta B / B_0$ in the range of a few percent, the exciter signal power is in the order of $P = 50$ W. The waves are detected by magnetic fluctuation probes ($\dot{B}$-probe) [8]. As the induced voltage at the probe is proportional to the exciter frequency ($U_{ind} \propto \omega$), the probe consists of 25 windings 25 mm in diameter to provide a sufficient sensitivity. A computer controlled high-resolution probe positioning system is used for two-dimensional (radial-axial) measurements of propagating wave fronts. Helium is used as filling gas with typical gas pressure of $0.2 - 3$ Pa.
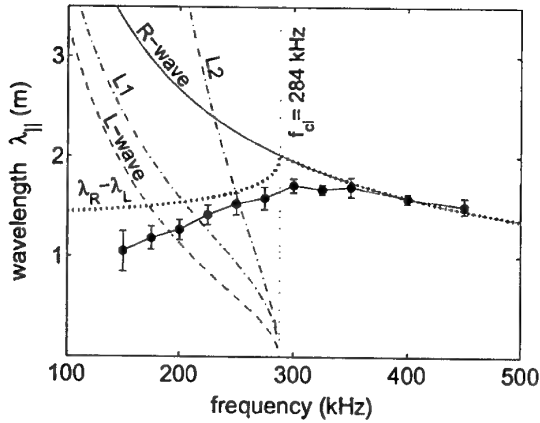
Figure 2: Measurements of whistler wave dispersion (markers). The calculated dispersion relations of an R-wave (solid line) and L-wave (dashed line) are shown as well. Superpositions of R- and L-waves $(L1, L2 = 2\pi/(k_L \pm k_R))$ are represented by dash-dotted lines and the dotted line is the difference wavelength $(\lambda_R - \lambda_L)$.

3. Results and Discussion

The experiments were done in a helium helicon discharge operated at a neutral gas pressure of $p = 2.5\,\text{Pa}$, magnetic field of $B_0 = 75\,\text{mT}$ and rf power of $P_{rf} = 5\,\text{kW}$. The plasma parameters are found to be $n \approx 4 \cdot 10^{18}\,\text{m}^{-3}$ and $T_e \approx 5\,\text{eV}$ from Langmuir probe characteristics. The experimental results for exciter frequencies in the range $100 - 500\,\text{kHz}$ are shown in Figure 2 (markers). The obtained wavelengths are in the range of $1 - 2\,\text{m}$. The increase of the errorbars at small frequencies is related to decreasing sensitivity of $\dot{B}$-probes. For frequencies above the ion gyro frequency $f_{ci} = 284\,\text{kHz}$, the measured wavelengths decrease with increasing frequency. These part of the dispersion has been identified as the R-wave dispersion in a previous measurement [6]. The present measurements agree very well with the calculated dispersion (solid line). Below the ion gyro frequency the observed wavelengths decrease with decreasing frequency. This behaviour can neither be described by R-wave (solid line) nor by L-wave (dashed line) dispersion. Since the antenna does not prescribe a polarisation direction, both R- and L-waves are excited simultaneously. Similarly the $\dot{B}$-probe measurement is sensitive to magnetic fluctuations only, hence different circular polarisations cannot be distinguished. Wavelengths (L1,L2) calculated from linear superposition of R-wave and L-wave cannot explain the measurements below f_{ci}. $L1 = 2\pi/(k_L + k_R)$ and $L2 = 2\pi/(k_L - k_R)$ are plotted dash-dotted in Figure 2. Especially, no

discontinuous jump is observed around f_{ci}. Nevertheless, the deviation form the R-wave dispersion below f_{ci} indicates that the L-wave is involved as well. Possibly, a non linear superposition of R- and L-wave necessary to explain the measurements (maybe due to the high excitation power used). A more appropriate (heuristic) agreement is to the difference wavelength $\lambda_R - \lambda_L$ (dotted line). This will be analysed in future investigations. To our knowledge, this is the first experimental observation of L-wave propagation under laboratory conditions.

4. Summary and Conclusion

Waves has been launched with frequencies near the ion gyro frequency. For frequencies above the ion gyro frequency, a decreasing wavelength with increasing frequency is observed. This behaviour is very well described by an R-wave dispersion. Below the ion gyro frequency a decreasing wavelength is observed for decreasing frequencies. Neither R-wave, L-wave dispersion nor a linear superposition of both can explain these measurements. A more reasonable approach, but so far only heuristic, is given by the difference wavelength of R-wave and L-wave.

Acknowledgement

References

[1] H. Barkhausen, *Physik Zeitschr. XX*, (1919) 401-403.

[2] R.L. Smith, N.M. Brice, J. Katsufrakis, D.A. Gurnett, S.D. Shawhan, J.S. Belrose, R.E. Barrington, *Nature* **204** (1964) 274-275.

[3] T.H. Stix, *Waves in Plasmas*, American Institute of Physics, New York 1992

[4] R.L Smith, N. Brice, *J. Geophys. Res.*, **69** (23) (1964) 5029-5040.

[5] T.S. Ruud, *Plasma Wave Phenomena observed with the FREJA satellite*, University of Oslo 2000.

[6] C.M. Franck, O. Grulke, T. Klinger, *Phys. Plasmas*, **9** (8) (2002) 3254-3258.

[7] R.L. Stenzel, J.M. Urrutia, C.L. Rousculp, *Phys. Fluids B* **5** (2) (1993) 325-338.

[8] C.M. Franck, O. Grulke, T. Klinger, *Rev. Sci. Instr.*, **73** (11) (2002) 3768-3771.

Formation of electron beam and volume discharge in air under atmospheric pressure

V.F. Tarasenko, V.M. Orlovskii

High Current Electronics Institute, 4, Akademichesky Ave., Tomsk 634055, Russia; vft@loi.hcei.tsc.ru

The conditions to form electron beams in air, nitrogen, and in the mixture CO_2 - N_2 - He under atmospheric pressure have been examined experimentally. At nanosecond pulses applied to the diode, e-beam was obtained in air with amplitude of 70 A. Electron beam appears at voltage pulse leading edge having duration at FWHM not higher than 0,4 ns. After beam current ends, the discharge is usually continued in quasi-stationary mode being of a volume character.

1. Introduction

In 2002, it was demonstrated in [1, 2] how amplitude of gas diode electron beam formed under atmospheric pressure of helium [1], as well as molecular gases (air, nitrogen, or gas mixture CO_2-N_2-He) [2] can be essentially increased. Electron beam was obtained under low values of E/p ~ 0,1 kV/cm×Torr (E is electrical field strength, p is gas pressure) being substantially smaller than critical ones necessary for achievement of effect of "running away electrons" [3]. Earlier many scientific teams investigated formation of accelerated electrons and X-ray radiation in gas-filled diodes (see for e.g., the monograph [3] and review [4], as well as references to these papers). However e-beam amplitudes obtained in molecular gases did not exceed fractions of an ampere, and interpretation of the effect was not simple, moreover, in a number of monographs devoted to gas discharge the effect was not considered at all [5].

In this paper, study devoted to mechanism of electron beam formation at low values of E/p in diode filled-in with air under atmospheric pressure is presented, preliminary results were earlier published in [6].

2. Experiment

Nanosecond pulse RADAN generators described in a more detail in [7, 8] were used in experiments. Generator 1 (RADAN-303) had impedance of 45 Ohm forming with matched load voltage pulses from 50 to 170 kV at voltage pulse duration at FWHM ~5 ns and voltage pulse leading edge of ~1 ns [7]. Generator 2 had impedance of 20 Ohm forming at discharge gap a voltage pulse with amplitude of up to 220 kV and duration at FWHM as ~2 ns under voltage pulse leading edge of ~0,3 ns [8]. Gas diode construction was similar to that described in [2]. Cathode – anode distance was 13-20 mm. Electron beam extraction was made through 45-μm AlBe foil or grid. Oscilloscope TDS-864B with 1 GHz-band and 5 GS/s was used in experiments to record shunt signals. Recording method resolution was not worse than 0,3 ns.

The following facts were established on the basis of voltage pulse measurements at gas diode and beam current (see for e.g., Fig.1) as well as gap discharge form observation with varying anode-cathode gap,
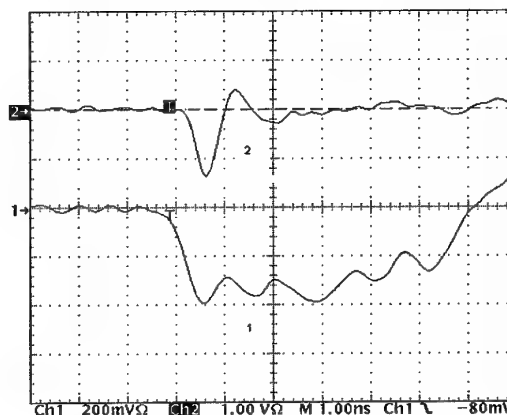
Fig.1. Oscilloscope traces of voltage pulses (1) and beam current (2). Voltage scaling is 45 kV/div, current - 20 A/div, and time - 1 ns/div. Generator 1.

cathode type, and gas diode voltage value. Electron beam appears at voltage pulse leading edge having duration at FWHM not higher than 0,4 ns. Maximum of beam current is usually fixed after voltage maximum at the gap. Amplitude of beam current in optimal conditions did not exceed 30 A for generator 1 and 70 A for generator 2. With voltage increasing, beam current maximum moves to start of voltage pulse and ends at maximal voltage values at leading edge. In parallel with beam current, discharge current flows through gas diode with substantially higher value and duration than beam current amplitude and duration. The maximum of e-beam energy distribution after 45-μm AlBe foil of the first generator under air pressure in diode of 1 atm corresponded to the electron energy of ~60 keV, and in the case of the second generator it was ~70 keV, Fig.2. After beam current ends, the discharge is usually continued in quasi-stationary mode being of a volume character. Within 5 ns (generator 1) during voltage pulse at the gap the anode current density reaches ~1 kA/cm², specific input energy in gas is ~1 J/cm³ and specific input power is ~200 MV/cm³. With maximal voltage at generator 1, the value of E/p parameter on end of beam current is equal to ~ 0,08 kV/cm×Torr.
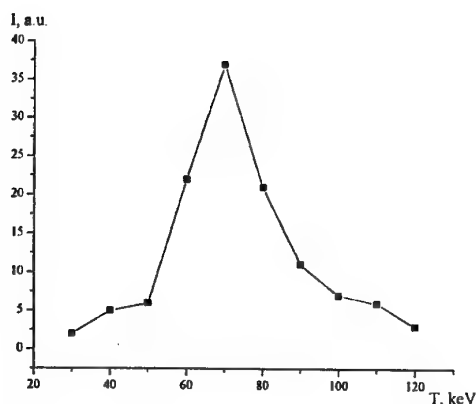
Fig.2. Distribution of electrons by energy in the beam behind the foil at air pressure in diode of 1 atm. Generator 2.

3. Discussion

Based on analysis of experimental data obtained as well as known processes occurring during gas discharge [3-5] we consider that the following dynamics of development of gas breakdown in a gap is being realized. With high-voltage pulse applied, at its leading edge the known process of electron avalanche multiplication starts with which electron concentration increases following the rule $N = N_0 exp(\alpha d)$, where α is coefficient of ionization, d is interelectrode gap. In order to obtain several kA of current during the time of ~1 ns being correspondent to the conditions of Fig.1, it is needed to have a sufficient amount of electrons near the cathode, $N_0 \sim 10^6$, which may appear due to cathode processes, during "pre-pulse" including. Along with development of discharge, the number of electrons in every avalanche could increase in ~10^8 times and above [5] without formation of streamer, and then within voltage pulse leading edge the electron amount reaches 10^{14} and more that with $E/p \sim 0,05-0,1$ kV/cm×Torr sufficient for discharge current of more than 1 kA. Electron beam is registered after ~0,5 ns following application of voltage pulse either with grid anode or foil one. Its formation, as we earlier supposed in [2], is connected with achievement of critical field in the space between plasma front from broadening to anode avalanches and anode. Note, that on avalanches growth plasma front consists of electrons, correspondingly, the space charge of electron cloud gives additional acceleration to anode for the electrons located at the edge of electron cloud. A part of electrons can have higher energy here than voltage at the diode is. It is clear that the number of electrons in a beam must be essentially smaller than number of electrons in avalanches, and the number of electrons with energy exceeding applied voltage value must be essentially lower than the number of them with average energy. After beam electrons reach anode, the field in the gap becomes rather improved, and electrical field gradient sufficient for "running away electrons" disappears.

Maintenance of volume character of discharge in gap within the whole voltage pulse, Fig.1, is determined by avalanche discharge character in the first stage and pre-ionization by electron beam formed during discharge. Stabilization of discharge current amplitude at high fields in the gap ($E/p \sim 0,05-0,08$ kV/cm×Torr) may be determined by increased energy losses of secondary electrons while they pass through plasma formed within discharge development as well as due to process of recombination. We consider this discharge type to be different from those described in [3-5] being in future widely applied in various fields (formation of subnanosecond electron beams, pumping of pulsed lasers on dense gases, etc.).

4. Conclusion

An electron beam has been obtained in atmospheric air with amplitude of 70 A with electron energy of 70 keV. Electron beam appears at voltage pulse leading edge having duration at FWHM not higher than 0,4 ns. The major part of running away electrons with rather low initial values of E/p ~ 0,05-0,1 kV/cm×Torr form in cathode plasma - anode gap. Cathode plasma propagates to anode at a high velocity, at that with electrical field distribution in gas diode area the critical value of E/p is being reached, either due to geometric quotient, leading to formation of subnanosecond electron beam. After beam current ends, the discharge is usually continued in quasi-stationary mode being of a volume character. The density of current reaches ~1 kA/cm^2, specific input energy in gas is ~1 J/cm^3 and specific input power is ~200 MV/cm^3.

5. Reference

[1] S.B. Alekseev, V.M. Orlovskii, V.F. Tarasenko, A.N. Tkachyov, S.I. Yakovlenko, *Pis'ma v JTF* **29** (2003) In publication.

[2] S.B. Alekseev, V.M. Orlovskii, V.F. Tarasenko, *Pis'ma v JTF* **29** (2003) In publication.

[3] Yu.D. Korolev, G.A. Mesyats, *Physics of pulsed gas breakdown. - Moscow: Nauka* (1991) 224 p.

[4] L.P. Babich, T.V. Loiko, V.A. Tsukerman, *UFN* **160**, No.7 (1990) 49.

[5] Yu.P. Raizer, *Physics of gas discharge.- Moscow: Nauka* (1987) 592 p.

[6] V.F. Tarasenko, V.M. Orlovskii, S.A. Shunailov, *Izvestiya VUZov, Fizika* **46**(3) (2003) 95.

[7] M.I. Yalandin, V.G. Shpak, *PTE*. No.3 (2001) 5.

[8] F.Ya. Zagulov, A.S. Kotov, V.G. Shpak, et al., *PTE* No.2 (1989) 146.

Wave modes in compressible collisionfree multi-species magnetoplasmas

K. Suchy

University of Düsseldorf, Universitätsstr. 1, D-40225 Düsseldorf, Germany [0211203410@t-online.de]

The dispersion equation and an expression for polarization ratios are derived using velocity moments up to second order.

For the calculation of the dispersion equation and polarization ratios of waves with phase velocities much higher than the thermal speed the latter is completely neglected in the so-called cold plasma approximation. A simple approach to taking the thermal speed into account is to add the gradient of a scalar pressure in the momentum balance equations for the mean velocities of the different species and to relate those pressures to the densities via an isothermal law.

An improvement of this simple approach is to use the pressure balance equations to obtain relations between the pressure tensors and the mean velocities. These are then introduced in the momentum balance equations. The third-order velocity moments in the pressure balance equations, whose traces are the heat flow vectors, are neglected. This reduces the accuracy by one sixth at the most [1].

After linearization of the mean velocities and of the electric field and Fourier transformation of the perturbation parts a set of algebraic equations, each combining the mean velocity of a species and the electric field, is established, i.e. a set of specific Ohm`s laws.

Maxwell`s curl-equations are likewise linearized and Fourier-transformed. The elimination of the magnetic perturbation field results in an equation combining the electric field with the sum of the partial current densities. The latter are replaced by the specific Ohm's laws. This leads to the dispersion system, i.e. the scalar product of the dispersion tensor with the electric field vector put equal to zero. The determinant of the dispersion tensor put equal to zero is the dispersion equation. The rows of the adjoint of the dispersion tensor (or linear combinations of them) are the polarization ratios of the electric field.

Taking in the dispersion equation the square of the refractive index as the unknown one obtains five roots for a one-species plasma, representing five wave modes, thus adding three acoustic modes to the two modes in a cold plasma [1]. One of these acoustic modes is predominantly longitudinal polarized, the two others predominantly transverse. Each additional species adds three additional modes.

Reference

[1] K. Suchy, C. Altman, *J. Plasma Physics* **69** (2003) 69.

Topic 14

Nonlinear phenomena, self-organization and chaos

Multidimensional solitons in complex media with variable dispersion: structure and evolution[1]

V.Yu. Belashov, A.V. Anoshen

Kazan State Power Engineering University, 51 Krasnosel'skaya, Kazan 420066 Russia

The problem of dynamics the multidimensional solitons in complex media with the dispersion is studied numerically. The applications to physics of the FMS waves in a magnetized plasma, and the 2-dimensional surface waves on shallow water are discussed.

In this paper we consider the problem of dynamics the multidimensional solitons which are described by the Kadomtsev-Petviashvili (KP) equation

$$\partial_t u + \alpha u \partial_x u + \beta \partial_x^3 u = \kappa \int_{-\infty}^{x} \Delta_\perp u \, dx, \qquad (1)$$

in complex media with the varying in time and/or space dispersive parameter $\beta = \beta(t, \mathbf{r})$. This problem is mainly interesting from the point of view of its evident applications in physics of the concrete complex media with the dispersion. For example, such situation may have place in the problems of the propagation of the 2D gravity and gravity-capillar waves on the surface of "shallow" water [1] when coefficient β is defined respectively as $\beta = c_0 H^2/6$ and $\beta = (c_0/6)\lfloor H^2 - 3\sigma/\rho g \rfloor$ where H is the depth, ρ is the density, and σ is the coefficient of surface tension of fluid. If $H = H(t, x, y)$ the dispersive parameter also becomes the function of the coordinates and time. Similar situation may have place on studying of the evolution of the 3D FMS waves in magnetized plasma in case of the inhomogeneous and/or non-stationary plasma and magnetic field [2] when β is function of the Alfvén velocity $v_A = f[B(t, \mathbf{r}), n(t, \mathbf{r})]$ (n is the plasma density) and an angle $\theta = (\mathbf{k}^\wedge \mathbf{B})$: $\beta = v_A (c^2/2\omega_{0i}^2)(\cot^2 \theta - m/M)$. It is well known that the 1D solutions of the KdV equation with $\beta = \text{const}$ in dependence on value of the dispersion parameter are divided into two classes: at $|\beta| < u_0(0, x) l/12$ (l is the characteristic wave length of the initial disturbance) they have soliton character, in a return case – they are the wave packets with asymptotes being proportional to the derivative of the Airy function. In this cases the KdV equation can be integrated analytically by the IST method. But, if $\beta = \beta(x, t)$ such approach is impossible principally, and it is necessary to resort to a numerical simulation in the conforming problems. Similar situation has place in a non-one-dimensional model described by the KP equation: if the analytical solutions of the KP equation are known that in case $\beta = \beta(t, \mathbf{r})$ the dispersion term of equation becomes quasi-linear

and the model being not exactly integrable [3].

In this paper the results of numerical experiments on study of structure and evolution of the nonlinear waves described by the KP equation with $\beta = \beta(t, \mathbf{r})$ are considered distracting from a concrete type of media. The numerical experiments were conducted for several model types of function β when at $t < t_{cr}$ $\beta = \beta_0 = \text{const}$, and at $t \geq t_{cr}$

$$1) \ \beta(x) = \begin{cases} \beta_0, & x \leq a; \\ \beta_0 + c, & x > a; \end{cases} \qquad (2)$$

$$2) \ \beta(x, t) = \begin{cases} \beta_0, & x \leq a; \\ \beta_0 + nc, & n = (t - t_{cr})/\tau = 1, 2, \ldots; \ x > a; \end{cases} \qquad (3)$$

$$3) \ \beta(t) = \beta_0 \left(1 + k_0 \bar{\beta} \sin \omega t\right), \ \bar{\beta} = (\beta_{max} - \beta_{min})/2, \qquad (4)$$
$$0 < k_0 < 1, \quad \pi/2\tau < \omega < 2\pi/\tau,$$

a and c are constants. In terms of the propagation of the waves on the shallow water that means that after reaching t_{cr}, respectively: 1) sharp "break of bottom"; 2) gradual "change of a height" of a segment of bottom; and 3) the "oscillations of bottom" with time are happen.

The results obtained in the numerical experiments on evolution of the 2D solitons described by the KP equation model (1) with $\beta = \beta(t, \mathbf{r})$ enable to obtain the different types of both stable and unstable solutions including the solutions of the mixed "soliton – non-soliton" type for different character of the dispersion variations in time and space. The obtained results open new perspectives in investigation of a number of applied problems of dynamics of the multidimensional nonlinear waves in concrete complex media with the dispersion.

References

[1] V.Yu. Belashov, *Ann. Geophys. Suppl.* **14** (1996) 91.

[2] V.Yu. Belashov, *XXV General Assembly of URSI*, Lille (1996) 475.

[3] V.Yu. Belashov, S.V. Vladimirov, *Solitary Waves in Dispersive Complex Media*, Springer-Verlag GmbH & Co.KG, 2003.

Numerical study of interaction of vortex structures in plasmas and fluids[1]

V.Yu. Belashov, R.M. Singatulin

Kazan State Power Engineering University, 51 Krasnosel'skaya, Kazan 420066 Russia

The results of numerical study of evolution and interaction of the vortex structures in the continuum, and, specifically, in plasmas and fluids in the 2D approach, when the Euler-type equations are valid, are presented. The set of the model equations $e_i d_t x_i = \partial_{y_i} H/B$, $e_i d_t y_i = -\partial_{x_i} H/B$, $\partial_t \rho + \mathbf{v} \cdot \nabla \rho = 0$, $\mathbf{v} = -(\hat{z} \times \nabla \psi)/B$, $\Delta \psi = -\rho$ describing the a continuum or quasi-particles with Coulomb interaction models, where ρ is a vorticity or charge density and ψ is a stream function or potential for inviscid fluid and guiding-centre plasma, respectively, and H is a Hamiltonian, was considered. For numerical simulation the CD method specially modified was used. In terms of vortex motion of fluids the results of numerical experiments, specifically, showed that for some conditions the interaction of vortexes in continuum may be nontrivial and, as for the "classic" FAVRs, lead to formation of complex forms of vorticity regions, for example, the vorticity filaments and sheets, and also can ended to formation of the turbulent field. The undertaken approach may be effective in studying of the atmospheric and Alfvén vortex dynamics, and also useful for the interpretation of effects associated with turbulent processes in fluids and plasmas.

1. Basic equations

In this paper we study numerically the evolution and interaction of the vortex structures (so-called FAVRs [1]) in the continuum, and, specifically, in plasmas and fluids in 2D approach, when the Euler-type equations are valid. In general case the set of the model equations describing the a continuum (inviscid incompressible fluid) or quasi-particles (charged filaments aligned with a uniform field **B**) with Coulomb interaction models is the following:

$$e_i d_t x_i = \partial_{y_i} H/B, \quad e_i d_t y_i = -\partial_{x_i} H/B, \quad \partial_\mathbf{v} \equiv \partial/\partial \mathbf{v},$$

$$\partial_t \rho + \mathbf{v} \cdot \nabla \rho = 0, \quad \mathbf{v} = -(\hat{z} \times \nabla \psi)/B, \qquad (1)$$

$$\Delta \psi - f = -\rho$$

where e_i is the charge per unit length of the filaments or the strength (circulation) of discrete vortex, ϕ is a z-component of vorticity ζ or charge density ρ, and ψ is a stream function or potential for 2D flow of inviscid fluid and guiding-centre plasma, respectively, and H is a Hamiltonian. Note, that in the continuum (fluid) model $B=1$ in the Hamiltonian eqs. (1). Function $f = 0$ for the continuum or quasi-particles (filaments) with Coulomb interaction models [2], and $f = k^2 \psi$ for a screened Coulomb interaction model [3]. We will consider here only a case $f = 0$, and generalization of our approach for $f = k^2 \psi$ is rather trivially.

For numerical simulation the contour dynamics (CD) method [1], to some extent modified, was used. This method gives a possibility not only to observe evolution of single contour, but also to study the interaction between vortexes having different symmetry order (different modes). Let us demonstrate it in the next paragraph.

2. Numerical results and discussion

Let us consider some results of numerical simulation in terms of the vortex motion of the inviscid incompressible fluid, as more visual. In general, to study the evolution of vortex structures with different symmetry orders it is necessary to insert a small amplitude disturbance $r = R_0[1 + \varepsilon \cos(m\alpha - \tilde{\omega}_m t)]$ (where R_0 is a conditional radius, ε is an eccentricity, m is symmetry order (mode), α is an angle and $\tilde{\omega}_m = \zeta_0 (m-1)/2$) to the constant vorticity circle region. But, accounting that the results of evolution for one and two vortices with different m were described in detail in [4], let us stay on results on interaction of vortices and consider the most simple case of circle vortices when $m=1$ and, therefore, $\tilde{\omega}_m = 0$. For two vortices the result of the interaction depends on sign of vorticity ζ ("polarity") and the distance δ between boundaries of vortices. For two vortices having opposite polarities for initial distance $\delta = d$ where d is a vortex diameter we observed that the vortices, rotating in opposite directions, move in the same direction and, practically don't interact independently on value of δ. For the vortices having opposite polarity the result of evolution depends essentially on δ. So, for rather small δ the vortices, on a level with rotation about their own axes and around of their common center, interact forming a common vortex region which consists of the vorticities of more small scales. For rather big δ the vortices on a level with rotation about their own axes rotate around of common center, at this, their interaction is reduced to a cyclic change of their shape (so-called "quasi-return" phenomenon [1] is observed). In our numerical experiments we have found that critical initial distance dividing these two types of interaction $\delta_{cr} = 3d/4$.

To study the interaction of the linearly disposed vortices in more details we have consider the problem for four vortices being at initial time along one line. The simulation of the interaction at linear disposition of four vortices one can observe that for rather big and equal initial distance between vortices the evolution leads to formation of two vorticity regions as a result of more strong interaction of the "outer" vortices with the "inner" ones. At this, the interaction of forming pairs is similar to that of two vortices case. In case $\delta_i = d/2$ we observed the formation of a complex vortex structure which consists of many vorticities of more small scales. The further evolution of this structure leads to formation of complex turbulent field. Let us note that in last case we can also see that the interaction between outer vortices is more strong. This fact can be explained by the fact of more strong "attraction" of outer vortices to the "center of mass" of the vortex system because the outer vortex is attracted to the center by three other vortices, and the inner vortex is attracted to the center by two vortices and, in opposite side, by one outer vortex. To test this statement in the next series of numerical experiments we have arranged outer and inner vortices on different initial distances. As a result, we observed the formation of vortex structure from two inner vortices.

In the next series of experiments we studied the interaction between the vortices disposed at initial time in the corners of appropriate equilateral figures. At this, the following results were obtained. In case of evolution of three vortices with opposite signs of ζ being at initial time in the corners of triangle, we have obtained that a pair of them, having opposite polarities, behaves as well as pair of vortices with opposite polarities in two vortices case, and third vortex does not participate in interaction almost, practically independently on value of δ_i $(i = 1, 2, 3)$. The similar character of interaction is observed for four vortices with opposite signs of ζ being at $t = 0$ in the corners of square.

The character of interaction of three and four vortices having the same polarities depends essentially on the distances between them like in the two vortices case. For example, for $\delta = d/2 < \delta_{cr}$ we observed that three vortices are rotated forming one big vortex which consists of many vorticities of more small scales. Similar picture is observed for four vortices being at $t = 0$ in the corners of square on distances smaller critical one from another.

3. Conclusion

So, we have presented, as more visual, some results of numerical simulation of eqs. (1) in terms of the vortex motion of the inviscid incompressible fluid. But, as we noted in the beginning, the set of eqs. (1) with $f = 0$ may describe also the quasi-particles with Coulomb interaction model. At this, the results presented above can be easily extended on the 2D simple system where the plasma is represented by charged filaments, aligned with a uniform field $\mathbf{B}$, that move with the guiding-

centre velocity $\mathbf{E} \times \mathbf{B} / B^2$. Moreover, the approach undertaken can be useful and also for other 2D continuum models when $f \neq 0$ in the Poisson eq. (1). They can describe the vortices or filaments with the non-Coulomb interaction. In the last case it is assumed that ions move with the guiding-centre velocity but electrons have a Boltzman distribution, at this, the additional term $f = k^2 \psi$ will describe the Debye screening [3]. Another plasma model that can be investigated using the described approach is the Hasegawa-Mima model [5], its equations can also be put in form (1) by way of inclusion of ion polarization drift through the ion equation of motion [3] $d_t \mathbf{v} = (e/M)(-\nabla\varphi + \mathbf{v} \times \mathbf{B})$. As to a hydrodynamic fluid model corresponding to a screened interaction that such model having form (1) has been proposed in [6] to describe the Earth's atmosphere with the equation of motion for the horizontal atmospheric flow $d_t \mathbf{v} = -g\nabla h + R\mathbf{v} \times \hat{z})$ where h is the atmospheric depth and R is the Coriolis force. Another possible application can take a place in the study of the problems associated with the dynamics of the Alfven vortices in the ionospheric and magnetospheric plasma [7].

In conclusion, let us note that the applications of the dynamics of different types' vortex structures will not rest the problems of study of the processes discussed above. in the power units. Such investigations are now one of the most perspective trends in some technical fields, for example in the problems of study of the vortex motions in working chambers of the varied types' power units, where the working substance may be water, vapor-gas mixtures and plasma [8]. At this, the most actual problem is the investigation of the vortex motions in the spatial regions where there are the flows with velocity shear (for example, near the walls of the boiler of thermal power units and the chambers of the gas turbines), and also the study of the vortex motions in magnetized plasma without dissipation (controlled thermonuclear fusion systems) where the electric currents can lead to formation of very complicated forms of the vortex regions.

References

[1] N.J.Zabusky, M.H.Hughes, K.V.Roberts, *J. Comput. Phys.*, **135** (1997) 220.

[2] J.B.Tailor, B.McNamara, *Phys. Fluids* **14** (1971) 1492.

[3] J.B.Tailor, *Plasma Phys. and Contr. Fusion*, **39** (1997) A1.

[4] V.Yu.Belashov, R.M.Singatulin, *Proc. RNSPE-3*, Kazan, Russia, **2** (2001) 61.

[5] A.Hasegawa, K.Mima, *Phys. Fluids*, **21** (1978) 87.

[6] J.G.Charney, *Geophs. Public. Kosjones Nors.* Videnshap-Acad. Oslo, **17** (1948) 3.

[7] O.A.Pokhotelov, L.Stenflo, P.K.Shukla, *Plasma Physics Reports*, **22** (1996) 941.

[8] V.Yu.Belashov, R.M.Singatulin, *Izv.Vuzov - Pow. Eng. Probl.*, **9** (2001) 103.

The multidimensional solitons in a plasma: structure, stability and dynamics

V.Yu. Belashov[1a], S.V. Vladimirov[2 b]

[1]Kazan State Power Engineering University, 51 Krasnosel'skaya, Kazan 420066 Russia
[2]School of Physics, University of Sydney, NSW 2006, Australia

The formation, structure, stability and dynamics of multidimensional nonlinear waves and solitons in a plasma with $\mathbf{v} = -(\hat{z} \times \nabla \psi)/B$ and $\beta > 1$ are studied. To study the stability of multidimensional solitons, the variation problem of the Hamiltonian bounding with respect to deformations conserving momentum is used. To study evolution of solitons and their collision dynamics the equations are integrated numerically. It was obtained that in both cases the formation of multidimensional solitons can be observed. It is found that the soliton elastic collisions can lead to formation of complex structures including the multisoliton bound states.

1. Basic equations

In this paper, we study formation, structure, stability and dynamics of multidimensional solitons formed on the low-frequency branch of oscillations in a plasma for $\beta \equiv 4\pi nT/B^2 \ll 1$ and $\beta > 1$. These oscillations are described by equation

$$\partial_t u + A(t,u)u = f, \quad f = \kappa \int_{-\infty}^{x} \Delta_\perp u dx, \quad (1)$$
$$\Delta_\perp = \partial_y^2 + \partial_z^2.$$

For $A_1(t,u) = \alpha u \partial_x - \partial_x^2(\nu - \beta \partial_x - \gamma \partial_x^3)$ Eq. (1) falls into GKP (Generalized Kadomtsev-Petviashvili) class of equations, and in the case when $\beta \equiv 4\pi nT/B^2 \ll 1$ for $\omega < \omega_B = eB/Mc$, $k\lambda_D \ll 1$, describe propagation of the fast magnetosonic (FMS) wave in a magnetized plasma with $k_x^2 \gg k_\perp^2$, $v_x \ll c_A$ near the cone of $\theta = \arctan(M/m)^{1/2}$ [1]. In this case, the function u is the dimensionless amplitude of the magnetic field of the wave $h = B_\sim/B$, the factors at the terms describing nonlinearity, dissipation and dispersion effects, respectively, are defined by plasma parameters and the angle $\theta = (\mathbf{B},\mathbf{k})$. In opposite case, $A_2(t,u) = 3s|p|^2 u^2 \partial_x - \partial_x^2(i\lambda + \nu)$, Eq. (1) converts into 3D derivative nonlinear Schrödinger (3-DNLS) equation class and in the case when $\beta > 1$ describes dynamics of the finite-amplitude Alfvén waves propagating nearly parallel to $\mathbf{B}$ for $u = h = (B_y + iB_z)/2B|1 - \beta|$, $\mathbf{h} = \mathbf{B}_\perp/B_0$ where $p = (1 + ie)$, and e is the "eccentricity" of the polarization ellipse of the Alfvén wave [2]. The upper and lower signs of $\lambda = \pm 1$ correspond to the right and left circularly polarized wave, respectively; the sign of nonlinearity is accounted by the factor $s = \text{sgn}(1 - p) = \pm 1$ in the nonlinear term; and $\kappa = -r_A/2$, $r_A = v_A/\omega_{0i}$.

Eq. (1) with A_1 or A_2 is not completely integrable. Therefore, excluding the stability and asymptotic analysis we used numerical integration for study of evolution of solitons and their collision dynamics using the special simulation codes.

2. Stability of 2D and 3D solutions

To study stability of the GKP equation solutions, we performed coordinate transformation and rewrite Eqs. (1,2) into the Hamiltonian form

$$\partial_t u = \partial_x(\delta H/\delta u), \quad (2)$$

where

$$H = \int \left[-\frac{\varepsilon}{2}(\partial_x u)^2 + \frac{\lambda}{2}(\partial_x^2 u)^2 + \frac{1}{2}(\nabla_\perp \partial_x v)^2 - u^3 \right] d\mathbf{r},$$

$\partial_x^2 v = u$, $\varepsilon = \beta |\gamma| \Gamma^{-1/2}$, $\lambda = \text{sgn}\,\gamma$. The stationary solutions of Eq. (2) are defined from the variation problem, $\delta(H + vP_x) = 0$, where $P_x = \frac{1}{2}\int u^2 d\mathbf{r}$ is the momentum projection onto the x axis, v is the Lagrange's factor, illustrating the fact that all finite solutions of Eq. (2) are the stationary points of the Hamiltonian for fixed P_x. Thus, conforming with Lyapunov's theorem, it is needed to prove the Hamiltonian's boundedness (from below) for fixed P_x.

Let's consider in real vector space R the scale transformations $u(x, \mathbf{r}_\perp) \to \zeta^{-1/2} \eta^{(1-d)/2} u(x/\zeta, \mathbf{r}_\perp/\eta)$ (where d is the problem dimension, and $\zeta, \eta \in$ R) conserving the momentum projection P_x. The Hamiltonian as a function of parameters ζ, η takes a form

$$H(\zeta,\eta) = a\zeta^{-2} + b\zeta^2\eta^{-2} - c\zeta^{-1/2}\eta^{(1-d)/2} + e\zeta^{-4} \quad (3)$$

where

$a = -(\varepsilon/2)\int(\partial_x u)^2 d\mathbf{r}$, $b = (1/2)\int(\nabla_\perp \partial_x v)^2 d\mathbf{r}$, $c = \int u^3 d\mathbf{r}$, $e = (\lambda/2)\int(\partial_x^2 u)^2 d\mathbf{r}$. In 2D case [$d=2$ in expression

(3)] one can obtain that for $\lambda = 1, \varepsilon \leq 0$ the Hamiltonian at fixed P_x is bounded from below, and, hence, the 2D solitons are absolutely stable. In cases $\lambda = 1, \varepsilon > 0$ and $\lambda = -1, \varepsilon < 0$ H has local minima, and Eq. (2) may have the locally stable solutions for some parameters. All other cases correspond to unstable 2D solutions.

In 3D case we obtain that the absolutely stable 3D solutions take place for $\lambda = 1, \varepsilon > 0$, and the locally stable solutions can be observed for $\lambda = 1, \varepsilon \leq 0$ if the condition $ab^2 e / c^4 < 9/512$ is satisfied. The analysis to the problem of the FMS waves beam's propagation in magnetized plasma enables us to prove [1], for example, that the 3D beam propagating at θ angle to the magnetic field is not focusing and therefore becomes stationary and stable within the cone $\theta < \arctan (M / m)^{1/2}$ when $(m / M - \cot^2 \theta)^2 [\cot^4 \theta (1 + \cot^2 \theta)]^{-1} > 4/3$. We also note that obtained results give us the possibility to interpret correctly some numerical and theoretical results on the dynamics of the internal gravity wave solitons induced by the pulse-type sources in the F-region of the ionosphere [3].

To study stability of the 3-DNLS equation solutions we used the formal change $u \to h$ and investigated the boundedness of the Hamiltonian [2]

$$H = \int_{-\infty}^{\infty} \left[\frac{1}{2} |h|^4 + \lambda s h h^* \partial_x \varphi + \frac{1}{2} \kappa (\nabla_\perp \partial_x w)^2 \right] d\mathbf{r}, \quad (4)$$
$$\partial_x^2 w = h, \ \varphi = \arg(h),$$

for transformation $h(x, \mathbf{r}_\perp) \to \zeta^{-1/2} \eta^{-1} h(x/\zeta, \mathbf{r}_\perp/\eta)$ ($\zeta, \eta \in \mathbf{C}$) conserving P_x, in complex vector space $\mathbf{C}$. The Hamiltonian as a function of ζ, η is given by

$$H(\zeta, \eta) = a \zeta^{-1} \eta^{-2} + b \zeta^{-1} + c \zeta^2 \eta^{-2} \qquad (5)$$

where $a = (1/2) \int |h|^4 \, d\mathbf{r}$, $b = \lambda s \int h h^* \partial_x \varphi \, d\mathbf{r}$, $c = (\sigma/2) \int (\nabla_\perp \partial_x w)^2 d\mathbf{r}$. Solving the extremum problem for functional (5) we obtain that Hamiltonian (4) is bounded from below, i.e.,

$$H > -3bd / (1 + 2d^2), \quad b < 0 \qquad (6)$$

if $ac^{-1} < d = \left(2\sqrt{2} \right)^{-1} \sqrt{13 + \sqrt{185}}$, and in this case 3D solutions of 3-DNLS equation are stable. The solutions are unstable in the opposite case, $ac^{-1} \geq d, b < 0$. Condition $b < 0$ corresponds to the right circularly polarized wave with $p = 4\pi n T / B^2 > 1$, i.e. when $\lambda = 1, s = -1$, and to the left circularly polarized wave when $\lambda = -1, s = 1$. It is necessary to note that the sign change $\lambda = 1 \to -1, s = -1 \to 1$ is equivalent to the change $t \to -t, \kappa \to -\kappa$ and for negative κ the Hamiltonian becomes negative in the area "occupied" by the 3D wave weakly limited in the $\mathbf{k}_\perp$-direction; in this case condition (6) is not satisfied. Change of sign of b to

positive (when $\lambda = 1, s = 1$ or $\lambda = -1, s = -1$) is equivalent to the analytical extension of solution from real y, z to pure imaginary values: $y \to -iy, z \to -iz$ and, therefore, equivalent to the change of sign of κ in the basic equations. In this case instead of inequality (6) the opposite inequality will take place. From the physical point of view this means that if the opposite inequality is satisfied, the right polarized wave with the positive nonlinearity and the left polarized wave with the negative nonlinearity are stable.

3. Numerical results

In our numerical experiments we have investigated two types of the low-frequency oscillations in a plasma with $\beta \ll 1$ and $\beta > 1$ which correspond to two types of waves and can lead to the formation of the multidimensional solitary wave structures. As a result, we have obtained that for FMS waves the 2D and 3D soliton formation can be observed. In particular, we observed the formation of a stable soliton with oscillating asymptotics, that corresponds to above mentioned analytical results. It is interesting to note that the 2D soliton interaction dynamics is not trivial for GKP equation unlike usual KP equation [4]. So, for example, for $\lambda = 1$, $\varepsilon > 0$ the formation of a stable two-soliton structure (so-called "bisoliton") can be observed as a final result of interaction of two initial pulses. In the 3D case for the FMS wave beam having the small angular distribution, the stationary propagation may be observed as a result of the nonlinear beam stabilization.

In the case of Alfvén waves propagating along the magnetic field lines, we have obtained that 3D stable solutions may be observed, with 3D spreading and collapsing ones. These results can be also interpreted in terms of the self-focusing phenomenon for the Alfvén waves' beam as the stationary beam formation, scattering, and self-focusing. Let's note that we observed the dynamics of the Alfvén waves' beam propagating in a plasma with $\beta > 1$ at angles near 0° with respect to the magnetic field, and the dynamics of the FMS wave beam propagating in plasma with $\beta \ll 1$ at angles near $\pi / 2$ with respect to the magnetic field. Let's note that for all cases the analysis of the Hamiltonian H deformations on the numerical solutions confirmed the stability of solutions considered above.

References

[1] V.Yu. Belashov, *Plasma Phys. and Contr. Fusion*, **36** (1994) 1661.
[2] V.Yu. Belashov, S.V. Vladimirov, *Solitary Waves in Dispersive Complex Media*, Springer-Verlag GmbH & Co.KG, 2003.
[3] V.Yu. Belashov, *Proc. 1989 Intern. Symp. on EMC*, Nagoya, Japan, **1** (1989) 228.
[4] V.I. Karpman, V.Yu. Belashov, Phys. Lett. 154A (1991) 131.

176

One-dimensional nonlinear and nonlocal oscillations of plasma

Paulius Miskinis

Vilnius Gediminas Technical University, Faculty of Fundamental Sciences, Department of Physics,
Sauletekio Ave. 11, LT-2040, Vilnius, Lithuania

A simple one-dimensional model describing nonlinear and nonlocal oscillations of electron plasma is considered. Due regard to the nonlocality of field potential allows to smooth down the peaks of nonlinear waves, to steep up the wave front, to modify the velocity amplitude and phase of the travelling wave.

1. Introduction

In many of the models of election magnetic hydrodynamics, a more complex spatial distribution of currents and fields is usually reduced by shifting to the corresponding two- or even one-dimensional systems, utilizing the symmetry of a model under study. Nevertheless, the magnetic field is essentially three-dimensional, and such simplifications can evoke manifestations of the effective nonlocality of a two- or one-dimensional medium. A good example of such nonlocality can be electron flows in a flat plasma layer [1], the Hall effect in thin films [2], in which the nonlocality of the medium is manifested in an integral relation between the current density J and the z-component of the magnetic field B_z expressed by the Ampere law:

$$B_z = \text{v.p.} \frac{2}{c} \int_{-\infty}^{+\infty} \frac{J(\xi)}{\xi - x} d\xi \qquad (1)$$

The nonlocality of vortex filaments in solitary thin film [3, 4] and layered superconductors [5], where nonlocality is manifested in the expression for the two-dimensional current function ψ related to the non-divergent current density j (e_z is the unit vector of the axis z)

$$j = \frac{c}{4\pi} \nabla \times (\psi e_z) . \qquad (2)$$

In the present work, on an example of a simple one-dimensional model, the problem of nonlinear and nonlocal oscillations of electron plasma is investigated. Due regard to the nonlocality of the field potential allows to smooth down the peaks of nonlinear waves, to steep up the wave front, to modify the velocity amplitude and to change the velocity phase of the travelling wave.

2. The nonlocal oscillations

The simplest model of electron plasma oscillation, which takes into account the influence of the potential nonlocality, is described by the model system of equations

$$\begin{cases} \dfrac{\partial \rho}{\partial t} + \dfrac{\partial (\rho v)}{\partial x} = 0, \\[2mm] \dfrac{\partial v}{\partial t} + v \dfrac{\partial v}{\partial x} = {}_a D_x^\alpha \varphi, \\[2mm] \dfrac{\partial^2 \varphi}{dx^2} = 4\pi (\rho - 1), \end{cases} \qquad (3)$$

where ρ is the density of plasma, v is the velocity, and φ is the potential. The system of units $e = m = \rho_0 = 1$ has been chosen. ${}_a D_x^\alpha \varphi$ is a fractional derivative [6, 7]:

$$ {}_a D_x^\alpha f(x) = \frac{1}{\Gamma(1-\alpha)} \frac{d}{dx} \int_a^x \frac{t(t)dt}{(x-t)^\alpha} \qquad (4)$$

and the order of the derivative $\alpha \sim 1$. Note here that at $\alpha = 1$ we have a classic system of evolution equations described in [8, 9] .

We will take into consideration only the travelling wave type solutions that depend only on the variable $\xi = x - ut$, where $u = const$ is the wave velocity. This assumption essentially simplifies the evolution equation (1) and leads to the system

$$\begin{cases} \dfrac{\partial}{\partial \xi} \rho(v - u) = 0, \\[2mm] \dfrac{\partial}{\partial \xi} \left(\dfrac{1}{2} v^2 - uv - {}_a I_x^{1-\alpha} \varphi \right) = 0, \\[2mm] \dfrac{\partial^2 \varphi}{d\xi^2} = 4\pi (\rho - 1), \end{cases} \qquad (5)$$

where ${}_a I_x^\alpha = {}_a D_x^{-\alpha} \varphi$ is the fractional integral of the order α [6] .

From the first equation in (5) follows the relation
$$\rho(v - u) = A , \qquad (6)$$
where $A = const$. It plays the role of the boundary condition. Also, from the other two equations of the system (5) it follows that

$$v = u - \sqrt{2 {}_a I_x^\alpha \varphi} \qquad (7)$$

and the Hamiltonian of the system

$$H = \frac{1}{2} v^2 - uv - {}_a I_x^{1-\varepsilon} \varphi = const \qquad (8)$$

Let us introduce the new variables

$$x = \frac{1}{4}v^2, \quad \frac{1}{2}y^{3-\alpha} = -_a I_x^{1-\alpha}\varphi .$$ (9)

Then the Hamiltonian H is

$$H = \frac{1}{2}y^{3-\alpha} - 2u\sqrt{x} + 2x = -\frac{1}{2}u^2 .$$ (10)

The phase trajectories in the phase plane (x, y) (see Fig.1) are closed curves surrounding the centre-focus $(0, u^2/4)$:

$$y^{3-\alpha} = 4u\sqrt{x} - 4x + 2E ,$$ (11)

and crossing the axis x in the points

$$x = \frac{1}{4}(u \pm s)^2, \quad s = \sqrt{u^2 + 2E} .$$ (12)

a)   b)
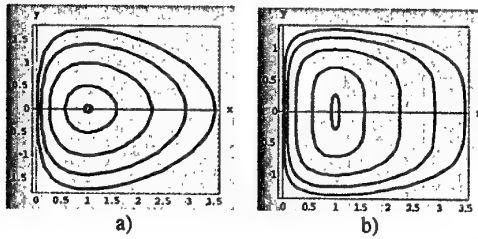
Fig. 1. Phase diagram of a system with the Hamiltonian $H = y^{3-\alpha}/2 - 2u\sqrt{x} + 2x$: a) for $\alpha = 1$ (local case) and b) $\alpha = 0.6$ (nonlocal case); $u = 2$ and $E = -3.995; -3; -2; -1$.

The bound states $E < 0$ are separated from the unbound ones by the condition $E = 0$, which leads to the region $x \in [0; u^2]$.

It is possible to show that the period of plasma oscillation for $\alpha = 1$

$$T = \oint \frac{dv}{\dot{v}} = \frac{2\pi}{\omega_o}$$ (13)

and does not depend on the oscillation energy E. At the same time the oscillations are unharmonic.

Interestingly, after substituting (7) the evolution equations turn into a system of separate equations:

$$\begin{cases} \rho = -\dfrac{A}{\sqrt{2_a I_\xi^{1-\alpha}\varphi}}, \\[2mm] v = u - \sqrt{2_a I_\xi^{1-\alpha}\varphi} , \\[2mm] \dfrac{d^2\varphi}{d\xi^2} = -4\pi\left(A\varphi^{-\frac{1}{2}} + 1\right) \end{cases}$$ (14)

Nevertheless, the velocity $v(\xi)$ can be derived from the Hamiltonian H (10). If $\psi(\xi) = v(\xi)/\varepsilon$, where $\varepsilon = \left(1 - |E|/(2\omega_o^2)\right)$, then

$$\psi(\xi) = -\cos\left[\pm\omega_o\xi - \varepsilon\left(1 - \psi^2\right)^{\frac{1}{3-\alpha}}\right],$$ (15)

where $\omega_o^2 = 4\pi e^2 n_o/m$ is the frequency of plasma oscillations, and "±" stands for the different half-

periods of oscillations. The explicit dependence $v(t)$ for a fixed value of the space variable x is shown in Fig.2. For $\alpha = 1$, we have only local oscillations:

$$\psi = -\cos\left[\pm\omega_0\xi - \varepsilon\left(1 - \psi^2\right)^{1/2}\right], \quad \psi = \frac{1}{\varepsilon}v .$$

3. Conclusions

The main peculiarities of the nonlocal plasma velocity oscillations are:
- steepening up of the wave front
- changes of the velocity amplitude

$$v \sim u - \omega_0^{\frac{\alpha-1}{2}}\sqrt{2\varphi}$$

- the smoothened peak of the nonlinear wave top
- the global phase shift $\Delta\psi \sim (\alpha-1)\pi/2$ of velocity oscillations
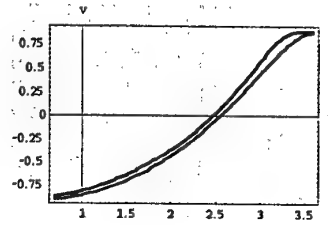
Fig. 2. Velocity of oscillations $v(t)$ in dependence on time at the frequency $\omega = 1$, parameter $\varepsilon = 0.9$, if nonlocality $\alpha = 0.05$ and phase shift $\Delta\varphi = 0.079$ (upper line) respect the local case (lower line). For simplicity, the next symmetric half-period of the periodic wave is omitted.

Note that all these peculiarities are of qualitative character. For quantitative assessments, a model of real plasma is advisable.

4. References

[1] E.B. Tatarinova, K.V. Chukbar. JETP **92**(3) (1987) 809.
[2] K.V. Chukbar. JETP **97**(4) (1990) 1362 .
[3] A.N. Artemenko, A.N. Kruglov, Phys. Lett. A **143** (1990) 485.
[4] M.V. Feigel'man, V.B. Geshkenbein, A.I. Larkin. Physica C 167 (1990) 177 .
[5] K.V. Chukbar, V.B. Yan'kov. JETP Letters. **61**(6) (1995) 487 .
[6] G.S. Samko, A.A. Kilbas, O.I. Marichev. *Fractional Integrals and Derivatives*. (Gordon and Breach; Amsterdam) 1993 .
[7] R.Hilfer. *Application of Fractional Calculus in Physics*. (World Scientific, Singapore) 2000.
[8] R.Z. Sagdeev. *Problems of Theory of Plasma*. Moscow: Atomizdat. **4** (1964) 20 (in Russian) .
[9] A.I. Achiezer, G.Ya.Liubarsky. Dokl. AN USSR. **80** (1951) 193 (in Russian) .

178

Controlling chaos caused by the current-driven ion acoustic instability

in a laboratory plasma using delayed feedback

Takao Fukuyama[1], Kazunari Taniguchi[2], Hiroyuki Shirahama[3], and Yoshinobu Kawai[1]

[1] Interdisciplinary Graduate School of Engineering Sciences, Kyushu University,

Kasuga-kouen 6-1, Kasuga, Fukuoka 816-8580, Japan

Electronic mail: fukuyama@aees.kyushu-u.ac.jp

[2] Department of Science, Kyoto University of Education,

Fujimori-cho 1, Fukakusa, Fushimi-ku, Kyoto 612-8522, Japan

[3] Division of Technology, Faculty of Education, Ehime University,

Bunkyo-cho 3, Matsuyama, Ehime 791-8577, Japan

Controlling chaos caused by the current-driven ion acoustic instability is attempted using the delayed continuous feedback method, i.e., the time-delay auto synchronization (TDAS) method introduced by Pyragas [Phys. Lett. A 170 (1992) 421.] with flexibility.

1. Introduction

Over the past decade, the problem of controlling chaos has attracted great interest in many fields, such as lasers,[1] motivated by the importance of the role. The serious role of turbulence in fusion-oriented plasmas creates a special interest in controlling chaos.

An effective method of controlling chaos, which has been proposed by Ott, Grebogi, and Yorke (OGY),[2] has attracted much attention. On the other hand, Pyragas[3] has proposed a time-delay feedback technique, i.e., the time-delay auto synchronization (TDAS) method,[4] which is appropriate for the experimental systems working in real time.

We have attempted chaos control using the TDAS method based on the Pyragas technique in order to attain stable chaos control.

2. Experimental set up

The experiments are performed using a Double Plasma device. Argon gas is introduced into the chamber at a pressure of 4.0×10^{-4} Torr. Typical plasma parameters are as follows: the electron density $n_e \sim 10^8$ cm^{-3}, electron temperature $T_e \sim 0.5$-1.0 eV.

The current-driven ion acoustic instability is excited by the two parallel mesh grids installed into the chamber (G_1 and G_2). A dc potential V_m is applied to G_1 in order to excite the current-driven ion acoustic instability, and G_2 is kept at floating potential. Time series signals for analysis are obtained from the fluctuating components of the currents on the V_m biased mesh grids.

The experiments in controlling chaos are performed by applying the feedback signal $F(x)$ to the floating mesh grid G_2. The feedback signal $F(x)$ is generated from $x(t)$, using the electronic circuit based on the TDAS method.

Chart of experimental setting is shown in Fig. 1.
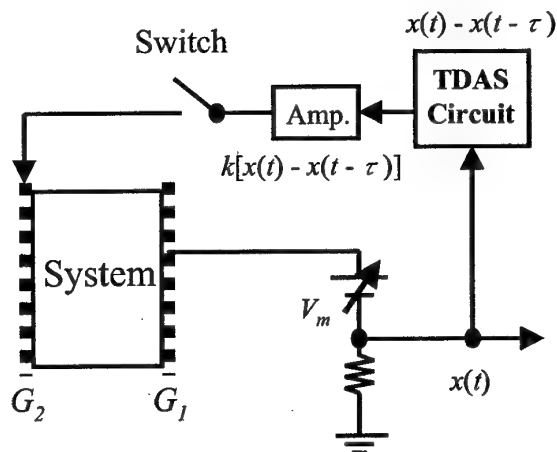
Figure1: Chart of experimental setting.

3. Experimental results and discussions

When the grid bias V_m exceeds a threshold, the current-driven ion acoustic instability is excited. When V_m exceeds 40 V, a limit cycle oscillation appears. Then, according to increasing V_m, the system becomes chaotic via bifurcation. The system presents a typical chaotic feature around $V_m = 54$ V. The TDAS control

is applied to the typical chaotic state.

Figure 2 shows the stabilization process of chaos using the TDAS method. Figure 2(a) and (b) correspond to the time series signal and the feedback signal during the transition from the uncontrolled to the controlled state, respectively. Here, τ and k are 20 μs ($\sim$ 1.16 period) and 0.28, respectively. The details of the state before and after switching on the control is depicted in Fig. 3, showing the time series signal, and $I(t) - I'(t)$ trajectories in the phase plane, the power spectra, respectively. It is found that the system changes from chaotic to periodic, maintaining the instability, and the fundamental mode ($\sim$ 70 kHz) of the unstable periodic orbit is selected during controlling process.[5]
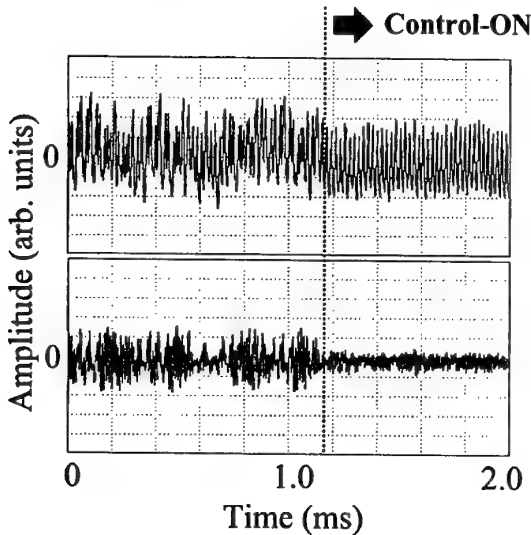
Figure2: The stabilization process of chaos using the TDAS method.
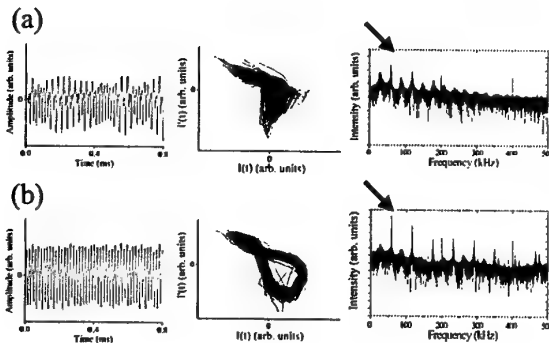
Figure3: The details of the state before and after switching on the control.
(a) Before control, (b) after control.

4. Further issue

Delayed feedback is applied to the periodic oscillation ($V_m = 40$ V), and the dynamical behavior is studied.

When the TDAS method is applied to periodic nonlinear regime and arbitrary delay time τ is chosen, the periodic state changes to various states such as "Type-1 intermittency" and unstable "period-3" orbits in period-doubling bifurcation, as shown in Fig. 4.
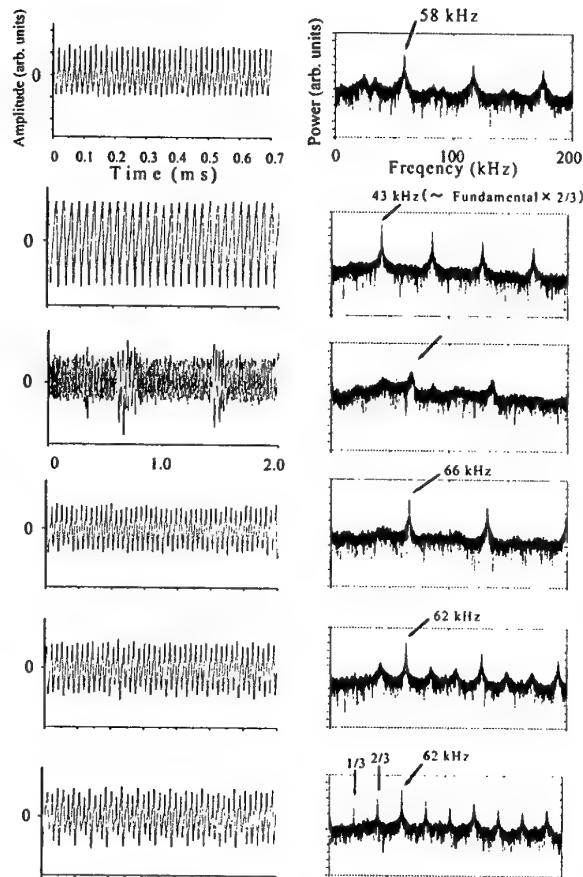
Figure4: Dynamical behavior of the system as a function of τ.

5. References

[1] S. Bielawski, D. Derozier, and P. Glorieux, Phys. Rev. E **49** (1994) R971.

[2] E. Ott, C. Grebogi, and J. A. Yorke, Phys. Rev. Lett. **64** (1990) 1196.

[3] K. Pyragas, Phys. Lett. A **170**, 421 (1992).

[4] Th. Pierre, G. Bonhomme, and A. Atipo, Phys. Rev. Lett. **76** (1996) 2290.

[5] T. Fukuyama, H. Shirahama, and Y. Kawai, Phys. Plasmas **9** (2002) 4525.

180

Dynamical behavior of coupled chaotic oscillators including phase synchronization and complete synchronization in plasma

Takao Fukuyama and Yoshinobu Kawai

Interdisciplinary Graduate School of Engineering Sciences,
Kyushu University, Kasuga-kouen 6-1, Kasuga, Fukuoka 816-8580, Japan
Electronic mail: fukuyama@aees.kyushu-u.ac.jp

The dynamical behavior of two coupled chaotic oscillators caused by the current-driven ion acoustic instability is experimentally studied. It is found that when two oscillators (two unstable waves) are interacting, and the dc potential applied to either of the two oscillators is varied gradually while maintaining coupling, the two oscillators synchronize in a certain region.

1. Introduction

Recently, the synchronization of two chaotic oscillators[1] has attracted much attention in many branches of science, motivated by the possibility of wide spread applications of coupled nonlinear oscillators. It is well known that two chaotic oscillators can synchronize through interaction, namely, coupling. This synchronization has useful applications in chaos control.[2] Coupled nonlinear oscillators exhibit a variety of fundamental dynamical phenomena in addition to the synchronization of mutual chaotic oscillators. The dynamical behavior of the coupled nonlinear oscillators including chaos synchronization has been studied in laser systems,[3] the electronic circuits[4] and so forth. The behaviors of coupled nonlinear oscillators are interesting phenomena in the study of plasma physics as well as other branches of science.

We have study the dynamical behavior of two coupled chaotic oscillators caused by the current-driven ion acoustic instability.

2. Experimental set up

The experiments are performed using a Double Plasma device. Argon gas is introduced into the chamber at a pressure of 4.0×10^{-4} Torr. Typical plasma parameters are as follows: the electron density $n_e \sim 10^8$ cm^{-3}, electron temperature $T_e \sim 0.5$-1.0 eV.

The current-driven ion acoustic instability is excited by the two parallel mesh grids installed into the chamber (G_1 and G_2). The dc potential V_m is applied to the mesh grid G_1 and V_S is applied to the mesh grid G_2 in order to excite the current-driven ion acoustic instability. V_m and V_s are control parameters which govern instability-1 and instability-2, respectively. Thus, interaction of two unstable waves (instabilities), namely coupling, is made.

Time series signals for analysis are obtained from the fluctuating components of the currents on the biased mesh grids on both ends (G_1 and G_2), and are sampled with a digital oscilloscope.

Figure 1 and 2 show schematic diagram of the experimental apparatus and chart of experimental setting, respectively.
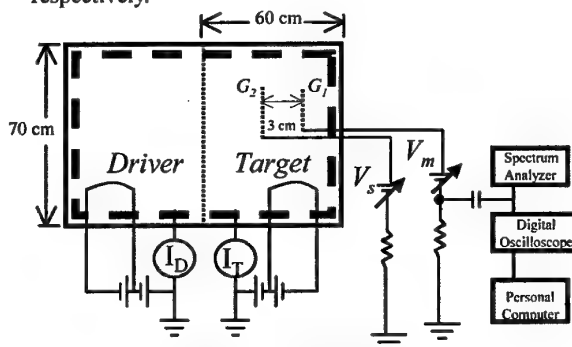
Figure1: Schematic diagram of the experimental apparatus.
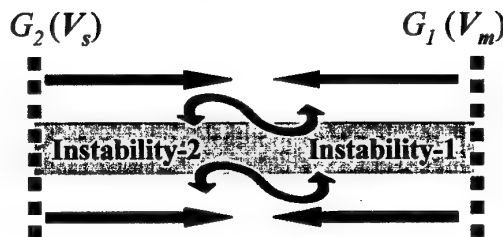
Figure2: Schematic of coupling of two oscillators.

3. Experimental results and discussions

When the grid bias exceeds a threshold, the current-driven ion acoustic instability is excited. We investigate the behavior of the coupled system where two chaotic oscillators caused by the instability interact. We change V_m gradually and the control parameter V_s governing instability-2 is fixed at 53 V.

For $0 V < V_m < 24$ V, only instability-2 oscillates since instability-1 is not yet excited in this range of the parameter. For $24 V < V_m < 38$ V, instability-1 is also excited and the system does not reach the synchronization state, as shown in Fig. 3. Figure 3(a) and (b) shows the time series of the signals and the X - Y plot of the two instabilities shown in (a). For $38 V < V_m < 60$ V, the phase synchronization[5] is observed. With increasing V_m, the two oscillators synchronize gradually, and finally for $60 V < V_m < 64$ V, the complete synchronization is observed, as shown in Fig. 4. For $V_m > 64$ V, instability-1 vanishes gradually.

(a)

(b)

Figure4: Complete synchronized state.
($V_m = 62$V, $V_s = 53$V)

4. Conclusion

Two oscillators caused by the current-driven ion acoustic instability have been coupled through the interaction of two unstable waves. When the control parameter V_m of instability-1 is changed gradually, with V_s fixed at 53 V, phenomena such as "phase synchronization" and "complete synchronization" have been observed. Thus, dynamical behavior of two coupled chaotic oscillators by mutual coupling has been observed in plasma.[6]

5. References

[1] L. M. Pecora and T. L. Carroll, Phys. Rev. Lett. **64** (1990) 821.

[2] K. Pyragas, Phys. Lett. A **170** (1992) 421.

[3] T. Heil, *et. al.*, Phys. Rev. Lett. **86** (2001) 795.

[4] R. D. Pinto, *et al*, Phys. Rev. E **62** (2000) 2644.

[5] S. Boccaletti, J. Bragard, F. T. Arecchi, and H. Mancini, Phys. Rev. Lett. **83** (1999) 536.

[6] T. Fukuyama and Y. Kawai, J. Phys. Soc. Jpn. **71** (2002)1809.

Figure3: Non synchronized state.

($V_m = 33$V, $V_s = 53$V)

Frequency up-shift in interaction of powerful plasma wave with an inhomogenous plasma

V.I. Arkhipenko, E.Z. Gusakov*, V.A. Pisarev, L.V. Simonchik

Institute of Molecular and Atomic Physics NASB, F.Skaryna Ave. 70, 220072 Minsk, Belarus
*Ioffe Physical-Technical Institute RAS, Politekhnicheskaya Str. 26, 194021 St. Petersburg, Russia

A frequency upshift of twenty megahertz is observed in the interaction of a high power microwave (f_0=2.84 GHz) with a magnetized inhomogeneous argon plasma. The dependencies of the frequency up-shift on the incident microwave power and frequency have been investigated. The induced frequency upshift is considered to be related to a rapidly growth plasma density in plasma waveguide.

The experiments were performed in a linear plasma device "Granite" [1] where plasma was produced using the electron cyclotron discharge in glass tube (Fig 1). The experiment parameters are as follows: external magnetic field is 0.35 T, the argon gas pressure is 2 Pa, the plasma inhomogeneity scale along magnetic field and across it are $a = 5$ cm and $b = 0.4$ cm accordingly, the maximal electron density is $n_e \sim 5 \times 10^{12}$ cm^{-3}, electron temperature is $T_e = 2$ eV. An electron plasma wave (EPW) at frequency $f = \omega/(2\pi) = 2.84$ GHz in the form of the fundamental Trivelpiece-Gould mode was launched into the plasma by waveguide. The dispersion relation for this wave is $k_\perp^2 = [\omega_{pe}^2 (r, z) / \omega^2 - 1] k_\parallel^2$, where $k_\parallel$ and $k_\perp$ are the components of the wave vector parallel and transverse to the magnetic field. The high density plasma ($n_e(r,z) > n_c$, where n_c - critical electron density) creates a plasma waveguide for EPW (Fig. 1). Propagating to a point of a plasma resonance (focal point), where $\omega = \omega_{pe}(0, z)$ the wave slows down and its electric field increases drastically. This electric field
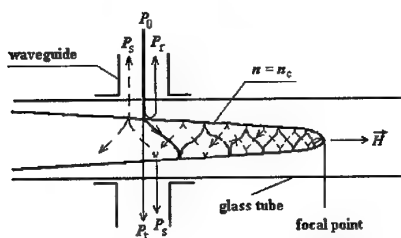
Fig. 1. Scheme of excitation and propagation of the EPW. P_0, P_t, P_s, P_r are incident, transient, scattered and reflected power correspondingly.

growth is so significant, that the incident wave power of 10 mW is enough for excitation of the parametric decay instability of stimulated backscattering $l \rightarrow l' + s$ [2].

At pump power $P \geq 5$ W the oscillatory energy of electrons exceeds already the ionisation energy of argon atoms. At this condition intensive resonance interaction of wave with electrons and, as a consequence, the capture of electrons and wave breakdown should take place [3, 4].

Parameters of microwave pump in present experiments are as follows: incident pulse power is $P \sim 50 - 200$ W, pulse duration is up to 2.5 μs, pulse rise time is $t_f \sim 40$

ns, repetition frequency is 300 Hz. The oscillogram of incident pulse is shown in fig. 2a. A number of diagnostics, possessing sufficient time resolution such as: multi-grid analyzer and spectroscopic, cavity, were used in the experiment.

As it is seen in oscillograms of multi-grid analyser (Fig. 2c) two separate bursts of electron current are generated in plasma after the microwave pulse is on. The first one is observed immediately after the application of microwave power, whereas the position of the second is determined by the pump power. The termination of the second fast electron current burst is always accompanied by oscillations observed on the microwave detector in the waveguide Fig. 2b. These oscillations indicate the wave reflected in plasma, which is up-shifted in frequency. The power of this wave is comparable to the launched one.

High energetic electrons produce the increased excita-
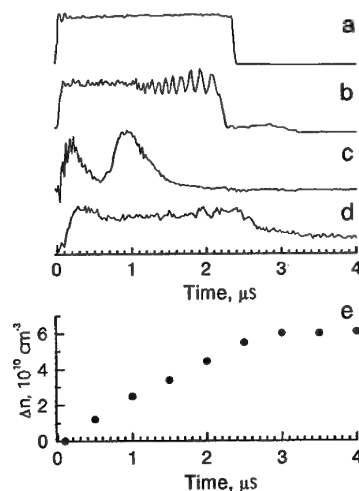
Fig. 2. Oscillograms of incident (a) and scattered (b) microwave pulses, currents of multi-grid analyzer (c), light intensity (d) and time behavior of electron number density (e) in focal region

tion and ionisation of argon atoms. To obtain the absolute spatial density distribution we used the data for average electron density and radial distribution of lu-

minosity integrated in visible spectral region, as radial distribution of plasma density. This method was tested earlier in [1]. The contours of electron density distribution at different time, calculated in this way, are plotted in fig. 6. Ten grey gradation were used in these pictures to scale the plasma density magnitudes. Maximal light hue corresponds to electron number density of $5 \cdot 10^{11}$ cm^{-3}.

These pictures obviously illustrate formation of longitudinal plasma channel, which serves as a waveguide for EPW. When the channel propagates down to the dis-

initial plasma   t = 0.5 μs

←—— 25 cm ——→

t = 1.1 μs   t = 2.4 μs

2 cm
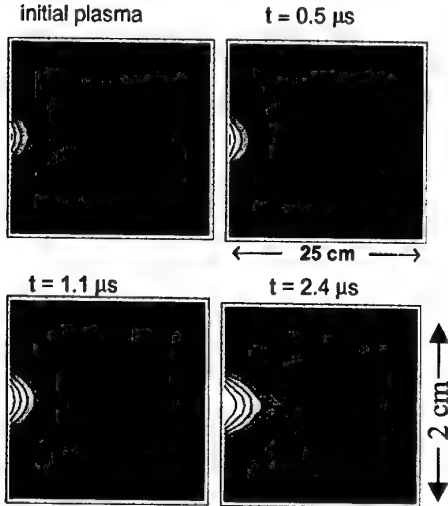
Fig. 3. Contours of the electron density distribution.

tance of 45 cm from the launcher it goes out from the magnetic system. The magnetic field quickly decreases and conditions for the EPW change drastically leading to its reflection. The reflection takes place also when the multi-grid analyzer is placed at distance less than 45 cm. Reflected wave propagates in opposite direction towards the launcher in non-stationary narrow channel with increasing density (see fig. 3). That leads to an additional phase taper and, correspondingly, to the frequency up-shift of the wave. The magnitude of frequency shift is changed in time and depends on both the frequency and power of pulses. It exceeds 20 MHz at the oscillation onset and then falls sharply to the frequency shift of ~5 MHz, which is weakly changed down to pulse termination (Fig. 4). The onset time of oscillations decreases with the pump power. It can be explained by quicker channel formation due to growth of electron energy and, as consequence, increasing of ionisation rate.

At the over and back wave propagation in plasma waveguide of length L the phase taper is $\delta\Phi = -2k_0L$. Using expression for k_0 from [1] we can obtained

$$\delta\Phi = -2\frac{L}{b}\frac{n_c}{n_c(z,t)-n_c}.$$

Phase factor have a following form $\Phi = \omega_0 t - 2\int k_0 dz$. Then wave frequency is $\omega = \frac{d\Phi}{dt} = \omega_0 + \frac{d\delta\Phi}{dt}$, and frequency difference is
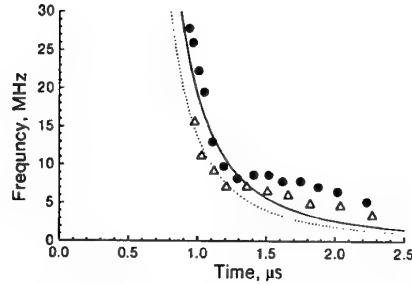
Fig. 4. Temporal dependences of the frequency up-shift experiment (•) and calculation (solid curve) for $f = 2840$ MHz; (Δ) and dashed curve for $f = 2400$ MHz, correspondingly

$$\delta f = \frac{\delta\omega}{2\pi} = \frac{1}{\pi}\frac{L}{b}\frac{n_c}{(n_c(z,t)-n_c)^2}\frac{dn_c}{dt}.$$

As it should be from time resolved plasma density measurements the plasma density in focal point changes linearly dependent. Using this fact we can obtain follow expression for frequency difference:

$$\delta f = \frac{1}{\pi}\frac{L}{b}\frac{n_c}{\frac{dn_c}{dt}(t-t_*)^2}, \qquad (1)$$

where t_* is is the time determined by plasma channel propagation up to reflection region.

Calculations fulfilled using (1) for experimental condition corresponding the plasma channel formation in fig. 3 at power ~100 W are shown in fig. 4. Apparently the frequency up-shift varies with t^{-2} and decreases with the incident wave frequency decrease.

References

[1] V.I. Arkhipenko, V.N. Budnikov et al, *Plasma Physics Reports* 7 (1981) 396.

[2] V.I. Arkhipenko, V.N. Budnikov et al, *Plasma Physics Reports* 13 (1987) 693.

[3] V.I. Arkhipenko, E.Z. Gusakov et al, *Proc. of the III Intern. Workshop "Strong microwaves in plasmas", Nizhny Novgorod* 2 (1996) 516.

[4] V.I. Arkhipenko, E.Z. Gusakov et al, Proc. *29th EPS Conference on Plasma Phys. and Contr. Fusion Montreux* ECA **26**B (2002) P-5.009.

Modelling the control of the space charge dynamics in a system of two electrical glow discharge plasma

Cristina Stan[1], C. P. Cristescu[1], D. Alexandroaei[2]

[1]Department of Physics, Polytechnic University of Bucharest, 313 Spl. Independentei, 77206-Bucharest, Romania,
[2]Department of Plasma Physics, "Al. I. Cuza" University of Iassy, 12 Blv Carol, Romania

This work present a comparative study between the experimental data on the system of two electrical glow discharge plasma and the simulated data from a system of ordinary differential equations based on van der Pol oscillators with reference to the control of the space charge dynamics.

1. Introduction

The dynamics of space charge structures in the form of a double layer, an arrangement of electric positive and negative charges localised in adjacent positions represent the subject of the present work. Experimentally it is found that these structures are very sensitive to the biasing conditions and that they cause most of the oscillatory phenomena of the plasma system as a whole [1,2].

We present a comparative study between the experimental control on of the dynamics of double layer structures and the computed results of a model consisting on two coupled perturbed van der Pol oscillators [3,4,5].

The numerical results of our computer model are in reasonable agreement with the experiment.

2. Experimental system

The experiments were carried out on the plasma created as a result of coupling of two adjacent independent glow discharges that are biased one against the other.

The experimental device consists of two short adjacent glow discharges, with plane cathodes and cylindrical anodes, all placed in the same glass tube, in argon at low pressure [2,4].

The plasma is formed in the contact region of the two negative glow plasmas, between the two anodes that are biased one against the other by a dc power supply whose voltage U_m is considered as the experimental control parameter. The ac mode of biasing is realized by connecting a corresponding power supply U_m in series with the dc biasing one U_m.

For certain experimental conditions, depending on the U_m biasing potential, coherent or non-coherent oscillations of the current I flowing through the inter-anode interval are observed. These oscillations are correlated with the dynamics of the DLs that appear in the plasma. Different complicated spatial-temporal patterns for different values of U_m have been observed [4,6].
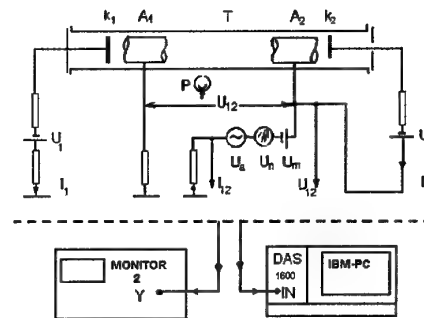
Fig. 1 Diagram of the experimental set-up

3. Mathematical model

For this experimental arrangement we proposed a model with two coupled perturbed van de Pol oscillators [3,4].

$$\begin{cases} \dot{x}_1 = x_2 + mx_4 \\ \dot{x}_2 = -c\left(x_1^2 - 1\right)x_2 - x_1 + e\cos x_5 \\ \qquad + m(x_4 + x_3) \\ \dot{x}_3 = x_4 - mx_2 \\ \dot{x}_4 = -f\left(x_3^2 - 1\right)x_4 - x_3 - e\cos x_5 \\ \qquad - m(x_2 + x_1) \\ \dot{x}_5 = 2\pi g \end{cases}$$

We consider the free oscillations of the plasma to be modelled by two van der Pol oscillators with dc and ac coupling.

4. Discussion and conclusion

The bifurcation diagram is a convenient way to identify values of the control parameter for which the system shows ordered and chaotic dynamics. However, there are situations, as shown in Fig.2, where the system presents intermittent transitions from periodicity to chaos. This behaviour could not be observed from the

bifurcation diagram, but it can be easily discerned from a stroboscopic representation as shown in Fig.2.

time (units of T)

(a)

time (units of T)
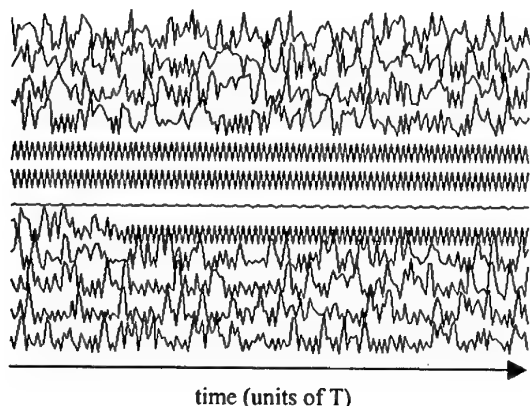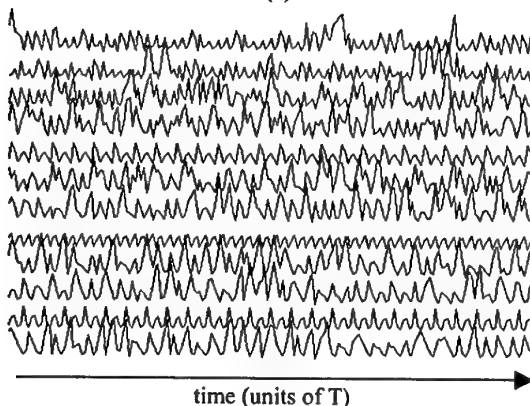
(b)

Fig. 2 Plot of the stroboscopically sampled amplitude x_1 in units of T, recorded for different values of the control parameter m, for $c=f=1$, $e=2$, $g=0.5$: (a) - for $m=1$ to $m=1.055$; (b) – for $m=1.07$ to $m=1.125$

In Fig.2 is shown the temporal behaviour of the amplitude of the first oscillator (x_1) for a range of values of the control parameter m.
The data were stroboscopically sampled with the period (T) of the forcing signal. The period of the fundamental of the oscillation is found to be a multiple of the forcing period, between T and $7T$. This obviously is a consequence of a frequency locking between the frequency of the forcing signal and the frequency of the free oscillation of the system ($e=0$). Spectral analysis confirms this conclusion.
The analysis of the dynamics of the system with respect to the amplitude of the forcing (e) for constant m shows that for values of e in excess of certain threshold values the forcing plays an important role in the synchronization of the system on frequencies which are subharmonics of the forcing.

The computed data of our model are in reasonable agreement with the experiment and shows the possibility of control of the dynamics of the system by an external source.

5. References

[1] D. Alexandroaei, M.Sanduloviciu, *Phys.Lett. A*, **122** (1987) 173.
[2] D. Alexandroaei, M. Sanduloviciu, *Rom. Journ. Phys.* **40**, 841 (1995)
[3] C. Stan, C. P. Cristescu, D. Alexandroaei, Proceedings of the XXV ICPIG, edited by T. Goto (Nagoya University, Nagoya, 2001), **3** (2001) 169
[4] C. Stan, C. P. Cristescu, D. Alexandroaei, *Contr. Plasma Phys.* **42** (2002) 81.
[5] C. P. Cristescu, C. Stan, D. Alexandroaei, *Phys. Rev. E* **65** (2002) 016602

On the Formation of Plasma Complex Structures
in Argon Glow Discharge

Georgeta Strat, S. Gurlui and M. Strat
"Al. I. Cuza" University of Iasi, Romania
*"Gh. Asachi" Tehnical University of Iasi, Romania

In this paper we show some of the phenomena which take place in the plasma complex structures
formed in the transition region between two negative glows.

1. Introduction

The complex plasma structures which appear in glow discharges such as a plasma formation near an anode, the stratification of the positive column of a glow discharge, the free formation formed at the contact region between two negative glows and others, are striking examples of the self-organization of a strongly nonechilibrum systems.

At the beginning of the 1970s interpretation of the moving striations (ionization waves) was based upon hydrodinamic fluid models. However, in the glow discharges (low pressures and small currents) where most theoretical and experimental studies applied, a nonlocal kinetic analysis of the plasma is required. In the glow discharges where inelastic collisions prevail in the electron energy balance, the instabilities that appear because of some resonance kinetic effects [1]

Other recent research concerning the origin of coherent space charge configurations formed in plasma underlined that the key processes related to self-organization are the symmetry breaking of both the excitation and ionization cross section functions together with their spatial separation [2].

In this paper we show that the same phenomena take place in the plasma complex structures formed in the transition region between two negative glows.

2. Experimental set-up and results

The experimental device is presented in Fig.1
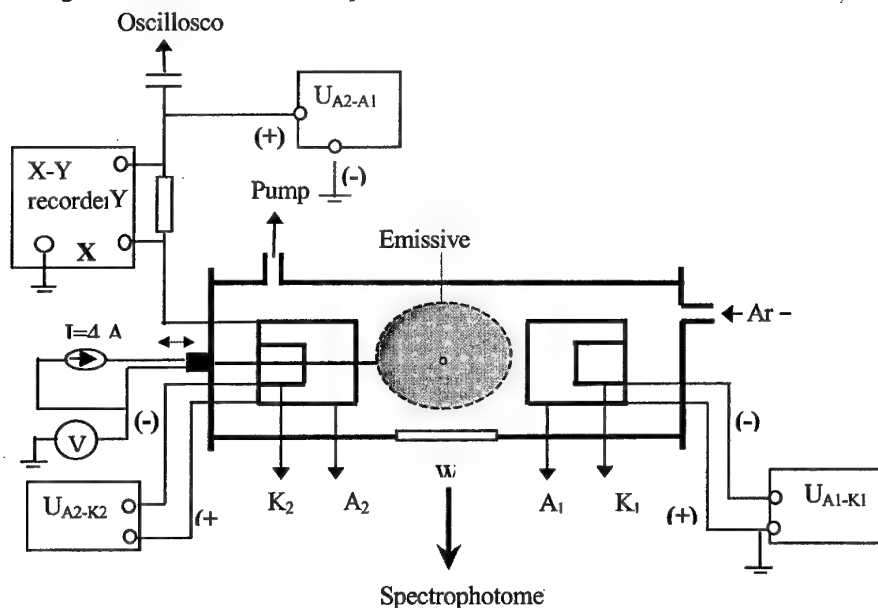
Figure 1 – The experimental set-up

A cylindrical stainless steel tube contains the following components: K_1, K_2-Al hole cathodes with 2.5 cm in diameter and 3.2 cm in lengths; A_1, A_2-cylindrical anodes with 7.0 cm in lengths and 4.0 cm in diameter, P– emissive probe (0.2 mm diameter Ta wire and 3 mm in lengths as a loop shape). Each anode was placed coaxial around the corresponding cathode and the probe, axially movable was passed through the K_2 axis. Axial and radial distributions of light intensity and corresponding optical spectra was obtained using a system of illumination of a entrance slit of a double mono-chromator with high spectral resolution (0,5 cm⁻¹). As it has been shown in many papers, the plasma double layers can be produced after a local acceleration

of the electrons towards a pozitevely polarized electrode which is imersed in a plasma at a thermodynamic equilibrum and asymptotically stable. Under such conditions the initially present symmetry of all the functions that describe the physical system took into consideration (DL) is broken. This is the initial condition for the appearance of self-organization. From these functions the most important are the following : the excitation cross section, the ionization cross section, the ionization rate and the electron density. In these conditions, the sudden increase in different but adjacent regions of these functions determines the self-assemblage of an instability (for example a DL) whose stability is assured by electrostatic forces acting as long range correlation between the two space charges. The development of the axial instability is caused by the nonlocality of the electron distribution and ionization threshold, which results in the presence of phase shifts between the ionization rate and electron density [3].

The experimental device described above allows us to prove the role of the self organization processes in the apparition of plasma formations in the region between A_1 and A_2 anodes.

Thus, gradually increasing and decreasing the biased voltage on the anode A_2 (U_{12}) we obtained the I(V)-characteristic shown in Fig.2. The I(V) characteristic presents some non-liniarities which emphasize the existence of a multiplicity of states of the plasma formations created in the contact region between two negative glows by applying a positive voltage on the anode A_2.

In the voltage range, (V_1-V_2) (see Fig.2), the current, I_{12}, increase only a little (biased voltage ≈ 50 V). A further increase of the biased voltage (at $V_3= 55$ V) produces a sudden jump in the current (V_3-V_4).

The free floating plasma formations generated
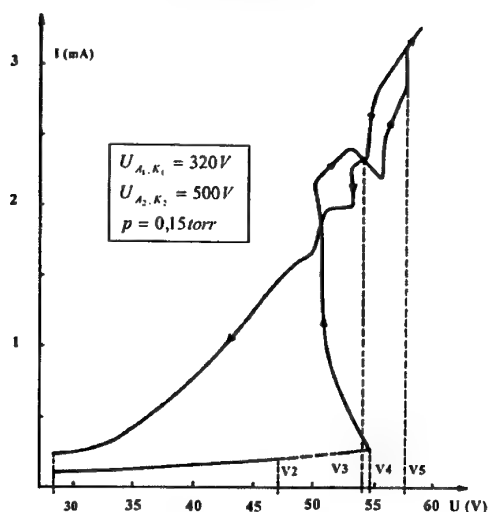
between V_3 and V_5. When V is further increased the plasma formation becomes pulsatory.

For initiating the cascading self-organization processes it is necessary to bring the gaseous conductor in a bi-stable state obtained when V-value is between V_1 and V_3 [2]. In this voltage range, the current is situated in the low current branch of I(V) characteristic and in the contact region between the negative glows, it spontaneously initiates the self assemblage of the plasma formations accompanied by a sudden jump of the current. The experimental investigations proved the presence of the complex space charge configurations whose self-consistances are ensured by electrical double layers.

The study of the plasma formations, by means of electrical and spectral methods, shows that at the origin of the coherent space charge configurations formed in the plasma are the self-organization processes which begin when the symmetry breaking of both the excitation and ionizations cross section functions together with their spatial separation appears.

The development of the axial instability (DL) appears when there are phase shifts between the ionization rate and electron density.

In Fig.3 the axial profiles of the electron density and of the ion spectral line intensities, measured in the maximum, at different distances from de anode A_2 along one plasma formation are given.
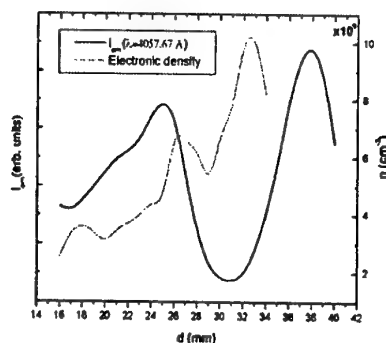
Fig. 3: The space shift between electron density and ionization rate

3. References

[1]   F. Sienger, Yu B. Golubovski, I. A. Prokhova, R. Winkler, *Plasma Chem. Plasma Process.* **18** (1998) 153;

[2]   M. Sanduloviciu, E. Lozneanu, S. Popescu, *J. Plasma Fussion Res. SERIES* **2** (1999) 486;

[3]   Yu B. Golubovskii, R.V. Kozakov, V.A. Maiarov, J. Behnke, *Phys. Rev. E* **62** (2000) 2707.

Fig. 2: The I(V)- characteristic in the case of existence of three plasma formations

this way are stable as long as the value of voltage V is

Control of Chaotic States in DP Machine Plasma by Using External Circuit Elements

Dan-Gheorghe DIMITRIU, Erzilia LOZNEANU, Codrina IONIȚĂ*, Mihaela MIHAI-PLUGARU,
George AMARANDEI, Cezar GĂMAN, Mircea SANDULOVICIU, Roman SCHRITTWIESER*

Faculty of Physics, "Al. I. Cuza" University of Iaşi, Bd. Carol I No. 11, RO-6600 Iaşi, Romania
*Institute for Ion Physics, "Leopold-Franzens" University of Innsbruck, Technikerstr. 25, A-6020 Innsbruck, Austria

We present a simple, effective and low-cost experimental method to control chaos in a DP-machine plasma. By using a capacitor, we can substitute the low-frequency chaos (uncorrelated oscillations), which appears in the S-type negative differential resistance region of the static I-V characteristic, by a nonlinear oscillation, the frequency of which is controlled by the external capacitance.

1. Introduction

Control of chaos is one of the most important problems of nonlinear physics [1]. In plasma physics a great interest exists in this subject [2,3], especially in the view of controlled fusion projects.

It is well known [4,5] that under certain experimental conditions in the front of a positively biased electrode immersed into plasma, a complex space charge configuration (CSCC) in form of an electrical double layer (DL) can appear. The static $I-V$ characteristic of the electrode shows at least two regions of negative differential resistance, one S-type and one N-type. The S-type negative differential resistance is related to the appearance and disappearance of a CSCC [4,5], whereas the N-type negative differential resistance is related to the spatio-temporal dynamics of a CSCC [6,7], or to the onset of a low-frequency instability [8]. Between these two regions uncorrelated low-frequency oscillations with a continuous spectrum can appear. Since the oscillations are not correlated, the plasma enters a chaotic state. To avoid this we have inserted a capacitor between the electrode and the ground. In this way a regular oscillatory state supersedes the chaotic one. The frequency of the observed oscillations depends on the time constants of the capacitor.

2. Experimental results and discussion

The experiments were performed in the DP machine of the University of Innsbruck, which was described elsewhere [9]. The plasma, created in the source chamber, was pulled away from thermal equilibrium by gradually increasing the voltage applied to a tantalum disk electrode with 2 cm diameter. The argon pressure was $p = 5 \times 10^{-3}$ mbar and the plasma density $n = 10^{10}$ cm^{-3}. At a certain value of the potential on the electrode a quasi-spherical luminous CSCC, confined by a space charge DL, appears in front of the electrode. Fig. 1a and 1c shows the current oscillations through the electrode and the FFT of these, respectively, recorded after the appearance of the CSCC. To characterise these oscillations, we present the autocorrelation function (Fig. 1e) and the reconstructed state space (Fig. 1g). From these figures we conclude that the oscillations are not corre-

lated, giving rise to a low-dimensional chaotic state. By introducing a capacitor into the external electronic circuit between the electrode and ground, we obtain a new oscillation [10], the period of which is determined by the charging and discharging time constants of the capacitor. Fig. 1b, 1d, 1f and 1h show the time series, the FFT, the autocorrelation function and the reconstructed state space, respectively, corresponding to these new current oscillations.

Because of the strong nonlinearity of the CSCC, the noise, which is permanently present in the system, can induce some uncorrelated oscillations of the current, corresponding to jumps of the structure between various unstable states, characterised by different electric conductivities. Usually it is very difficult to control the noise level experimentally. An alternative is to substitute the chaotic dynamics by a periodically one and to control its dynamics by the frequency of the oscillations. This is the method, which also we use. As described above, the periodical state is obtained by inserting a capacitor into the external electrical circuit. In this way we can control the dynamics of the CSCC by modifying the capacitance of the capacitor.

3. Conclusion

We propose a simple, effective and low-cost method to control chaos in a DP-machine plasma. The method permits the substitution of a chaotic state (uncorrelated low-frequency oscillations) by a periodical one, the frequency of which can be easily controlled. For this we only need a capacitor.

References

1. T. Shinbrot, *Adv. Physics* **44** (1995) 73;
2. T. Mausbach, T. Klinger, A. Piel, *Phys. Plasmas* **6** (1999) 3817;
3. T. Klinger, C. Schröder, *Phys. Plasmas* **8** (2001), 1961;
4. R. A. Bosch, R. L. Merlino, *Contrib. Plasma Phys.* **26** (1986) 1;
5. B. Song, N. D'Angelo, R. L. Merlino, *J. Phys. D: Appl. Phys.* **24** (1991) 1789;

6. M. Sanduloviciu, C. Borcia, G. Leu, *Phys. Lett. A* **208** (1995) 136;

7. E. Lozneanu *et al.*, *J. Plasma Fus. Res. SERIES* **2** (1999) 389;

8. C. Avram, R. W. Schrittwieser, M. Sanduloviciu: *J. Phys. D: Appl. Phys.* **32** (1999) 2750 and 2758;

9. R. Schrittwieser *et al.*, *Physica Scripta* **T84** (2000), 122;

10. D. Dimitriu *et al.*, *Proc. 29th EPS Conf. on Plasma Phys. and Control. Fus* (Montreux, Switzerland, 2002), *Europ. Conf. Abstr.* **26B** (2002), p. 2.003.
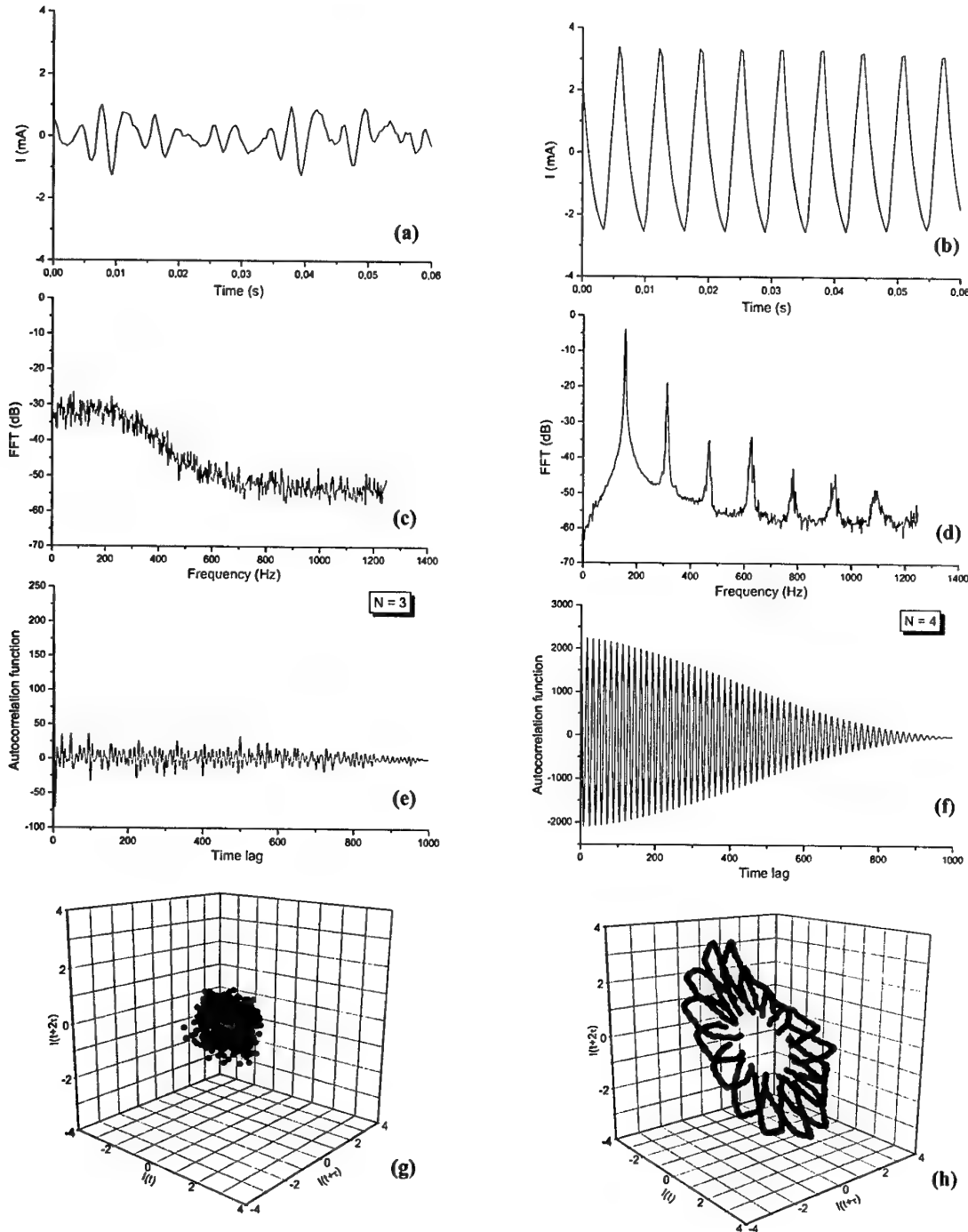
Fig. 1: Time series, FFT, autocorrelation function and reconstructed space of the current oscillations, respectively, before (left column) and after (right column) insertion of a capacitor.

Simple Method to Control the Nonlinear Dynamics of a Ball of Fire in a DP Machine Plasma

Dan-Gheorghe DIMITRIU, Erzilia LOZNEANU, Codrina IONIȚĂ*, Mihaela MIHAI-PLUGARU, George AMARANDEI, Cezar GĂMAN, Mircea SANDULOVICIU, Roman SCHRITTWIESER*

Faculty of Physics, "Al. I. Cuza" University of Iasi, Bd. Carol I No. 11, RO-6600 Iași, Romania
*Institute for Ion Physics, "Leopold-Franzens" University of Innsbruck, Technikerstr. 25, A-6020 Innsbruck, Austria

We present a simple experimental method to obtain harmonic oscillations of the current in the presence of a ball of fire, in a DP machine plasma. By insertion of a coil in the external electrical circuit we can suppress all the higher harmonics, transforming the nonlinear oscillations into sinusoidal ones.

1. Introduction

By applying a positive potential to an electrode immersed in a plasma, in front of it a complex space charge configuration (CSCC) in form of a spherical double layer (DL) can appear [1,2], which is also sometimes called ball of fire. If the value of the potential on the electrode is large enough, the CSCC shows spatio-temporal dynamics related with the formation and disruption of the DL [3,4]. The plasma system performs strongly nonlinear oscillations, characterised by the presence of many higher harmonics in their spectrum. But, for many applications, purely harmonic oscillations are required, so we need to suppress the higher harmonics. This is possible by inserting an inductance into the external electronic circuit, in series with the electrode and the power supply. The oscillation frequency depends on the inductance according to Thomson's formula.

2. Experimental results and discussion

The experiments were performed in the DP machine of the University of Innsbruck, which has been described elsewhere [5]. The plasma created in the source chamber was pulled away from thermal equilibrium by gradually increasing the voltage applied to a tantalum disk electrode with 2 cm diameter. The argon pressure was $p = 5 \times 10^{-3}$ mbar and the plasma density $n = 10^{10}$ cm^{-3}. By applying a voltage $V_E = 75$ V to the electrode we obtain high-amplitude current oscillations, represented in Fig. 1a. Fig. 1c shows the spectrum of these oscillations. We observe the existence of many higher harmonics, and the oscillations are strongly nonlinear. To characterise the oscillations, we present the autocorrelation function (Fig. 1e) and the reconstructed phase space (Fig. 1g), obtained by using the method of delays, proposed by Packard et al. [6], Ruelle [7] and Takens [8]. To control these current oscillations we have inserted a coil with the inductance L into the external electrical circuit, in series with the electrode and the power supply. The proper choice of L can lead to the transformation of nonlinear oscillations into harmonic ones. Figs. 1b, 1d, 1f and 1h show the current oscillations, the FFT, the autocorrelation function and the reconstructed space, respectively, for the case when the coil is inserted. We observe the disappearance of all higher harmonics from the spectrum, with the oscilla-

tions assuming a sinusoidal shape. The reconstructed space has a perfect circular shape, which is characteristic for harmonic oscillations. The square of the oscillation frequency depends on the inverse of the inductance, according to Thomson's formula.

The oscillatory state before connecting the coil corresponds to the transition of the DL into a propagating state, during which new DLs are successively generated and detaching from the electrode [3,4]. The frequency of these oscillations is determined both by the values of external circuit elements and by the characteristics of the plasma (including the DL). The existence of many higher harmonics in the spectrum (Fig. 1c) is an indication for the strong nonlinearity of the oscillations. These higher harmonics can be very advantageous in some applications, as e.g. high frequency generators. But in most of the applications it is preferable to generate harmonic (sinusoidal) oscillations. According to the Thomson formula, we can obtain harmonic oscillations by modifying the capacitance or the inductance either of the plasma, or of the external electrical circuit elements (capacitors and coils). Our choice was to insert an inductance into the external electrical circuit and to find a suitable value of the inductance in such a way that the obtained current oscillations will be harmonic (Fig. 1b). In this case we obtain a resonance between the power source of oscillations (the dc power supply) and the oscillatory circuit (plasma together with the external electrical circuit elements).

3. Conclusions

We propose a simple method to control the nonlinear dynamics of a ball of fire in DP machine plasma. The method eliminates all higher harmonics of a strongly nonlinear oscillation obtaining a purely sinusoidal one.

References

[1] R. A. Bosch, R. L. Merlino, *Contrib. Plasma Phys.* **26** (1986) 1;
[2] B. Song, N. D'Angelo, R. L. Merlino, *J. Phys. D: Appl. Phys.* **24** (1991) 1789;
[3] M. Sanduloviciu, C. Borcia, G. Leu: *Phys. Lett. A* **208** (1995) 136;
[4] E. Lozneanu *et al.*: *J. Plasma Fus. Res. SERIES* **2** (1999), 389;

[5] R. Schrittwieser et al., Physica Scripta T84 (2000), 122;

[6] N. H. Packard et al.: Phys. Rev. Lett. 45 (1980) 712;

[7] D. Ruelle: in Chaotic Evolution and Strange Attractors, Cambridge University Press, Cambridge 1989;

[8] F. Takens: in Dynamical Systems and Turbulence, Lecture Notes in Mathematics vol. 898 (Eds. D. A. Rand, L. S. Young). Springer-Verlag, Berlin 1981.
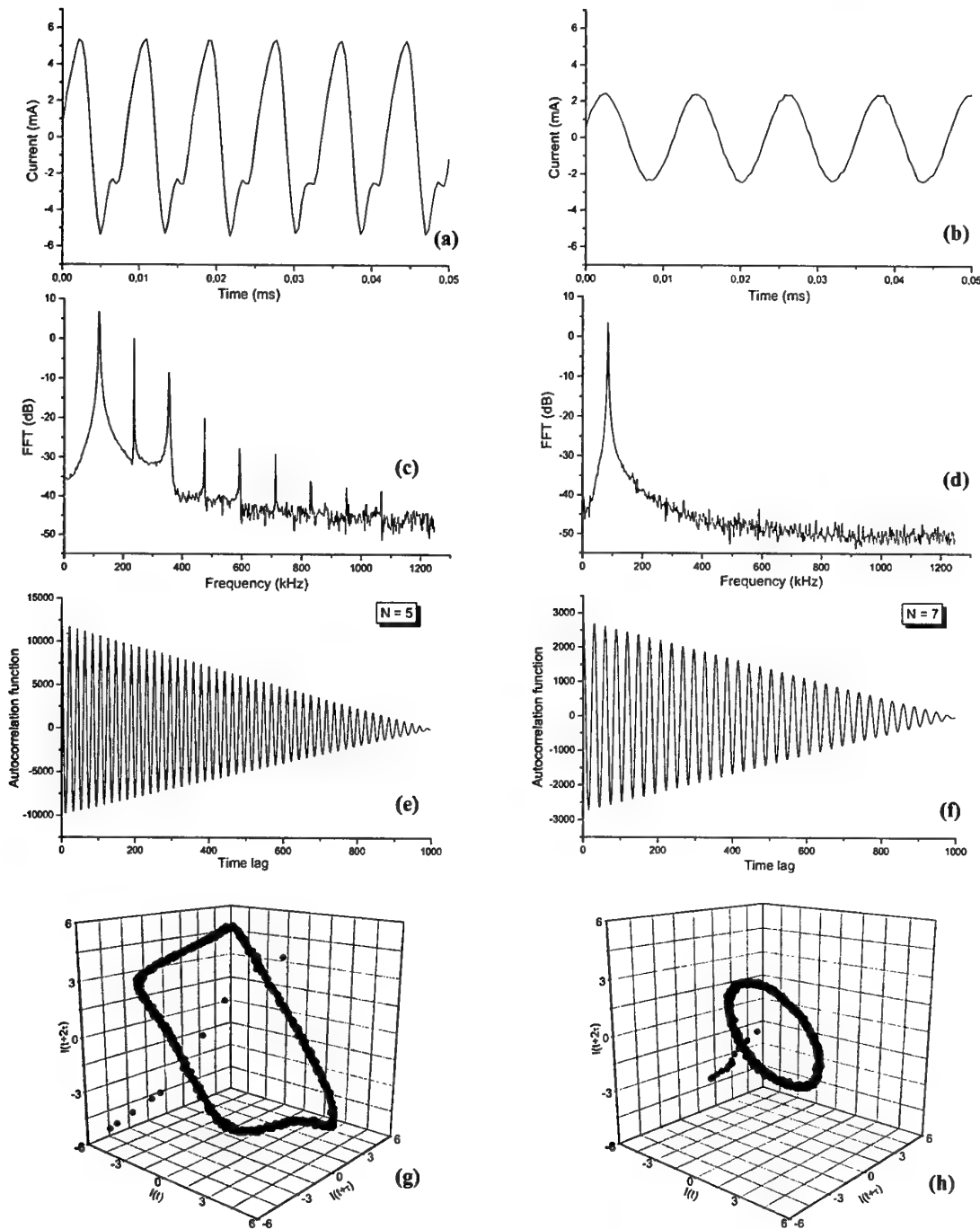
Fig. 1: Time series, FFT, autocorrelation function and 3D Poincaré map through the reconstructed phase space of the current oscillations, respectively, before (left column) and after (right column) the insertion of the coil.

Self-organization acting as physical basis for stimulation of oscillations in plasma devices

E. Lozneanu, V. Pohoata, S. Popescu and M. Sanduloviciu

Department of Plasma Physics, Al. I. Cuza University, 6600 Iasi, Romania

C. Ionita and R. Schrittwieser

Institute for Ion Physics, L. Franzens University, 6020 Innsbruck, Austria

Oscillations stimulated by two kinds of negative differential resistance related to self-organized spatial, respectively spatio-temporal patterns are presented and discussed.

1. Introduction

When a gaseous conductor in a plasma device is subjected to an external constraint (electric field) that gradually drives the gaseous conductor away from the thermodynamic equilibrium, two phases of self-organization can be observed [1-3]. The first one is finished with the emergence of a stable complex space charge configuration known as fireball (FB). The second one is related to the transition of FB into an unstable steady state (regular in behavior) during which a proper dynamics of the double layer (DL) from its border ensures its existence [2,3]. Both phases of self-organization are related to abrupt nonlinear variations of the current transported by the gaseous conductor experimentally observed as an S-shaped, respectively a Z-shaped bistability. Their appearance attributes to the gaseous conductor the ability to work as an S-respectively an N-shaped negative differential resistance (NDR) [2-5].

2. Experimental results and discussion

In this paper we present experimental results obtained on the DP-machine of the University of Innsbruck, Austria [6]. Thus, in Fig. 1(a) the current I_E collected by a positively biased disk electrode E immersed in the plasma of the DP-machine is plotted as a function of the potential V_E of E. The critical points on this characteristic are marked by letters. Note that the external dc power supply was connected to E through a resistor $R = 10 \, \Omega$. Fig. 1(b) presents the oscillations that appear simultaneously with the abrupt increase of I_E (branch c-d), respectively those that appear when I_E suddenly decrease (branch e-f). The corresponding power spectra are shown in Fig. 1(c). The electrode potential values for which the signals were collected are marked with the same letters in all graphs.

From Fig. 1(a) results that the abrupt increase of I_E marked by the branch c-d is accompanied by the appearance of strong oscillations in the voltage range d-e, the frequency of which depends on V_E. The shape of the oscillations and the corresponding power spectra immediately after their appearance (point d in Fig. 1) and the abrupt transition of the system into another oscillation regime (point e in Fig. 1) are shown in Fig. 1(b) respectively Fig. 1(c). When the voltage of the external dc power supply is gradually decreased the
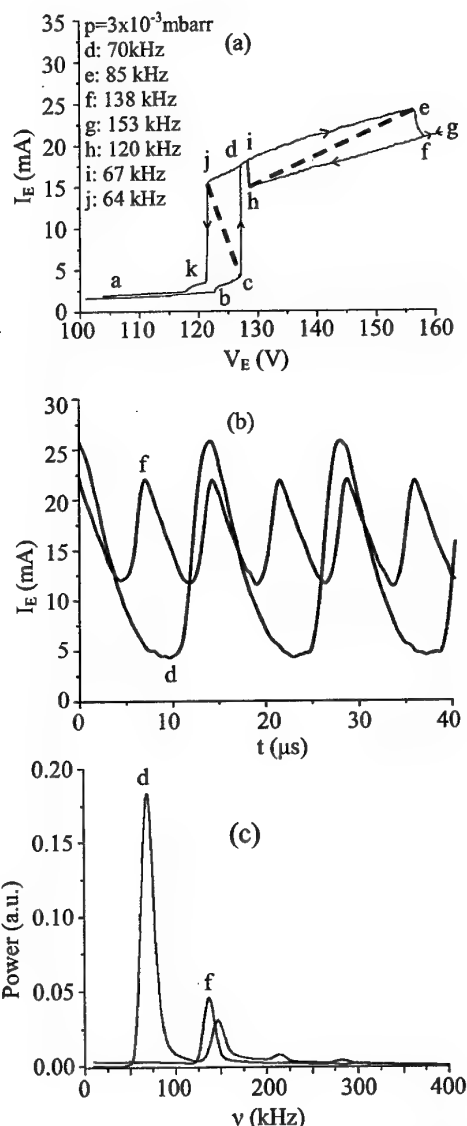
Fig. 1 (a) Current *versus* voltage static characteristic; (b) oscillations stimulated by S-, respectively Z-shaped bistability; (c) power spectra of the oscillations shown in Fig. (b)

I(V)-characteristic presented in Fig. 1(a) emphasizes two hysteresis loops, the first one proving the presence of an S-shaped bistability (that corresponds to an S-shaped NDR [3,4]) and the second one the presence of a Z-shaped bistability (that corresponds to an N-shaped NDR [3,5]). The NDR corresponding to the voltage intervals in which the gaseous conductor reveals bistability are marked in Fig. 1(a) by broken lines.

For explaining the two kinds of the oscillations generated by the DP-machine we take into account that the oscillations with lower frequencies (64-85 kHz) are related to the presence of the S-shaped NDR, whereas the oscillations with higher frequencies (120-153 kHz) to the presence of the N-shaped NDR. As already shown [4], the S-shaped NDR stimulates oscillations only when the system is suitably connected to a resonant circuit able to perform natural oscillations with an amplitude sufficient to trigger the self-assembling and de-aggregation of FB formed in front of E. In that case the oscillations appear spontaneously with the maximal value of their amplitude. Such a stimulation mechanism corresponds to a subcritical Hopf bifurcation. In the case investigated by us the oscillatory circuit contains as reactive elements the capacitance of the DL from the FB border and an inductance related to the phase difference of the electrons and positive ions emphasized during the self-assembling and de-aggregation processes of the FB. The other kind of oscillations, the frequency of which is twice the frequency stimulated by the S-shaped NDR, is related to the N-shaped NDR. Usually the amplitude of these oscillations softly increases, so that this can be classified as a supercritical Hopf bifurcation.

The experimental results presented in Fig. 1 emphasize two essential facts. First, during the self-assembling process of FB matter and energy delivered from the external dc power supply are used to produce the ordered arrangement of opposite space charges inside FB, *i.e.* its self-organization process. Secondly, during FB de-aggregation the stored matter and energy can be used for stimulating oscillations when FB is suitably connected to a resonant system [4] or when FB acts itself as a resonant system. The sudden change of the oscillations regime at a frequency twice the frequency related with the self-assembling and de-aggregation of the FB and half of amplitude proves the appearance of a shelling-off process of FB (the DL periodically detaches from the FB border [2]), a dynamics that involves the presence of two DLs that form and disrupt successively. Since every of these DLs contains at its negative side a well located net negative space charge acting as a barrier for I_E, this new kind of oscillation regime appears simultaneously with the decrease of I_E, *i.e* the appearance of the N-shaped NDR.

For explaining the obtained experimental results it is necessary to elucidate the physical processes at the origin of the FB emergence. The knowledge of these physical processes also offers answers to the mechanism that explains the genuine origin of the nonlinear behavior of the studied gaseous conductor. These phenomena are explained in detail elsewhere [3,4]. The

most difficult problem that must be solved concerning the phenomena described in this paper resides from the discrepancy between the well-located optical phenomena observed when FB emerges and the values of the mean-free path of electron impact excitation and ionization processes. For example, typical for the DP-machine plasma, the mean-free path for the ionization processes is in the range of 2m. Considering the very small value of the excitation and ionization probabilities corresponding to such large value of the mean-free path, such a plasma is usually considered collisionless. However, the observed light phenomena contradict this assertion. The emergence of FB with dimensions (2-3 cm in diameter) much smaller than the mean-free-path of inelastic electron-neutrals collisions proves that the collision-less plasma model spectacularly fails when common experimental data, as those presented in this paper, have to be explained. In this context it is worth to mention that many important plasma theorists [7,8] have already expressed the opinion that the understanding of plasma experiments needs a substantial improvement of the used theoretical models. In this context, we agree with the opinion expressed by T. Sato [9], that this improvement is possible only by a paradigmatic shift in plasma theory. We consider that this shift needs the abandonment of the collisionless plasma model when the nonlinear phenomena related with self-organization, and implicitly the stimulation of instabilities have to be explained. We consider that unsolved problems as those mentioned in [8] become potentially resolvable when collective effect related to the symmetry breaking and spatial separation of the regions where the excitation and ionization cross-sections suddenly increase are considered [3]. Such phenomena always appear when a gradient of electrons kinetic energy is locally maintained. In magnetically confined plasma as those produced in fusion devices such phenomena appear at the plasma edge where conditions for DL assembly are present. The collisionless plasma model remains, however, as a useful model for solving a part of the problems of the plasma physics, namely that do not imply the nonlinear behavior.

References

[1] E. Lozneanu *et al.*, *IEEE Trans. Plasma Sci.* **30** (2002) 30.
[2] E. Lozneanu, M. Sanduloviciu, *J. Plasma Fusion Res. SERIES* **4** (2001) 532.
[3] M. Sanduloviciu *et al.*, *Chaos, Solitons &Fractals* **17** (2003) 183.
[4] E. Lozneanu *et al.*, *J. Appl. Phys.* **92** (2002) 1195.
[5] E. Lozneanu *et al.*, *J. Plasma Fusion Res. SERIES* **2** (1999) 389.
[6] R. Schrittwieser *et al.*, *Physica Scripta* **T84** (2000) 122.
[7] H. Alfven, *Trans. Plasma Sci.* PS **14** (1986) 669.
[8] D. Montgomery, *J. Plasma Phys.* **56** (1996) 387.
[9] T. Sato *et al.*, *Phys. Plasmas* **3** (1996) 2135.

Instabilities in inductive discharges with electronegative gases

P. Chabert, H. Abada, and J.-P. Booth

LPTP, Ecole Polytechnique, 91128 Palaiseau cedex, France

A.J. Lichtenberg, M.A. Lieberman, A. M. Marakhtanov

Department of EECS, UC Berkeley, Berkeley CA, USA

Relaxation oscillations in charged particle densities are seen in low-pressure electronegative inductive discharges, in the neighborhood of the transition between lower power capacitive operation and higher power inductive operation. The region of oscillatory behavior in both pressure and power increases as the plasma becomes more electronegative. Charged particle and free radical dynamics were investigated experimentally. A global model was developed which allowed to determine the parameters governing the transition to instability.

1. Introduction

Instabilities in electronegative discharges have been studied in high-pressure dc glows [1-3], in rf capacitive discharges [4] and recently in low-pressure inductive discharges [5,6]. An inductive discharge can exist in two modes: the capacitive (E) mode, for low power, and the inductive (H) mode, for high power. As the power is increased, transitions from capacitive to inductive modes (E-H transitions) are observed [7,8]. When operating with electropositive gases the transition occurs at a given power, and the discharge is always stable. In contrast, when operating with electronegative gases, the transition is usually unstable, and a wide range of powers exist where the discharge oscillates between E and H modes [5,6,9]. The relaxation oscillations in this E-H transition cause charged particle density, electron temperature and plasma potential modulations. The free radical concentration may also oscillate if the frequency is low, as observed by laser induced fluorescence in a CF_4 inductive discharge.

2. Experiments in CF_4 and SF_6

We have studied two different systems. The first device, located in Berkeley (USA), is a planar TCP, 30 cm in diameter and 19 cm long, working with Ar/SF_6 gas mixtures. The coil is powered by 13.56 MHz rf power supply through a match box. The second device, located in the Ecole Polytechnique (France), is also a TCP (same diameter but 6 cm long) working with CF_4 gas. In both systems, oscillations are seen in charged particle density, electron temperature and plasma potential using probes and OES measurements. When increasing power, we see a low power transition to enter the unstable region, and then an upper transition to a stable inductive mode as seen in figure 1. The instability windows get smaller as the argon partial pressure increases. It is also important to mention that a change in the matching network settings usually leads to a change in the frequency.

The frequency of the oscillations lies between 5 and 100 kHz for SF_6, and are about 30 times smaller for CF_4 (see figure 2). This is predicted by theory and is mainly due to the fact that the attachment coefficient in CF_4 is a lot smaller than in SF_6, although there are some second order effects.
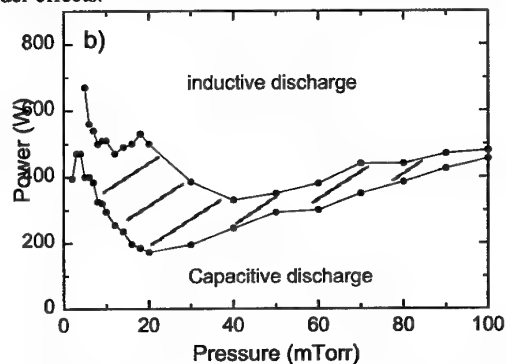
Figure 1: Instability window in (1:1)Ar/SF_6 mixture.
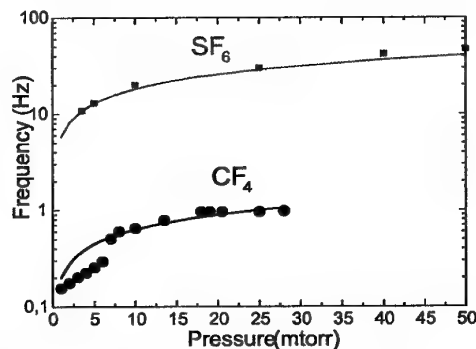
Figure 2: Instability frequencies versus pressure.

Results presented figure 3 for Ar/SF_6 show that the electron and ion dynamics are different. This was not studied in CF_4 since probe measurements are difficult in polymerizing chemistries. The electron density typically changes by a factor of 25, with fast rise and decay times. Over the same time, the ion densities only change by a factor of five and exhibit slower rise and decay times. Positive and negative ion densities decay at the same rate, which suggests that the ion losses are mainly due to mutual recombination.
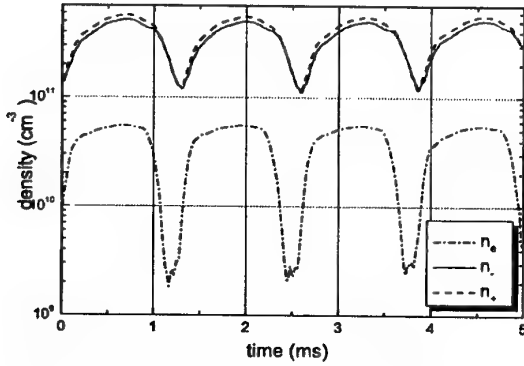
Figure 3: Densities vs time in (1:1)Ar/SF$_6$ mixture.

The free radical dynamics were investigated using space and time-resolved laser-induced fluorescence. The CF and CF$_2$ radical densities are strongly modulated during low-frequency instabilities, i.e. at low pressure. Several mechanisms were examined both from experimental and model results. Chemical reactions (either in the gas phase or at the wall) seem to be mainly responsible for the radical density fluctuations. Gas heating effects, observed previously in the inductive mode, probably make some contribution to the radical dynamics, but do not explain the major part of the observed time variations.

3. Theory

A global model has been developed to describe the instability [6,9]. This model is based on three differential equations: the particle and energy balance equations.

$$\frac{dn_e}{dt} = n_e n_g K_{iz} + n_- n_g^* K_{det} - n_e n_g K_{att} - \Gamma_e \frac{A}{V}$$

$$\frac{dn_-}{dt} = n_e n_g K_{att} - n_- n_g^* K_{det} - n_- n_+ K_{rec} - \Gamma_- \frac{A}{V}$$

$$\frac{d}{dt}\left(\frac{3}{2} n_e T_e\right) = P_{abs} - P_{loss}$$

These equations can be integrated considering quasi-neutrality in the plasma volume and at the walls to produce the dynamical behavior. However, to better understand the physics, one can look at equilibrium curves, i.e. setting $dn_e/dt = 0$, $dn_-/dt = 0$, $dT_e/dt = 0$, and examine the stability in the $n_-(n_e)$ phase plane. In figure 4d the phase space representation of $dn_e/dt = 0$ (dashed line) is shown in the n_- vs n_e plane. "Below" the dashed line, dn_e/dt is positive. We also plot (dot-dashed line) the equation for $n_-(n_e)$ obtained by setting $dn_-/dt = 0$. Again, "below" the dot-dashed line, dn_-/dt is positive. The crossing of the two $n_-(n_e)$ curves gives the equilibrium. An examination of a small departure from the equilibrium will convince the reader that the equilibrium can be unstable only if both slopes obtained from the $dn_e/dt = 0$ and $dn_-/dt = 0$ curves are positive at the crossing, and it is sufficient for instability if the slope of the dn_-/dt curve is larger. For the example shown in figure 4d we would therefore predict unstable behaviour. Superimposed on figure 4d is the actual trajectory in the phase plane, for which the complete time-dependent equations are solved. The intersection of the dynamical phase space trajectory with the $dn_e/dt = 0$ curve indicates the stabilization of the falling electron density.

To explore the details of the bifurcation we need to examine the dynamical behaviour in the transition regions between stability and instability. We do this for small variations of power near the capacitive-to-inductive transition. With increasing power where the $dn_-/dt = 0$ curve intersects the $dn_e/dt = 0$ curve near its minimum, the trajectory goes through a series of steps, as shown in figure 4. In figure 4a the motion is stable, collapsing to the fixed point. In figure 4b the bifurcation has occurred, leading to a periodic solution that grows out of the fixed point. In figure 4c the motion has become more complicated with a larger amplitude oscillation appearing somewhat randomly, which is often seen in certain types of chaotic dynamics [10, Sec. 7.5]. Finally, in figure 4d the attractor of the large amplitude relaxation oscillation has been established.
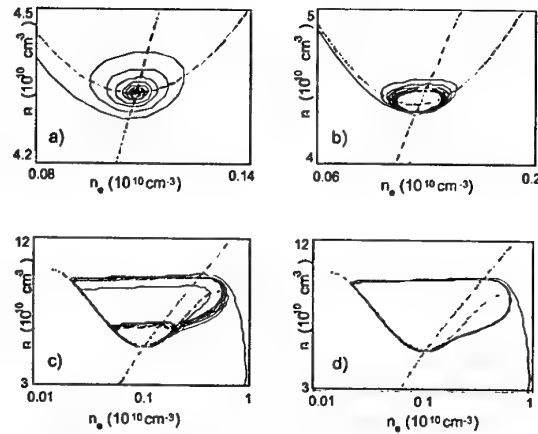
Figure 4: Trajectories when increasing power near the capacitive-to-inductive transition.

4. References

[1] R.A. Hass, Phys. Rev. A 8, 1017 (1973)

[2] W.L. Nighan and W.J. Wiegand, Phys. Rev. A 10, 922 (1974)

[3] A.D. Barkalov and G.G. Gladush, Sov. Phys. Tech. Phys. 24, 1203 (1979)

[4] E. Metsi, E. Gogolides, A. Boudouvis, Phys. Rev. E, 54, 782 (1996)

[5] M. Tuszewski, J. Appl. Phys. 79, 8967 (1996)

[6] M.A. Lieberman, A.J. Lichtenberg, and M.A. Marakhtanov, Appl. Phys. Lett. 75, 3617 (1999)

[7] I.M. El-Fayoumi, I.R. Jones, and M.M. Turner, J. Phys. D 31, 3082 (1998)

[8] M.A. Lieberman and R.W. Boswell, J. Phys. IV 8, Pr7 (1998)

[9] P. Chabert, A.J. Lichtenberg, M.A. Lieberman, and M.A. Marakhtanov Plasma Sources Sci. Technol 10 (2001) p.478

[10] A.J. Lichtenberg and M.A. Lieberman, *Regular and Chaotic Dynamics*, 2nd Ed. Springer-Verlag, New York, 1992

Topic 15

Particle and laser beam interaction with plasmas

Dynamics of carbon plasma induced by an excimer laser in nitrogen environment

S. Messaoud-Aberkane, T. Kerdja, S. Abdelli, S. Nait-Amor,
S. lafane, S. Malek and K. yahiaoui.
Centre de Développement des Technologies Avancées
Lot.20 Aout 1956,BP17. Baba Hassen, Alger, Algeria.
Email: aberkane_sabrina@yahoo.fr

Abstract. The dynamics of laser-ablated carbon plume propagation through different background Nitrogen pressure have been investigated with time and space-resolved emission spectroscopy. Results of temporal and spatial evolution of CI and CII emissions lines at4267A° and 2478A°4267A° respectively under different nitrogen pressure show that there are two stages of expansion in accordance with shock wave and drag force model propagation model

1. Introduction

Reactive pulsed laser ablation deposition (RPLAD) consisting on the laser ablation of target in reactive gas has become an attractive technique for a wide variety of compound thin films synthesis. In order to produce high quality films with desired properties, the well understanding of the temporal behaviour of ejected species in the ablated plume is necessary. In this work, we report on emission spectroscopic diagnostic of carbon plasma in nitrogen environment at different pressures.

2. Experimental set-up

Carbon plasma is induced by KrF excimer laser radiation (ë=248 nm, ô =25 ns, f =10 Hz) at a fixed fluence of 12 J/cm². The laser beam is focused under an angle of 45°, onto a rotating graphite target surface. The chamber is evacuated at 10^{-6} mbar and then filled with N_2 at pressures in the range of 0.5 to 2 mbar.

In order to identify the emitting species and to analyse the plasma propagation, the plasma plume is imaged on the entrance slit of 0.8m spectrometer (Spex, 1200tr/mm) with a spatial resolution of 100 µm and a spectral resolution of 0.8Å. The light emission is collected by a fast photo-multiplier tube (Hamamatsu R928) connected to a fast digital oscilloscope (Tektronix TDS3032).

3. Experimental results

3.1. Temporal evolution

we have studied the spatio-temporal evolution of CI and CII lines at 247.8 and 426.7nm respectively, starting from d =3mm to avoid the continuum emission in the vicinity of the target.

The fig.1 a,b shows the time of flight of the transient maximum emission intensity of the CI and CII lines for different observation distances, at different pressures.

We show that as the gas pressure is increased, the propagation of the carbon species is more affected. We can see two stages of expansion. The first is well fitted using drag force model according to the following formula:

$$d = d_f [1 - exp (-\beta t_{max})] + d_0 \qquad (1)$$

Where $d_f = v_0/\beta$ is the stopping distance, v_0 the initial velocity, β the damping coefficient and d_0 a boundary condition [1].

The second stage is well fitted by the shock wave model according to the expression [2]:

$$d = a.t^{(0.4)} + d_0 \qquad (2)$$

Where a is constant.
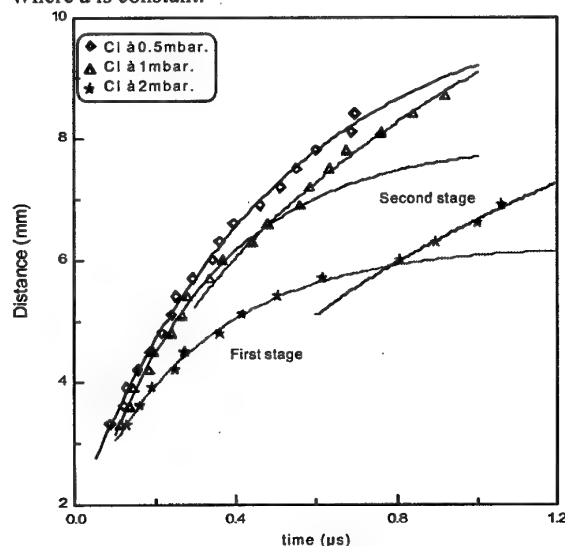
Fig (1.a): (t_{max}, d) plots of the C I emission line (247.8 nm) at different nitrogen pressures.

The drag model fit parameters and the initial velocity v_o, are reported in table1, showing that the stopping distance d_f decreases with increasing pressure in agreement with the expected confinement effect. The coefficient β increases with increasing gas pressure. Initial velocity v_o remains the same independently from the used pressure.
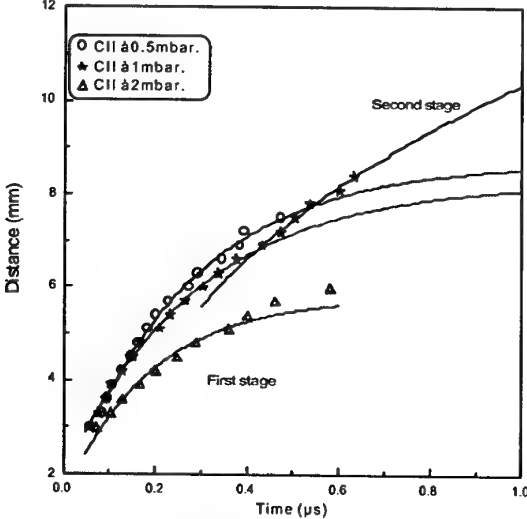
Fig (1.b): (t_{max}, d) plots of the C II emission line (427.6 nm) at different nitrogen pressures.

C II (λ = 427.6 nm)			
	$d_f(mm)$	$\beta(\mu s^{-1})$	v_o (m/s)
0.5mb	7.27	3.74	2.7×10^4
1mb	6.03	4.75	2.8×10^4
2mb	4.36	5.18	2.3×10^4
C I (λ = 247.86 nm)			
	$d_f(mm)$	$\beta(\mu s^{-1})$	v_o (m/s)
0.5mb	8.07	2.15	1.7×10^4
1mb	7.44	2.12	1.6×10^4
2mb	4.51	3.02	1.4×10^4

Table1: d_f, β values inferred from the simulation of the experimental data for the emission lines of C I and of CII by using the drag model and the corresponding calculated initial velocity.

3.2. Spatial distribution

Figures (2.a) and (2.b), show the spatial evolution of maximum emission intensities of CI and CII respectively, at different nitrogen pressures.
The curves are characterised by a strong continuum emission up to 3mm from the target surface, which masks the transitions lines emission. At larger distances, the one can see a structure with maximum moving to the target surface as the pressure is increasing.
This effect is due to the plasma confinement by N_2 gas molecules as it was previously observed with an inert gas [3]
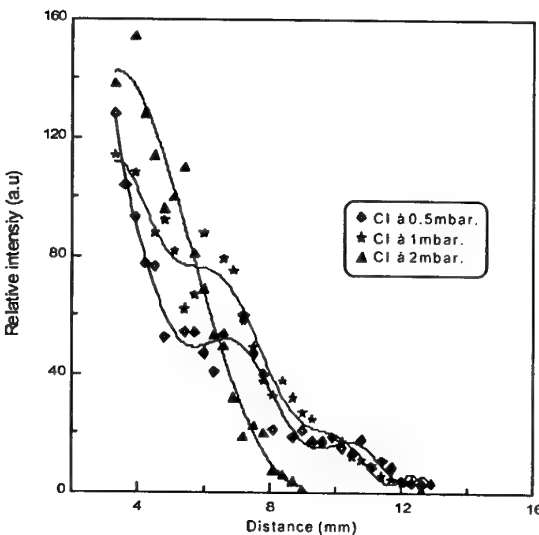
Figure (2.a): The maximum emission intensity of the CI transition at 247.8nm as a function of the distance at different nitrogen pressures.
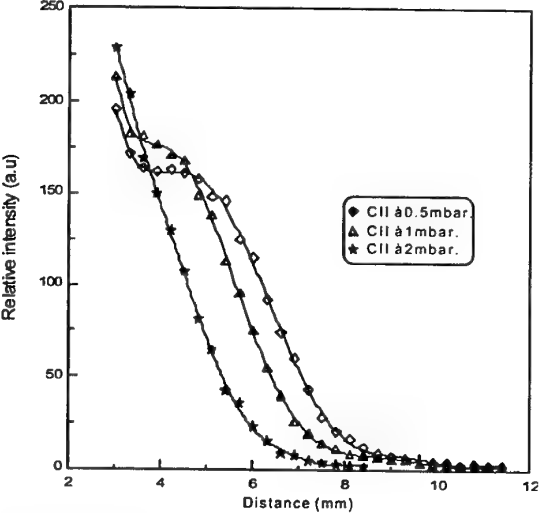
Figure (2.b): The maximum emission intensity of the CII transition at 426.7nm as a function of the distance at different nitrogen pressures.

4. References

[1] S. Acquaviva, M. L. De Giorgi. Applied Surface Science 197-198 (2002), pp. 21-26.
[2] J.Gonzalo, F.Vega and C.N. Afonso, J.appl. phys, 77, 12, (1995).
[3] T. Kerdja, S. Abdelli, D. Ghobrini, and S. Malek, J. Appl. Phys. 80 (8) 5365, (1996).

ELECTRON DENSITY AND TEMPERATURE DIAGNOSTIC OF LASER CREATED TITANIUM PLASMA

S. Nait Amor, T. Kerdja, S. Abdelli, S. Lafane,
S. Messaoud-Aberkane, K.Yahiaoui, and S. Malek

Centre de Developpement des Technologies Avancées.
Lot. 20 Aout 1956, BP17. Baba Hacen, Alger. Algeria
E-mail: naitamorsamir@hotmail.com

In this contribution we present time and space evolution of plasma parameters during ablation of titanium target in vacuum and at low nitrogen pressure using KrF laser. Electron density is measured from Stark Broadening of singly ionised species; electron temperature is determined from Boltzmann plot of lines intensities of the same species.

1 Introduction

In recent years, pulsed laser deposition has become an attractive technique for depositing a wide variety of materials. Optimisation and control of such process require the understanding of vaporisation and plasma build-up mechanism, plasma playing a key role since it determine the formation of reactive species and high-energy ions [1].

Among the several diagnostics technique generally used to probe plasma plume, optical emission spectroscopy appear to be popular choice owing to its non-intrusive. Electron density and temperature can also be determined from spectral lines analysis. In this contribution, we present the spatial and temporal evolution of electron density and electron temperature at early stage of ablation. For electron density measurement, we have adopted a technique based on the line width analysis of selected emission lines. The electron plasma temperature is determined using the Boltzmann plot method.

2 Experimental arrangements

Material vapour is produced by focusing a KrF laser beam (248 nm, 30 ns) on a pure titanium target surface at fixed laser fluence of 16J/cm² and at 1 mbar ambient nitrogen pressure. The plasma plume is imaged onto the entrance slit of 0.8m spectrometer (Spex 1704) equipped with 1200 grooves mm⁻¹ grating, blazed at 0.3 µm. The entrance and exit slits of spectrometer are adjusted to 80µm, giving spectral resolution of 0.64A° and spatial resolution of 80µm. Signals are recorded by means of a fast phototube (Hamamatsu R928) and digital oscilloscope (Tektronix TDS3032).

3 Results and discussions

3.1 Electron density

Titanium plasma emission is collected from region along the axis of the plume, and shows Ti^{++}, Ti^{+} and Ti emission. Assuming that the Stark effect is the mean

broadening process taking place in the plasma, the electron density can be determined by measuring the line width through the relation $\Delta\lambda_{1/2} = 2w(n_e/10^{16})$ Å, where w, $\Delta\lambda_{1/2}$ and n_e are the electron impact parameter, line width (FWHM) and the electron density respectively [2]. In our case, the electron density is determined from line width of Ti^{+} line at 3483A°. At each given distance of observation, the temporal evolution of electron density shows a fast increase with delay time up to the maximum value and decreases with increasing delay time (fig.1). The increase of electron density in titanium plasma at earlier times can be attributed to the low density of electrons reaching the observation zone with Ti^{2+}. The plasma front is mainly constituted from Ti^{2+} and Ti^{+} ions. Assuming LTE equilibrium, the Ti^{2+} density is lower than the Ti^{+} density, so the electron density in the plasma front can be assumed less than the electron density in the plasma core. The fast droop of electron density after maximum value is due to the recombination process and the plasma expansion.
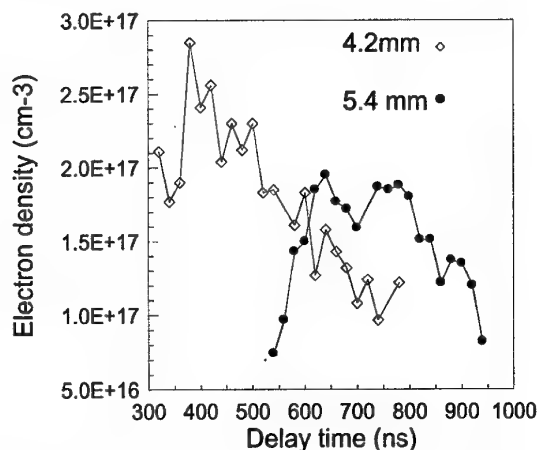
Figure (1): Temporal evolution of electron density at two distances from the target surface.

On fig.2 the temporal evolution of the maximum electron density is well fitted by t^{-1} scaling law up to 350ns and t^{-3}

scaling law beyond. Assuming one-dimensional expansion at low distances and three dimensional for higher distances, our experimental results are in good agreement with theoretical plasma dynamics models [1].
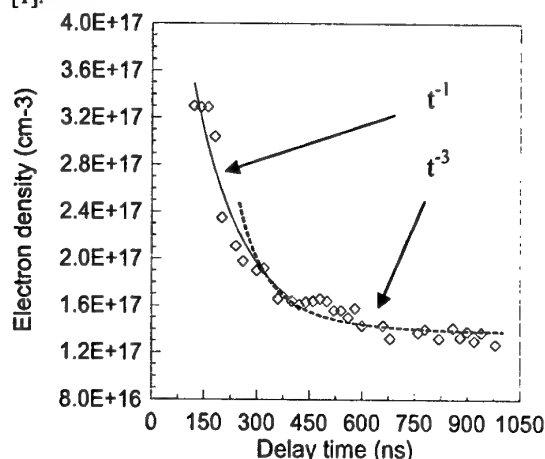
Figure (2): Temporal evolution of maximum electron density at different distances from the target surface.

3.2 Electron temperature

Plasma electron temperature is determined from Boltzmann plot method of 399.8nm, 334.1nm and 319.9nm Ti lines. Fig.3 represents the temporal evolution of the electron temperature at 2.4mm and 6mm from the target surface. At both distances, temporal evolution of plasma electron temperature shows a temperature increase with time at earlier stage of plume expansion and decreasing shape at longer time, the decreasing became slower at longer delay. The collision of the gas molecules with the plasma front leads to the dissociation and ionisation of the gas molecules, so the plasma thermal energy shows a decrease.

Decreasing of electron temperature is due to the adiabatic expansion of plasma plume. During this expansion thermal energy is converted into kinetic energy and plasma cools down rapidly [3]. At later time electron temperature begins to decrease more slowly due to the energy released by the recombination, which compensates the cooling due to expansion process. Temporal evolution of plasma electron temperature is well fitted by t^{-1} in good agreement with adiabatic model of plasma expansion where γ is equal to 1.33, fig.(3,4).

4 Conclusions

In this contribution, we report the spatio-temporal evolution of plasma parameters using lines emission of titanium plasma species. Both electron density and electron temperature show fast increasing shape at earlier times up to the maximum values and then decrease rapidly with increasing delay times.

Increasing of electron density is due to the low electron density in the plasma front reaching the observation zone with Ti^{++} species. For electron temperature, collisions of plasma front species with gas molecules lead to cooling down of plasma front and increasing gas molecule temperature. The droop of both electron density and electron temperature after reaching maximum values is due to the plasma expansion.
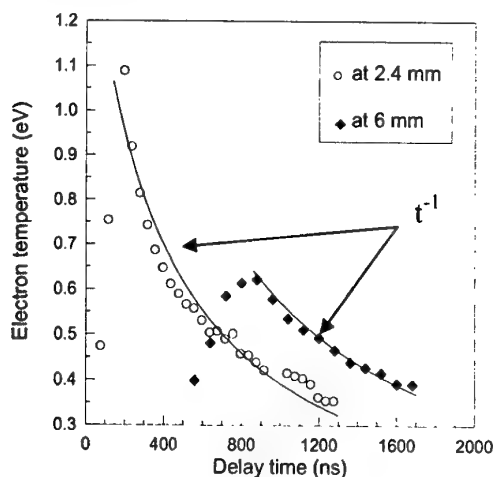
Figure (3): Temporal evolution of electron temperature at two distances from the target surface.
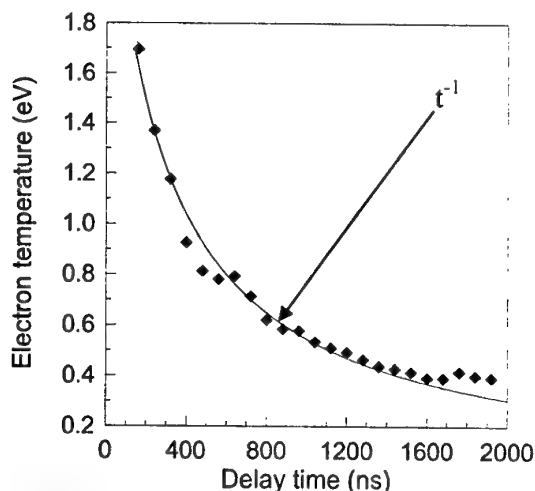
Figure (4): Temporal evolution of maximum electron temperature at different distances from the target surface.

4 References

[1] F. Fuso, L.N. Vyacheslavov and G. Masciarelli, J. Appl. Phys., 76, (1994), 12.
[2] J. Hermann, Al. Thomann, C. Boulmer-Leborgne, B. Dubreuil, M.L. Degiorgio, A. Luches, and I.N. Mihaiescu, J. Appl. Phys., 77, (1995), 2829.
[3] S.S. Harilal, C.V. Bindhu, C. Issac, V.P.N. Nampoori, and C.P.G.Vallabhan, J. Appl. Phys., 82, (1997), 5.

202

Dissipative Instability of Overlimiting Electron Beam

E.V.Rostomyan

Institute of Radiophysics and Electronics Electronics National Ac.Sci.of Armenia
Alikhanyan str 1, Ashtarack, 378410, Armenia

Influence of dissipation on development of overlimiting electron beam instability caused by aperiodical modulation of beam density in medium with negative dielectric constant is investigated. It is shown that growth rates of dissipative instability of overlimiting electron beam depend on parameter characterizing dissipation more critically as compared with sublimiting e-beams. The influence of dissipation on mode structure, space distribution and development dynamics of overlimiting e-beam instability and its gradual transition to that of dissipative type with increase in level of dissipation is investigated in detail.

Recently most of beam-plasma interaction experiments are gradually changed over to more and more high-current electron beams. It is known that beam current that can pass through given vacuum electrodynamic system is limited by the beam space charge. Plasma filled systems can operate with beams current that are several times higher that limiting vacuum current. Overlimiting electron beam instability has distinction in kind of physical nature [1-4]. As the beam current increases the fields of beam space charge play more and more significant role and change physical character of beam-plasma interaction as compared with subliming electron beams. Traditional statement about physical nature of electron beam instability related to induced radiation of the system proper waves by beam electrons might not be applied to overlimiting beams. Physical character of their instability is due either to aperiodical modulation of the beam density in medium with negative dielectric constant [1,3] or to excitation of beam pace charge wave with negative energy.

Along with the increasing of the beam current one more trend is dominant in contemporary microwave electronics: change over to higher frequencies. This trend leads to increasing of energy active losses in the walls of resonators due to decreasing of the skin depth. The Q-quality of resonators falls dawn and dissipation increases. Apart from increasing of beam current dissipation of high level also changes the physical nature of beam instability. Dissipation can play an important role in the dynamics of beam-plasma instability development. It can become not only deciding factors in the limiting spatial and temporal growth and determining the magnitude of the fields. The dissipation can also significantly influence on the mode structure of instability and reduce the growth rate [5-7]]. But dissipation never suppresses beam instability completely. Dissipation of high level transforms conventional beam instability to that of another type - dissipative beam instability. This type of instabilities comes to be developing in systems with electron beams where the beam space charge wave with negative energy exists. Actually dissipation is nothing else as a channel of energy withdrawal for excitation of the beam wave with negative energy. Growing of slow space-charge wave causes instability of charged particle beam under its interaction with dissipative or inductive walls. This type of dissipative instability is an important issue in particle accelerators and applications to microwave devices. Recently this phenomenon has received new attention especially in connection with its role in high current induction linacs as drivers for heavy ion inertial fusion. Dissipative beam instabilities have an array of characteristic peculiarities [5-7]. In particular dissipative instabilities differ from conventional beam instability by low growth rates as well as by relatively low energy of excited oscillations. Some aspects of gradual transition of monoenergetic e-beam instability to that of dissipative type with increase on level of dissipation are investigated in [8]. Dissipative and resistive wall instabilities of electron beam underly on the operation of so-called amplifier on dissipation. The idea of such a type of amplifier was proposed comparatively long ego and was developed further [9]. It has some characteristic peculiarities as compared with traditional TWT – wide bandwidth, absence (or very weak) of inner feedback, and its amplification does not depend on operation regime (beam current etc). It seems, change over to overlimiting electron beams keeps these properties unchanged.

Dissipative instability of overlimiting electron beam has not been considered yet. Present investigation considers the influence of dissipation on development of overlimiting electron beam instability caused by aperiodic modulation of beam density in media with negative dielectric constant. Fully magnetized beam-plasma waveguide is considered. It is shown that the well-known dispersion relation [1-4] in the case of overlimiting beam currents has solutions for growth rates that are proportional (in absence of dissipation) to the beam Lengmuire frequency and inverse proportional to the parameter characterizing dissipation (in systems with high level of dissipation). But for subliming al) e-beams the respective growth rates have another dependence on these parameters. The change in the physical nature of the instability relates to the effect of beam space charge fields, which leads to distortion of the polarization of the waveguide fields. As we think, the dependences become more critical because of with

increasing of the beam current its proper oscillations of reveal themselves more efficiently, the mode related to beam wave with negative energy is excited and serve as a channel for energy withdrawal.

In order to investigate the influence of dissipation on mode structure, space distribution and development dynamics of overlimiting electron beam instability we proceeded from the initial set of equations (Maxwell's, continuity and motion eqs for the beam and plasma electrons) and considered the evolution of an initial perturbation in the system. Using wide spread representation of growing fields as wave train with slowly varying amplitude we obtained equation for the envelope of waveform. This equation was solved and analytical expression for space-time distribution of the fields upon overlimiting e-beam instability development is actually derived. Characteristic properties of the wave train are following. It can be thought of as consisting of many unstable modes. In absence of dissipation the envelope is symmetric (see curve 1 in Fig1). The front of induced waveform moves at beam velocity u, back edge – at group velocity of resonant wave in considered system $v_0 < u$. This shows the convective character of overlimiting electron beam instability in laboratory frame and the frames moving at velocities $v < v_0$, and $v > u$. Unlike to the case of sublimiting beam, in the absence of dissipation, the waveform induced by overlimiting beam is symmetric i.e. its peak places on its middle at all instants.
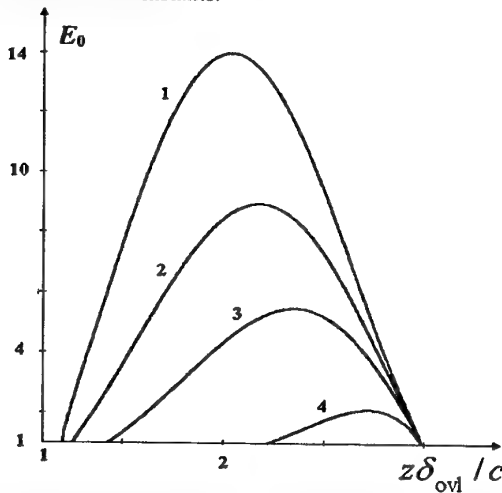
Fig1. Shapes of waveform vs on longitudinal coordinate z at fixed instant $t = 3/\delta_{ovl}$ (δ_{ovl} is the max growth rate overlimiting e-beam instability) of for various values of parameter $k = v/\delta_{ovl}$; $k_1 = 0$; $k_2 = 0.4$; $k_3 = 1.3$; $k_4 = 2.5$; ($v_0/u = 0.4$)

The growth rate of most unstable mode is equal to maximal growth rate of overlimiting e-beam instability. In other words the maximal growth rate of instability usually describing instability in given system in fact is nothing else that the growth rate in the peak of wave packet. For conventional beam instability the peak placed on 1/3 of its length from front [14]. As the beam current increases the peak of induced waveform shifts

backward to the middle of wave packet and the growth rate essentially changes its value and dependence on beam density $\omega_b^{2/3} \rightarrow \omega_b$ (ω_b is the Lengmuire frequency of the beam).

Dissipation significantly effects on growth rates and suppresses low-velocity modes. The length of induced waveform depends on dissipation level and tends to zero when the level of dissipation increases. In the limit of high-level dissipation, unstable perturbations move at velocity u and their growth rate is equal to growth rate of overlimiitng e-beam dissipative instability. If one considers injection and further propagation of an overlimiting electron beam into plasma-filled waveguide the dissipative instability can develop mainly near beam front.

The dependence of maximal spatial growth rate on dissipation level is given by simple expression

$$q_{ovl}^{(max)}(v) = q_{ovl}\left(\sqrt{1+\lambda} - \sqrt{\lambda}\right)$$

where q_{ovl} is the spatial growth rate in the absence of dissipation, $v = \mathrm{Im}\, D_0/(\partial D_0/\partial \omega)$ characterizes dissipation in considered system, $\lambda = (v/\delta_{ovl})(u/v_0)$, δ_{ovl} is the maximal growth rate of overlimiting e-beam instability in plasma-filled waveguide. The dependence of the maximal growth rate on dissipation level is shown in Fig 2.
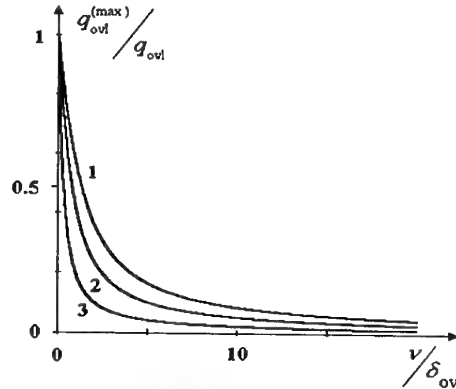
The maximal spatial growth rate of overlimiting e-beam instability vs on dissipation level and parameter $p = u/v_0$. $p_1 = 1.5$, $p_2 = 4$, $p_3 = 25$.

References

[1] M.V.Kuzelev, A.A.Rukhadze, *Electrodynamics of Dense El. Beams in Plasma*, (Moscow) 1990.
[2] T.Tadjima, *Phys Fluids*, **22**, 1157, (1979).
[3] N.I.Aizatski, *Sov. J. Plasma Phys.* **6**, 597, (1980)
[4] E.V.Rostomyan, *Eur J. Appl. Phys*, **14**, 177, (2001)
[5] H.Bohmer,et al *Phys Fluids*, **14**, 150, (1971).
[6] V.U.Abramovich, V.V. Shevchenko, *Zhurn Eksp. teor. fiz* **62**, 1386, (1972)
[7] D.Winske, E.A. Jackson, *Phys Fluids* **18**, 389,(1975)
[8] E.V.Rostomyan, *Phys Plasmas,* **7**, 1595, (2000).
[9] C.K.Birdsall, et al *Proc. IRE,* **41**,.865, (1953).

Effect of Dissipation on Excitation of Beam Wave with Negative Energy

Eduard V. Rostomyan

Institute of Radiophysics & Electronics National Ac. Sci. of Armenia
Alikhanyan st. 1, Ashtarack, 378410, ARMENIA

The effect of dissipation on the instability of overlimiting electron beam caused by excitation of the beam wave with negative energy and transition of this instability to that of dissipative type as the level of dissipation increases is investigated. Growth rates are obtained. The interplay of two effects both leading to excitation of the beam wave with negative energy leads to more critical (as compared with the case of dissipative instability of sublimiting electron beam) dependence of the growth rate on dissipation. An equation describing the influence of dissipation on space-time development of the fields is derived and solved. Analysis of the solution is presented

Two basic trends of high power microwave electronics are following: increasing power and frequency of output radiation [1,2]. First trend leads to increasing of beam current. In plasma-filled devices it can several times exceed limiting current in vacuum devices. But the physical character of beam-plasma interaction changes. Instability of overlimiting electron beam is due not to induced radiation of system proper waves, but either to excitation of the beam wave with negative energy, or to aperiodic modulation of the beam space charge in medium with negative dielectric constant [3-5]. The first type of overlimiting electron beam instability realizes in beam-plasma systems that are no uniform in cross section. Moreover many new physical phenomena exhibit themselves if system consists of spatially separated beam and plasma [6]. Change of the physical character of beam plasma interaction results in change of energy transfer from beam electrons to excited oscillations.

At changing over to higher frequencies, for effective interaction of beam electrons with slowing down space harmonics the beam should be driven into resonators' walls [2]. The skin depth decreases, and the Q-quality of resonators falls dawn. Energy loss in the walls of resonators increases. Influence of dissipation on interaction of overlimiting electron beam with plasma may leads to an array of new phenomena that are significant for microwave generation because of dissipation also leads to excitation of the beam wave with negative energy. Dissipation is nothing else as a channel of energy withdrawal and such an excitation actually is dissipative beam instability. In systems with overlimiting electron beams the influence of dissipation is significant because (in contrary to sublimiting beams) actually the same mechanism of instability takes place without dissipation and dissipation intensify it. Influence of dissipation on the operation of microwave devices with overlimiting beam has not been considered yet. Superposition of the two effects that led to excitation of the beam wave with negative energy, results in critical effect of dissipation on the instability. The dependence of the growth rate on the parameter characterizing dissipation becomes more critical. The influence of dissipation on spatial-temporal development and mode structure of the instability is investigated. Gradual transition of this type of

overlimiting beam instability to that of dissipative type is elaborated.

Consider fully magnetized plasma filled waveguide penetrated by overlimiting relativistic electron beam. In such a system physical character of beam-plasma interaction essentially depends on transversal geometry. In the case of inhomogeneous beam and/or plasma the instability is due to excitation of beam wave with negative energy.

Generally say, rigorously treatment of the problem may not be developed based on the perturbation theory with small parameter. But in the case of spatially separated beam and plasma when the integral describing fields overlap is small, the effect may be considered analytically. In this case $p_b(\mathbf{r}_\perp)p_p(\mathbf{r}_\perp) = 0$ (functions $p_{p,b}(\mathbf{r}_\perp)$ represent the profiles of the plasma and beam densities in the waveguide cross-section; for homogeneous beam and plasma $p_{p,b}(\mathbf{r}_\perp)=1$ for thin annular beam $p_b = \delta(r-r_b)$, where δ is the Dirac function and r_b is the beam radius). In zero approximation the system may be described by solving of following two independent problems

$$\Delta_\perp E_{z\alpha} - \left(k^2 - \frac{\omega^2}{c^2} \right)\left[1 - p_\alpha(r_\perp)\delta\varepsilon_\alpha \right]E_{z\alpha} = 0 \qquad (1)$$

with the conditions $E_{z\alpha}= 0$ on the metallic surfaces. Here $\alpha = p, b$ for plasma and beam respectively, $\delta\varepsilon_p = \omega_p^2 / \omega(\omega + i\nu)$; $\delta\varepsilon_b = \omega_b^2\gamma^{-3}(\omega\text{-}ku)^{-2}$, $\Delta_\perp$ is the Laplace operator with respect to transversal coordinates, ω and k are the frequency and wave vector of perturbations E_z is the longitudinal electric field which is represented in a form $E_z(\mathbf{r}_\perp,z,t)=E_z(\mathbf{r}_\perp,\omega,k)\exp(-i\omega t+ikz)$, z is the coordinate along the waveguide axis, t is the time, $\omega_{p,b}$ are the Lengmuire frequencies for plasma and beam respectively, γ is the relativistic factor of beam electrons $\gamma = (1-u^2/c^2)^{-1/2}$, u is the velocity of beam electrons, c is the speed of light. The zero order dispersion relations are

$$D_\alpha(\omega,k) = k_{\perp\alpha}^2 + \left(k^2 - \frac{\omega^2}{c^2} \right)(1-\delta\varepsilon_\alpha) = 0 \qquad (2)$$

where $k_{\perp\alpha}$ are determined by the proper function of zero

order problems respectively. If one applies the perturbation theory to this state he can obtain after cumbersome calculations the dispersion relation, which takes into account the beam-plasma interaction in first order approximation

$$D_p(\omega,k)D_b(\omega,k)=G[(k^2-\frac{\omega^2}{c^2})^2\delta\varepsilon_p\delta\varepsilon_b] \quad (3)$$

Here $G>0$ and it is nothing else as so-called geometrical factor of the space charge. It shows the overlap of the plasma and the beam fields and represents all specific properties of considered system. The factor D_b in the dispersion relation (3) coincides with the dispersion relation describing beam oscillations in magnetized waveguide in the case of full filling. In the simplest one dimensional limit the spectra of beam oscillations are given by well known simplest expression

$$\omega=ku\pm\Omega_b \quad (4)$$

where $\Omega_b=\omega_b\gamma^{-3/2}$. In general case $\Omega_b=\Omega_b(\omega,k)$ and the spectra take complicate form. Obvious expression for the spectra can be obtained if one neglects the biased current as compared with the high frequency beam current i.e. $k\ll k_\perp\gamma$

$$\omega_\pm=ku\pm\alpha^{1/2}/\gamma \quad (5)$$

where $\alpha=\omega_b^2/k_{\perp b}^2u^2\gamma^3$. Non-potential character of the beam waves is intrinsic for high beam current only, comparable or higher than the limiting vacuum current. If one search the solutions of (3) for the form $\omega=ku+\delta$ dispersion relation takes the form

$$\left(x+\Delta+i\frac{v_0}{ku}f\right)\left(x^2-\frac{\alpha}{\gamma^2}\right)=-\frac{G}{2\gamma^4}\alpha\frac{\omega_p^2}{k^2u^4/c^2-\omega_p^2} \quad (6)$$

where

$$\Delta=\frac{k^2u^2-\omega_0^2}{2\gamma^2\left(\omega_p^2-k^2u^4/c^2\right)} \qquad f=\frac{\omega_p^2\left(1-2\beta^2\gamma^2x\right)}{2\gamma^2\left(k^2u^4/c^2+\omega_p^2\right)},$$

v_0- is the effective collision frequency in plasma. The growth rate attains its maximum if (in absence of dissipation) $\Delta=-\sqrt{\alpha}/\gamma$ and is equal

$$\delta_{sl}=(2\gamma)^{-1}(Gf)^{1/2}\left(\omega_b^2/k_{\perp b}^2u^2\gamma^5\right)^{1/4} \quad (7)$$

If dissipation in the system is high enough ($v_0\gg\delta_s$) the instability become of dissipative type with following growth rate

$$\delta_v=\frac{\omega_0}{v}\left(G/4\gamma^3\right)\!\alpha^{1/2}\omega_p^2/(k^2u^2-\omega_0^2) \quad (8)$$

It can be written as $\delta_v=\delta_{sl}^2/v$

where $v=\left[\mathrm{Im}\,D_p/(\partial D_p/\partial\omega)\right]\big|_{\omega=\omega_0,\,k=k_0}$

Consider now in detail how the increasing in level of dissipation changes the character of instability and transform it. The development of an initial perturbation in the system and influence of the dissipation on the shape of induced waveform will show as the details of this transition. In so doing we represent the field E_z in form with slowly varying amplitude

$$E_z(\mathbf{r}_\perp,z,t)=E_0(\mathbf{r}_\perp,z,t)\exp(-i\omega_0t+ik_0z) \quad (9)$$

where the dependence $E_0(z,t)$ is week in following mean

$$\left|\partial E_0/\partial t\right|\ll\omega_0 E_0\,,\qquad \left|\partial E_0/\partial z\right|\ll k_0 E_0\,, \quad (10)$$

ω_0 and k_0 is solution of zero order equations (2). The transversal structure of the fields may be obtained in the normal way by expanding on series of the eigenfunctions of given system. Longitudinal structure of induced waveform is described by equation

$$\left(\frac{\partial}{\partial t}+v_b\frac{\partial}{\partial z}\right)\left(\frac{\partial}{\partial t}+v_p\frac{\partial}{\partial z}+v\right)E_0(z,t)=\delta_{sl}^2E_0(z,t) \quad (11)$$

where v_p and v_b are the group velocities of plasma and beam waves respectively. Solution of equation (11) gives us the following expression for slowly varying amplitude

$$E_0(z,t)=-\frac{J_0}{2\sqrt{\pi}}\frac{e^{\chi(z,t)}}{(u-v_0)^{1/2}\delta_{sl}^{1/2}(ut-z)^{1/2}} \quad (12)$$

$$\chi(z,t)=\frac{2\delta_{sl}}{u-v_p}\{[(z-v_pt)(v_bt-z)]-v(v_bt-z)\}^{1/2} \qquad J_0=\text{const.}$$

This expression explicitly shows convective character of instability in separated beam-plasma system. Unstable perturbation ranges as $v_p\le v\le v_b$. Growth rate in the peak is equal to (7). The peak of the wave train moves at average velocity $w_g=(v_p+v_b)/2$. Dissipation suppresses slow perturbations. The threshold velocities $v_{th}=(\lambda v_b+v_p)/,/(1+\lambda)$ where $\lambda=v^2/4\delta^2$. Dynamics of instability in presence of dissipation may be obtained by analyzing the following equation

$$\lambda(v_bt-z)(z-v_pt)=(w_gt-z)^2 \quad (13)$$

Exact solution of the equation (11) leads to following expression for point of peak

$$z=\frac{t}{2}\{v_b+v_p+\lambda'(v_b-v_p)\} \qquad \lambda'=\sqrt{\lambda/(1+\lambda)} \quad (14)$$

Substitution of (14) into χ (see (12)) leads to following maximal growth rate depending on dissipation level

$$\delta_{max}(v)=\delta_{sl}\left(\sqrt{1+x^2}-x\right) \quad \text{where } x=v/\delta_{sl}.$$

In the limit $v\gg\delta_{sl}$ the wave train significantly shortens and the growth rate in the peak is equal δ_v (9) i.e. the dissipative instability of overlimiting electron beam develops and its growth rate has more critical dependence on dissipation

References

[1] . D.M. Goeble et al, *Phys Plasmas*, **6**, 2225, (1999).
[2] *Relativistic High Frequency Electronics*. Edited by A.V. Gaponov-Grekhov, Gorki, (1981)
[3] M.V.Kuzelev, A.A.Rukhadze, *Electrodynamics of Dense Electron Beams in Plasma*,(Nauka), 1990,
[4] N.I.Aizatski, *Sov. J. Plasma Phys.* **6**, 597, (1980)
[5] E.V.Rostomyan, *Eur. J Appl. Phys.* **14**, 177, (2001)
[6] N.I.Karbushev, E.V.Rostomyan, *J Contemporary Phys.* **27**, #1, 50, (1992)

Optical emission characteristics of carbon plasma produced by single- and double-pulse laser ablation

Burakov V.S., Bokhonov A.F., Nedel'ko M.I., Savastenko N.A., and <u>Tarasenko N.V.</u>

Institute of Molecular and Atomic Physics National Academy of Sciences of Belarus, 70 Scaryna Ave., 220072 Minsk, Belarus

The effect of additional laser irradiation on the optical emission of laser ablated carbon plasma have been examined to define plasma conditions for the controlled synthesis of carbon structures.

1. Introduction

Laser ablation carbon plasmas have been intensively examined during the last years to define plasma conditions for the synthesis of carbon structures with unique properties in particular, fullerenes and nanotubes [1,2]. The physical properties of plasma plume, such as species concentrations and temperature, directly affect the properties of the material being formed. Successful synthesis is strongly dependent on the formation of atomic and molecular species with required chemistry and energy. For selection of optimal plasma conditions the detailed understanding the basic physical and chemical processes governing the ablation plume composition and reliable methods for controlling of the relative amounts of plume species are needed. Different laser-induced effects through mechanisms of laser-surface and laser-plasma interactions may be useful for the control of ablation plume characteristics. In this context, the double-pulse laser ablation technique leading to better coupling of laser pulse energy to the target and ablated matter is of great interest. This paper presents time-resolved emission spectroscopic studies of C_2 and C_3 species produced by single- and double-pulse laser ablation of graphite in helium atmosphere. It is suggested [1] that the small carbon molecules may serve as feedstock for carbon nanotubes formation. In this connection the study of the dynamics of these species in the plume is important for establishment of the growth mechanisms of carbon nanotubes in the laser ablation processes.

2. Experimental

The experiments were carried out using a set-up described elsewhere [3]. The Nd-YAG (1064 nm, 10 ns, $5 \cdot 10^8$ W/cm^2) laser radiation in combination with the second harmonic (532 nm, $5 \cdot 10^7$ W/cm^2) radiation of another Nd-YAG laser at different temporal delays between pulses were employed for ablation. The laser beams were focused on the surface of the graphite sample placed in the chamber under helium environments. The pressure of the helium atmosphere was about 600 Torr. In the experiment the sample was a new surface for each pulse that was achieved by rotating the target.

Spectroscopic characterization of the ablated plume was performed by the time resolved emission spectroscopy and laser-induced fluorescence methods. The details of these diagnostic techniques were described in [4].

Optical observation of the plasma emission was performed by imaging the section of the plasma plume onto the entrance slit of monochromator equipped by the fast photomultiplier. The detection of the photomultiplier signals was accomplished by a digitizer, connected to a personal computer for data processing, storage and analysis. The review emission spectra of plasma were recorded in the UV and visible region using a spectrograph with a reciprocal dispersion of 1.6 nm/mm. Kinetic energies of ablated species were determined by measuring their time-of-flight characteristics.

3. Results and discussion

The plasma emission spectra (300-700nm) were recorded and compared for different ablation regimes (single pulse and double pulse in coincidence and in sequence at various delays between pulses and laser fluences). The major species including CI, CII, and C_2, C_3 radicals within the plume have been identified. The spectra were dominated by the C_2 Swan bands ($d^3\Pi_g$ - $a^3\Pi_u$). The recorded Swan bands included $\Delta\upsilon = +1$ (470-475 nm); $\Delta\upsilon = 0$ (510-516nm); $\Delta\upsilon = -1$ (550-565 nm); and $\Delta\upsilon = -2$ (595-615 nm); where $\Delta\upsilon$ is the difference of the vibrational quantum numbers between the upper and the lower states of transition. The emission in the wavelength range 390 - 410 nm was identified as the C_3 (Comet Head System: $A^1\Pi_u$ - $X^1\Sigma_u^+$). The C_2 high-pressure bands in the spectra were also recorded including the (6 - 7) band at 543.4 nm and (6 - 8) band at 589.9 nm. The high-pressure bands are known to be part of the Swan system with $\upsilon' = 6$ levels excited at relatively high pressures.

Transient emissions from the plume zone (1 mm from the target) were detected at 543.4 nm, at 473.7 nm, (C_2 Swan system), and at 404.9 nm (C_3 Comet Head System). The emission of C_2, C_3 molecules persisted for 3-5 µs after the laser pulse, although the radiative lifetime of the upper states much shorter (only about 100 ns for C_2 Swan bands). This implies that formation of the excited carbon species must continue for at least a few microseconds after the laser pulse. A maximum of emission is reached not later than after 300 ns. Except for amplitudes there were no significant differences between wave forms of molecular emissions originated from different electronic-vibrational levels as well as between the temporal shapes of C_2 and C_3 bands.

The coupling of the second laser beam into the laser-ablated plume caused changes of molecular plume dynamics. The temporal evolution of the emission of C_3 molecules is presented in Fig.1. As can be seen from Fig.1 the C_3 band intensity in plasma produced by the sequence of two laser pulses is larger in comparison to the single pulse mode. In contrast to the ionic lines in double-pulse laser produced plasma [5] the enhancement of molecular emission was observed in a rather small interval of pulse separations (0-5 μs for C_3 molecules). It should be noted that when two pulses were fired simultaneously the effect was more than just additive both for the C_3 and C_2 band intensities.

The effect of preplasma produced by the first (IR) laser pulse on the spectrum of plume formed by the second (green) laser depends on the time delay between pulses. Fig.2 presents the ratio of the emission amplitudes of C_2, C_3 molecules from the 1064-532 nm double-pulse and from the 532 nm single-pulse laser ablation plasma versus the temporal delay between two laser pulses (Δt). It should be noted that for Δt ≤2 μs the intensity of C_2 emission from the double-pulse plasma increases but for 2 ≤Δt < 30 μs decreases. The intensity of C_3 emission from the double pulse produced plasma increases until the time separation between laser pulses does not exceed of 5 μs. For time delays Δt > 5 μs the presence of preplasma does not exert influence on the emission characteristics of C_3 molecules. As for C_2 emission it ceases to be influenced by the preplasma for time delays Δt > 30 μs. So, plasma produced by the first laser pulse seems to decay completely after 30 μs.

Several mechanisms may be responsible for the observed features of double-pulse laser-produced plasma spectra. The enhancement of the molecular emission may be related to the production of the excited C_2, C_3 molecules through the decomposition of carbon clusters (fullerenes) and evaporation of the particulates (soot particles) formed after action of the first laser pulse. The Rayleigh scattering measurements supported the presence of particulates in the plume. The subsequent laser pulse may fragment carbon clusters as well as heat and evaporate carbon particles. It is known that electronically excited C_2 is a photo-fragmentation product of laser-excited fullerenes [6]. Laser vaporization of suspended particles also generates C_2 and other small carbon molecules. It should be noted that surface temperature increasing after the first laser pulse resulting in enhancement of the amount of vaporized species may also contribute in observed emission features.

So, experiments demonstrate increased plasma emission, higher degree of particle atomization in dual-pulse ablation regime at the optimal pulse separations compared to the plasma produced by one laser. The double-pulse laser ablation enables the plasma to be further affected in a controlled way. By proper selection of the pulse separations and wavelengths in the sequence of two laser pulses the parameters of the

near-surface plasma can be adjusted to optimize its applications.
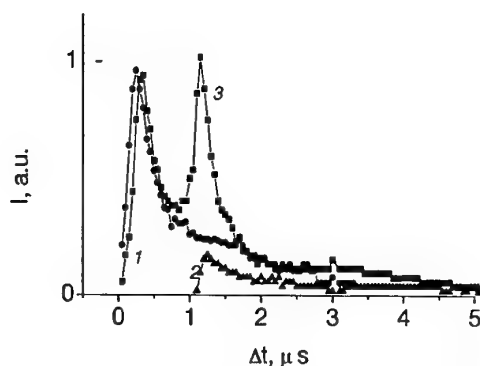
Fig.1. Time-resolved C_3 band emission intensities (λ=404.9nm) for the cases of single-pulse 1064 nm laser ablation (1), single-pulse 532 nm laser ablation (2), and double-pulse mixed wavelength
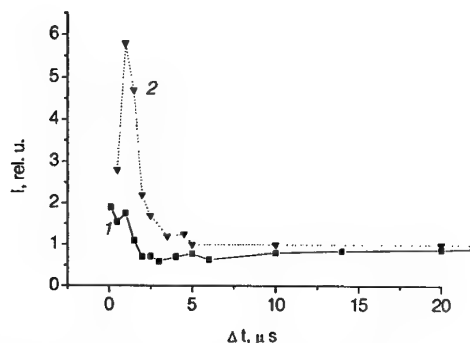
Fig.2. The ratio of the emission amplitudes of C_2 (1) and C_3 (2) molecules from the 1064 - 532 nm double pulse and from the 532 nm single-pulse laser ablation plasmas as a function of the temporal delay between laser pulses (Δt).

References

[1] C.D.Scott, S.Arepalli, P.Nikolaev, R.E.Smalley, *Applied Physics.* **A72** (2001) 573.
[2] A.A. Puretzky, D.B. Geohegan, X. Fan, S.J. Pennycook - *Applied Physics.* **A70** (2000) 153.
[3] V.S. Burakov, N.V. Tarasenko, N.A. Savastenko, *Spectrochimica. Acta.* **B 56** 961 (2001).
[4] V.S.Burakov, A.F. Bokhonov, P.A.Naumenkov, M.I. Nedel'ko, and N.V.Tarasenko, *Zh. Prikl. Spectrosk.* **65** (1998) 426.
[5] V.S.Burakov, A.F. Bokhonov, P.A.Naumenkov, M.I. Nedel'ko, and N.V.Tarasenko, *Quantum Electronics* (in press).
[6] D.M.Gruen, S.Liu, A.R.Krauss, X.Pan *J Appl. Phys.* **75** (1994) 1758.

Direction-Selective Free Expansion of Laser-Plasmas From Planar Targets

Th. Müller[1], B. K. Sinha[2] , S. N. Srivastava[1] and K. P. Rohr[1]

1. Fachbereich Physik, Universitaet Kaiserslautern,
D-67663 Kaiserslautem, Germany
2. Laser & Plasma Technology Division, Bhabha Atomic Research Centre,
Mumbai – 400 085, (India)

Direction-selective expansion of laser-plasmas from planar, slab targets of Al, Ni, Mo and Ta are reported. Angular distributions of the particles emitted from the targets, produced by a 130mJ-5nsec, NdLYAG laser, were obtained by means of a retarding potential analyzer and a quartz crystal. It was observed that the angular distribution of the particles was preferentially focussed towards the target normal with the increase in the focal spot size, atomic mass of the target material and the ionization state of the expanding particles, for a given value of the laser energy. Our experimental results confirm, for the first time, the Monte Carlo simulation results of the earlier workers, taking into account collision and recombination processes.

I. Introduction

In the field of material preparation such as fabrication of thin films of high T_c superconductors, oxides, semiconductors and diamond-like carbon laser pulsed-deposition technique (LPD) has been found to be interesting and useful [1-3]. The partition of energy as well as the angular distribution of the emitted materials have a great influence on the quality of the deposited layers [4]. Experimental investigations of Mueller and Rohr [5] demonstrated that the free-expansion of laser-produced plasmas from planar targets is directed essentially towards the normal to the target surface. The causes for this direction-selective behaviour of the freely expanding plasma are not well known. Itina et al [6] observed that the non-equilibrium chemical reactions in the gas phase during ablation affected the angular distributions in the way opposite to elastic collisions. Itina et al [7], in their subsequent works, presented the results of a Monte Carlo simulation of the laser desorption-process. They concluded that the chemical process, the recombination-dissociation one, gave rise to the broadening of the angular distribution and the collisions were found to be responsible for the focussing effect.

In the present work we have investigated the direction-selective free-expansion of laser-produced plasmas from the slab targets of Al, Ni, Mo and Ta using a 130mJ-5nsec, Nd:YAG laser. We report the experimental observation of the following results. For a given laser energy and the target material the angular distribution showed more preferential focusing towards the target normal as the values of the focal spot size B increased. For the given laser-energy and the given focal spot diameter, the focusing toward the target normal was more pronounced as the value of the atomic mass number increased. For a given laser-energy, a given focal spot diameter and a given target element, the angular distribution showed more preferential focusing as the ionization state of the emitted particles increased. The results are well explained on the basis of the estimates of recombination and collision rates.

II. Experiment

The plasma is created by an Nd:YAG laser (E_L = 130mJ, τ = 5nsec and λ = 1.06μm) incident on planar, slab targets at a fixed angle of −45° with respect to the target normal [5]. Target materials consisted of Al, Ni, Mo and Ta. The particles of the freely expanding plasma were detected in an angular range relative to the target normal between 50° to −10° for ions and 80° to −15° for the total number of particles by moving the analyzers within the plane of incidence, at a distance of 35° from the target. Positive sign before the angle signifies the analyzer being away from the direction of incident laser with reference to target normal. The ion-spectra were fully resolved by the time-of-flight/retarding-potential method, which made it possible to obtain the absolute number of each species. The second detector consisted of an rf-excited quartz crystal. From the frequency change of the crystal after the plasma has been deposited, one obtains the total mass or, in the case of monoatomic beams, the total number of particles. The number of the neutral particles could be deduced from the difference between the total particle signal and the summed spectra of the different ion-species. Full experimental details are given in the works of Mueller and Rohr [5].

III. Results

Fig.1 typically displays the integrally normalized angular distributions of the total number of particles of Ni as a function of the angle θ for three sizes of the spot size B, where θ is the angle between the direction of observation and that of the target normal. We note that although all the distributions are focussed towards the direction of the target normal, the focussing effect increases as the focal spot size increases. The combined result from Al, Ni, Mo and Ta were observed and found that the focussing significantly increases with increase in atomic mass number. For two focal sizes B = 8.34mm^2 and 0.61m^2,

^{59}Ni
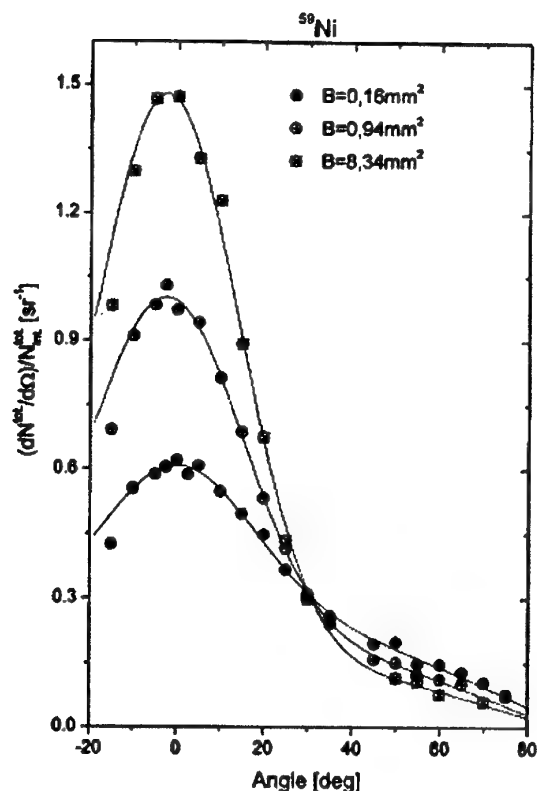
Fig.1 A typical distribution of normalized integrated emissions from Ni for three focal spot sizes

the experiments were repeated on the four materials and the angular distributions of neutral as well as upto three times ionized particles were obtained. The results showed that the particles with higher ionization states were much more focussed towards the target normal. Approximate calculations of the recombination rates and the particle collision frequencies were performed. It was seen that when recombination rate dominated, the focussing was less pronounced and when particle collision frequencies dominated, the focussing effect was sharper, in agreement with the results of Monte Carlo simulations of Itina et al [6,7] and Sibold and Urbassek [2].

Experimentally obtained maximum ionization states for Al, Ni, Mo and Ta were observed to be approximately as 2.4, 1.9, 1.5 and 1.3 respectively. It should be noted that these values represent the average values of the ionization states after the recombination, in the core of the plasma, has taken place. The estimated values of the average ionization states from Mosher's calculations [8] are approximately 11, 16, 17 and 22. This means that a strong recombination has taken place during the time-interval of the laser pulse duration. But this is not enough. One has to know which process,

collisional or recombination is dominating, which seems, at this stage, a difficult question. When the focal spot size varies from B=0.16mm^2 to B=8.34mm^2, Te decreases from 85 to 75 eV i.e. by a factor of 1.2 and the average decrease in the average ionization states, for all the four elements is also around a factor of 1.17. That is to say, the fractional decrease in Te and Z is nearly the same. From a simple calculation one can see that, because of this change in the plasma parameters three-body recombination rate decreases by a factor of approximately 1.3. The electron-ion collision frequency v_{ei} also increases by a factor of about 1.1. Hence, these two processes nearly neutralize each other. But when we consider the radiative recombination rate and the electron-electron collision frequency v_{ee} we find encouraging results. For the same amount of variation in the plasma parameters the radiative recombination rate decreases by a factor of 1.31 and, at the same time, the electron-electron collision frequency also increases by a factor of 1.31. As a result, for larger values of the focal spot size, the focusing toward the target normal increases. These experimental results support the simulation results of Itina et al [6,7].

References :

[1]   R. K. Singh, J. Narayan, Phys. Rev. (B), 41, (1990) 8843.

[2]   D. Sibold, H. M. Urbassek, J. Appl. Phys., 73, (1993) 8544.

[3]   A. Thum-Jäger, K. Rohr, J. Phys. (D), 32, (1999) 2827.

[4]   D. H. Lowendes et al, Surf. Science, 273, (1996) 898.

[5]   T. Müller, K. Rohr, J. Phys. (D), 35, (2002) 352.

[6]   T. E. Itina et al, J. Chem. Phys., 106, (1997) 8905.

[7]   T. E. Itina et al, Appl. Surf. Science, 127-129, (1998) 171.

[8]   D. Mosher, Phys. Rev. (A), 10, (1974) 2330.

Plasma Channel Dynamics Created by High-Current Relativistic Electron Beam When Being Distributed in Gaseous Media of Various Types

N.A. Kondratiev, G.E.Remnev, V.I.Smetanin

Nuclear Physics Institute at Tomsk Polytechnic University

634050, Tomsk, Russia, E-mail: alex@npi.tpu.ru

Experimental results of determination of plasma channel dynamics created by high-current beam (energy of electrons $E_e = 1,1 \cdot 10^6$ eV, beam current $I_b = 2,4 \cdot 10^4$ A, with pulse duration $t=60 \cdot 10^{-9}$ c.) in gases: helium (He), nitrogen (N_2), neon (Ne), Air (Air), argon (Ar), krypton (Kr), xenon (Xe), humid air (Air:H_2O) at pressure from 1 to 760 Tor are presented. It is showed that in gases with low value relation of collision rate v to ionization rate u_i ($v/u_i < 1$) electron beam forms wide plasma channel of high conductivity: $R_b/R_p < 1$, (where R_b- beam radius, R_p- plasma channel radius), which provides suppression of large-scale resistive hose instability (RHI).

1. Introduction

Great interest towards applied utilization of high-current relativistic electron beams (REB) interacting with various gaseous media is predetermined not only by their unique capacity for transportation of energy of high density through gas, but also by possibility of realization of a number of selective plasma chemical reactions or synthesis of compounds in beam plasma [1]. Immediate research of REB distribution dynamics in various gaseous media can give a full idea about development and effect of large-scale instabilities among which the dominant is: resistive hose instability (RHI) [2]. The results of this research can built the basis for RHI suppression or stabilization methods being worked out.

2. Experimental technique

Research was done at accelerator «Tonus» [3] generating high-current REB with the following parameters: electron energy $E_e = 1,1 \cdot 10^6$ eV, beam current $I_b = (2,0-2,4) \cdot 10^4$ A, pulse duration $t=60 \cdot 10^{-9}$ c. Electron beam with a diameter at accelerator outlet of $\sim 5 \cdot 10^{-2}$ m, was injected through anodic titanic foil $50 \cdot 10^{-6}$ m. thick, to metal drift tunnel (DT) with a diameter of $9,2 \cdot 10^{-2}$ m, and being filled up with one of the gases mentioned above at pressure from 1 to 760 Tor. In order to determine plasma channel dynamics created by heavy-current REB in various gaseous media previously used equipment and technique for radial conductivity profile measurements was utilized [4].

3. Results and discussion

Radial conductivity profile of plasma channel created by REB in gases (at pressure P = 300 Tor) and its time dynamics are displayed at Fig. 1. Formed by heavy-current REB, homogeneous wide plasma channel $R_b / R_p < 1$, (where R_b- beam radius, R_p- plasma channel radius) of high conductivity in Ne, Ar, Kr, Xe with characteristic maximum at beam periphery testifies for past gas electrical break-down in radial direction. This provides REB steady distribution and dampening its transverse vibrations throughout the whole distribution length. At the same time, for gases He, Air, N_2, Air : H_2O, with the increase of pressure P radial conductivity profile tends to $R_p=R_b$ and experiences synchronous

vibrations corresponding to REB displacement relative to distribution axis thus decreasing its effectiveness essentially. Differences obtained in conductivity profiles of plasma channels can be explained with the help of distinctions of gas and kinetic parameters of the gases used.

After full REB space charge neutralization is reached, secondary electrons do not leave beam anymore and take part in ionization process, accelerating in induced longitudinal electrical field E_z. Appearance of induced field E_z is conditioned by rate of beam current change I_b and is proportional to $\sim L \, dI/dt$, where L - inductance of system. This field induces plasma current I_p flowing inside the beam and by its field compensating REB magnetic field. Electrons accelerated in induced field and reaching the energy of keV, form electron avalanche.

Process of electrical break-down has strongly pronounced threshold character. Existence of such a threshold is connected with strong dependence of atoms ionization rate by electron impact u_i from the value of electrical field and also with the fact that besides ionization there are mechanisms which prevent avalanche from development. In work [5] by the example of numerical model it was shown that for gases in which relationship of collision rate v to ionization rate u_i is relatively small, i.e. ($v/u_i < 1$) formation of wide ($R_b/R_p < 1$) plasma channel is the most possible. The results which we obtained for gases: Ar , Ne , Kr , Xe can serve as experimental confirmation to this numerical model. Of course, one of the most important addition to the mechanism of plasma channel formation described above is taking into account radial constituent of electrical field determined from the condition: $E(r) = U/r \, \ln(r_2/r_1)$, where U-voltage (V), r_2–drift tunnel radius, r_1- beam radius. Value estimation E (r) gives the order of magnitude $\sim 10^5$-10^6 kV/sm. In [6] it was demonstrated that in this case radial electrical field is displaced to beam periphery in charge neutralization process. At the same time amplitude maximum of electrical field $E = (E_z^2+E_r^2)^{1/2}$ moved to the "wings" of the beam and avalanche multiplication of electrons lead to formation

of conductive channel wrapping beam, essentially decelerating development of resistive hose instability (Fig.2.) It is break-down in the radial direction that forms maximum of radial conductivity profile at the edge of REB (gases: Ar, Ne, Kr, Xe).

4. References

[1] V.D. Rusanov, A.A. Fridman. Physics of chemically active plasma. Moscow, 1984. P.230-232.

[2] H.S. Uhm, M. Lampe. Phys. Fluids. 1980. Vol. 21. N 8. P. 1574-1585.

[3] I.Za. Gleizer, et al. At. Energy. 1974. N.36. P.378.

[4] N.A. Kondratiev, et al. Physical Letters A. 1990.Vol. 148. N 2. P.89-94.

[5] G.A. Sorokin. Collective acceleration methods and beam-plasma interactions. 1982. P.180-185.

[6] G.Y. Kurevlev, G.A. Sorokin. THT. 1990. Vol.28. N. 3. P.433-438.
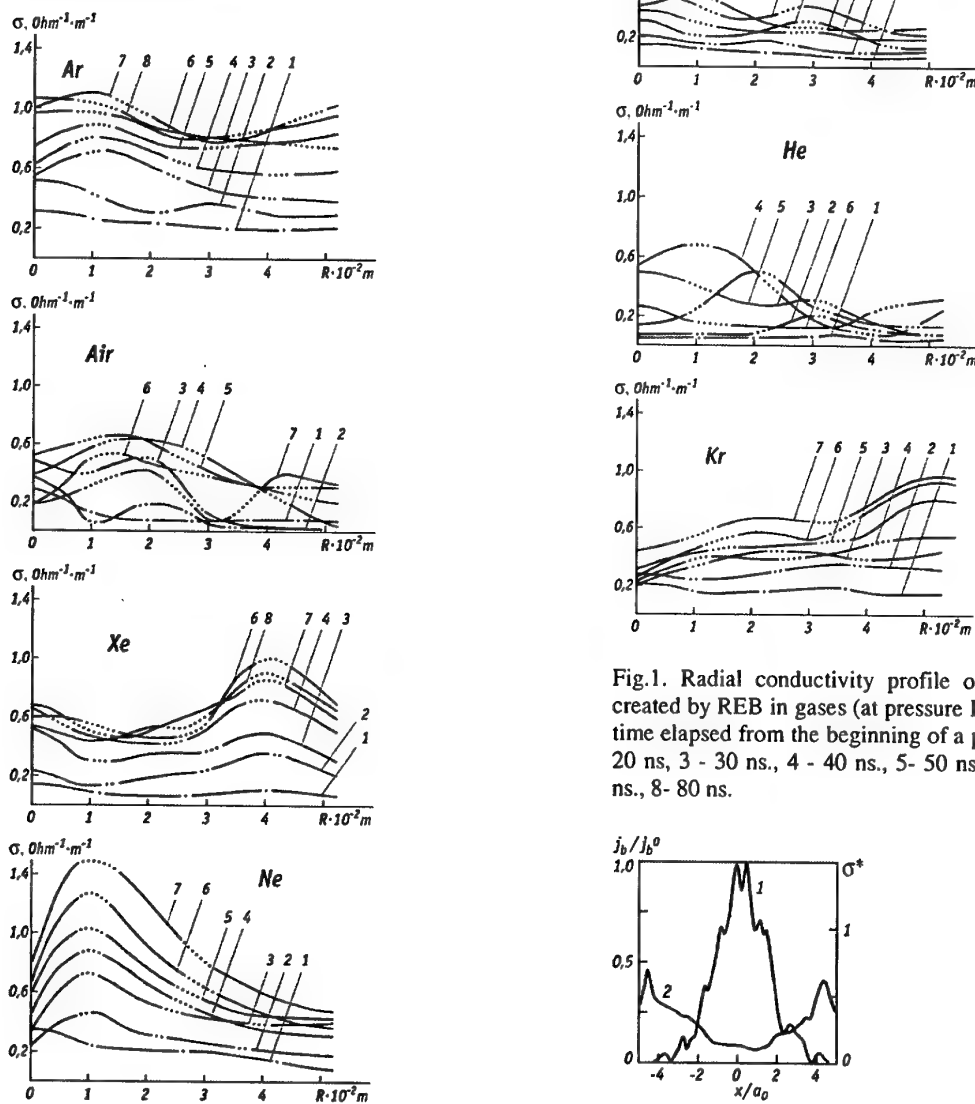
Fig.1. Radial conductivity profile of plasma channel created by REB in gases (at pressure P = 300 Tor.). The time elapsed from the beginning of a pulse: 1- 10 ns., 2- 20 ns, 3 - 30 ns., 4 - 40 ns., 5- 50 ns., 6- 60 ns., 7- 70 ns., 8- 80 ns.
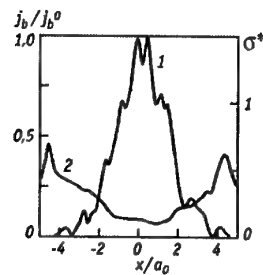
Fig.2. Formation of conductive (σ*)(2) channel wrapping beam j_b(1). Ref. [6].

Discharge features in a non-chain HF-laser

V.F Tarasenko, and A.N. Panchenko

High Current Electronics Institute, 4, Akademichesky Ave., 634055 Tomsk, Russia
Phone: (3822) 258685, Fax: (3822) 259410, E-mail: VFT@loi.hcei.tsc.ru

Electric discharge parameters and amplitude-temporal and spectral parameters of laser radiation in gas mixtures of SF_6 with hydrogen and hydrocarbons are studied. High discharge uniformity obtained with the use of special shaped electrodes along with uniform UV preionization is key parameter for improving intrinsic efficiency of discharge HF-laser. Experimental conditions providing high intrinsic efficiency of a non-chain HF laser are determined.

1. Introduction

Lasers with non-chain chemical reaction excited by a self-sustained discharge are the most promising for many practical applications [1-7]. In certain experimental conditions high radiation parameters were obtained without preionization of the laser active volume [1,2]. The use of intense preionization allow us to obtain the same pulsed energy of HF laser using mixtures of SF_6 with hydrogen and hydrocarbons and it was suggested to use profilated electrodes for improving discharge stability and output parameters of non-chain chemical lasers [3]. Importance of preionization for efficient operation of HF laser was also demonstrated in [4,5]. In [3,6] intrinsic efficiency of a non-chain HF laser was improved using pulse generator with inductive energy storage. In the present paper, effects of preionization and pumping pulse parameters on output parameters of discharge HF laser are studied.

2. Experimental technique

The installation was similar to the long pulse excimer laser excited by the inductive energy storage with semiconductor opening switch [7]. The laser has active volume $2-3,8\times0,6-1,4\times70$ cm^3 (discharge gap d = 2 or 3,8 cm). The active volume and cathode surface was uniformly preionized by 72 spark gaps evenly distributed along both sides of anode. Some experiments were made without preionization. Six SOS-50-2 diodes were used as the opening switch.

3. Discharge stability and HF laser output

Gas mixture of non-chain HF laser contains more than 70% of SF_6. However volume discharge in these mixtures is relatively easy to form. The laser action was obtained in wide range of gas mixture composition and pumping pulse parameters. Development of small-scale roughness on electrode surfaces (especially on cathode surface) improves conditions for volume discharge formation in gas mixtures with hydrocarbons without or at low intensity preionization. Therewith uniform electric field in the discharge gap of a laser on SF_6-hydrocarbone mixture is not necessary [4]. However, discharge in H_2-based mixtures is more sensitive to the preionization conditions and electric field strength in the laser gap. In our experiments, the

laser output lower 0,2 J was obtained with the gap of d = 2 cm. Arc formation was evident 50-200 ns later the gap breakdown due to non-uniform electric field strength across the laser gap and on the cathode surface independently on the preionization parameters. Therefore further experiment were made with d = 3,8 cm and electrodes providing uniform electric field. Disconnection of preionization results in two – tree fold increase of the breakdown voltage. However, strong deterioration of discharge stability is evident in hydrogen based mixtures. At low pressure chaotically distributed anode and cathode flares with different length penetrate into the discharge volume and short down the gap, the laser output decreases by a factor of 1,5. The number of these arc channels in the laser gap increases with the mixture pressure accompanied by sharp increase of discharge current and 50-100 ns later the breakdown and further decrease of the laser output. The use of preionization removes anode flares and arcs from the laser volume and improve the laser output. However, large number cathode flares grows into the laser gap during current pulse.

In the case of gas mixtures with pentane preionization has much lower effect on the discharge quality. In both cases a large number of small bright spots on the cathode surface and very uniform discharge luminescence without any sign of arcing and minor difference of the laser output only at low U_0 are evident. In the absence of preionization discharge appears in several local points and than expands on full electrode surface, the time of discharge formation decreases at high U_0 resulting in lower energy losses during discharge formation [2]. Therefore the laser output was independent on preionization at $U_0>30$ kV. Additional indication of the discharge uniformity is partial discharge of the storage capacitor C_0 and residual voltage U_{res} is measured across the gap after the discharge current termination. U_{res} increases directly to the mixture pressure and inversely to the charging voltage. Maximal U_{res} was observed in the mixtures with H_2 (see Figure 1). Development of discharge non-uniformities results in zero U_{res}. At low pressure and high U_0 stored energy is totally deposited into the volume discharge (see Figure 2) and $U_{res}=0$, as well.

The use of the inductive generator and preionization similarly to [3,6] increases breakdown voltage by a
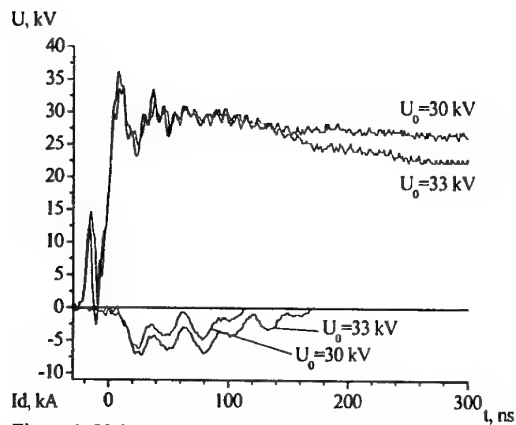
Figure 1: Voltage across the laser gap and discharge current in SF_6:H_2=60:7,5 Torr mixture.

Figure 2: Waveforms of voltage across the laser gap and discharge current and discharge view (negative) in SF_6:H_2=24:3 Torr mixture. U_0=33 kV.

factor of 1,5-2, shortens rise-time of discharge current and in some conditions increases discharge current amplitude. In the case of the inductive generator U_{res} depends on the discharge resistance and is determined by recharging of capacitor C_p from C_0 during current pulse. Breakdown voltage up to 50-60 kV and 50-100 ns excitation pulse with current amplitude up to 30 kA was obtained with the inductive generator. It is important that considerable part of input energy is deposited into the laser active media at high E/p across the laser gap during voltage drop after the gap breakdown. As it is seen from Figure 2, the inductive generator improves discharge homogeneity. Similarly to pentane based mixtures highly uniform discharge fluorescence without cathode flares was observed in mixtures with H_2. Note that about half of the energy stored in C_0 is lost in SOS diodes during current interruption and remains in the C_p-L_p-C_0-L_0 circuit. With the use of preionization the laser output in H_2 based mixtures was close to that with the capacitor generator, and decreases in C_5H_{12} based mixtures. Without preionization the output decreases by a factor of about 2 for all mixtures with H_2.

The laser efficiency with respect to deposited energy up to η_{in} ~10 % is obtained using discharge excitation by the inductive and capacitor generators in the SF_6-H_2 mixtures. Therewith output spectra of the HF laser significantly widens and cascade laser action on some rotational lines of HF molecule vibrational transitions $v(3-2) \rightarrow v(2-1) \rightarrow v(1-0)$ is observed. Specific output of the non-chain HF-laser over 8 J/l (140 J/l×atm) and total laser efficiency η_0 ~4,5% were achieved., as well.

4. Conclusion

It was shown that discharge parameters have strong effect on the HF laser output. Application of the inductive generator, electrodes of uniform field and intense preionization allows to form uniform volume discharge and improves intrinsic laser efficiency. Excitation modes with maximal intrinsic efficiency η_{in} =10% was realized using the capacitor and inductive
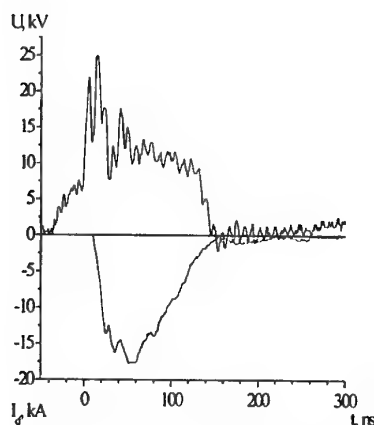
generators. The use of the inductive generator allows to improve η_{in} in wide range of input electric energy (10 - 100 J/l). The generator provides breakdown electric field strength up to E_0/p = 200 kV/cm×atm and significant part of stored in the inductor energy is deposited into the laser active volume at high E/p value across the laser gap during short current pulse. The laser energy up to 1,4 J, specific output of 7 J/l and total laser efficiency over 3% were easily achieved.

Discharge uniformity, increase of the rate of fluorine atom formation in the laser active volume [4] and cascade laser action can explain high intrinsic efficiency of the discharge HF laser.

Maximal output up to 1.9 J and total laser efficiency η_0 = 4,5% were obtained in the SF_6-H_2-C_5H_{12} mixtures using the capacitor generator with low circuit inductance, electrodes of uniform field and intense preionization.

4. References

1. A.F. Zapolsky, K.B. Yushko, *Kvant. Electron.* 6 (1979) 408.
2. V.V.Apollonov, S.Yu.Kasantsev, V.F.Oreshkin, K.N.Firsov, *Kvant. Electron.* 25 (1998) 123.
3. V.F. Tarasenko, V.M. Orlovskii, and A.N. Panchenko, *Quant. Electronics* 31 (2001) 1035.
4. L. Richeboeuf, S. Pasquiers, M. Legentil and V. Puech, *J. Appl. Phys.* 31 (1998) 373.
5. B. Lacour, S. Pasquiers, S. Postel, V. Puech, *Appl. Phys. B* 72 (2001) 45.
6. V.F. Tarasenko, V.M. Orlovskii, and A.N. Panchenko, *Technical Physics* 48 (2003) 267.
7. E.H. Baksht, A.N. Panchenko, V.F.Tarasenko, T. Matsunaga, and T. Goto, *Jap. J. Appl. Phys.* 41 (2002) 3701.

Formation of an electron beam in helium at elevated pressure

V.F. Tarasenko[*], S.B. Alekseev[*], V.M. Orlovskii[*], A.N. Tkachov[**], S.I. Yakovlenko[**]

[*]High Current Electronics Institute, 4, Akademichesky Ave., Tomsk 634055, Russia; vft@loi.hcei.tsc.ru
[**]General Physics Institute, Russian Academy of Science, Vavilova St. 3., Moscow, 119991, Russia

1. Introduction

There exist many papers devoted to investigations of X-ray radiation and electron beams formed in gases at elevated pressures (see [1], and references to this paper). However, electron beams with high current density and efficiency is actually achieved at relatively small gas pressures [2,3]. A number of papers report on accelerated electrons obtained at pressure of about 1 atm, still there are either small current and e-beam densities realized [1]. This work was aimed at theoretical and experimental study of the probability to obtain high e-beam current at elevated pressure values of helium.

2. Theory

A theoretical examination and simulation of multiplication process of electrons in discharge gap was done in order to recognize the conditions for running electrons. The main results obtained are as follows: Some part of electrons (~1%) start to run away when the electron accumulates the energy $\varepsilon \equiv m_e v^2/2 = eEl$ of about two energy orders of atom ionization on the free path $l = 1/\sigma_i N$. Here σ_i is cross section of ionization; N is density of neutral atoms; v, m_e are velocity and mass of an electron; E is strength of electrical field. Correspondingly, the condition for the voltage U between anode and cathode when electrons appear has the following form: $U > U_{cr1} \equiv NL\sigma_0\varepsilon_0/e$, where L is distance between planes; σ_0 is cross section of ionization with energy of an electron as $\varepsilon \sim \varepsilon_0 \sim 2J$.
The fair quantity of electrons (~50%) run away at the condition realized $\dfrac{m_e N}{eE} \displaystyle\int_0^{\sqrt{2U/m_e}} \sigma_i(v)v\,dv > 1$. If in the range of energies $\varepsilon_1 < \varepsilon < eU$, most significant for integration, the cross section of ionization may be approximated by dependence inversely proportional to the energy $\sigma_i(\varepsilon) = \sigma_1\varepsilon_1/\varepsilon$, one might write the condition of running away electrons in the following way:
$$U > U_{cr2} \equiv NL\sigma_1\varepsilon_1 \ln(eU/\varepsilon_1)/e.$$
We may set for helium $\sigma_1 \approx 4\cdot10^{-17}$ cm², $\varepsilon_1 \approx 500$ eV. Being headed for $U \sim 100$ kV, for the presented critical field strength we will have $E_{cr2}/N \equiv U_{cr2}/LN = \sigma_1\varepsilon_1\ln(eU/\varepsilon_1)/e \approx 10^{-13}$ cm³·V/cm or $E_{cr2}/p \equiv U_{cr2}/Lp = (N/p)\cdot\sigma_0\varepsilon_1\ln(eU/\varepsilon_1)/e \approx 3.4$ kV/Torr·cm. Here p is pressure of gas at room temperature.
Numerical simulation of the processes of electron multiplication and running away between two planes at distance L and voltage U was performed using one of particle method modifications. The results of modeling

are in accord with presented estimation. For example, for the pressure values of 13.5 Torr and 25 Torr corresponding to the part $\eta = 50$ % of accelerated electrons (from the total number of the electrons reached the anode) at $E = 62.5$ kV/cm and $E = 125$ kV/cm, we have accordingly $E/p = 4.6$ kV/Torr·cm and $E/p = 5$ kV/Torr·cm. Notice that with $E < E_{cr2}$ at intensive multiplication of electrons the beam current occurs to be much higher than with $E > E_{cr2}$, though the part η of running away electrons with $E < E_{cr2}$ is less than with $E > E_{cr2}$. In other words, at the given electrodes voltage, the beam current may increase both with pressure and distance between electrode increase. It should be noted, by the way, that the mentioned above takes place only in the case if the field strength in plasma is not yet dropped due to screening by free charges.

3. Experiment

The pulsed generator earlier used for e-beam formation in vacuum [4] was taken for experiments. The generator had 30-Ohm impedance and formed with matched load an impulse with voltage of 200 kV and duration at FWHM 4 ns at voltage leading edge of about 1 ns. The diode used in experiments was filled in with helium at pressure from 0.1 up to 760 Torr. Two cathodes were used in experiments. The cathode №1 constituted a set of three coaxial cylinders (12, 22, and 30 mm in diameter) made from 50-μm Ti foil, inserted one into other and fixed on duralumin substrate 36-mm in diameter. Height of rings decreased by 2 mm from the smaller to the greater. The cathode №2 was made from graphite in the form of a tablet of 29-mm in diameter with rounded edges being convex in the foil direction with 10-cm radius of curvature. The graphite cathode was placed on a copper holder of 30-mm in diameter. E-beam extraction was realized through 45-μm thick AlBe foil mounted at the end flange. The beam current was measured using graphite electrode mounted at the distance of 10 mm from the foil and connected by low-value shunt with the case of accelerator. Besides that, at the same time, the total diode current on the end flange was measured too, the end flange being connected with cylindrical case of vacuum diode through the second shunt.
The basic experimental results are as follows. There were four typical modes of diode operation. The first mode was observed at small helium pressure in the diode (0.1÷1 Torr, $E/p > 70$ kV/Torr·cm) for the cathode №1 which provided additional electrical field acceleration on the foil selvages. With this well-known mode of accelerator operation, the highest beam

current values behind the foil (> 1 kA) were registered. With further decrease of residual pressure of helium in the diode (>0.01 Torr) the diode beam current was equal by amplitude to the "total" diode current.

The second mode was observed at average pressures of helium ($1\div10$ Torr, $E/p > 7$ kV/Torr·cm) being different by high instability from pulse-to-pulse due to helium breakdown with low voltage values. In this mode, beam current was registered only in separate pulses for the cathode №1 made from foil. As for the cathode №2 made from graphite, it was not possible to register the beam current in the first and second modes. The third mode was observed with helium pressure values 10-40 Torr ($E/p > 1.5$ kV/Torr·cm) also for the cathode №1 made from foil. Increase of helium pressure leaded as compared with the second mode to increasing of the time of breakdown delay, voltage increase at the gap, and appearance of beam current comprising behind the foil of up to 30 % as compared to the bean current of the mode 1.

At helium pressures above 100 Torr for the graphite cathodes №1 and №2, there was observed the fourth mode. This mode is characteristic for low values of E/p < 0.7 kV/(Torr·cm).

It is necessary to note that with the use of this generator with the pulse of 4-ns duration, a short-circuit discharge and (or) the discharge between anode (foil) and cathode was observed in the diode resulting in diode short-circuit to voltage pulse end, correspondingly, the total diode current was close to short-circuit current, and beam current pulse was shorter than the voltage pulse on the matched load.

Increase of the beam current extracted behind the foil was recorded with increasing of the cathode-anode gap from 7.5 to 28 mm. The electron energy estimation show that the half current is being transferred by the electrons possessing energy above 100 keV (the current beam behind two foils) and the part of such electrons is proportional to the total current of the beam. For the graphite cathode №2, the maximum of beam electron distribution by energy was corresponded to the energy of ~150 keV. Let us note that similarly to [1], we registered electrons with abnormally high energy exceeding the value of eU.

The form of the gas-filled diode discharge during the fourth mode essentially differed for the cases of cathodes №1 and №2. With the foil cathode №1, there were observed single channels, and with the graphite cathode №2, the discharge was more uniform, similar form of discharges was earlier observed in [1].

In our opinion, most important is the experimental result obtained with the use of the graphite cathode №2, when essentially higher beam current (up to 140 A, current density above 10 A/cm^2) was increased. In these conditions, in contrast to [1], the beam electrons reached anode either with greater gaps. Diameter of the electron beam trace of the foil in the case of the cathode was ~40 mm, and uniform change of foil color along the beam aperture was registered.

4. Discussion

Numerical analysis of theoretical and experimental results is difficult due to the circumstance that there are no yet means to take into account shielding of electrical field correctly. Really, plasma is formed during breakdown having high conductivity as compared with the rest part of the discharge gap, and within fractions-units of nanoseconds it bridges the gap. The plasma may serve, in particular, as a source of electrons, i.e. to be plasma cathode. Nevertheless, some qualitative conclusions may be drawn.

It is possible to determine the value of the parameter $E/p > 3$ kV/cm×Torr with which an essential rise of beam current was observed. This value of E/p is in accord with calculated value of E/p, when the part of running away electrons increases (the mode 3). Some difference is connected with change of voltage value at the gap in experimental conditions. Duration of voltage pulse of 4 ns was sufficient for gap short-circuiting in all modes with which e-beam was stably registered.

The beam current behind the foil was registered with both cathodes cases at E/p < 0.7 kV/cm×Torr when the part of beam electrons is small. As for the cathode №1 made from the foil, the beam current value increased with pressure from 150 to 760 Torr, with that the value of the parameter E/p decreased from 0.5 to 0.1 kV/cm×Torr. It may be connected with the results of calculations, demonstrating the rise of beam current with decrease of E/p.

5. Conclusion

Thus the experimental and theoretical investigations performed with the aim to study conditions for obtain of running away electrons in helium show that the accelerated electrons are being formed both at the values of E/p above 3 kV/cm×Torr (in these conditions a high e-beam efficiency may be reached) and at the comparatively low values of the parameter E/p = 0.1-0.5 kV/cm×Torr. An electron beam has been obtained in atmospheric helium with amplitude of 140 A (beam current density is above 10 A/cm^2) with electron energy of ~150 keV.

6. Reference

1. L.P. Babich, T.V. Loiko, V.A. Tsukerman, *UFN* **160**, No.7 (1990) 49.
2. A.P. Sorokin, *Pis'ma v JTF* **28**, No.9 (2002) 14.
3. A.P. Bokhan, P.A. Bokhan, *Pis'ma v JTF* V.**28**, No.11 (2002) 21.
4. V.P.Gybanov, S.D. Korovin, I.V. Pegel' et. al. *Izv. VUZov. Fizika* No.12 (1996) 110.

Optical collective phenomena with participation of metastable atoms in decaying plasma of pulsed discharge

S.N. Bagayev[1], V.V. Vasilyev[2], V.S. Egorov[2], V.N. Lebedev[2], I.B. Mekhov[2], P.V. Moroshkin[2], A.N. Fedorov[2], I.A. Chekhonin[2], E.M. Davliatchine[3], and E. Kindel[3]

[1] Institute of Laser Physics, Siberian Branch of RAS, Lavrentyeva 13/3, 630090 Novosibirsk, Russia

[2] St. Petersburg State University, Department of Optics, Ulyanovskaya 1, 198504 St. Petersburg, Russia

[3] Institute of Low-Temperature Plasma Physics, Friedrich-Ludwig-Jahn-Str. 19, 17489 Greifswald, Germany

Considering new methods of nonstationary plasma diagnostics, we investigate an appearance of a new type of laser spectrum generation, which is a direct consequence of underlying principles of light-matter interaction. The spectrum "condensation" and amplification observed originate from the collective coherent interaction between atoms of a dense resonant medium trough the electromagnetic field.

With a view to develop new methods of nonstationary plasma diagnostics, experiments on probing the decaying plasma of pulsed discharge, which contains great amount (10^{13} cm^{-3}) of metastable atoms, were carried out by the intracavity-laser-spectroscopy method using a dye laser. The essential role of collective phenomena under interaction between polychromatic laser radiation and a dense resonantly absorbing medium was shown for this method of plasma diagnostics. The principle possibility for two types of generation spectrum to appear is proved under intracavity spectroscopy with broadband pumping: (1) ordinary type, with a deep at week absorption lines, (2) the so-called "collective" type of generation spectrum.

On the basis of experimental and theoretical results obtained, a new method of light generation under intracavity interactions with broadband pumping is proposed and proved – parametric excitation of collective effects under interaction of electromagnetic field and matter, which is accompanied by the so-called "condensation" of lasing spectrum.

In the intracavity experiments, decaying plasma of a Ne pulsed discharge (initial gas pressure is 4 Torr, current density is tens of A/cm^2, current pulse duration is 10–100 µs) was placed inside a dye laser with lamp pumping. Figure 1 shows a set of "condensation" spectra corresponding to generation close to 594.5 nm spectral line, that were obtained at different phases of pulsed-discharge plasma decay.
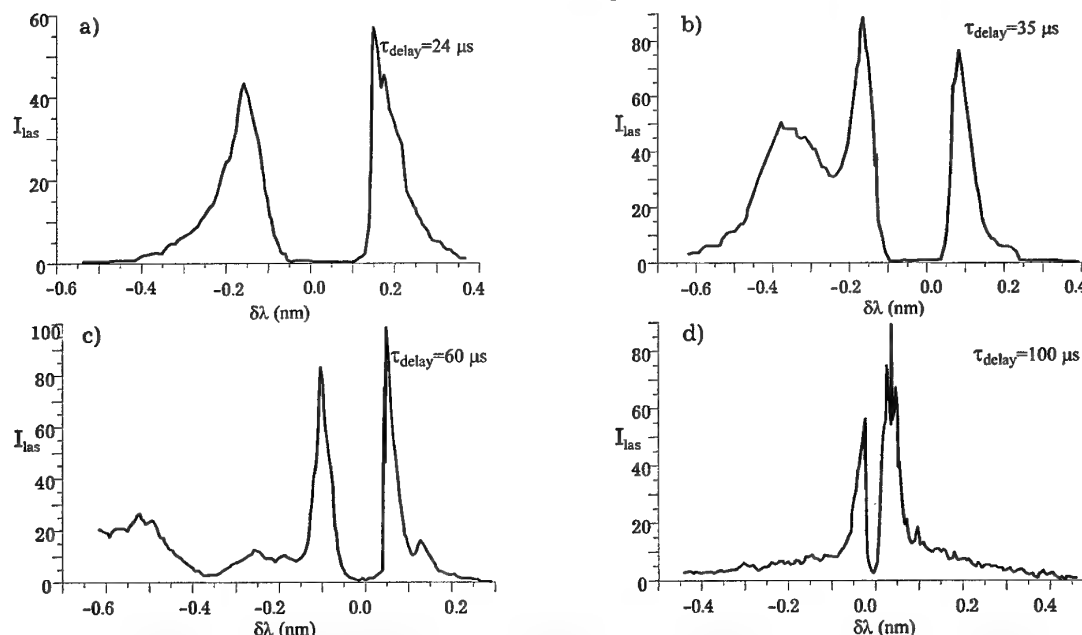
Fig. 1. "Self-splitting" of the generation spectrum at different time moments in the afterglow pulsed discharge, that corresponds to different absorbing metastable atom densities in the intracavity absorbing cell; Ne, λ=594.5 nm.

The density of absorbing atoms, calculated by expression $\Delta = \omega_c^2 T_2$ (Δ is a distance between components of "condensation" spectrum, ω_c is a cooperative frequency, which is also known as optical plasma frequency, T_2 is a phase relaxation time of the corespondent spectral transition), are in agreement, at least in order, with analogous measurements by the Rozhdestvensky "hook" method.

It should be emphasised, that the results obtained are truly the consequence of the fundamental principles of light–matter interactions, but not that of some cavity effects. To demonstrate that, we carried out the free-space experiments on the dye-laser pulse amplification under pumping of afterglow plasma of a Ne pulsed discharge. In these experiments, the decaying plasma was created after a current pulse of 10–100 μs with current density of tens A/cm^2 and initial Ne pressure of 18 Torr. Under certain experimental conditions, the spectrum "condensation" at a strong absorption line was also observed. The correspondent effective amplification coefficient of a laser beam, probing the plasma, is shown in Fig. 2.

References

[1] S.N. Bagayev, V.S. Egorov, I.B. Mekhov, P.V. Moroshkin, I.A. Chekhonin, Opt. Spectrosc. V. 93, N 6, pp. 955 – 962 (2002);

[2] S.N. Bagayev, V.S. Egorov, I.B. Mekhov, P.V. Moroshkin, I.A. Chekhonin, E. M. Davliatchine, and E. Kindel, Opt. Spectrosc. V. 94, N 1, pp. 126 – 133 (2003)
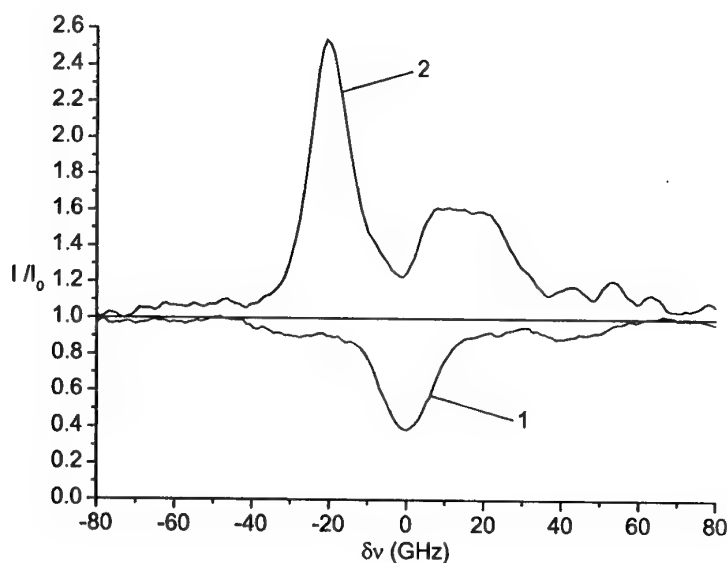
Fig. 2. Transmission of the probe laser field in the absence of the pump beam (1) and it's amplification in the presence of the pump (2); Ne, λ=640.2 nm.

Ionization-induced generation of strong Langmuir waves by high-intensity Bessel beam

V.B. Gildenburg and N.V. Vvedenskii

Institute of Applied Physics, Russian Academy of Sciences, 46 Ul'yanov Street, Nizhny Novgorod, 603950, Russia

Dynamics of the field and plasma at the gas breakdown produced by the Bessel (axicon-focused) laser beam is studied with the effects of natural plasma waves generation and reflected wave spectrum conversion taken into account

We study in this paper the dynamics of the field and plasma in the discharge column created by axicon focusing [1-3] of a high-intensity laser radiation in homogeneous gas. We focus on the effect of natural plasma waves generation considered previously for other types of the optical and microwave discharges [4, 5].

The spatiotemporal evolution of the electric field $\widetilde{\mathbf{E}} = \mathrm{Re}[\,\mathbf{E}(\mathbf{r},t)\exp(-i\omega t)]$ is calculated numerically based on the vector wave equation for the slow time envelope of the field $\mathbf{E}(\mathbf{r},t)$:

$$\frac{2i}{\omega}\frac{\partial \mathbf{E}}{\partial t} + \delta^2 \nabla(\nabla\cdot\mathbf{E}) + \varepsilon\mathbf{E} - \frac{1}{k_0^2}[\nabla\times[\nabla\times\mathbf{E}]] + \hat{\Gamma}\mathbf{E} = 0 \quad (1)$$

This equation takes into account the spatial and time dispersion and allows us to describe the processes of resonance excitation and Landau damping of Langmuir waves in the time-varying plasma. In Eq. (1), $\hat{\Gamma}$ is the model dissipation operator: $\hat{\Gamma}\mathbf{E} = -i\,a\,\delta^2\nabla(\nabla\cdot\mathbf{E})$, $\varepsilon = 1 - (N/N_c)(1 - i\nu/\omega)$ is the complex permittivity of the plasma, $N_c = m(\omega^2 + \nu^2)/4\pi e^2$ is the critical density, ν is the electron collision frequency, a is the coefficient of order unity, $k_0 = \omega/c$, $\delta = \sqrt{3}\,V_T/\omega$, $V_T \ll c$ is the thermal electron velocity.

Gas breakdown is caused by the optical-field-induced ionization processes. As an example we consider tunnel ionization of hydrogen atoms and determine the time averaged ionization rate by the known expression

$$\frac{\partial N}{\partial t} = 4\Omega\left(N_g - N\right)\sqrt{\frac{3E_a}{\pi|\mathbf{E}|}}\exp\left(-\frac{2E_a}{3|\mathbf{E}|}\right). \quad (2)$$

Here $E_a = 5.14\times10^9$ V/cm and $\Omega = 4.16\times10^{16}\,\mathrm{s}^{-1}$ are the atomic field and frequency units, and N_g is the concentration of neutral atoms before the process of ionization. The parameter range we are interested in here is the following: the wavelength $\lambda \sim 0.6 - 10$ μm, laser pulse intensity $S \sim 10^{14} - 10^{16}$ W/cm^2, and gas pressure $p \sim 0.3 - 70$ atm.

We consider the model of the axially symmetric discharge: $N(\mathbf{r},t) = N(r,t)$ produced by the rotating cylindrical wave with the complex envelope of electric field $\mathbf{E}(\mathbf{r},t) = \mathbf{E}(r,\varphi,z,t) = \mathbf{E}(r,t)\exp(i\varphi + ik_0 z\cos\theta)$ (r,φ,z are the cylindrical coordinates). Outside the plasma ($r \geq R$, $N(r \geq R) = 0$) the field is a superposition of the converging (incident) and diverging (reflected) TE and TM waves with a given angle of inclination θ to the axis of symmetry z. The incident wave is given by the axial components of electric and magnetic fields: $E_z^{(in)} = C(t)H_1^{(2)}(k_0\,r\sin\theta)$, $H_z^{(in)} = -i\cos\theta E_z^{(in)}$, $C(t) = A\exp(-(t-t_0)^2/\tau^2)$, $H_1^{(2)}$ is the first-order Hankel function describing the converging wave. The correlation between the amplitudes of these components (the coefficient $-i\cos\theta$) is chosen so that the transversal components of the fields in the absence of plasma are circular polarized and are the zero-order Bessel function of radius r: $E_\varphi(r) = iE_r(r) \sim J_0(k_0\,r\sin\theta)$. We note that, in the presence of plasma, the field remains circularly polarized only on the axis.

Equations (1) and (2) were solved numerically in the space interval $0 \leq r \leq R$ with the initial conditions: $N(r,0) = 0$, $E_\varphi(r,0) = -2C(0)\cot\theta J_0(k_0 r\sin\theta) = iE_r(r,0)$, $E_z(r,0) = 2C(0)J_1(k_0\,r\sin\theta)$ and the following boundary conditions: (i) the solution is analytical at $r = 0$: $E_z = 0$, $\partial E_{r,\varphi}/\partial r = 0$, (ii) all field components (including E_r) are continuos at $r = R$ (for detailed expressions and explanation see [6]).

It has been found that the scenario of the breakdown process depends greatly on the convergence angle of the wave. If this angle is less than some critical value $\theta_c \approx 25^0$, the maximum plasma density $N_{max} \sim N_c\theta^2$ that is less than the critical one. However, at the angle exceeding the critical one, the plasma density at the axis increases in the sharpening regime and passes the critical point, after that the fast ionization wave containing the plasma resonance point at the leading front propagates in the radial direction. The results of numerical calculations are presented on Figs. 1 and 2 in dimensionless variables $k_0 r \to r$, $\omega t \to t$, $\mathbf{E}/E_a \to \mathbf{E}$, $N/N_c = n$ for the parameter values: $\theta = 30^0$, $\Omega/\omega = 22$, $k_0\delta = \sqrt{3}V_T/c = 0.02$, $\nu/\omega = 0.01$, $a = 0.1$, $N_g = 1.5N_c$, $t_0\omega = 100$, $\tau\omega = 50$, $A/E_a = 0.0204$, $k_0 R = 4$. At the given values of A, the maximum field at the axis in the absence of plasma
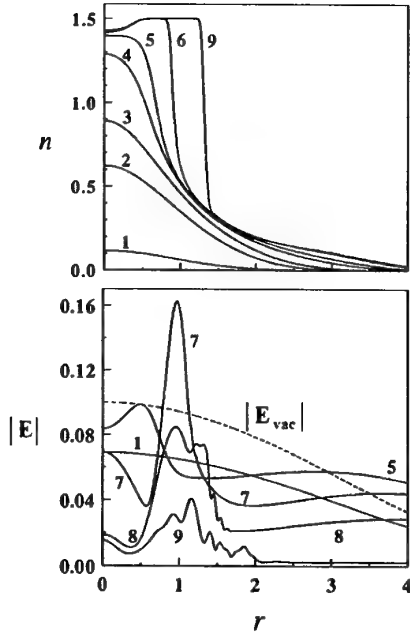
Fig. 1. Evolution of the plasma density $n(r,t)$ and the field amplitude $|\mathbf{E}(r,t)|$ at $\theta = 30^0$. Curves 1-9 correspond to the time instants $t = 80$, 90, 95, 105, 110, 120, 130, 150, and 200, respectively. The dashed curve shows the unperturbed field $|\mathbf{E}_{vac}(r)|$ (in the absence of a plasma) at $t \approx t_0 = 100$.

is the same: $|\mathbf{E}|_{max} / E_a = 0.1$. The above dimensionless parameters correspond to the vacuum wavelength $\lambda \approx 0.8$ μm, maximum pulse intensity $S \approx 3 \times 10^{14}$ W/cm^2, pulse duration (at the level of $1/e$) $\tau\sqrt{2} \approx 30$ fs, and the gas pressure $p \approx 60$ atm.

The transition of the plasma density through the critical value at $\theta > \theta_c$ (Fig. 1) is accompanied by the excitation of intense Langmuir oscillations, whose amplitude reaches its maximum (twice as high as the amplitude of the unperturbed electric field at the axis) at the front of the ionization wave at $r = 1$.

The coupling of the excited Langmuir oscillations to an external electromagnetic field (due to the presence of a fairly sharp boundary of the ionized region) gives rise to the partial emission of their energy into the surrounding space, i.e., to the occurrence (along with the fundamental frequency component ω) of one or several components at frequencies close to $\omega_{p max} = \sqrt{4\pi e^2 N_g / m} \approx 1.22\omega$ in the spectrum of the cylindrical wave reflected from the discharge. In view of the linear character of the "transition" resonant excitation of Langmuir oscillations, the intensities of the shifted spectral components are proportional to the intensity of the incident wave. This linear parametric conversion of
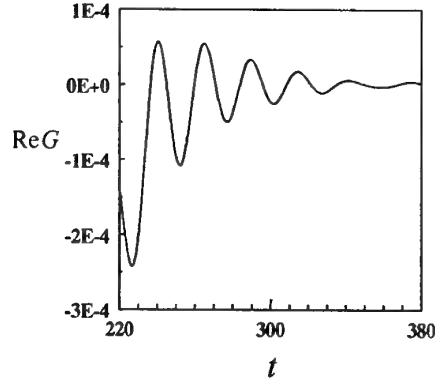
Fig. 2. Time behavior of the amplitude function $\mathrm{Re}\,G(t)$ of the reflected TE wave at large times. The curve illustrates the radiation from the discharge at the upshifted frequency $\omega_{p\,max} \approx 1.22\omega$.

the scattered spectrum of an ionizing electromagnetic wave (previously described in the model of a thin gas slab [5]) is illustrated in Fig. 2 by the time dependence of the quantity $\mathrm{Re}\,G(t)$ determining the amplitude of H_z-component of the reflected wave $H_z^{(r)} = G(t)H_1^{(1)}(k_\perp r)$ at large times $t > 220$ (after the end of the incident pulse), when the signal amplitude at the fundamental frequency has already substantially decreased, but the Langmuir oscillations still exist and continue emitting. The transversal wave number at the frequency $\omega_{p\,max}$ is $k_\perp = (\omega_{p\,max}/c)\sin\theta_p = \sqrt{(\omega_{p\,max}/c)^2 - k_0^2\cos^2\theta}$, that is, the corresponding reflected cylindrical wave is inclined to z-axis at the angle $\theta_p > \theta$ ($\cos\theta_p = (\omega/\omega_{p\,max})\cos\theta$). In the given numerical example, $\theta = 30^0$, $\theta_p = 45^0$; at $t \approx 250$ the intensity of the frequency shifted component is about 10^{-4} of the maximum intensity of the incident wave.

References

[1] L.Ya. Margolin *et.al.*, Sov. Tech. Phys. Lett. **13** (1987) 89.
[2] H.M. Milchberg *et.al.*, Phys. Plasmas **3** (1996) 2149.
[3] A.A. Babin *et.al.*, Physics-Uspekhi **42** (1999) 74.
[4] V.B. Gildenburg and N.V. Vvedenskii, Phys. Plasmas **8** (2001) 1953.
[5] M.I. Bakunov *et.al.*, Phys. Plasmas **9** (2002) 2803.
[6] N.V. Vvedenskii and V.B. Gildenburg, JETP Lett. **76** (2002) 380.

Overcooling of the Hot Spot of Laser Plasma by Electron Conductivity

S. A. Maiorov

General Physics Institute of Russian Academy of Science, ul. Vavilova 38, Moscow, 119991 Russia

A hot spot of laser plasma is surrounded by extensive region of weakly ionized gas and the electron conductivity in background cold plasma is main reason for plasma electrons cooling.

1. Introduction

The possibility of developing a x-ray recombination laser by intense, ultrashot laser pulse has been considered in many papers [1-3]. But a residual energy is determining by above-threshold ionization and inverse-bremsstrahlung heating may be significant. Cooling is usually achieved either by hydrodynamic expansion or by radiative cooling. A hot spot of laser plasma is surrounded by extensive region of weakly ionized gas. Our calculations indicate that the main channel of a plasma electrons cooling of a hot spot is electron conductivity in background cold plasma.

2. Radiative cooling of laser plasma spot

Let us estimate the time of radiative cooling for high residual energy of electrons after laser pulse.

The energy withdraw from the electron component due to bremsstrahlung is expressed as [4]

$$Q_{bs} = 1.54 \times 10^{-32} z^2 T_e^{1/2} N_i N_e \quad \text{W/cm}^3.$$

The energy loss due to photorecombination is expressed as [5]

$$Q_{pr} = 5. \times 10^{-31} z^4 T_e^{-1/2} N_i N_e \quad \text{W/cm}^3.$$

The ratio of specific powers of bremsstahlung and photorecombination radiation is $Q_{bs}/Q_{pr} = T_e/30z^2$. For $z=7$ and $T_e < 1$ keV photorecombination radiation is predominant over bremsstrahlung radiation. At first let us consider a low electron density case

$$N_e < N_{e\,pr} = 3.1 \times 10^{13} T_e^{3.75}/z \quad \text{cm}^{-3},$$

where photorecombination is predominant collisional ion-electron recombination [6]. For $z=7$ and $N_e = 2 \times 10^{20}$ cm^{-3} the electron temperature $T_{e\,pr} = 50$ eV is lower bound of the low electron density case. The time of electron cooling due to photorecombination at initial electron temperature $T_e = 100$ eV is $\tau_{ph.rec} = 3T_e N_e/2Q_{pr} = 1$ ns, the time cooling from 1 keV is $\tau_{ph.rec} = 30$ ns. Thus the cooling due to bremsstahlung and photorecombination radiation in not effective to create overcooled plasma with $z \gg 1$.

3. Overcooling by electron conductivity

We shall consider the problem, from which it is possible to determine time dependence of hot spot temperature due electron conductivity in surround weakly ionized gas.

Suppose, that hot spot of plasma is surrounded by cold plasma. Assume, that a cold surrounded plasma has a mean ion charge z_0, electron temperature $T_0 \ll T_{max}$, density if ions N_i in hot spot and surround plasma are equal. Let the hot spot of laser plasma has radius r_0, electron temperature T_{max}, mean ion charge z_{max}. Propagation of heating wave is described by equation

$$\frac{\partial T}{\partial t} = \frac{1}{r^s} \frac{\partial}{\partial r} (r^s \chi \frac{\partial T}{\partial r}),$$

where $s=0, 1, 2$ for plane, cylindrical and spherically symmetric cases. A temperature conductivity coefficient may be writing as $\chi = aT^n$, for the electron conductivity $n=5/2$. Let background electron temperature is $T_0=0$ and instantaneous thermal energy put in point $r=0$ at time $t=0$.

In spherical symmetry case $s=2$ the solution depends from self similar variable $\xi = r/(aQ^n t)^{1/(3n+2)}$ and this solution is $T(\xi) = T_c[1-(r/r_f)^2]^{1/n}$, where thermal heating front radius is $r_f = \xi_1 (aQ^n t)^{1/(3n+2)}$, T_c - temperature at center, constant $\xi_1 \approx 1$, a temperature source constant $Q = \int T dV$ [6]. A mean temperature of electrons in volume inside heating wave $r < r_f$ is $T_{pl} = 3Q/4\pi r_f^3$ and one little differents from temperature in center T_c [6]. Therefore for estimation of T_c value we will consider

$$T_c \approx (Q^{2/3}/at)^{3/(3n+2)} \sim t^{-6/19}$$

The validity of this model is districted by condition $T_0 < T_c < T_{max}$. Here Q is a temperature source constant

$$Q = 4\pi z_{max} N_i r_0^3 T_{max}/3z_0,$$

a coefficient electron temperature conductivity at $z_0=1$ is $\chi = 2\kappa_e/3N_e \approx 6.32 T_e \tau_e/m_e$, where κ_e is the thermal electron conductivity, $\tau_e = 3.5 \times 10^4 T_e^{3/2}/(\Lambda/10) z^2_0 N_i$ sek is the time between electron collisions, Λ - Coulomb logarithm [7]. When $r_f < r_0$, the self similar solution is not correct. In this case we can use the estimation for r_f as $r_f = r_0 + (\chi t)^{1/2}$. Therefore for T_c value we will consider

$$T_{pl} = 3Q/4\pi(r_f^3 + (z_{max}/z_0 - 1) r_0^3) =$$
$$= z_{max} T_{max} /(r_f^3/r_0^3 + z_{max}/z_0 - 1).$$

In cylindrical symmetry case $s=2$ for T_c estimation we will consider

$$T_c \approx (Q/at)^{1/n+2} \sim t^{-2/7},$$

where $Q = \pi r_0^2 z_{max} T_{max}/z_0$. When $r_f < r_0$, we will estimate r_f as $r_f = r_0 + (\chi t)^{1/2}$ and for mean plasma temperature have

$$T_{pl} = Q/\pi(r_f^2 + (z_{max}/z_0 - 1) r_0^2) =$$
$$= z_{max} T_{max} /(r_f^2/r_0^2 + z_{max}/z_0 - 1).$$

Plasma temperature depends from time as $T_c \sim t^{-6/19}$ for spherical symmetry and as $T_c \sim t^{-2/7}$ for cylindrical symmetry case. Space picture of plasma spot may be

very complex in real experiment. Simple formula for $T_e(t)$ allows to estimate a temperature with good accuracy.

Table presents same results of calculation [8]. A hot spot plasma parameters r_0 , T_{max} , z_{max} and surround plasma parameter z_0 are taken from experiments for nitrogen [9], neon [2] and helium [10]. Calculations 1-12 are for nitrogen, 1-8 in spherical symmetry and 9-12 in cylindrical symmetry, the electron density in hot spot is $N_e=2\times10^{20}$ cm^{-3} and $z_{max}=7$. Calculations 13-18 are for neon in cylindrical, electron density in hot spot is $N_e=10^{20}$ cm^{-3} , $z_{max}=10$. Calculations 19-23 are for helium in cylindrical symmetry, electron density in hot spot is $N_e=6\times10^{19}$ cm^{-3} , $z_{max}=2$.

Recent studies have extended the validity of the electron conductivity equation in collisionless limit by using non local transport coefficients [11,12]. It makes possible using of the simple self similar solution in a weakly collisional regime.

4. Ionization cooling in heating wave

The velocity of heating wave is rapidly decreased after 30 - 100 μm in our plasma parameters of a hot spot and a background plasma. The ionization of surrounded gas by electron impact is a next possible cause of the hot spot cooling. For example, the time of ionization is $\tau_{ion}=1/\sigma_{ion}N_a v_e \approx 10$ ps and this time corresponds to the time of ionization cooling in heating wave.

5. Conclusion

The results of the estimations and calculation permit to do the following conclusion. The main reason of plasma electrons cooling of a hot spot of laser-produced multicharged ion plasma is electron conductivity in background cold plasma.

6. References

[1] B.M. Penetrante and J.N. Bardsley: Phys. Rev. A, 43, 3100(1991).

[2] W.J. Blyth, S.G. Preston, A.A. Offenberger et al.: Phys. Rev. Lett., 74, '4, p.554 (1995).

[3] T.E. Glover, J.K. Crane, M.D. Perry, R.W. Lee, R.W. Falcone: Phys. Rev. E, 57, p.982(1998).

[4] V.I. Kogan and A.B. Migdal. Plasma Physics and the Problem of Controllable Thermonuclear Reactions, Vol. 1, ed. by M.A. Leontovich (Izd. Akad. Nauk SSSR), p.172(1958)

[5] V.I. Kogan. Plasma Physics and the problem of Controllable Thermonuclear Reactions, Vol. 3, ed. by M.A. Leontovich (Izd. Akad. Nauk SSSR), p.99 (1958)

[6] Ya.B. Zel'dovich and Yu.P. Raiser "Physics of shock waves and high-temperatute hydrodynamic phenomena", Moscou, Nauka, 1966.

[7] S.I. Braginskii in Review of Plasma Physics edited by M.A. Leontovich (Consultans Burean, New York, 1965) Vol.1, p.205.

[8] S.A.Maiorov: Bulletin of the Lebedev Physics Institute, No. 5 (1997) 3.

[9] A.Ya. Faenov (private communication).

[10] G.S. Sarkisov, V.Yu. Bychenkov, V.T. Tikhonchuk, et all. Pis'ma v ZETF,66 (1(12), p.778 (1997).

[11] V.Yu. Bychenkov, W. Rozmus, and V.T. Tikhonchuk: Phys. Rev. Lett., 75(24), p.4405 (1995).

[12] A.V. Brantov, V.Yu. Bychenkov, and V.T. Tikhonchuk: Phys. Plasmas, 5, p.2742 (1998).

Table

N	z_0	r_0 μm	T_{max} eV	$T_e(t)$, eV, at time (s)				
				10^{-13}	10^{-12}	10^{-11}	10^{-10}	10^{-9}
1	1	5	100	49	30	17	9	4
2	1	5	1000	121	62	31	15	7
3	5	5	100	91	51	27	13	7
4	5	5	1000	183	94	46	22	11
5	1	20	100	74	53	33	19	10
6	1	20	1000	254	138	71	36	18
7	1	5	100	60	42	26	15	8
8	1	5	1000	200	113	62	33	17
9	5	5	100	86	64	37	20	11
10	5	5	1000	272	146	77	40	21
11	1	20	100	82	64	45	29	17
12	1	20	1000	367	224	128	70	37
13	1	5	200	80	50	29	16	9
14	1	5	2000	218	119	63	33	17
15	8	5	200	141	78	42	22	1,7
16	8	5	2000	307	161	84	44	3
17	1	20	200	123	87	56	33	8
18	1	20	2000	431	246	135	72	38
19	1	2	100	42	24	13	7	4
20	1	2	500	77	41	22	12	6
21	0,1	2	100	26	15	8	5	2,4
22	0,1	2	500	48	26	14	73	4
23	0,1	10	500	07	61	34	18	9

Theory of Skin Depth Interaction of Lasers with Plasmas

Heinrich Hora[1,2], J. Badziak[3], Y. Cang[2,4] S. Jablonski[3], K. Jungwirth[5], L. Laska[5], F. Osman[2],P. Parys[5],K. Rohlena[5], J. Wolowski[3], E. Woryna[3] and J. Zhang[4]

[1]Department of Theoretical Physics, University of New South Wales, Sydney 2052, Australia
[2]School of Quantit. Methods and Mathemat. Science, Univ. Western Sydney-Penrith, Australia
[3]Institute of Plasmas Physics and Laser Microfusion, 00-908 Warsaw
[4]Institute of Physics, Academia Sinica, Beijing, China
[5]Institute of Physics, ASCR, 18221 Prague 8, Czech Republic

The measured anomalous low maximum energy of ions emitted by TW-ps laser pulses in contrast to ns pulses led to the skin layer interaction model. Consequences are the nonlinear (ponderomotive) force acceleration of plasma blocks against the laser and into the target for a possible alternative laser-fusion scheme.

The measured drastic difference between the maximum ion energies from targets irradiated by TW-ps laser pulses was explained [1] by a skin layer interaction mechanism. This is basically different to the generation of very high ion energies by relativistic self-focusing and implies a very high contrast ratio for the suppression of any prepulse before the main pulse arrived at the target apart from the some pre-irradiation of less than 500 ps before the main pulse. Details of the theory of the involved nonlinear (ponderomotive) force generation [2 of plasma blocks will be reported. The main energy of the laser energy is converted into the fast motion of the two plasma blocks,

- one moving against the laser light and
- the other into the target.

Numerical results indicate that the reflectivity losses are low as long as the von-Laue-type density ripple is moderate as known for longer pulses as the reason for the stochastic pulsating interactions [3]. The block motion of the plasma against the laser light

    a)   may advantage the application of this operation as laser ion source while the block into the target and

    b)   is important for application to laser fusion.

For the case (a) a detailed explanation of different plasma groups for longer pulse interaction [4] needed a detailed interpretation. These include relativistic self-focusing as confirmed experimentally ant theoretically in numerous experiments. The second fast group can be identified as due to the generated hot electron as detected from the energetic x-ray spectrum where the thermalization is immediately given by the quantum correction of the collision frequency. This is a proof of mutual agreement of these theories and splendidly explains also recent measurement for ions emitted with 0.6 GeV energy. For further slower ion groups further mechanisms for ion generation [5] were considered. In contrast to theses processes, the (prepulse controlled) TW-ps interaction is very different and simplified as seen from the experiments and as expected from the model of the skin layer laser plasma interaction as expected form the theory of nonlinear (ponderomotive) acceleration and as shown in extensive numerical calculations.

For the process (b) or results is essential that the blocks moving into the target produce ion current densities exceeding 10^{10} A/cm^2 as necessary from the earlier theory of light ion beam fusion. In order to achieve the necessary energy flux density of more than 2×10^7 J/cm^2, the application of shorter laser wavelengths may be interesting. We further studied the need of some prepulse during the last 100 ps before interaction of the ps mail laser pulse in order to receive some swelling of the laser field energy density in the interaction range and for enlarging the effective skin depth as a result of swelling..

Further questions refer to the generation of the fusion reaction front in uncompressed (or low compression) nuclear fusion fuel. These are discussed in view of the recent Nuckolls-Wood model [6] of an electron beam mechanisms for ignition for the fast ignitor. The Nuckolls-Wood scheme needs the usual very high-density pre-compression of DT fuel as usual in the fast ignitor but the basic aim of the PW-ps laser pulse is to produce a very high intensity relativistic electron beam. The physics problems of the relativistic effects are not all e4xploerd yet, even the ele4ctron acceleration mechanism is still open whether it is a wake field acceleration of the "free wave acceleration" which was succesccul to explain recent experiments quantitatively.

In contrast to this Nuckolls-Wood scheme, the nonlinear force produced plasma block ignition excludes the relativistic effects from the beginning, and it does not need the compression of the plasma beyond about ten times the solid state density what process is performed automatically by the one dimensional ablation process of the skin layer process. which conditions may now be applied for the ignition similar to the well known light ion beam fusion.

[1] H. Hora, J. Badziak, F.P. Boody, R. Höpfl, K. Jungwirth, B. Kralikowa, J. Kraska, L. Laska, P. Paris, V. Perna, M. Pfeifer, K. Rohlena, J. Skala, J. Ullschmied, J. Wolowski, E. Woryna, *Opt. Commun.* 207, (2002) 333

[2] H. Hora, *Laser Plasma Physics and the Nonlinearity Principle* (SPIE Books, Bellingham 2000)

[3] H. Hora and M. Aydin, *Phys. Rev.* A45, (1992) 6123

[4] J. Wolowski et al Plasma Physics and Controlled Fusion 44, (2002) 1277

[5] H. Hora, F. Osman, R. Höpfl, J. Badziak, P. Paris, J. Wolowski, W. Woryna, F. Boody, K. Jungwirth, B. Kralikova, J. Kraska, L. Laska, M. Pfeifer, K. Rohlena, J. Skala, and J. Ullschmied, Skin depth Theory explaining anomalous picosecond laser plasma interaction, *Czechoslovak J. Physics*, 52, Suppl. D (CD No.7), (2002) D349

[6] J.L Nuckolls and L. Wood, *Future of Inertial Fusion Energy*, Preprint UCRL-JC-149860 (September 4, 2002) www.llnl.gov/tid/ Library..html

Liquid plasma produced by intense laser light

Norio Tsuda and Jun Yamada

Dept. of Electronics, Aichi Institute of Technology

1247, Yachigusa, Yakusa, Toyota, 470-0392 Japan

The plasma produced in liquid by the excimer and YAG laser light is studied and the basic data about breakdown threshold of liquid and the development behavior of plasma are examined.

1. Introduction

When the laser light is focused at the solid or gas, a hot and dense plasma is produced.[1~7] However, the laser induced plasma in liquid hasn't been studied enough. When a laser light is focused in liquid, a hot plasma is produced at the focal spot. The mechanisms of the breakdown and the plasma development have not almost been investigated. In liquid, the laser induced plasma may be able to resolve the hazardous material called the environment material, or the plasma produced in a physiological saline may become to be the basic data when the human body is irradiated by the laser light. Then, plasma produced in liquid by the laser light is studied and the basic data about breakdown threshold of liquid and the development behavior of plasma are examined.

2. Experimental arrangement

The experiment arrangement is shown in Fig. 1. Excimer or YAG laser light is focused in liquid. The maximum laser power of excimer laser is 500 mJ with a wavelength of 308 nm and a pulse half width of 30 ns. While the maximum laser power of YAG laser is 340 mJ with a wavelength of 1064 nm and a pulse half width of 15 ns. Moreover, the YAG laser is able to drive the second harmonic oscillation with a power of 180 mJ, a wavelength of 532 nm and a pulse half width of 15 ns. The YAG laser is operated at the wavelength of 532 nm. The chamber is made of acrylic and has three quarts glass windows of height of 25 mm, width of 30 mm and thickness of 2 mm. The ultra pure water or the ultra pure water with a melted NaCl is used as a test liquid. The excimer laser is focused using the concave mirror to avoid influence of refraction at liquid surface. The backside of acrylic chamber is able to attach the concave mirror. The diameter of the focal spot is 96 μm when the laser light is focused using the concave mirror of focal length 25.4 mm. On the other hand, the YAG laser light is focused from the out side of the chamber using the lens of the focal length 60 mm, because the intensity of YAG laser light is so high that the concave mirror can not be used. The diameter of focal spot is 130 μm. The laser power is controlled using the optical filter.

To examine the attenuation of laser light in liquid, the photodiodes are set up at back and front of the chamber. The transmittance is measured from the ratio of transmitted laser power to the incident one.

When NaCl concentration is varied, the threshold value of light intensity is measured taking into account the absorption of laser light in liquid. The threshold laser intensity is defined as an intensity at which the plasma production probability is 50 %.

The plasma development is observed using the streak camera. The plasma luminosity is focused on the incident slit of the streak camera by relay lens with a focal length of 100 mm. The streak image is displayed on a monitor by a dummy color of light intensity. The plasma boundary is determined by a threshold intensity because the plasma boundary of the streak image is not so clear. The plasma boundary is drawn by a plotter.
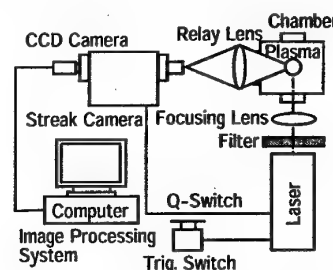
Fig. 1. Experimental arrangement.

3. Experimental results

3.1 Transmittance

The transmittance of the laser light through NaCl solution is measured. The transmittance as a function of NaCl concentration is shown in Fig. 2. When the excimer laser is used, the transmittance decreases with increasing concentration. The attenuation of laser light in NaCl solution is not negligible because NaCl molecular absorbs the laser light. However, the transmittance of YAG laser is 40 %, which is almost a constant independent on NaCl concentration. The scattering loss of YAG laser light may be so large that the transmittance turns out large because the temporal coherent of YAG laser is better than one of excimer laser.

3.2 Threshold characteristic

When NaCl solution is irradiated by the laser light with the intensity near threshold, we watch whether the plasma is produced or not. From 20 observations, a plasma production probability is examined. The threshold characteristic for NaCl concentration using

excimer laser or YAG laser is shown in Fig. 3. The threshold intensity of plasma produced by YAG laser is lower than that by the excimer laser, because the spot size and the absorption coefficient of YAG laser are bigger than those of the excimer laser. The threshold values decrease with increasing NaCl concentration because the ionization coefficient increases with increasing the NaCl concentration. If the NaCl concentration increases moreover, the threshold value may increase again because the collision occurs more frequently with increasing NaCl concentration.
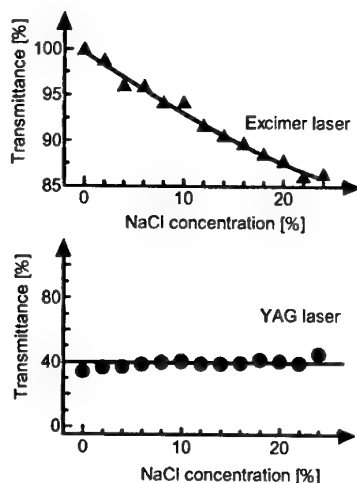
Fig 2. Transmittance.
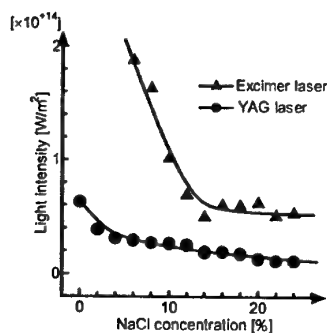
Fig. 3. Threshold characteristic.

3.3 Streak image

The typical streak image of the plasma, which is produced by YAG laser, is shown in left figure of Fig. 4. The laser light is irradiated from the right hand side, the time is scanned from top to bottom, and the inside of the boundary shows the plasma. The YAG laser is operated at 1064 nm. The plasma produced in liquid develops only backward because the plasma frequency is higher than the laser frequency and laser light is absorbed at only backward plasma surface. The plasma consists of a group of plasmas produced from many seeds because the electrolytes in liquid as seed may initiate the plasma

production.

On the other hand, the plasma produced by the excimer laser is produced at the focal spot and develops backward and forward asymmetrically as shown in right figure of Fig. 4. The development mechanism of forward plasma is different from that of backward plasma. When the concentration of sodium chloride is higher, the plasma develops forward widely. However, when the concentration is too high, the plasma develops hardly because the laser light is absorbed in liquid.
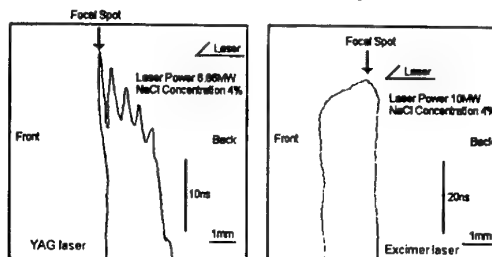
Fig. 4. Streak image.

4. Conclusion

When the liquid is irradiated by the ultraviolet laser light or visible laser light, the plasma is produced at the focal spot. The characteristic of transmittance is different when the YAG laser or excimer laser is used. The transmittance of excimer laser light decreases with increasing the NaCl density. However, the transmittance of YAG laser light is a constant. Threshold intensity decreases with increasing NaCl concentration. Threshold intensity of plasma produced by YAG laser is lower than that by excimer laser, because the focal spot size of YAG laser is bigger than that of the excimer laser. The dynamic behavior of the laser produced plasma is observed by the streak camera. The plasma produced by excimer laser develops not only backward but also forward. However, The plasma produced by YAG laser develops only backward.

5. References

[1] R.G. Meyerand, and A.F.Haught, Phys.Rev.Lett. **11** (1963) 401.
[2] Yu.P.Raizer, Sov.Phys.JETP, **21** (1965) 1009.
[3] G.V.Ostrovskaya, and A.N.Zaidel', Sov.Phys.Usp, **16** (1974) 834.
[4] J.Yamada, and T.Okuda, Jpn.J.Phys, **18** (1979) 139.
[5] J.Yamada, and T.Okuda, Laser Particle Beams, **7** (1989) 531.
[6] J.Yamada, N.Tsuda, Y.Uchida, H.Huruhashi, and T.Sahashi, Trans. IEE Jpn, **114** (1994) 303.
[7] N.Tsuda, and J.Yamada, J.App.Phy, **81** (1997) 582.

Effect of ultraviolet light irradiation on thermionic energy converter

Norio Tsuda and Jun Yamada

Dept. of Electronics, Aichi Institute of Technology

1247, Yachigusa, Yakusa, Toyota, 470-0392 Japan

The laser light is irradiated to the converter and the output current characteristics are studied. The output current may be mainly produced by light of ultraviolet region when the sun light is irradiated to the converter.

1. Introduction

A thermionic energy converter is a generator that directly converts a heat into an electricity. In order to operate with lower emitter temperature, the method of light irradiation to the converter is proposed.[1] The output characteristics are examined in detail when the visible light is irradiated.[2] In wide wavelength range about 627nm, the output current is increased, and the peak current is about 40A/m² at the laser energy of 15mJ. But, this value is not enough for the practical application. The resonance light of infrared region is irradiated and the output current characteristics are measured. The very high output current is obtained by irradiating the resonance light at fairly lower laser energy comparing with that by the visible light.[3,4] When the wavelength is 852 nm, the emitter temperature of 945K, the vapor pressure 1.93Pa and the laser energy 1mJ, the output current is about 500A/m², the peak current is more than the 100 times of the visible light irradiation. However, the wavelength width of resonance light is very narrow. Then, the ultraviolet laser light is irradiated to the thermionic energy converter and the output characteristics are examined.

2. Experimental arrangement

The experimental arrangement is shown in Fig.1. The converter is made of cylindrical Pyrex glass with a diameter of 50mm and a length of 140mm. The converter has three windows for an incident light. The emitter has a tungsten spiral heater inside a cylinder made of nickel. The heater current can control the emitter temperature. On the other hand, the collector is a disk made of stainless steel and has a mesh made of molybdenum with a diameter of 20mm in center. The converter is set in an electric oven. The vapor pressure of cesium gas can be controlled by adjusting the oven temperature. A light source is a XeCl excimer laser. The excimer laser is a wavelength of 308 nm and a pulse half width of 30 ns. The diameter of laser beam is about 8mm and the maximum laser power is 15 mJ, because an aperture puts on the optical pass of the laser light. The laser light is irradiated to the space between the electrodes being parallel to both electrodes.

3. Output characteristics with ultraviolet light irradiation

3.1 Voltage-current characteristic

The voltage–current characteristic is shown in Fig. 2. "Short circuit current density" is defined by the output current density when the voltage between the electrodes is 0V. The waveform of the output current by the ultraviolet light irradiation has a very long half width comparing with that by the visible light irradiation, which is same as that by resonance light irradiation.

Fig. 1. Experimental arrangement

Cesium vapor pressure 7.10 Pa
Emitter Temperature 1150 k
Wave length 308 nm
Laser energy 15 mJ
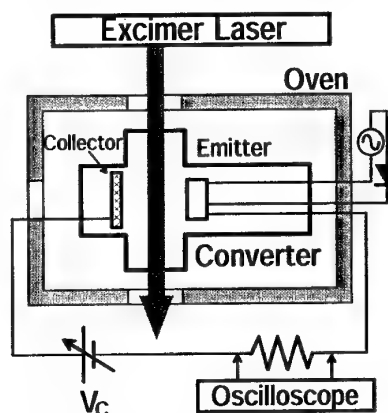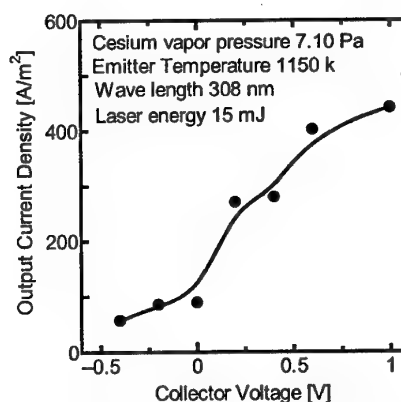
Fig. 2. Voltage-current characteristic

3.2 Cesium vapor pressure characteristic

The cesium in the converter adheres the electrodes and effectively reduces the work function. The work

function of emitter is decided by the cesium coating rate. The work function of cesium is 1.69 eV and one of tungsten is 4.62 eV. In high cesium vapor pressure, the work function of emitter reduces by absorbing the cesium on the surface of emitter. On the other hand, since the cesium of emitter surface evaporates in high emitter temperature, the work function increases.

The dependence of short circuit current density on cesium vapor pressure is shown in Fig. 3. The short circuit current density increases and reaches a peak because the work function of emitter decreases with increasing cesium vapor pressure. The movement of thermal electron and diffusion of cesium ion are prevented by cesium atoms. Therefore, the short circuit current density may increase by closing the space between the electrodes in high cesium density. When the emitter temperature is higher, the cesium vapor pressure at which the short circuit current density reaches a peak shifts to higher vapor pressure.

Fig. 4. Short circuit current density vs. laser power

Fig. 3. Short circuit current density vs. cesium vapor pressure

3.3 Laser power characteristic

The short circuit current density vs. laser power is shown in Fig. 4. The short circuit current density increases with increasing laser power. In low cesium vapor pressure, the work function of emitter is the value which is high value of closely tungsten. The ion to neutralize the space charge is few, because the emitted thermal electron and the space charge are low. When the cesium vapor pressure is low, the short circuit current density shows a saturation.

3.4 Absorption characteristic

The absorption rate of ultraviolet light by cesium vapor is shown in Fig. 5. The absorption rate of ultraviolet light increases with increasing cesium vapor pressure. The absorption rate of ultraviolet light is lower than one of resonance light. However, it reaches to 70 % in this experimental condition, and is not negligible small.
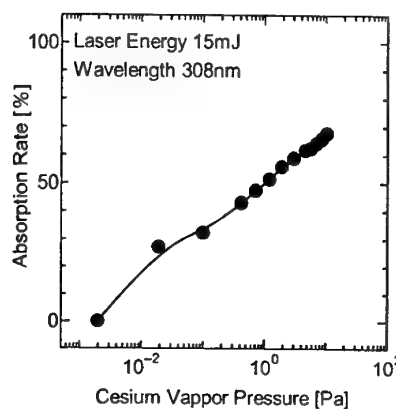
Fig. 5. Absorption rate

4. Conclusion

The ultraviolet laser light is irradiated to the thermionic energy converter and the output characteristics are measured. The short circuit current density obtained by ultraviolet irradiation is higher than that by visible light. The maximum short circuit current density reaches about 400 A/m^2. This is slightly low comparing with that by the resonance light. However, the absorption of ultraviolet light hardly depends on the wavelength, while the wavelength width of resonance absorption is very narrow. The output current may be fairly improved by ultraviolet light when sun light is irradiated to the converter.

5. References

[1] M. Knado, H. Furukawa, M. Ichikawa and S. Yokoi: Proc. 29th Intersociety. Energy Conversion Engineerign Conf., U.S.A., (1994).
[2] J. Yamada, T. Kawaguchi, N. Tsuda, and M. Kando: IEE. Jpn, **120A** (2000) 357.
[3] T. Inaguma, N. Tsuda, and J. Yamada: IEE. Jpn, **122A** (2002) 977.
[4] T. Inaguma, N. Tsuda, and J. Yamada: XXV ICPIG, **1** (2001) 287.

228

Sunday, July 20

Guided-wave-produced-plasmas

A. Shivarova

Faculty of Physics, Sofia University, 5 J. Bourchier Blvd., BG-1164 Sofia, Bulgaria

The abstract of a topical lecture on diffusion-controlled gas discharges sustained in the field of travelling waves is presented in this contribution. Based on discharge models within the fluid plasma theory, the maintenance of discharges without and in external magnetic field is discussed. The mechanisms of the discharge self-consistency and of the electron heating are shown. The final results from the models are for the self-consistent axial structure of the discharges.

1. General comments on guided-wave-produced plasmas

The guided-wave-sustained discharges (GWSDs) are comparatively new plasma sources [1]. In these discharges, the wave produces the plasma and the plasma produced sustains the wave propagation. Depending on the type of the waves, the GWSDs show up in two modifications: surface-wave-sustained discharges as plasma sources without external magnetic field and Trivelpiece-Gould sustained discharges for plasma production in an external magnetic field. These discharges exist in the total gas-pressure range ($p = 10^{-5}$ Torr ÷ 1 Atm) of the gas discharges and in a very wide range of variation of the wave frequency ($f = 500$ kHz ÷ 10 GHz). This flexibility makes the GWSDs very attractive for the gas-discharge applications [2].

In the GWSDs, the plasma column is extended far away from the wave launcher. The characteristics of the plasma (plasma density n, electron temperature T_e, etc.) and of the wave (wavenumber $k = \beta + i\alpha$, wave energy flux S, intensity of the wave electric field $|E|^2$) vary along the discharge length (z-direction) being self-consistently related to each other. This clear display of self-consistency makes the GWSDs a "pure" example for the definition of the gas discharges – as nonlinear systems which unify in a self-consistent manner plasmas and fields – and motivates the interest in their modelling [3].

2. Structure of the fluid-plasma models of the guided-wave-produced plasma sources

According to the nature of the GWSDs, the models of the discharges combine electrodynamics with gas-discharge physics.

The wave-energy balance – $d\bar{S}/dz = -\bar{Q}$ – is the first equation of the electrodynamical part of the models, with Joule heating $Q(r,z)$ and S integrated over the cross section of the waveguide structure (a plasma column in a glass tube with permittivity ε_g and internal and external radii R and R_1, surrounded by free space). This equation is usually used in its well-known form [4]:

$$\frac{d\bar{n}}{dz} = \frac{-2\alpha\bar{n}}{1 + \dfrac{\bar{n}}{\Theta}\dfrac{d\Theta}{d\bar{n}} - \dfrac{\bar{n}}{\alpha}\dfrac{d\alpha}{d\bar{n}}} \qquad (1)$$

where $\bar{n}$ is the averaged – over the plasma column cross section – plasma density, α is the space damping rate of the wave and $\Theta(z) = \overline{Q}(z)/\pi R^2 \bar{n}(z)$ is the power absorbed on average by an electron.

Equation (1) shows that the self-consistent description of the axial structure of the discharge requires to have the $(\bar{n} - \alpha)$- and $(\bar{n} - \Theta)$- relations known.

The $(\bar{n} - \alpha)$-relation comes out from the dispersion law of the wave

$$D(\omega, k = \beta + i\alpha, \varepsilon, R, R_1, \varepsilon_g) = 0 \qquad (2)$$

which is the second equation of the electrodynamical part of the discharge models. Here $\varepsilon(r, z)$ is the plasma permittivity.

The $(\bar{n} - \Theta)$-relation results from the gas-discharge part of the models. It is completed by the balance equations of production and losses of charged particles

$$\left(\frac{\delta n_{e,i}}{\delta t}\right)_{loss} = \left(\frac{\delta n_{e,i}}{\delta t}\right)_{gain} , \qquad (3)$$

specified for the given discharge considered, and by the electron energy balance

$$dP_\chi + dP_{coll} = Q \qquad (4)$$

in which, energy losses through thermal conductivity and collisions are taken into account.

Equation (3), describing the radial (r-) structure of the discharge, results into the condition of the discharge maintenance expressed by a $[T_e - n(r = 0)]$-relation provided nonlinear processes are taken into account. With eq. (4) relating T_e to Θ, both (3) and (4) finally determines the $(\bar{n} - \Theta)$-relation. Since Θ is related to the maintenance field intensity, the $(\bar{n} - \Theta)$-relation expresses the basis of the description of the discharge as a nonlinear structure. Whereas the $(\bar{n} - \alpha)$-relation is a specific characteristic of the GWSDs, the $(\bar{n} - \Theta)$-relation is a basic concept of self-consistency of the high-frequency discharges, in general.

The numerical models [5-12] presented here of discharges in different gases (argon, helium, helium-argon gas mixtures and hydrogen) as well as of discharges in an external magnetic field, being extension and further development of ideas from the analytical modelling of surface-wave-sustained discharges [3], stresses the mechanisms of discharge

self-consistency and of the electron heating in the wave field.

3. Electron heating in the wave field

The mechanisms of the wave damping determine the mechanisms of the electron heating. In the numerical models presented here, the wave dispersion law (2) is for radially-inhomogeneous collisional plasmas, with radial profile of the plasma density and electron-neutral elastic collision frequency as obtained in the gas-discharge part of the models. Regimes of weak ($\nu < \omega$) and strong ($\nu \geq \omega$) collisions could be considered which permits covering the total range of the variation of the gas pressure of diffusion-controlled discharges in a combination with the total range of variation of the wave frequency. A display – along the discharge length – is shown of conditions of local heating with wave power deposition in the total plasma volume and of nonlocal heating with spacially-localized power deposition, including regions of resonance absorption of the waves.

4. Mechanisms of the discharge self-consistency

The nonlinear mechanisms relating n to Θ or, equivalently, to the maintenance field intensity, ensures a self-consistent description of the discharge. It could be achieved if the condition for the discharge maintenance obtained from the charged-particle balance (3) relates the plasma density n to the electron temperature T_e.

In the models of discharges in atomic gases – argon, helium and helium-argon gas mixtures – the nonlinear processes of step ionization and recombination are the mechanisms, which ensure the self-consistency. The condition for the discharge maintenance obtained, e.g., in the models of argon discharges is:

$$\left(\frac{\mu}{R}\right)^2 D_{A\perp} + \rho_r n(r=0) = \nu_i + \frac{\rho_{si} n(r=0)}{1+\eta n(r=0)} . \quad (5)$$

Here $D_{A\perp}$ is the corresponding – without and with external magnetic field – ambipolar diffusion coefficient, μ is the parameter characterizing the radial plasma density inhomogeneity, ν_i is the frequency of direct ionization, ρ_{si} is the rate of step ionization with η being the coefficient of its saturation and ρ_r is the recombination coefficient.

Being an obvious generalization of the Schottky condition – $(\mu/R)^2 D_{A\perp} = \nu_i$ – in a sense that the total losses through diffusion and recombination are compensated by the total ionization (direct and step ionization), condition (5) relates the plasma density n to T_e and, respectively, to Θ, and ensures the self-consistency of the models. Regarding GWSDs, this means that the required interrelation between the axial profiles of $\overline{n}$ and Θ is achieved.

The models of gas discharges in helium and helium-argon gas-mixtures show that the ambipolar diffusion coefficient defined – after detailed analysis of the ion dynamics – as an effective one, is an additional factor of self-consistency.

The model of hydrogen discharges shows that the hydrogen atom yield in the discharge is the main factor which ensures the discharge self-consistency.

5. Axial self-consistent structure of the discharges

The final results from the models are for the self-consistent axial structures of the discharges composed out from the interrelated axial variation of $\overline{n}$, T_e, Θ, β and α. In discharges in helium-argon gas mixtures and in hydrogen discharges, the axial profiles of the concentration of the ion components also enter the discharge structure. Moreover, in hydrogen discharges, the axial variations of the concentration of the neutral gas species and of the gas temperature are important component of the structure of the discharge.

References

[1] M. Moisan, C. Beaudry, P. Leprince, *Phys. Lett.* **50A** (1974) 125.

[2] M. Moisan, J. Hubert, J. Margot, Z. Zakrzewski, in: *Advanced Technologies Based on Wave and Beam Generated Plasmas*, eds. H. Schlüter and A. Shivarova, Kluwer, Dordrecht, 1999, p. 23.

[3] Yu.M. Aliev, H. Schlüter and A. Shivarova, Guided-Wave-Produced Plasmas, Springer, Berlin, 2000.

[4] Z. Zakrzewski, *J. Phys. D: Appl. Phys.* **16** (1983) 171.

[5] K. Makasheva, A. Shivarova, *Phys. Plasmas* **8** (2001) 836.

[6] J. Berndt, K. Makasheva, H. Schlüter, A. Shivarova, *Plasma Sources Sci. Technol.* **11** (2002) 208.

[7] J. Berndt, K. Makasheva, H. Schlüter, A. Shivarova, *J. Appl. Phys.* **92** (2002) 6461.

[8] I. Koleva, Ts. Paunska, H. Schlüter, A. Shivarova, Kh. Tarnev, *Plasma Sources Sci. Technol.* (2002) submitted.

[9] Ts. Paunska, H. Schlüter, A. Shivarova, Kh. Tarnev, *Plasma Sources Sci. Technol.* (2002) submitted.

[10] A. Shivarova, Kh. Tarnev, *Plasma Sources Sci. Technol.* **10** (2001) 260.

[11] H. Schlüter, A. Shivarova, Kh. Tarnev, *Plasma Sources Sci. Technol.* **10** (2001) 267.

[12] H. Schlüter, A. Shivarova, Kh. Tarnev, *Contr. Plasma Phys.* (2002) submitted.

Nonlinear Effects in Low Frequency Inductive Plasmas

A. I. Smolyakov, V. A. Godyak[*], Yu. O. Tyshetskiy

Department of Physics and Engineering Physics,
University of Saskatchewan, Saskatoon, SK, S7N 5E2 Canada
[*]OSRAM SYLVANIA, Beverly, MA 01915, USA

1. Introduction

Modern inductively coupled plasma (ICP) sources tend to operate at low frequencies (several MHz and less) that reduces capacitive coupling and transmission line effects and leads to simpler and lower cost rf power sources and matching circuits. Together with a low neutral gas pressure (1-10 mTorr) this creates a unique combination of conditions where two features of inductively coupled plasmas become most prominent: anomalous (non-collisional) heating and nonlinearity due to the Lorentz force. When the electrons are weakly collisional, the collisionless wave particle interaction (Landau damping) replaces real collisions and becomes the main mechanism of the wave absorption and plasma heating [1]. In this regime, the electron mean free path exceeds the characteristic plasma length scale so that electrons ``sample'' the electric field over large distance resulting in the electric current being not a local function of the electric field. This regime is often referred to as nonlocal regime as opposite to the local, or short mean free path, highly collisional regime of the classical skin effect. The related propery of the low frequency ICP is due to the fact that the nonlinear Lorentz force can be much larger than the force of the inductive electric field [regime of the electron Hall magnetohydrodynamics (EMHD)]. Nonlinear forces in ICP may significantly affect plasma density profile [2], generate higher harmonics of the electric current [3], electrostatic potential [4,5], and modify the skin-effect [6]. In this paper we review the experimental data and theoretical models describing these effects.

Experiments have been carried out in a cylindrical low pressure argon ICP, with a metallic chamber with diameter $2R = 20$ cm and length $L = 10.5$ cm, and a quartz window separating a planar coil from plasma [7]. To enhance nonlinear processes the driving frequency and gas pressure were reduced, correspondingly, to 0.45 MHz and 1 mTorr. The rf discharge was maintained at a discharge power $P = 200$ W. The basic plasma parameters: n_e, T_e, the rf and dc plasma potential have been measured with a Langmuir probe moved along the axial (z) direction. Nonlinear harmonics of the electrostatic potential were directly obtained from Langmuir probe measurements. The ponderomotive potential was calculated as the difference between the dc potential and plasma density. Measurements were made on the discharge axis (r= 0) and at a fixed radial position r = 4 cm, which corresponds to the maxima of the radial distribution of the azimuthal rf electric field and the radial magnetic field. The electromagnetic fields and the plasma current density distributions were inferred from magnetic probe measurement made along the axial direction at r=4 cm and along the radial direction at z=3.2 cm. Langmuir and magnetic probe measurement were made over a wide frequency range (0.45 - 13.56 MHz) but here we mainly consider data for f = 0.45 MHz where nonlinear effects are largest.

2. Nonlinear plasma polarization in the ICP

Nonlinear polarization potential has not been observed earlier in experiments with inductive discharges. One of the reasons for this was that for a typical ICP driven at 13.56 MHz nonlinear effects are negligibly small. They are significantly increased for lower frequency. Polarization potential is created due to the potential component of the nonlinear Lorentz force [5], while the solenoidal component of the Lorentz force is responsible for the nonlinear harmonics in the electric current [3,5].
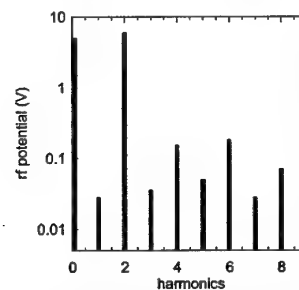
Fig. 1 The frequency spectrum of the polarization potential in the middle of the skin layer, at a distance of 1 cm from the quartz window (z=1cm, r=4 cm) in an ICP driven at 0.45 MHz.

Note that dc plasma potential (zero frequency, ω=0) has been deduced from the plasma density and plasma potential profiles while the oscillating rf harmonics have been measured directly. The dc potential corresponds to the nonlinear ponderomotive force. As it is seen in Fig. 1, the first (fundamental) harmonic, induced by parasitic (capacitive) coupling from the induction coil, is smallest, while the second harmonic exceeds the electron temperature and dominates all others. Amplitudes of the second harmonic and dc (ponderomotive) potential are approximately equal for small dissipation.
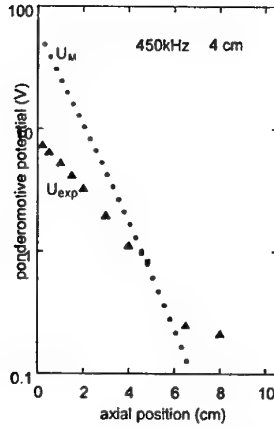
Fig. 2 The experimental value of the ponderomotive potential U_{exp} shown together with the Miller potential U_m.

As shown in Fig. 2 the experimental value of the ponderomotive potential is significantly different from the classical expression for the cold plasma (Miller potential). We have derived an expression for the ponderomotive force in hot plasmas (the strongly nonlocal regime) [8]. This expression can be cast in a form similar to that of the local case, i.e. $F_p = \omega_{pe}^2/8\omega\pi E_0^2/\delta_{th}$, where the characteristic gradient length of the electric field δ is replaced with the characteristic length of the particle excursion over the wave period, $\delta_{th} = v_{th}/\omega$.

$$F_p = \frac{\omega_{pe}^2}{8\pi\omega} E_0^2 \frac{\sqrt{\pi}\omega}{v_{th}}$$

This expression is in reasonable agreement with the experimental data [8].

3. Plasma heating at low frequencies

Typically, in the low pressure ICP operating in the anomalous regime, the power absorption due to the interaction with thermal electrons significantly exceeds the collisional absorption. There is an optimal frequency when the power absorption reaches the maximal value. It has been shown that for low driving frequencies and low collisionality $\nu < \omega$ the effects of the particle thermal motion reduce the absorption below the collisional value so that the total electron heating due to both collisional and collisionless mechanisms of wave energy dissipation becomes smaller than it would have been if only the collisional mechanism was involved. This linear effect is illustrated in Fig. 3. Nonlinear effects that are most important for low frequencies may further affect plasma heating [3]. Nonlinear effects have been investigated via direct numerical simulations. In Fig. 2 the ratio of total S_{tot} to the collisional S_{coll}
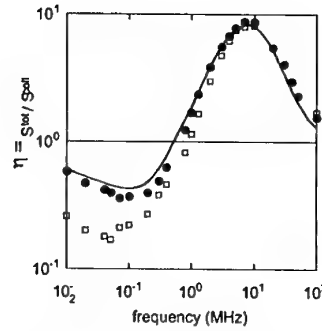
Fig. 3: Ratio of the total to collisional absorbed power. Solid curve represents the linear theory (without rf magnetic field), circles -- the result of PIC simulation without rf magnetic field, squares -- the PIC simulation with rf magnetic field. The parameters are: E=0.5 V/cm, T=10 eV, $n=2.7\times10^{10}$ cm^{-3}, $\nu=1.5\times10^6$ s^{-1}.

heating, $\eta = S_{tot} / S_{coll}$, is shown as a measure of the influence of the electron thermal motion on the electron heating. In numerical calculations the measured absorbed power is averaged over the rf field period. The simulations included electron-atom collisions (implemented into the PIC code with a direct Monte-Carlo method) and the electron-electron collisions (implemented via the Langevin equation) as a mechanism for the "maxwellization" of the electron distribution function. At low frequency there is significant reduction of plasma heating due to the rf magnetic field as a result of expulsion of electrons from the skin layer by the ponderomotive force leads as well as a result of nonlinear trapping of electrons in the rf magnetic field [3].

References

[1] M. Lieberman and V.A. Godyak, IEEE Trans. Plasma Sci. **26**, 955 (1998).

[2] R. H. Cohen and T. D. Roglnien, Plasma Sources Sci. Technol. **5**, 442 (1996); Phys. Plasmas **3**, 1839 (1996).

[3] V.A. Godyak, R.B. Piejak, B.M. Alexandrovich, Phys. Rev. Lett. **83**, 1610 (1999).

[4] V.A. Godyak, R.B. Piejak, B.M. Alexandrovich and A.I. Smolyakov, Plasma Sources: Sci. Technol. **9**, 541 (2000).

[5] A.I. Smolyakov, V. Godyak and A. Duffy, Phys. Plasmas **7**, 4755 (2000).

[6] J.D. Evans and F.F. Chen, Phys Rev. Lett. **86**, 5502 (2001); F. F. Chen, Phys. Plasmas **8**, 3008 (2001).

[7] V.A. Godyak, R.B. Piejak, B.M. Alexandrovich, J. Applied Phys. **85**, 703 (1999).

[8] A. Smolyakov, V. Godyak, and Y. Tyshetskiy, Phys. Plasmas **8**, 3857 (2001).

234

Recombining Plasma Expanding in Low-Pressure Region

R.P. Dahiya
Centre for Energy Studies
Indian Institute of Technology Delhi
New Delhi – 110 016, India
E-mail: rpdahiya@ces.iitd.ernet.in

High density thermal plasma expanding in low-pressure region is of immense scientific interest and has numerous applications. The monomer seeded plasma is utilised for plasma processing of surfaces, i.e. deposition, surface etching, nitriding and for many more applications depending on the seeding materials. Conditions prevailing in the Tokomak edge plasma can also be simulated using the low temperature, high flux obtained with cascaded arc thermal plasma source. Various species of the high density flowing plasma generated in a narrow channel (few mm diameter) of an arc discharge are usually in thermal equilibrium. In this presentation experimental measurements made in the thermal plasma with particular reference to the kinetics in molecular plasma and surface nitriding will be discussed. The cascaded arc source is coupled to a low-pressure chamber wherein the plasma generated in the source expands while propagating in the axial direction. Typical parameters of argon plasma in the expansion region are: plasma density, 10^{19} m^{-3}, electron temperature, 3000 K for argon flow rate of 3 slpm and 60 A arc current. The current in the arc is distributed over three water-cooled tungsten cathodes, which not only prolongs the life of electrodes but also improves the uniformity of the system. If argon is replaced with molecular gas hydrogen / nitrogen, recombination processes set in the expanding plasma. The plasma density drops significantly and the electron temperature also reduces. In hydrogen plasma, charge transfer between the rovibrationally excited hydrogen molecules followed by dissociative recombination reactions provides the fast loss mechanism. Axial magnetic field helps to contain and prolong the hydrogen plasma beam in the chamber. Side injection of hydrogen in one of the cascaded arc plates stabilises the arc, improves the ion flux, and is also beneficial for improving the cathode life. A combination of nitrogen and hydrogen plasma generated in the system has led to an efficient process for nitriding of machinery components.

Aspects of Turbulent Transport

V. Naulin and J. Juul Rasmussen

Association EURATOM-Risø National Laboratory

Turbulence is an ubiquitous phenomenon in plasmas, which have usually large amounts of free energy available that can drive the turbulent velocity fluctuations. Universal properties of turbulence are its abilities to mix and to transport. The turbulent transport is often found not to be described by a transport coefficient, as Fick's law suggests. We discuss the consequences of this and the relationship between passive particle and plasma transport, that is mixing and transport.

1. Introduction

A characteristic feature of turbulence is the ability to disperse and mix particles and heat. This process is rather complicated even under idealized conditions of homogeneous and isotropic turbulence and is after many years of research still far from being understood in general. Covering a variety of important areas from the diffusion of pollutants in environmental flows to the particle and heat diffusion in magnetized plasmas this topic connects basic research with applications.

For magnetized plasmas it is agreed that the enhanced levels of cross-field transport (anomalous transport), observed in a wide variety of devices including tokamaks and stellarators is due to low-frequency, electrostatic, micro-turbulence, with the $E \times B$-drift as the dominating velocity. A good candidate to understand and explain the anomalous transport from first principles is drift-wave turbulence [1, 2, 3]. We investigate turbulence of magnetized plasmas and discuss the influence of structures on the transport.

2. Particle Dispersion...

The mean square displacement of an ensemble of particles in a velocity field $\vec{u}(\vec{x}, t)$ is given by [5]:

$$\left\langle \vec{x}^2(t) \right\rangle = 2t \left\langle u^2 \right\rangle \int_0^t \left(1 - \frac{\tau}{t} \right) R_L(\tau) d\tau \qquad (1)$$

with $\langle \vec{u}(\vec{x}(t)) \cdot \vec{u}(\vec{x}(t'), t') \rangle = R_L(t - t') \left\langle u^2 \right\rangle$. Here R_L is the normalized Lagrangian velocity correlation. For very short times the correlation is close to unity in the so-called ballistic limit:

$$\left\langle \vec{x}^2(t) \right\rangle = t^2 \left\langle u^2 \right\rangle . \qquad (2)$$

For very long times the integral evaluates to the Lagrangian integral τ_l

$$\int_0^t R_L(\tau) d\tau \approx \int_0^\infty R_L(\tau) d\tau =: \tau_L . \qquad (3)$$

and provided that τ_l is finite we obtain

$$\left\langle \vec{x}^2(t) \right\rangle = 2t\tau_L \left\langle u^2 \right\rangle = 2\tau_L D \qquad (4)$$

This limit $(t \gg \tau_L)$ is often called the diffusion limit. Note that τ_L differs from the Eulerian correlation time available to laboratory measurements. For homogeneous, isotropic turbulence and times longer than the Lagrangian correlation time the particle diffusion will thus be normal. However, there might be large intermediate ranges depending on the correlation times and scales, especially if the correlations reach the spatial or temporal extend of the system.

3. ... and Transport

The question if test particle transport is connected to the turbulent radial transport of plasma

$$\Gamma = \langle n v_r \rangle$$

by the $E \times B$ velocity ($v_r = -\partial_y \phi$) is far from trivial. We consider the Hasegawa-Wakatani equations (HWE) [4] as minimal model for drift-wave type plasma turbulence:

$$\partial_t n + \partial_y \phi + \{\phi, n\} = -C (n - \phi) + \mu \nabla^2 n , \quad (5)$$

$$\partial_t \nabla^2 \phi + \{\phi, \nabla^2 \phi\} = -C (n - \phi) + \mu \nabla^4 \phi \quad (6)$$

The deviation from adiabaticity, given by the parameter $1/C$, leads to an instability. The HWE Eqs. (5, 6) contain two limits: i) $C \to 0$, where the density and potential decouples, thus the system describes standard 2D Navier-Stokes turbulence with n passively advected. ii) $C \to \infty$, which corresponds to the adiabatic density response $\phi \approx n$ and the HWE reduce to the Hasegawa-Mima equation (HME).

The evolution of the energy $E \equiv \frac{1}{2} \int ((\nabla \phi)^2 + n^2) dV$ and generalized enstrophy $W \equiv \frac{1}{2} \int (\omega - n)^2 dV$ is governed by

$$d_t E = \int -n\partial_y \varphi - C (n - \phi)^2 - \mu(\omega^2 + (\nabla n)^2) d^2 r , (7)$$

$$d_t W = \int -n\partial_y \phi - \mu(\nabla(n - \omega))^2 d^2 r . \qquad (8)$$

Here $\omega = \nabla \times \mathbf{v} = \nabla^2 \varphi$ is the vorticity. The driving term is the integrated $E \times B$-flux

$$\Gamma_0 = \int \Gamma d^2 r = \int n u \varphi d^2 r = \int -n\partial_y \varphi d^2 r,$$

which mediates the instability when $n \neq \phi$. In the inviscid limit the HWE has a Lagrangian conserved quantity $\Pi = (\omega - n + x)$. We employ the conservation of Π to estimate the radial dispersion of the fluid elements. From $x - x_0 = -(\xi - \xi_0)$, where $\xi = \omega - n$. We obtain:

$$\langle (x - x_0)^2 \rangle_p = \langle \xi^2 \rangle_p + \langle \xi_0^2 \rangle_p - 2\langle \xi_0 \xi \rangle_p, \qquad (9)$$
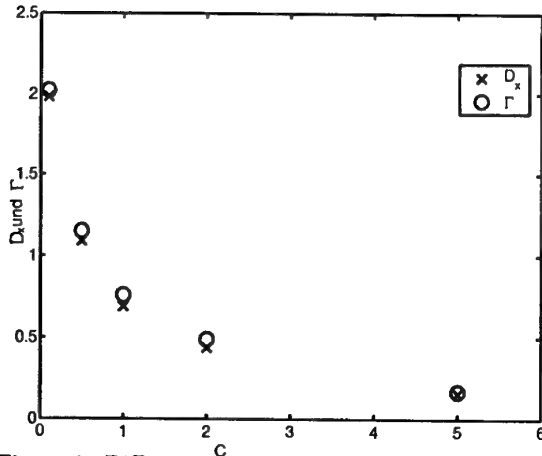
Figure 1: Diffusion coefficient and Flux for various values of C.

where the average $\langle \cdot \rangle_p$ is taken over all fluid elements/particles. If the turbulence is homogeneous, we can replace the averaging over the fluid elements with averaging over the fields ($\langle \cdot \rangle_p = \langle \cdot \rangle_f$). In the time asymptotic limit we may then assume that the last term on the rhs vanishes (this designates the correlation between the fluid PV and the initial fluid PV). Taking the time derivative and using Eq. (8) we obtain:

$$d_t \langle (x - x_0)^2 \rangle_p = d_t \langle \xi^2 \rangle_f = 2 d_t W. \tag{10}$$

Finally we arrive at

$$D_x = \Gamma_0 , \tag{11}$$

what is confirmed by numerical experiment see Figure 1.

4. Transport PDF

In models where the fluctuations are driven by a local instability and the density fluctuation-level is small compared to the background density the probability distribution function (PDF) of as well density and radial velocity is given by a normal distribution.

When evaluating for the PDF of Γ we note that the folding of two normal distributions is not a normal distribution. Moreover if n and ϕ are correlated the average of the PDF may become non-zero and lead to a net transport.

If the transport PDF is evaluated not for the local values of the transport, but averaged over some domain, the transport PDF has to converge to a stable distribution. If the second order moment is finite, the central limit theorem tells us that this is a normal distribution. If the second order moment does not exist, than we have a Levy-Pareto stable PDF and thus expect a power law tail in the PDF, as long as all the averaging procedures are carried out for times/lengths well below the correlation length/time-scales. A power law tail in the PDF of

the averaged flux reflects thus the existence of long range correlations in the system, respectively that the turbulence is intermittent. Correlations that can manifest themselves via the occurrence of coherent structures within the turbulence.

5. Turbulence and Structures: The quest for correlations

Two dimensional turbulence, as the turbulence of magnetized plasmas, is characterized by a dual cascade: of enstrophy to the small scales and energy to large scales. Moreover if the vorticity is a function of the potential, then the convective non-linearity vanishes and thus turbulent de-correlation mechanisms are no longer very effective. The regions of reduced nonlinearity and correlated potential and vorticity are also known as coherent structures. These structures form out of the turbulence and can survive for long times compared to the turbulence de-correlation time. Tracking particles in the turbulence and stating if they are trapped inside structures we could find that this introduces an intermediate regime for the transport [6].

6. Turbulent Equipartition

Usually turbulence takes place in an confined vessel with boundary conditions and the plasma is continuously driven. The arguments used above are then no longer valid. Indeed based on the conservation of Lagrangian invariants we could show, that the turbulence sets up characteristic gradients, independently of the magnitude of the flux generated. Clearly this breaks Fick's law. Moreover it leads to a bursty type of transport, where plasma is pushed outwards in large structures [7].

7. Summary

It is found that as long as the spatial/temporal extend of the plasma is close to correlation times/length scales the turbulent structures induce a power law tail in the PDF of the transport. This transport is then not described by Fick's law on diffusion and turbulent profiles might be sustained at various levels of flux through the system.

8. References

[1] B.D. Scott, Plasma Phys. Contr. Fusion, **39**, 1635 (1997).

[2] B.D. Scott, Phys. Plasma, **7**, 1845 (2000).

[3] V. Naulin, New J. Phys. **4** , 28 (2002).

[4] A. Hasegawa and M. Wakatani, Phys. Rev. Lett. **50**, 682 (1983).

[5] H. Tennekes and J.L. Lumley, *A first course in turbulence*, MIT Press, Cambridge, MA (1972).

[6] V. Naulin, A.H. Nielsen, and J. Juul Rasmussen, Phys. Plasmas **6**, 4575 (1999).

[7] V. Naulin, J. Nycander, and J. Juul Rasmussen, Phys. Plasmas to appear April 2003.

Turbulence and anomalous transport in magnetized plasmas: hints from the Reversed Field Pinch configuration

V. Antoni[a,b], M. Spolaore[a], N. Vianello[a],
R. Cavazzana[a], E. Martines[a], G. Regnoli[a,b], G. Serianni[a], E. Spada[a]
[a] Consorzio RFX, Associazione Euratom-ENEA sulla Fusione, corso Stati Uniti 4, Padova, Italy
[b] INFM, Unità di Padova, Sez.A, Italy

H. Bergsåker, J. Drake
Alfvèn Laboratory, Royal Institut of Technology, Association EURATOM/NFR,10044 Stockholm,
Sweden

V. Carbone
Dipartimento di Fisica, Università degli Studi della Calabria- 87036 Rende (CS), Italy
INFM, Unità di Cosenza - 87036 Arcavacata di Rende (CS), Italy

Coherent structures are observed to emerge from turbulence background in the edge region of plasmas confined in Reversed Field Pinch configurations. These structures have features reminiscent of single vortices in ordinary fluids and their versus of rotation depends on the local shear of the plasma mean velocity.

Plasma fluctuations are commonly recognised as the leading mechanisms ruling particle and energy transport in magnetically confined plasmas for thermonuclear fusion research [1]. This enhanced transport is commonly referred as 'anomalous' transport as it is much larger than the classical one due to collisions. Fluctuations contributing to the transport span a finite range of frequencies usually comprised between the ion cyclotron frequency and frequencies close to those of magnetohydrodynamic (MHD) activity. The time behaviour reveals that both electrostatic and magnetic fluctuations exhibit bursts in a wide range of frequencies including those relevant for transport and this feature seems independent of the specific magnetic configuration, as it is observed in tokamaks [2, 3], stellarators [4] and Reversed Field Pinch (RFP) experiments [5]. An extensive study of the features of these bursts has been carried out in the edge region of RFP experiments RFX and EXTRAP-T2R. In this region it has been found that most of the particle transport is carried by electrostatic fluctuations. It results that the range of fluctuations time scale contributing to the transport are respectively from 5 to 50 μs in RFX and from 2.5 to 20 μs in T2R, while the corresponding toroidal wave length ranges from 0.15 m to 1 m in RFX and from 0.06 m to to 0.6 m in T2R. The statistical analysis of the Probability Distribution Function (PDF) of fluctuations has shown that these bursts belong to the tail of the distribution and that the PDF's tend to develop non gaussian tails at the smaller time scales. These statistical features allowed the bursts to be classified as 'intermittent' events according to the fluid turbulence theory [6].

In both experiments, intermittency was observed in primary electrostatic quantities, such as floating potential and electron density, as well as in derived quantities, like the electrostatic particle flux [5,7]. A study of the bursts observed in the electrostatic particle flux, [5]; has evidenced that these events, although representing a small fraction of the signal, carry a large fraction of the particle flux losses up to 50%. The investigation of their time behaviour has shown that they tend to cluster during magnetic relaxation processes which cyclically takes place in a RFP [8]. This property has lead to the interpretation that they are the effect of some non linear coupling of the internal resonant MHD modes [7]. Sorting out the intermittent events from the turbulent background has allowed the reconstruction of the spatial structure associated to these bursts, to be carried out using different arrays of Langmuir probes inserted in the edge region of the two experiments. In this contribution a review of the salient properties of these structures is presented.

RFX and EXTRAP-T2R experiments are both toroidal devices with aspect ratio R/a = 2m/0.5m and R/a = 1.2m/0.183m respectively. More detailds on the experiments can be recovered from references [9,10]. The results presented refer to data collected in low current discharges, 300 kA and 80 kA respectively, to allow the insertion of the probes. The average electron density was about $1.5 \ 10^{19} m^{-3}$ in RFX and $1 \ 10^{19} m^{-3}$ in T2R. The statistical analysis was performed taking into account the most significant time scales for the electrostatic flux, which are peaked around 10 μs and 5 μs respectively for the two experiments.
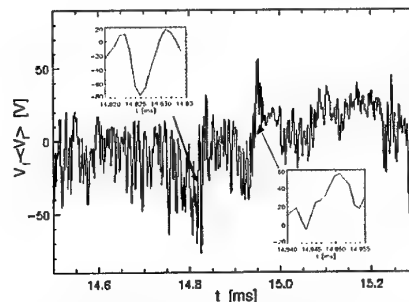
Fig.1 Floating potential fluctuations vs time, the small frames show an expansion of a negative and a positive intermittent event respectively.

Measurements were performed with 1 MHz sampling rate for RFX data and 3 MHz for T2R data; the maximum bandwidth was 400 kHz in both cases

due to the electronic conditioning of signals. In fig.1 is shown a floating potential signal with the characteristics bursts. An expansion of positive and negative bursts is also shown. The bursts correspond to intermittent events identified with the above mentioned technique.

Time correlation indicate that 'frozen turbulence' hypothesis [6] can be applied, so that the bi-dimensional structure can be reconstructed from a radial array of probes and assuming the structure flowing through the probe by a velocity equal to the local electric drift flow. Since in a RFP the magnetic field in the outer region is mainly poloidal and a radial electric field is commonly observed to set up directed inward, the drift velocity is in the toroidal direction with versus opposite to that of the toroidal current.

An example of the radial structure of floating potential for positive and negative intermittent events is shown as a function of time in figure 2. The radial-toroidal structures for the two classes of events are also shown in fig. 2: the corresponding electric field can be deduced and the E×B velocity pattern is derived. In the same fig. 2 the resulting drift velocity is overlaid. The intermittent events are found to correspond to single vortex structures rotating in different versus depending on the sign of the the peak of the floating potential. In RFX the toroidal extension of these structures results in the range 10÷15 cm while their average radial extent, obtained by a weighted averaging, results $3 \div 4$ cm, almost independent of the radial position where the centre of the structure lies. The versus of rotation of the vortices has been found to be strongly dependent on the local mean E×B velocity shear [11].
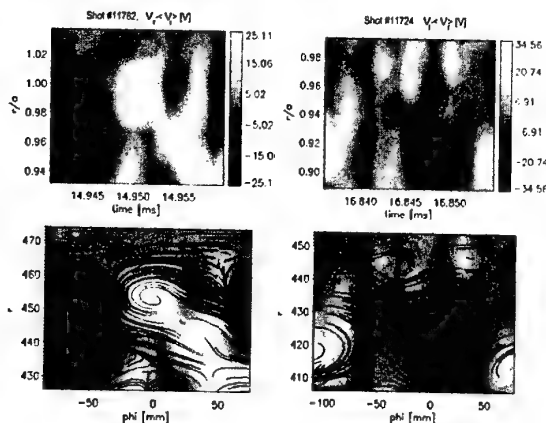
Fig.2 Upper part: radial structure vs time of positive (left) and negative (rigth) floating potential events. Bottom part: deduced radial-toroidal structure for the two classes, the vector plots represent the calculated E×B velocity patterns, data from RFX.

Figure 3 shows the relative fraction of negative and positive peaks vs normalised radial position r/a obtained in the edge of T2R. It can be observed that in the region r/a<1 negative peaks are the majority while the opposite occurs in the outermost region.

In the same figure the radial profile of the mean ExB velocity is also shown. A correlation has been deduced

between the two mentioned regions and the sign of the shear $dv_{E×B}/dr$. A similar correlation has been observed also in RFX. The relative abundance of vortices with a preferred rotation direction, has suggested that they survives longer when the condition $\omega \cdot \nabla \times \overline{V} > 0$ applies, where $\overline{V}$ is the mean flow velocity, i. e. $v_{E×B}$ in our approximation, and $\omega=\nabla \times \delta v$ represents the structure vorticity with δv the fluctuating part of flow velocity[11]. The result has a remarkable analogy with vortex dynamics in ordinary sheared fluids and in non neutral plasmas [11]. In particular it has been shown that vortices with versus 'adverse' to the mean vorticity, i.e. with $\omega \cdot \nabla \times \overline{V} < 0$, are fragmented and eventually expelled from the region with unfavourable shear, therefore shortening their average life-time. This result confirms the role of the E×B velocity shear in turbulence regulation as it affects not only the background turbulence but also the emerging structures.

In conclusion intermittent events which emerge from turbulent background as bursts of activity have features reminiscent of single vortices observed in ordinary fluids. These vortices have preferred versus of rotation depending on the local mean E×B shear.
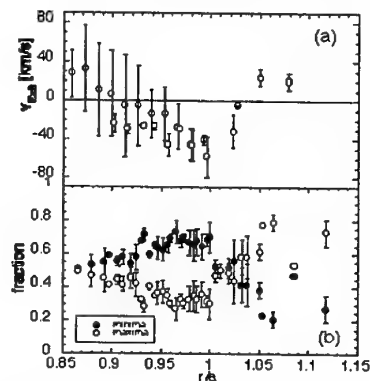
Fig.3 Radial profile of $v_{E×B}$ measured in the edge of EXTRAP-T2R experiment (a), relative fraction of positive and negative events in the same region (b).

[1] B. A. Carreras, IEEE Trans. Plasma Science **25** (1995) 1281
[2] R. Jha *et al.*, Phys. Rev. Lett, **69** (1992) 1375
[3] J. A Boedo *et al.*, Phys. Plasmas, 8 (2001) 4826
[4] O. Grulke *et al.*, Phys. Plasmas, **8** (2001) 5171
[5] V. Antoni *et al.*, Phys. Rev. Lett., **87** (2001) 045001 1-4
[6] U. Frish, *Turbulence the Legacy of A. N. Kolmogorov*, Cambridge University Press, Cambridge, 1995, p. 58.
[7] N. Vianello *et al.* Plasma Phys. Control. Fusion **44** (2002) 2513
[8] V. Antoni et al., Europhys. Lett., **54** (2001), 51
[9] G. Rostagni, Fus. Eng. Design, **25** (1995) 301.
[10] P. R. Brunsell *et al.* Plasma Phys. Control. Fusion **43** (2001) 1457
[11] M. Spolaore *et al.*, Phys. Plasmas **9** (2002) 4110

Experimental Studies of MHD Dynamics in a RFP Magnetically Confined Plasma

J. R. Drake, J.-A. Malmberg and the EXTRAP T2R Team

Division of Fusion Plasma Physics, EURATOM / VR Fusion Association

Alfvén Laboratory, Royal Institute of Technology KTH, SE 100 44 Stockholm.

Studies of non-linear dynamics of MHD modes in the EXTRAP T2R reversed-field pinch experiment have demonstrated such phenomena as mode rotation, phase-locking and wall locking.

1. Introduction

The reversed field pinch (RFP) is a magnetic fusion device. It is similar to the Tokamak in that it is a toroidal configuration. However a significant difference between the RFP and the Tokamak is that for an RFP the toroidal magnetic field, B_ϕ, and the poloidal magnetic field, B_θ are about equal in magnitude whereas for the Tokamak, B_θ is much stronger than B_ϕ. In the RFP equilibrium, the toroidal magnetic field is maximum on the minor axis of the torus and decreases with increasing radius. At the plasma edge, the toroidal field is reversed relative to the field on axis. Clearly B_ϕ, and B_θ vary strongly over the minor cross-section of the reversed-field pinch.

Tearing mode instability is a common phenomenon in magnetised plasmas. In the RFP configuration, the tearing modes exhibit very complex (and very interesting) dynamics. Indeed the non-ideal tearing mode fluctuations produce electric fields in a non-linear dynamo action. This well-known "RFP dynamo" sustains a part of the plasma current and is therefore important for sustaining the characteristic RFP equilibrium. The process that establishes the RFP equilibrium is called relaxation. The dynamic behaviour, described by Taylor [1], is based on the general principle that the plasma tends to relax toward a state of minimum magnetic energy. Magnetic reconnection (tearing modes), leading to a redistribution of helicity, characterises the relaxation.

The MHD modes in an RFP are characterised by a toroidal mode number n and a poloidal mode number m. The tearing modes are resonant with the magnetic field when $\mathbf{k} \cdot \mathbf{B} = 0$ where $\mathbf{k}$ is the wave vector of the mode and $\mathbf{B}$ is the equilibrium field. This resonance occurs on rational flux surfaces where the field winding number, $q = rB_\phi/RB_\theta$ has the value $q = m/n$. Since the fields vary strongly over the cross-section, there are potentially a large number of resonant modes in the RFP.

2. Experimental observations

A variety of MHD modes are predicted by theory and are indeed seen in experiments. Studies of tearing mode dynamics have been made in the EXTRAP T2R RFP located at the Alfvén Laboratory. The device is a medium-sized RFP with an aspect ratio R/a = 1.24 m /

0.18 m [2]. A unique feature of the device is that the conducting boundary, or shell, has a magnetic penetration time of about 6 ms, which is shorter than the pulse duration (20 ms) but much longer than the typical tearing mode growth rates. The RFP configuration is dependent on a conducting wall for MHD stability. The device is therefore suitable for the study of the effects of a non-ideal boundary on both ideal MHD modes and tearing modes.

For tearing modes, there is good agreement between linear MHD stability theory and the observed existence of the modes. The perturbations associated with the observed modes are $m=1$ (resonant on flux surfaces where $1/n = rB_\phi/RB_\theta$) and $m=0$ (resonant at the reversal surface where $B_\phi = 0$). The qualitative picture is that the tearing modes form magnetic islands lying on nested (resonant) toroidal flux surfaces.

The existence of the perturbations is predicted by linear theory but the dynamics of the modes that are experimentally observed is of course generally non-linear. Therefore the RFP is a very good device for the study of non-linear MHD mode phenomena. Examples of phenomena that have been experimentally studied in the EXTRAP T2R device are as follows [3]:

- Spectra of saturated mode amplitudes.

- Phase alignment (locking) of several modes to form a localised perturbation in the flux surfaces.

- Toroidal rotation of the modes due to viscous drag on the islands produced by the flowing plasma fluid, either in a phase-locked formation or with velocities independent of each other.

- Wall locking of the modes due to electromagnetic braking forces on the modes caused by stationary fields from currents in the boundary structure.

Saturated modes form magnetic islands that are immersed in the plasma. In Fig. 1 the power spectrum for $m = 1$ modes is shown as a function of the toroidal mode number n. The spectrum is derived from measurements of the magnetic perturbations made using arrays of pick-up coils placed at the plasma edge. Each mode is a Fourier harmonic of the total perturbation. The dominant n-numbers are in good agreement with the predicted values of n for the equilibrium magnetic field profiles. The amplitude of a

mode perturbation is typically about 1% of the equilibrium field.

Three or more modes can interact with each other and become phase-locked thus producing a localised flux surface perturbation at the point where the phases are aligned. The inter-mode electromagnetic forces between the different modes cause the phase-locking. This phase-aligned state often appears spontaneously and is quite robust. Indeed the phase-aligned configuration is frequently observed to rotate in the rest frame of the torus in a direction determined by the global toroidal flow of the plasma fluid.
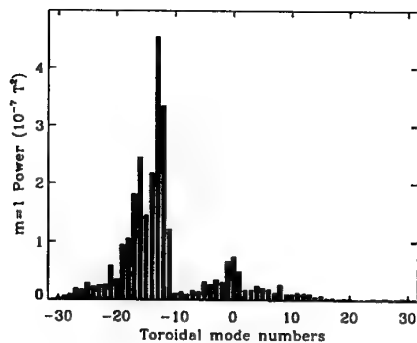
Fig. 1 Power spectrum of m = 1 tearing modes.

The degree of phase alignment can be quantitatively represented by a quantity called σ, which is the sine of the phase difference between two modes summed over a collection of at least three modes. If the phases are aligned, the sine of the phase difference between two modes is zero at that toroidal position. Three or more modes must be involved for the alignment to be non-trivial. The phase alignment is visualised by examining the inverse of this sum and a plot of $1/\sigma$ versus toroidal position and time is shown in Fig. 2.
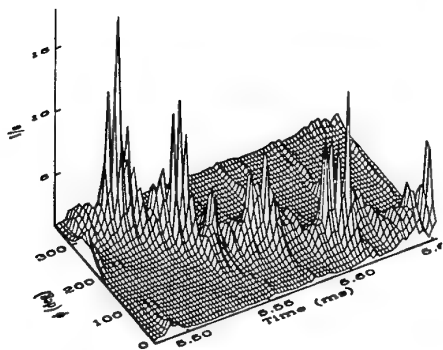
Fig. 2. The signature of phase-alignment, $1/\sigma$, as a function of toroidal position, ϕ, and time.

In Fig. 2 it can be seen that the phase aligned structure makes a complete toroidal revolution in about 150 μs, which corresponds to a velocity of about 50 km/s. This velocity is comparable to the $E \times B$ drift velocity of the plasma fluid in the toroidal direction.

The dynamics of a mode is affected both by viscous forces due to plasma flow relative to the island and electromagnetic forces between the mode and other modes or between the mode and externally produced fields. For example, image currents in the in the close-fitting conducting boundary surrounding the toroidal pinch interact with the rotating perturbations causing a drag which slows down the rotation. Also, non-axisymmetric magnetic field errors due to ports or gaps in the conducting boundary produce electromagnetic forces on the modes that lead to wall-locking, which is a form of phase-locking to stationary features.

One extremely important phenomenon is the fact that rotation of tearing modes suppresses the radial component of the magnetic perturbation at the conducting boundary. In Fig. 3 the amplitude of the radial component of the $n = 12$ tearing mode and its helical phase velocity are shown as a function of time.
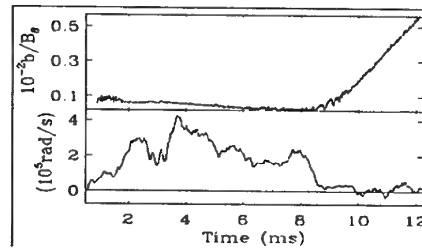
Fig. 3. Perturbation amplitude and helical phase velocity for the n = 12 tearing mode.

At about t = 8 ms, the rotation frequency goes to zero due to wall locking of this mode. The perturbation immediately starts to grow at a rate determined by the magnetic penetration time of the wall.

3. Concluding remarks

The presence of MHD activity of course negatively affects the confinement properties of the RFP experiments. The goal is to reduce the fluctuations. However the studies of the non-linear MHD dynamics that are carried out on RFP configurations contribute to the general understanding of MHD.

4. References

[1] J. B. Taylor *Reviews of Modern Physics* **58** (1986) 741.

[2] P.R. Brunsell, H. Bergsåker, M. Cecconello, J.R. Drake R.M. Gravestijn, A. Hedqvist, J.-A. Malmberg, *Plasma Phys. Control. Fusion* **43** (2001) 1457.

[3] J.-A. Malmberg and P.R. Brunsell, *Phys of Plasmas* **9** (2002) 212.

242

A New Cyclotron Maser Mechanism Observations and Theory

R. Bingham[1], A. Cairns[2], A. D. Phelps[3]

[1]Rutherford Appleton Laboratory, Chilton, Didcot, Oxon., OX11 0QX, UK
[2]University of St Andrews, Fife, Scotland, KY16 9SS
[3]University of Strathclyde, 16 Richmond Street, Glasgow G11XQ

We present a new cyclotron maser type instability driven by a crescent or horseshaped electron distribution function. Such distribution functions are easily created by an electron beam moving into a stronger magnetic field region, where conservation of the first adiabatic invariant causes an increase in their pitch angle. This produces a broad region on the distribution function where there is a +ve slope in the perpendicular component of the velocity space distribution function. Planetary dipole magnetic fields are examples of where these types of distributions can be found, giving rise for example to the earth's auroral kilometric radiation and Jupiter's decametric radiation signatures.

We examine the stability of these electron horseshoe distribution functions for right-hand extraordinary mode (R – X mode) radiation close to the electron cyclotron frequency propagating perpendicular to the magnetic field using both non-relativistic and relativistic beams. A quasi-linear theory is developed which is used to analyze the saturation process. Saturation occurs when the perpendicular slope in velocity space forms a plateau. This provides an estimate of the efficiency of such a process. Calculations suggest that efficiencies as high as 20% can be achieved. Finally, a laboratory experiment to investigate this new type of instability will be discussed.

Author Index